ISSN 2542-1565

Vol. 14 2021 No. 04

GEOGRAPHY ENVIRONMENT SUSTAINABILITY

Special Issue «PERMAFROST REGIONS IN TRANSITION»
Special Issue «GEOGRAPHY OF COVID-19 PANDEMIC: ENVIRONMENTAL ISSUES, PUBLIC HEALTH AND SOCIO-ECONOMIC CONSEQUENCES»

«The journal GEOGRAPHY, ENVIRONMENT, SUSTAINABILITY was founded in 2008 by Russian Geographical Society, the Lomonosov Moscow State University Geography Department, and the Russian Academy of Sciences Institute of Geography. Since that time the journal publishes **4 issues per year**, containing original research papers and reviews. The journal issues are open source and distributed through subscriptions, library exchanges of leading universities, and via the website through the world»

FOUNDERS OF THE JOURNAL: Russian Geographical Society, Faculty of Geography, Lomonosov Moscow State University and Institute of Geography of the Russian Academy of Sciences

The journal is published with financial support of the Russian Geographical Society.

The journal is registered in Federal service on supervision of observance of the legislation in sphere of mass communications and protection of a cultural heritage. The certificate of registration: ПИ № ФС77-67752, 2016, December 21.

PUBLISHER
Russian Geographical Society
Moscow, 109012 Russia
Novaya ploshchad, 10, korp. 2
Phone 8-800-700-18-45
E-mail: press@rgo.ru
www.rgo.ru/en

EDITORIAL OFFICE
Lomonosov Moscow State University
Moscow 119991 Russia
Leninskie Gory, 1,
Faculty of Geography, 1806a
Phone 7-495-9391552
Fax 7-495-9391552
E-mail: ges-journal@geogr.msu.ru
www.ges.rgo.ru

DESIGN
Layout designer: Tereshkin Anton
Moscow, 115088,
26 Simonovsky Val str., bldg. One
Phone: +7 (903) 108-04-44
E-mail: smile.tai@gmail.com

DOI prefix: 10.24057

Format A4 (210x297mm)

"GEOGRAPHY, ENVIRONMENT, SUSTAINABILITY" is the only original English-language journal in the field of geography and environmental sciences published in Russia. It is supposed to be an outlet from the Russian-speaking countries to Europe and an inlet from Europe to the Russian-speaking countries regarding environmental and Earth sciences, geography and sustainability. The main sections of the journal are the theory of geography and ecology, the theory of sustainable development, use of natural resources, natural resources assessment, global and regional changes of environment and climate, social-economical geography, ecological regional planning, sustainable regional development, applied aspects of geography and ecology, geoinformatics and ecological cartography, ecological problems of oil and gas sector, nature conservations, health and environment, and education for sustainable development.

OPEN ACCESS POLICY. "GEOGRAPHY, ENVIRONMENT, SUSTAINABILITY" is an open access journal. All articles are made freely available to readers immediately upon publication. Our open access policy is in accordance with the Budapest Open Access Initiative (BOAI) definition - it means that articles have free availability on the public internet, permitting any users to read, download, copy, distribute, print, search, or link to the full texts of these articles, crawl them for indexing, pass them as data to software, or use them for any other lawful purpose, without financial, legal, or technical barriers other than those inseparable from gaining access to the internet itself.

Date of publication: December 31st, 2021.

CONTENTS

EDITORIAL PAPER

PERMAFROST REGIONS IN TRANSITION: INTRODUCTION

Dmitry A. Streletskiy[1,2*], Alexey A. Maslakov[3], Irina D. Streletskaya[3], Frederick E. Nelson[4,5]
[1]Department of Geography, The George Washington University, Washington, DC, USA.
[2]Earth's Cryosphere Institute, Tyumen Scientific Centre, Siberian Branch of Russian Academy of Sciences, Tyumen, Russia.
[3]Faculty of Geography, Lomonosov Moscow State University, Leninskie Gory 1, Moscow 119991, Russia
[4]Department of Geography, Environment, and Spatial Sciences, Michigan State University, East Lansing, MI, USA
[5]Department of Earth, Environmental, and Geographical Sciences, Northern Michigan University, Marquette, MI, USA
***Corresponding author:** strelets@gwu.edu
Received: November 3rd, 2021 / Accepted: November 9th, 2021 / Published: December 31st, 2021
https://doi.org/10.24057/2071-9388-2021-081

ABSTRACT. Russian permafrost regions are unparalleled in extent, history of development, population presence, and the scale of economic activities. This special issue, «Permafrost Regions in Transition», provides a timely opportunity to (a) examine major issues associated with changing permafrost conditions in natural environments and areas of economic development; (b) present insights into new methods of permafrost investigations; and (c) describe new opportunities and risks threatening sustainable development of Arctic populations and industrial centers in Russia. The issue begins with papers focused on methods of permafrost research, followed by papers focused on examining changes in permafrost under natural conditions, and in Arctic settlements. The last two papers examine potential impacts of permafrost degradation on the Russian economy and potential health implications.

KEYWORDS: permafrost, thermokarst, climate change, infrastructure, Arctic, massive ice, permafrost landscape, petrography, radon

CITATION: Dmitry A. Streletskiy, Alexey Maslakov, Irina D. Streletskaya, Frederick E. Nelson (2021). Permafrost Regions In Transition: Introduction. Geography, Environment, Sustainability, Vol.14, No 4, p. 6-8
https://doi.org/10.24057/2071-9388-2021-081

ACKNOWLEDGEMENTS: This research was performed according to the Development program of the Interdisciplinary Scientific and Educational School of M.V.Lomonosov Moscow State University «Future Planet and Global Environmental Change»

Conflict of interests: The authors reported no potential conflict of interest.

INTRODUCTION

Russian permafrost regions are unparalleled in extent, history of development, population presence, and the scale of economic activities. This special issue, «Permafrost Regions in Transition», provides a timely opportunity to (a) examine major issues associated with changing permafrost conditions in natural environments and areas of economic development; (b) present insights into new methods of permafrost investigations; and (c) describe new opportunities and risks threatening sustainable development of Arctic populations and industrial centers in Russia. The issue begins with papers focused on methods of permafrost research by **Vasil'chuk et al. (2021), Tikhonravova et al. (2021), and Zotova (2021)**, followed by papers focused on examining changes in permafrost under natural conditions by **Tregubov et al. (2021) and Grebenets et al. (2021)**, and in the Russian Arctic settlements by **Kotov** and **Khilimonyuk (2021)** and **Kamnev et al. (2021)**. The last two papers examine potential impacts of permafrost degradation on the Russian economy **(Badina and Pankratov 2021)** and potential health implications **(Puchkov et al. 2021)**.

METHODS OF PERMAFROST RESEARCH

Geocryological conditions and the response of permafrost landscapes to changing climate and economic development depend on several factors, including permafrost extent, temperature regime, the thickness and cryogenic structure of permafrost, the depth of seasonal freezing and thawing, as well as the combination of area-specific cryogenic processes. The paper by **Zotova (2021)** reviews the main landscape indicators used in geoecological assessments and mapping of permafrost conditions, arguing that the landscape-indicator method is an effective tool, but only at large to medium geographic scales (1: 25 000–1: 100 000), as generalization of permafrost properties at smaller geographic scales hinders the real distribution of permafrost characteristics. Generally, in similar landscape conditions, the resilience of permafrost to economic development increases toward the northern and eastern parts of Russia.

Petrographic methods are commonly used in paleo reconstructions. However, ice recrystallization is a major limiting factor in arriving at correct interpretation of sedimentary environments, and significantly limits the use of petrographic methods in the determination of ground ice genesis in permafrost. **Tikhonravova et al. (2021)** examine the processes responsible for ice crystal growth and provide examples of characteristic patterns of crystal arrangements for various types of ice, including glacier ice, lake ice, segregated ice, and injection ice, among others that can be useful for determining ice genesis. The authors also discuss the formation of secondary ice structures resulting from ice recrystallization, which have to be considered in effective applications of petrographic methods.

Massive ice bodies are widespread in the coastal lowlands of the Chukotka region, yet the origin of these bodies is not well understood. Vasilchuk et al. (2021) use cryostratigraphy and stable isotopic composition methods to evaluate the genesis of ground ice collected at seven coastal exposures in the northern part of Chukotka. Depletion of isotopic composition in massive ice bodies was found with increasing climate continentality, moving from coastal locations inland. This is attributed to the corresponding depletion of precipitation, which is the major source of water for massive ice formation. The authors determined that the ice was formed underground from atmospheric precipitation, surface, and ground waters, and is not the product of buried glacier ice. More dating and pollen analysis is needed to reinforce this conclusion.

Permafrost in Natural Landscapes

Monitoring of permafrost temperature and the active layer facilitates comprehensive understanding of changing climatic conditions in cold regions. The importance of permafrost is underscored by its recognition as one of the essential climatic variables by the Global Climate Observing System of the World Meteorological Organization (Biskaborn et al. 2019). Progressive thickening of the active layer under a warming climate has the potential to involve previously frozen organic material, which may have global implications for climate, while changing permafrost at local and regional scales has detrimental impacts on ecosystems, hydrology, and vegetation (Streletskiy et al. 2021). The response of permafrost to climate forcing differs substantially between different landscape types, so considerable knowledge is required at site-specific scales, where the roles of non-climatic factors and vegetation feedbacks may modulate the atmospheric signals and the response of permafrost to them.

Grebenets et al. (2021b) provide a thorough analysis of long-term active layer thickness (ALT) and dynamics, and their relations with climate variables and micro-landscape features at a Circumpolar Active Layer Monitoring (CALM) site in a remote region of Western Taymyr, Russia (Nelson et al. 2021). One of the main results of the study is that a strong statistical relationship was not found between ALT and summer air temperature. The effects of precipitation have an important modulating effect on this relationship. The study also found evidence of shrub expansion within the 1 ha monitoring site over the 16 years of observation.

Lakes in permafrost areas are another important indicator of changing climatic conditions in the Arctic (Kravtsova and Rodionova 2016; Veremeeva et al. 2016). Tregubov et al. (2021) analyze the dynamics of thermokarst lakes in the Anadyr lowland of northeast Russia over the last 65 years. Their study reveals that under the combined influence of climate warming, active layer thickening, and thermal erosion, lake area has shrunk 24% over this period. Based on field observations and remote sensing data, the authors propose two main scenarios of lake drainage in this area. They discovered 3-12 year cycles of intensive lake drainage and formation of frost-mound bogs within drained lake basins. The authors were also able to distinguish cases of lake drainage having ameliorative effects through both natural and anthropogenic causes.

Permafrost in Arctic settlements

Permafrost degradation is commonly execrated in areas of human presence and economic activities, and may negatively impact the sustainable development of the regions. Indigenous communities practicing subsistence lifestyles have first-hand experience with the direct impacts of permafrost degradation on food security, water quality, infrastructure stability, and thermal erosion. The majority of the population in the Russian permafrost regions is, however, concentrated in large industrial settlements, many of which have a substantial number of thaw-related deformations of building and structures (Grebenets et al. 2012).

Vorkuta is one of the largest settlements built on permafrost. Due to the complexity of its geological environment, its long history of development, and the diversity of construction techniques employed there, Vorkuta presents an unparalleled opportunity to examine various principles of construction used historically in permafrost regions (Shiklomanov et al. 2020). Using a combination of archival materials and field surveys, Kotov and Khilimonyuk (2021) assess the housing stock in the city and outline the major reasons responsible for infrastructure failure, including lack of proper attention to geocryological conditions, lack of high-quality construction materials, improper operation of building crawl spaces, limited ventilation, and inadequate water drainage, among others. An important conclusion from this study is that structures built using passive methods of construction on permafrost (also known as Principle I) are most vulnerable to climate warming.

Permafrost monitoring in areas of concentrated human activities is essential to support sustainable development of the Arctic regions, yet many settlements built on permafrost lack reliable and up-to-date data on changes in permafrost temperature under buildings and other infrastructure that can be used to assist geotechnical evaluations and prevent deformation within the built environment. Kamnev et al. (2021) provide methodological approaches and discuss preliminary results from the establishment of a program of permafrost temperature monitoring under a residential building in Salekhard, Russia. Preliminary results from this combined program of automated temperature monitoring in boreholes and computer modeling indicate that this is a promising approach that provides improved reliability and safety to residential buildings on permafrost, and can be implemented widely in settlements built on permafrost.

Permafrost impacts on economy and health

Permafrost degradation under projected climate warming can have severe economic consequences in terms of direct damage to infrastructure, as well as indirect costs associated with maintenance, insurance, salability, and mortgage availability. Better understanding of the extent and magnitude of potential risks is critically important for planning and development of adaptation strategies in the Russian Arctic regions. However, the economic forecast of permafrost-related damage is a relatively new area of research. Previous estimates (Streletskiy et al. 2019; Melnikov et al. 2021) relied on governmentally available statistics on regional values of fixed assets on permafrost in relation to population distribution at municipal levels.

Badina and Pankratov (2021) argue that using economic data directly from the enterprises operated in permafrost regions may significantly improve the evaluation of costs associated with permafrost degradation. This is because population distribution in the Arctic does not always correspond with fixed asset allocations, such as buildings and structures. The authors compiled a database on more than thirteen thousand enterprises operating in the Arctic regions and estimated the market value of buildings and structures based on the average share values of those assets in the total structure of fixed assets, by economic sector. The total value of fixed assets in the Arctic Zone of the Russian Federation's (AZRF) Asian sector was 14.8 trillion rubles with 10.7 in buildings and structures. The authors, in collaboration with permafrost scientists, plan to overlay this information with regions where permafrost degradation is projected to have the highest risks.

Permafrost regions are known for having large quantities of materials that may have health implications, such as mercury, as well as byproducts of mining, petroleum development, and solid waste (Grebenets et al. 2021a; Schaefer et al. 2020). **Puchkov et al. (2021)** present a compelling review focused on yet another potential hazard associated with permafrost degradation – release of radon that may have detrimental impacts on the health and well-being of communities and industrial centers on permafrost. The authors outline major areas where permafrost degradation and a large presence of radionuclides in the environment may result in elevated radon concentrations. They call for development of radon monitoring programs and legislation focused on mitigating potential threats from release of radon to improve public health and safety in regions on permafrost.

CONCLUSION

Historically, permafrost has played a very important role in the advancement of Russian science and engineering. Under rapidly changing climatic conditions and in areas of economic development, international attention should be focused on Russia's regions on permafrost in transition by virtue of the degree of development and extent of infrastructure on permafrost, as well as the accomplishments of Russian scientists and engineers engaged in permafrost research and applied work. Unfortunately, much of the research on this topic is not readily available to non-Russian speaking audiences. We hope that the papers in this special issue of Geography, Environment, Sustainability will narrow this gap and provide a diverse readership with an opportunity to delve more deeply into the latest developments and advances of research focused on Russia's permafrost regions.

REFERENCES

Badina S.V., Pankratov A.A. (2021). The value of buildings and structures for permafrost damage prediction: the case of the Eastern Russian Arctic. Geography, Environment, Sustainability, 4(14), 83-92, DOI: 10.24057/2071-9388-2021-058.

Biskaborn B.K. et al. (2019). Permafrost is warming at a global scale. Nature communications, 10(1), 1-11, DOI: 10.1038/s41467-018-08240-4.

Grebenets V.I., Tolmanov V.A., Iurov F.D. & Groisman P.Y. (2021a). The problem of storage of solid waste in permafrost. Environmental Research Letters, 16(10), 105007, DOI: 10.1088/1748-9326/ac2375.

Grebenets V.I., Tolmanov V.A., Streletskiy D.A. (2021b). Active layer dynamics near Norilsk, Taimyr peninsula, Russia. Geography, Environment, Sustainability, 4(14), 55-66, DOI: 10.24057/2071-9388-2021-073.

Grebenets, V., Streletskiy, D., & Shiklomanov, N. (2012). Geotechnical safety issues in the cities of Polar Regions. Geography, Environment, Sustainability, 5(3), 104-119. DOI: 10.24057/2071-9388-2012-5-3-104-119.

Kamnev Ya.K., Filimonov M.Yu., Shein A.N., Vaganova N.A. (2021). Automated monitoring of the temperature under buildings with pile foundations in Salekhard. Geography, Environment, Sustainability, 4(14), 75-82, DOI: 10.24057/2071-9388-2021-021.

Kotov P.I., Khilimonyuk V.Z. (2021). Building stability on permafrost in Vorkuta, Russia. Geography, Environment, Sustainability, 4(14), 67-74, DOI: 10.24057/2071-9388-2021-043.

Kravtsova V.I., Rodionova T.V. (2016). Investigation of the dynamics in area and number of thermokarst lakes in various regions of Russian cryolithozone, using satellite images. Earth's Cryosphere, 1(20), 81-89 (In Russia with English abstract).

Melnikov V.P., Osipov V.I., Brushkov A.V. et al. (2021) Assessment of damage to residential and industrial buildings and structures during temperature changes and permafrost thawing in the Arctic zone of the Russian Federation by the middle of the XXI century, Geoecology, 1, 14-31 (in Russian).

Nelson F.E., Shiklomanov N.I. & Nyland K.E. (2021). Cool, CALM, collected: the Circumpolar Active Layer Monitoring program and network. Polar Geography, 1-12, DOI: 10.1080/1088937X.2021.1988001.

Puchkov A.V., Yakovlev E.Y., Hasson N., Sobrinho G., Tsykareva Y.V., Tyshov A.S., Lapikov P.I., Ushakova E.V. (2021). Radon hazard in permafrost conditions: current state of research. Geography, Environment, Sustainability, 4(14), 93-104, DOI: 10.24057/2071-9388-2021-037.

Schaefer K., Elshorbany Y., Jafarov E., Schuster P.F., Striegl R.G., Wickland K.P. & Sunderland E.M. (2020). Potential impacts of mercury released from thawing permafrost. Nature Communications, 11(1), 1-6, DOI: 10.1038/s41467-020-18398-5.

Shiklomanov, N., Streletskiy, D., Suter, L., Orttung, R., & Zamyatina, N. (2020). Dealing with the bust in Vorkuta, Russia. Land Use Policy, 93, 103908. DOI: 10.1016/j.landusepol.2019.03.021.

Streletskiy D. 2021. Permafrost Degradation. Snow and Ice-Related Hazards, Risks, and Disasters. In: Haeberli W. and Whiteman C. (ed.). Oxford, Elsevier, 297-322, DOI: 10.1016/B978-0-12-817129-5.00021-4.

Streletskiy D. A., Suter L. J., Shiklomanov N. I., Porfiriev B. N., & Eliseev D. O. (2019). Assessment of climate change impacts on buildings, structures and infrastructure in the Russian regions on permafrost. Environmental Research Letters, 14(2), 025003. DOI: 10.1088/1748-9326/aaf5e6.

Tikhonravova Ya. V., Rogov V. V., Slagoda E. A. (2021). Genetic identification of ground ice by petrographic method. Geography, Environment, Sustainability, 4(14), 20-32, DOI: 10.24057/2071-9388-2021-063.

Tregubov O.D., Glotov V. E., Konstantinov P. Ya., Shamov V. V. (2021). Hydrological conditions of drained lake basins of the Anadyr lowland under changing climatic conditions. Geography, Environment, Sustainability, 4(14), 41-54, DOI: 10.24057/2071-9388-2021-030.

Vasil'chuk Yu. K., Maslakov A. A., Budantseva N. A., Vasil'chuk A. C., Komova N. N. (2021). Isotope signature of the massive ice bodies on the northeast coast of Chukotka peninsula. Geography, Environment, Sustainability, 4(14), 9-19, DOI: 10.24057/2071-9388-2021-020.

Veremeeva A., Glushkova N., Günther F., Nitze I., and Grosse G. (2016). Landscapes and thermokarst lake area changes in Yedoma regions under modern climate conditions, Kolyma Lowland tundra, XI. International Conference on Permafrost, Potsdam, Germany, 20 June 2016 - 24 June 2016. DOI: 10.2312/GFZ.LIS.2016.001.

Zotova L. I. (2021). The landscape indication of permafrost conditions for geoecological assessments & mapping at various scales. Geography, Environment, Sustainability, 4(14), 33-40, DOI: 10.24057/2071-9388-2021-039.

RESEARCH PAPER

ISOTOPE SIGNATURE OF THE MASSIVE ICE BODIES ON THE NORTHEAST COAST OF CHUKOTKA PENINSULA

Yurij K. Vasil'chuk[1*], Alexey A. Maslakov[1], Nadine A. Budantseva[1], Alla C. Vasil'chuk[1], Nina N. Komova[1]
[1]Faculty of Geography, Lomonosov Moscow State University, Leninskie Gory, 119991 Moscow, Russia
***Corresponding author:** vasilch_geo@mail.ru
Received: February 25th, 2021 / Accepted: November 9th, 2021 / Published: December 31st, 2021
https://doi.org/10.24057/2071-9388-2021-020

ABSTRACT. The massive ice (MI) bodies are widespread phenomena on Chukotka coastal plains. Although they have been studying since 1930s, stable isotope method was applied for the ice beds quite recently. In this study cryostratigraphy and stable oxygen and hydrogen isotope composition of MI bodies on the extreme North-Eastern Chukotka (near Lavrentiya settlement and Koolen' lake) have been studied in detail. It was concluded that studied MI bodies have intrasedimental origin and most likely are dated back to the Late Pleistocene age. Mean $\delta^{18}O$ values range from –18.5 ‰ to –15 ‰ whereas mean $\delta^{2}H$ values range from –146‰ to –128 ‰ that is higher than expected for the Late Pleistocene ice bodies in this region, which most likely resulted from isotopic fractionation during freezing of water-saturated sediments in a closed system when forming ice became isotopically enriched compared with initial water. The analysis of co-isotope ratios for MI shows that initial water is mainly of meteoric origin (precipitation, water of lakes and taliks).

KEYWORDS: massive ice (MI), cryostratigraphy, stable isotopes, freezing conditions, North-Eastern Chukotka

CITATION: Yurij K. Vasil'chuk, Alexey A. Maslakov, Nadine A. Budantseva, Alla C. Vasil'chuk, Nina N. Komova (2021). Isotope Signature Of The Massive Ice Bodies On The Northeast Coast Of Chukotka Peninsula. Geography, Environment, Sustainability, Vol.14, No 4, p. 9=19 https://doi.org/10.24057/2071-9388-2021-020

ACKNOWLEDGMENTS: This work was supported by Russian Scientific Foundation [grant № 19-77-00045, field studies] and Russian Foundation of Basic Research [grant № 20-05-00782, methodology of the study and calculations and grant № 18-05-60272 «Arctic», isotope analysis]. The contribution of Alexey Maslakov was supported by State Assignment 121051100167-1

Conflict of interests: The authors reported no potential conflict of interest.

INTRODUCTION

Massive ice bodies represent thick, often bedded, and sometimes deformed layers of massive ground ice and icy sediment and are the most spectacular of ground-ice forms. Massive ice bodies were described in west and east Siberia, Chukotka, Alaska and Yukon, the Tuktoyaktuk Coastlands, the Canadian Arctic Archipelago and Russian Arctic islands, China and the Antarctic. These icy bodies are important not only because of their origin and the light this may throw upon permafrost history but also because of the thaw-settlement properties of terrain underlain by such bodies. There are two explanations advanced for the origin of these massive icy bodies. The first is that it is intra-sedimental and formed largely of segregated ice supplemented by water-injection processes that give rise to intrusive ice. The second is that they are bodies of buried glacier ice, without a clear distinction being made between glacier ice derived from snow and sub-glacier regelation ice (French 2018). For massive ice bodies of intra-sedimental origin the study of stable isotope composition may allow to establish the nature of initial water and the conditions of ice formation (Vasil'chuk 2012; Vasil'chuk & Murton 2016).

Massive ice bodies of different genesis are widely distributed in the Eastern Chukotka seacoast. They have been studying for over than 80 years – since 1930s in Anadyr settlement and Ugolnaya Bay vicinities (Shvetsov 1938, 1947; Soloviev 1947). In the 1950–1960s the MI bodies of Chukotka were studied by Vtyurin (1964, 1975) and Gasanov (1964, 1969) in many parts of the region: the valley of the Anadyr River, the coast of the Krest Bay, Mechigmen Gulf, the Uelen lowland, the coast of Kolyuchinskaya Bay, and in the coastal part of Nizhne-Anadyr lowland.
Isotope composition was defined for MI beds of Koolen' lake coast, Amguema and Anadyr River valleys, Anadyr vicinity, and Onemen Bay coast (Vasil'chuk 1992, 2012; Korolev 1993; Kotov 1997a, b, 1998 a, b, 1999, 2001, 2005; Vasil'chuk & Kotlyakov 2000).

Recent climate warming in the Arctic (IPCC 2013) and in Chukotka region in particular (Bulygina et al. 2020; Maslakov et al. 2020a) facilitated deeper active layer thickening (Abramov et al. 2019) and more intensive thaw slumps formation. Exposed MI beds in vicinities of Lavrentiya and Lorino settlements (Eastern Chukotka Peninsula) allowed conducting detailed cryostratigraphic and stable isotope studies in the summer seasons of 2015–2020.
The purpose of this paper is to identify the conditions for the formation of MI beds and their distribution within northeast of the Chukotka Peninsula based on field studies and stable oxygen isotope data.

MATERIAL AND METHODS

Study region

Chukotka Peninsula is the easternmost part of Siberia; it is washed by the Bering Sea from the south and southeast and by the Chukchi Sea from the north (Fig. 1).

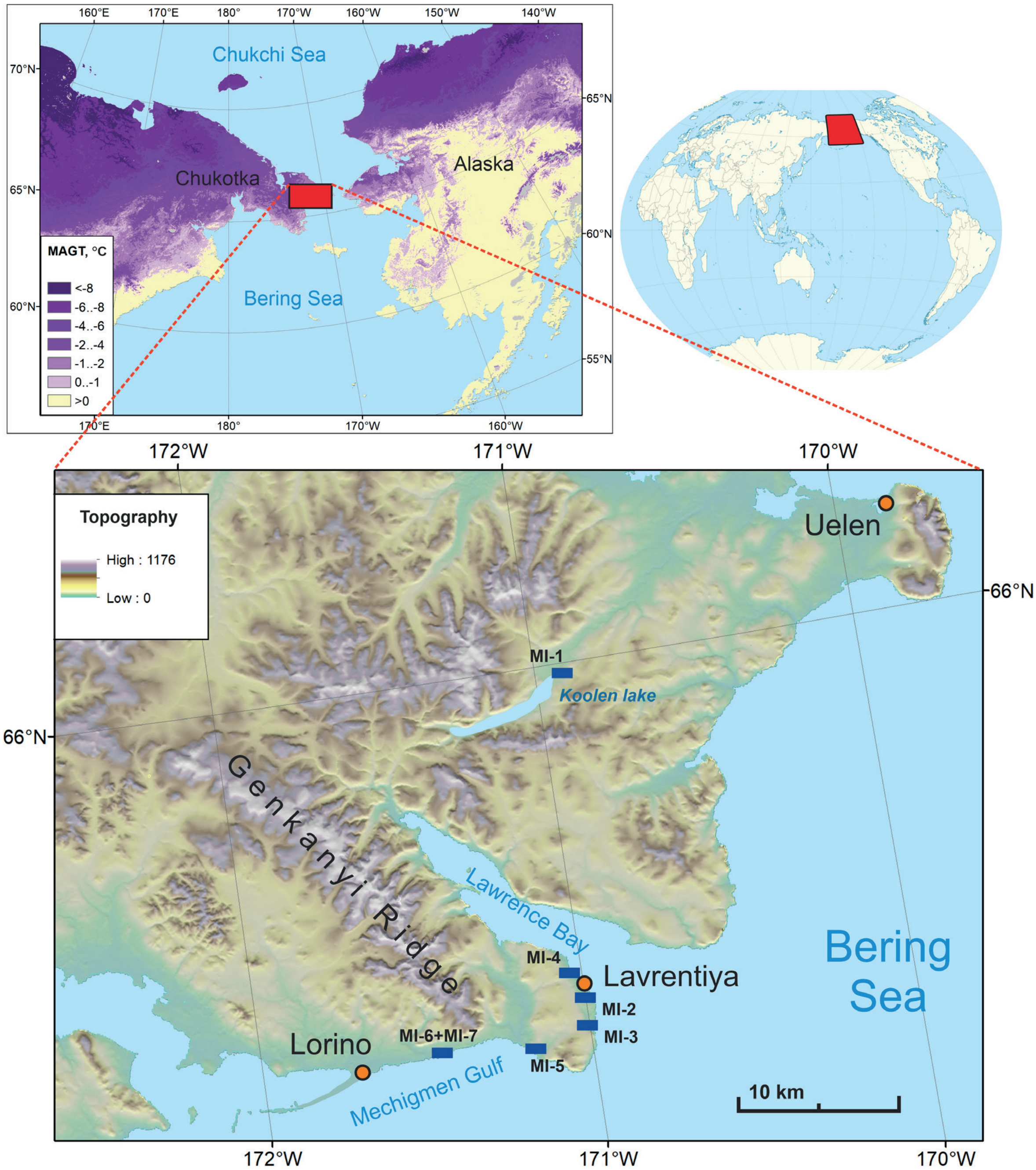

Fig. 1. Map of the study area with MI sites. Massive ice sampled for stable isotope analysis: MI-1 – Koolen' Lake valley; MI-2-7 – near the Lavrentia settlement

Approximately 80% of Chukotka Peninsula is occupied by flattened low-hill terrain of Mesozoic age with a height of up to 1200 meters above sea level (m asl). The height of plains and lowlands ranges from 10 m asl to 80 m asl; they are confined to sea coast and large lagoons. They are composed of marine and fluvial sediments of the Middle and Late Pleistocene and Holocene age.

Climate. The climate of the peninsula is arctic and maritime subarctic. Winter lasts up to 10 months a year. The average annual air temperature at the nearest weather station Uelen for 1989–2019 was –6.0 °C (Bulygina et al. 2020). Average air temperature for July is +7.1 °C (interannual variance lies within the range from +5.4 °C to +11.3 °C); for January it is –20.0 °C (interannual variance lies within the range from –13.7 °C to –26.8 °C). The area is experiencing significant climate warming: in the period 1960s–2020s mean annual air temperature increased by 0.6–0.7 °C per decade (Maslakov et al., 2020a). Interannual variance in the precipitation amount lies within the range from 300 mm to 690 mm (Bulygina et al. 2020) with the absence of the long-term trend.

Permafrost. Permafrost is continuous. Non-through taliks (up to 40 m thick) are found only in the lower reaches of large rivers and under the large thermokarst lakes. The mean annual ground temperature for the coastal plains varies from –2°C to –4°C. The permafrost thickness varies from 500–700 m in the highest parts of the ridges to 100–300 m in the valleys and coastal plains of the Chukchi Peninsula (Kolesnikov & Plakht 1989).

Massive ice bodies are widespread in Chukotka; they often confined to the coasts of the gulfs (Krest, Onemen, etc). The Late Pleistocene and Holocene ice wedges are also widespread in the region. They represent an excellent paleoarchive of the Late Quaternary winter climate changes (Vasil'chuk 2006; Opel et al. 2011).

Vegetation. At the altitudes of up to 100 m asl coastal plains of the Eastern Chukotka are covered by a typical Far Eastern hummocky tundra. The hummocks are occupied by dwarf shrubs *Salix pulchra*, *Betula exilis*, and *Ledum decumhens*. Herbaceous plants are represented by *Eriophorum vaginatum*, *Carex lugens*, *C. rariflora*, *Poa*

Arctica, etc. Humid depressions are mainly occupied by *Eriophorum vaginatum* and *Carex stans* with *Salix pulchra* (Zamolodchikov et al. 2004). The slopes of the hills at the altitudes of up to 250–300 m asl are covered by lichen and low-shrubs tundra. Hilltop surfaces are mostly barrens.

Field studies and analytical methods

Massive ice (MI) bodies exposed in floodplain and terraces at 7 sites (MI-1–7, see Fig. 1) have been studied from 1985 to 2020 (Fig. 2-7). For stable isotope analysis, ice was sampled both vertically and horizontally from the ice beds, depending on the outcrop accessibility.

Isotope oxygen in MI sampled in 1985–1987 was measured using a G-50 device in the isotope geology laboratory at the Institute of Geology, Tallinn, Estonia (Prof. R. Vaykmäe) and in the isotope hydrology laboratory at the Institute of Water Problems of Russian Academy of Science (Dr. A. Esikov). Control measurements were taken in both laboratories.

The massive beds sampled during field studies in 2015–2020 were analyzed in the stable isotope laboratory of the Geography Faculty at Lomonosov Moscow State University (Prof. Yu. Vasil'chuk and Dr. N. Budantseva) using a Finnigan Delta-V Plus mass spectrometer applying equilibration techniques. International water standards (SMOW, GRESP, and SLAP) were used for calibration. Analytical precision was ±0.4‰ for $\delta^{18}O$ and ±1‰ for $\delta^{2}H$. All values are presented in δ-notation in per mille (‰) relative to the Vienna Standard Mean Ocean Water (VSMOW).

RESULTS

Site MI-1. A homogeneous autochthonous MI body is located on the northern coast of the Koolen' lake, 2 km from the mouth of the Koolen'veem River, in a ravine that opens up to the lake at an altitude of 25 m above the lake level.

Cryostratigraphy. Thick ice layer was exposed a 0.4–0.7 m (possibly up to 1.2 m) at a depth of approximately 3 m. The body is overlain by a bedded formation of sand and peat. The sand is coarse-grained, gray-yellow, with inclusions of gravel. The peat contains remnants of grasses, mainly mosses, rarely twigs of shrubs. At an altitude of 0.1 m above the top of the formation we found a boulder with a diameter of 10 cm. Higher up in the sand and peat there are blocks of granodiorites with a diameter of 20–30 cm, which are exposed in the nearby rocky slope at an altitude of 200 m. The ice of the exposed layer is gray, with a weakly expressed vertical banding due to interlayers saturated with yellow and black sand. The ice is saturated with air bubbles ranging in size from 1 mm to 12 mm.

Oxygen isotopes. The values of $\delta^{18}O$ in the MI range from −20.6‰ to −22.4‰ (Fig. 8a) For comparison, the values of $\delta^{18}O$ in the modern seasonal injection ice mound on the floodplain of the lake Koolen' vary from −13.4‰ to −15.3‰; in the Holocene ice wedges on the floodplain of Koolen' lake the values of $\delta^{18}O$ vary from −14.7‰ to −16.2‰ (Vasil'chuk, 2012; Vasil'chuk et al., 2018a,b).

Site MI-2. Homogeneous MI body (Fig. 2) was studied in the summer season of 2017. It is located on the coast of the Lavrentiya Bay (St. Lawrence Bay), 2 km south of the Lavrentiya settlement (65°32 ' 51 "N; 171°58'24" W).

Cryostratigraphy. The MI body is exposed in a thermocirque on the seashore, at an altitude of 5 m asl. The width of the body is 18.6 m; the visible thickness is 3.1 m. It is covered with a layer of unsorted dark yellow loam with inclusions of gravel and boulders with a diameter of 10 cm. The thickness of the overlying sediments varies from 1.5 m to 3.0 m. The ice boundary is smooth and fuzzy. The body is represented by sequence of clear and bubbly ice layers and dark gray ice-rich loam with the inclusions of debris (Fig. 2b, c). The size of the ice bubbles is 0.2–0.9 cm, without orientation. The thickness of the ice layers varies from 0.5 cm to 10 cm; the thickness of the loam layers is 0.2–5.0 cm. The layers are tilted in the opposite direction from the shore at an angle of 45°.

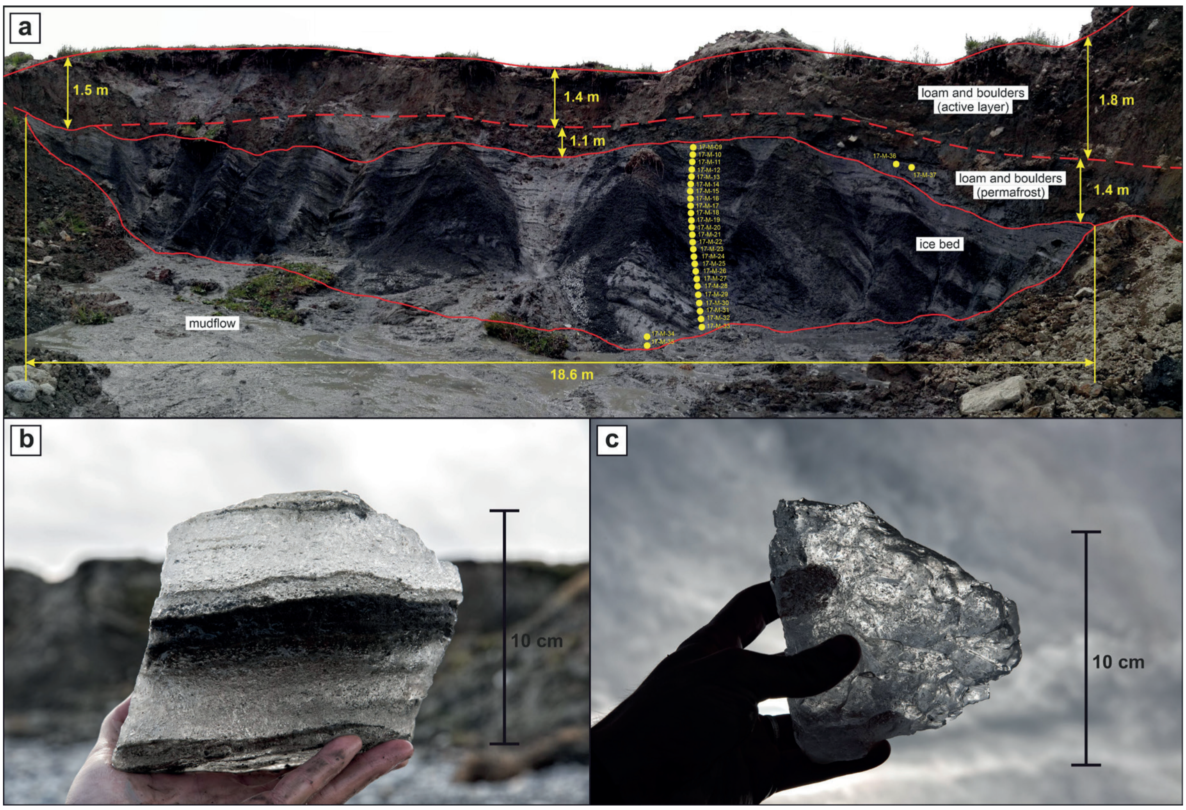

Fig. 2. Massive ice (MI-2): a) general view and sampling scheme; b) and c) detailed views of ice matter. (Photos by A. Maslakov)

Oxygen isotopes. The values of δ^{18}O in MI range from −18.96‰ to −14.84‰ (Fig. 8b). The distribution of the values δ^{18}O with the depth traces the change in the trend of isotopic values from positive in the lower part of the bed to negative in the upper one.

Site MI-3. The homogeneous the MI body studied in 2019 and 2020. It is located on the coast of the Lavrentiya Bay (St. Lawrence Bay), 7 km south of the Lavrentiya settlement (Fig. 3).

Cryostratigraphy. The vertical thickness of the body MI-3 is approximately 2.5 meters; the upper boundary is smooth, clear and discordant. The overlying sediment is 0.7–2.0 thick. It is dark grey loam, with gravel inclusions and bunches of black peat. The layer has a vertical and horizontal lenticular cryogenic structure (ice fills the cracks between the slab ground particles). The MI bed is composed of pure, dislocated layered ice. Layers with a thickness of from 0.2–0.3 cm to 20 cm are sustained with horizontal extent (see Fig. 3d). The layering is emphasized due to the interlayers of the grey loam, including 0.2–3.0 cm thick rubble. Sometimes, layering is disordered with the inclusion of slightly rolled boulders 30 cm in diameter. The boundary with overlying sediments is clear and discordant. The foot of the ice body lies beneath the mudflow.

Stable isotopes. The values of δ^{18}O in MI-3 range from −24.5‰ to −17‰ (Fig. 8b); the values of δ^{2}H range from −148.4‰ to −116.3‰. The values of δ^{18}O are distributed fairly uniformly along the depth and are close to −18‰, −17‰, while at a depth of approximately 1 m from the top (and slightly away from the main section), one sharply negative peak of the values of δ^{18}O −24.5‰ and δ^{2}H −148.4‰ was recorded.

Site MI-4. A homogeneous ice body discovered in a thermocirque 2.5 km north of the Lavrentiya settlement (Fig. 4) was studied in 2019 and 2020.

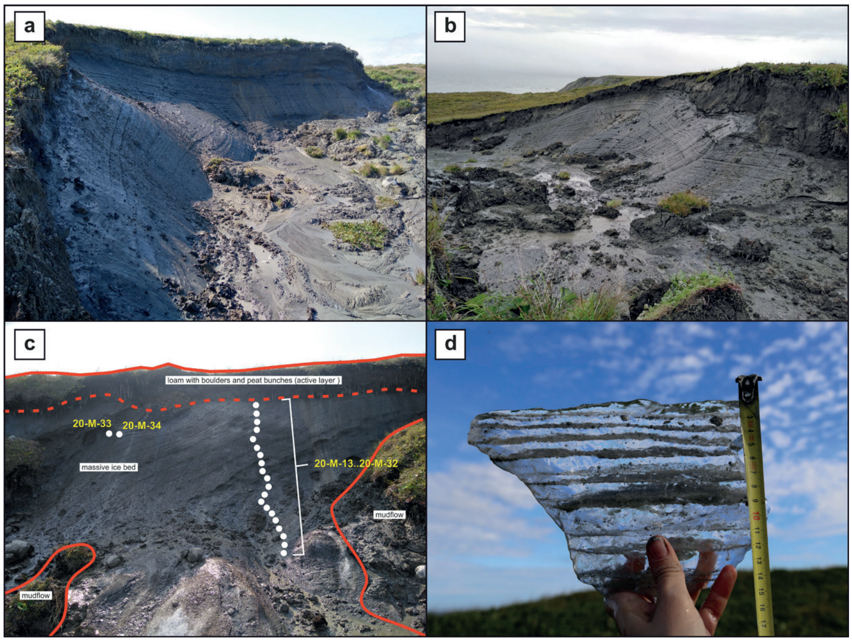

Fig. 3. Massive ice body MI-3: general view (a, b), sampling scheme in 2020 (c), and detailed view of the ice (d). (Photos by A. Maslakov)

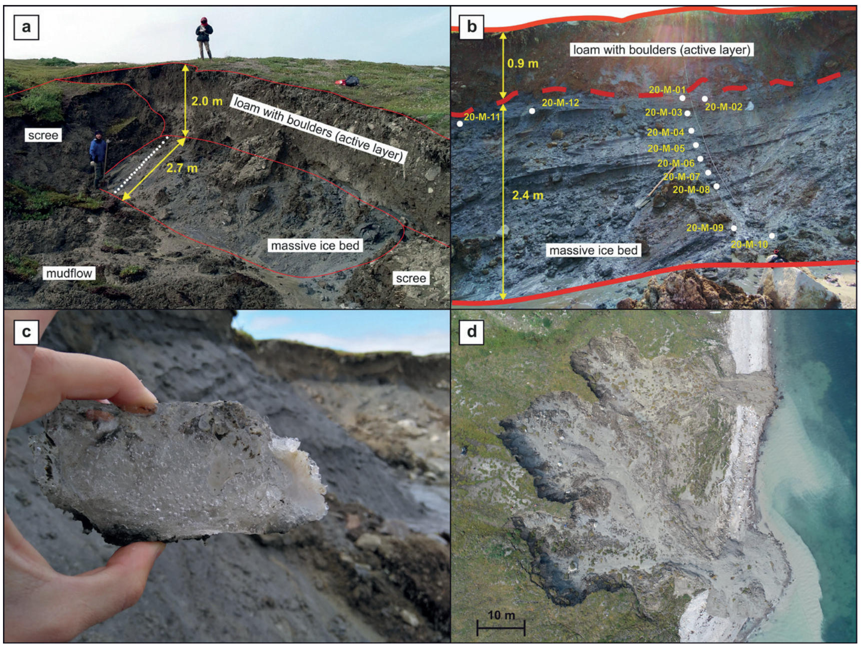

Fig. 4. Massive ice body MI-4: sampling schemes: a – 2019, b – 2020; c – detailed view of ice matter; d – aerial photo of the thermocirque from UAV. (Photos by A. Maslakov)

Cryostratigraphy. MI body is exposed in a large thermocirque (approximately 70 m wide, 45 m deep), eroding lower levels of the plain. Covering sediments are dark beige loam with the inclusion of boulders up to 1 m in diameter and bunches of black peat. Near MI top, the color of the loam changes to gray and blue-gray. The thickness of the overlying sediments is 1–2 m. The upper boundary of the body is smooth and discordant. Apparently, the overlying sediments were formed from Pleistocene loam with coarse-grained material, which was reworked after subsequent thaw slumps and armored the ice body. This is evidenced by the occurrence of black peat bunches and inclined lenses, which were buried by slump. MI body is an interlayer of clear, transparent ice (with a rare inclusion of bubbles) with gray loam, including boulders and gravel. The thickness of the ice layers varies from 2–3 cm to 20–30 cm; the thickness of the soil layers varies from 0.5 cm to 10 cm. These layers are inclined by 5–8° to the horizon line. The ice body is slightly dislocated with rare inclusions of boulders up to 20 cm in diameter, which though do not break the layering sequence.

Stable isotopes. The values of $\delta^{18}O$ in the MI-4 samples of 2019 vary from −19.02‰ to −18.16‰. The values of $\delta^{18}O$ are distributed fairly uniformly over the depth and are close to −18.5‰ (Fig. 8d). The range of values of $\delta^{18}O$ for the same body in the samples of 2020 is wider (from −21.3‰ to −16.6‰) whereas the values of $\delta^{2}H$ lie in the range from −163.9‰ to −123.9‰. More negative isotopic values are observed in the middle part of the ice layer (Fig. 8e).

Site MI-5. Heterogenic MI body was studied in 2016. It was located (65°30'28,4" N, 171°11'50,2" W) 2 km south-east from Chulkheveem (Akkani) river mouth and 1 km west from Akkani sea hunters base, on the Mechigmen Gulf coast (Fig. 5).

Cryostratigraphy. A thick and relatively extended layer of ice 45 m wide and up to 2.7 m thick was exposed in a thermocirque 25 meters from shoreline, 50 m wide with walls up to 4.5 m high. The thermocirque foot is located at an altitude of 3 m asl. The ice in the entire massif is clean and bubbly. It has a slightly dislocated layered structure. Ice layers of 10–15 cm alternated with 0.1–3.0 cm layers of grey loams. The boundary between the ice and the overlying sediments is smooth, clear, and discordant. The overlying deposits are 1.7–3.0 meters thick and represented by dark-yellow and blue-gray loam with boulder inclusions. The structure of the dark yellow loam is slab parting with traces of layering and smears of ocher loam. The blue-gray loam is confined to the base of the overlying sediment layer with a maximum thickness (2.1 m) in the central part of the outcrop; it is structureless, occasionally contains interlayers and bunches of black peat. The cryogenic structure near the contact is oblique lenticular with a lens up to 3 mm thick and up to 5 cm long. The more detailed cryostratigraphy is presented in (Vasil'chuk et al., 2018c). Apparently, the presented ice body is the remnant of the larger one exposed in the grassed thermocirque (see Fig. 5c) and buried by thawed slump deposits.

Stable isotopes. Variations of $\delta^{18}O$ and $\delta^{2}H$ values in ice samples were insignificant – $\delta^{18}O$ varied from −16.6‰ to −17.88‰; $\delta^{2}H$ varied from −123.7‰ to −135.8‰ (Fig. 8f).

Site MI-6. A homogeneous ice body was studied in 2015. It was exposed in a coastal thermocirque in an outlier of a Pleistocene 30–50 m high terrace, 8 km west of the mouth of the Chulkheveem (Akkani) river mouth (65°31'10.8" N; 171°25'04.9" W). The thermocirque base was at an altitude of approximately 5 m asl. (Fig. 6).

Cryostratigraphy. The width of the thermocirque was approximately 20 m; the width of the exposed ice body was approximately 6 m. The upper contact was clear and discordant; the foot of the body lied under the mudflow. The visible thickness of the ice was up to 4.7 m (see Fig. 6a). The overlying deposits 17 m thick are entirely represented by heavy, ice-poor loam of slab parting structure with rare inclusions of small boulders and pebbles and rare detritus of marine mollusks shells. The ice of the body is clean, with rare inclusions of bubbles and well-visible layering, which does not conform to the upper contact. The thickness of pure ice layers varies from 5 cm to 15 cm; they are interspersed with thin films (up to 5 mm) of bubbly ice, muddy ice, or grey loam (Maslakov et al. 2018).

Stable isotopes: Variations of $\delta^{18}O$ values in the body are insignificant – from −16.1‰ to −14.8 ‰ for $\delta^{18}O$ (Fig. 8g).

Site MI-7. Massive ice body on the coast of the Mechigmen Gulf is located 8.3 km west of the Chulkheveem (Akkani) river mouth, in front of the picket «23 km» of road from Lavrentiya to Lorino, 300 m west from site MI-6 (65°31'07.5" N, 171°25'29.9" W) and was studied in 2018 (Fig. 7).

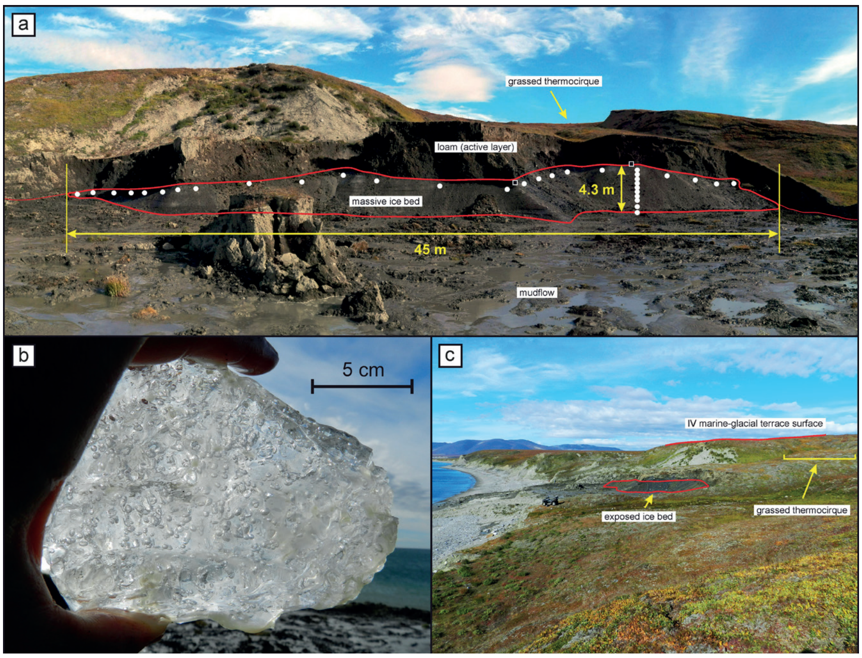

Fig. 5. Massive ice body MI-5: a) sampling scheme; b) detailed view of ice matter; c) general view from the side. (Photos by A. Maslakov)

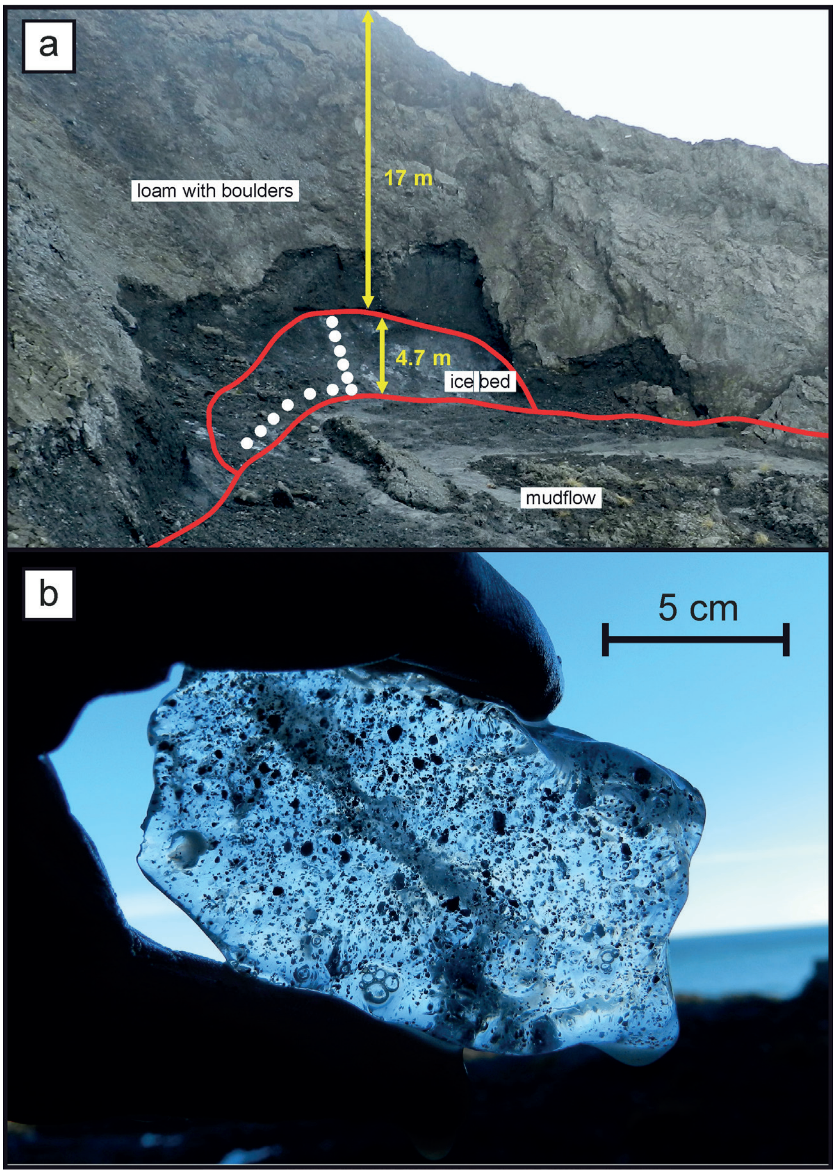

Fig. 6. Massive ice MI-6: a) sampling scheme; b) detailed view of ice matter. (Photo by A. Maslakov)

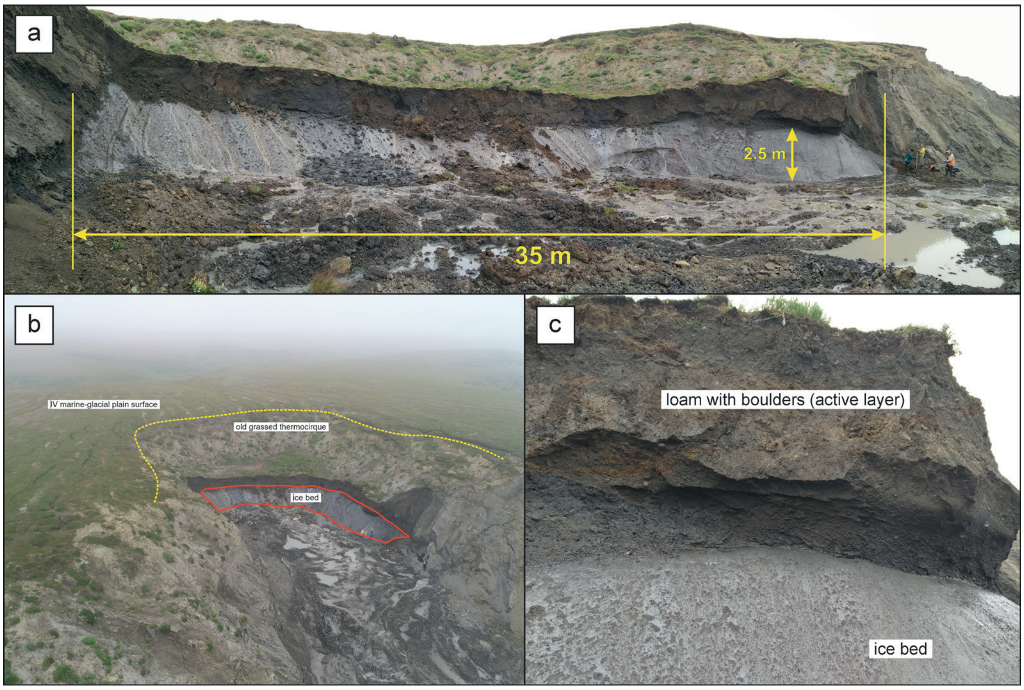

Fig. 7. Massive ice MI-7: a) and b) general view; c) the upper boundary with overlying sediments. (Photo by A. Maslakov, 2018)

Cryostratigraphy. The body was discovered in a thermocirque approximately 30 meters wide eroding IV marine terrace with surface altitudes of 40–60 m asl. The apparent thickness of the ice layer varies from 1.5 m to 3.5 m. The body top is smooth, discorded with overlying sediment's structure; the bottom of the body goes under the mudflow. The thickness of the overlying sediments in the central part of the cirque is approximately 1 m, increasing to 5–7 m at the edges. These are unsorted loams of dark beige color with inclusions of boulders and peat bunches. The ice is clear, bubbly; the bubbles do not have a strict orientation and reach 3–5 mm in diameter. Stratification in the ice can be traced only in the upper part of the deposit. Ground layers are found on the edges of the ice body; they are lying according to the top of the formation. The main part of MI is pure bubble ice, almost devoid of ground inclusions. In polarized light, ice is coarse-grained, with crystals ranging in size from 1–2 cm to 5 cm in width. Layered ice is characterized by smaller crystals (several mm wide). This thermocirque is embedded in an older one, and the exposed ice body had been forming the lower or middle part of a more massive ice body, partially degraded as a result of the formation of the previous thermocirque. The isotope analysis has not yet been performed in this body, and here it is listed as one of the best outcrops of MI in the north-east of Chukotka, studied by A. Maslakov, N. Belova, F. Romanenko, and A. Baranskaya (Maslakov et al. 2018).

DISCUSSION

Isotope composition of MI bodies of Chukotka

Although MI beds in Chukotka have been studied for more than 80 years, their isotopic study began less than 30 years ago. There are some publications devoted to isotope composition of MI near Anadyr and the coast of Onemen Bay (Vasil'chuk 1992; Kotov 2001, 2005), in the Amguema River valley (Korolev 1993; Kotov 1997a, b) and in the Tanyurer River valley (Kotov, 1998a), located in Western and Central Chukotka region.

Massive ice near the city of Anadyr. Massive ice body exposed in a quarry on a slope near the city of Anadyr was 2 m thick and was dissected by syngenetic ice wedges more than 5 m high. $\delta^{18}O$ values in MI varied from −19.6‰ to −19.7‰, while in wedge ice they varied in more wide range – from −23.4‰ to −18.6‰; in segregated ice from enclosing sand they varied from −22.7‰ to −18.6‰. Higher isotope values (from −17.3‰ to −16.4‰) were obtained for Holocene epigenetic ice wedges from the upper part of slope deposits (Vasil'chuk 1992).

Massive ice in the Amguema River valley. In the middle course of the Amguema River (130 km north of the Arctic Circle), Korolev (1993) and Kotov (1997a) studied the structure and isotope composition of MI in the exposure of the ridge. Isotope composition of MI at the depth 4–12 m is uniform; $\delta^{18}O$ values vary from −26.6‰ to −25.2‰. Isotope oxygen composition of modern snow in this area is much heavier, average $\delta^{18}O$ value is −21‰; $\delta^{18}O$ value in Holocene ice wedges and modern ice veinlets vary from −20‰ to −18‰.

In total 30 samples were analysed from these MI bodies. The range of $\delta^{18}O$ values in vertical and horizontal directions is insignificant, not more than 4‰: from −29‰ to −25‰ (mean value is −26.1‰). Isotope composition of the Late Pleistocene ice wedge is generally lighter than that of the MI: $\delta^{18}O$ values in the ice wedge range from −29.2‰ to −27.3‰ (Korolev 1993). A radiocarbon date of 20600±600 years BP (MAG-1309) obtained from a peat layer in slope sediments from a depth of 12 m indicates that the slope complex and the end-moraine ridge were formed in the Late Pleistocene (Kotov, 1997a).

Homogeneous autochthonous MI on the Onemen Bay coast. On the northern coast of the Onemen Bay, 25 km from the city of Anadyr, MI bodies were studied by Kotov (1997a,b, 2001) in two thermocircues exposed to the east of Cape Rogozhny. In the outcrop located at Cape Glubokiy, three cryogenic horizons of different ages with polygonal ice wedge structures were identified. Based on radiocarbon dates, it was determined that two lower cryogenic horizons were formed in the last stage of the Late Pleistocene (after 40 ka BP), and upper one is of Holocene age. In similar and apparently synchronous strata on the northern coast of Onemen Bay, 4 km southeast of the Cape Rogozhny outcrop, we studied ice wedges, in which $\delta^{18}O$ values vary from −27.3‰ to −23.8‰.

In one thermocircus, two layers of MI were separated by a layer of loam with coarse-grained material with a thickness of up to 8 m. The isotope-oxygen composition was studied for the four MI layers. One of them was analyzed in the Estonian Academy of Sciences: $\delta^{18}O$ values in the upper part of the ice ranged from −16.7‰ to −20.7‰. Other three layers were analyzed in the Alfred Wegener Institute for Polar and Marine Research in Potsdam: $\delta^{18}O$ values ranged from −20.64‰ to −20.03‰. Higher values (−19.78‰ to −18.99‰) were obtained in the ice layers enriched with soil.

Heterogeneous allochthonic MI in the Tanyurer River valley. In the middle and lower reaches of the Tanyurer River (in the valley of the Kuiviveyem River) A.N. Kotov traced a series of long and rather high arc-shaped ridges. The age of the outer ridge is determined on the basis of ^{14}C dates between 16.86 ka and 21.5 ka BP from plant residues from peaty sand (Kotov, 1998a). $\delta^{18}O$ values in MI range from −23.56‰ to −21.73‰; the mean value is −22.96‰. $\delta^{2}H$ values vary from −181.3‰ to −165.2‰. In the Late Pleistocene ice wedge $\delta^{18}O$ values vary from −24.9‰ to −21.3‰; $\delta^{2}H$ values vary from −191.5‰ to −165.9‰ (Kotov, 1998a).

The analysis of the obtained isotope data showed that $\delta^{18}O$ values in MI bodies in most areas of continental Chukotka vary from −29‰ to −23‰, and in the coastal areas, for example, near the city of Anadyr, they are closer to −20‰, −18‰.

Preliminary interpretation of the isotope composition of the studied massive ice bodies of the North-East Chukotka

New stable isotope data do not allow clearly establishing the age and conditions of the ice formation yet, but some conclusions can be made:

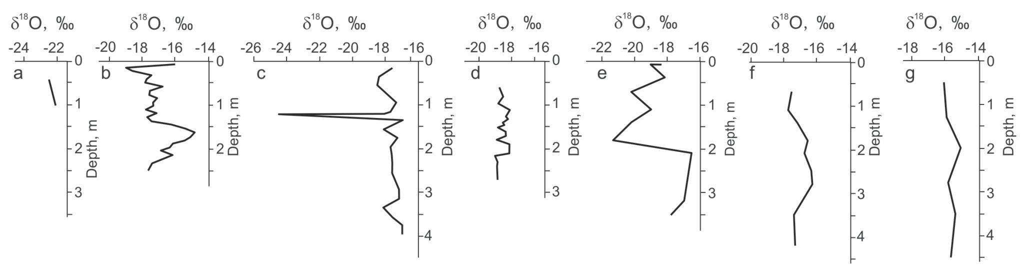

Fig. 8. Distribution of $\delta^{18}O$ values in the MI bodies of the north-eastern Chukotka by depth (the depth of the bodies roof is taken as 0 m): a – MI-1; b – MI-2; c – MI-3; d – MI-4 (2019); e – MI-4 (2020); f – MI-5; g – MI-6

1. First of all, most of the six studied MI bodies have a relatively «enriched» isotope composition, the mean $\delta^{18}O$ values vary from −15.4‰ to −18.7‰, mean $\delta^{2}H$ values vary from −128.1‰ to −145.8‰. And only MI near the Koolen' lake has mean $\delta^{18}O$ value of −21.5‰ (Table 1).

2. Two patterns of vertical isotope profiles are clearly observed for MI bodies. The first pattern is a uniform distribution of the $\delta^{18}O$ values in the range from −17‰ to −18‰; the second pattern presents significant variations of the $\delta^{18}O$ values in the range from −16‰ to −22‰. In the first case, the monotonous vertical distribution indicates a single rapid freezing of water by the congelation type. In the second case, sharp changes of isotope values reflect gradual freezing by segregation type, most likely upward and downward from the horizon, where the ice has the most positive value. In this case, more and more isotopically negative ice is formed during gradual freezing.

3. $\delta^{18}O$ values for the MI close to −17‰ and −18‰ are almost equal to the winter Holocene precipitation in this region (Vasil'chuk et al. 2018), which would seem to indicate a possible Holocene age of the ice. However, it is known that during water freezing, forming ice always became «heavier» by 2–3‰ compared to the original water due to fractionation, even at one stage of freezing. In this regard, we can suppose that $\delta^{18}O$ values of the source water are close to −20––21‰. Moreover, evaporation from water reservoirs that served as a source for MI formation, should not be excluded. Thus, it can be assumed that the initial water was characterized by $\delta^{18}O$ values in the range from −23‰ to −25‰. These values are undoubtedly more realistic for the Late Pleistocene surface waters of the Eastern Chukotka. Modern surface waters are usually isotopically enriched by 6-10‰ for the $\delta^{18}O$ values (Table 2). According to our data, the waters of rivers, streams, and lakes sampled in summer are characterized by $\delta^{18}O$ values from −9.6‰ to −14.7‰, in snowpatches $\delta^{18}O$ values vary from −10.4‰ to −18.9‰; in the ground water $\delta^{18}O$ value is −14.6‰. Our data are consistent with the data obtained by Polyak et al. (2008), who studied isotope composition of hydrotherms and surface waters of the Eastern Chukotka: according to them $\delta^{18}O$ values in surface waters vary from −11.1‰ to −16.4‰.

Slopes of the $\delta^{2}H$-$\delta^{18}O$ lines lower than eight commonly indicate the evaporation of initial water. On the co-isotope diagram (Fig. 9), the slope of the $\delta^{2}H$-$\delta^{18}O$ ratio line for MI-5 is close to 6 that may indicate evaporation of water before freezing and massive ice formation. For two MI bodies (MI-2 and MI-4, 2020) the slopes of the $\delta^{2}H$-$\delta^{18}O$ ratio lines are close to the global meteoric water line (GMWL) and are equal to 7.71 and 8.36, respectively (Fig. 9). This most likely indicates that in this case we studied lower part of a once thick MI body, where ice was formed under the equilibrium conditions of a closed system according to the Rayleigh type. This is also indicated by contrast distribution of the $\delta^{18}O$ values in these ice bodies (see Fig. 2, b, e).

For the MI-3 clustering of the isotope values does not allows to construct a regression line, moreover, for one sample the much lower value was obtained (see Fig. 8c, 9). Such negative shift (compared to the other values) most likely indicates a noticeable fractionation during ice formation when isotopically enriched ice was formed at the first stages of water freezing, and isotopically depleted ice – on the last stage of water freezing.

Table 1. Stable isotope ($\delta^{18}O$, $\delta^{2}H$ and d_{exc}) minimum, mean, and maximum values; standard deviations, slopes, and intercepts for MI bodies, eastern Chukotka

Site ID	Field site ID	N	$\delta^{18}O$ (‰)			$\delta^{2}H$ (‰)			d_{exc} (‰)			Slope	Intercept	R^2
			Min.	Mean	Max.	Min.	Mean	Max.	Min.	Mean	Max.			
MI-1	343-YuV	2	−22.4	−21.5	−20.6	–	–	–	–	–				
MI-2	17-M	26	−18.96	−16.97	−14.84	−148.4	−131.4	−116.3	−2.48	4.52	11.02	7.71	−0.6	0.9
MI-3	20-M	20	−24.5	−18.0	−17	−191.3	−142.6	−121.1	−8.6	−0.5	11.7	6.86	−19.5	0.7
MI-4 (2019)	19-M	19	−19.02	−18.57	−18.16	–	–	–	–	–	–	–	–	–
MI-4 (2020)	20-M	11	−21.3	−18.7	−16.6	−163.9	−145.8	−123.9	−6.5	4.1	14.2	8.36	11	0.8
MI-5	16-M	33	−17.88	−17.13	−16.27	−135.8	−128.1	−121.6	4.2	9.0	15.8	6.42	−18.1	0.5
MI-6	15-L	12	−16.1	−15.4	−14.8	–	–	–	–	–	–	–	–	–

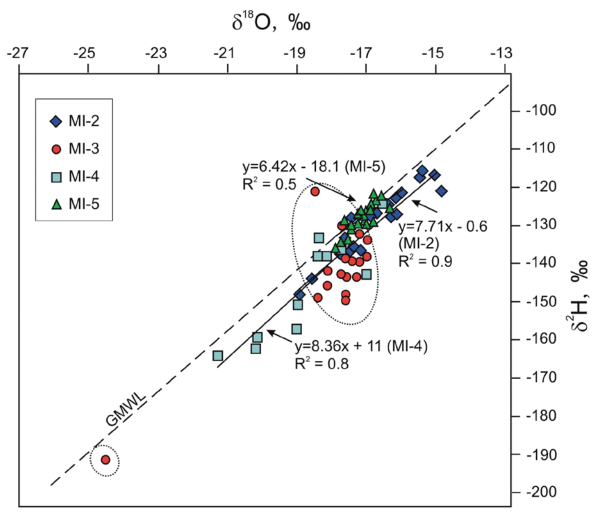

Fig. 9. Co-isotope $\delta^{2}H$-$\delta^{18}O$ lines for the MI bodies of the extreme northeast of Chukotka. GMWL (global meteoric water line) is given for comparison

Table 2. The $\delta^{18}O$ values in the surface water (spring – SW, river – RW, creek – CW, lake water – LW, bay – BW), snowpatches (S) of the northeast coast of Chukotka. From Vasil'chuk (1992, vol. 2) and additional data

Sample ID	Location	Type of water	$\delta^{18}O$, ‰
342-YuV/1	Creek near Lavrentia settlement (sampled in July)	CW	–11.7
342-YuV/2	Snowpatch 1 near Lavrentia settlement	S	–18.9
342-YuV/5	Snowpatch 2 near Lavrentia settlement	S	–10.4
342-YuV/3	Water of Lavrentia Bay	BW	–1.4
342-YuV/4	Small lake near Lavrentia settlement (sampled in July)	LW	–9.6
342-YuV/8	Snowpatch 3.7 km southern Lavrentia settlement (sampled in July)	S	–14.4
342-YuV/9	Water of Chul'cheveem River	RW	–12.2
343-YuV/37	Creek near Koolen' lake (sampled in August)	CW	–14.7
17-M-01-17-M-02	Near glacier lake in the car (sampled by A.Maslakov in 2017)	LW	From –10.67 to –11.97
17-M-03-17-M-08	Snowpatch 4 in glacier car, near Lavrentia settlement (sampled by A.Maslakov in 2017)	S	From –12.39 to –12.69
17-M-70	Spring water at 21 km picket of «Lavrentia –Lorino» road (sampled by A.Maslakov in 2017)	SW	–14.6

Analysis of the isotope composition of MI bodies of Chukotka shows a negative trend from the coast inland: mean $\delta^{18}O$ values of MI bodies near the Lavrentiya settlement vary from –15.4‰ to –18.7‰; MI on the coast of the Onemen Gulf and near the city of Anadyr vary from –19.6‰ to –20.6‰; in the more continental areas, i.e. at the Koolen' Lake, mean $\delta^{18}O$ value for MI is –21.5‰; for farther inland, in the Tanyurer River and Amguema River valleys, $\delta^{18}O$ values of MI bodies vary from –21.7‰ to –23.6‰ and from –25‰ to –29‰, respectively. This is most likely due to the continental isotope effect of precipitation (which was the primary source of water for ice formation), when precipitation becomes more isotopically depleted from coastal to continental areas.

4. If to assume that studied MI bodies are the fragments of burial glacial ice, then, first of all, it should be noted that modern glaciation in the highest mountains of the Eastern Chukotka is mainly of the glacial cirque type, less often of the cirque-valley type. This involves approximately 25–30 small glaciers. For the largest of them, the margin moraine forms were noted near the edge of the glacier. In total, there were 47 glaciers in Chukotka with an area of 13.53 km^2 (Sedov 1997) divided into five groups. The largest group is represented by 21 glaciers with a total area of 8.65 km^2. They were discovered near the Iskaten ridge, most of them are of cirque, cirque-valley, and cirque-hanging types. In the mountain range near the Provideniya Bay (1194 m), there is enough moisture from the Pacific Ocean, the total area of glaciers is approximately 2.5 km^2 (Sedov 1997).

In the Late Pleistocene these glaciers could advance only by 100–300 meters. By morphology and environmental conditions, they are very close to the glaciers of the Polar Ural mountains (Vasil'chuk et al. 2016). According to Mangerud et al. (2008), in the Late Pleistocene these glaciers never occupied a much larger area compared to the present time.

5. In the Arctic Siberia, we studied territories such as the Arctic islands with glacial domes – Severnaya Zemlya, Novosibirsk Islands, Wrangel Island, the mountainous areas of Verkhoyansk mountains, Sayan, and Stanovoy Ridge, etc. and could not find any Late Pleistocene glacier or its part under the Holocene glacier. There is no reason to assume the active disappearance of the Pleistocene glaciers during the Holocene, as along the extensive north Siberian coast and on the arctic islands Late Pleistocene ice wedges not only degraded but are also located directly beneath the modern active layer (Vasil'chuk Yu., Vasil'chuk A. 2018).

At the same time, the Late Pleistocene glaciers are quite widespread in the North American Arctic and on the islands of the Canadian Arctic Archipelago – these are, first of all, the glacial domes of Greenland, Ellesmere, Devon, Agassiz, etc. Therefore, the preservation of the buried Late Pleistocene glacial ice is possible in the permafrost sediments of the North America, whereas their existence in the Eurasian Arctic, including Chukotka, is impossible (Vasil'chuk 2020).

6. Isotopic curves for polar caps of the Russian Arctic can demonstrate a very contrasting distribution of $\delta^{18}O$ values (even in the bottom ice the range is more than 5–6‰, in spite of the compacted ice and almost untraceable seasonal differences) as a quite uniform distribution of $\delta^{18}O$ values with the range of no more than 2–4‰. Vasil'chuk (2020) observed that the isotopic composition of the majority of the MI bodies of the Northern Eurasia is very close to the Holocene values.

7. It should be noted that the existence of the Late Pleistocene yedoma strata with thick ice wedges in Chukotka, in the valleys of the Main, Tanyurer, and Ekityki rivers (Kotov, 1997a,b, 2001; Vasil'chuk, Vasil'chuk, 2021) near mountains with glacial cirque glaciers clearly indicate the impossibility of glaciation expanding in these valleys, since syngenetic ice wedges do not form under glaciers.

8. Ice bodies MI 2- MI 7 were found either within Pleistocene plain (MI 2-4) or under sediments of Pleistocene terrace (MI 5-7) that allows assuming that MI bodies are confined to Pleistocene deposits and may be formed during epigenetic freezing. Among the studied MI bodies, three of seven objects (MI 3, 5, and 7) were found in the old grassed thermocirques, which were possibly activated by the recent climate warming. Apparently exposed ice bodies are the parts of larger ones, which were partly melted from the top during previous period of increased summer temperatures. The foot of the bodies was not exposed in all outcrops. In this way, core drilling may be a potential direction of further studies of the distribution and morphology of the MI bodies in the Chukotka region.

9. Summing all the presented reasons it may be concluded that the studied MI bodies are of intrasedimental genesis; they were formed by congelation and congelation-segregation processes. However, this is still only a motivated assumption. A more definite conclusion about the age and origin of MI can be made after its dating and pollen analysis.

CONCLUSIONS

a. Recent climate warming in the Arctic and in the Chukotka region in particular facilitated deeper active layer thickening and more intensive thaw slumps formation. Exposed MI beds in vicinities of Lavrentiya and Lorino settlements allowed conducting detailed cryostratigraphic and stable isotope studies in the summer seasons of 2015–2020.

b. For the first time cryostratigraphy and stable isotope composition of six MI bodies of the extreme north-east of Chukotka (Koolen' Lake – Lavrentiya settlement) were studied.

c. $\delta^{18}O$ and $\delta^{2}H$ values in the MI samples were rather high: the mean $\delta^{18}O$ values vary mainly from −18.5‰ to −15‰; $\delta^{2}H$ values vary from −146‰ to −128‰.

d. The studied MI bodies are of intrasedimental genesis and highly likely are dated back to the Late Pleistocene age.

e. Analysis of the isotope composition of MI bodies of Chukotka shows a negative trend of $\delta^{18}O$ values from the coast inland, from −15.4‰ to −18.7‰ (near the Lavrentiya settlement) and from −25‰ to −29‰ (in Amguema River valley) that is mainly explained by continental isotope effect for precipitation, which was the primary source of water for ice formation.

f. More definite conclusion about the age and origin of the MI can be made after their direct dating and pollen analysis direct from ice.

REFERENCES

Abramov A., Davydov S., Ivashchenko A., Karelin D., Kholodov A., Kraev G., Lupachev A., Maslakov A., Ostroumov V., Rivkina E., Shmelev D., Sorokovikov V., Tregubov O., Veremeeva A., Zamolodchikov D. & Zimov S. (2019). Two decades of active layer thickness monitoring in northeastern Asia, Polar Geography, DOI: 10.1080/1088937X.2019.1648581.

Bulygina O.N., Razuvayev V.N., Trofimenko, L.T., Shvets, N.V. (2020). Automated Information System for Processing Regime Information (AISPRI). Available at: http://aisori.meteo.ru/ClimateR [Accessed on 28 February 2020].

French H.M. (2018). The Periglacial Environment, 4th Edition. Wiley, 544.

Gasanov Sh.Sh. Ground ice of the Chukotka Peninsula. In Permafrost of Chukotka. Magadan. Publ: SVKNII SO AN SSSR, 1964, 14-41. (in Russian).

Gasanov Sh.Sh. (1969). Structure and formation history of permafrost of the Eastern Chukotka. Moscow: Nauka, 168. (in Russian).

Kolesnikov S.F., Plakht I.R. Chukotka Area. (1989). In: Popov A. I, ed. Regional'naya Kriolitologiya (Regional Cryolithology). University Press: Moscow; 201-217. (in Russian).

Korolev S.Yu. (1993). Late Pleistocene glacier ice finding in the valley of the Amguema River (Northern Chukotka). Doklady of the Russian Academy of Sciences, 329(2), 195-198. (in Russian).

Kotov A.N. (1997a). Features of cryolithogenesis in the ablation zone of Late Pleistocene glaciers. In: Results of fundamental studies of the Earth's cryosphere in the Arctic and Subarctic. Novosibirsk: Nauka, 249-259. (in Russian).

Kotov A.N. (1997b). Massive ice on the northern coast of Onemen Bay (Chukotka). In: Late Pleistocene and Holocene of Beringia. Magadan. Publ: SVKNII SO AN SSSR, 92-98. (in Russian).

Kotov A.N. (1998a). Cryolithogenic ridges in the Tanurer River valley (Chukotka). Earth's Cryosphere, II(4), 62-71. (in Russian).

Kotov A.N. (1998b). Ground ice formation and problems of the regions of new development of Chukotka. In: Chukotka: nature and man. Magadan. Publ: SVKNII SO AN SSSR, 38-51. (in Russian)

Kotov A.N. (1999). Late Pleistocene cryolithogenic deposits and glacier ice in the valley of the Ekityki River (northern Chukotka). In complex studies of Chukotka (problems of geology and biogeography). Magadan. Publ: SVKNII SO AN SSSR, 93-102. (in Russian).

Kotov A.N. (2001). Peculiarities of occurrence, composition, and structure of layer-type ice deposits on the northern coast of Onemen Bay (Chukotka). Materials of the second conference of geocryologists of Russia, volume 1, part 2. Lithogenetic geocryology. Engineering geocryology. Moscow State University M.V. Lomonosov 6–8 June 2001 Moscow: Moscow University Press, 218-225. (in Russian).

Kotov A.N. (2005). Comparative analysis of the composition and structure of stratal ice deposits of Chukotka. In Materials of the third conference of geocryologists of Russia. Moscow State University M.V. Lomonosov June 1-3, 2005 Volume 1. Part 2. Lithogenetic geocryology and soil cryogenesis. M .: Moscow University Press, 168-175. (in Russian).

Mangerud J., Gosse J., Matiouchkov A., Dolvik T. (2008). Glaciers in the Polar Urals, Russia, were not much larger during the Last Global Glacial Maximum than today. Quaternary Science Reviews, 27(9), 1047-1057, DOI: 10.1016/j.quascirev.2008.01.015.

Maslakov A.A., Belova N.G., Baranskaya A.V., Romanenko F.A. (2018). Layered ice on the eastern coast of the Chukchi Peninsula during climate warming: some results of expeditions in 2014–2018. Arctic and Antarctic, 4, 30-43. (in Russian)).

Maslakov A.A., Nyland K.E., Komova N.N., Yurov F.D., Yoshikawa K., Kraev G.N. (2020). Community Ice Cellars In The Eastern Chukotka: Climatic And Anthropogenic Influences On Structural Stability. Geography, Environment, Sustainability, 13(3), 49-56, DOI: 10.24057/2071-9388-2020-71.

Opel T., Dereviagin A.Yu., Meyer H., Schirrmeister L., Wetterich S. (2011). Palaeoclimatic Information from Stable Water Isotopes of Holocene Ice Wedges on the Dmitrii Laptev Strait, Northeast Siberia, Russia. Permafrost and periglacial processes, 22, 84-100, DOI: 10.1002/ppp.667.

Polyak B.G., Dubinina E.O., Lavrushin V.Yu., Cheshko A.L. (2008). Isotopic Composition of Thermal Waters in Chukotka. Lithology and Mineral Resources, 43(5), 429-453, DOI: 10.1134/S0024490208050027.

Soloviev P.A. (1947). Ice in permafrost soils in the Anadyr city area. Mineral resources of Arctic, Iss. 2, Moscow-Leningrad, 213-232. (in Russian).

Shvetsov P.F. (1938). Permafrost and geotechnical conditions of the Anadyr region. Edited by Sumgin M.I. and Efimov A.I. (eds.). Moscow-Leningrad: Publ. Glavsevmorput, 78. (in Russian).

Shvetsov P.F. (1947). Groundwater and fossil ice in the area of the city of Anadyrand the Ugolnaya bays. Nedra of Arctic. Iss. 2. Moscow-Leningrad, 204-211. (in Russian).

Sedov R.V. Chukotka glaciers. Materials of glaciological research, iss. 82. 1997, 213-217.

Vasil'chuk Yu.K. (2012). Isotope Ratios in the Environment. Part 2: Stable isotope geochemistry of massive ice. Moscow: Moscow University Press, 472. (in Russian).

Vasil'chuk Yu. K. (2006). Massive ice bodies. In Vasil'chuk Y., Krylov G., Podborny Y. Eds. Cryosphere of oil-gas fields of Yamal Peninsula. Vol. 1. Cryosphere of the Kharasavey gas-condensate field.: Nedra, 160-193. (in Russian).

Vasil'chuk Yu. K. (1992).Oxygen isotope composition of ground ice (application to paleogeocryological reconstructions). Volume 1, 420 pp., Volume 2, 264 pp. Theoretical Problems Department, Russian Academy of Sciences and Lomonosov Moscow University Publications, Moscow (in Russian with English contents section).

Vasil'chuk Yu. K. (2020). Some clear evidences of the intrasedimental origin of massive ice in northern Eurasia. Arctic and Antarctic, 1, 23-34, DOI: 10.7256/2453-8922.2020.1.32283 (in Russian).

Vasil'chuk Yu.K., Budantseva N.A., Vasil'chuk A.C., Podborny Ye.Ye., Chizhova Ju.N. (2016). Multistage Holocene massive ground ice in Northern West Siberia. Earth's Cryosphere, XX(1), 34-45. http://www.izdatgeo.ru.

Vasil'chuk Yu.K., Budantseva N.A., Farquharson L., Maslakov A.A., Vasil'chuk A.C., Chizhova Yu.N. (2018a). Isotopic evidence for Holocene January air temperature variability on the East Chukotka Peninsula. Permafrost and Periglacial Processes, 29(4), 283-297, DOI: 10.1002/ppp.1991.

Vasil'chuk Yu.K., Budantseva N.A., Vasil'chuk A.C., Maslakov A.A., Chizhova Ju.N. (2018b). Oxygen isotope composition of Holocene ice wedges of the Eastern Chukotka. Doklady Earth Sciences, 480(2), 759-763, DOI: 10.1134/S1028334X18060107.

Vasil'chuk Yu.K., Chizhova Ju.N., Maslakov A.A., Budantseva N.A., Vasil'chuk A.C. (2018c). Oxygen and hydrogen isotope variations in a recently formed massive ice at the mouth of the Akkani River, Eastern Chukotka. Led i Sneg. Ice and Snow, 58(1), 78-93, DOI: 10.15356/2076-6734-2018-1-78-93 (in Russian).

Vasil'chuk Yu.K., Vasil'chuk A.C. (2017). Ice wedges in the Mayn River valley and winter air paleotemperature in the Southern Chukchi Peninsula at 38-12 Kyr BP) // Earth's Cryosphere, XXI(5), 27-41, DOI: 10.21782/KZ1560-7496-2017-5(27-41)

Vasil'chuk Yu.K., Kotlyakov V.M. (2000). Principles of Isotope Geocryology and Glaciology. A comprehensive textbook. Moscow University Press, 616. (in Russian).

Vasil'chuk Yu.K., Murton J.B. (2016). Stable isotope geochemistry of massive ice // Geography, Environment, Sustainability, 3, 4-24, DOI: 10.15356/2071-9388_03v09_2016_01

Vasilchuk Yu.K., Vasilchuk A.C. (2018). The oxygen isotope composition of ice wedges of Ayon Island and paleotemperature reconstructions of the Late Pleistocene and Holocene of the North of Chukotka. Moscow University Geology Bulletin, 73(1), 87-99, DOI: 10.3103/S0145875218010131.

Vtyurin B.I. (1964). Cryogenic structure of Quaternary deposits (the case of the Anadyr lowland). Moscow: Nauka, 152. (in Russian)

Vtyurin B.I. (1975). Ground ice of the USSR. Moscow: Nauka, 214. (in Russian).

Zamolodchikov D.G., Kotov A.N., Karelin D.V., Razzhivin V.Y. (2004). Active-Layer Monitoring in Northeast Russia: Spatial, Seasonal, and Interannual Variability. Polar Geography, 28(4), 286-307.

RESEARCH PAPER

GENETIC IDENTIFICATION OF GROUND ICE BY PETROGRAPHIC METHOD

Yana V. Tikhonravova[1*], Viktor V. Rogov[2], Elena A. Slagoda[3]
[1]Melnikov Permafrost Institute, Siberian Branch, Russian Academy of Sciences, Yakutsk, 677010, Russia
[2]Lomonosov Moscow State University, Moscow, 119991, Russia
[3]Earth Cryosphere Institute Tyumen Scientific Centre Siberian Branch, Russian Academy of Sciences, Tyumen, 625026, Russia
*Corresponding author: tikh-jana@yandex.ru
Received: May 31th, 2021 / Accepted: November 9th, 2021 / Published: December 31st, 2021
https://doi.org/10.24057/2071-9388-2021-063

ABSTRACT. The advantages and limitations of the petrography method and the relevance of its use for the study of natural ice are reviewed in the present work. The petrographic method of ground ice study is often used for solving paleogeographic issues. The petrofabric analysis of ground ice is not only useful for descriptive purposes but, like the study of cryostructures, helps to infer growth processes and conditions. Different types of natural ice have specific features that can help us to determine ice genesis. Surface ice, such as glacier ice is often presented by foliation formed by large crystals (50-60 mm); lake ice is characterised by the upper zone of small (6 mm x 3 mm) dendritic and equigranular crystals, which change with increasing depth to large (may exceed 200 mm) columnar and prismatic crystals; segregated ice is composed by crystals forming foliation. Ground ice, such as ice wedge is presented by vertical-band appearance and small crystals (2-2.5 mm); closed-cavity ice is often distinguished by radial-ray appearance produced by elongated ice crystals; injection ice is composed by anhedral crystals, showing the movement of water; snowbank ice is presented by a high concentration of circular bubbles and small (0.1-1 mm) equigranular crystals; icing is described by foliation and mostly columnar crystals. Identification of the origin of ground ice is a complicated task for geocryology because it is difficult to distinguish different types of ground ice based on only visual explorations. The simplest way to get an ice texture pattern is by using polarized light. Distinctions between genetic types of ground ice are not always made in studies, and that can produce erroneous inferences. Petrography studies of an ice object are helpful to clarify the data interpretation, e.g., of isotopic analyses. It is particularly relevant for heterogeneous ice wedges' study.

KEYWORDS: ice texture, ice appearance, polarized light, ice crystallography

CITATION: Yana V. Tikhonravova, Viktor V. Rogov, Elena A. Slagoda (2021). Genetic Identification Of Ground Ice By Petrographic Method. Geography, Environment, Sustainability, Vol.14, No 4, p. 20-32
https://doi.org/10.24057/2071-9388-2021-063

ACKNOWLEDGEMENTS: The research was carried out within the state assignments of the Research work Plan of the Melnikov Permafrost Institute, SB, RAS, project No. AAAA-A20-120111690012-6 and the Research work Plan of the Earth Cryosphere Institute Tyumen Scientific Centre, SB, RAS, project No. 121041600042-7. We would like to thank Mr. Muse Tarekegn for his help with translation.

Conflict of interests: The authors reported no potential conflict of interest.

INTRODUCTION

One approach to the study of ground ice is crystallography. The idea of using the petrographic method to establish the ice appearance and textural characteristics of ground ices for their genetic indication has been developing since the mid-20th century (Vtyurin and Vtyurina 1960; Savel'ev 1963; Shumskii 1964; Vtyurin 1975; Rogov 1996, 2009; Solomatin 2013). Sander B. was the first to propose using the petrographic method in glaciology (Shumskii 1964). The petrographic method of ground ice study for solving paleogeographic problems has become standard procedure for many researchers (Katasonov and Ivanov 1973; Katasonov 1975; Pewe, 1967; Sher and Kaplina 1979; French and Pollard 1986; Solomatin 1986; Pollard 1990; Coulombe et al. 2019; Tikhonravova et al. 2017, 2019, 2020; et al.).

The study of the ground ice texture has great value for paleogeographic reconstructions in the permafrost zone. A set of data on the composition, sediments micromorphology, ice appearance, and texture of ground ice and their relationship allows us to determine the genesis of sediments and ice and the conditions for their accumulation. Ice is very sensitive to changes in environmental conditions and exogenous processes. It demonstrates this information in its texture (Golubev 2000; Rogov 2009). Geological processes cause the formation of various elements of the constitution within ice objects: ice wedge's shoulder (Tikhonravova et al. 2020); composite zone within an ice wedge (Tikhonravova et al., 2019); closed-cavity ice over an ice wedge (Kanevskiy et al. 2017) that can be involved to ice-wedge composition (Tikhonravova 2021), etc. The elements of constitution are associated with different genetic types of ice (Popov 1955; P. Shumskii 1960; Solomatin 1965; Murton 2013). Petrographic analysis helps to define the ratio of different ice types within an ice object and allows establishing the primary and secondary processes of their formation.

Although the petrographic approach has been used in the study of ground ices in the past (Shumskii 1964; Gell 1973, 1975; Savel'ev 1980; Rothschild 1985; Pollard 1990; Golubev 2000; Tyshko et al. 2000; Solomatin 2013; and others) there is still a relative lack of data upon the characteristics of different genetic types of ice. Present work aims to to review the advantages and limitations of the petrography method; to review the different approaches and used terminology; to estimate the relevance of using this method for studying of natural ice in the currently.

PROBLEMS OF TERMINOLOGY

Currently, there are many synonyms and confusion in terminology on currently. For example, the term «cryotexture» is used in Russian terminology to describe the structural characteristics of frozen deposits caused by the configuration of ground ice and sedimentary material (Kotlyakov 1984). While North Americans use the term «cryostructure» to describe this phenomenon. Also, the term «cryotexture» is used in English terminology to describe the grain and/or ice crystal size and shape, and the nature of the contacts between grains and ice crystals in frozen earth materials (French 2007). The Russian classifications of frozen ground blur the distinction between cryotexture (i.e., grain size by English terminology) and cryostructure (i.e., aggregate shape by English terminology) and mainly use just one term «cryotexture». Alan William Gell (1975) remarks that terminology hasn't been consistent in papers concerned with ice petrology.

Ice appearance (Pollard 1990) is ice characteristics that can be obtained without ancillary equipment – colour, different inclusions, fissures, etc. Terms used as synonyms: texture of ice in Russian terminology (Vtyurin 1975; Tyshko et al. 2000; Lein et al. 2005; Solomatin 2013;).

Ice texture (Gell 1973; Rothschild 1985; Pollard and French 1985; Petrich and Eicken 2010; St-Jean et al. 2011) is crystal characteristic of ice that can be obtained with ancillary equipment. Terms used as synonyms: crystal pattern (son Ahlmann and Droessler 1949b); ice microstructure (Kipfstuhl et al. 2006; Petrich and Eicken 2010; Faria et al. 2014a, 2014b; Coulombe and Fortier 2015), internal structure (Bonath et al. 2018), crystal structure (Kawano and Ohashi 2006; Slagoda et al. 2012; Orekhov et al. 2017), structure of ice in Russian terminology (Savel'ev 1980; Tyshko et al. 2000; Rogov 2009; Solomatin 2013; Golubev 2014; Gorgutsa et al. 2016).

Ice fabric (Rothschild 1985; Pollard and French 1985; French and Harry 1988; Faria et al. 2014a) is the preferred orientation of the crystalline lattices of a population of grains, i.e. c-axis orientations. Terms used as synonyms: petrofabric (French and Pollard 1986); lattice preferred orientation (Faria et al. 2014b); crystallographic fabric (Minchew et al. 2018), crystallographic preferred orientation (Wheeler et al. 2001).

METHODOLOGY

The techniques and procedures of determining ice texture follow closely those developed for glacier ice (Ostrem 1963). Determination of ice texture and fabric is possible using its optical features (Savel'ev 1963; Shumskii 1964). One of the features is double refraction, which realizes the decomposition of a plane-polarized light beam in the crystal to two mutually perpendicular planes with constant and variable refractive indexes. This feature is demonstrated in a thin ice section (0.8-1.0 mm) under cross-polarized light. Two polarizing filters are arranged perpendicular to each other, with a light source installed underneath the lower polarizer. A polarizing filter allows only light waves of the same orientation to pass through, which means two perpendicularly positioned filters block visual light waves completely. The light source goes through the first polarizer and becomes linearly polarized light, which is completely blocked by the perpendicularly arranged second polarizer. When the thin ice section is placed between the two polarizers, the polarized light is refracted to multiple directions due to the different orientations of individual ice crystals within the ice sample. This technique reveals the otherwise transparent and indistinguishable crystal morphology. Each crystal acquires its interference colour, which allows judging about its size, shape, and orientation in the thin section. These studies are better produced at a negative temperature, standard methods were proposed by Shumskii (1964) and Savel'ev (1963). The method is often applied directly in the field, when it is difficult to transport a large number of frozen samples.

X-ray-computed tomography (CT) scanning is also used (Dillon et al. 2008; Calmels et al. 2010; Fortier et al. 2012; Coulombe et al. 2019) to study ice and icy soil. This technique relies on the calculation of the linear attenuation coefficient that measures the density of an object passed through an X-ray beam at different angles. In frozen samples, sediments and rock appear white, gases inclusions and water appear black, and ice can have various shades of grey depending on their density. Different shades of grey are assigned specific CT numbers to create the displayed image using a specific image processing software like Fiji (Schindelin et al. 2012). This technique produces cross-sectional images of an object, and allows visualizing (2-D and 3-D) and reconstructing the internal constitution (Calmels et al. 2010; Fortier et al. 2012).

Sample preparation

Large ice monoliths (15x15x10 or larger depending on the task) are sampled using a chainsaw or axe from a cross section. The monoliths should be oriented in space. To study the internal constitution characteristics from oriented monoliths of ice or icy ground, we need to make thin sections of different sides: vertical transverse, vertical longitudinal, and horizontal. The monoliths are cut into 6-10 mm thick sections using a band saw. Thin ice sections (0.5-1.5 mm) are procured by slowly melting down the thick ice specimen via manually rubbing the surface with a thick, warm aluminium plate. There is also a new procedure of shaving thick ice sections with a microtome (Bruneau et al. 2015). The authors propose the microtome to overcome the flaws and tedium of the melting procedure. After melting down or cutting, the ice surface is wiped with dry tissue paper to avoid refreezing of meltwater on the ice surface and is then settled on a glass plate.

Ice appearance study

The study of an ice object starts during fieldwork. The ice object is observed in the cross section. The relationship and position between the ice object and enclosing sediments, ice morphology and configuration, ice colour, and different inclusions (bubbles, organic, and mineral particles) are recorded. The ice appearance is studied in more detail in thin section under the diffused light. The colour, fissures, and location of bubbles and organo-mineral inclusions are marked. Bubbles can indicate the relative speed of freezing and the direction from which freezing occurred (Rothschild 1985). As crystallization takes place, the air is rejected from the freezing water and accumulates at the ice/water interface until its concentration is high enough for bubbles to nucleate. Under a relatively low freezing rate, a bubble will continue to grow as the freezing front moves forward thus forming a cylindrical bubble parallel to the direction of ice growth. Slightly faster freezing produces oval-shaped bubbles oriented away from the freezing interface. Fast freezing produces small spherical bubbles as there is insufficient time for more air to diffuse into the initial bubbles. Very slow freezing produces ice without bubbles since in the former, the air can diffuse away from the ice, and in the latter, the continuous removal of water prevents the build-up of air bubbles sufficient for nucleation. Very high freezing rates initially give clear ice, but over a while, bubbles nucleate and grow at grain boundaries within the ice. According to Mélanie St-Jean (2011), bubble configuration can indicate the water state of matter for ice formed by snow densification or the freezing of liquid water.

Ice texture study

Polarized light is often used to view ice texture. This can be a handmade polaroid or polarized light microscopy. The thin sections of ice are photographed under crossed polarization to quantify ice crystals and their shapes on photographs. In absence of polarized light, texture patterns can also be received by the method of making rubbings with a pencil on paper (Seligman 1950): selected ice area is dried if necessary, a piece of soft, unglazed, and slightly absorbent printing paper is then placed over it and «rubbed» with a soft pencil. It can also be received through rubbing a mixture insoluble in water over an ice surface, placing and gently pressing absorbent kitchen paper over the treated area, and after, when the outlines of the crystals appear, the paper is gently removed and dried (son Ahlmann and Droessler 1949a). One of the techniques for displaying the ice texture is scanning the ice's thin or thick section and producing digital black-and-white images at microscopic resolution (Kipfstuhl et al. 2006). Consecutive images are taken every 2 mm in the x-direction. An overlapping of 0.5 mm is helpful for the later reconstruction of the full mosaic figure. A series of about 1,500 images are needed to map a section of 45 by 90 mm.

The crystal shape, texture pattern, crystal boundary characterization, and crystal relationships are recorded. Crystal shape (habit) is the characteristic external shape of an individual crystal or crystal group: euhedral (idiomorphic or automorphic crystals), subhedral (hypidiomorphic), and anhedral (xenomorphic or allotriomorphic) (Shumskii 1964; Gell 1975; Rothschild 1985; Pollard 1990; St-Jean et al. 2011; Golubev 2014). Euhedral crystals are well-formed, have a hexagonal or cubic shapes, and are bounded by regular faces (Fig. 1a). Anhedral crystals are opposite, they have no regular crystal faces (Fig. 1b). Subhedral is an intermediate texture, they have some regular faces and bear some resemblance to a hexagonal shape. Shumskii (1964) also distinguished: prismatic-granular (parallel-fibrous oriented growth; also called panidiomorphic-granular); intersertal (rejected impurities arranged on grain boundaries); poikilitic (crystals containing insoluble, solid impurities or fine air inclusions); cataclastic (large primary crystals remain among fine crushed granules). Gell (1973) suggested the classification of different texture pattern types by the grain boundary shapes: straight, curved, sutured, and cuspate.

Quantitative characterization of ice crystals

Determination of quantitative characterization of ice crystals is needed for an objective comparison of different ice types. Qualitative indicator of crystal sizes is individual for each genetic type of ice.

A crystallographic analysis is produced with manually delineated ice crystal boundaries on the photos of ice thin sections under polarized light and calculation of crystallographic parameters using special software. Viktor

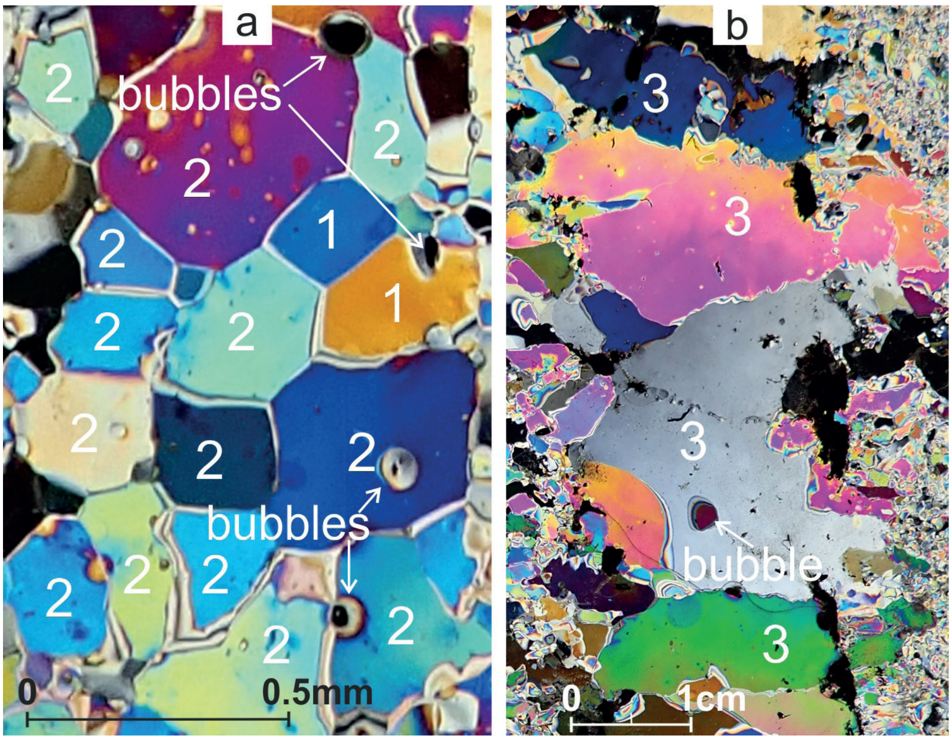

Fig. 1. Ice grain shapes (habit) of ice wedge (a) and crack ice (b) from Kurunrnakh Island, Lena Delta: 1 – euhedral; 2 – subhedral; 3 – anhedral

Rogov and colleagues have developed an addon called «Crystal» for MapInfo. Ice crystal boundaries are delineated manually using MapInfo (Fig. 2), and automatic calculations are undertaken using the «Crystal» addon. The parameters that characterize crystal size, shape, and orientation at the thin section are calculated in the program using the equations of Shumskii (1964) and Rogov. Main parameters: maximum diagonal (l_{max}) for each crystal determined; average diameter of the crystals (D) calculated as the average diameter of circles that included the crystals' area; the average area of the crystal (S) is determined using Shumskii's correction coefficient equalled as 1.5625; the minimum and maximum areas (S_{min}, S_{max}); coefficient of difference in the size of crystals (C_{diff}) calculated as the ratio of the maximum perimeter of the crystal to the minimum.

Some researchers also use other software, like Fiji (Coulombe et al. 2019) or the Clemex Application Suite (St-Jean et al., 2011) to measure the area, long axis, and circularity ratio of each crystal.

Ice fabric study

The ice fabric refers to the distribution of crystal axes in an assemblage of ice crystals and contains a fingerprint of the history of the ice deformation. There is a classic manual technique for fabric measurement. Petrofabric diagram illustrates the 3-dimensional orientations of fabric elements. The optic-axis orientations in ice are determined using special equipment – the universal stage. A detailed description of the universal stage and the standard technique for the determination of orienting crystals can be found in papers of Langway (1958) and Savel'ev (1963); as well as in the modification (Hill and Lasca 1975) and development of this technique (Wilen et al. 2003). Inclinations of 0° and 90° correspond to vertical and horizontal c-axes of crystals, respectively. One orientation measurement is made for each ice crystal in a sample, and these data are plotted on a Schmidt equal-area net that represents the surface of a hemisphere of unit radius. Fabric diagrams are plotted as projections of this Schmidt net with data. To identify the regularity of the crystal orientation distribution, the isolines of the points on 1% of the area or the isolines of the points concentration are plotted.

Modern automated ice fabric techniques produce a digital mosaic trend representation of the azimuth (colour) and colatitude (brightness) of c-axes in a thin section. The development of these automated techniques is facilitating many applications as the knowledge of the c-axis direction for large numbers of grains – the spatial relationship, size, and shape of the grains (Wilen et al., 2003). Unlike traditional fabric analysis, the information allows considerable interactive data processing with a strong link between fabric and texture data.

RESULTS AND DISCUSSION

The petrography analysis of ground ice is not only useful for descriptive purposes but, like the study of cryostructures, helps to infer growth processes and conditions. The crystal size, shape, boundary characteristics, and c-axis orientations are directly related to the direction and speed of the freezing process. Ice crystals normally grow at a right angle to the freezing front, and crystal size varies inversely with the rate of freezing.

The techniques of scanning for displaying the ice texture previously mentioned or crystal-orientation measurements on the universal stage can give interesting data but they are often difficult to implement. The main problem using the scanning techniques for displaying the ice texture is the alignment (matching) of the individual images. Another problem is the large size of the reconstructed images (Kipfstuhl et al. 2006). Consequently, research often doesn't include the ice petrographic study, with just the external description of the morphology and appearance of ice. Sometimes this is not enough to determine the genetic type of ice, freezing direction, and conditions. Different types of ground ice are difficult to distinguish based only on visual field research (French and Harry 1990). Visualization of an ice texture pattern is one of the primary tasks to the determination of ice type. The texture pattern can be found between crossed polarizers. Polaroid is an easy tool; it is possible to use both in the laboratory and the field.

Although different ice types may display a characteristic range of fabric and texture patterns, the reality is that a range of textures exists for each ice type. Without a complex study approach and good crystallographic control, just the ice textures do not permit the unambiguous identification of ice types. The perfect methods and diagnostic criteria allowing to distinguish one type from another do not yet exist. Research should be based on combining two or more different approaches to overcome this difficulty. However, different genetic types of ice have special features:

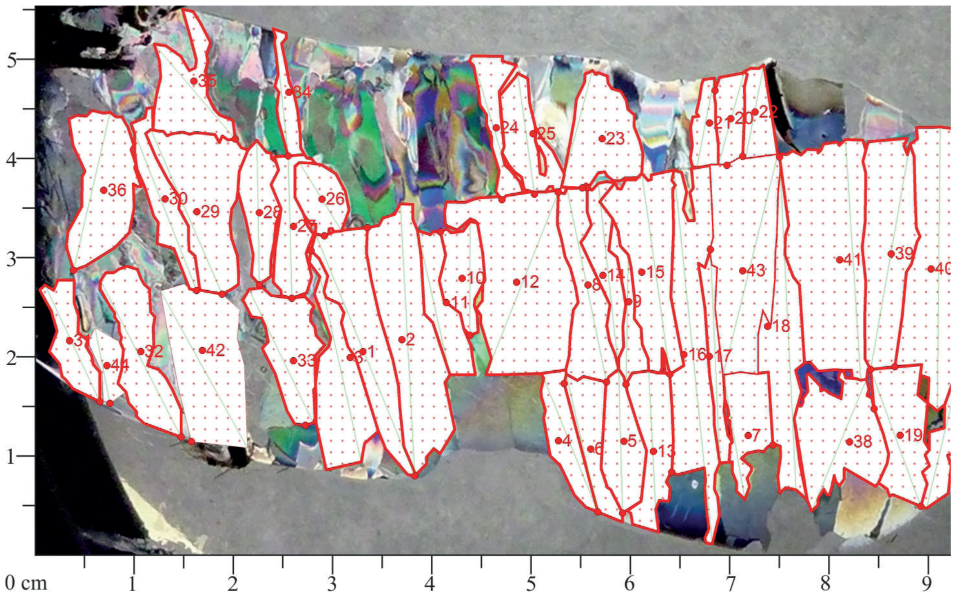

Fig. 2. Crystal boundaries delineated manually using "Crystal" addon for MapInfo (vertical thin section of the closed-cavity ice from Bovanenkovo area, the Yamal Peninsula, Russia)

Glacial ice

Glacial ice appearance is characterised mainly by foliation often in the form of distinct, typically discontinuous, bands of bubbles. That foliation is defined by variations in crystal size, crystal shape, bubble concentration, and bubble distribution (Fig. 3). Glacial ice has a wide range of crystal sizes (submillimetre to tens of centimetres), grains are mostly large (5-6 cm) (Gow et al., 1997). Crystal characteristics vary greatly depending on the location within the glacier (Rothschild 1985; Gow et al. 1997; Coulombe et al. 2019). Ice fabric may or may not have a well-defined relationship to the foliation. The foliation may take different forms in glacier ice. Deformation in glaciers often leads to a complex suite of textures. This is due to the combination of brittle fracture and plastic flow affecting ice with inherited and induced heterogeneities, largely visible through variations in bubble content. Dynamic recrystallization on the grain scale also contributes to the foliation, leading to a reorganization of bubbles and grain boundaries (Hudleston 2015). Different investigations show that crystal characteristics vary greatly depending on the location within the glacier (Diprinzio et al. 2005). For example, ice near the top of a glacier is generally more granular with a less pronounced crystal orientation. As one progresses through the glacier, the preferred crystal orientation reflects ice flow. Finally, near the tongue or edges of the glacier (the ice parts which are most likely to be buried in a moraine), crystals are usually large (several centimetres in diameter) and exhibit preferred orientations (Rothschild 1985).

Lake, river, and sea ices

Ice cover formation occurs due to cooling and heat outflow from the water surface. The ice is affected by the freezing temperature, insoluble inclusions and mineralisation, gases in the water, and the water movement. The ices of bulk water are characterised by layering, showing different formation stages (Savel'ev 1980). There is a gradual increase in the crystals' area from the upper layers to the lower ones, which is caused by an increase in the ice thickness and a decrease in the rate of heat transfer during crystallization, and a slowdown in crystal growth. The ices of bulk water are characterised by a wedging out zone of competing crystals.

Lake ice appearance has a high concentration of randomly scattered spherical bubbles of different diameters in the upper part, followed below by a mostly bubble-free zone and (rarely) beds of very small (up to 1 mm) bubbles (Fig. 4). Lake ice texture is characterised by an upper zone of relatively small randomly arranged dendritic crystals first (Golubev, 2014), and small euhedral equigranular crystals following. It changes with increasing depth to large anhedral columnar and prismatic crystals (Fig. 4). In the upper section crystals are generally relatively small, 6 mm x 3 mm; there is an increase in size downwards, it may exceed 200 mm in length (Gell, 1975). There are randomly oriented rapidly equidimensional crystals in the upper section; large columnar and prismatic crystals usually form with horizontally oriented c-axes at first, and after the large crystals with their basal planes oriented vertically eventually wedge out others (Rothschild, 1985).

The formation of ice in rivers is more complex than in lakes, largely because of the effects of water velocity and turbulence. Lake ice also grows differently from sea ice: microscopically, at the scale of brine inclusions and below. Typically, more than 99.9% of the impurities such as ions dissolved in lake water are expelled from the ice cover. In sea ice, brine is trapped between the lamellae at the bottom of the ice, allowing for ion retention of between 10 and 40% in the ice (Petrich and Eicken 2010). That affects the sea ice morphology (Tyshko et al. 2000). Different

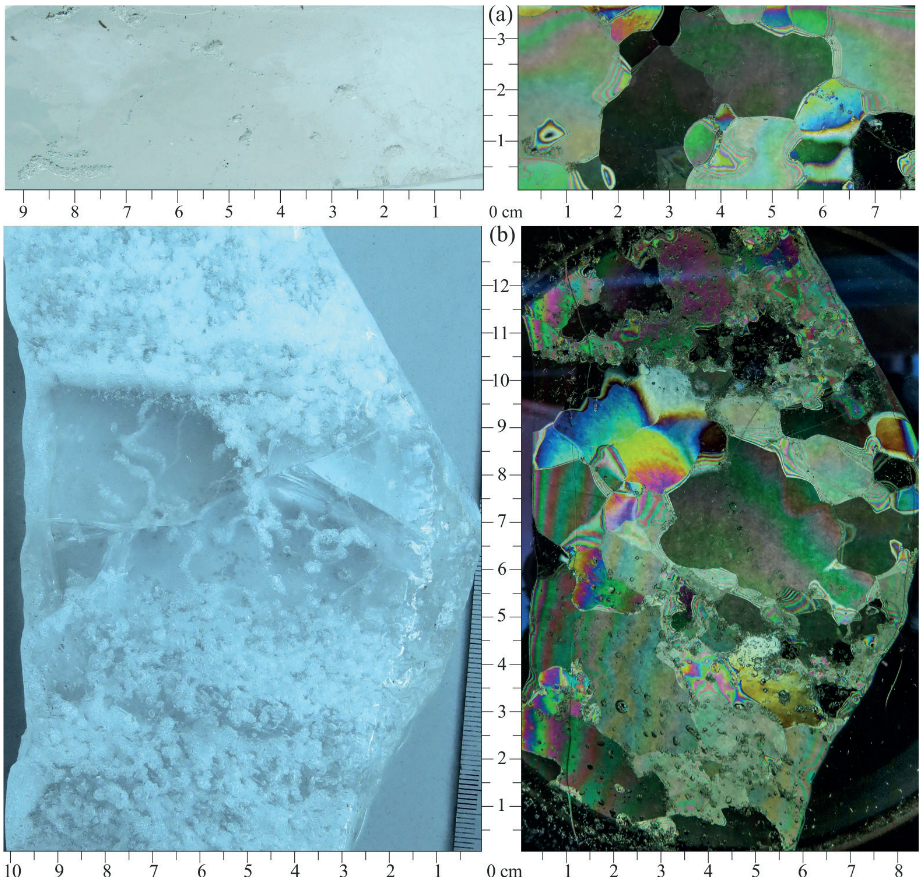

Fig. 3. Appearance and texture of glacial ice (crevasses in lateral margins of Romantic's Glaciar, the Polar Urals, Russia), horizontal thin section (a) and vertical thin section (b)

impurities (e.g., organo-minerals particles, ions) are freezing nuclei. Moreover, perennial sea ice is different from annual sea ice (Savel'ev 1980; Tyshko et al. 2000) and fast sea ice. The availability of freezing nuclei and the speed at which freezing takes place are important factors in determining the exact ice texture and fabric.

Segregated ice

Segregated ice is formed from pore water migrating to the freezing front (Shumskii 1964). It forms a unique cryostructure (by English terminology) including pore ice (Rogov 2009). Segregated ice appearance is often pure and clean. There may be mineral particles suspended in ice. Segregated ice is often characterised by the lamination of crystals. Bubbles and crystal c-axes are often oriented normally to the freezing front (Rothschild 1985). Segregated ice tends to be composed of equigranular anhedral crystals whose c-axes form a loose girdle normally oriented to the plane of the ice layer (Fig. 5). Also, the crystal shape may be irregular or slightly elongated parallel to the compositional layering. Petrographic characteristics of segregated ice are closely related to sediment banding (Pollard 1990). The crystal sizes directly depend on pore water quantity and freezing rate.

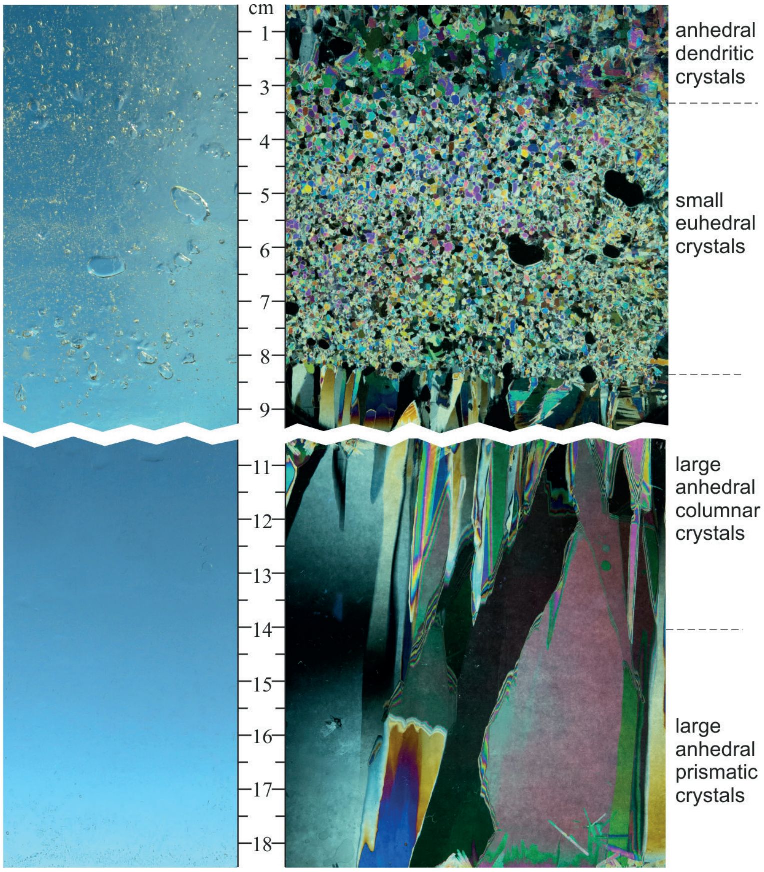

Fig. 4. Appearance and texture of lake ice (Lake Lipovoe, Tyumen, Russia), vertical thin section: small crystals are the first crystallization stage, large crystals are the second one (Savel'ev, 1980)

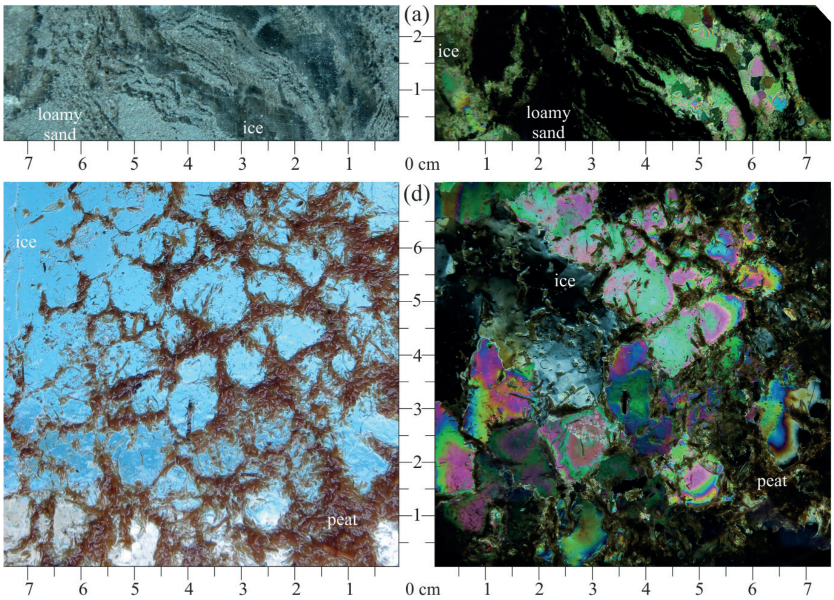

Fig. 5. Appearance and texture of segregated ice (horizontal thin section) in loamy sand within the ice wedge from Gyda area, Northern West Siberia, Russia (Y.V. Tikhonravova et al., 2019) (a); appearance and texture of segregated ice (horizontal thin section) forming the suspended cryostructure within the peatland of Pur-Taz interfluve, Northern West Siberia, Russia (b)

Ice wedge

The ice-wedge formation process is caused by thermal contraction cracking: frost cracking in winter, infilling the crack mostly by snow meltwater (Lachenbruch 1962) in spring, and the meltwater fast freezing in the crack as an ice vein (Leffingwell 1915; French 2007). Thus, ice veins compose an ice wedge. A specific feature of the vein ice is a vertical axial seam and small crystals (up to 20 mm (Shumskii 1964)). There are small crystals oriented horizontally from crack walls towards each other (Fig. 6, a). An axial seam is formed by bubbles and organo-mineral inclusions on the contact of the ice crystals (Shumskii 1964). If the ice wedge is located at a layer of annual negative temperature fluctuations for a long time, the wedge ice recrystallizes (Shumskii 1964): old ice crystals of the ice vein enlarge and round, but the ice vein's axial seam remains.

The ice wedge appearance is characterised mainly by vertical bands of bubbles (Fig. 6b,d). Wedge ice texture is composed of small subhedral to euhedral crystals for Holocene age ice (Fig. 6, c); and of small euhedral equigranular crystals for Pleistocene age ice (Fig. 6e). Crystal size depends on freezing temperature, crack wall form and its width, the composition of infilling water and enclosing deposit, and recrystallization (Solomatin 2013). However, due to their mode of formation, crystal size is generally larger in the upper portion of the wedge (up to 1-2 cm in diameter (Shumskii 1964)) than in the lower part (<0.15 cm in diameter (Rothschild 1985)). Crystal size of a young ice wedge varies from 0.18 to 8 mm (on average 1.6-2 mm); of ice wedge – from 0.19-30 mm, on average 2-2.5 mm in diameter (Vtyurin and Vtyurina 1960). The ice texture of the vertical section is comparable with the ice texture of the horizontal section. Wedge ice's crystal c-axis orientation may vary from chaotic to distinctly linear (Shumskii 1964; Rothschild 1985). Occasionally, accompanying processes participate in ice-wedge formation and form other genetic types of ice (closed-cavity ice, segregated ice, etc.) within the ice-wedge structure (Romanovsky 1959; Shumskii 1964; Popov et al. 1985; Murton 2013; Gilbert et al. 2016; Kanevskiy et al. 2017; Tikhonravova et al. 2019, 2020).

Closed-cavity ice

Closed-cavity ice (Everdingen 2005) is formed by the freezing of water trapped in underground cavities cut into permafrost by flowing water. This ice is also called thermokarst-cave ice (Kanevskiy et al. 2017) or pool ice (Mackay 2000), or pond ice (Gell 1975). Closed-cavity ice usually forms within and next to ice wedges (Kanevskiy et al. 2017). Closed-cavity ice is characterised by radial-ray appearance and texture (Fig. 7a) (Shumskii 1964) due to forming through multilateral slow freezing of free water, and seam of spherical bubbles formed by the collision of the ice crystals. The radial-ray appearance is presented by elongated bubbles directed to the seam. Additionally, ice appearance can be pure. The closed-cavity ice is composed of congelation elongate ice crystals (congelation ice is ice formed in bulk water). The crystals are anhedral and have serrated boundaries. The ice crystals vary from being small (~0.2 cm in diameter (Y.V. Tikhonravova et al. 2020)) to large according to cavity size. Crystal size depends on freezing rate, cavity form and its size, and water amount. The ice texture of the vertical section is different from the ice texture of the horizontal section (Fig. 7).

Injection ice

Injection (intrusive) ice is formed by the freezing of water moving under hydraulic or hydrostatic pressure. Its appearance is often pure and clean. Soil particles can occur at the base of intrusive ice in the form of streaks parallel

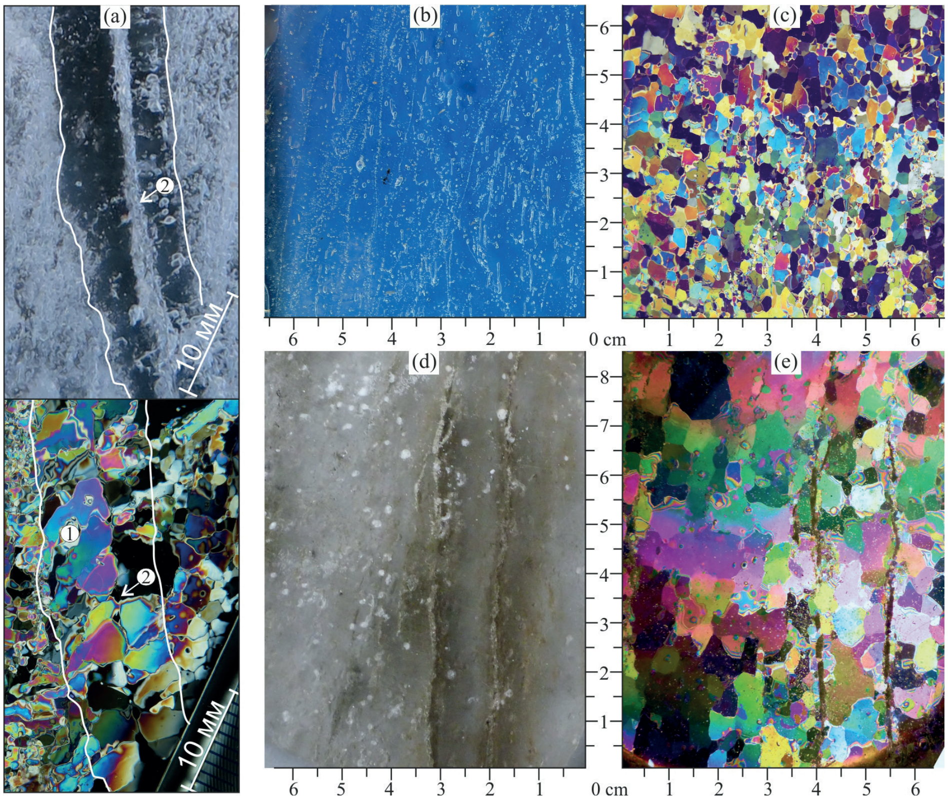

Fig. 6. Ice-wedge petrography, vertical thin section: appearance and texture of ice vein from Pur-Taz interfluve, Northern West Siberia, Russia (a); ice appearance (b) and texture (c) of Holocene ice wedge (>4 m high and 3 m wide) from Pur-Taz interfluve (67°20'N, 078°55'E), Northern West Siberia, Russia (Y.V. Tikhonravova et al., 2020); ice appearance (d) and texture (e) of Pleistocene ice wedge (>4 m high and ~2 m wide) from Gyda area (70°53'N, 078°27'E), Northern West Siberia, Russia (Y.V. Tikhonravova et al. 2019). 1 – ice vein's crystals; 2 – axial seam

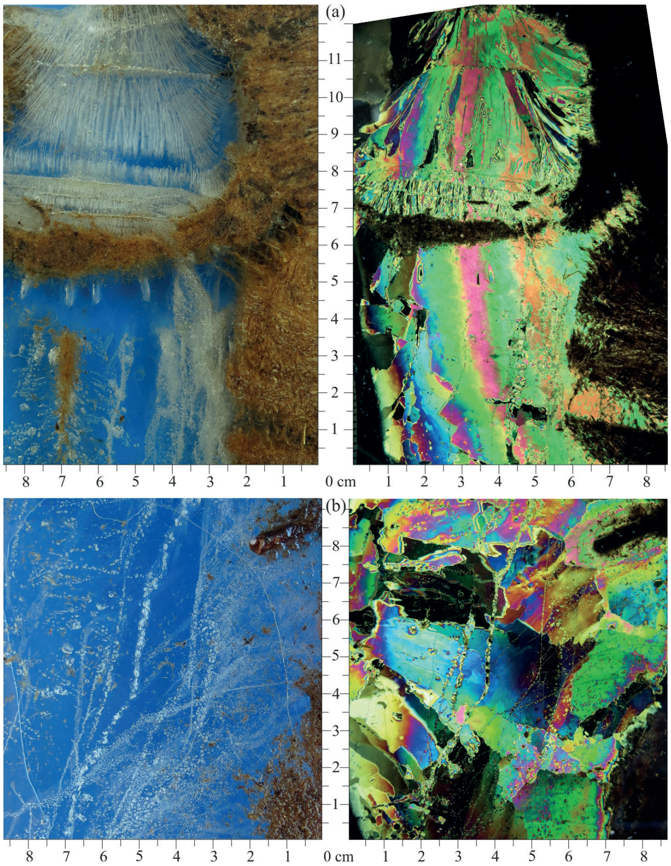

Fig. 7. Appearance and texture of closed-cavity ice from the peatland of Pur-Taz interfluve, Northern West Siberia, Russia: vertical thin sections (a); horizontal thin sections (b)

to the plane of water movement at the time of intrusion (Fig. 8). Sometimes, layering occurs in the form of distinct bubble bands parallel to the overlying ground surface. Injection ice texture is characterised by large tabular crystals oriented normally to the freezing direction (Slagoda et al. 2012). Intrusive ice crystals vary from being small (<1 mm in dimensions) and equidimensional in upper chill zones to large (up to 200 mm long), columnar, and dimensionally oriented parallel to the freezing direction (Rothschild 1985). Shumskii (1964) notes anhedral grains with crystals size from 1-2 cm to 16 cm. Crystal size is mostly dependent on moisture amount and freezing rate. The texture pattern of intrusive ice reflects the groundwater transfer mechanism and freezing conditions. C-axis orientation is random in the upper chill zone and becomes more concentrated with depth becoming preferred normal to the direction of crystal elongation (horizontal) (Pollard and French 1985).

Icing

Icing (aufeis) forms on the ground surface, or on river or lake ice, by freezing of successive flows of water that may seep from the ground, flow from a spring or emerge from below river or lake ice through fractures (Everdingen 2005). The water does not always reach the ground surface; sometimes it spread laterally into or between sediment horizons (Gell 1975). The icing appearance is characterised by foliation in the form of distinct bands of spherical bubbles (Fig. 9a). Bubble sizes and shapes are uniform within a given band but varied from band to band. The bubbles are both inter- and intragranular. Icing texture is characterised mostly by columnar crystals oriented vertically in vertical thin sections; by elongated crystals randomly oriented (Fig. 9b). The crystals are anhedral to subhedral. Small crystals occur in the bubble foliation (Fig.

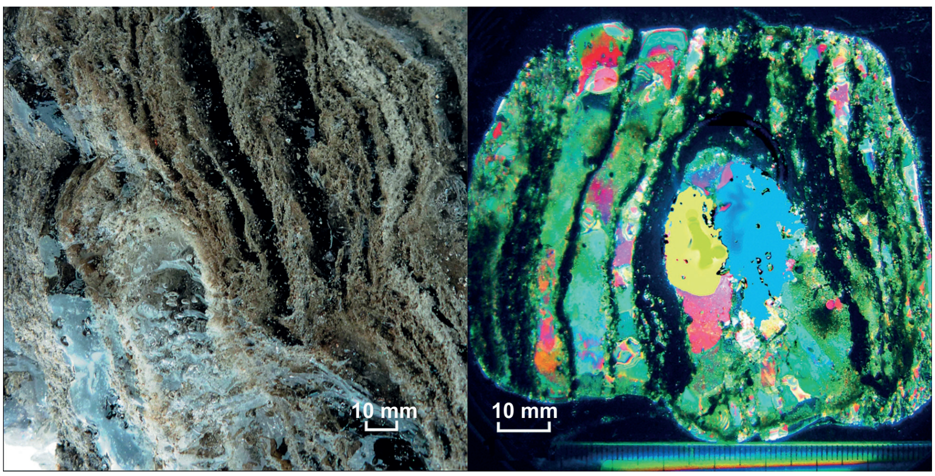

Fig. 8. Appearance and texture of injection-segregated ice (ice laccolith with a teardrop-shaped core and vertically-wavy bands formed mostly sand, Marre-Sale Cape, Western Yamal, Russia), vertical thin section (Slagoda et al., 2012)

9a). A zone of small crystals indicates a chill zone (Gell 1975). Crystal size is variable. In Gell's research (1975), icing crystal size upped to >80 mm. C-axis preferred orientation is orthogonal to the growth direction (Gell 1975).

Snowbank ice

Burial of ice is frequently encountered in the Arctic. Along with glaciers and ice of bulk water (lake, river, and sea), snowbanks can be buried and conserved in deposit. Snowbank ice is characterised by a milky appearance due to a high concentration of circular bubbles. Snowbank texture is presented by small euhedral equigranular crystals (Fig. 10a). The crystal size in the snowbank ranges between 0.1-0.2 mm and 1 mm in diameter, whereas the average crystals in the firn may be up to 3 mm (Shumskii 1964). It is necessary to consider that texture of all surface ice types may change after burial (Fig. 10b). The longer the ice has been buried, the greater are the chances of its transformation.

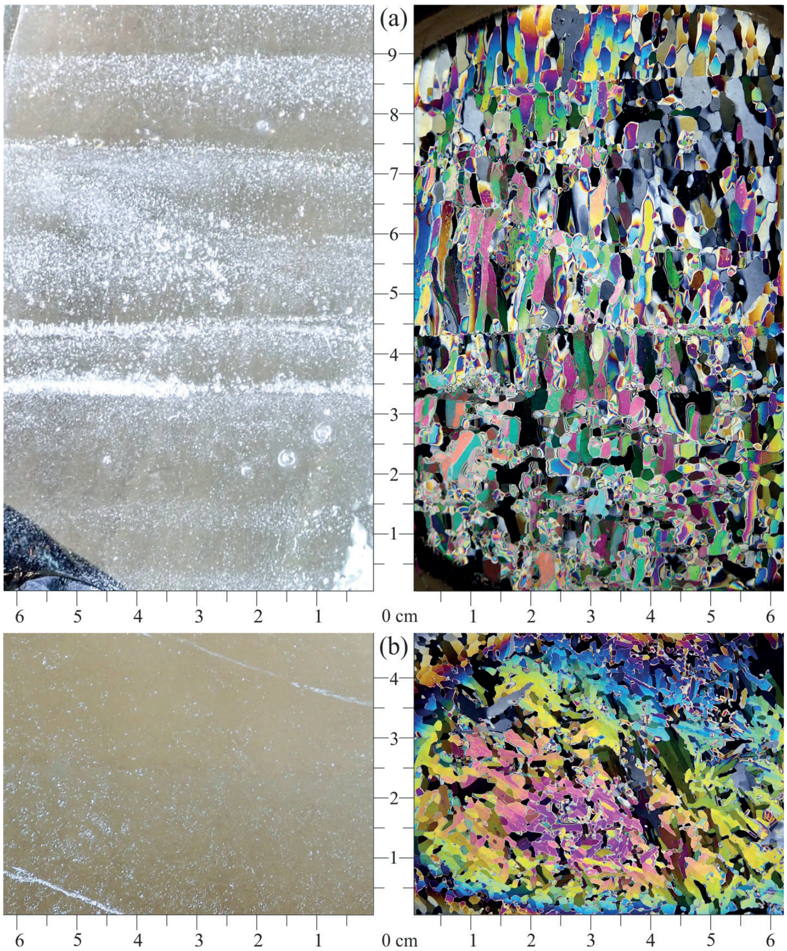

Fig. 9. Appearance and texture of icing from Kyzyl-Syr area, Central Yakutia, Russia: vertical thin sections (a); horizontal thin sections (b)

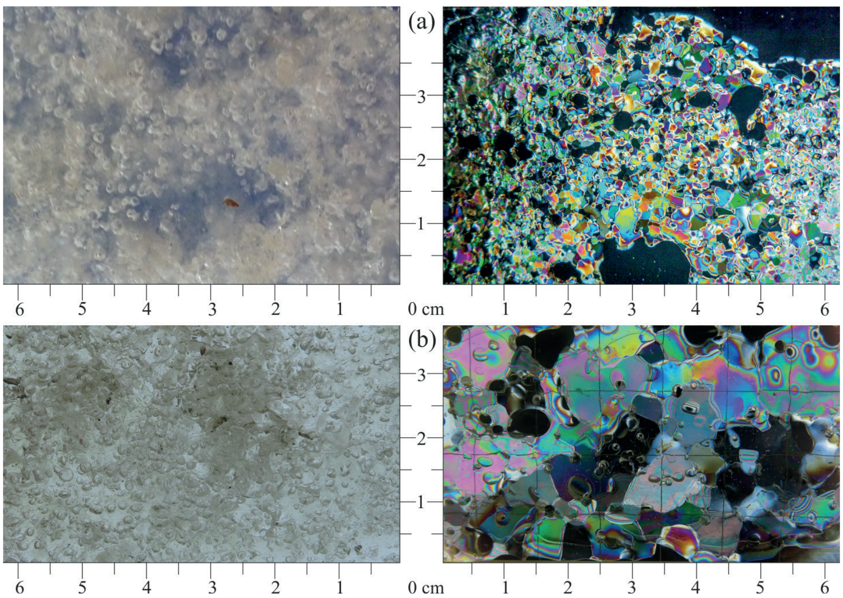

Fig. 10. Appearance and texture of one-year snowbank ice from Marre-Sale Cape, Western Yamal, Russia (a), of buried recrystallized snowbank ice from Central Yamal, Russia (b)

Based on the data analysis of ice appearance, texture features, crystal size, and its orientation, it is possible to conclude that some genetic types of ices are similar in ice texture pattern, and some are difficult to distinguish. The glacier ice is comparable with the old buried snowbank ice; upper part of lake/river/sea ice is comparable with one-year snowbank ice. Whereas other genetic types of ices are highly different and can be distinguished via polarized light or with even visual examination. Wedge ice has a unique feature – the ice vein formed by small crystals directed horizontally to the axial seam. The unique feature of closed-cavity ice is the radial-ray texture. The segregated ice forms a unique cryostructure (from pore ice to suspended cryostructure (Rogov 2009)). Icing appearance is comparable with glacier in foliation, whereas icing texture is different from glacier texture. The icing texture is comparable with ice of bulk water.

Identification of the origin and nature of ground ice is a complicated task for geocryology. An understanding of how the more common types of ice textures and fabrics form aids in the interpretation of petrographic data. The primary features of the ice composition and constitution are controlled mostly by the growth mechanisms of the ice, while the conditions for ice preservation are controlled by the characteristic of enclosing sediments or mode of burial. The constitution of ice may change within a deposit, as shown in the example of buried snowbank ices. This might occur from additional stresses (e.g., sediments pressures, cracking, and creep), changes in ground temperature, and flooding. As a result, the ice may undergo recrystallization (enlarging and rounding of ice crystals) and/or develop a secondary structure (Rothschild 1985) that bears little resemblance to the original texture. This makes it difficult to identify the ice origin. The presence of faults, cracks, strain shadows, grain boundary irregularities and dislocations, and crystal substructure (Rothschild 1985) in ice constitution can be transformation indicators. Crystal substructure includes grain boundary migration, incorporation of smaller crystals within a larger one, and recrystallization (Rothschild 1985). It can occur when a grain is subjected to a bending stress. Dislocations accumulate along walls between different parts of the grain and form subgrain boundaries and substructure patterns, respectively. Therefore, it is important to continue ice studies using petrography methods and collecting characteristics of the different genetic types of ice.

Petrography studies of an ice object help clarify the data interpretation of isotopic and chemical compositions. It is particularly relevant at heterogeneous (formed by several genetic types of ice) ice wedge's study because the different genetic types of ice within an ice wedge produce distorted air paleotemperature assessment by the isotopic signature ($\delta^{18}O$ and δD). The information about winter paleotemperatures preserved in wedge ice is related directly to the mechanism of ice-wedge formation. The ice wedge is formed via fast freezing of mainly meltwater (Lachenbruch 1962) and its isotopic composition reflects air paleotemperature. Fast water crystallization within a thermal contraction crack reduces the fractionation process (Vasil'chuk 1991). Hence, ice wedges are considered to be climate archives for the cold period. Currently, ice wedges cannot provide an absolute quantitative evaluation of past winter temperatures (Galanin 2021), but they can contribute valuable time-averaged information on past climate development (Opel et al. 2018). Meanwhile, if the crystallization mechanism changes, the fractionation process cannot be ignored. The isotopic fractionation depends on source water and soil compositions, soil moisture migration, and freezing conditions. Unfortunately, distinctions between genetic types of ice within ground ice do not always appear in ice wedges' studies. That can produce erroneous inferences. Wedge ice texture may indicate paleoclimatic conditions of ice veins formation (Solomatin and Kryuchkov 1981) and help identify other genetic types of ice (Y.V. Tikhonravova et al. 2019, 2020).

CONCLUSIONS

The petrography method is essential for geocryology and glaciology scientists. Ice petrography studies help produce correct data interpretation of ice-formation mechanism and its metamorphosis, isotopic and chemical compositions. That is of great importance for paleogeographic reconstructions in the permafrost zone. The simplest way to get an ice texture pattern is by using polarized light. Additionally, petrography study has to be continued to accumulate more information about different genetic types of ice. The different ice types have specific features that can help us determine ice genesis. For example, the glacier is often presented by foliation defined by variations in crystal configuration and bubble distribution. Lake ice is characterised by an upper zone of mostly small randomly arranged dendritic and equigranular crystals, which change with increasing depth to large columnar and prismatic crystals. Segregated ice forms a unique cryostructure, and is often characterised by the lamination of crystals. Ice wedge is presented by a vertical-band appearance, and small crystals directed horizontally to axial seam. Closed-cavity ice is characterised by radial-ray appearance produced by elongated ice crystals that can be of different sizes. Injection ice is often distinguished by anhedral crystals, showing the movement of water. Icing is described by foliation and mostly columnar crystals that are comparable with ice crystals of water bulk. Snowbank ice is presented by the high concentration of circular bubbles and small equigranular crystals that may transform after burial.

The ice constitution may change due to metamorphism within the permafrost. It may undergo recrystallization or develop a secondary structure. More work remains to be done to distinguish genetic types of ice.

REFERENCES

Bonath V., Petrich C., Sand B., Fransson L. and Cwirzen A. (2018). Morphology, internal structure and formation of ice ridges in the sea around Svalbard. Cold Regions Science and Technology, 155, 263-279, DOI: 10.1016/j.coldregions.2018.08.011.

Bruneau S., Sullivan A., Zhang Z. and Colborne B. (2015). Ice-microtome design for procurement and crystal analysis of ice thin sections. 25th CANCAM.

Calmels F., Clavano W.R. and Froese D.G. (2010). Progress on X-ray computed tomography (CT) scanning in permfrost studies. 63rd Canadian Geotechnical Conference & 6th Canadian Permafrost Conference, January, 1353-1358.

Coulombe S. and Fortier D. (2015). Cryofacies and cryostructures of massive ice found on Bylot Island , Nunavut. 68e Conférence Canadienne de Géotechnique et 7e Conférence Canadienne Sur Le Pergélisol, 20 Au 23 Septembre 2015, Québec, Québec., August 2016.

Coulombe S., Fortier D., Lacelle D., Kanevskiy M. and Shur Y. (2019). Origin, burial and preservation of late Pleistocene-age glacier ice in Arctic permafrost (Bylot Island, NU, Canada). Cryosphere, 13(1), 97-111, DOI: 10.5194/tc-13-97-2019.

Dillon M., Fortier D., Kanevskiy M. and Shur Y. (2008). Dillon-2008. Ninth International Conference on Permafrost, 361-366.

Diprinzio C.L., Wilen L.A., Alley R.B., Fitzpatrick J.J., Spencer M.K. and Gow A.J. (2005). Fabric and texture at Siple Dome, Antarctica. Journal of Glaciology, 51(173), 281-290, DOI: 10.3189/172756505781829359.

Everdingen, R. O. van, ed. (2005). IPA – Multi-language glossary of permafrost and related ground - ice terms.

Faria S.H., Weikusat I. and Azuma N. (2014a). The microstructure of polar ice. Part I: Highlights from ice core research. Journal of Structural Geology, 61, 2–20, DOI: 10.1016/j.jsg.2013.09.010.

Faria S.H., Weikusat I. and Azuma N. (2014b). The microstructure of polar ice. Part II: State of the art. Journal of Structural Geology, 61, 21-49, DOI: 10.1016/j.jsg.2013.11.003.

Fortier D., Kanevskiy M., Shur Y., Stephani E., Dillon M. and Jorgenson M.T. (2012). Cryostructures of Basal Glacier Ice as an Object of Permafrost Study: Observations from the Matanuska Glacier, Alaska. 10th International Conference on Permafrost, 107-112, DOI: 10.13140/2.1.4876.2569.

French H.M. (2007). The Periglacial Environment. In: Angewandte Chemie International Edition, 6(11), 951-952. , third. Addison Wesley Longman Limited, John Wiley and Sons; Hoboken.

French H.M. and Harry D.G. (1988). Nature and origin of ground ice, Sandhills Moraine, southwest Banks Island, Western Canadian Arctic. Journal of Quaternary Science, 3(1), 19-30, DOI: 10.1002/jqs.3390030105.

French H.M. and Harry D.G. (1990). Observations on buried glacier ice and massive segregated ice, western arctic coast, Canada. Permafrost and Periglacial Processes, 1(1), 31-43, DOI: 10.1002/ppp.3430010105.

French H.M. and Pollard W.H. (1986). Ground-ice investigations, Klondike District, Yukon Territory. Canadian Journal of Earth Sciences, 23, 550-560.

Galanin A.A. (2021). About the incorrectness of Yu.K. Vasil'chuk's method for the reconstruction of paleotemperatures using isotope composition of wedge ice. Review of the article by Yu.K. Vasil'chuk, A.C. Vasil'chuk "Air January paleotemperature reconstruction 48–15 calibrat. Earth's Cryosphere, 2, 62–75, DOI: 10.15372/KZ20210206 (in Russian with English summary).

Gell A.W. (1973). Ice petrofabrics, Tuktoyaktuk, N.W.T., Canada. Liverpool University.

Gell A.W. (1975). Underground ice in permafrost, Mackenzie. Delta -Tyktoyaktuk Peninsula. N.W.T. the University of British Columbia.

Gilbert G.L., Kanevskiy M. and Murton J.B. (2016). Recent Advances (2008–2015) in the Study of Ground Ice and Cryostratigraphy. Permafrost and Periglacial Processes, 27(4), 377-389, DOI: 10.1002/ppp.1912.

Golubev V.N. (2000). Structural Glaciology. Cogelation ice structure. MSU. (In Russian).

Golubev V.N. (2014). Formation of ice cover on fresh-water reservoirs and water courses. Vestnik MGU. Series 5. Geography, 2, 9-16. (In Russian).

Gorgutsa R., Ksenofontova D. and Sokolov A. (2016). The Effect of S alinity and Structure of Ice on Its Strength. Polar Mekhanics, 43–53. (In Russian).

Gow A.J., Meese D.A., Alley R.B., Fitzpatrick J.J., Anandakrishnan S., Woods G.A. and Elder B.C. (1997). Physical and structural properties of the Greenland Ice Sheet Project 2 ice core: A review. Journal of Geophysical Research: Oceans, 102(C12), 26559-26575, DOI: 10.1029/97JC00165.

Hill J.R. and Lasca N.P. (1975). An improved method for determining ice fabrics. Journal of Glaciology, 10(58), 113-138.

Hudleston P.J. (2015). Structures and fabrics in glacial ice: A review. Journal of Structural Geology, 81, 1-27, DOI: 10.1016/j.jsg.2015.09.003.

Kanevskiy M., Shur Y., Jorgenson T., Brown D.R.N., Moskalenko N., Brown J., Walker D.A., Raynolds M.K. and Buchhorn M. (2017). Degradation and stabilization of ice wedges: Implications for assessing risk of thermokarst in northern Alaska. Geomorphology, 297, 20-42, DOI: 10.1016/j.geomorph.2017.09.001.

Katasonov E. and Ivanov M. (1973). Cryolithology of Central Yakutia. Guidebook of 2nd International Conference on Permafrost. (In Russian).

Katasonov E.M. (1975). Frozen-ground and facial analysis of Pleistocene deposits and paleogeography of Central Yakutia. Biuletyn Peryglacjalny, 24, 33-40. (In Russian).

Kawano Y. and Ohashi T. (2006). Numerical simulation of development of sea ice microstructure by Voronoi dynamics technique. The 18th IAHR International Symposium on Ice, 97-103.

Kipfstuhl S., Hamann I., Lambrecht A., Freitag J., Faria S.H., Grigoriev D. and Azuma N. (2006). Microstructure mapping: a new method for imaging deformation-induced microstructural features of ice on the grain scale. Journal of Glaciology, 52(178), 398-406, DOI: 10.3189/172756506781828647.

Kotlyakov V.M., ed. (1984). Glaciological dictionary. Gidrometeoizdat. (In Russian).

Lachenbruch A.H. (1962). Mechanics of thermal contraction cracks and ice-wedge polygons in permafrost. Geological Society of America Special Papers, 70, 69.

Langway C.C. (1958). Ice fabrics and the universal stage. In: US Amy, Snow and Ice Research Establishment, 62.

Leffingwell E.K. (1915). Ground Ice-Wedge – the Dominant Form of Ground Ice on the North Coast of Alaska. J. Geol., 23(7), 635-654.

Lein A.Y., A.S. S., Leibman M.O. and Perednya D.D. (2005). Ice Record: an Example of Deciphering Using Isotopic Tracers. Priroda, 7, 25-34.

Mackay J.R. (2000). Thermally induced movements in ice-wedge polygons, western Arctic coast: a long-term study. Geographie Physique et Quaternaire, 54(1), 41-68.

Minchew B.M., Meyer C.R., Robel A.A., Gudmundsson G.H. and Simons M. (2018). Processes controlling the downstream evolution of ice rheology in glacier shear margins: case study on Rutford Ice Stream, West Antarctica. Journal of Glaciology, 64(246), 583-594, DOI: 10.1017/jog.2018.47.

Murton J. (2013). Permafrost and periglacial features: ice wedges and ice-wedge casts. In: Encyclopedia of Quaternary Science, 436-451. Elsevier, DOI: 10.1016/b978-0-444-53643-3.00097-2.

Opel T., Meyer H., Wetterich S., Laepple T., Dereviagin A. and Murton J. (2018). Ice wedges as archives of winter paleoclimate: A review. Permafrost and Periglacial Processes, 29(3), 199-209, DOI: 10.1002/ppp.1980.

Orekhov P.T., Popov K.A., Slagoda E.A., Kurchatova A.N., Tikhonravova Y.V., Opokina O.L., Simonova G.V. and Melkov V.N. (2017). Frost mounds of bely island in coastal marine settings of the Kara Sea. Earth's Cryosphere, 21(1), 46-56, DOI: 10.21782/KZ1560-7496-2017-1(46-56). (In Russian).

Ostrem G. (1963). Comparative crystallographic studies on ice from ice-cored moraines, snowbanks and glaciers. Geografiska Annaler, 45(4), 210-240.

Petrich C. and Eicken H. (2010). Growth, Structure and Properties of Sea Ice. In: N. T. David and S. D. Gerhard eds., Sea Ice , Second, 23-78. Blackwell.

Pewe T.L. (1967). Quaternary geology of Alaska. In: Angewandte Chemie International Edition, 6(11), 951-952. United States Government Printing Office, DOI: 10.3133/pp835.

Pollard W. (1990). The nature and origin of ground ice in the Herschel Island area, Yukon Territory. The Fifth Canadian Conference on Permafrost, 23-30. http://pubs.aina.ucalgary.ca/cpc/CPC5-23.pdf.

Pollard W.H. and French H.M. (1985). The Internal Structure and Ice Crystallography of Seasonal Frost Mounds. Journal of Glaciology, 31(108), 157-162, DOI: 10.3189/s0022143000006407.

Popov A.I. (1955). The origin and development of a thick fossil ice. USSR Academy of Sciences. (In Russian).

Popov A.I., Rozembaum G.E. and Tumel' N.V. (1985). Cryolithology. MSU. (In Russian).

Rogov V.V. (1996). Classification of structures of ground ice. Vestnik MGU. Series 5. Geography, 3, 93-101. (In Russian).

Rogov V.V. (2009). Fundamentals of Cryogenesis. Geo. (In Russian).

Romanovsky N.N. (1959). On the question about syngenetic ice wedge formation. Glaciological Studies during the MGG (1), 83-86. (In Russian).

Rothschild A. (1985). Ground ,Ice Petrography, Sand Hills Moraine, Southern Banks Island, N.W.T. In: Psychology. University of Ottawa.

Savel'ev B.A. (1963). Guide to the study of the ice characteristic. Moscow State University. (In Russian).

Savel'ev B.A. (1980). Structure and Composition of Natural Ice. Moscow State University. (In Russian).

Schindelin J., Arganda-Carreras I., Frise E., Kaynig V., Longair M., Pietzsch T., Preibisch S., Rueden C., Saalfeld S., Schmid B., Tinevez J.Y., White D.J., Hartenstein V., Eliceiri K., Tomancak P. and Cardona A. (2012). Fiji: An open-source platform for biological-image analysis. Nature Methods, 9(7), 676-682, DOI: 10.1038/nmeth.2019.

Seligman G. (1950). Instruments and Methods: Improvement in Making Rubbings of Glacier Crystals. Journal of Glaciology, 1(7), 361-361, DOI: 10.3189/S0022143000012533.

Sher A. and Kaplina T. (1979). Late Cenozoic of the Kolyma Lowland. Tour XI Guidebook, XIV Pacific Science Conference, Khabarovsky, USSR Academy of Sciences, 115. (In Russian).

Shumskii P. (1960). About ice wedge formation. In: Articles collection of Melnikov Permafrost Institute AS USSR, 81-97.

Shumskii P.A. (1964). Principles of Structural Glaciology. Dover. (In Russian).

Slagoda E., Opokina O., Rogov V. and Kurchatova A. (2012). Structure and genesis of the underground ice in the Neopleistocene-Holocene sediments of Marre-Sale Cape, Western Yamal. Earth's Cryosphere, 16(2), 9-22. (In Russian with English summary).

Solomatin V.I. (1965). About the ice-wedge structure. In: Ground ice, 46-72. Moscow State University. (In Russian).

Solomatin V.I. (1986). Petrology of Ground Ice. Academy Nauk. (In Russian).

Solomatin V.I. (2013). Physics and geography of underground glaciations. Geo. (In Russian).

Solomatin V.I. and Kryuchkov M.V. (1981). Ice veins of ice wedges and reconstruction of paleotemperature of ice formation. Problems of Cryolithology, 9, 179-183. (In Russian).

son Ahlmann H.W. and Droessler E.G. (1949a). Glacier Ice Crystal Measurements at Kebnekajse, Sweden. Journal of Glaciology, 1(5), 269-274, DOI: 10.3189/002214349793702665.

son Ahlmann H.W. and Droessler E.G. (1949b). Glacier Ice Crystal Measurements at Kebnekajse, Sweden. Journal of Glaciology, 1(5), 269-274, DOI: 10.3189/002214349793702665.

St-Jean M., Lauriol B., Clark I.D., Lacelle D. and Zdanowicz C. (2011). Investigation of ice-wedge infilling processes using stable oxygen and hydrogen isotopes, crystallography and occluded gases (O2, N2, Ar). Permafrost and Periglacial Processes, 22(1), 49-64, DOI: 10.1002/ppp.680.

Tikhonravova Y.V., Lupachev A.V., Slagoda E.A., Rogov V.V., Kuznetsova A.O., Butakov V.I., Simonova G.V., Taratunina N.A. and Mullanurov D.R. (2019). Structure and formation of ice-ground veins of the second lake-alluvial terrace in the North of Gydan in the late Neopleistocene–Holocene. Ice and Snow, 59(4), 557-570, DOI: 10.15356/2076-6734-2019-4-367 (In Russian with English summary).

Tikhonravova Y.V., Slagoda E.A., Rogov V.V., Butakov V.I., Lupachev A.V., Kuznetsova A.O. and Simonova G.V. (2020). Heterogeneous ices in ice wedges structure on the Pur-Taz interfluve peatlands (The North West Siberia, Russia). Ice and Snow, 60(2), 225-238, DOI: 10.31857/S2076673420020036. (In Russian with English summary).

Tikhonravova Y.V., Slagoda E.A., Rogov V.V., Galeeva E.I. and Kurchatov V.V. (2017). Texture and structure of the Late Holocene ground ice in the Northern West Siberia. Led I Sneg-Ice and Snow, 57(4), 553-564, DOI: 10.15356/2076-6734-2017-4-553-564. (In Russian with English summary).

Tikhonravova Ya.V. (2021). The problem of isotope-oxygen determination in heterogeneous ice wedges. Sixth Forum for Young Permafrost Scientists «Current Challenges and Future Prospects for Geocryology», June 28 –July 13, 2021, 66-68. (In Russian).

Tyshko K., Cherepanov N. and Fedotov V. (2000). Crystallian structure of sea ice cover. Gidrometeoizdat. (In Russian).

Vasil'chuk Y. (1991). Reconstruction of the paleoclimate of the Late Pleistocene and Holocene on the basis of isotope studies of subsurface ice and waters of the permafrost zone. Water Resources, 17(6), 640-647.

Vtyurin B. (1975). Ground ice of the USSR. Nauka. (In Russian).

Vtyurin B. and Vtyurina E. (1960). Winter observations on formation and behavior of thermal-contraction crack within ice wedge. In: Data of general geocryology, 98-105. AS USSR. (In Russian).

Wheeler J., Prior D., Jiang Z., Spiess R. and Trimby P. (2001). The petrological significance of misorientations between grains. Contributions to Mineralogy and Petrology, 141(1), 109-124, DOI: 10.1007/s004100000225.

Wilen L.A., Diprinzio C.L., Alley R.B. and Azuma N. (2003). Development, principles, and applications of automated ice fabric analyzers. Microscopy Research and Technique, 62(1), 2-18, DOI: 10.1002/jemt.10380.

RESEARCH PAPER

LANDSCAPE INDICATION OF PERMAFROST CONDITIONS FOR GEOECOLOGICAL ASSESSMENT & MAPPING AT VARIOUS SCALES

Larisa I. Zotova
Faculty of Geography, Lomonosov Moscow State University, Moscow 119991, Russia
Corresponding author: zotlar@mail.ru
Received: April 5th, 2021 / Accepted: November 9th, 2021 / Published: December 31st, 2021
https://doi.org/10.24057/2071-9388-2021-039

ABSTRACT. In this paper, the features of landscape indication of permafrost characteristics required for assessing the environmental state at various research scales are discussed. A number of permafrost characteristics affect the geoecological state and stability of natural landscapes, especially in the context of climate warming and technogenic surface disturbances. These include the distribution, temperature regime, thickness and cryogenic structure of permafrost, seasonal freezing and thawing, as well as the development of cryogenic processes. Their determination through the landscape view, however, is ambiguous. The choice of certain permafrost characteristics for geoecological assessment is based on many years of experience in creating cryo-ecological maps on a landscape basis by the school of Faculty of Geography, Moscow State University. The recent studies on the identification of regional cryoindicators are analyzed, including the issues of cryogenic landscapes classification and clarification of the boundaries of geocryological zones using the landscape structural method. The content of the two maps, «Permafrost Landscape Differentiation Map of the Russia Cryolithozone» at a scale of 1: 15,000,000 and «Permafrost Landscape Map of the Republic of Sakha (Yakutia)» at a scale of 1: 1,500,000, is presented, as well as their use as a basis for environmental planning and geoecological assessment.

KEYWORDS: permafrost; cryolithozone; landscape indication, cryogenic processes, geoecological mapping

CITATION: Larisa I. Zotova (2021). Landscape Indication Of Permafrost Conditions For Geoecological Assessment & Mapping At Various Scales. Geography, Environment, Sustainability. Vol.14, No 4, p. 33-40
https://doi.org/10.24057/2071-9388-2021-039

ACKNOWLEDGMENTS: This study was supported by State Assignment «The cryosphere evolution under climate change and anthropogenic impact» No. 121051100164-0 and Russian Foundation for Basic Research No. 18-05-60080. The author expresses deep gratitude to Nelly Tumel for ideas, guidance and many years of collaboration. Many thanks to editors and anonymous reviewers for their helpful comments that improved the manuscript.

Conflict of interests: The authors reported no potential conflict of interest.

INTRODUCTION

Landscape indicators related to permafrost characteristics have found wide application in scientific research and survey, especially in engineering and geocryological mapping. The method is based on the relationship between the external appearance of landscape components and their internal structure followed by interpretation based on reliable indicators (Viktorov and Chikishev 1990). The relief, vegetation and ground cover are the most indicative physiognomic components of the landscape.

Since the 1930s, landscape indication of the permafrost state has been used in different regions, especially if the information on the research subject was limited. V. Tumel (1945), A. Tyrtikov (1956, 1969) and V. Kudryavtsev (1961) were the first scientists to point out the benefits of this landscape indication method in permafrost studies. In 1960, I. Baranov (1960) compiled the first landscape-based geocryological map of the USSR at a scale of 1:10,000,000. In the 1970s, the first surveys and mapping using the landscape indication method were carried out in Alaska (Everett et al.1978), Canada and in the north of Western Siberia (Melnikov et al.1974). A special place in landscape indication studies of permafrost is occupied by the pioneering developments of E. Melnikov (1983) on the taxonomy and classification of landscapes in the north of Western Siberia.

The permafrost landscape indication is the main method of geocryological mapping at all scales. It is an important research tool for the interpretation of remote sensing data, as well as studying the dynamics and evolution of permafrost, including the problems caused by the current climate warming. This article considers some ecological aspects of this method for assessing and mapping the permafrost zone.

Ambiguity of landscape indication

The development of landscapes within the permafrost zone and their recovery after disturbances largely depends on the properties of permafrost, which include the permafrost distribution, temperature and thickness, ground ice composition, depth of seasonal thawing-freezing and presence of cryogenic processes. These parameters are usually used as criteria for the classification and mapping of permafrost landscapes. However, not all of these features are equally amenable to landscape indication.

Permafrost distribution. In the continuous permafrost zone, taliks under river beds and lakes are present, while outside this zone, islands of frozen rocks, in which permafrost is primarily formed and preserved, can be found. Accordingly, a reliable indicator of permafrost distribution is peat and peat landscapes. Permafrost develops in these landscapes because in summer, due to the high heat capacity of water, peat prevents soil heating, while in winter high ice content determines the soil thermal conductivity and its intense cooling.

For the *permafrost average annual temperature*, there is no indicator. Only a qualitative assessment of the heat content can be given based on the physiognomy of a landscape: the coldest or the «warmest» permafrost areas can be identified.

Permafrost thickness is poorly amenable to landscape indication, except for the southern isolated permafrost zone. In conditions of continuous permafrost distribution and its significant thickness (more than 100 m, up to 500-700 m), the indication is impossible.

Permafrost ice content is an indicated characteristic since it depends primarily on the composition of rocks, which is quite simple to distinguish based on vegetation using aerial and satellite images. At any scale, the ice content increases from minimum to maximum values is as follows: bedrocks – sand – sandy loam – loam – peat. On a small scale, this is a fairly reliable indicator, but on a large scale, the composition of rocks is insufficient to indicate their ice content. Within one lithological type, it is necessary to know the genesis of rocks, which determines moisture (ice content). For example, ice content in lacustrine loams is much higher than in moraine loams.

Depth of seasonal thawing/freezing is usually mapped on a medium to large scale. Tundra vegetation is clearly correlated with the depth of seasonal thawing. However, without field studies of the active layer depth, its interpretation is possible only at the qualitative level – deep, medium, shallow, etc. The primary indicator of the depth is the composition of rocks. This is followed by the presence of moss vegetation cover. The latter is an indisputable indicator of shallow thawing. For seasonal freezing, vegetation is replaced by snow cover.

Cryogenic processes such as thermokarst, thermoerosion, solifluction, etc., usually create forms of meso- and micro-relief, which are easily recognized on images and mapped on large and medium scales. To identify these processes, a complex of geomorphological indicators is used, which includes the relief dissection, presence of lake depressions and small erosional forms, nature of the meso- and microrelief, as well as the appearance of landscapes along with the hydrographic network. These indicators have their own set of features – a characteristic color, tone, structure, pattern, etc.

Cryogenic landforms, which develop as a result of a certain process, are indicated on any scale with one caveat. The larger are these forms, the more reliable is their identification. Cryogenic relief is the most significant indicator of geocryological zoning in the northern territories. In the southern permafrost zone, it is mainly represented by vast areas occupied by frost heave mounds in the growth stage; in the north, there is ancient polygonal block relief (Osadchaya and Tumel 2012). The most reliable landscape indicator of cryogenic processes is the tundra zone. Forested permafrost is a very difficult object to interpret. Within its boundaries, depending on the region, only some physiognomic landscapes work. In Western Siberia, for example, these are lacustrine-bog landscapes; in Central Yakutia – negative landforms, alases; in Transbaikalia – slope exposure.

Indicators of relief-forming processes in different regions of the Russian permafrost zone are well studied and published in scientific literature. For Western Siberia, these are the works of E. Melnikov et al (1974), N. Ukraintseva et al (2011), M. Pupyrev (2013) and others. For the European North – the works of G. Osadchaya (2012,2015), F. Rifkin et al (2008), for Yakutia – numerous works of the Permafrost Institute (Fedorov 1991; Fedorov et al. 2004; Shestakova 2011; Torgovkin 2005, etc.). A. Kizyakov and M. Leibman (2016) published a review of 110 publications of Russian and international researchers devoted to the study of cryogenic relief-forming processes.

Reliability of landscape indication in the permafrost zone increases from north to south which is explained by the increasing role of vegetation cover in the indication. In the north of cryolithozone, the value of geobotanical indicators is not so high and landscape indication of temperature conditions depends to a greater extent on the relief. The most reliable indicators in the permafrost zone are the external appearance of the landscape, its pattern and combinations with each other (Viktorov and Chikishev 1990; Tumel and Zotova 2017).

The landscape permafrost classification

The level of detail used for the indicators is determined by the research scale. When creating maps on a small scale for evaluation, strategic and scientific purposes, indicators at the level of landscapes are used. On a larger scale, at the design stages for specific engineering projects, the type of terrain, tracts and facies are analyzed. Thus, only natural complexes of a certain rank can reliably characterize the geocryological situation. For example, in the area of the Spasskaya Pad station near the city of Yakutsk, based on long-term studies it was established that, at the local level, the type of natural boundaries (tracts) is a good indicator of thickness and moisture content of the seasonally thawed layer. On a medium scale, the differentiation of landscapes according to the cryogenic structure and ice content, annual mean temperature of rocks and seasonally thawed layer thickness is well indicated by the type of terrain. Higher rank geosystems used in small-scale research (1: 5,000,000) in the basin of the Lena River only allowed to reveal the nature of frozen and thawed rocks distribution (Torgovkin 2005).

The functioning of landscapes in the permafrost zone and their transformation after disturbances largely depends on the permafrost properties – frozen rocks distribution, their temperature regime, cryogenic structure, ice content and active layer thickness, which are used as the lithocryogenic factors of landscapes stability. A striking example of their practical use in classification and mapping is the digital version of the «Permafrost landscape map of the Republic of Sakha (Yakutia) at a scale of 1: 1,500,000.

The map was compiled in ArcGIS 10.1 based on the interpretation of Landsat and Modis satellite imagery and a specialized base of geocryological data with more than 800 geocryological observation points, including individual geothermal wells. In total, 20 types of terrain and 36 types of plant groupings were identified, the combination of which made it possible to systematize 145 types of permafrost landscape (Fedorov et al. 2018).

To develop the classification, the authors used permafrost criteria corresponding to taxonomic units. The type of landscape corresponds to the nature of permafrost distribution; types of terrain (identified by the stratigraphic-genetic complex) – to the cryogenic structure and ice content in the sediments; types of tracts and facies – to the temperature of rocks and active layer thickness. In this case, geological and geomorphological factors (rank of terrain types) were compared with vegetation groups. This permafrost landscape classification can serve as a basis for assessing the resilience of landscapes to climate change and anthropogenic impact in this region. The unified matrix legend (Fig.1) allows to quickly determine physiographic and permafrost characteristics of the selected landscapes. This map introduces new methodological and classification solutions.

Forecasting indication studies of permafrost conditions

In recent years, a number of scientists have carried out significant studies to identify tracts as indicators of permafrost conditions in various regions to optimize environmental management in the permafrost zone (Osadchaya 2012, 2015; Medvedkov 2018; Shestakova 2011; Makarycheva 2015 etc.).

For example, based on the detailed long-term studies in the European North-East, it has been established that in this region peatlands are a universal cryoindicator of geocryological zoning. Their characteristics were used to clarify the boundaries between geocryological subzones. On the border between the sporadic and isolated permafrost, the change of subzones is indicated by the appearance of flat-topped polygonal peatlands, while on the border between discontinuous and continuous permafrost, an abrupt disappearance of dome-shaped peatlands and appearance of polygonal ones can be observed. As a result, the Bolshezemelskaya tundra geocryological map at a scale of 1: 1,000,000 was compiled and environmental restrictions on nature management were formulated taking into account the differences in permafrost landscapes (Osadchaya 2012, 2015).

The response of landscapes in the boreal isolated zone of permafrost rocks in the Yenisei River basin to climate warming was determined based on reliable indicators of their frozen and thawed state. The number of biogenic landforms in the landscape structure of this subzone increases and the processes of solifluction and kurum desertification are intensified (Medvedkov 2018).

A separate field of studies is focused on the indication of the temperature of rocks along with the thickness of seasonally thawed and protective layers using the successive stages of vegetation development after an external impact. The well-known monograph by N. Moskalenko (1999) describes a technique for constructing ecological genetic series of phytocenoses on the example of Western Siberia northern natural zones. The work of Shestakova (2011) is devoted to mapping geocryological conditions based on the identification of the vegetation succession series on different scales. For example, in a comparative analysis of natural and disturbed landscapes of the Prilenskoye plateau, it was found that the temperature of frozen rocks in new successions increases by 1°C, and the seasonal thaw layer thickness increases by 0.5–1.0 m compared to natural ones. These works make it possible to model the development of permafrost landscapes after disturbance, which is necessary for predicting and assessing environmental impact.

From the regional perspective, the work on the identification of thermokarst phenomena in the southern permafrost zone within the route «Eastern Siberia-Pacific Ocean» should be noted. Based on the interpretation of aerial images, the areas with loose cover and presence of ice were identified, indicating all types of thermokarst phenomena, which are confined to peatlands, bush mari, river floodplains, etc. As a result, the zoning of the oil pipeline 3 km buffer zone was carried out over more than 2,600 km in order to locate the observation points for monitoring thermokarst processes (Makarycheva 2015).

It is known that the dynamics of thermokarst lakes is considered as an indicator of climate change in the Arctic regions (Kravtsova and Tarasenko 2011). The reliability of this indication is confirmed by the spatial data obtained from a series of satellite images and the results of their automatic interpretation using the ERDAS Imagine package combined in ArcGIS (Kravtsova and Rodionova 2016). Remote sensing data have been widely used for monitoring thermokarst lake dynamics not only in the Russian permafrost zone but also in Alaska, Canada, China and Sweden (Kizyakov and Leibman 2016). The established decrease in the surface area of lakes (due to the formation of coastal strips with floating bog vegetation) has the paramount importance in the context of active thermokarst development (Chen et al. 2013). Thermokarst

Terrain type	Designation	Stratigraphic-genetic complex	Prevailing criogenic textures and trapped ice	Volumetric ice content	Basic cryogenic processes	Tundra			
						Tundra in continuous cryolithozone			
						Arctic tundra grassinoid	Typical tundra low shrub/lichen and moss	Scutherm tunra shrub	Sparse vegetation of marshes
						1	2	3	4
Marshes		mH, mH1-2	Massive, lenticular	<0.2...0.2-0.4	Frost cracking, heaving	-11...-13 / 0.2-0.4			-11...-13 / 0.2-0.6
Low terrace		aH, aIII-H	Massive, lenticular, layered; Hclocene ice wedges	0.2-0.4	Frost cracking, thermokarst, heaving				
Mid terrace		aII-III	Massive, rarely sheet ice	0.2-0.4	Frost cracking, thermosuffusion	-10...-12 / 0.2-0.4	-8...-10 / 0.3-0.5	-6...-8 / 0.5-0.8	
Inter-ridge-lowland		aII-III, bH	Massive, lenticular, layered	0.2-0.4 (0.6)	Frost cracking, thermokarst, heaving				
High terrace		aI, aI-II	Massive	<0.2...0.2-0.4	Frost cracking			-6...-8 / 0.5-0.8	
Old terrace		lpH, LH	Massive, cortiical, lenticular	<0.2...0.2-0.4	Frost cracking				
Inter-alas		LedIII, laII-III,aIII	Layered, lenticular, reticular; Pleistocene ice wedges	0.4-0.6 (0.8)	Thermokarst	-10...-12 / 0.2-0.4	-8...-10 / 0.3-0.5	-7...-8 / 0.4-0.6	

Fig. 1. Fragment of the legend to Permafrost Landscape Map of the Republic of Sakha (Yakutia) (Fedorov et al. 2018)

lakes tend to increase in number and size within the continuous permafrost zone and decrease in its more southern parts (Jones et al. 2011). Thus, the response of thermokarst to recent climate warming shows no uniform trend for the permafrost zone. In the context of climate change, methods for mathematical modeling of the landscape morphology in thermokarst lake and erosion plains are being developed. (Victorov et al. 2015).

The landscape indication method is widely used in international monitoring programs TSP (Thermal State of Permafrost) and CALM (the Circumpolar Active Layer Monitoring) – the world's main information sources on the permafrost temperature as well as seasonal freezing and thawing layer (Brown et al. 2000). CALM monitoring network, established in the late 1990s, observes the long-term response of the active layer and near-surface permafrost to changes and variations in climate at more than 125 sites distributed in both hemispheres. Several groups of sites are used to create regional maps of the active layer thickness (Ukraintseva et al.2011; Maslakov et al. 2019 etc.)

Permafrost landscape structure

In the permafrost area mapping one more indicator is used – the landscape structure, which characterizes its spatial organization. Taking this indicator into account, the boundaries of regions, zones, and provinces can be identified more reliably based on inter-component relationships (Osadchaya et al.2016). Secondly, more informed decisions on the economic development of a particular region can be made when considering possible environmental risks of nature management related to the complex differentiation of permafrost landscapes (Osadchaya and Hohlova 2013).

Application of the landscape indication method on a small scale can be seen in «Permafrost Landscape Differentiation Map of the Russia Cryolithozone» on a scale of 1: 15,000,000 (Fig. 2), compiled based on the A. Isachenko's map on a scale of 1: 4,000,000. The permafrost characteristics were obtained from the synthesis of geocryological maps on scales of 1: 2,500,000 (1997) and 1: 5,000,000 (1977), Permafrost landscape map of Yakut ASSR on a scale of 1: 2,500,000 and a number of maps from regional atlases.

In terms of permafrost distribution (% of the area occupied by permafrost), four types of areas can be defined: with continuous (> 95%), discontinuous (50-95%), sporadic (10-50%), isolated (<10%) distribution. Permafrost distribution is shown on the map with a colored background, types of landscapes – with indices and boundaries of different thickness. Figure 3 shows the 23 zonal landscape types, which are subdivided into regional sectors (European, Siberian, Far Eastern, etc.) denoted by letters (Tumel and Zotova 2017).

The comparison of regions with four main types of permafrost distribution and zonal types of landscapes within their boundaries was made back in 1954 by I. Baranov. N. Tumel and N. Koroleva (2008) conducted a similar analysis on their map using modern GIS technologies and have got interesting conclusions. For example, several tundra and taiga landscapes are found in each permafrost subzone (from continuous to isolated), which means that they cannot be used as indicators of the permafrost conditions (this statement does not apply to regions). The most homogeneous landscape structure is observed within the continuous permafrost zone, while the greatest diversity corresponds to the sporadic permafrost zone (Fig 4).

Also, it was established that allocation of the sporadic zone as a separate area is not justified since the set of landscapes and their percentage in this area is similar to the discontinuous zone, which means they can be combined. Moreover, permafrost occupies more than 40%

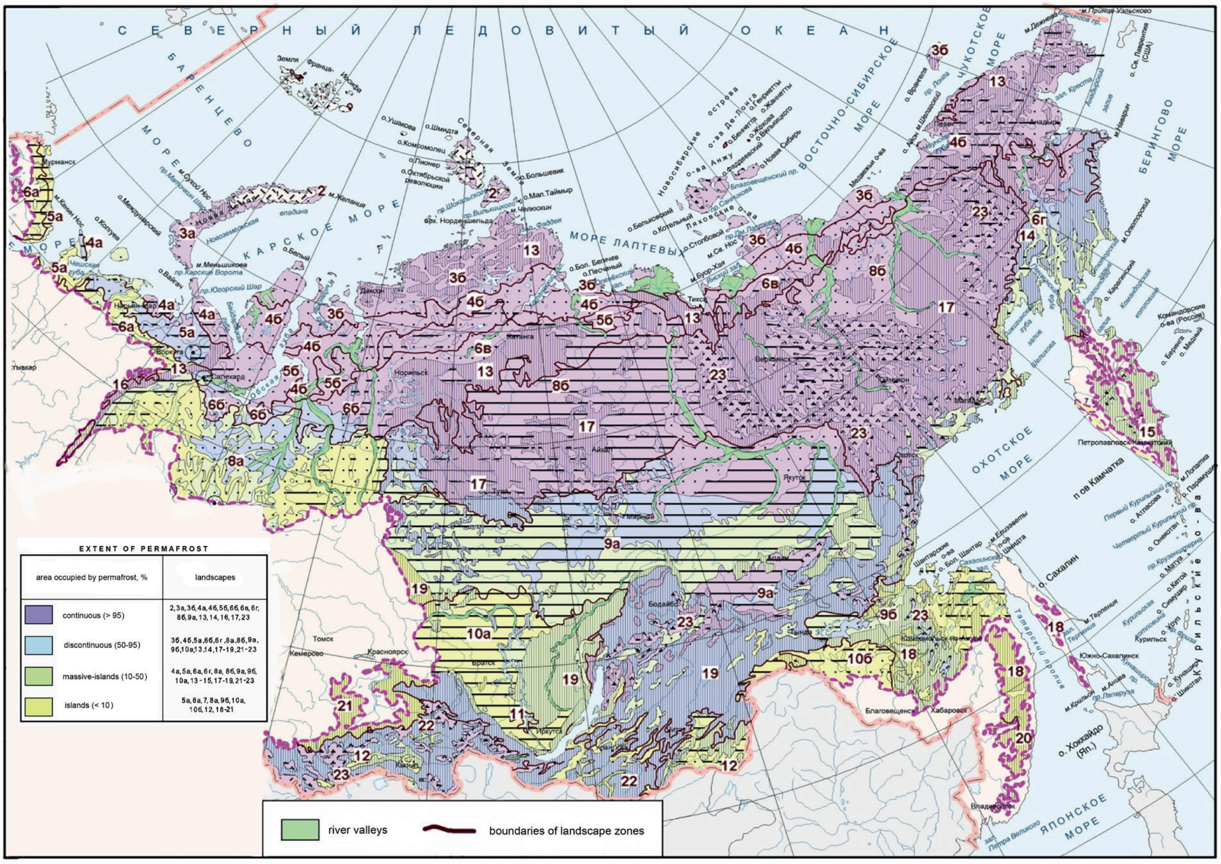

Fig. 2. «Permafrost Landscape Differentiation Map of the Russia Cryolithozone» on a scale of 1: 15,000,000 (Tumel and Koroleva 2008)

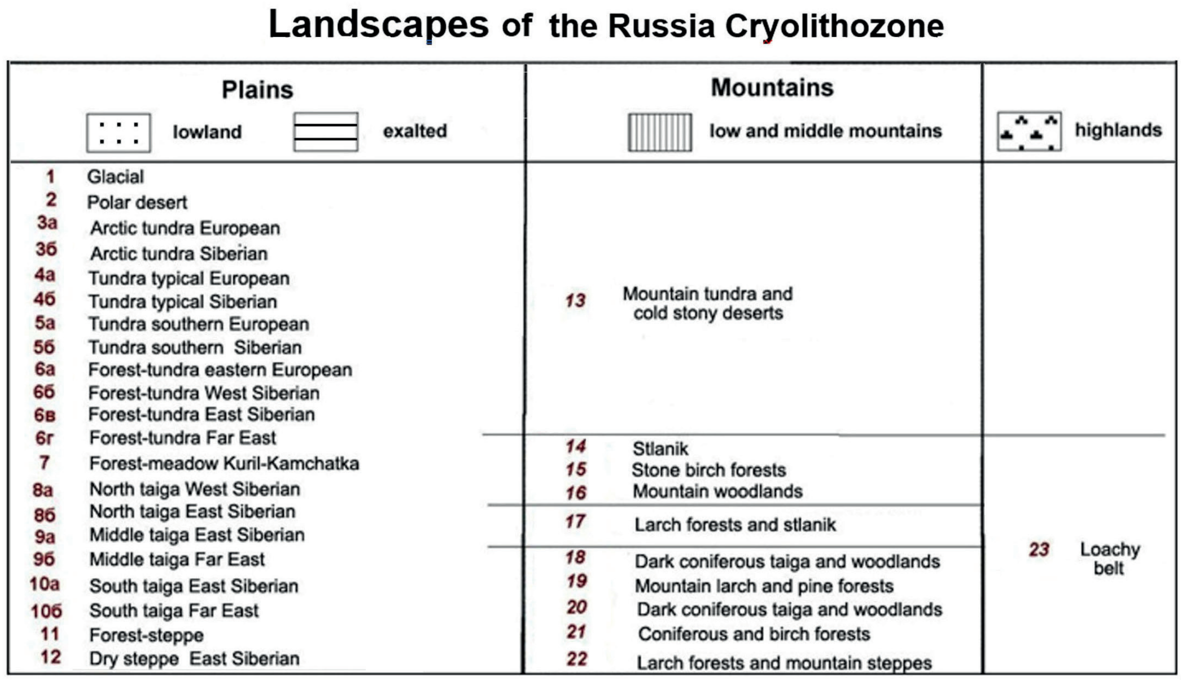

Fig. 3. «Fragment of the legend to the Permafrost Landscape Differentiation Map of the Russia Cryolithozone» (Tumel and Koroleva 2008)

there. Therefore, not four, but only three areas of permafrost distribution should be distinguished, as it is done in the well-known circumpolar permafrost map (Brown et al. 2002). This statement, however, cannot be considered as universal. It is applicable to the entire permafrost zone, which is characterized by a contrasting landscape structure. At the same time, in the western sector of cryolithozone, including the Bolshezemelskaya tundra, it is not recommended to combine the sporadic and discontinuous distribution subzones due to its flat topography, which determines the leading role of zonal factors (climate and vegetation) in the formation of permafrost conditions.

The absence of a definite connection between the boundaries of zonal landscapes and the main types of permafrost distribution can be seen in the behavior of the southern border of the Russian permafrost zone. In the west of the European North, it runs along the border of the southern tundra, while in the Bolshezemelskaya tundra and Western Siberia it «cuts» through the northern taiga, descends far to the south approximately along the Yenisei river meridian and then cuts the southern taiga and steppes of Central Siberia (Fig. 2). Approximately the same discrepancy is observed between the landscape boundaries and the main types of permafrost distribution,

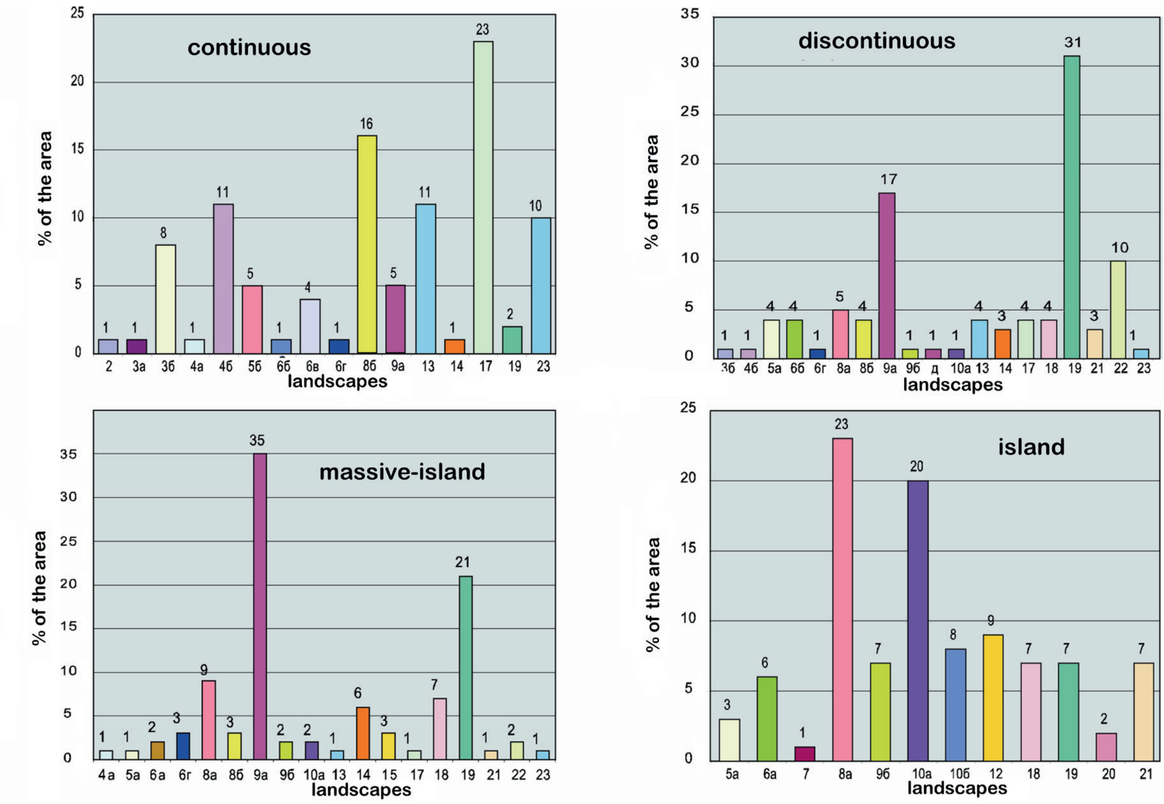

Fig. 4. Landscape differentiation of the four permafrost distribution zones in Russia, % of the area in each zone (Tumel and Koroleva 2008)

especially when considering the Russian permafrost zone in general. However, if we consider small-scale maps (from 1: 2,500,000 and smaller) of individual regions (European North, Western Siberia, Yakutia, Eastern Siberia), landscape indication starts to work very effectively again. This primarily applies to accumulative and denudation plains, within which the permafrost distribution, temperature, thawing depth, and often ice content, correspond to one of the landscapes.

The ambiguity of landscape indication should be taken into account when performing geoecological sustainability assessment of identical landscapes with different permafrost characteristics. In the northern geocryological area it easier to assess the resilience of landscapes to mechanical disturbances of the surface, hydrocarbon pollution, climate warming, etc. since the variety of permafrost conditions within the same landscape there is significantly lower compared to landscapes located to the south. In the central part of the permafrost zone, within the discontinuous and sporadic permafrost subzones, it is most difficult to determine the degree of ecological risk due to the maximum variety of permafrost landscape conditions. Such landscape diversity defines the spatial variation of the mean annual temperature, seasonal thawing and cryogenic structures. The southern permafrost zone is less difficult for economic development (Tumel and Koroleva 2008). The most typical landscapes in all permafrost regions correspond to Central and Eastern Siberia, which include the most extensive platform massifs with similar landscape conditions prevailing in a long historical development.

DISCUSSION

Indication of permafrost conditions is very complex. It is based on the idea of dependence of the vegetation cover in the permafrost zone on the thermal properties of substrate and seasonal processes of thawing and freezing. The combination of geomorphological, geobotanical and hydrological indicators can be used to identify the permafrost properties of landscapes with certain accuracy.

However, the degree of the «landscape – permafrost» connection is different. Zonal landscape indicators, with rare exceptions, are not universal and can be used only for a specific region. So, on a small scale, most landscapes are not reliable indicators of permafrost conditions. Thus, the scale of research imposes limitations on the effectiveness of the landscape indication method. It is most effective for medium-scale mapping (1:25,000–1:100,000). Small-scale studies within the permafrost zone require a more careful approach to the «permafrost-landscape» relationship, although in this case, landscape units serve as the basis for the permafrost mapping.

When creating small-scale maps, a large amount of information is generalized using landscape classification and geoinformation mapping. In the most famous geocryological maps, such as the «Geocryological map of the USSR» (Baranov 1960) and «Circum-Arctic map of permafrost and ground ice conditions» (Brown et al. 2002), the method of landscape indication was used indirectly. The only map of permafrost that fully exploits regional landscape differentiation is the updated «Map of Permafrost and Landscapes of the Republic of Sakha (Yakutia)» on a scale of 1:1,500,000 (Fedorov et al. 2018), as well as a number of maps created by the Earth Cryosphere Institute (Drozdov et al. 2003; Drozdov et al. 2018). Successful examples of cryogenic landscape mapping in high-altitude areas are the latest maps of the Tibet Plateau based on the new MODIS land surface temperature method (Zou et al. 2017; Wu et al. 2018).

Cryoindication studies are of great importance for the development of geoinformation technologies in permafrost research. Individual landscape components are considered in GIS as permafrost indication factors. GIS technologies simplified permafrost landscape classification as well as interpretation of maps by introducing overlay methods and approaches such as attribute tables (Drozdov et al. 2003; Torgovkin 2005; Fedorov et al. 2018 etc.). GIS is widely used in engineering and geocryological research, geoinformation modeling of permafrost conditions and mapping (Drozdov 2004; Rivkin et al. 2008; Torgovkin 2005; Victorov et al. 2015 etc.). New methods of spatial analysis significantly increase the content of various maps allowing for a more comprehensive analysis of permafrost regions.

In Russia, the most significant results in the field of regional, local, and regime studies of landscape-based permafrost mapping were obtained by the Earth Cryosphere Institute, Tumen, Moscow (ECI SB RAS) (Melnikov 1983; Drozdov et al. 2018, etc.), Melnikov Permafrost Institute SB RAS, Yakutsk (Fedorov 1991; Fedorov et al. 2018, etc.) and Lomonosov Moscow State University, Faculty of Geography (Shpolyanskaya and Zotova 1994; Tumel and Koroleva 2017; Tumel and Zotova 2019; Maslakov et al. 2021 etc.). These are well-known scientific schools with many years of research and mapping experience. Their works fully reflect the current state of landscape indication research in the permafrost zone.

CONCLUSIONS

The study and mapping of the permafrost zone are based on the geosystem approach, in which landscape indication is considered as one of the main methods. It is important to pay attention to two points when using it in environmental assessment studies. Firstly, to the reliability of displaying the boundaries of permafrost zones, because as the boundaries change, the qualitative characteristics of permafrost and its stability also change. Secondly, to the manifestation of cryogenic processes, such as thermokarst, thermoerosion, solifluction, frost heaving, ice formation, etc., which are dangerous both for natural landscapes and for the functioning of engineering structures. These processes are the most important indicator of the reaction of northern landscapes to anthropogenic disturbances.

There is a certain sequence in the cryogenic processes indication. First of all, the ice content of frozen rocks is identified, as it determines the activation of cryogenic processes. After that, islands of frozen and thawed landscapes are revealed, which are associated with the manifestation of ecologically hazardous cryogenic processes. This is followed by the thickness of the seasonal thawing and freezing layer (a key indicator of the degree of cryogenic processes development) and, in some cases, the average annual temperature of permafrost. Permafrost temperature is a background characteristic that promotes or prevents the development of cryogenic processes. Temperature above -5°C is favorable for their activation, while temperature below -5°C contributes to their attenuation. Permafrost thickness affects the ecological situation mainly in the south of the permafrost zone, where its profile is no more than 5–20 m and there is a danger of complete thawing. Cryogenic processes themselves and the cryogenic landforms they produce are an integral part of the indicative landscape properties.

The use of landscape indication in the studies of permafrost conditions has large-scale limitations. The smaller is the scale of research, the more limited is the application of the landscape indication method. For small-scale studies, the reliability of the «landscape – permafrost» relationship decreases from north to south. Resistance to anthropogenic surface disturbances in the same landscapes with different permafrost characteristics increases to the north and east. The central part of the Russian permafrost zone is the most difficult to develop due to the maximum variety of permafrost landscape conditions.

REFERENCES

Baranov I. (1960). Geocryological Map of the USSR at a Scale of 1:10,000,000; Explanatory note; Obruchev Permafrost Institute: Moscow, Russia (in Russian).

Brown J., Ferrians O., Heginbottom J., Melnikov E. (2002). Circum-Arctic Map of Permafrost and Ground-Ice Conditions, Version 2.; NSIDC—National Snow and Ice Data Center: Boulder, CO, USA.

Brown J., Hinkel K., Nelson F. (2000). The circumpolar active layer monitoring (CALM) program: Research designs and initial results. Polar Geogr., 24, 166-258.

Chen M., Rowland J., Wilson C., Altmann G., Brumby S. (2013). The importance of natural variability in lake areas on the detection of permafrost degradation: A case study in the Yukon Flats, Alaska. Permafrost and Periglacial Processes, 24, 224-240, DOI: 10.1002/p.1783.

Drozdov D., Korostelev Y., Malkova G., Melnikov E. (2003). The set of eco-geologic digital maps of the Timan-Pechora province. In Proceedings of the Permafrost: 8th International Conference on Permafrost, ICOP, Zurich, 21 July–25 July 2003, 205-210.

Drozdov D., Malkova G., Romanovskij V., et al. (2018). Digital maps of permafrost zone and estimation of modern first name in the permafrost zone. In Actual Problems of Permafrost; Collection of Reports. 15-16 May 2018, 1. Part 4; KDU University Book: Moscow, Russia, 295-301.

Everett K., Webber P., Walker D., Parkinson R., Braun J. (1978). A geoecological mapping scheme for Alaskan coastal tundra. In Proceedings of the Third International Conference of Permafrost, Edmonton, AB, Canada, 10–13 July 1978, 359-365.

Fedorov A. (1991). Permafrost landscapes of Yakutia: a method of isolation and mapping issues / A.N. Fedorov. – Yakutsk, 140. (in Russian).

Fedorov A., Vasilyev N., Torgovkin Y., Shestakova A., Varlamov S., Zheleznyak M. et al. (2018). Permafrost-landscape map of the Republic of Sakha (Yakutia) at scale 1:1,500,000. Geosciences, 8, 465, DOI: 10.3390/geosciences8120465.

Geocryologic Map of the USSR. Scale 1:2, 500,000 (1997). Yershov E.D., Ed.; State Cartographic Factory: Vinnytsia, Ukraine. (in Russian).

Jones B., Grosse G., Arp M., Jones K., Walter A., Romanovsky V. (2011). Modern thermokarst lake dynamics in the continuous permafrost zone, northern Seward Peninsula, Alaska. J. Geophys. Res., 116, G00M03, DOI: 10.1029/2011JG001666.

Kizyakov A., Leibman M. (2016). Cryogenic relief formation processes: a Review of 2010-2015 Publications. Earth's Cryosphere, XX(4), 40-52, DOI: 10.21782/ KZ1560-7496-2016-4(45-58).

Kravtsova V. and Rodionova T. (2016). Investigation of the dynamics in area and number of thermokarst lakes in various regions of Russian cryolithozone, using satellite images. Earth's Cryosphere, XX(1), 81-89 (in Russian with English summary).

Kravtsova V. and Tarasenko T. (2011). Thermokarst lakes dynamics in Central Yakutia under climate changes since 1950. Earth's Cryosphere, XV(3), 31-42 (in Russian with English summary).

Kudryavtsev V. (1961). Permafrost survey as the main type of permafrost research. In Permafrost Research; MSU: Moscow, Russia, 3-10. (in Russian).

Makarycheva E. (2015). Thermokarst phenomenon typification approaches near the southern border of the permafrost zone. In: Engineering Geology for Society and Territory. Vol. 1. Springer International Publishing Switzerland, Torino, 331-334.

Maslakov A., Shabanova N., Zamolodchikov D., Volobuev V., Kraev G. (2019). Permafrost degradation within Eastern Chukotka CALM sites in the 21st century based on CMIP5 climate models. Geosciences, 9(5), 232, DOI: 10.3390/geosciences9050232

Maslakov A., Zotova L., Komova N., Grishchenko M., Zamolodchikov D., Zelensky G. (2021). Vulnerability of the Permafrost Landscapes in the Eastern Chukotka Coastal Plains to Human Impact and Climate Change. Land, 10, 445, DOI: 10.3390/land10050445.

Medvedkov A. (2018). Indication of the state of taiga permfrost landscapes on the southern periphery of cryolithozone under conditions of a changing climate. in: Bulletin of the Moscow Region State University. Series: Natural Sciences, 1, 18-28, DOI: 10.18384/2310-7189-2018-1-18-28.

Melnikov E. (1983). Landscapes of the permafrost zone of West-Siberian Gas-Bearing Province; Nauka: Novosibirsk, Russia. (in Russian).

Melnikov E., Veisman L., Kritsuk L., Moskalenko N., Tagunova L., Todosiichuk I. (1974). Landscape indicators of engineering geocryological condition of the North of the Western Siberia and their interpretive signs. Nedra: Moscow, 132. (in Russian).

Moskalenko N. (1999). Anthropogenic dynamics of the plain vegetation within permafrost zone of Russia. Nauka: Novosibirsk, Russia, 280. (in Russian).

Osadchaya G. and Tumel N. (2012). Local landscapes as indicators of geocryological zoning (case study: European north-east) Earth's Cryosphere, XVI(3), 62-71 (in Russian with English summary).

Osadchaya G. and Hohlova E. (2013). Optimisations of nature management during the industrial exploitation of territorial resources of Bolshezemelskaya Tundra southern cryolitozone. Earth's Cryosphere, XVII(3), 35-43 (in Russian with English summary).

Osadchaya G., Tumel N., ZenginaT., Lapteva E. (2015). The development of the review Geocryologic Map of Bolshezemelskaya Tundra on the bases of landscape method. In Proceedings of the International Conference «Arctic, Subarctic: mosaic, contrast, variability of the Cryosphere»/V.P.Melnikov and D.S. Drozdov(ed) – Tyumen: Epoha publishing house, 2015, 287-290.

Osadchaya G., Tumel N., Koroleva A. (2016). Morphological structure of cryogenic landscapes of the Bolshezemelskaya Tundra. Earth's Cryosphere, XX(3), 14-23. (in Russian with English summary).

Pupyrev M. (2013). Deciphering and indication of modern exogenous processes in permafrost geocryological monitoring // Vestn. Tyum. State University, 4. 67-75 (in Russian with English summary).

Rivkin F., Popova A. et al. (2008). Mesoscale and detailed geocryological mapping as a basis for carbon budget assessment (East European Russian Arctic, CARBO-North Project). 9th International Conference on Permafrost, University of Alaska, Fairbanks, Volume 2,1493-1498

Shestakova A. (2011). Mapping of the permafrost landscapes taking into account vegetation succession. Ph.D. Thesis, Permafrost Institute, Yakutsk, Russia. (in Russian).

Shpolyanskaya N. and Zotova L. (1994). Map of potential landscapes stability of Western Siberia Cryolithozone; Moscow University Bulletin, Series 5. Geography; Moscow University Press: Moscow, Russia, 56-5. (in Russian with English summary).

Torgovkin Ya. (2005). Landscape indication and mapping of the river Lena permafrost conditions. Ph.D. Thesis, Permafrost Institute, Yakutsk, Russia. (in Russian).

Tumel N. and Koroleva N. (2008). Permafrost-landscape differentiation Russian permafrost zone as the basis of ecological and geological studies. Eng. Geol. 2, 11-14. (in Russian).

Tumel N. and Koroleva N. (2017). Ecological Atlas of Russia; LLC Feoriya: Moscow, Russia, 183-188, ISBN 978-5-91796-034-0. (in Russian).

Tumel N. and Zotova L. (2019). Diagnostics and Mapping of Geoecological Situations in the Permafrost Zone of Russia. Geosciences, 9, 353, DOI: 10.3390/geosciences9080353.

Tumel N. and Zotova L. (2017). Permafrost Geoecology: Training Aid for Bachelors and Masters, 2nd ed.; Yurite: Moscow, Russia, 2017, 220, ISBN 978-5-534-04227-6. (in Russian).

Tumel V. (1945). About permafrost survey. Izv. AN USSR Ser. Geogr. Geophys. 9, 135-144. (in Russian).

Tyrtikov A. (1969). Vegetation cover influence on freezing and thawing of soils Moscow: Moscow State University Publishing House, 192. (in Russian).

Ukraintseva N., Drozdov D., et al. (2011). Landscape indication of local variability of permafrost properties (Urengoyskoye field in Western Siberia). Earth,s Cryosphere, XV(4), 37-40. (in Russian).

Victorov A., Kapralova V., Trapeznikova O. (2015). Mathematical model of the thermokarst lake plain morphostructure under changing climatic conditions. Earth's Cryosphere, XIX(2), 23-31.

Viktorov S. and Chikishev A. (1990). Landscape indication and its practical application. Moscow: Moscow State University Publishing House, 200. (in Russian).

Wu X., Nan Z., Cheng G., Zhao S. (2018). Spatial modeling of permafrost distribution and properties on the Qinghai-Tibet Platea. Permafr. Periglac. Process. 29, 86-99, DOI: 10.1002/ppp.1971.

Zou D., Zhao L., Sheng Y., Chen J., Wu T., Wu, J., Xie C., Wu X., Pang Q., Wang W., et al. (2017). A new map of permafrost distribution on the Tibetan Plateau. Cryosphere, 11, 2527-2542.

RESEARCH PAPER

HYDROLOGICAL CONDITIONS OF DRAINED LAKE BASINS OF THE ANADYR LOWLAND UNDER CHANGING CLIMATIC CONDITIONS

Oleg D. Tregubov[1*], Vladimir E. Glotov[1], Pavel Ya. Konstantinov[2], Vladimir V. Shamov[3,2]
[1]North-Eastern Interdisciplinary Scientific Research Institute N.A. Shilo FEB RAS, 16 Portovaya St., 685000, Magadan, Russia
[2]Melnikov Permafrost Institute SB RAS, 36 Merzlotnaya St., 677010, Yakutsk, Russia
[3]Pacific Geographical Institute FEB RAS, Radio 7, 690041, Vladivostok, Russia
*Corresponding author: tregubov2@yandex.ru
Received: March 19th, 2021 / Accepted: November 9th, 2021 / Published: December 31st, 2021
https://doi.org/10.24057/2071-9388-2021-030

ABSTRACT. The lakes of the Arctic lowlands are both the unique indicator and the result of climatic and permafrost changes. Remote sensing methods and field measurements were used to consider the patterns and features of the morphometric indicators dynamics of the Anadyr lowland lakes over 65 years. We analyzed the parameters of 36 lakes with an area of 0.02–0.3 km^2 located in the bottoms of drained lake basins, in river floodplains, on sea-shore terraces. Field studies were conducted on 22 typical lakes. The considered dynamics of seasonal thawing are based on the monitoring of the active layer for 1994–2020. Due to an increase of mean annual air temperature by 1.8 °C, as well as an increase and then a decrease in the mean annual precipitation by 135 mm, the average share of a lake area in the study area decreased by 24%. It is shown for the first time that cryogenic processes of the lacustrine coastal zone affect the change in the area of lakes simultaneously with the influence of precipitation and air temperature. Based on field observations, we considered two causes of natural drainage: discharge of the lakes through newly formed thermokarst and thermoerosional surface flow channels and decrease in suprapermafrost groundwater recharge as a result of changing depth of seasonally thawed active layer in the coastal zone.

KEYWORDS: thermokarst lakes, active layer, suprapermafrost groundwaters, climate warming, Chukotka

CITATION: Oleg D. Tregubov, Vladimir E. Glotov, Pavel Ya. Konstantinov, Vladimir V. Shamov (2021). Hydrological Conditions Of Drained Lake Basins Of The Anadyr Lowland Under Changing Climatic Conditions. Geography, Environment, Sustainability, Vol.14, No 4, p. 41-54 https://doi.org/10.24057/2071-9388-2021-030

ACKNOWLEDGEMENTS: The study was financially supported by the Russian Foundation for Basic Research, projects 18–05–60036, the Russian Foundation for Basic Research, and the State Foundation for Basic Research of China (project no. 20–55–53014). The authors thank K.K. Uyagansky for participation and assistance in field observations.

Conflict of interests: The authors reported no potential conflict of interest.

INTRODUCTION

The article is devoted to the search and study of the impact of climatic changes on the feed and discharge of lakes in the drained lake basins of the Anadyr lowland. The research methodology included remote analysis of water capacity in basins and field observations of cryogenic processes. The novelty of the research lies in the detailed analysis of the climate influence on the hydrology of lakes through cryogenic processes in the shore zone of water bodies.

The drained permafrost lake basins (Alas, Khasyrey, and Emylkyn[1]) occupy a special place among the natural complexes studied by remote sensing methods. This is due to their wide distribution on the arctic plains, as well as to interaction of surface and ground waters in drained lake basins (DLB) of surface and ground waters, embedded and seasonally thawed ice-containing peat deposits, and a vegetation cover with specific heat-insulating and water-retaining properties. In contrast to autonomous landscapes, the response of the super-aquatic system to climatic changes is multifactorial and variable (Konishchev 2011). It depends not only on the climate but also on sources of feed and the intensity of water exchange in lakes and bogs, geomorphology and hydrography of the basins, permafrost top ice content, hydrophysical and chemical properties of peat soils, and lake sediments. Most of DLB in the cryolithic zone was formed during climate warming at the Pleistocene and Holocene boundary as a result of thawing and shrinkage of soils of the ice complex (General geocryology, 1978; Romanovsky 2003; Rodionova 2013). In the river basins of the Anadyr lowland, there are observed modern cryogenic processes: frost heaving, formation of wedged ice, thermal erosion, thermal abrasion, and various forms of thermokarst (Chukotka: Natural-economic essay 1995, Krivoshchekov 2000).

Since recently, scientists have been widely using remote sensing methods in spatial analysis to generalize

[1]Chukchi name of drained lake basins used by reindeer herders

changes in the natural environment. This, first, concerns the processing of data from space imagery and aerial photography. The effectiveness of such work is determined by the quality of the interpretation of the surface images and the representativity of the samples of the studied area. The percentage of deciphered objects confirmed by field observations is essential. In conditions of climate fluctuations, the use of remote sensing methods together with monitoring of the components of the natural environment enables identifying the factors and mechanisms of the impact of global warming on natural landscapes.

DLB are attractive for remote sensing since they enable retrospective analysis of the morphology of lakes based on cartographic data and satellite images of different years. The list of works devoted to the remote study of the dynamics of the lake area in the Arctic lowlands is very long. This article does not overview these publications and is not intended to provide their exhaustive analysis. We considered the works listed below as the most interesting and significant ones.

It was found that during 1965-2016, the area of lakes in the Kolyma R. lowland decreased by 7%, averagely (Veremeeva, 2017). At the same time, it was noted that the interannual dynamics of climatic indicators does not affect the water capacity of the objects. The later study (Veremeeva et al. 2021) of the lower reaches of the Kolyma River indicated an increase in precipitation and thermokarst-dependent water capacity of lakes in 1999–2013 and 1999–2018 by 0.89% and 4.15%, respectively. The work (Kapralova 2014) shows that changes in the total area of lakes within one area are subject to statistical laws. Methodological aspects of remote retrospective analysis are considered in the case of the Eurasian lowlands (Rodionova 2013). At the same time, the author notes a slight increase in the water capacity of lakes and expresses the opinion that global climate warming slightly effects the water capacity of the lowlands in the northern hemisphere. Other studies consider dynamics of areal thermokarst and number of thermokarst lakes in Western and Eastern Siberia (Dneprovskaya 2009; Bryskina 2015; Salva 2020) and track the changes in the water capacity in Yamal areas caused by anthropogenic impact (Sannikov 2012).

Intensive remote studies of the lakes in the Arctic plains were conducted in North America. In 1948–2013, the authors noted a decrease in the area and number of lakes in northern Alaska by 30.3% and 17.1%, respectively (Andresen 2015). An earlier study in western Alaska conducted in the period from 1949 to 2002 showed draining of 50 out of 7,400 remotely analyzed lakes (Hinke 2005). The reduction in the area of lakes in northern Canada is described by researchers (Labrecque 2009; Marsh 2009; Lantz 2015). The authors draw attention to the drainage of large lakes due to the extension of existing lakes and the formation of new surface flow paths. The problem of water discharge under abnormal weather conditions is considered in the example of lakes in northeastern Alaska (Nitze 2020). Abnormal precipitation in the winter period of 2017–2018 led to erosion of the shores and a one-time discharge of 192 lakes.

Changes in the water capacity of lakes were recorded in mountain permafrost conditions of China, on the Qinghai-Tibet Plateau (Luo 2015). Researchers noted an increase in the number of small and large thermokarst lakes in 1969–2010.

The estimates of changes in the lakes' water capacity in the Arctic latitudes contradict hypotheses about the change in the water capacity of the basins. Most of the works register decrease in the area of water bodies and lack of evidence of thermokarst activation during an over 50-year observation period (Romanenko 1999; Jones 2011, 2015). In a short, about 10–20 year long, observation series, we registered activation of thermokarst and an increase in ratio of lake surface in the basins due to the formation of new small water bodies (Tomirdiaro 1973; Sannikov 2012; Chen 2013; Arp, 2015; Boike 2016; Nesterova 2020). At the same time, it is confirmed that the area of large lakes is reduced. Drainage of reservoirs, increased evaporation, accumulation of bottom sediments and overgrowing of reservoirs, complete thermokarst, thermal abrasion, and processing of icy soils along the shores of lakes are indicated as the reasons for the drainage of the basins.

Lakes and thermokarst in Chukotka and in particular in the Anadyr lowland were actively studied by geocryologists and hydrogeologists in the last century. Among the recent works that consider in detail the problems of the genesis and transformation of water bodies, the works (Lyubomirov 1990; Krivoshchekov 2000; Tregubov 2010; Ruzanov 2014) should be noted. Lyubomirov examines the conditions for the formation and evolution of the lakes of the Anadyr lowland. Krivoshchekov analyzes the experience of reclamation of lakes for meadow cultivation. Tregubov and Ruzanov focus on the applied significance of lakes as sources of water supply, analyze the genesis of water bodies and their interaction with submerged taliks. The results of remote sensing studies of 8,305 thermokarst lakes in the Anadyr lowland are provided in the work by Rodionova (2013). According to the interpretation of Landsat satellite images made in the period from 2009 to 2013, the surface area of 338 water bodies (4% of the sample) was reduced by 86 km^2 (3.3%). And only one lake out of the surveyed water bodies slightly increased its water capacity. Field observations were not conducted; hydrological processes and overgrowth of water bodies were named as the reasons for the change in the area of the lakes.

The Study Area

The Anadyr lowland is located in the southeastern outskirts of Chukotka covering an area of 35 thousand km^2 (Fig. 1). The climate of the territory is subarctic marine. According to the Anadyr meteorological station, the mean annual temperature for the period 1981–2010 is -5 °C. Annual precipitation is 382 mm; most of it falls in winter. The thickness of continuous permafrost decreases from 300 m to 50 m from north to south, where it becomes discontinuous. The temperature of frozen soils at the bottom of the layer of annual heat turnover varies from north to south from -7.1 °C to -1 °C. The depth of seasonal thawing in undisturbed lowland landscapes is 45–55 cm.

The area occupied by lakes ranges from 20% to 60% (Geophysics ... 1987; Krivoshchekov 2000; Rodionova 2013). The area of the lakes varies from hundreds to several square kilometers. Lake water is characterized by a hydrocarbonate and sodium composition, neutral or slightly acidic reaction, and low salinity of 15–30 mg/L (Lyubomirov 1990). As for chemical composition of waters of the lakes located on low sea-shore terraces near the coastline, the proportion of chlorides in them increases; salinity can increase from 20–50 mg/L to 1.5–2.0 g/L. The waters of the drained lake basins are color and contain increased concentrations of total iron.

Despite the long history of studying the lakes of the Anadyr lowland, there is no consensus on their origin, and no optimal classification of water bodies has been proposed

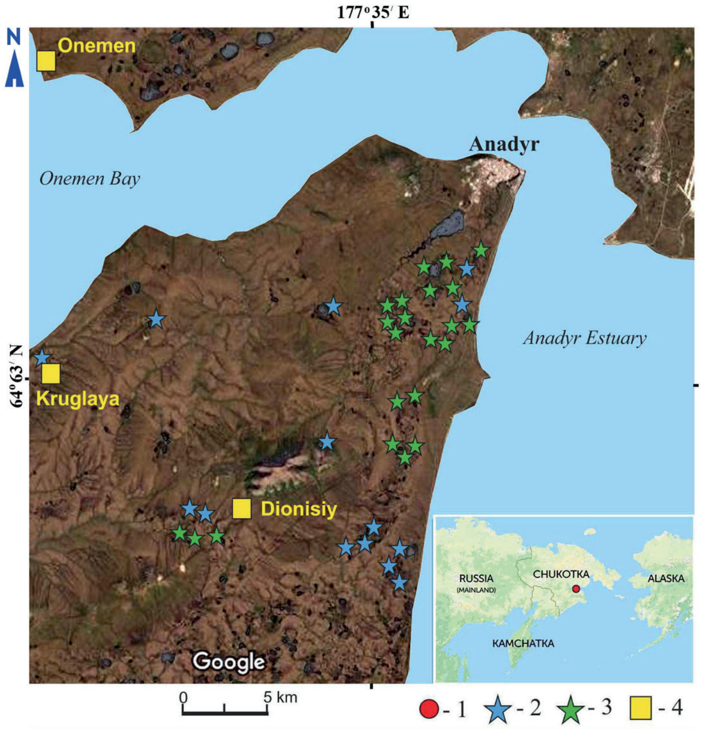

Fig. 1. Study area scheme: 1 – study area in the inset; 2 and 3 – lakes studied based on cartographic data only (2), based on cartographic data and field observations (3); 4 – active layer monitoring sites

(Ruzanov 2014). Summary of the different points of view on the conditions of their formation allows distinguishing aqueoglacial lakes, glacial fluviatile dam lakes, water-erosion flood plain lakes, water-fluviatile lagoon-like lakes, thermokarst cave-in lakes, and thermokarst secondary lakes. Groups of erosion-fluviatile and thermokarst lakes are confined to drained lake basins. Floodplain and lagoon-like lakes are found in river valleys and on the coast of the Anadyr Estuary. Thermokarst cave-in lakes are found in elevated areas of distribution of embedded relict glacial landforms and Late Pleistocene permafrost. These are deep (3–5 m) lakes with an uneven funnel-shaped bottom formed when embedded ice deposits thawed out and the surface subsided (Tregubov 2010). Secondary thermokarst lakes with a flat bottom and a depth of 1.2–3.0 m are the most widespread, occupying the bottom of the DLB or flattened watershed saddles (Tomirdiaro 1972). It is important to note that old or modern thermokarst as a cryogenic phenomenon is inherent more or less in all categories of lakes. Therefore, S.V. Tomirdiaro classified most of the lowland lakes as thermokarst lakes (Tomirdiaro 1972, 1973).

The objects of our direct study included 36 lakes with an area of 0.01–0.50 km^2 located at a distance of 7–36 km south and southwest of the city of Anadyr (see Fig. 1). The reservoirs are located within the DLB, confined to the inter-ridge watershed relief depressions (5)[2], gentle slopes (10), river valleys (15), and sea-shore terraces (6). The absolute marks of the water's edge vary from 8 m to 80 m, the depth of the lakes is 1–4 m, the salinity of the waters is 15–60 mg/L. According to the pattern of water exchange, we classified all surveyed lakes into landlocked lakes and lakes with seasonal overflow (20), lakes with permanent overflow (11), and drainage lakes (5).

The dynamics of the depth of seasonal thawing were analyzed based on the results of long-term monitoring of the active layer (AL) at the sites of the international CALM[3] program (see Fig. 1), (Abramov et al., 2019). This is the Onemen platform, which occupies the flattened top of a tundra ridge, 26 m high, with hummocky moss and cotton grass vegetation. The Dionisiy site, covered with spotty-lumpy large-grained dwarf moss-forb tundras, is located on a slope of 2–3° in the mountain foot at an altitude of 120 m. The Kruglaya site was laid out in 2010 on the bottom of the DLB with a polygonal relief and moss-dwarf shrub vegetation. The absolute bottom heights are approximately 6 m. In general, the sites represent typical landscapes of catchments and the bottom of the DLB.

METHODS

The choice of research methods was determined by the need to answer the questions:

1. How has the water content of the Anadyr lowland lakes changed over the past 65 years against the background of climatic changes?
2. Is it true that water bodies really form a single general set of objects and are characterized by general patterns of morphometric changes? To what extent do the geomorphological position, feeding, and discharge conditions of lakes determine the change in their morphometric parameters?
3. What are the current exogenous-cryogenic processes occurring in the coastal zone of lakes, in their catchment area, and along the surface flow paths?
4. How does the depth of seasonal thawing change in the catchment area, in the bottoms of basins, and along the shores of lakes?
5. What permafrost reliefs are formed on the bottoms of inflows and outflows?

Substantially, it was necessary to check the assumptions of predecessors about the reasons for the drainage of reservoirs located in different climatic and geocryological conditions.

According to the order and content of the tasks determined, the methods were divided into the auxiliary laboratory and basic field methods. The laboratory research methodology is based on a comparative analysis on one

[2]Here and below, the number of lakes is indicated in brackets
[3]Circumpolar Active Layer Monitoring

scale (1: 25000) of the contours of lakes on a topographic map compiled from aerial photography of 1953 and satellite images from the Google Maps application based on the results of the 2018 survey (Fig. 2). Morphometric characteristics of lakes, i.e. perimeter, area, and linear dimensions, were defined using the Universal Desktop Ruler V. 3.8.6498 software. Statistical lake parameters (arithmetic mean, skewness, kurtosis, and frequency) were calculated using Microsoft Excel tools.

During the fieldwork in August 2020, 22 lakes were surveyed. The technical capabilities of instrumental measurements allowed studying reservoirs with an area of 0.01–0.4 km^2. Transverse dimensions were measured using an RGK D1000 laser rangefinder. The measurement range was 3–1000 m; technical accuracy at a distance of 500 m was 1.0–1.8 m (depending on weather conditions).

Each water body was surveyed along the perimeter. We obtained information on the state of coastal ledges, feeder creeks, and surface flow channels; we revealed ground sloughing and determined depth at the coast, shoals, composition of the bottom soil, groundwater outlets, as well as salinity (electrical conductivity) and pH of lake waters. In the coastal zone, we recorded floodplain terraces, polygonal relief, frost mounds, and thermokarst depression lakes with a diameter of 3–15 m.

The depth of seasonal thawing along the shores of lakes in swampy areas and dry terraces was measured with a 1.2 m metal probe. Soil moisture was measured at a depth of 25 cm using a TK-100-01 moisture meter. In the monitoring sites with a size of 100 × 100 m, the thawing depth in the active layer was measured annually from August 25 to September 5 using a 10 × 10 m pattern (Onemen since 1994, Dionisy since 1996, Kruglaya since 2010).

RESULTS

The table in the appendix A summarizes laboratory and field research data. The results of a comparative analysis of the morphometric characteristics of the lakes are summarized in the diagrams below. The histogram shows the frequency distribution of lakes with different water capacity variability (Fig. 3a).

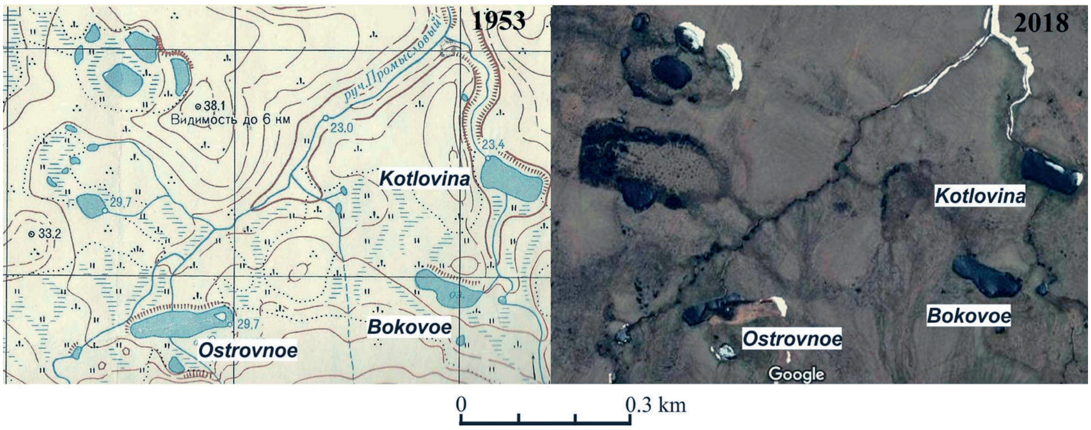

Fig. 2. An example of a comparative analysis of lakes in the valley of the creek Promyslovyy on a topographic map (left) and on a satellite image (right)

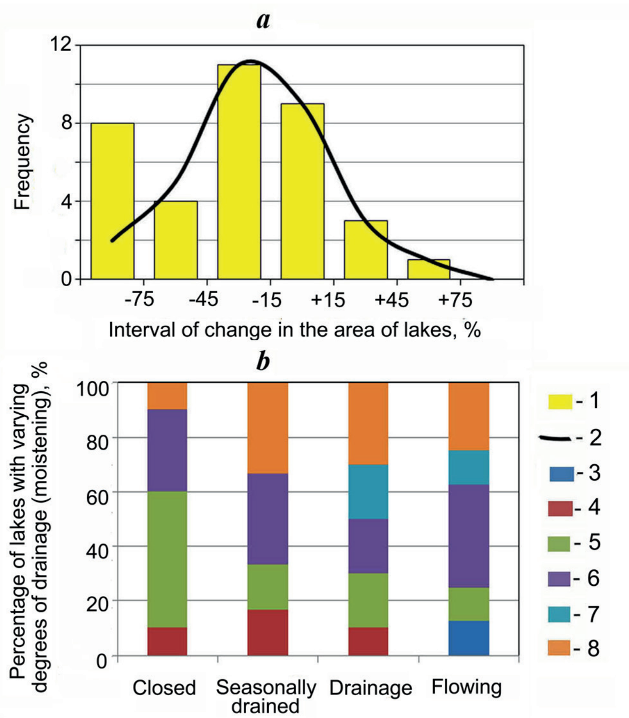

Fig. 3. Distribution of occurrence frequency of lakes with different drainage-watering degrees and the proportion of lakes with different drainage-watering degrees – in groups with different types of water exchange (b). Color and symbols designate: 1 – distribution histogram, 2 – distribution curve without taking into account the lakes drained by land melioration; lakes with varying drainage-watering degrees: 3– 75:45%, 4– 45:15%, 5– 15:(-15)%, 6– (-15):(-45)%, 7– (-45):(-75)%, 8– (-75):(-100)%

The normal distribution of frequencies is disturbed by a large number of water bodies dried up by 90% or more. As it was found out, five out of eight such lakes were drained during melioration in the 1970s for meadow cultivation. These are the lakes Glubokoe, Peschanoe, Kamenistoe, Yazyk, and Sosednee (see Appendix A). After excluding them from analysis, the empirical distribution acquired a normal form (see the distribution curve) with an average percentage of reduction in the area of the water surface of -0.24 (-24%), a standard deviation of 0.36, an asymmetry of -0.31, and a peaked kurtosis of 0.52.

Terminal lakes have retained their water capacity to the greatest extent, in comparison with open and drainage lakes (Fig. 3b). The dotted graph of the distribution of lakes according to the absolute height of the water's edge shows two clouds of scattered objects separated by a height interval of 40–60 m (Fig. 4a). In the relief of the territory, this height interval corresponds to the mountain foothills covered with a trail of diluvial sediments and tundra ridges, the outliers of the 3rd sea terrace, composed of low ice-bearing glacial–marine sediments dated back to the early interglacial transgression (Newest ... 1980; Lyubomirov 1990). This partly explains the absence of lakes at these heights. In another dot plot, lakes are grouped according to their original size (Fig. 4b). The scattering cloud bounds an almost isosceles triangle of 0.2 km^2 horizontally and -24% vertically. As the initial area of water bodies increases, the spread in the amount of their drainage-watering degrees decreases. This is probably because parameters of small water bodies change rapidly and reflect current, possibly cyclical, changes. The larger the reservoir, the more resistant it is to local impact and the more slowly its parameters change.

Field measurements of the transverse dimensions of the reservoirs showed that the size of seven lakes remained almost the same; five lakes were completely dry; in three lakes, water surface area increased; and in seven lakes, it reduced.

In comparison with the result of the analysis of satellite images in 2018 (June), the deviation of the observed parameters, i.e. lake area increase and lake shore draining, in 2020 from the calculated ones was 5–10%. Morphology of the shores (open shoals or flooded shores) indicates that this is a consequence of the interannual dynamics of the feeding and discharge of water bodies. The size of open water bodies with low, bogged shores and small bogged catchments decreased. Field transverse dimensions of terminal, seasonally open, and drainage lakes, which constitute the majority, were increased compared to the 2018 image.

The results of the field survey proved the complex structure of the shore zone of the lakes. It is expressed in presence or absence of lake terraces, degree of development of thermal erosion, thermokarst, and thermal abrasion along the shores, in the morphology of the drainways, in the material of bottom sediments of lakes and groundwater outlets. Fragments of two terraces with ledges 0.3–0.5 m high were found in the DLB of various drainage degrees (Fig. 5a).

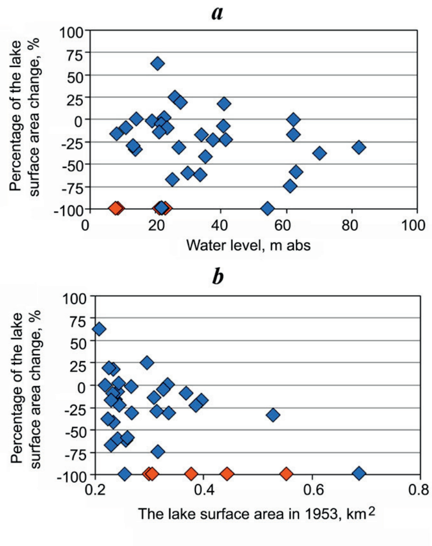

Fig. 4. Distribution of lakes with different degrees of drainage – watering, depending on hypsometric position (a) and area of water bodies according to aerophotos taken in 1953 (b): 1 – lakes without traces of technogenic impact, 2 – lakes with proven facts of melioration

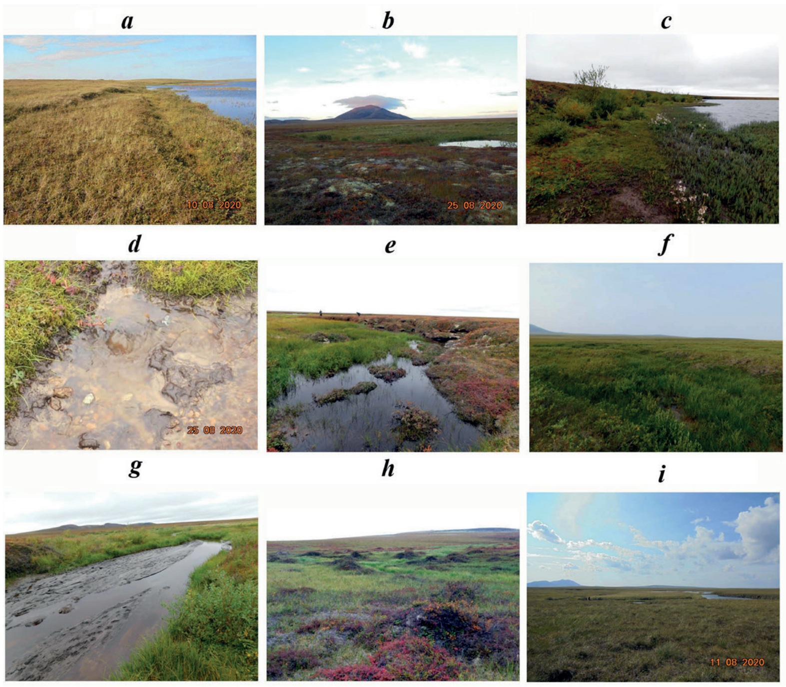

Fig. 5. Field observations of the shore zone of the Anadyr lowland lakes:
a – ledges of lake terraces, b – polygonal dwarf shrubs of the upper terrace of the lake, c – large shrubs along the coast at the footslope, d – outflows of suprapermafrost waters at the footslope, e – thermokarst and thermal erosion along the sides of the lake drainage channel, f – newly formed drainways on thawing ice of polygons, g – traces of water discharge from a drained lake in a channel, h – frost heave mounds on the lake shores, i – thermokarst lake 10 m from a drying lake

The upper terrace is distinguished by a polygonal relief, composed of peat deposits with a thawing depth of 50–55 cm and a moisture content of 65–75% (Fig. 5b). Vegetation cover is represented with shrub moss-and-lichen. The lower terrace is mostly boggy; areas with a polygonal, sometimes mound relief are subject to thermokarst – the intersections of polygonal wedges are filled with water. The vegetation cover varies from moss-cotton grass to forb-sedge and sedge-sphagnum. The depth of seasonal thawing is 45–50 cm; humidity is more than 80%. The shores of the lakes adjacent to the ridges' convex slopes are distinguished by solifluction sloughing and thermal erosion ditches. Drainage of the coast at the footslope causes springs with woody shrubs along the shores (Fig. 5c).

Thermoabrasive shores, due to the relatively small size of the reservoirs, are developed to a limited extent, mainly on elongated reservoirs oriented to the south-east (Skvazhinnoye, Ovalnoye, and Mysovoye). Among the general regularities, more or less inherent in all lakes, there is a combination of a coastline of ledges and cliffs with a height of 0.3–0.5 m and boggy coastal shoals. Another regularity concerns new or renewed surface flow channels in the majority of drained lakes. These can be both rectilinear melioration canals and natural zigzag paths of the surface flow along the thawed polygonal wedges of the first DLB terrace, or pre-existing inter-lake channels widened and deepened by thermokarst and thermal erosion (Fig. 5d, 5e).

Monitoring of the geocryological conditions of the Anadyr lowland is limited to a 25-year period (Tregubov 2019) (Fig. 6).

During the observation period, the thawing depth at the Onemen reference site, which occupies an autonomous position in the relief, increased by 15 cm, or 36% of the initial value. A slightly smaller increase (by 27%) in the thawing depth was noted in the transit (transsuperaqual) conditions of the Dionisiy site. An intermediate position is occupied by the superaqual Kruglaya platform. Taking into account the retrospective data interpolation, the increase in the thickness of the AL within its limits was 12 cm, or 34%. All landscapes are characterized by fluctuations in the depth of seasonal thawing lasting from 2.7 to 9–11 years. The mean annual temperature of the active layer in the depth interval of 20–50 cm at the Onemen site increased by 2.5 °C over 20 years of observations (Tregubov 2020). The mean annual temperatures of the active layer of the Dionysiy site remained unchanged.

The result of observations of seasonal thawing at the northwest and southeast ends of the Kruglaya site, located at the DLB bottom, is shown in Fig. 7.

These are the shores of two secondary thermokarst lakes: gentle boggy (point 1) shore of the terminal lake Severnoye and steep, 1.2 m high (point 2), shore of the open lake Yuzhnoye. As can be seen, the dynamics of the active layer seasonal thawing of the two shores over the 10-year observation period is different (see Fig. 7b, 7c). Against the background of the general increase in the magnitude of seasonal thawing, the thickness of the thawed layer on the boggy shore decreased sharply in 2011–2015 and thawing depth decreased on the elevated dry shore of the lake in 2013–2014. Analysis of the dynamics of climatic indicators suggests that this is due to an abnormally sharp drop in precipitation in 2010–2013 (by 302 mm) in relation to an increase in the mean annual air temperature in 2012–2014 from -7.5 °C to -4.5 °C. Amplitude of fluctuations in precipitation in 2016–2017 is twice less (140 mm). Consequently, the thawing depth on the boggy coast slightly decreased in 2017 (see Fig.

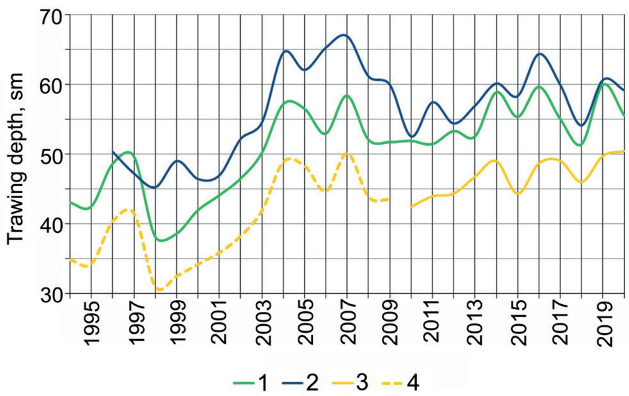

Fig. 6. Dynamics of seasonal thawing at the active layer monitoring sites: 1 – Onemen (Rogozhnyy), 2 – Dionysiy, 3 – Kruglaya, 4 – Kruglaya (retrospective)

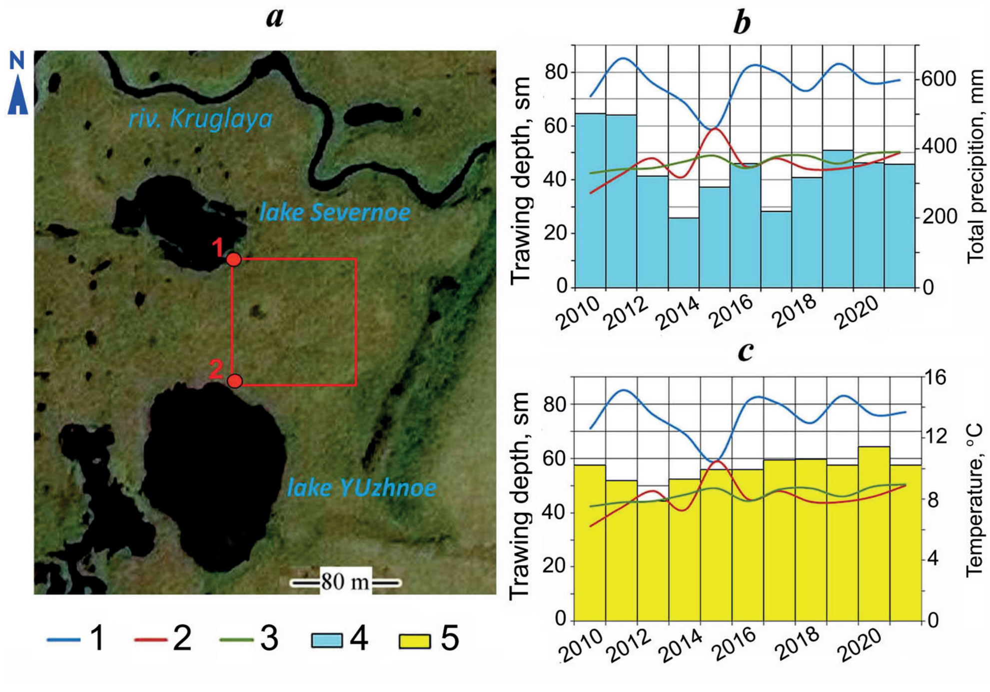

Fig. 7. Dynamics of seasonal thawing at the Kruglaya site (a) against the background of changes in the annual precipitation (b) and air temperature (c): thawing depth at point 1 (1), at point 2 (2) on average over the site area (3); 4 – the annual amount of precipitation; 5 – mean air temperature of the frost-free period of the year

7b). Such phenomena are in good agreement with the well-known conclusions of geocryologists about the dual effect of moisture on the thawing and freezing regime of the active layer (General Geogcryology 1978). A decrease in the precipitation volume leads to drainage of the low shores of thermokarst lakes and a decrease in the depth of thawing along the shores of coastal bogs. At the same time, a decrease in the moisture content of high shores, on the contrary, contributes to an increase in the depth of seasonal thawing due to the higher intensity of heat turnover in polygonal tundras as compared to tundra bogs.

DISCUSSION

Elementary statistical analysis of permafrost climatic conditions showed that the area of water bodies tends to decrease. The average drainage volume is 24%; the confidence interval for a normal distribution of changes in the area of lakes with a probability of 95% is in the range from 46.6% to -94.6%. Analysis of possible hydrological and geomorphological reasons for drainage shows a completely explainable causal relationship. It is expected that the smallest losses of the area of the water mirror are inherent in terminal and seasonally-overflow lakes. The change in the area of the lakes is associated with their position within the DLB and the relative excess of the water edge over the erosion basis. The lakes located in the headwaters of creeks or occupying the upper position in a cascade of lakes turned out to be significantly drained: Beloye, Uvalnoe 2, Verkhovoe, Mezhdurechnoye, Ostrovnoye, and Gusinoe 3 (see Appendix A). These lakes are characterized by the formation of the new or deepening existing surface flow paths. In most cases, the lakes located along the edge of the hollows at the foot of the slope retained their water content: Severnoye, Uvalnoye, Ovalnoye, Bokovoe, and Podgornoye. This is due to the larger catchment area and stable feeding of the lakes with suprapermafrost waters. At the same time, the sample contains quite a few exceptions from the patterns described above. For example, the lake Skvazhinnoe, the area of which increased due to thermal abrasion by 18%; the open lake Novoe, the bed of which expanded by 63% due to activating thermokarst along the repeatedly wedged ice of the above-floodplain terrace; the terminal lake Mysovoye, located in the center of the boggy bottom of the basin, the water surface of which decreased by 33%. And also a group of the terminal and seasonally open lakes located at the foot of the slope, with an area varying from -17% to -60% (Besstochnoye, Uglovoe, Ostrovnoe, and Poduvalnoe). Thus, information on the conditions facilitating the drainage of lakes or preservation of their water capacity is insufficient to predict hydrological processes. Thus, it is required to conduct a more detailed analysis, taking into account the regime of lake feeding and discharge, climatic changes and cryogenic processes.

For this purpose, it is necessary to consider the changes in the climatic conditions of the territory. From the middle of the last century to the present, the mean annual air temperature has increased by 1.81 °C, with year-to-year fluctuations of 1.5–3 °C (Fig. 8). The annual precipitation increased by 61.6 mm with the amplitude of interannual fluctuations up to 300 mm. The duration of the frost-free period increased by 4 days (Tregubov 2020). Variations in the values of climate indicators are due to fluctuations of different amplitude with a period of 3–5 years. Over the past 25 years, the air temperature has increased by 1.7 °C, and the annual precipitation has decreased by 135 mm. The amplitude of interannual fluctuations in temperature and precipitation has decreased (see Fig. 8). The duration of the frost-free period increased by 12 days with an average value of interannual fluctuations of 5 days (Tregubov 2020).

The information on evaporation capacity dynamics is not available. According to the known calculation schemes of zoning and literary sources for the warm season in the studied area, it is approximately 200–250 mm (Geofizika ... 1987; Postnikov 2014). Evaporation capacity probably increased with an increase in temperature and duration of the warm frost-free period.

Open and seasonally open secondary thermokarst lakes with an increase in air temperature, and hence evaporation, will have a negative long-term water balance even with a constant or partially increasing amount of precipitation. This is due to the limited capabilities of the lake basin in the accumulation and retention of moisture and the absence of other feed sources, except for atmospheric precipitation. An increase in the water content and area of such lakes is possible only due to the deepening and expansion of the bed during the development of thermokarst and thermal abrasion.

A local source of replenishment of lake water and preservation of the area of water bodies can be ground ice meltwater in the composition of the increasing suprapermafrost flow. In the present case, this applies to the lakes located at the foot of extended slopes. The intensity and availability of this feed source are limited by the ice content of the permafrost roof and wedges and icy horizons' melting time.

But the hydrological regime of the lakes is influenced not only by long-term changes in climate indicators but also by short-term fluctuations in their values. Often, fluctuations in the mean annual temperature and the amount of precipitation are in antiphase. Hot dry summers and warm winters precede years with high water and summer-autumn floods, i.e. 1962–1966, 1978–1979, 1991–1994, 1996–1997, 2004–2006, 2011–2013, 2017–2018 (see Fig. 8). Positive temperature extremes correspond to the maxima of interannual fluctuations in the depth of seasonal thawing (see Fig. 6). These facts, as well as the field observations by the authors, make it possible to represent the stages of formation of lake water discharges:

1. The maximum seasonal thawing is reached in conditions of dry hot summer, long autumn, and warm snowy winter; thermokarst is activated along the surface ground ice; talik zones that do not freeze completely during winter are formed in flow troughs.

2. With the onset of floods, the hollows of the lake flow paths are subject to thermal erosion; they deepen and provide a flow of meltwaters, which drain before the

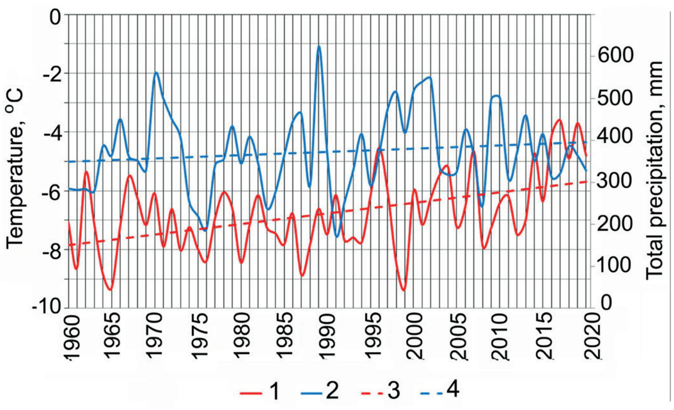

Fig. 8. Dynamics of mean annual temperature and precipitation according to the Anadyr weather station: 1 – mean annual temperature, 2 – total precipitation, 3 – linear trend of temperature, 4 – linear trend of total precipitation

beginning of the intensive melting of the lake ice cover. The main water discharge falls on the summer-autumn floods caused by prolonged rains. This is the period of the maximum thawing depth along the lake shores in the surface flow paths.

3. In the years following the draining of the lake, the flow channel is closed due to silting and sloughing of the washed-out and thawed shores. Drainways become useless. Given sufficient feed, the lake bed is filled with water. In the event of insufficient atmospheric precipitation, absence or interception of suprapermafrost flow, the lake bottom overgrows and becomes a tundra bog or a herb-grass meadow.

Discharges as a reason for the drainage of the DLB were noted in (Lantz 2015; Nitze 2020). But the authors describe this process more as an extraordinary event and do not consider it as a natural phenomenon for the permafrost zone. According to residents, the bed of the lake Gusinoe 3, which is often visited by hunters and gatherers of wild plants, since 1994 has been drained three times and re-filled with water.

Despite the attractiveness of the discharge model as a reason for the cyclic change in the water content of lakes, it does not explain the variety of hydrological drainage regimes. In most of the surveyed lakes, water surface area decreased slightly and they do not contain any newly formed elements of the drainways. Among these reservoirs, there are many terminal or seasonally open lakes, differing in the catchment area. The last remark makes it impossible to unambiguously relate the drying up of these lakes only with an increase in evaporation, since lakes with a large catchment area should be less affected by a decrease in precipitation and an increase in the mean annual temperature.

The results of the analysis of the seasonal thawing dynamics of the shores of the lake Severnoe (see Fig. 7), together with observations of thermokarst and frost heaving in the coastal strip of drying water bodies, allowed proposing a cryogenic hypothesis of their partial natural drainage. It is based on the interaction of lakes with the suprapermafrost aquifer of the DLB. Figure 9 shows a schematic model of this interaction.

With a constant amount of annual precipitation and seasonal thawing depth, area of the water surface and depth of the reservoir are within the seasonal dynamics (Fig. 9, a). During the floods period, the lake feeds the suprapermafrost aquifer at the bottom of the basin. In May–June, the overflow floods the adjacent marshy shore. In August–September, this occurs due to the reverse filtration of the flood excess of lake waters through the deeply thawed active layer of the coastal strip. The return flow into the lake occurs during the summer dry season through the suprapermafrost horizon, if the thawing front of the active layer occupies a position above the water level in the lake.

Under conditions of interannually fluctuated climatic parameters, the dynamic equilibrium is violated. A decrease in precipitation and an increase in the mean annual temperature lead to increased evaporation, water recedes from the shores, decreased level and water surface area. This, in turn, leads to deeper freezing and a decrease in the depth of seasonal thawing of the coastal strip (see Fig. 9, b). Therefore, for example, over a ten-year observation period, the interannual decrease in the area of the lake Severnoye reached 27% – the water receded from the control point (No. 1) by 6 m. This happened in 2014, with a decrease in the annual precipitation in 2013 to 200 mm (see Fig. 7 b). When the low shores are drained, the suprapermafrost aquifer is separated from the lake by a frozen bulkhead and forms two unequal areas – coastal and drainage areas (Fig. 9b). The dependence of lake feeding on the catchment area decreases. Water exchange is disturbed. In short-term periods of high water level, the lake still feeds the suprapermafrost horizon, but the reservoir does not recharge during the summer low-water period. As a result, drying out intensifies and reaches a maximum in 1–2 years after the decrease in the amount of precipitation.

Within the catchment area in the suprapermafrost horizon, with an increase in thawing depth, activation of thermokarst along icy horizons and underground ice is followed by the formation of subaerial talik zones. Freezing of such taliks result in heaving mounds (Fig. 5h). As a result, after the establishment of a new dynamic equilibrium of water exchange, this leads to the development of hilly tundra bogs with thermokarst satellite lakes of a large partially drained reservoir on the catchment in the bottom of the DLB (Fig. 5i). This situation has not been previously described, but it is quite typical. It is easily recognized on satellite images and during field observations in the DLB. Sometimes the associated lake is located 10–15 m from a large partially drained reservoir. Moreover, there are no signs of modern thermokarst on the shores of the dying lake.

The proposed conceptual dynamic model is not universal. Under conditions of increasing atmospheric humidity, the water exchange between the lake and the suprapermafrost aquifer can increase. An increase in air temperature will lead to the activation of thermokarst and an increase in the area of the reservoir. The lack of atmospheric nutrition may not immediately affect the water content of the lakes located at the foot of the extended slopes of the ridges. An increase in the depth of seasonal thawing in the catchment area leads to the melting of the icy horizons of the transitional layer, ground ice, and an increase in the suprapermafrost flow and feeding of such lakes (see Fig. 6d).

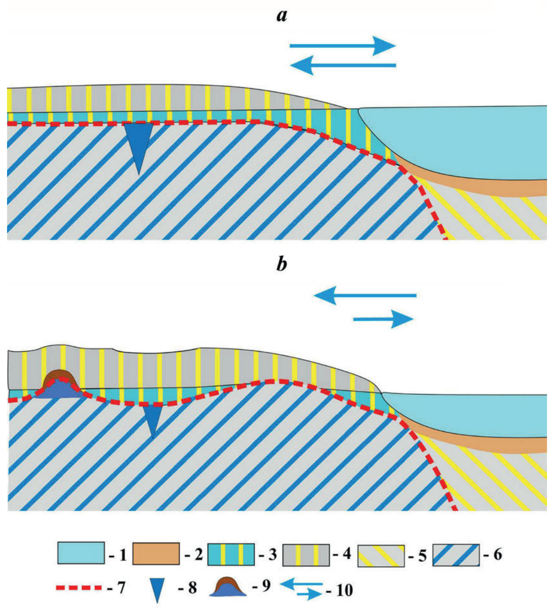

Fig. 9. Model of interaction of lake waters and suprapermafrost aquifer under static climatic conditions (a) and with a decrease in precipitation against the background of an increase in air temperature (b): 1 – lake; 2 – bottom sediments; 3 – suprapermafrost aquifer; 4 – active layer; 5 – underlake talik zone; 6 – permafrost; 7 – permafrost roof; stylized image of wedge ice (8) and permafrost heaving mounds (9); 10 – direction and intensity of water exchange (description in the text)

The dynamic model partly explains the paradox of simultaneous development of thermokarst in the bottom of the DLB along the ice wedges, formation of new wedge ice, attenuation of thermokarst along the shores and drainage of large lakes, and formation of new local point thermokarst lakes, which confused the predecessors and modern researchers (Lyubomirov 1990; Labrecque 2009; Boike 2016; Nesterova 2020). Within the framework of the considered model, the nature of the process is determined by the excess of the shores and the surface of the terraces relative to the water edge in the lake and the topography of the permafrost roof.

CONCLUSIONS

1. In the period from 1953 to 2018, the area of the water surface in the drained lake basins of the Anadyr lowland, ranging in size from 0.008 km2 to 0.5 km2, reduced by an average of 24%. The largest percentage (40–100%) of drainage was registered in open and flowing water bodies located at the sources of streams and cascades of lakes. The smallest decrease in the water surface (0–40%) is typical for closed water bodies located at the foot of long slopes. The area of three out of 36 lakes was increased. Field observations conducted in these lakes recorded manifestations of thermokarst and thermal abrasion, as well as the inflow of drainage water from drained lakes.

2. The reasons for the drainage of reservoirs included anthropogenic and natural processes: melioration of lakes for meadow growing (1965–1985); natural discharges of lake waters; changing conditions for feeding reservoirs with suprapermafrost waters. Discharges occur in conditions of abnormally high precipitation preceded by an increase in the depth of seasonal thawing, activation of thermokarst, and thermal erosion. Changes in the surface flow conditions of suprapermafrost waters are caused by a differentiated change in the depth of seasonal thawing in the coastal zone of closed and seasonally drained lakes.

3. Favorable conditions for the discharge of lake waters are repeated at intervals of 3–12 years; this is typical of open lakes with an excess of the water edge over the base of erosion by 1 m or more. The area of the water surface of closed lakes located in the central part of the depressions decreases due to the weakening of the supply of groundwater from the suprapermafrost horizon. The coastal zone of drying lakes are characterized by bogging areas, frost heaving, and thermokarst, isolated from the reservoir by frozen barriers. It is assumed that this is the main mechanism of drainage of secondary thermokarst lakes, which have exhausted their expansion potential due to thermokarst and thermal abrasion. In the 20-year perspective, permafrost drainage of lakes in the bottom of the DLB is expected to be followed by expansion of the area of mound tundra bogs with numerous thermokarst lakes.

REFERENCES

Abramov A., Davydov S., Ivashchenko A., Karelin D., Kholodov A., Kraev G., Lupachev A., Maslakov A., Ostroumov V., Rivkina E., Shmelev D., Sorokovikov V., Tregubov O., Veremeeva A., Zamolodchikov D., Zimov S. (2019). Two decades of active layer thickness monitoring in northeastern Asia // Polar Geography, 42(3), 1-17.

Andresen C.G. and Lougheed V.L. (2015). Disappearing of Arctic tundra ponds: Fine-scale analysis of surface hydrology in drained thaw lake basins over a 65-year period (1948–2013) // J. Geophys. Res. Biogeosci, 120, 466-479, DOI: 10.1002/2014JG002778.

Arp C.D., Jones B.M., Liljedahl A.K., Hinkel K.M., and Welker J.A. (2015). Depth, ice thickness, and ice-out timing cause divergent hydrologic responses among Arctic lakes // Water Resources, 51, 9379–9401, DOI: 10.1002/2015WR017362.

Boike J., Grau T., Heim B., Günther F. et al. (2016). Satellite-derived changes in the permafrost landscapes of Central Yakutia, 2000–2011: Wetting, drying, and fires // Global Planet. Change, 139, 116–127, DOI: 10.1016/j.gloplacha.2016.01.001.

Bryksina N.A., Polishchuk Yu.M. (2015). Analysis of changes in the number of thermokarst lakes in the permafrost zone of Western Siberia based on satellite images // Cryosphere of the Earth, XIX(2), 114-120.[Bryksina N.A., Polishchuk Yu.M. Analiz izmeneniya chislennosti termokarstovykh ozer v zone mnogoletney merzloty Zapadnoy Sibiri na osnove kosmicheskikh snimkov // Kriosfera Zemli. 2015. T. XIX. № 2. C. 114–120.]

Chen M., Rowland J.C., Wilson C.J. et al. (2013). The importance of natural variability in lake areas on the detection of permafrost degradation: a case study in the Yukon Flats, Alaska // Permafrost and Periglacial Processes, 24, 224-240, DOI: 10.1002/ppp.1783.

Chukotka: Natural-economic essay (1996). Moscow: «Art-Litex», 370.

Chukotka: Prirodno-ekonomicheskiy ocherk (1996). Moscow: «Art-Litex», 370.

Dneprovskaya V.P., Bryksina N.A., Polishchuk Yu.M. (2009). Izucheniye izmeneniy termokarsta v zone preryvistogo rasprostraneniya vechnoy merzloty Zapadnoy Sibiri na osnove kosmicheskikh snimkov // Issledovaniye zemli iz kosmosa, 4, 1-9.

Dneprovskaya V.P., Bryksina N.A., Polishchuk Yu.M. (2009). Study of changes in thermokarst in the zone of discontinuous distribution of permafrost in Western Siberia on the basis of satellite images // Earth research from space, 4, 1-9.

General Permafrost Science (1978). / Ed. by V.A. Kudryavtseva. – M.: Publishing house of Moscow University, 464.

Geofizika i antropogennyye izmeneniya landshaftov Chukotki (1987). / I.V. Ignatenko, I.M. Papernov, B.A. Pavlov, M.N. Zamoshch, I.N. Skorodumov. Moscow: Nauka, 271.

Geophysics and anthropogenic changes in the landscapes of Chukotka (1987). I.V. Ignatenko, I.M. Papernov, B.A. Pavlov, M.N. Zamoshch, I.N. Skorodumov. Moscow: Nauka, 271.

Hinkel K.M., Frohn R.C., Nelson F.E., Eisner W.R., and Beck R.A. (2005). Morphometric and spatial analysis of thaw lakes and drained thaw lake basins in the western Arctic coastal plain, Alaska // Permafrost and Periglacial Processes, 16(4), 327-341.

Jones B.M., and Arp C.D. (2015). Observing a Catastrophic Thermokarst Lake Drainage in Northern Alaska // Permafrost and Periglac. Process, 26, 119-128, DOI: 10.1002/ppp.1842.

Jones B.M., Grosse G., Arp C.D., Jones M.C., Anthony K.W., Romanovsky V.E. (2011). Modern thermokarst lake dynamics in the continuous permafrost zone, Northern Seward Peninsula, Alaska // Journal of Geophysical Research, 116: G00M03, DOI: 10.1029/2011JG001666.

Kapralova V.N. (2014). Regularities of the development of thermokarst processes within the lacustrine-thermokarst plains (based on the approaches of the mathematical morphology of the landscape): dis. ... Cand. geological miner. Sciences: 25.00.36. Moscow, 109.

Kapralova V.N. (2014). Zakonomernosti razvitiya termokarstovykh protsessov v predelakh ozer-no-termokarstovykh ravnin (na osnove podkhodov matematicheskoy morfologii land-shafta): dis. ... kand. geol.-miner. nauk: 25.00.36. Moscow, 109.

Kislov A.V., Grebenets V.I., Evstigneev V.M., Konishchev V.N., Sidorova M.V., Surkova G.V., Tumel N.V. (2011). Consequences of possible climate warming in 21st century in the north of Eurasia // Bulletin of Moscow University. Series 5. Geography, 3. [online] URL: https://cyberleninka.ru/article/n/posledstviya-vozmozhnogo-potepleniya-klimata-v-xxi-veke-na-severe-evrazii8 (date of access: 12.07.2021).

Kislov A.V., Grebenets V.I., Yevstigneyev V.M., Konishchev V.N., Sidorova M.V., Surkova G.V., Tumel N.V. (2011). Posledstviya vozmozhnogo potepleniya klimata v XXI veke na severe Yevrazii // Vestnik Moskovskogo universiteta. Seriya 5. Geografiya, 3. [online] URL: https://cyberleninka.ru/article/n/posledstviya-vozmozhnogo-potepleniya-klimata-v-xxi-veke-na-severe-evrazii8 (data obrashcheniya: 12.07.2021).]

Konischev V.N. (2011). Response of permafrost to climate warming // Cryosphere of the Earth, XV(4), 15-18.

Konishchev V.N. (2011). Reaktsiya vechnoy merzloty na potepleniye klimata // Kriosfera Zemli, XV(4), 15-18.

Krivoshchekov V.S. (2000). Land reclamation and land development in Chukotka. Magadan: Chukotka branch of SVKNII FEB RAS, 274.

Krivoshchekov V.S. (2000). Melioratsiya i osvoyeniye zemel na Chukotke. Magadan: Chukotskiy filial SVKNII DVO RAN, 274.

Labrecque S., Lacelle D., Duguay C.R., Lauriol B., Hawkings J. (2009). Contemporary (1951–2001) evolution of lakes in the Old Crow Basin, Northern Yukon, Canada: remote sensing, numerical modeling, and stable isotope analysis // Arctic, 62(2), 225-238.

Lantz T., Turner K. (2015). Changes in lake area in response to thermokarst processes and climate in Old Crow Flats, Yukon // J. Geophys. Res. Biogeosci., 120, 513-524, DOI: 10.10 02/2014JG00274 4.

Luo J., Niu F., Lin. Z., Liu M., Yin G. (2015). Thermokarst lake changes between 1969 and 2010 in the Beilu River Basin, Qinghai–Tibet Plateau, China // Science Bulletin, 60(5), 556-564, DOI: 10.1007/s11434-015-0730-2.

Lyubomirov A.S. (1990). Chukotka permafrost lakes. Yakutsk: Permafrost Institute of the Siberian Branch of the USSR Academy of Sciences, 176.

Lyubomirov A.S. (1990). Ozera kriolitozony Chukotki. Yakutsk: In-t merzlotovedeniya SO AN SSSR, 176.

Marsh P., Russell M., Pohl S., Haywood H., Onclin C. (2009). Changes in thaw lake drainage in the Western Canadian Arctic from 1950 to 2000 // Hydrol. Process, 23, 145-158.

Nesterova N.V., Makarieva O.M., Fedorov A.N., Shikhov A.N. (2020). Geocryological factors of activation of thermokarst processes in Central Yakutia / Collection of reports of FOURTH VINOGRADOVSKIE READINGS. HYDROLOGY FROM KNOWLEDGE TO WORLD VIEW (St. Petersburg, October 23–31, 2020). St. Petersburg: LLC Publishing house VVM, 739–744.

Nesterova N.V., Makaryeva O.M., Fedorov A.N., Shikhov A.N. (2020). Geokriologicheskiye fak-tory aktivizatsii termokarstovykh protsessov v Tsentralnoy Yakutii / Sbornik dokladov CHETVERTYYE VINOGRADOVSKIYE CHTENIYA. GIDROLOGIYA OT POZNANIYA K MIROVOZZRENIYU (Sankt-Peterburg, October 23–31, 2020). Sankt-Peterburg: OOO Izdatelstvo VVM, 739-744.

Newest Deposits and Paleogeography of the Pleistocene of Chukotka (1980). / Ed. by P.A. Kaplina. Moscow: Nauka, 295.

Nitze I., Cooley S. W., Duguay C. R., Jones B. M., and Grosse G. (2020). The catastrophic thermokarst lake drainage events of 2018 in northwestern Alaska: fast-forward into the future, The Cryosphere, 14, 4279-4297, DOI: 10.5194/tc-14-4279-2020.

Noveyshiye otlozheniya i paleogeografiya pleystotsena Chukotki (1980). / Pod red. P.A. Kaplina. M.: Nauka, 295.

Postnikov A.N. (2014). Distribution of evaporation from the water surface on the territory of Russia // Scientific notes of the Russian State Hydrometeorological University, 36, 22-28.

Postnikov A.N. (2014). O raspredelenii ispareniya s vodnoy poverkhnosti na territorii Rossii // Uchenyye zapiski Rossiyskogo gosudarstvennogo gidrometeorologicheskogo universiteta, 36, 22-28.

Rodionova T.V. (2013) Issledovaniye dinamiki termokarstovykh ozer v razlichnykh rayonakh kriolitozony Rossii po kosmicheskim snimkam: dis. ... kand. geogr. nauk: 25.00.33. Moscow, 196.

Rodionova T.V. (2013). Investigation of the dynamics of thermokarst lakes in different regions of the permafrost zone of Russia using satellite images: Thesis of PhD in geography: 25.00.33. Moscow, 196.

Romanenko F.A. (1999). Dinamika ozernykh kotlovin na tsentralnom Yamale // Erozionnyye protsessy tsentralnogo Yamala. SPb., Izd-vo Gomelskogo TSNTDI, 1999. 350

Romanenko F.A. (1999). Dynamics of lake basins in the central Yamal // Erosion processes of central Yamal. St. Petersburg., Publishing house of the Gomel TsNTDI, 350.

Ruzanov V.T. (2014). Kharakter ozer Anadyrskoy nizmennosti i ikh osvoyeniye // Inzhenernyye izyskaniya, 7, 68-72.

Ruzanov V.T. (2014). The nature of the lakes of the Anadyr lowland and their development // Engineering research, 7. 68-72.

Salva A.M. (2020). Otslezhivaniye uchastkov termokarstovykh proyavleniy po kosmicheskim snimkam (na primere trassy magistralnogo vodovoda v Tsentralnoy Yakutii) // Ark-tika i Antarktika, 2, 126-137.

Salva A.M. (2020). Tracking areas of thermokarst manifestations using satellite images (the case of the main water conduit route in the Central Yakutia) // Arctic and Antarctica, 2, 126-137.

Sannikov G.S. (2012). Cartometric studies of thermokarst lakes on the territory of the Bovanenkovskoye field, Yamal Peninsula // Cryosphere of the Earth, XVI(2), 30-37.

Sannikov G.S. (2012). Kartometricheskiye issledovaniya termokarstovykh ozer na territorii Bovanenkovskogo mestorozhdeniya, poluostrov Yamal // Kriosfera Zemli, XVI(2), 30-37.

Tomirdiaro C.B., Ryabchun V.K. (1973). Ozernyy termokarst na Nizhne-Anadyrskoy nizmenno-sti // Dokl. II Mezhd. konf. po merzlotovedeniyu. Yakutsk, 58-67.

Tomirdiaro C.B., Ryabchun V.K. (1999). Lake thermokarst on the Lower Anadyr lowland // Reports of 2nd Int. conf. on permafrost. Yakutsk, 58-67.

Tomirdiaro S.V. (1972). Permafrost and the development of mountainous countries and lowlands. Magadan, 174.

Tomirdiaro S.V. (1972)Vechnaya merzlota i osvoyeniye gornykh stran i nizmennostey. Magadan, 174.

Tregubov O.D. (2010). Reconstruction of glacial processes and the search for water supply sources for the Zapadno-Ozernoye gas field // Bulletin of the North-Eastern Scientific Center of the Far Eastern Branch of the Russian Academy of Sciences, 4, 20-27.

Tregubov O.D. (2010). Rekonstruktsiya lednikovykh protsessov i poiski istochnikov vodosnab-zheniya dlya Zapadno-Ozernogo gazovogo mestorozhdeniya // Vestnik Severo-Vostochnogo nauchnogo tsentra DVO RAN, 4, 20-27.

Tregubov O.D. (2019). The nature of short-period fluctuations in the depth of seasonal thawing // Geoecology. Engineering geology. Hydrogeology. Geocryology, 4, 3-17.

Tregubov O.D., Uyagansky K.K., Nuteveket M.A. (2020). Monitoring of permafrost-climatic conditions of the Anadyr lowland // Geography and natural resources, 2, 143-152.

Veremeeva A., Nitze I., Günther F., Grosse G., Rivkina E. (2021). Geomorphological and Climatic Drivers of Thermokarst Lake Area Increase Trend (1999–2018) in the Kolyma lowland Yedoma Region, North-Eastern Siberia. Remote Sensing, 13(2), 178, DOI: 10.3390/rs13020178. Veremeeva A.A. (2017). Formation and modern dynamics of the lacustrine-thermokarst relief of the tundra zone of the Kolyma lowland according to space survey data: Thesis of PhD in geography: 25.00.25,134.

Veremeyeva A.A. (2017). Formirovaniye i sovremennaya dinamika ozerno-termokarstovogo relyefa tundrovoy zony Kolymskoy nizmennosti po dannym kosmicheskoy syemki: dis. ... kand. geogr. nauk: 25.00.25 Pushchino, 134.

Appendix

Appendix A. Results of survey of the Anadyr lowland lakes

Name of the lake; center coordinates	Landscape position; relief height (m)	Morphometric characteristics: transverse dimensions (m); perimeter (m); area (km^2)		Area fluctuation (%)	Field observations:	
		1953	2018		lake dimansions, m	Feed and discharge, landforms, coastal conditions, cryogenic processes, M (mg/L); pH
Mysovoe; 64.683469, 177.430887	Bottom of a bogged basin, head; 13.7	750x525; 2743; 0,328	750x410; 2400; 0,219	-33	745x410	Suprapermafrost groundwater, seasonal discharge, swampy overgrown shores, fragments of a 0.3 m high terrace. 21; 5.63
Severnoe; 64.688643, 177.4444	Bogged basin bottom, head; 14	500x475; 1490; 0,134	495x485; 1436; 0,135	1	522x475	Suprapermafrost groundwater, seasonal discharge, steep shores 0.3–0.5 m high. 44; 6,3
Yazyk; 64.681728, 177.453460	Footslope, head; 8,5	563x225; 1487; 0,099	350x45; 726; 0,02.	-80	325x30	Suprapermafrost groundwater, seasonal discharge, melioration canal, swampy overgrown shores, drained bays. 31; 6.12
Yuzhnoe; 64.670861, 177.430286	Seashore terrace 2, head; 18,8	385x190; 950; 0,066	390x200; 1000; 0,067	-1	401x205	Suprapermafrost groundwater, seasonal discharge, steep shores 0.3–0.5 m high, drowned valleys. 26; 6,06
Kamenistoe; 64.695155, 177.48887	Seashore terrace 1; 7,8	500x325; 1500; 0,105	Drained	-100	-	-
Sosednee; 64.689982, 177.481490	Seashore terrace 1; 8	275x250; 747; 0,038	240x200; 693; 0,032	-16	-	-
Klin; 64.615247, 177.409687	Footslope, river terrace; 41,3	375x225; 974; 0,045	220x200; 782; 0,035	-22	225x196	Suprapermafrost surface and groundwater, flowing, permanent surface flow, steep shores 0.5 m high, new runoff channel, thermal erosion. 19; 5.45
Uvalnoe; 64.607151, 177.389345	Footslope, river terrace; 40,6	377x130; 918; 0,042	312x120: 893; 0,039	-7	315x120	Suprapermafrost groundwater, seasonal discharge, top overgrown and solifluction sloughing shores
Skvazhinnoe; 64.594008, 177.411146	Gentle slope, inter-ridge saddle; 40,8	378x127; 983; 0,034	310x175; 900; 0,040	18	320x181	Suprapermafrost groundwater, surface flow paths not found, steep shores 0.3–0.5 m high, thermal abrasion, rafts. 15; 5.7
Poduvalnoe; 64.586863, 177.395439	Footslope, river terrace; 33,5	400x175; 1069; 0,057	346x100; 756; 0,022	-61	330x90	Surface (stream) and underground suprapermafrost waters, constant discharge, steep sloughing shores, extended surface flow path, thermal erosion. 15; 7.2
Krugloe-Protochnoe; 64.593050, 177.392006	River terrace; 35,1	250x250; 725; 0,034	200x210; 516; 0,020	-41	200x196	Surface (stream) and underground suprapermafrost waters, constant discharge, steep sloughing shores, extended surface flow path, thermal erosion. 21; 6,46
Glubokoe; 64.671840, 177.39019	Seashore terrace 2; 21,3	750x500; 2038; 0,244	Drained	-100	-	Dried bottom, overgrown with herbs, woody forms of shrubs, terraces 0.5–1 m high, bogged melioration canal, frost mounds 0.5–1 m high
Peschanoe, 64.664826, 177.39526	Seashore terrace 2; 23	875x750; 3032; 0,352	Drained	-100	-	Dried bottom, overgrown with herbs, woody forms of shrubs, terraces 0.5–1 m high, bogged melioration canal, frost mounds 0.5–1 m high
Peremychka; 64.662108, 177.383331	Seashore terrace 2; 22	600x525; 1727; 0,177	Drained	-100	-	Drained, bogged bottom, terraces 0.5–1 m high, constant discharge (creek), frost mounds 0.5–1 m high
Gusinoe 1; 64.656010, 177.404789	River terrace; 25,8	425x275; 1227; 0,096	440x250; 1443; 0,120	25	442x255	Discharge from the lake Gusinoe 2, underground suprapermafrost waters; seasonal drainage; bogged shores, flooded lowlands, thermokarst in the coastal zone. 22; 5.82

Gusinoe 2; 64.652299, 177.394060	River terrace; 22,5	250x200; 743; 0,044	250x150; 806; 0,045;	2	250x141	Discharge from the lake Gusinoe 3, underground suprapermafrost waters; seasonal drainage; bogged shores, thermokarst in the coastal zone. 24; 5,6
Gusinoe 3; 64.655679, 177.385734	River terrace; 25	325x200; 753; 0,030	110x100; 406; 0,010	-67	120x84	Underground suprapermafrost waters; constant drainage; terrace 0.5 m high, shallows, frost mounds in the coastal zone.15; 5,4
Ovalnoe; 64.659132, 177.471565	Seashore terrace 2, slope; 21,6	510x275; 1640; 0,126	460x290; 1365; 0,120	-5	465x290	Underground suprapermafrost waters; seasonal discharge; two terraces 0.3–0.5 m high, thermal abrasion, overgrown shallows. 84; 5,93
Kotlovina; 64.651674, 177.458261	Seashore terrace 2, drainage; 23,4	312x180; 763; 0,033	230x100; 737; 0,030	-9	235x96	Drainage lake; steep shore 0.5–1 m high; overgrown sandy shore. 39; 7,02
Bokovoe; 64.647322, 177.452596	Seashore terrace 3, slope; 27,5	310x120; 753; 0,026	280x120; 817; 0,031	19	300x120	Suprapermafrost surface and underground waters, head; steep shore 1 m high; flooded lowland. 19; 6,11
Ostrovnoe; 64.645962, 177.427963	Seashore terrace 3, slope; 29,7	475x175; 1045; 0,042	240x90; 767; 0,017	-60	248x88	Suprapermafrost groundwater, constant discharge, bogged overgrown bottom, two terraces 0.5–1 m high, frost mounds, thermokarst in the coastal zone
Novoe; 64.663313, 177.462295	River terrace, head	125x75; 345; 0,008	140x140; 423; 0,013	63	-	-
Istochnoe; 64.663783, 177.301417; 33,9	Basin divide, saddle, head; 20,5	750x500; 1952; 0,196	620x410; 1684; 0,163	-17	-	-
Beloe; 64.617337, 177.327010	River terrace, slope; 54,1	425x275; 998; 0,055	Drained	-100	-	-
Pribrezhnoe; 64.540627, 177.404515	Seashore terrace 1, footslope; 10,8	573x475; 1536; 0,168	480x430; 1506; 0,153	-9	-	-
Gus; 64.551546, 177.355764	Seashore terrace 3; 27	625x300; 1786; 0,136	500x250; 1544; 0,094	-31	-	-
Uzkoe; 64.530183, 177.379367	Seashore terrace 1, footslope; 13	1000x250; 2322; 0,114	650x180; 1556; 0,081	-29	-	-
Mutnoe; 64.513347, 177.311217	Slope, head; 21,7	875x750; 3102; 0,486	130x90; 382; 0,009	-98	-	-
Mutnoe-Maloe; 64.515231, 177.323835	River terrace, slope; 21	425x400; 1203; 0,109	400x300; 1106; 0,094	-14	-	-
Uglovoe; 64.511094, 177.226073	Footslope; 37,4	650x575; 1865; 0,186	550x350; 1501; 0,144	-23	-	-
Istok; 64.656823, 177.099387	Basin divide, saddle, head; 82	400x250; 986; 0,068	310x170; 837; 0,047	-31	-	-
Mezhdurechnoe; 64.549186, 177.139899	Basin bottom, head; 61	575x325; 1625; 0,116	Drained	-100	-	Suprapermafrost underground waters; steep sloughing shore. Frost mounds and thermokarst in the coastal zone, deep surface flow path

Besstochnoe; 64.546604, 177.126166	Footslope; 62	325x175; 698; 0,030	400x220; 621 0,025	-17	-	-
Podgornoe; 64.545534, 177.143676	Footslope; 62	350x120; 684; 0,019	280x90; 667; 0,019	0	287x94	Suprapermafrost underground waters, springs, seasonal discharge; steep sloughing shore 0.3–2 m high. Solifluction. 15; 6,11
Verkhovoe; 64.546308, 177.182986	Slope, head; 65,8	425x230; 1063; 0,060	300x140; 720; 0,025	-58	-	-
Uvalnoe 2; 64.557926, 177.136895	basin divide, saddle top; 70	250x150; 619; 0,024	190x110; 489; 0,015	-38	-	-

RESEARCH PAPER

ACTIVE LAYER DYNAMICS NEAR NORILSK, TAIMYR PENINSULA, RUSSIA

Valery I. Grebenets[1], Vasily A. Tolmanov[1*], Dmitry A. Streletskiy[2]
[1]Department of Cryolithology and Glaciology, Geographic Faculty, Lomonosov Moscow State University, Leninskiye Gory 1, Moscow, 119991, Russia
[2]Department of Geography, The George Washington University, 2036 H Street, Washington, DC 20052, USA
***Corresponding author:** vasiliytolmanov@gmail.com
Received: June 24th, 2021 / Accepted: November 9th, 2021 / Published: December 31st, 2021
https://doi.org/10.24057/2071-9388-2021-073

ABSTRACT. This paper provides information on active layer thickness (ALT) dynamics, or seasonal thawing above permafrost, from a Circumpolar Active Layer Monitoring (CALM) site near the city of Norilsk on the Taimyr Peninsula (north-central Siberia) and the influences of meteorological and landscape properties on these dynamics under a warming climate, from 2005 to 2020. The average ALT in loamy soils at this 1 ha CALM site over the past 16 years was 96 cm, higher than previous studies from 1980s conducted at the same location, which estimated ALT to be 80 cm. Increasing mean annual air temperatures in Norilsk correspond with the average ALT increasing trend of 1 cm/year for the observation period. Active layer development depends on summer thermal and precipitation regimes, time of snowmelt, micro-landscape conditions, the cryogenic structure (ice content) of soils, soil water content leading up to the freezing period, drainage, and other factors. Differences in ALT, within various micro landscape conditions can reach 200% in each of the observation periods.

KEYWORDS: Active Layer Thickness (ALT), permafrost, thaw subsidence, CALM (Circumpolar Active Layer Monitoring) program, Russia, Taymyr Peninsula

CITATION: Valery I. Grebenets, Vasily A. Tolmanov, Dmitry A. Streletskiy (2021). Active Layer Dynamics Near Norilsk, Taimyr Peninsula, Russia. Geography, Environment, Sustainability, Vol.14, No 4, p. 55-66 https://doi.org/10.24057/2071-9388-2021-073

ACKNOWLEDGEMENTS: Fieldwork to collect the data presented here was conducted in the 2005–2021 period, supported by the U.S. National Science Foundation-funded project The Circumpolar Active Layer Monitoring Network [OPP-0352958, OPP-1304555, OPP-1836377] to George Washington University and Northern Michigan University. The paper was written within the framework of the project «Cryospheric Evolution Under Climate Change and Anthropogenic Impacts» [CITIS 121051100164]. The authors are grateful to the Norilsk Meteorological Observatory staff for providing valuable meteorological information, and to the leading engineer of the Norilsk Scientific and Production Association «Fundament» Alovsat G. Kerimov for participation in the geodetic work. We are grateful to the researchers and students who assisted in the field by conducting CALM observations and participated in obtaining primary data. We thank two reviewers for many helpful suggestions.

Conflict of interests: The authors reported no potential conflict of interest.

INTRODUCTION

The active layer is a soil or rock layer between the ground surface and permafrost that thaws in the summer season and freezes again in the winter (General Permafrost Science 1978). Active layer thickness (ALT) is highly variable owing to high spatial variability in vegetation and soil conditions, local topography, and geomorphic conditions. ALT is recognised as one of the most important variables used to characterise the permafrost system and its response to climate change (French 1999). Determination of ALT in various landscapes and soils is also a necessary step in many engineering and geocryological surveys, as well as in ecosystem studies. The active layer is sensitive to changing climatic conditions and can be used as an indicator for the assessment of the state and rate of transformation of permafrost (Kudryavtsev 1954; Shur 2005).

Detailed studies of ALT variability have always been at the center of permafrost research, including pioneering works by V. Kudryavtsev, V. Tumel, I. Redozubov, G. Feldman, A. Pavlov, D. Gilichinsky, N. Tumel, A. Washburn, J. Brown, T. Péwé, F. Nelson). Previous studies established patterns of ALT and factors influencing ALT dynamics, revealed its role in determining the stability of engineering structures built on permafrost, and provided an assessment of settlement of thawing or heaving during the freezing season.

Active layer dynamics depend on the climatic, landscape, and soil conditions characteristic of specific areas (Nelson et al. 1998). The Circumpolar Active Layer Monitoring Program (CALM) was created in 1991 to track long-term changes in ALT. It currently includes more than 250 active sites with standardized observations in permafrost regions of both hemispheres (Brown et al. 2000; Nelson et al. 2021).

This report is focused on a CALM site established in the north of central Siberia (Taimyr), near city of Norilsk in 2005. The site is among the locations where changes in climatic and near-surface permafrost temperature are most pronounced in recent years (Streletskiy et al. 2015). In this paper we evaluate the spatial and temporal variability of the active layer within the Western Taymyr region, particularly Norilsk. The study is based on data collected at the Norilsk CALM site over 16 years and assesses the role of rapidly changing climatic conditions and landscape transformations on active layer dynamics.

Background

The first known report on the conditions of the active layer in the region is attributed to the first geological expedition led by N.N. Urvantsev in the valley of the river Norilskaya in 1918, which reported difficulties in transporting cargoes by carts as they became mired repeatedly in thawed loamy-clayey soils. However, the report noted that excavation of soil pits was much easier in the thawed layer, as compared to frozen soils. The first instrumental measurements of active layer thickness in this area were conducted in the 1920s and 1930s by the Northern Sea Route Committee on the route of the proposed Dudinka – Norilsk railway. Measurements were unsystematic and were made in different periods during the summer season. Construction of the Norilsk Mining and Metallurgical Plant was initiated in 1935, and created high demand for engineering and geological surveys. Specialists from the Committee for the Study of Permafrost of the Academy of Sciences of the USSR arrived in Norilsk in 1936 under the leadership of V.F. Tumel, who organized a special group under the management of NorilskStroy. A laboratory for the study of physical and mechanical properties of soils and a permafrost station under the leadership of engineer M.V. Kim were organized. This group paid particular attention to the permafrost mechanical properties and permafrost temperature regime of foundations and basements. The employees of the permafrost laboratory collected information about the depth of thawing in various types of soils, which allowed estimation of the range of the maximum depth of seasonal thawing of soils (depending on soil type, the impact of groundwater, vegetation, etc.) from 0.5 to 3.5 m (Sheveleva, Khomichevskaya 1967). In later work it was noted that the smallest depths of seasonal thawing in the Norilsk region were typical for floodplains and terraces covered with peat, and are 0.3 to 0.8 m; maximum thickness was from 4.5 to 5.5 m on gently sloping areas of the plateau, which is composed of highly fractured, highly conductive basalts covered by thin (up to 0.5 m) Quaternary sediments (Demidyuk 1989). Thaw depth data were obtained during thermal measurements in boreholes by interpolation to determine the depth of the 0°C isotherm.

No regular observations of ALT dynamics were conducted before the start of measurements within the framework of the Circumpolar Active Layer Monitoring program (CALM). The CALM program utilizes various methods to determine ALT, and detection of the surface elevation to estimate the effect of the winter heaving and subsequent thaw subsidence (Brown et al. 2002).

Results obtained through the CALM program demonstrate strong spatial heterogeneity in ALT worldwide (Luo et al. 2016; Abramov et al. 2019). Regional research conducted in the Putorana Plateau near Norilsk shows expansion of forest vegetation due to an increase in winter precipitation during the 20th century (Kirdyanov et al. 2012). A case study based on remote sensing (Nyland et al. 2017) showed that maximum changes (17%) occurred in closed forest areas. These closed forest areas experienced rapid tree growth and expansion of shrubs, while open forest expanded with individual trees up to 20 m apart and herbaceous and moss layers between. Numerous studies conducted in West Siberia have also documented expansion of southern species into the northern territories. One of the most dramatic changes is the replacement of the southern tundra by forest-tundra (Moskalenko, 2003; Vasiliev et al. 2021; Frost et al. 2019). Such change is usually connected with increases in average annual air temperature and subsequent increases in permafrost temperature.

For engineering purposes, specialists from the Norilsk permafrost laboratory experimentally produced data on the potential thaw settlement of thawing soils in the area (Sheveleva, Khomichevskaya 1967). Potential thaw settlement varies over a wide range, from 0.5-2 %/m for fluvial-gravel pebbly rocks; 10-20 %/m- for lacustrine loams; and up to 48 %/m in icy lacustrine clays dominated by ground ice. Subsidence was studied in the laboratory using frozen soil samples. However, in natural conditions the process is more complicated by patterns of water drainage in the active layer and the high variability of soil conditions. Ground subsidence in tundra landscapes depends on weather conditions in particular warm seasons and on ice content (Streletskiy et al. 2017).

Study Area

The geographic location of the site is shown in Figure 1. The site is on the Taimyr Peninsula of northern Siberia, in the Norilsk-Rybninskaya valley, 1 km south of the Kharaelakh Mountains, part of Putorana Plateau. The site is 2.5 km southeast of the Talnakh city part of the Norilsk industrial area of the Krasnoyarskiy Kray. The site is located within the Valkovskaya lacustrine-alluvial valley terrace, on the watershed surface between two streams and has a slight (1-2o) slope in the southwest direction. The formation of the terrace is associated with the drainage of a lake known as Valyok Basin at the end of the Late Pleistocene. Lake drainage resulted in accumulation of loamy-clayey sediment, in which formed ice-rich permafrost (Sheveleva and Khomichevskaya 1967). The valley is bordered by the steep spurs of the Putorana Plateau located 1 km northeast from the R-32 site. The plateau protects the study area from cold northern winds and contributes to increased snow accumulation. Our research (May 5th 2019) showed that the height of the snow cover at the site was about 120 cm relative to 70 cm at the Norilsk meteorological observatory. Higher snow accumulation leads to later onset of thawing, the reason why we chose the sum of positive degree-days for the period after snow melt (see below).

METHODS, MATERIALS AND DATA

Field methods

The CALM site was established in 2005 near Talhakh (69°26'N, 88°28'E), a satellite city of Norilsk. The site is registered within CALM database as R32 «Talnakh» (www.gwu.edu/~calm). Data are available at the Arctic Data Center web site (https://arcticdata.io/catalog/view/doi:10.18739). Active layer thickness was measured on a 1 ha grid using mechanical probing with a metal probe (Brown et al. 2000; Fagan and Nelson 2017). The probe is a pointed metal rod with a cross section of 10 mm and a length of 1.6 m. Three measurements were made at each of the 121 equally spaced grid points (10 m spacing) at the end of August or beginning of September, from 2005 to 2020. The total number of measurements was approximately 6000 during this period.

Geodetic surveys for evaluation of thaw subsidence were conducted at the site in 2007. Geographic location and surface elevation were determined by theodolite surveys, relative to a fixed benchmark. Subsidence was

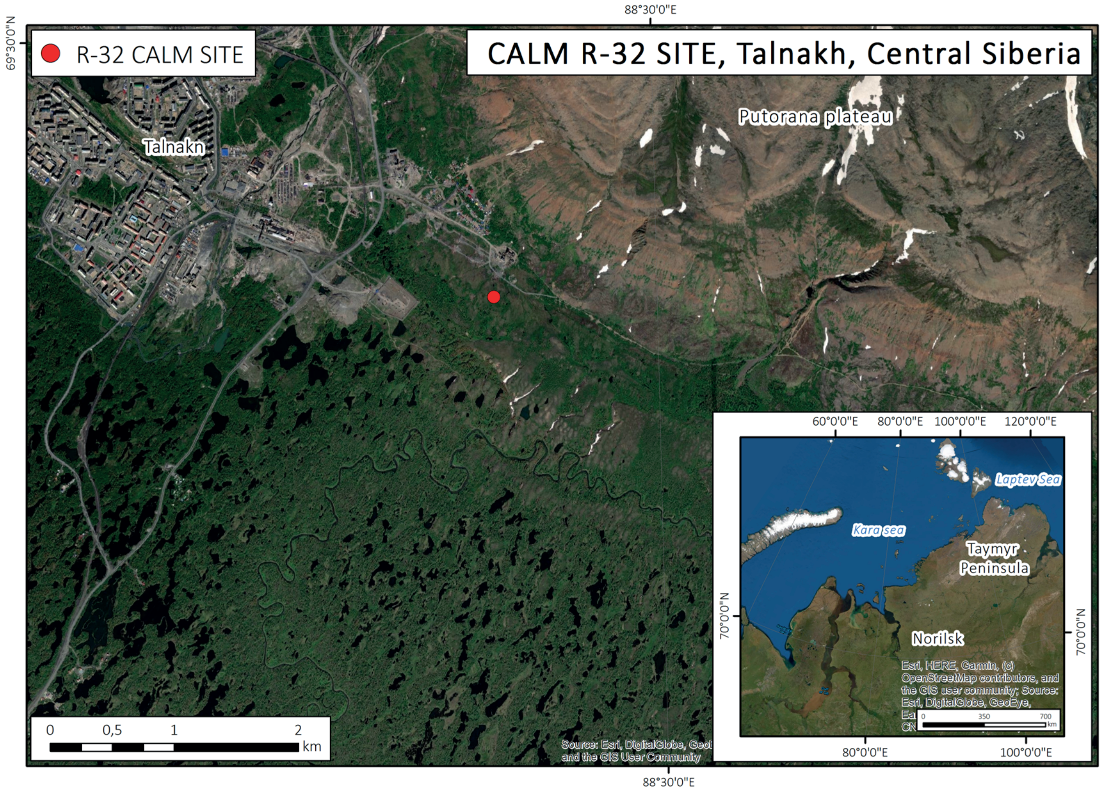

Fig. 1. Location of the R-32 site

estimated as the difference in elevation between the benchmark and the 121 marked points of the grid.

Landscape maps were compiled for 2005, 2008 and 2017. Geobotanical mapping of landscape complexes enabled assessment of transformations in the site's landscape structure, and guided the landscape-specific analysis of thaw values by landscape group. Landscape groups were delimited using several parameters, including microrelief (lower parts and higher parts based on the geodetic surveys of the site), surface hydrologic regime, and vegetation. Vegetation descriptions were conducted within the defined microrelief types, e.g., runoff hollow. The dominant vegetation type was recorded for the different levels.

Analytic procedures

Degree-days of thawing (DDT) were used for the analysis of the influence of warm-season air temperature on ALT. DDT is the sum of the positive average daily temperatures from the beginning of the warm period to the time of ALT measurement (Boyd 1973). In this study, the sum of positive temperatures from the date of snowmelt to the ALT measurement date was used.

Traditionally, a version of the Stefan Solution is used to compute ALT (General Permafrost Science 1967; Harlan and Nixon 1978). The latter was applied in the form of the equation $Z = E\sqrt{DDT}$, where E is the «edaphic factor», describing the thermal properties of the surface and thawing soils (Nelson and Outcalt 1987).

Meteorological data were obtained from the Norilsk Meteorological Observatory (WMO ID 23078), located 17 km southwest of the CALM grid, at the elevation of the Valkovskaya lacustrine-alluvial terrace.

The normalized variability index (I_v) was used to estimate the spatial variability of thaw over the time series following Brown et al. (2000) and Hinkel and Nelson (2003). Iv is determined by:

$$I_v = [(Z_i - Z_{avg}) / Z_{avg}] \quad (1)$$

where Z_{avg} is the average thaw depth for a specific year, and Zi is the value for a specific grid point. The variability for the 16-year series is calculated as the difference in the ratios (expressed as per cent) of the minimum and maximum achieved over these years. Some researchers have suggested classifying low variability when the Interannual Node Variability index INV = 0-19%; medium with INV = 20-29%; and 3) high - with INV> 30% (Smith et al. 2009).

The Pearson Product Moment Correlation method was used to assess changes in the micro-landscape structure of the site by the annual datasets (Gmurman 2010). We measured the strength and direction of the relationship between two variables using the nonparametric Spearman rank correlation coefficient. We conducted pointwise analysis between every single point from the 121-point dataset. We correlated every point from the dataset with its analogue from different years. The result is a matrix with the correlation between datasets from different years. Another important statistical parameter that we used is the coefficient of variation (2)

$$C_v = \sigma / \bar{a} \quad (2)$$

where σ is the standard deviation and ā is the arithmetic mean of ALT values (Ivchenko, Medvedev 2010).

Maps were made using the Surfer software package (Surfer 1999), which facilitated creation, comparison, and analysis of the spatial distribution of ALT values at the site between the years following (Hinkel and Nelson, 2003; Kaverin et al. 2019).

Climate data

The territory is characterized by a polar tundra climate (Kottek et al. 2006), with polar nights and polar days, long snowy winters, and relatively short cool summers. According to meteorological data obtained at the Norilsk Meteorological Observatory, the average annual wind speed is 6.3 m / s; rainfall – 340 mm per year; the height of the snow cover is 80 cm.

Analysis of meteorological data from the Norilsk Hydrometeorological Observatory (1938-2020) shows that after a sufficiently long period of increased climate severity and its subsequent relative stabilization there is a pronounced warming trend since the 1960s (Fig. 2). The averaged MAAT was -9.8 0C, and the duration of the warm period was about 120 days in the 1970s (Handbook of Construction 1977); while in the 1988–2020 period mean annual temperature was -8.2 0C. The temperature in 2020 was -3.80C, which is 4.70 OC higher than the climatic norm (1981–2010). The season with positive daily air temperature lasted 150 days in 2020. There was an almost weeklong period with a temperature above 00C in mid-April, which contributed to early snowmelt.

An increase in air temperature with a slight increase in snow cover depth in the winters led to the growth of trees and shrubs, creating a transition to southern tundra (Nyland et al. 2017). Thermokarst processes on the Valkovskaya terrace, thermal erosion on river banks and ice-rich shores of large lakes were also more common. The number of deformed engineered works on frozen piles has significantly increased in the cities and industrial zones of the region. According to our observations (Grebenets et al. 2016) the reason was an increase in the permafrost temperature of the upper permafrost (8-10 m), and the subsequent decrease in the freezing forces on the foundations.

The region lies within the zone of continuous permafrost. Taliks underlie the largest rivers (Norilskaya and Rybnaya), and the largest lakes on the Valkovskaya terrace. Permafrost temperature decreases with elevation (Sheveleva and Khomichevskaya 1973).

Permafrost underlies the entire CALM site. The upper part of the permafrost section is dominated by loamy strata with a relatively small amount of gravel-pebble material. Loams have a thin layer of partially decomposed peat from the surface in some places. Mean annual ground temperature (MAGT) at the level of zero annual amplitude is -3.8 ° C. These data were acquired from the archives of the Research Institute of Foundations and Underground Structures, Norilsk.

RESULTS

Impact of climatic conditions on active layer dynamics

Sixteen years of observations show that ALT has an increasing trend of 1 cm / year (Fig. 3). Thawing rate depends primarily on the cumulative effect of DDT and the warming effect of precipitation in summer (Fig. 3).

Fig. 3 shows that average ALT at the site varies from 81 cm (2005) to 113 cm (2019). DDT varies from 794 (2010)

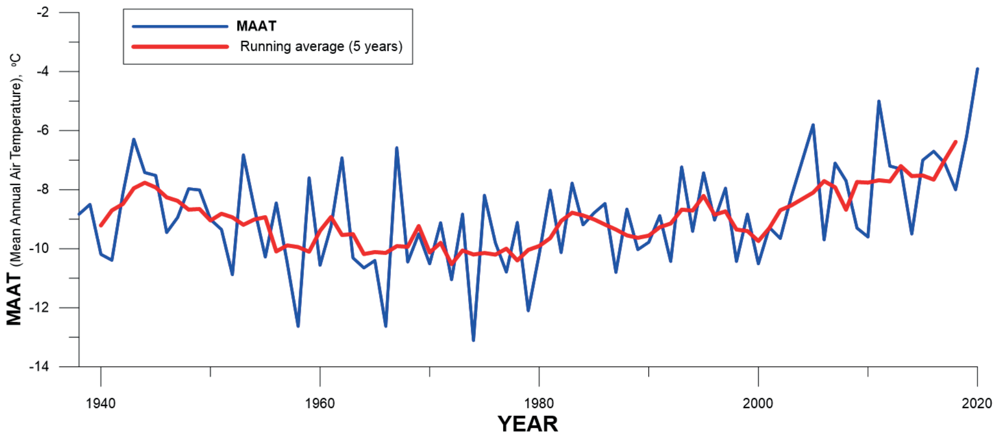

Fig. 2. Changes in mean annual air temperature in Norlilsk (data from the Norilsk Meteorological Observatory). Blue line represents mean annual air temperature (MAAT). Red line represents the 5-year running average

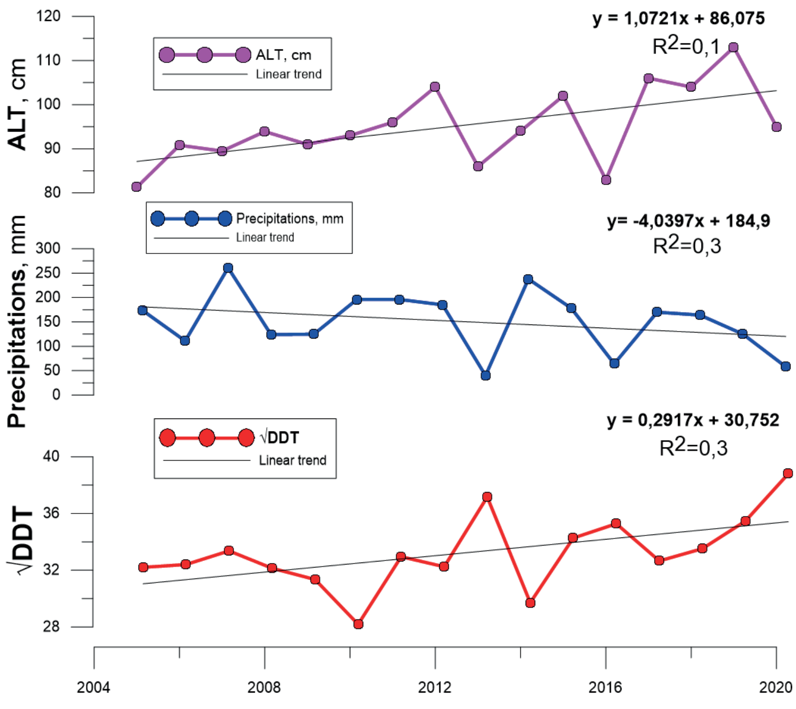

Fig. 3. Time series of active layer thickness, degree days of thawing, and precipitation for the 2005–2020 period

to 1506 degree-days, (2020). Most variable is the regime of summer precipitation: from 40 mm (2013) to 261 (2007) mm. Cv=0.4. (C_v for √DDT=0.1; for ALT=0.15) Average thaw depth over the last 16 years at the R-32 site is 96 cm. According to the generalized results of measurements in the loamy strata of the region until the 1980s, ALT was 80 cm.

Bivariate regression analysis revealed the absence of a linear dependence over 16 years only on DDT and the amount of precipitation (Fig. 4).

Figure 4 shows that in both cases the coefficient R^2 was less than 0.1 Active layer thickness did not exceed the long-term mean values (95, 86, 83 cm) in dry years, even with extremely hot summers and maximum values of positive degree days (2020 – 1506, 2013 – 1381, 2016 – 1244).

A clearer dependence of ALT on DDT is manifested if we group the measurement results (average values for the site) by years with warm and humid conditions (Fig. 5, a) and a relatively dry summer (Fig. 5, b). The relationship between soil thawing and air temperature is quite strong for the first case, with R^2 value of 0.7.

Higher than average ALT was reached in 2012, 2015, 2017, 2018, and 2019, when the amount of precipitation was higher than or near the mean annual values. More than half (56%- 103 mm) of precipitation fell in the second half of July, at the beginning of August in 2012, with very high average (for this period) air temperature of 15.8°C (this value is higher than the average annual temperature values at that time). These conditions resulted in a well-developed active layer of 104 cm. A total of 179 mm of precipitation fell in 2017. This is 1.14 times greater than the average for the season. The bulk of precipitation fell in July and August (61 and 103 mm); the soil had thawed to a sufficient depth by this time that downward water drainage activated thaw.

The summer of 2018 was abnormally warm in June (13.8° C, which is 3.8 ° C higher than the average value for the 16 years of this research project). A total of 66 mm of precipitation fell during this period (1.53 times higher than the average value for this month). Consequently, a thick active layer formed during the cold remaining months (72 and 44 mm of precipitation). The increase in ALT was most pronounced in August of 2019, when the average air temperature was 4.6°C higher than the mean temperature for this month for the period 2005–2021. The month was very rainy (72 mm of precipitation) leading to record for seasonal thaw (113 cm). The influence of the combination of high DDT and high precipitation on the active layer thickness is significantly «corrected». The first correction is the shift of the maximum air temperature late in the warm season. The second is the regime of summer precipitation: at the beginning of the warm season when most of the precipitation drains atop the frozen soils near the surface, or drains along the peat loam in the upper part of the section. The maximum impact on ALT from these positions is recorded during rainy Augusts.

Table 1 shows the results of measurements that emphasize the peculiarities of the influence of the number of positive degree-days in combination with the amount of precipitation in the warm period.

An interesting pattern occurred in years with abnormally hot and dry summers (2013, 2016, and 2020). Only 40 mm of precipitation fell over the summer of 2013, (ALT 86 cm) and only 4 mm of precipitation fell in July 2016 (ALT 83 cm) at an average monthly temperature of 18 ° C. The total amount for the 2016 warm season was 64 mm. ALT was only 95 cm in dry 2020 (precipitation of 58 mm), with an early snowmelt (April 24). The date of transition to positive air temperatures was also abnormally early (May 8th). The amount of DDT was maximal (1506 degree-days).

The formation of the seasonally thawed layer at the site cannot always be explained by the cumulative effects of only heat and moisture. One of the lowest values of ALT was observed in 2007 with greater than average precipitation and DDT. Similar results have been obtained by other researchers (Maslakov et al. 2019).

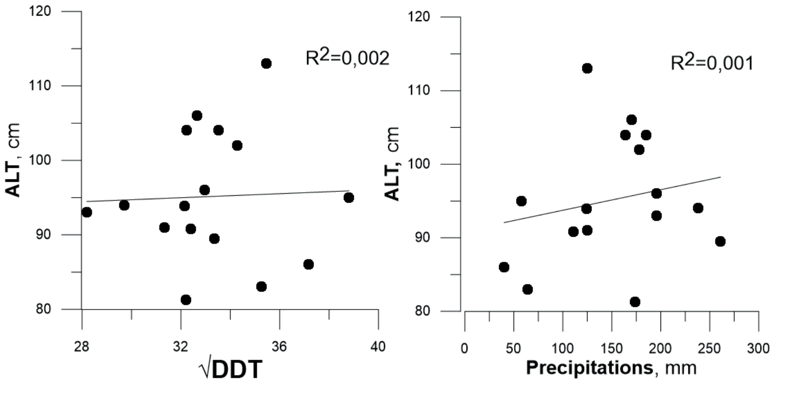

Fig. 4. Dependence of thawing depth on two main factors: the root of positive degree days (a) and summer precipitation (b)

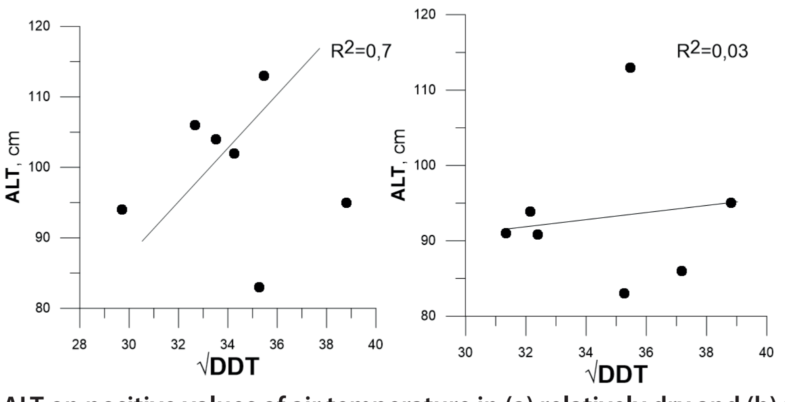

Fig. 5. Dependence of ALT on positive values of air temperature in (a) relatively dry and (b) more humid summer periods

Table 1. The main parameters of active layer and weather conditions affecting its formation

Year	DDT	Precipitations, mm (May-August)	Mean ALT, cm	Cv	INV, min %	INV, max,%
2005	1037	174	81	23.4	-40	84
2006	1050	111	90	24.7	-53	56
2007	1113	261	90	22.2	-45	57
2008	1033	124	94	22.5	-42	58
2009	982	125	92	21.4	-44	57
2010	795	196	93	26.9	-54	71
2011	1086	196	96	23.4	-47	67
2012	1040	185	104	23.0	-43	54
2013	1381	40	**86**	15.4	-100	34
2014	882	238	94	21.2	-44	80
2015	1174	178	102	20.5	-38	43
2016	1244	64	83	20.0	-42	41
2017	1066	170	106	23.8	-39	51
2018	1124	164	104	24.2	-35	54
2019	1258	125	113	19.7	-40	41
2020	1506	58	**95**	18.8	-45	67
Average	1111	150	95	21.9	-47	57

Very high variability in ALT was observed at the site. The interannual variability is 184% in comparison with the average value over 16 years, which is extremely high (Table 1). This result is due to the large differentiation of the site in terms of microrelief, vegetation conditions, and thickness of the peat causing different rates of infiltration, transpiration, and other influential processes.

The coefficient of variation of ALT and the amount of precipitation in the summer period are very high (Fig. 6). The values of the coefficient are minimal in relatively dry summer periods. This indicates that the values of the ALT are grouped near average values. The coefficient is much higher for wet summers. They are more differentiated and grouped around the minimums / maximums in wet years. This is explained by the redistribution of moisture over the site, which leads to higher differentiation of soil thawing.

The annual contrasts of ALT are clearly visible in the maps showing ALT from 2005 to 2020 (Fig. 7). The difference between individual measurement points reach factors of 3–4 in some cases. The contrast in local conditions of heat transfer through the surface lead to this variability.

The R-32 site has a slight southward slope (Fig. 8), which allows water to move to the lower (southeast) part of the site or to stagnate in microtopographic depressions. Two runoff hollows (Fig. 8) redistribute water through the site. ALT values are higher than average in these types of landscapes. The second zone with the highest values of thawing is characteristic of the small well-drained areas occupied by bushes and trees (Alnus Fruticosa, Larex Sibirica and Betula Nana). This is due to the almost complete absence of moss and peat cover, the presence of roots, and increased pathways for summer precipitation through these more porous soils to lower areas.

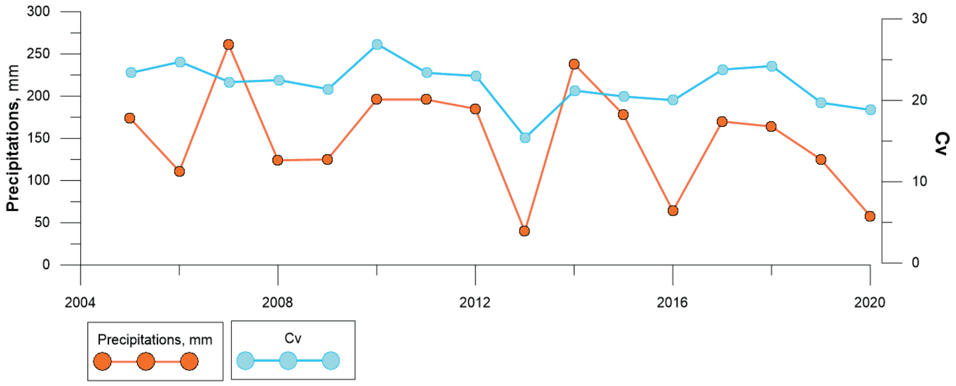

Fig. 6. Graph of the coefficient of variation (standard deviation of indicators for all points from the average value for a particular year) and the amount of summer precipitation

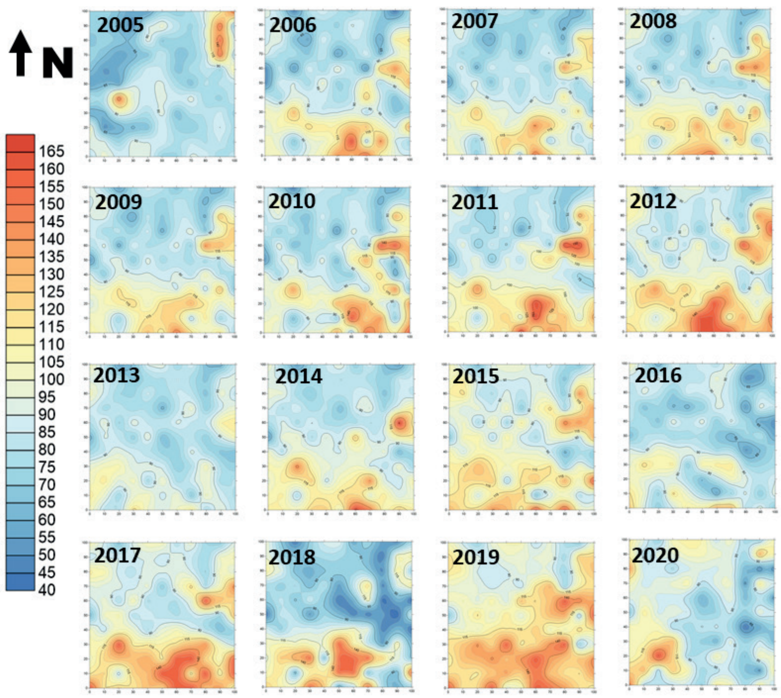

Fig. 7. Active layer thickness maps from 2005 to 2020

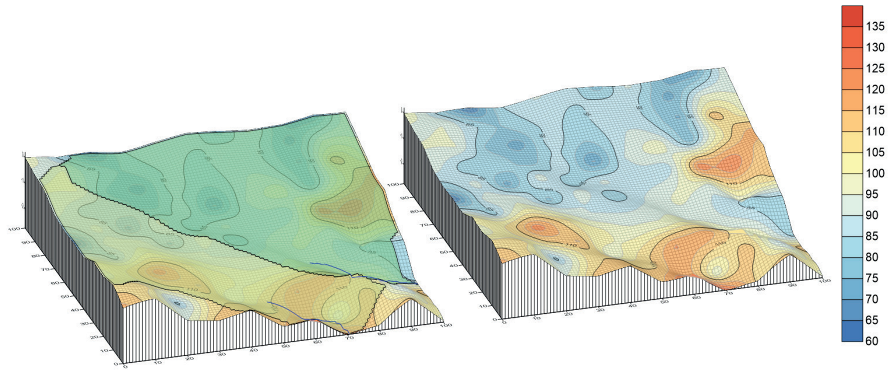

Fig. 8. The microrelief of the site R – 32 with (a) potential water tracks and (b) the average ALT map (2005–2020)

Microlandscape Control Over ALT

The moisture content of the soil affects the depth of thaw. Observations of microlandscape conditions over 12 years show that shrubs are growing rapidly in the eastern and southern parts of the site, which could enhance transpiration and decrease the water content of the active layer. The substrate base remains an inert system. Significant changes have taken place in the microlandscape environment. The height of the shrubs has noticeably increased in the southeastern part of the site compared to 2005. Differences in surficial water content have also increased. We observed, for example, formation of a new water track in the weak runoff hollow. This part of the site tends to be wetter than it was before during the previous decade of the research Water has stayed in this feature during the last 3-4 years of probing. The processes of uneven cryogenic heaving became noticeably more active in the southwestern part of the site (frost-boils on tundra).

The results from Spearman's correlation analysis confirmed that restructuring of the landscape is occurring in the site (Fig. 9).

The 121-point annual datasets were correlated between each other. Thaw values at specific points («thaw patterns») were similar and had a fairly high degree of correlation ($r > 0.75$) between the different years in the period from 2005 to 2010. All landscape-restructuring processes, such as growth of shrubs, the new small water track, and activation of spot medallions (frost boils), altered heat transfer through the surface. This demonstrates that patterns of ALT within the sites were substantially altered over the past decade. Correlation between the datasets for the last five years (2015 to 2020) is quite low and does not exceed 0.4 in general. The changed landscape conditions are shown in Fig. 10 and presented in Table 2. General changes include: the shrubs Salix pulchra and Betula nana have been vigorously expanded into a typical tundra community, consisting of Vaccinium vitis, Vaccinium uliginosum, Carex, Sphagnum for the last decade; the height and coverage area of shrubs and trees are noticeably increased due to growth of Alnus fruticosa and Larix sibirica.

The highest values of soil thawing are noted in those places where microrelief features contribute to thawing, for example, the lowest parts of the site containing stagnant water.

Additional research conducted in 2011 showed that thaw values vary significantly in different parts of frost boils. A large variability in thawing was recorded between the center of medallion spots with an open ground surface, a ridge with a dwarf-sedge-moss cover and a crack with a moist sedge-moss cover for 12 fresh medallion spots. The average depths in these features were 104, 87, and 91 cm.

We compared microlandscape differentiation in the four types of microlandscape that contrast most strongly in terms of heat transfer through the surface:

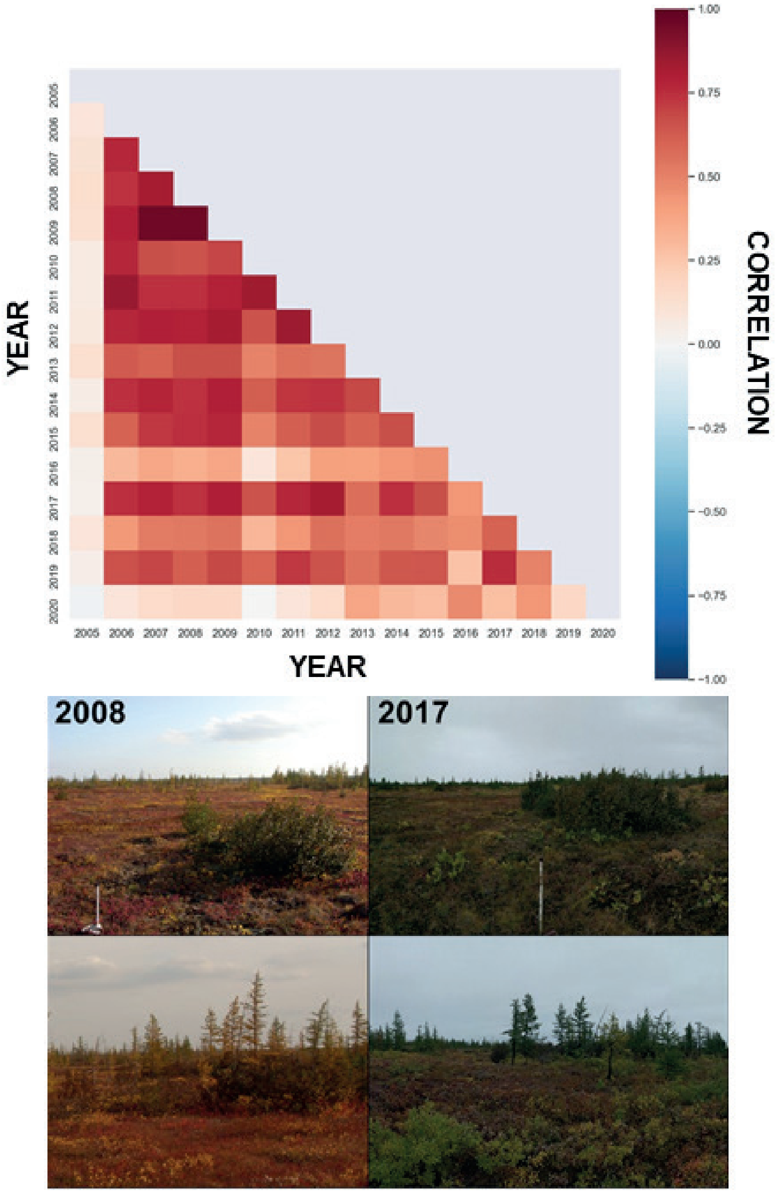

Fig. 9. Results from correlation analysis between the series of active layer thickness data (121 points) for different years. Each cell of the matrix represents the correlation value between two datasets from different years. The bottom part of the figure shows the expansion of bushes at the site. Photos are taken the first point and from the middle of the grid for the period 2008–2017

Table 2. Main landscape types at the site

Landscape type	Vegetation type
High and well-drained areas, with expanding shrubs, which contributed transpiration and decrease in active layer moisture	Larix sibirica, height up to 4-5 m Alnus fruticosa, height up to 2.5-3 m. Betula nana – up to 40-50 cm, Seldom – Salix pulchra, Exus, Vaccinium uliginosum, Vacinium Vitis), seldom -Carex
Frost boils on tundra with fresh frost boils (round loamy soil spots), with predominant sizes about 80-100 cm, the diameter of individual spots reaches 1,5 m, cracks between spots reach 20-30 cm in width and 10-15 depth.	Betula nana 40-50 cm, Ledum palustrum, Vaccinium uliginosum, Vacinium Vitis, seldom Carex, Sphagnum, lichen Cetraria islandica
Relatively flat, slightly swampy surface occupied by birch shrubs, hummocky-hillock surface, chaotic arrangement of hillocks and hummocks, the size of hollows does not exceed 30-40 cm	Betula nana, Salix Polarica, Vaccinium uliginosum, Carex, Sphagnum
Growing runoff hollows, going through all the site. Runoff hollows are most wet and low landscape type.	Salix pulchra, Betula nana, Vaccinium uliginosum, Rubus chamaemorus, Carex, Ereophorum vaginatum, Sphagnum
Downstream swamp, in the place of an overgrown thermokarst lake	Carex, Ereophorum vaginatum, Sphagnum
Thermokarst lake	

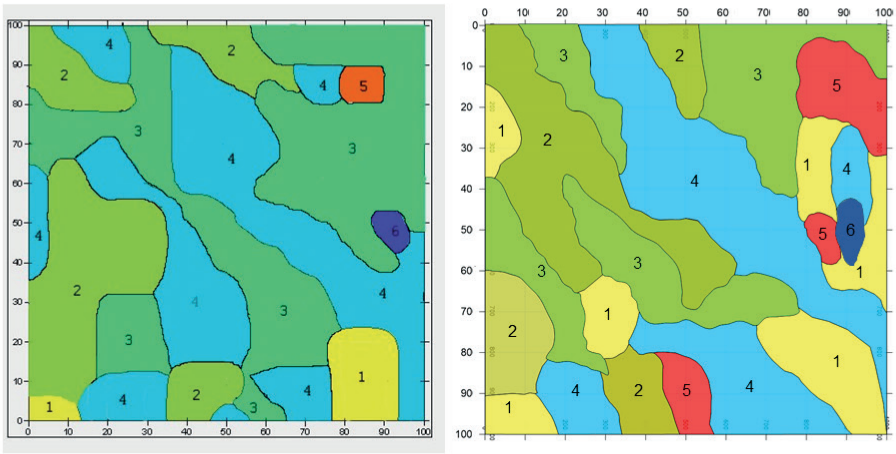

Fig. 10. Active layer thickness maps from 2005 to 2020

a) hummocky tundra with a dense and relatively thick moss-peat cover and shrub vegetation; b) runoff hollows with vegetation represented by sedge-moss communities with separate, low Salix pulchra bushes that have appeared in recent years; c) areas occupied by frost boils on tundra with minimal amounts of moss-peat cover; and d) hillocks with relatively high tree and shrub vegetation. Fig. 11 reflects the differentiation of ALT by landscapes for the observation period (from 2005 to 2020).

The highest values of thawing were found in waterlogged depressions between positive microforms of the relief, and in areas with frost-boils or well drained relatively elevated areas. ALT is lower (much less susceptible to weather fluctuations in different years) within the hummocky tundra occupied by shrub-sedge-moss communities. Moss is a good thermal insulator and provides a relatively uniform heat supply and moisture to soils.

Thaw subsidence

Geodetic surveys of surface elevation were performed at the end of the thawing period, relative to the first point. Because measurements of the surface level at the beginning of the thawing season were not conducted at the site, it is possible to monitor only relative interannual subsidence. Data on intra-annual surface changes, including heaving and subsidence organised at another CALM sites in the Russian northwest and Alaska's North Slope show the importance of thaw subsidence monitoring (Mazhitova and Kaverin, 2007; Shiklomanov et al. 2013; Streletskiy et al. 2017).

Surface elevation remains relatively stable, but it is apparent that the lower, wet areas with a sufficient amount of snow accumulation experience more active subsidence. Analysis of the thaw subsidence rate in various types of landscapes showed that the most stable type of landscapes are areas with well-developed moss cover. Thaw depth here is also minimal. (Table 3). The maximum subsidence rate was found in runoff hollows and open areas of the frost-boil tundra.

There is a very slight difference in surface changes in different years. The thaw subsidence rate does not always directly follow the value of the ALT.

The minimum ALT over 16 years of observations occurred in 2013. The thaw subsidence rate in that year, however, was close or greater than the average in 2013. This is attributed to excessive precipitation in the previous

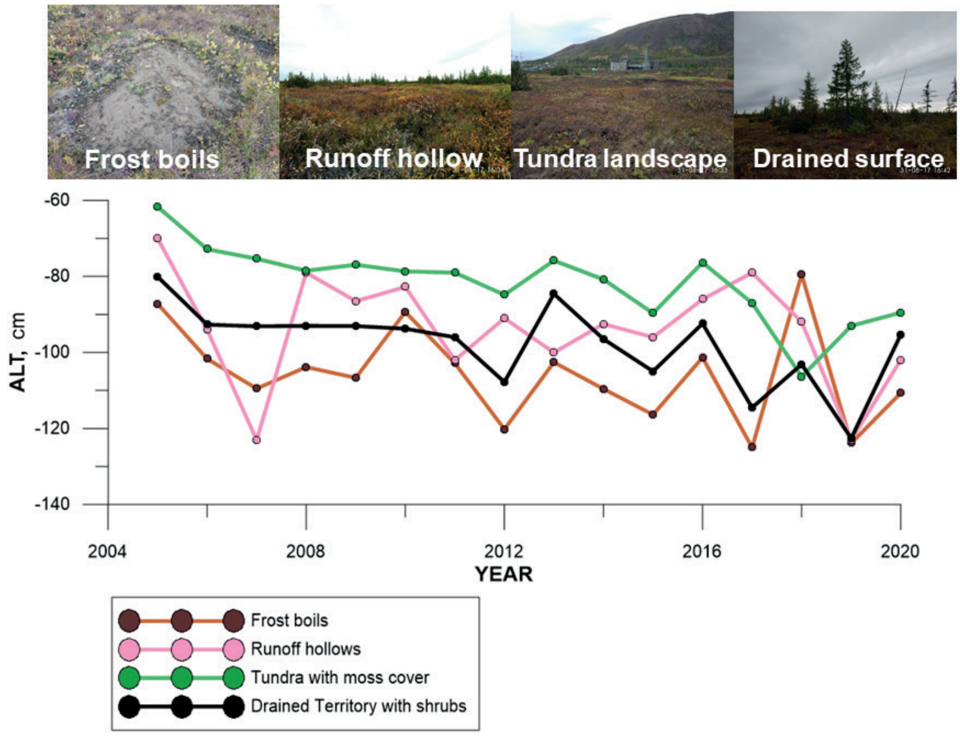

Fig. 11. Active layer thicknesses in different landscape types

Table 3. Thaw subsidence rates in different landscapes

Year	Frost Boil	Frost Boil	Tundra	Tundra	Runoff Hollow	Runoff Hollow
	Geodetic changes, cm	ALT	Geodetic changes, cm	ALT	Geodetic changes, cm	ALT
2010	-3	112	0	84	-4	101
2011	3	110	0	90	16	108
2012	-3	113	1	105	6	121
2013	0	76	-1	84	-21	84
2015	-1	94	-1	101	-4	98
2016	-1	76	0	82	4	79
2017	2	116	0	105	0	123
2018	-1	105	0	101	0	121
2019	2	125	0	101	0	121
2020	-4	92	0	96	-5	96
Total.subsidence	-4		-3		-8	

autumn (2012). The active layer had the maximum moisture saturation, leading to formation of segregation ice. Summer melt of a large amount of ice in the active layer increased the surface settlement. The precipitation regime also played an important role in warm seasons. Heavy rains occur after snowmelt and during the first period of thawing moisten the soil. Water has low compressibility in its liquid state and ice-rich permafrost has low infiltration capacity. These factors lead to the water-stagnant regime of the active layer, protecting it from thaw subsidence. It called «weighing» action of water (SP 25.13330.2012).

The northern part of the site is more stable (relative to point 1). The southwestern part contains more wet soils at the end of the warm period. The latter area recorded a wide range of changes in the soil surface due to higher ice content and the existence of the runoff hollows as water tracks here. Surface «breathing» affects the regimes of floods in each of the specific summer period. These factors can cause local («point») places of desiccation or stagnancy of the soil.

DISCUSSION

Additional work will be required to identify other factors affecting the formation of the active layer at this site. In particular, information about changes in soil moisture and temperature, pre-winter moisture and ice content of frozen soil, the number of frosts during the warm season will be needed. Some researchers state that ALT can be forecast with a sufficient degree of accuracy for most purposes (Bonnaventure and Lamoureux 2013). This does not work for all monitoring sites. Field-based studies (Kaverin et al. 2019) have shown that estimated and forecast ALT, based only on analysis of the sums of positive air temperatures, are not sufficient for soils with different peat content. This conclusion also applies to the Talnakh research site.

The heterogeneity of heat transfer results from soil type and vegetation cover, the thickness and duration of snow cover in certain areas, differences in the ice content of the frozen soils, the porosity of thawing soils and presence of peat formation, temperature regime and the micro-relief of the study area (Nelson et al. 1998; Kaverin 2014, 2019). These factors affect the depth of the active layer.

The depth of thaw based on the results of field observations at the R-32 (Talnakh) site depends on the amount of heat transferred to the soil surface. It includes the multiple factors discussed above, including air temperatures and rain. A combination of these meteorological parameters in certain years («warm – humid», «warm – dry», etc.) and its details during the summer period peaks of temperature increase and precipitation (coincidence / non-coincidence of the rainiest and the warmest periods, and a shift of the maximums of these weather characteristics by the end of July – August, when the thawing is already deep enough) are responsible for the formation of active layer.

Record values of active layer thickness were observed in 2012. These could affect the icy transition layer. During the subsequent heat wave in 2013 accelerated growth of shrubs and landscape restructuring of the site occurred. Differentiation of landscapes within the site is quite noticeable in recent years. This is very apparent in the photos of Fig. 9. These changes determine different conditions of heat transfer, which are enhanced by the dissection of the relief caused by topoclimatic and geomorphic processes.

One of the features of the site is the presence of patches of frost boils on tundra. The processes leading to their formation have been observed during some years (e.g., 2018). According to our hypothesis, its intensification is associated with high pre-winter humidity in some years and low values of negative temperatures in November – December, when the active layer is nearly completely frozen. The activation of the processes of frost boil formation in the southwestern part of the site is associated with the destruction of the soil and vegetation cover, the protective role of which is well known. It significantly affects ALT values.

CONCLUSIONS

A decrease in the severity of the climatic conditions in Taimyr has contributed to major changes in the natural and anthropogenic systems (Kirdyanov et al. 2012; Nyland et al. 2017; Grebenets et al. 2016). These changes are growth of shrubs and trees, an increase in moss and peat cover; increases in the occurrences of building deformations, rising permafrost temperatures, and decreases in the bearing capacity of piles. Field measurements of the parameters of the active layer conducted within the framework of the CALM program at the R-32 (Talnakh) site, showed that over the past 16 years, there has been a tendency towards an increase in the thaw depth of 1 cm / year.

The depth of thawing and the number of positive degree-days illustrates that ambiguity can exist in the relationship between these two parameters. There was no statistical relationship found between the amount of summer heat expressed as degree-days of thawing and active layer thickness. This is associated with the extremely high variability of the amount of atmospheric precipitation during the warm period, with variability in precipitation from year to year reaching up to six times. Statistical analysis shows that the dependence of thaw depth on DDT can be improved if summers with a similar amount of precipitation are compared, underscoring the importance of precipitation on active layer dynamics. The seasonal thaw of soils will be higher if the peak in precipitation shifts from June to the second half of July and August, when the underground runoff in soil is limited and precipitation penetrates deeper and enhances thawing.

Changes in landscape structure were detected at the site during the 16-year observation period, associated particularly with active growth of shrubs and trees. Polar willow has spread quite widely, occupying places that were not previously covered by this species. The maximum seasonal thawing of soils is recorded in runoff hollows, relatively elevated and well-drained areas with trees and shrubs, and in the centres of frost boils. These types of landscape occupy about half of the site. The diversity in vegetation and large differences in the thickness of the moss-peat cover has led to a significant difference in ALT in different years. Interannual differences can involve factors of two or three.

Thaw subsidence rate has a relative relationship with the depth of thawing. The properties of soils have a noticeable effect on thaw values. Local conditions of drainage and surface runoff, types of vegetation, and soil characteristics play important roles in thaw subsidence rate.

The study of active layer dynamics in Taimyr is important, as the region is relatively lacking in permafrost observations and is one of the areas being affected by pronounced climatic warming and the presence of a substantial human population and extensive infrastructure built in permafrost terrain. ■

REFERENCES

Alaska, U.S.A., in Proceedings of the Seventh International Conference.

Abramov A., Davydov S., Ivashchenko A., Karelin D., Kholodov A., Kraev G., Lupachev A., Maslakov A., Ostroumov V., Rivkina E., Shmelev D., Sorokovikov V., Tregubov O., Veremeeva A., Zamolodchikov D., and Zimov S. (2019). Two decades of active layer thickness monitoring in northeastern Asia. Polar Geography, 0(0), 1-17, DOI: 10.1080/1088937X.2019.1648581.

Bonnaventure P.P. and Lamoureux S.F. (2013). The active layer: A conceptual reviewof monitoring, modelling techniques and changes in a warming climate. Progress in Physical Geography, DOI: 10.1177/0309133313478314.

Boyd D.W. (1973). Normal freezing and thawing degree days for Canada: 1931–1960. Downsview. Ontario, Canada: CLI 473 Publ.

Brown J., Nelson F.E. and Hinkel K.M. (2000). The circumpolar active layer monitoring (CALM) program research designs and initial results. Polar Geography, 3, 165-258.

Fagan J.E. and Nelson F.E. (2017). Sampling designs in the circumpolar active layer monitoring (CALM) program. Permafrost and Periglacial Processes, 28(1), 42-51.

French H.M. (1999) Past and present permafrost as an indicator of climate.

Change. Polar Research, 18:2, 269-274, DOI: 10.3402/polar.v18i2.6584.

Frost G.V., Epstein H.E., Walker D.A., Matyshak G. and Ermokhina K. (2018). Seasonal and long-term changes in active-layer temperatures after tall shrubland expansion and succession in Arctic tundra. Ecosystems, 21(3), 507-520.

Gmurman V.E. (2010). Probability theory and mathematical statistics: Textbook for universities. Moscow, Russia: Vyshaya shkola Publ. (In Russian) Golden Software, Inc., SURFER for Windows, version 7 User's Guide, Golden, Colo., 1999.

Grebenets V.I., Streletskiy D.A., Shiklomanov N.I., Kerimov A.G., Ostroumova E.A., Konovalov Y.V. and Andruschenko F.D. (2016). Thermal state dynamics of permafrost basement on engineering objects in cryolithozone of Russia. (2016). In: Book of abstracts of XI International Conference On Permafrost Exploring Permafrost in a Future Earth. Potsdam, Germany: Bibliothek Wissenschaftspark Albert Einstein Telegrafenberg, 1080-1083, DOI: 10.2312/GFZ.LIS.2016.001.

Harlan R.L. and Nixon J.F. (1978). Ground thermal regime. In: O. Andersland and D. Anderson ed., Geotechnical Engineering for Cold Regions. New York: Mc Craw Hill, 103-163.

Hinkel K.M. and Nelson F.E. (2003). Spatial and temporal patterns of active layer thickness at Circumpolar Active Layer Monitoring (CALM) sites in northern Alaska, 1995–2000. Journal of Geophysical Research, 108(D2), 8168, DOI:10.1029/2001JD000927.

Ivchenko G.I. and Medvedev Y.I. (2010). Introduction to mathematical statistics. Moscow: LKI Publ. (In Russian).

Kaverin D.A., Pastukhov A. V. and Mazhitova G.G. (2014). Temperature regime of tundra soils and underlying permafrost (Northeastern European Russia). Earth's Cryosphere, 18(3), 23-32. (In Russian).

Kaverin D.A., Pastukhov A.V., Novakovsky A.B., Biasi K., Maruschak M. and Elsakov V.V. (2019). Landscape and climatic factors impacting the thaw depth in soils of permafrost peat plateaus (on the example of Calm R52 site). Earth's Cryosphere, 23(2), 62-71, DOI: 10.21782/KZ1560-7496-2019-2(62-71) (In Russian).

Kirdyanov A.V., Hagedorn F., Knorre A.A., Fedotova E.V., Vaganov E.A., Naurzbaev M.M. and Rigling A. (2012). 20th century tree-line advance and vegetation changes along an altitudinal transect in the Putorana Mountains, northern Siberia, Boreas, 41(1), 56-67.

Konischev V.N. (2011). The response of permafrost to climate warming. Earth's Cryosphere, 15(4), 15-18 (In Russian with English summary).

Kudryavtsev V. (1954). Thermal regime of the upper horizons of rocks Moscow: Publ. of the Academy of Sciences of the USSR (In Russian).

Kudryavtsev V. and Dostovalov V. (1967). Obschee merzlotovedenie. Moscow: Publ. of Moscow State University (In Russian).

Laval, Laval, Quebec, 1998

Laval, Laval, Quebec, 1998

Luo D., Wu Q., Jin H., Marchenko S.S., Lü L. and Gao S. (2016). Recent changes in the active layer thickness across the northern hemisphere. Environmental Earth Sciences, 75(7), DOI: 10.1007/s12665-015-5229-2.

Maslakov A., Shabanova N., Zamolodchikov D., Volobuev V. and Kraev G. (2017). Permafrost Degradation within Eastern Chukotka CALM Sites in the 21st Century Based on CMIP5 Climate Models. Geosciences, 9(5), 232, DOI: 10.3390/geosciences9050232.

Mazhitova G.G. and Kaverin D.A. (2007). Thaw depth dynamics and soil surface subsidence at a Circumpolar Active Layer Monitoring (CALM) site, the European North of Russia. Earth's Cryosphere, 11, 20-30 (In Russian).

Mazhitova G.G. & Kaverin Dmitry. (2007). Thaw depth dynamics and soil surface subsidence at a Circumpolar Active Layer Monitoring (CALM) site, the European North of Russia. Earth's Cryosphere. 11. 20-30. Miller L.L., K.M. Hinkel, F.E. Nelson, R.F. Paetzold and S.I. Outcalt, Miller L. L., K. M. Hinkel F. E. Nelson R. F. Paetzold and S. I. Outcalt,TMoskalenko N.G. (1999). Anthropogenic dynamics of vegetation of the plains of the permafrost zone of Russia. Novosibirsk: Nauka Publ. (In Russian)

Nelson F.E. and Outcalt S.I. (1987). A computational method for prediction and regionalization of permafrost. Arctic and Alpine Research, 19(3), 279-288.

Nelson F.E., Outcalt S.I., Brown J., Shiklomanov N.I. and Hinkel K.M. (1998). Spatial and Temporal Attributes of the Active-Layer Thickness Record, Barrow, Alaska, U.S.A. Permafrost – 7th International Conference, 55, 797-802.

Nyland K.E., Shiklomanov N.I. and Streletskiy D.A. (2017) Climatic – and anthropogenic-induced land cover change around Norilsk, Russia, Polar Geography, 40(4), 257-272, DOI: 10.1080/1088937X.2017.1370503.

General Permafrost Science (geocryology). (1978). Moscow: Publ. of Moscow State University (In Russian).

General Permafrost Science. (1974). Novosibirsk: Nauka Publ. (In Russian) on Permafrost, vol. 1, pp. 731 – 737, Cent. d'Etud. Nordiques, Univ.

Popov A.I., Arkhangelov A.A., Velikotsky M.A., Zhigarev L.A., Konishchev V.N., Marakhtanov V.P., Tumel N.V. and Shpolyanskaya N.A. (1989). Regional cryolithology. Moscow: Publ. of Moscow State University (In Russian)

Sheveleva N.S. and Homichevskaya L.S. (1967). Geocryological conditions of the Yenisei north. Moscow: Nauka Publ. (In Russian)

Shiklomanov N., Streletskiy D., Little J. and Nelson F. (2013). Isotropic thaw subsidence in undisturbed permafrost landscapes. Geophysical Research Letters, 40, 6356-6361.

Smith S.L., Wolfe S.A., Riseborough D.W. and Nixon M. (2009) Active-Layer Characteristics and Summer Climatic Indices, Mackenzie Valley, Northwest Territories, Canada. Permafrost and Periglacial processes, 20, 201-220

SP 25.13330.2012 Basements and foundations on permafrost soils (In Russian) Spatial and temporal patterns of soil moisture and thaw depth at Barrow,

Streletskiy D.A., Shiklomanov N.I., Little J.D. and Nelson F.E. (2017). Thaw subsidence in undisturbed tundra landscapes, Barrow, Alaska, 1962–2015. Permafrost and Periglacial Processes, 28(3), 566-572.

Streletskiy D.A., Sherstiukov A.B., Frauenfeld O.W. and Nelson F.E. (2015). Changes in the 1963–2013 shallow ground thermal regime in Russian permafrost regions. Environmental Research Letters, 10(12), 125005.

SURFER for Windows, version 7 User's Guide. (1999). Colorado: Golden Software Inc.

GWU.edu/calm (2021). CALM program web-site. [online] Available at: https://www2.gwu.edu/~calm/ [Accessed 1 May 2021].

ArcticData.io (2021). Arctic Data Center. [online] Available at: https://arcticdata.io/catalog/view/doi:10.18739/A2KP7TS45 [Accessed 1 May 2021].

REVIEW

BUILDING STABILITY ON PERMAFROST IN VORKUTA, RUSSIA

Pavel I. Kotov[1*], Vanda Z. Khilimonyuk[1]
[1]Lomonosov Moscow State University, Faculty of Geology, Moscow, Russia.
***Corresponding author:** kotovpi@mail.ru
Received: April 18th, 2021 / Accepted: November 9th, 2021 / Published: December 31st, 2021
https://doi.org/10.24057/2071-9388-2021-043

ABSTRACT. The Infrastructure stability on permafrost is currently an important topic as the Arctic countries are developing climate change adaptation and mitigation programs. Assessing the sustainability of infrastructure facilities (especially in urban environments) is a difficult task as it depends on many parameters. This article discusses the city of Vorkuta, which is located in the northwest of Russia. This city differs from many others built on permafrost because most of buildings were built according to Principle II (The Active Method) of construction on permafrost with thawing soil prior to construction. Assessments of the engineering and geocryological conditions, basic principles of construction in the city, and reasons for building failures, were carried out within this study. The research is based on publications, open data about buildings, and visual observations in Vorkuta. About 800 buildings are in use in Vorkuta in 2020 (43% of what it was 50 years ago). According to the analysis, about 800 houses have been demolished or disconnected from utility lines over the past 50 years (about 250 of these are still standing, pending demolition). Since 1994, the construction of new residential buildings has almost stopped. Therefore, buildings that have been in use for over 50 years will account for 90% of the total residential housing stock by 2040. The effects of climate change in the city will depend primarily on the principle of construction employed and on the geocryological conditions of the district. Buildings constructed according to Principle I (The Passive Method) were found to be more vulnerable due to a decrease in permafrost bearing capacity. The impact of increasing air temperature on some of the buildings built on bedrock (the central part of the city) and some built on thawing soil will be minimal, as other factors are more significant.

KEYWORDS: Vorkuta, permafrost, Arctic cities, urban infrastructure, foundation, climate change

CITATION: Pavel I. Kotov and Vanda Z. Khilimonyuk (2021). Building Stability On Permafrost In Vorkuta, Russia. Geography, Environment, Sustainability, Vol.14, No 4, p. 67-74 https://doi.org/10.24057/2071-9388-2021-043

Conflict of interests: The authors reported no potential conflict of interest.

INTRODUCTION

Permafrost covers 21 million km^2. This accounts for 22% of the Northern Hemisphere's exposed land area (Obu et al. 2019). There are 1162 permafrost settlements with a total of 5 million inhabitants. Most of these settlements are relatively small (with a median size of 622 inhabitants), but 123 of them had a population of over 5000 inhabitants in 2017. Eighty-five percent of these large permafrost settlements are located in the Russian Arctic. These Russian settlements are mostly located on continuous permafrost, except for in a few regions (the Komi and Nenets regions), where settlements are located in zones of sporadic and discontinuous permafrost. The majority of settlements in the Arctic are in continuous permafrost zones (Ramage et al. 2021).

The major factor of infrastructure accidents in permafrost regions is the change of the soil temperature regime, which may be caused by natural or anthropogenic factors. Several studies focused on the assessment of the climate change impact on permafrost, including (Nelson et al. 2001; Romanovsky et al. 2010; Aalto et al. 2018; Vasiliev et al. 2020). Near-surface permafrost in the Arctic warmed by over 0.5°C between 2009 and 2017 (Biskaborn 2019), leading to changes in the stability of infrastructure, on which Arctic inhabitants are directly dependent.

Cities on permafrost (especially in the Russian Arctic) are very complex systems, which combine natural and technical sites. A city is a center of concentrated anthropogenic impact on the natural environment, covering a large area. The consequences of this negative impact depend both on natural conditions (climatic, geocryological) and on the intensity of the anthropogenic impact, which leads to a significant change in the natural conditions. Geocryological conditions are a set of permafrost characteristics that affect the construction and use of infrastructure facilities. These characteristics include the distribution of permafrost, composition and properties of frozen soil (the physical, mechanical and thermal properties), mean annual ground temperature, morphology and genesis of taliks, composition, properties and depth of the active layer, and also geocryological processes. Cities in the Arctic develop their own special microclimate: their radiation balance, air temperature and humidity, wind conditions and precipitation, along with the spatial distribution of these characteristics, are changing (Khrustalev et al. 2011). As a result, there is a significant transformation of geocryological conditions and change in the thermal state of the environment. Moreover, each city has its characteristics that must be taken into account. A series of works is devoted to urban infrastructure in the Arctic (Khrustalev and Davidova 2007;

Grebenets et al. 2012; Streletskiy et al. 2012b; Melvin et al. 2017; Shiklomanov et al. 2017; Hjort et al. 2018; Streletskiy et al. 2019; Shiklomanov et al. 2019).

This work focused on Vorkuta, as one of the largest Arctic cities built on permafrost (with a population of 73,100 in 2020). Vorkuta is located in the European part of Russia. It was founded in 1930 as a GULAG mining camp and experienced intensive urban development between the 1960s and 1990s (Barenberg 2014). The region of Vorkuta is unique because, within a small area of the city, there is a wide variety of geological and geocryological conditions as well as economic activities (from coal mining to agricultural facilities). Practically all known methods of construction on permafrost can be found in the city.

The infrastructure of Vorkuta consists of buildings, underground, surface, and above-ground utility lines, roads and parking lots, pedestrian paths, green spaces, and parks. Contact areas of these elements with the ground surface form places with heat sources and temperature sinks. The sources of heat include the areas occupied by buildings built according to Principle II, underground utility lines, and green spaces (they accumulate snow and have a warming effect on permafrost). Temperature sinks (cold spots) include the areas occupied by buildings built according to Principle I, roads, parking lots, and any other surfaces where snow cover is removed. The temperature regime of soils can be affected by changing the structure of urban space. For example, this could be a change in the density of buildings, roads, the ratio of areas subject to technical reclamation (drainage, backfilling with sand, landscaping, snow removal). The density of buildings in the residential part of Vorkuta varies from 13 to 24% (Khrustalev et al. 2011).

The transport system consists of roads, railway lines, and an airport. The length of highways throughout the region is 120 km, and in the central part of Vorkuta it is 70 km. There is no road connection between Vorkuta and any other cities, it is connected with the center of Russia by the railway line Vorkuta - Kotlas -Moscow and with Western Siberia by the railway line Vorkuta -Labytnangi. Transport infrastructure is not considered in this research. It is necessary to take into account another set of permafrost parameters to assess the stability of transport infrastructure (Isaev et al. 2020).

Recently, there have been many assessments of the climate change impact on infrastructure (Khrustalev and Davidova 2007; Streletskiy et al. 2012a; Hjort et al. 2018). For example, according to one modelling study, Vorkuta is a high-risk infrastructure hazard area in the Russian Arctic (Hjort et al. 2018). However, most of the models do not consider the complex integral impact of all factors (geocryological conditions, features of the territory, principles of construction), which may lead to an incorrect interpretation of modelling results.

This paper discusses the role of permafrost conditions in the urban development of Vorkuta, the basic methods of construction, the reasons for infrastructure failure, and the impact of climate change on building stability.

STUDY AREA

Vorkuta is located in the Ural region of the Bolshezemelskaya tundra, which is characterised by a gentle hilly plain with average elevations of 50–180 m. The climate is determined by the location of the region in the subarctic with low solar radiation in winter, the proximity to the northern seas, and intense westerly air mass transfer. The frost-free period is about 70 days, and winter lasts about eight months. The average air temperature is -5.53°C. An important factor of the temperature regime of frozen soils is snow cover (Isaev et al. 2020). The duration of the period with a stable snow cover is about 200 days. The average thickness of the snow cover is 62 cm; in urban areas it is 88 cm. In winter, some parts of the territory are exposed to snowdrifts, the thickness of which, in some places, can reach over 3.0 m.

Geological structure of the Vorkuta region includes deposits of the Devonian, Carboniferous, Permian, and Quaternary ages. Carbonate sediments (dolomites, limestones, and marbles) represent Carboniferous and Devonian deposits. Terrigenous sediments (conglomerates, sandstones, siltstones, mudstones, and coals) represent Permian deposits. These Paleozoic and Mesozoic rocks are covered by Quaternary sediments (Geocryology 1986).

The thickness of the Quaternary sediments cover varies from several meters up to 80-120 meters. It is uneven in thickness and complex in structure (Geocryology 1986). Genetically, Quaternary sediments are subdivided into four main types: diluvial, upper moraine, fluvioglacial, and lower moraine. There are some water-logged areas in the Vorkuta region, which contain lacustrine-boggy sediments and peat (Markizov 1991).

Silty clays with gravel mainly represent diluvial sediments, the amount of which increases with depth. The thickness of the cover-diluvial formations most often ranges from 0.5 to 1 m, going up to 3 m on the slopes, and 5 m at the bottom of the slopes.

Silty clays are characterized by a high content of clay particles (45–55%) and water content (25 - 30%). Silty clays and loams mainly represent the soils of the upper moraine. The content of clay particles is 35 to 45%, gravel – up to 10%. The water content is close to the liquid limit.

Fluvioglacial sands are usually water-saturated in the thawed state. Because of their high infiltration capacity, these deposits often contain groundwater.

Silty clays and loams with inclusions of gravel represent the lower moraine. These soils are often frozen. The ice content in the upper part is 25–31% and decreases with depth.

Lacustrine-bog sediments consist mainly of silty clay and clay. They contain thick (up to 0.2-0.4 m and more) ice layers and ice lenses. After thawing, these sediments have a low bearing capacity.

Thaw subsidence of Quaternary sediments depends on the quantitative content of ice inclusions, their shape, and position within the ground. For example, the maximum thaw subsidence of diluvial sediments is 0.2-0.3 m/m, whereas for lacustrine-boggy sediments it is 0.7 m/m. The minimum subsidence is observed in sandy and gravel deposits with a massive cryogenic texture (less than 0.01 m).

The features of the relief, widespread presence of clay in the Quaternary sediments and the permafrost extent result in a high occurrence of swamps and lakes, mainly of thermokarst genesis.

Vorkuta belongs to the subzone of discontinuous high-temperature permafrost, which occupies up to 80-90% of the area (Geocryology 1986). The area contains many taliks of various genesis. The most common permafrost thickness is 40-80 m. The permafrost table is uneven, varying from several meters to 40 m. The smallest depth of the permafrost base is 15–20 m, the highest is 200 m. The mean annual ground temperature varies from -0.1 to -1.5 °C (rarely -2.0°C). The thickness of the active layer varies from 0.3 to 2.5 m. Unfrozen soils are found near the Vorkuta River (Khilimonyuk et al. 2011).

METHODS

Several reported cases of collapsed buildings were evaluated to determine the reason for such incidents, and then fieldwork was carried out to determine whether faulty design, faulty maintenance, or both, caused the failure. The current state of buildings in Vorkuta was examined during fieldwork, with analyses of relevant scientific publications, official reports, and reports from the municipal authorities. Building observations were carried out as part of the field courses for master students, organized by the Geocryology Department of MSU. Master students, led by representatives of the geocryological service of the Komi Republic, studied the experience of construction and use of buildings in Vorkuta and carried out visual and instrumental surveys of the foundations. Building observations consisted of the following stages:

- Gathering of information about the history of the building;
- A visual inspection, during which the presence of structural defects and deformations of the building and its structures (deflections, rolls, bends, distortions, faults, etc.), features of nearby areas of the territory, vertical planning, organization of surface water drainage were determined;
- An instrumental inspection, which consisted of measuring the geometric parameters of buildings, determining the actual characteristics of building materials, and the parameters of cracks;
- Surveys of foundations, which included the excavation of pits near the foundations with a description of the soil and an examination of the condition of the foundation. Cracks in structures (transverse, longitudinal, inclined, etc.), bare reinforcement, concrete falls, areas of concrete with discoloration, and the most damaged areas of foundation structures were all recorded to assess the condition.

Based on a literature review and field research, the information on the engineering design of foundations in Vorkuta and the main reasons for urban infrastructure failure in the city was summarized.

RESULTS AND DISCUSSION

ENGINEERING DESIGN OF FOUNDATIONS

Practically all major methods of construction on permafrost (construction on bedrock, Principle I, Principle II) can be found in Vorkuta. The most common type of foundation is piling foundation (accounting for about 80% of the housing stock) (Eroshenko et al. 1979). In this section, the engineering design of foundations is considered in more detail.

Construction on bedrock

In some areas of Vorkuta, bedrock is found at a depth of 1.5 to 5 meters. This is enough for the construction of pile or column foundations. Most of the buildings, built on bedrock, currently are in a stable state (Vorkuta thermal power station, city center, Northern and Leninsky districts).

Principle I

A major task is to preserve the soil in the frozen state during the construction and lifespan of the structure. A crawlspace foundation is the most common foundation type in Vorkuta. Quarter 22 (comprising 2-storey wooden panel and stone buildings) was built in the 1950s according to Principle I. During the first 9 years of the use of buildings, the permafrost table rose due to clearing and removing snow from the streets (Khrustalev et al. 2011).

In Vorkuta, about 100 wooden one- and two-storey buildings were built on shallow foundations according to Principle I from 1950 to 1960 (Markizov 1991). Slag, gravel, natural sand-gravel mixture, burnt rock from mine waste heaps, and other local materials were used for backfilling (Romanenko et al. 1974).

Principle II

Since 1970, most of the buildings in Vorkuta were built according to Principle II. This principle includes three major methods of foundation construction: adaptation of the building to uneven subsistence during thawing; preliminary thawing of the permafrost and stabilization of the permafrost's initial position.

The method of adapting a building to uneven subsidence during thawing is the oldest method of foundation construction in the North, which was used in the 1930-1950s. A survey of 94 buildings in Vorkuta showed that 29 of them were deformed within 5-10 years after they began to be used (Bondarev 1964). The average relative subsidence of the buildings was 0.25 m (for some buildings, up to 1 meter). Such large subsidence of the foundation is not possible to compensate for due to the destructive stresses that arise in it.

V.F. Zhukov (Zhukov 1958) proposed possibilities and outlined major conditions of using preliminary thawing of permafrost in 1958. Following that work, wide practical implementation of an alternative method of foundation construction began (Bondarev 1964). Calculations showed that to ensure the stability of buildings in Vorkuta, it is necessary to pre-thaw the permafrost to a depth of 18-31 m. But such a large pre-thawing depth also leads to enormous capital expenditures for preparing the foundation. This method became dominant in Vorkuta since 1970.

The method of stabilizing the permafrost's initial position was developed by the employees of the Gersevanov Research Institute of Bases and Underground Structures (which has a branch in Vorkuta) and engineers of Vorkutaugol (Khrustalev and Nikiforov 1990). This method was used when an unfrozen layer was detected below the active layer and the permafrost table. Frozen soils in this case are characterized by significant compressibility during thawing (over 0.02 m/m) and the foundations are located in a layer of thawed soil. The stabilization method relies on the fact that the permafrost table is stable all the time due to the alternating mode of operation of foundation ventilation. Alternating periods last 5-15 years with a negative average annual air temperature in the foundation (cold period) and 2-5 years with a positive average annual air temperature (warm period). It is necessary to consider frost heaving forces. A few 26-panel five-story buildings (1975–1978) were constructed in the settlement Vorgashor using this method. A modification of the stabilization method used cooling devices instead of ventilated foundations. Ten structures were built in 1980 using this modified method.

In Vorkuta, about 237 one- and two-story buildings were built on shallow foundations according to Principle II (Markizov 1991).

Combination of Principle I and Principle II

This approach was used for Quarter 7 in the city center, where some houses were built according to Principle I, and others according to Principle II. This part of the city is characterized by an intense degradation of permafrost. The building density in this area is about 24% and there is a developed network of underground utility lines (heat pipelines, hot and cold water supply lines, sewerage).

High building density and significant thickness of snow cover led to the thawing of frozen soil near the buildings (Khrustalev et al. 2011). In addition, because of the deep thawing, infiltration of groundwater had increased, which further impacted the thermal regime as well. The cooling of soils only due to the presence of ventilated crawlspaces is insufficient to withstand the general changes in the permafrost conditions. The possibility of intensive thawing of frozen soils was not taken into account in this area, so most of these buildings were deformed. Buildings constructed according to Principle I have the greatest deformations. A similar situation was observed in the Railroad District of Vorkuta (Belotserkovskaya et al. 1989).

HISTORY OF THE DEVELOPMENT OF VORKUTA

The history of Vorkuta began in 1921, when the first expedition, headed by Alexander Alekseevich Chernov started to study the Pechora region. A large Pechora coal deposit was discovered in 1924. In 1930, the Vorkuta coal deposit was discovered and the first coal was mined in 1934 (Strategy 2020). From 1934 to 1960, a railway, a thermal power station, 15 mines, woodworking and cement plant, residential and industrial buildings, along with roads in the city were built. Of 953 buildings constructed on permafrost soils in 1961, 856 were built without consideration of the frozen state of the ground (Bakalov 1964).

In 1960–1970, Vorkuta developed at a rapid pace: the volumes of coal production were constantly growing. Among the large new buildings of these years are the Khalmer-Yu, Yun-Yaga, and Vorgashorskaya mines, a dairy plant, a distillery, a poultry factory, and a garment factory. In 1977, there were 1.184 buildings in the Vorkuta region (Belotserkovskaya and Ponomarev 1985).

Vorkuta reached its greatest prosperity in the 1980s. In those years, the population reached 200 thousand people, while the production of cement and reinforced concrete structures in the city grew, and the volume of coal production increased significantly. About 100 thousand square meters of housing were commissioned annually (Barenberg 2014).

The period from 1991 to 2006 turned out to be difficult and unstable years for the city. The political, economic, social crisis in the country also affected coal mining, and production began to decline. Most of the mines were closed and the population began to decline likewise (Shiklomanov et al. 2019).

In 2006, the municipal formation of the urban Vorkuta district was established, consisting of the city of Vorkuta and several settlements (Vorgashor, Eletsky, Zapolyarny, Komsomolsky, Meskashor, Mulda, Oktyabrsky, Promyshlenniy, Severny, Seida, Sivomaskinsky, Khanovei, and Yurshor). Most of the settlements were closed and abandoned (Shiklomanov et al. 2019). Since 2006, statistical processing of the socio-economic state of the city has been carried out, which was subsequently used for data processing.

The current state of the housing stock in Vorkuta is assessed using the online service of The Ministry of Construction, Housing and Utilities (https://dom.mingkh.ru/), which contains information about the housing stock in the Russian Federation, as well as statistics from 2006 to 2019 (Passport 2015; Passport 2020).

After the collapse of the USSR and the crisis in the mining industry, many residents left the city, moving to the southern regions of the country. The population of the city continues to decline annually, from 108.9 thousand (2006) to 73.1 thousand (2020) (Fig. 1).

This reduction in the number of people leads to the need to reduce the number of buildings since most of them are not used (Shiklomanov 2019). Thus, there is a constant reduction in the number of residential buildings in settlements. Compared to 2006, only 20% of the housing stock in the satellite settlements remains, whereas in Vorkuta it is still 80% (Fig. 1).

In 2020, about 800 residential buildings were in use in Vorkuta. There is no complete data for 41 houses, so further processing was carried out for 759 houses. Figure 2 shows the current state of the housing stock. 55% of the buildings have 5 floors, 15% have 2 floors, 12% have 3 floors, and the remaining 18% make up buildings with other numbers of floors - less than 5% each (Fig. 2).

According to Russian standards, buildings are expected to be used for 50 years (GOST 27751-2014). Thus, houses built before 1970 have been in use for more than this period. There are 43% of such buildings in Vorkuta. Every year the number of such buildings will increase and by 2040 it will reach 90% if the current trends continue.

Every year the number of buildings in a «critical» state increases (Passport 2020). It means a critical technical state of the building, characterized by its destruction or damage and deformations, which can cause loss of stability. As of January 1, 2019, 47 residential buildings were officially deemed critical and unusable. Thus, the number of critical houses in the city does not exceed 6%.

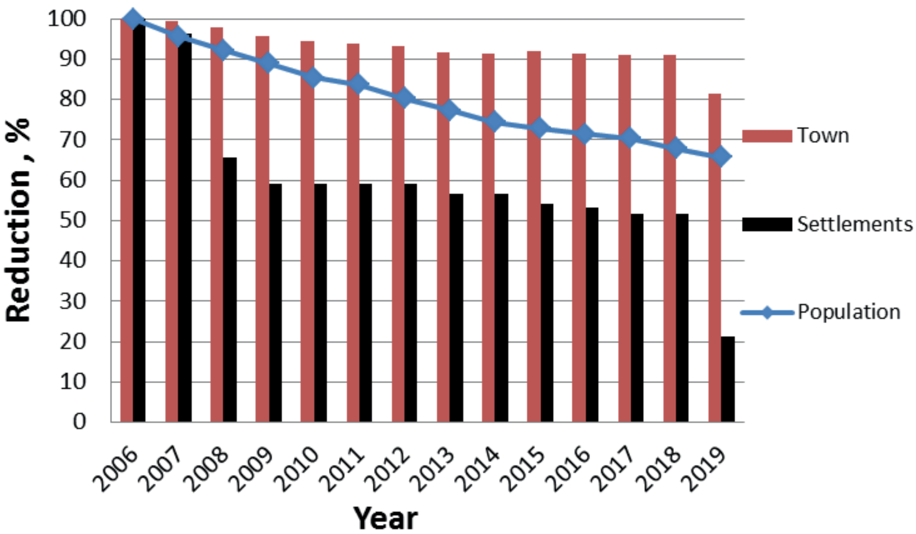

Fig. 1. The reduction of total residential housing stock (in the city and satellite settlements) and population (total population in 2006 is taken as 100%)

After resettlement of such buildings, it is necessary to demolish them and reclaim the territory. However, at present, these works are practically not carried out. The mayor of Vorkuta said in an interview that there are 155 abandoned buildings in the city (Interview 2020). It is almost 20% of the total residential housing stock. A special municipal program provides for the relocation of the population to the central part of Vorkuta to reduce the ineffective expenditures of the local budget for the maintenance of excess infrastructure (Strategy 2020). It includes the closure of several settlements and the disconnection of 47 buildings from utility lines. Over the four years of the program, 71 houses were disconnected from utilities, and 27 houses were demolished (Passport 2020).

If we compare how the housing stock has changed over time, then the following stages can be distinguished. Until 1961, mainly two and three storey wooden houses were built. Currently, 163 such houses are still in use, i.e. only 17% of the total number of houses existed in 1961.

From 1964 to 1994, active construction of brick (and later panel) 5-story buildings began. Currently, 417 houses built before 1977 are in use, i.e. only 35% of the total number of houses. Thus, 800 houses have been demolished or disconnected from utility lines over the past 50 years.

It is also necessary to take into account the deterioration of utility lines. In 2018 and 2019, there was an increase in the number of accidents at sewerage facilities and heating pipelines. Furthermore, leaks and unaccounted water consumption increased from 28 to 62% (2006–2019). It will lead to a more rapid thawing of permafrost and the modification of cryogenic processes.

THE MAIN REASONS OF INFRASTRUCTURE FAILURE

The analysis of infrastructure failure was carried out based on data from scientific publications of employees of the Gersevanov Research Institute of Bases and Underground Structures (Vorkuta branch), where systematic long-term observations of building stability were started (Bakalov 1964; Bondarev 1964; Belotserkovskaya and Ponomarev 1985; Belotserkovskaya et al. 1989). As a result, the following reasons can be distinguished.

1. Ignoring geocryological conditions, composition, and properties of frozen soils. During construction in the period 1930-1950, the depth of boreholes during engineering survey was 5-8 meters, in the 1960s and even at the beginning of the 1970s, it was increased to 10-12 m. The buildings were constructed according to Principle II without taking into account the high compressibility of soils during thawing below 10 meters depth, which led to significant and uneven settlement of soil during the building's use. Examples of buildings deformed for this reason are numerous.

The design and construction of the administrative building of construction department No. 6 (1970-72) was carried out without preliminary research. Although a solid reinforced concrete slab with rib beams was used as the foundation, the building experienced uneven settlement of soil and was later demolished in 1978 (Khrustalev et al. 2011). The railroad district of Vorkuta is one of the most complex areas. The upper part of the cross-section consists of ice-rich lacustrine-boggy soil (0.2-2.5 m thick) and diluvial sediments (1.0-4.5 m thick) with ice interlayers. The depth of foundation under each building was made the same, and adjacent foundations were located in both thawing and frozen soils since pre-construction preparation of the soil base was not considered in these projects (Belotserkovskaya et al. 1989). Ignoring the geocryological conditions and the compressibility of frozen soil after thawing led to the failure of some buildings.

2. Using two principles of construction in the same district. Sometimes a project was carried out when the facility was already in use, such as during the ground or underground laying of plumbing and heating networks in the immediate vicinity and even inside the contour of structures constructed according to Principle I. Such violations were very common for buildings constructed in the 1950s and 1960s, for example the city hospital, school, Krasnoarmeyskaya and Suvorov streets, and the railroad district. The principle of construction was independently selected for each building without considering the railroad district development as a whole (Belotserkovskaya et al. 1989).

3. Mistakes made during the construction processes. The most common and constantly occurring mistakes of construction technology are:
- waterlogging of foundation pits and construction sites;
- failure to perform adequate planning to provide a slope necessary for surface water runoff;
- allowing freezing of the thawed soil base during the construction processes;
- failure to design adequate ventilation of the foundation during the lifespan of structures.
- failure to ensure the design bearing capacity of piles due to under-loading of piles to design elevations.

4. Poor quality of construction materials. Northern climate combined with the possible effect of salt solutions

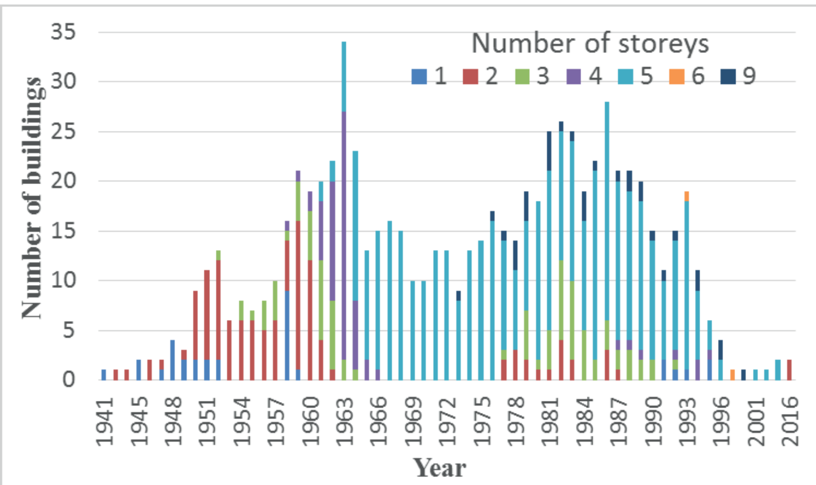

Fig. 2. Breakdown of the current (2020) existing structures in Vorkuta, according to the year of construction (1941-2016) and the number of storeys. There are no 7- or 8-storey buildings

in soils significantly intensify destructive processes in concrete, leading to a premature decrease in its strength (Grebenets et al. 2002; Grebenets and Ukhova 2008). When examining buildings in Vorkuta, wall panels were found with damage over the entire surface. Balcony slabs, canopies, and basement panels collapse very quickly under these conditions. After 2-3 years of use, almost all buildings showed traces of frost damage. A survey of Vorkuta foundations showed that up to 50% of columnar and pile foundations show signs of concrete damage in the form of cracks (20–30 cm long and more than 1 mm thick) after 10 years of use (Pantileenko 2016). The strongest concrete damage is observed in the active layer or above the surface. There is no concrete damage to the foundation below the active layer.

5. Improper building use. This can lead to changes in temperature and humidity conditions near the foundation. It is possible to subdivide improper building use into the following:
- the impact of water: repeated natural and technogenic flooding of the foundation, especially accumulation of chemically aggressive wastewater;
- improper use of the crawlspace foundation limiting ventilation;
- long-term heat sources near buildings constructed according to the first principle (hot water pipelines, coal ash dumps, waste heaps, rainwater pits).

CLIMATE CHANGE IN THE VORKUTA REGION

Processing of the average annual air temperature at the Vorkuta meteorological station showed that from 1937 to 1998, temperatures did not change dramatically, but from 1998 to the present, a steady increase in air temperature has been observed (fig. 3).

Monitoring of the soil temperature began in Vorkuta at the beginning of the 1960s (Oberman 2008). The mean annual ground temperature in the western Russian Arctic has increased by 0.03 to 0.06°C/yr, and the permafrost table has lowered by up to 8 m in the discontinuous permafrost zone (Vasiliev et al. 2020). According to the observation data, the permafrost temperature near Vorkuta has increased by 0.02 °C to 0.68 °C/yr. The thickness of taliks has increased by 2 meters in some areas (Report 2019). Winter climatic parameters and thickness of the peat horizon of soils have a major impact on the active layer thickness in the Vorkuta region according to long-term active layer monitoring (over 17 years) (Kaverin et al. 2017).

Another factor that must be taken into account in the Vorkuta region is the influence of coal dust because it changes the radiation balance of the area. Snow melts in the city almost a month earlier than in natural conditions. The results of modelling in the northern part of Vorkuta (with ground temperatures of -1.5 to -2.0°C) showed only an insignificant influence of this factor. Snow pollution will have a stronger effect in the central part of Vorkuta, where the ground temperature is -0.5 °C (Khilimonyuk et al. 2011). The effect of climate change on the stability of infrastructure will depend on the construction principle (Belotserkovskaya 1990). The least stable foundations, constructed according to Principle I will decrease their mechanical characteristics (Kotov and Stanilovskaya 2021) and bearing capacity (Streletskiy et al. 2012a) due to an increase of ground temperature. There is no official data about how many buildings were built according to Principle 1. However, according to our estimates, their number does not exceed 20% of the housing stock in Vorkuta.

Climate change will not have a significant effect on buildings constructed on bedrock. In this case, the stability of structures will depend only on the mechanical properties of the rock. The upper part of the rocks in Vorkuta has many cracks, therefore it has a low bearing capacity. It is also necessary to take into account the effect of tangential heaving forces on the stability of low-rise buildings.

The stability of buildings constructed according to Principle II also depends on thermal influences and the thickness of thawing. The thawing depth for a typical 5-story residential building in Vorkuta is about 30 m. With climate warming, it is possible to assume an increase in soil temperature and even a decrease in the permafrost table. However, this effect will be very insignificant at depths greater than 42 m for Vorkuta (Khrustalev et al. 1993). Improper use can lead to much larger changes in soil temperature. The stability of buildings depends on thaw settlement. Thaw settlement calculations are performed using deformation characteristics (thawing and compressibility coefficients). These characteristics can be determined by field (hot stamp) and laboratory tests (compression and triaxial test) (Kotov et al. 2017; Kal'bergenov 2019). Deformation characteristics for different test methods can differ by several times in magnitude (Kotov et al. 2015). There are many factors influencing thaw settlement: the cryogenic structure, water/ice content, density, cryogenic texture, thawing conditions, and stresses. Therefore, thaw settlement varies widely. Indeed, settlement may not occur with increasing thawing depth due to the low compressibility of the soil (especially for sand and gravel).

Buildings constructed according to the method of stabilization of the permafrost's initial position have practically no thermal influence on each other. In addition, the buildings provide good snow and wind protection. This construction method is practically insensitive to climate change, which only affects the alternating mode of the needed ventilated foundation operation.

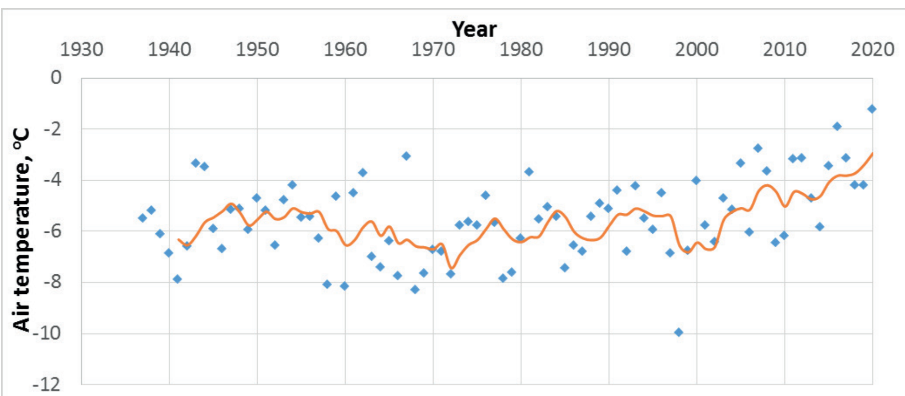

Fig. 3. Annual mean of air temperature in Vorkuta (raw data (blue dots) and 5 years running mean (orange line))

CONCLUSIONS

This article describes various principles of construction in Vorkuta. According to the literature review and field observations, there are several reasons for infrastructure failure, which include ignoring the geocryological conditions, composition, and properties of soils; using two construction principles in the same city district; using poor-quality construction materials; mistakes made during the construction processes; and improper building use. Among those, improper building use is one of the major reasons.

The analysis of infrastructure stability in the context of climate change was carried out. Buildings constructed according to Principle I were found to be more vulnerable due to a decrease in foundations bearing capacity. The increasing temperature will not affect the stability of buildings built on bedrock (which depends on the mechanical properties of rock). Most of the buildings in the city were built according to Principle II, where the influence will depend on the method of construction and the thickness of thawing. There is no impact of climate change for two methods: the stabilization of the permafrost's initial position and the preliminary thawing of permafrost (if the thawing thickness was more than 42m). A slight increase in air temperature can accelerate thawing, but will not play a decisive role in comparison with the improper use of the infrastructure.

Currently, there is an unfavorable situation with residential buildings in Vorkuta due to the increasing share of housing stock being deemed critical (6% every year) and presence of several abandoned and unused buildings. About 800 buildings are in use in Vorkuta in 2020 (43% of what it was 50 years ago). According to the analysis, about 800 houses have been demolished or disconnected from utility lines over the past 50 years (about 250 of these are still standing, pending demolition). Since 1994, the construction of new residential buildings has almost stopped. Therefore, buildings that have been in use for over 50 years will account for 90% of the total residential housing stock by 2040.

REFERENCES

Aalto J., Karjalainen O., Hjort J. and Luoto M. (2018). Statistical forecasting of current and future circum-Arctic ground temperatures and active layer thickness. Geophysical Research Letters, 45(10), 4889-4898, DOI: 10.1029/2018GL078007.

Bakalov S.A. (1964). Construction experience on permafrost soils at Vorkuta. Soil Mechanics and Foundation Engineering, 1(5), 306-309, DOI: 10.1007/bf01704066.

Barenberg A. (2014). Gulag Town, Company Town: Forced Labor and Its Legacy in Vorkuta. Yale University Press, New Haven.

Belotserkovskaya G.V. and Ponomarev V.D. (1985). Selection of method of construction on permafrost soils. Soil Mechanics and Foundation Engineering, 22(6), 205-209, DOI: 10.1007/bf01706375.

Belotserkovskaya G.V., Fedoseev Y.G., Yanchenko O.M. (1989). Causes of deformation of buildings on permafrost in railroad district of Vorkuta. Soil Mechanics and Foundation Engineering, 26(3), 102-106, DOI: 10.1007/bf02302818.

Belotserkovskaya G.V. (1990). Effect of permafrost conditions and type of foundations on deformation of building in Vorkuta. Soil Mechanics and Foundation Engineering, 27(4), 161-163, DOI: 10.1007/bf02305648.

Biskaborn B.K., Smith S.L., Noetzli J., Matthes H., et al. (2019). Permafrost is Warming at a Global Scale. Nature Communications, 10(1), 264, DOI: 10.1038/s41467-018-08240-4.

Bondarev P.D. (1964). Problems of experimental construction under permafrost soil conditions. Soil Mech Found Eng 1, 91-94, DOI: 10.1007/BF01703649.

Eroshenko V.N., Targulyan Y.O., Vlokh V.P. (1979). Experience in the construction of pile foundations under frozen-ground conditions in the Vorkuta region. Soil Mechanics and Foundation Engineering, 16(4), 180-185, DOI: 10.1007/bf01704128.

Geocryology of the USSR (1986). European territory of the USSR. Moscow: Nedra. (in Russian).

GOST 27751–2014 (2015). Reliability for Constructions and Foundations. General Principles. Standardinform, Moscow. (in Russian).

Grebenets V.I., Konishchev V.N., Rogov V.V. (2002). Cryogenic Destruction of Construction Materials in Foundations of Buildings Erected in the Permafrost Zone. Soil Mechanics and Foundation Engineering 39, 106-111, DOI: 10.1023/A:1020372002621.

Grebenets V.I. and Ukhova Y.A. (2008). Decreasing geotechnical reliability with worsening frozen-bed conditions. Soil Mechanics and Foundation Engineering, 45(5), 186-192, DOI: 10.1007/s11204-008-9023-y.

Grebenets V., Streletskiy D. and Shiklomanov N. (2012). Geotechnical safety issues in the cities of Polar Regions. Geography, Environment, Sustainability, 5(3), 104-119, DOI: 10.15356/2071-9388_03v05_2012_08.

Hjort J., Karjalainen O., Aalto J., Westermann S., Romanovsky, V.E., Nelson F.E., Bernd Etzelmüller and Luoto M. (2018). Degrading permafrost puts Arctic infrastructure at risk by mid-century. Nature communications, 9(1), 1-9, DOI: 10.1038/s41467-018-07557-4.

Interview (2020). In Vorkuta, residents of the empty Sovetsky microdistrict will be resettled as part of a large-scale plan. (in Russian). Available at: https://tass.ru/v-strane/7684471 [Accessed on 29 March 2021].

Isaev V., Kotov P., Sergeev D. (2020). Technogenic hazards of russian north railway. Lecture Notes in Civil Engineering, 1(49), 311-320, DOI: 10.1007/978-981-15-0450-1_32.

Kal'bergenov R.G., Kotov P.I., Tsarapov M.N. (2019). Determination of the deformation characteristics of thawing soils by the triaxial compression method. Soil Mechanics and Foundation Engineering, 56(1), 65-69, DOI: 10.1007/s11204-019-09571-0.

Kaverin D.A., Pastukhov A.V., Novakovskiy A.B. (2017). Active layer thickness dynamics in the tundra permafrost: affected soils: a calm site study, the European north of Russia. Earth Cryosphere XXI, 6, 30-38, DOI: 10.21782/EC1560-7496-2017-6(30-38).

Khilimonyuk V.Z., Pustovoit G.P., Filatova M.V. (2011). Changes in the temperatures of perennially frozen rocks due to pollution of the earth's surface by coal dust in the territory of the Pechorsk coal basin. Moscow Univ. Geol. Bull. 66, 207-212, DOI: 10.3103/S0145875211030069.

Khrustalev L.N. and Nikiforov V.V. (1990). Stabilization of Perennially Frozen Grounds in the Base of Buildings. Novosibirsk: Nauka. (in Russian).

Khrustalev L.N., Pustovoit G.P., Emel'yanova L.V. (1993). Reliability and durability of bases of engineering structures on permafrost soils under global climatic heating conditions. Soil Mechanics and Foundation Engineering, 30(3), 92-96, DOI: 10.1007/bf01712793.

Khrustalev L.N. and Davidova I.V. (2007) Forecast of climate warming and account of it at estimation of foundation reliability for buildings in permafrost zone. Earth Cryosphere, 11, 68-75. (in Russian with English summary).

Khrustalev L.N., Parmuzin S.Y., Emelyanova L.V. (2011) Reliability of Northern Infrastructure in Conditions of Changing Climate. Moscow: University Book Press. (in Russian).

Kotov P.I., Roman L. T., Sakharov I.I., Paramonov V.N., Paramonov M.B. (2015). Influence of thawing conditions and type of testing on deformation characteristics of thawing soil. Soil Mechanics and Foundation Engineering, 52(5), 254-261, DOI: 10.1007/s11204-015-9337-5.

Kotov P.I., Roman L.T., Tsarapov M.N. (2017). The influence of thawing and consolidation conditions on the deformation properties of thawing soils. Moscow University Geology Bulletin, 72(2), 153-158, DOI: 10.3103/S014587521702003X.

Kotov P.I. and Stanilovskaya, Y.V. (2021). Predicting changes in the mechanical properties of frozen saline soils. European Journal of Environmental and Civil Engineering, DOI: 10.1080/19648189.2021.1916604.

Markizov L.P. (1991). Buildings on bedding from drainage materials. Leningrad: Stroyizdat. (in Russian).

Melvin A.M., Larsen P., Boehlert B., Neumann J.E., Chinowsky P., Espinet X., Martinich J., Baumann M.S., Rennels L. and Bothner A. (2017). Climate change damages to Alaska public infrastructure and the economics of proactive adaptation Proc. Natl Acad. Sci. 114 E122-31, DOI: 10.1073/pnas.1611056113.

Nelson F.E., Anisimov O.A. and Shiklomanov N.I. (2001). Subsidence risk from thawing permafrost. Nature, 410, 889-890, DOI:10.1038/35073746.

Oberman N. G. (2008). Contemporary permafrost degradation of the European north of Russia Proc. Ninth Int. Conf. on Permafrost, 1305–1310.

Obu J., Westermann S., Bartsch A., Berdnikov N., et al. (2019). Northern Hemisphere Permafrost Map Based on TTOP Modelling for 2000–2016 at 1 km2 Scale. Earth-Science Reviews, 193, 299-316, DOI: 10.1016/j.earscirev.2019.04.023.

Pantileenko V.N. (2016). Construction and technological problems of the Arctic development. European North Resources, Technology and Development Economics, 1(3), 21-29. (in Russian).

Passport (2015). Passport of the socio-economic situation of the Vorkuta for 2006-2015. (in Russian). Available at: http://xn--80adypkng.xn--p1ai/ [Accessed on 29 March 2021].

Passport (2020). Passport of the socio-economic situation of the Vorkuta for 2010-2019. (in Russian). Available at: http://xn--80adypkng.xn--p1ai/ [Accessed on 29 March 2021].

Ramage J., Jungsberg L., Wang S. et al. (2021). Population living on permafrost in the Arctic. Popul Environ, DOI: 10.1007/s11111-020-00370-6.

Report (2019). An informational report with an assessment of the current state natural and technogenical situation of the Russian Arctic including Marre-Sale and Vorkuta test sites]. The Ministry of Natural Resources and the Environment of the Russian Federation. (in Russian). Available at: https://geomonitoring.ru/download/pshz/arctic2018.pdf [Accessed on 29 March 2021].

Romanenko I.I. (1974). Constructional properties of burned coalmine rocks and pebble-sand mixtures of Vorkuta. Soil Mechanics and Foundation Engineering, 11(2), 126-128, DOI: 10.1007/bf01710949.

Romanovsky V.E., Drozdov D.S., Oberman N.G. et al. (2010). Thermal State of Permafrost in Russia. Permafrost and Periglacial Processes, 21(2), 136-155, DOI: 10.1002/ppp.683.

Shiklomanov N., Streletskiy D., Grebenets V., Suter L. (2017). Conquering the permafrost: urban infrastructure development in Norilsk, Russia. Polar Geography 40, 4, 273-290, DOI: 10.1080/1088937X.2017.1329237.

Shiklomanov N., Orrtung R. Suter L., Streletskiy D, Zamyatina N. (2019). Dealing with the Bust in Vorkuta, Russia. Land Use Policy 103908, DOI: 10.1016/j.landusepol.2019.03.021.

Strategy (2020). The strategy of socio-economic development of the municipal formation of the urban district Vorkuta. (in Russian). Available at: http://xn--80adypkng.xn--p1ai/ [Accessed on 29 March 2021].

Streletskiy D.A., Shiklomanov N.I. and Grebenets V.I. (2012a). Changes of foundation bearing capacity due to climate warming in Northwest Siberia. Earth Cryosphere, 16(1), 22-32. (in Russian with English summary).

Streletskiy D.A., Shiklomanov N.I. and Nelson F.E. (2012b). Permafrost, infrastructure, and climate change: a GIS-based landscape approach to geotechnical modeling Arctic, Antarctic, Alpine Res, 44, 368-80.

Streletskiy D., Suter L., Shiklomanov N., Porfiriev B., Eliseev D. (2019). Assessment of Climate Change Impacts on Buildings, Structures and Infrastructure in the Russian Regions on Permafrost. Environmental Research Letters 14, 025003, DOI: 10.1088/1748-9326/aaf5e6.

Vasiliev A.A., Drozdov D.S., Gravis A.G., Malkova G.V., Nyland K.E. and Streletskiy D.A. (2020). Permafrost degradation in the Western Russian Arctic Environ. Res. Lett. 15 045001 DOI: 10.1088/1748-9326/ab6f12.

Zhukov V.F. (1958) Pre-construction thawing of frozen soil during the construction of structures on them. Moscow: Publishing house of the Academy of Sciences of the USSR. (in Russian).

RESEARCH PAPER

AUTOMATED MONITORING THE TEMPERATURE UNDER BUILDINGS WITH PILE FOUNDATIONS IN SALEKHARD

Yaroslav K. Kamnev[1], Mikhail Yu. Filimonov[2,3], Aleksandr N. Shein[1*], Nataliia A. Vaganova[2,3]

[1]Arctic Research Center of the Yamal-Nenets autonomous district, Respubliki str. 20, Salekhard, Yamalo-Nenetskiy Autonomous District, Tyumen region, 629008, Russia

[2]Krasovskii Institute of Mathematics and Mechanics, Ural Branch of RAS, S. Kovalevskaya str. 16, Yekaterinburg, 620108, Russia

[3]Ural Federal University Institute, Mira str. 19, Yekaterinburg, 620002, Russia

***Corresponding author:** A.N.Shein@yandex.ru

Received: March 2th, 2020 / Accepted: August 2nd, 2021 / Published: October 1st, 2021

https://doi.org/10.24057/2071-9388-2021-021

ABSTRACT. In the paper, we consider a method of ground temperature monitoring using the thermometric boreholes and computer modeling the residential buildings with the pile foundation in the city of Salekhard; note that it is located in the permafrost zone. Construction of the residential buildings and industrial structures in the permafrost zone and their operation is carried out according to the principle of preserving the frozen state of foundations. For ground temperature monitoring, thermometric boreholes are used. In a given time period, the measured temperatures are transferred to a server for further processing. Information about the temperature is an important factor for the safety of the buildings and it can be used to evaluate the piles bearing capacity. It allows to propose options for the soil thermal stabilization or to eliminate the detected technogenic heat sources. An approach of mathematical modeling to reconstruct the temperature fields in the pile foundation base of a building is discussed taking into account the data of temperature monitoring. 24 boreholes were equipped with more than 400 in-borehole thermal sensors for testing the method under the residential building I. The preliminary modeling is carried out for December and January 2020 for the contact thermal conductivity model with phase transition with the upper part of the geological section typical for Salekhard (the sandy soils). The modeling describes the freezing processes during the months in detail. The thermal monitoring allows to say that the ground in the base of the Residential building I is stable. But there are detected heat transfers near the borehole T1 at the depth of 12–14 m. The combination of monitoring and computer modeling makes it possible to assess the safety of the operation of the residential buildings in cities located in the permafrost zones.

KEYWORDS: permafrost, remote monitoring, thermometry, computer modelling, climate warming

CITATION: Yaroslav K. Kamnev, Mikhail Yu. Filimonov, Aleksandr N. Shein, Nataliia A. Vaganova (2021). Automated Monitoring The Temperature Under Buildings With Pile Foundations In Salekhard. Geography, Environment, Sustainability, Vol.14, No 4, p. 75-82 https://doi.org/10.24057/2071-9388-2021-021

Conflict of interests: The authors reported no potential conflict of interest.

INTRODUCTION

The cryolithozone covers 35 million km^2, which are more than a quarter of the Earth's land. The part of cryolithozone is the permafrost soils that are found not only in the Arctic, but, also, outside it; for example, in the highlands (Anisimov et. al 1996; Nelson et. al 2002; Zhang et. al 1999). Russia is directly related to the cryolithozone where permafrost occupies 60-65% of the territory or 11 million km^2 (Brown et al. 1997, 2002). It is most widespread in the Eastern Siberia and Transbaikalia. There are different types of the permafrost distribution (continuous, sporadic, isolated), different types of cryogenic structures (massive, layered, mesh form), and different temperature conditions. The different features, physical and chemical properties of the permafrost soils are taken into account in the construction of various engineering structures and residential buildings in the cryolithozone.

Today, the Russian Arctic is developing rapidly; the planning, construction, and exploitation of facilities in the cryolithozone are accompanied by a number of problems. Those are caused not only by the complex structure of the soils, but, also, by the processes of permafrost degradation that is accelerated due to the climate warming. Therefore, newer scientific investigations are in progress. They are aimed on researching the current state of the cryolithozone and assessing the impact of climate change on the permafrost (Nelson et. al 2001; Romanovsky et al, 2001; Zhang et. al. 2003; Streletskiy et al. 2012, 2019; Hjort et al. 2018; Aalto et al. 2018). In particular, assessments of the sustainability of the existing and planning infrastructure are carried out in the Arctic and Sub Arctic territories. A series of works is devoted to the assessment of the bearing capacity of the permafrost soils (Streletskiy et al. 2012, 2019; Hjort et al. 2018). These works indicate the permafrost temperature increasing in the period over 30 years (1960–1990) related to the climate warming. The investigations pointed out up to 45% foundations bearing capacity decreasing in certain areas and that this tendency will entail another 25% decreasing by 2050. The various countries budget's losses (due to possible destructions) are estimated as hundreds of billions of dollars (Streletskiy et al. 2019, Luis Suter et al. 2019). At present, for the Russian Federation, the annual losses related to the operation of infrastructure and the residential buildings on the permafrost reach up to $2 billion. In the future, according to the above predictions, the amount of damage will only grow.

Such predictions and assessments seem quite realistic when considering the current situation (Grebenets et al. 2012; Shein et al. 2020), since the number of disasters and damages to the infrastructure facilities in the cryolithozone has significantly increased recently (BBC News. Russian Arctic… 2020; BBC News. Norway landslide… 2020; The Siberian Times. Two-storey residential… 2020). The current trend of the climate warming leads to the temperature of the permafrost increasing that directly affects the bearing capacity of the soils. The human influences on the state of permafrost are stipulated by development and operation of objects (Filimonov et al. 2017; Kiselyov et al. 2020; Vaganova et al. 2017, 2019).

Most of all buildings and structures in the cryolithozone of Russia are built and operated on the principle of the preservation of the frozen ground foundation. However, outdated norms and rules are used in the building and further operation of the facilities (SP 25.13330.2012, 2012; Resolution of the State Construction Committee of the Russian Federation of 27.09.2003 N 170, 2003). Note that the existing documents indicate the necessity of geotechnical monitoring of all types of the buildings and structures in the permafrost zone during both the construction and operation. It is necessary to «ensure that stakeholders are informed in a proper time about the detected deviations of the controlled parameters ... from the project values and the results of the thermal and geotechnical prediction» (SP 25.13330.2012, 2012). First of all, this relates to the temperature, the control of which is necessary to confirm the bearing capacity of the foundation soil and to prevent the dangerous permafrost geological processes (thermokarst, subsidence, frost heaving, etc.). Therefore, monitoring and modeling (predicting) the changes in the temperature fields in the site of pile foundations of buildings will increase the operational reliability of engineering structures and residential buildings. Note that in addition to the temperature, to evaluate the bearing capacity of the foundation soil, it is necessary to know other characteristics of the soil, such as wetness, granular mineralogical composition, etc.

Beginning from 2018, for the safe operation of the buildings and structures in the permafrost zone in the Yamal-Nenets Autonomous District, a methodology of automated temperature monitoring is developed (Gromadsky et al. 2019). It includes a program for calculating non-stationary thermal fields under buildings with the pile foundations. In the future, it is planned to expand the functionality of the program and add the ability to recalculate the obtained temperature values into the bearing capacity of the soil for the current state and for the prognosis. In 2020, to test the methodology, the administration of the Salekhard city provided four capital buildings where about 80 boreholes were drilled and equipped with the thermometric equipment.

According to (Kuzin 1963) the territory of the modern development of the city of Salekhard and the surrounding area is located on the V sea terrace (Q1) and on the I and II alluvial terraces of the Ob and Polui rivers (Q3-Q4). The average depth of the active layer is 1.5-2 m and has recently been increasing. The thickness of the permafrost reaches 150 m, and its temperature within the depth of the zero annual amplitude varies from -0.5 to -2ºC. The upper part of the section is dominated by sandy. With depth, sandy loam and loam appear, and clay is less common. Salekhard is located near the border, where the continuous permafrost turns into intermittent. Therefore, the monitoring of the permafrost under the objects is particularly relevant here.

This paper focuses on monitoring and studying the processes of propagation of the thermal fields in the site of the pile foundation of the residential building in the city of Salekhard using the thermometric boreholes.

The paper presents and analyzes the preliminary temperature data obtained for the foundation of the residential building in the city of Salekhard, Zoya Kosmodemyanskaya str. 68 (hereinafter referred to as the Residential building I). An enough dense grid of the borehole thermal sensors allows us to obtain unique data that can be used for the numerical modeling and prediction of the permafrost soil temperature in the entire area of the pile foundation.

In combination with temperature monitoring of the soil in the area of the pile foundation the possibility and the promises of the method of mathematical modeling application are discussed. It is suggested that the combination of the methods allows one to analyze, predict and prevent the destructive tendencies in the permafrost foundations.

METHODOLOGY OF REMOTE MONITORING THE GROUND TEMPERATURE

Automated monitoring of the temperature of the soil demands thermometric boreholes arrangement in a ventilated basement to a depth of at least the actual length of the pile under residential building (10 meters or more). The drilled boreholes are equipped with the systems of automatic monitoring of the permafrost temperature SAM-Permafrost (Kurakov Sergey Anatolyevich, Tomsk) that are designed for the remote autonomous registration and data transmission from the connected thermometric cables (maximum 4 cables and 1 air temperature thermistor) in a single database and, further, to the remote server using the GSM module. The client software allows one to configure controllers, read, export, and visualize the data. Error of calibration of the sensors of temperature measurement is ±0.1°C. The resolution of the temperature measurement is 0.07°C. Such characteristics of the thermometric equipment correspond to modern developments in the field of geotechnical monitoring (kriolab.ru, 2021; msu-geophysics.ru/uslugi/geotexnicheskij-monitoring, 2021; rgtekh.ru, 2021).

The thermistors are installed in boreholes on the thermometric cables with the step of 0.5 m until the depth of 5 m, and with the step of 1 m in the tail. To exclude the influence of the air temperature, the thermometric boreholes are covered with a wooden box with the proper insulation. Four air temperature thermistor are installed in different parts of the ventilated basement at a height of 1-1.5 m. The results of temperature measurements are automatically collected on the server and duplicated on a specially developed web resource (https://monitoring.arctic.yanao.ru) where it is possible to analyze, visualize, and export the data about the temperature of the soil. Now this site is running in a test mode and only the specialists have the access. In addition to the automated data collecting, there is a mode of importing data from files; the mode allows one download files from the SAM-Permafrost terminals without the built-in GSM module. The full access to the web-resource is provided for specialists and all

stakeholders. There, the following options are provided:
• display the monitoring the objects on the map with the ability to view advanced information (number of boreholes, installation time, etc.);
• display the scheme of the set of thermometric boreholes for the monitoring objects with the ability to view information on each of the boreholes;
• visualization of data in the form of tables and graphs and export of data for the selected thermometric boreholes.

RESULTS OF REMOTE MONITORING THE GROUND TEMPERATURE (07.2018 – 12.2020) UNDER RESIDENTIAL BUILDING I

In the city of Salekhard, the municipality provided four capital buildings to test the automated temperature monitoring methodology. In 2018, four thermometric boreholes were equipped by the thermometric cables (Fig. 1, red dots) in the ventilated basement of the Residential building I. These boreholes were projected according to the standards of construction and operation (SP 25.13330.2012, 2012; and Resolution of the State Construction Committee of the Russian Federation of 27.09.2003 N 170, 2003). In 2020, 20 additional boreholes were drilled and equipped with the thermometric cables (Fig. 1, black dots). The thermometric boreholes were drilled in the ventilated basement under the existing objects with the drilling equipment UKB 12/25 (the height of the ventilated basement is 120-170 cm). Drilling was carried out with the selection of soil samples and a detailed description of the geological section. The upper part of the section is dominated by sandy. With depth, sandy loam and loam appear. According to (Kuzin 1963) is a typical geological section for Salekhard. The boreholes were cased with the solid polyethylene pipe with a diameter of 40 mm. The upper part of the casing pipe was covered with the heat-insulating box.

Thus, 24 boreholes were equipped for testing the method under the Residential building I (Fig. 1). The enough dense grid of the boreholes is installed due to necessity to develop and to verify the methodology and serves to solution of a number of scientific problems. The aim of this project is, in particular, testing the developed program of calculating of the non-stationary thermal fields and to determine the optimal distance between the boreholes. The first task is partially solved in this work, the second one will be solved in the future. The temperature is measured every 3 hours (synchronized with the nearest weather station at the airport of the Salekhard). The accumulated data is transferred to the server every 12 hours.

Figure 2 (a, b c, d) shows the average monthly ground temperatures for the October 2018, 2019, and 2020. The comparison of the data of the soil temperatures in the boreholes in different years shows the temperature decreased in all boreholes at the depth of 9–11 m. This tendency is presumably caused by reaching the projected influence of the seasonal cooling devices (SCDs). Note that they are inserted into the foundation construction. Undoubtedly, it is worth to highlight the temperature change at the depths of 12–14 m in the borehole T1. Here, the temperature in 2020 has increased by 2.5°C. This indicates unwanted effects (possibly, permafrost thawing) below the project depth of the foundation. To find out the reason of this temperature behavior in 2020, it is necessary to carry out additional investigations using, for example, the geophysical methods. In general, the situation with the permafrost in the base of the foundation of the Residential building I can be described as stable, since the soils at the base of the pile foundation are in frozen state.

To determine the moment of the beginning of the permafrost thawing in the borehole T1, the results of the temperature measurements at the depths of 11, 12, 13, and 14 meters for the two-year monitoring period were analyzed (Fig. 2e). The measurement results show that the depth of zero annual amplitude under Residential building I and on this type of the landscape is more than 10 meters. We can assume that at the depths greater than 10 m, the SCDs reached its projected power only in 2019, because the temperature in the borehole T1 at a depth of 11 m was close to zero in 2018 (Fig. 2e, gray curve), and since the winter 2019, the thermistors showed a stable negative temperature. The moment of the beginning of the permafrost thawing is clearly defined. In the borehole T1, the temperature at the depth of 13–14 m began to increase in early summer, 10.06.2020. Apparently, it is due to the spring melt water, which initiated the process of thawing. The further temperature monitoring is necessary to determine the power of the heat source and to predict the state of the permafrost. In addition, it is necessary to identify the nature and issue of the heat source. If our assumptions are correct and the permafrost thawing is caused by the groundwater, then the underground leakage can be determined using the electrical resistivity tomography (ERT). The ERT method is successfully used to solve the problems of mapping permafrost, determining the depth of the active layer and tails (You et al. 2013; McClymont et al. 2013; Yeltsov et al. 2017; Olenchenko et al. 2019).

In 2020, for further testing of the automated temperature monitoring methodology, 20 more boreholes were drilled and equipped with the thermometric cables (Fig. 1, black dots). Note that the automatic transmission of temperature

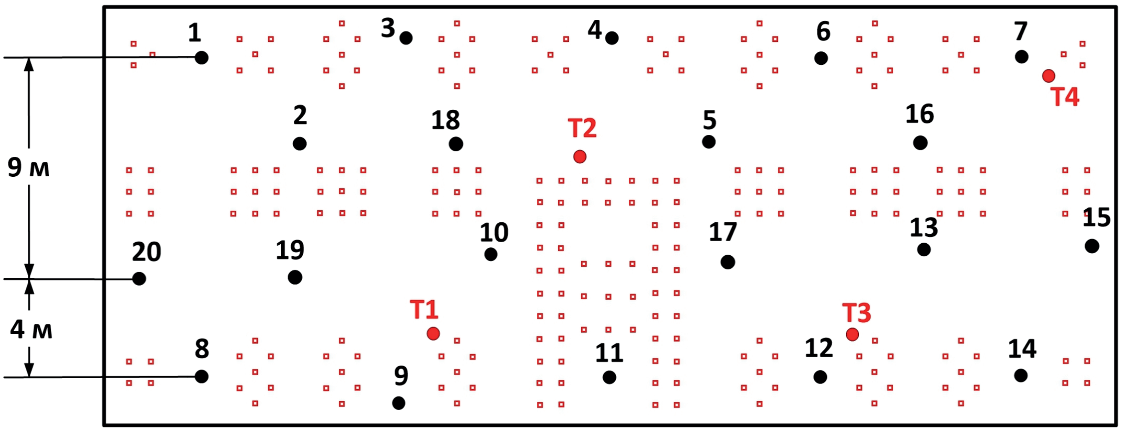

Fig. 1. Scheme of the pile base (red squares) and the location of the thermometric boreholes (black and red circles) under the Residential building I in the horizontal plane

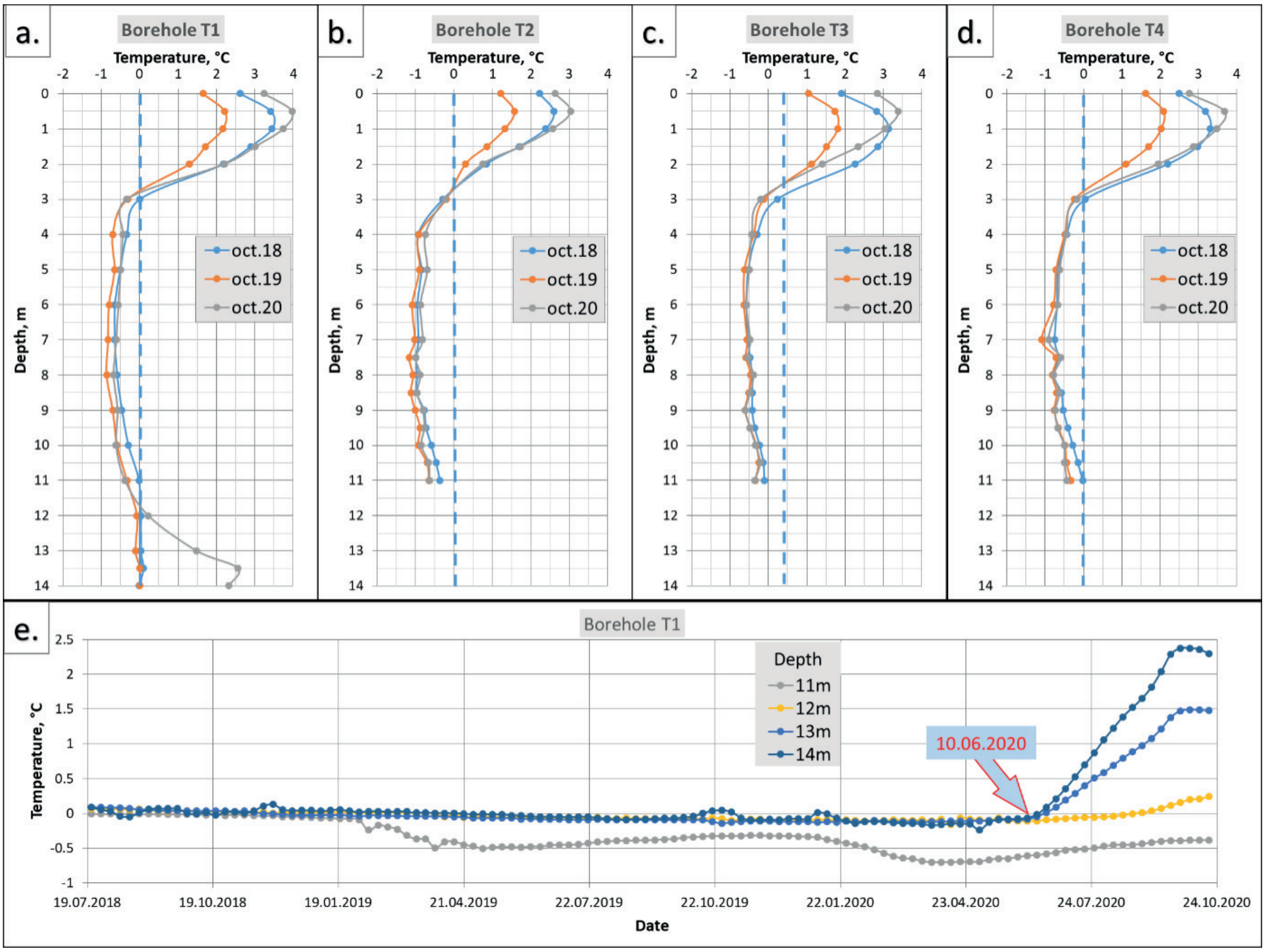

Fig. 2. The results of measuring the temperature of soils under the Residential building I: monthly average temperature for the October 2018-2020 in the boreholes T1-T4 (a, b c, d); (e) is the temperature in the borehole T1 for 19.07.2018-24.10.2020 at depths 11, 12, 13, and 14 meters

to the server from boreholes T1-T4 was interrupted on 23.10.2020 due to the technical difficulties and at the time of writing, the data received after 23.10.2020 has not been processed. Therefore, for three-dimensional analysis (interpolation) and modeling, only the wells 1-20, equipped at the end of 2020, are used.

The first temperature monitoring data transferred to the server from the new 20 wells allowed us to visualize the three-dimensional distribution of the temperature field under the Residential building I by the interpolation at different time points up to the depth of 12m (Fig. 3). The interpolation was carried out without taking into account geology, using the tools of programs designed to visualize geodata. We considered two cases: the weekly average temperature (30.11.2020–06.12.2020) at the beginning of monitoring (Fig. 3a) and the weekly average temperature (11.01.2021–17.01.2021) at the beginning of 2021. As a result, it was found that there is a zone of thawing under Residential building I (Fig. 3, shaded in of red), which is probably caused by leaks from the water lines. The pipes go into the ground directly above the thawing zone. Moreover, the location of the detected thawing coincides with the T1 borehole where, at the depth of 12–14 m, the permafrost thawing began in the summer of 2020 (according to the temperature observations). These two temperature anomalies are highly likely related due to their localization. The further monitoring will possibly predict the impact of these anomalies on the permafrost under the building.

Let analyze the ground temperature at the base of the foundation of the Residential building I in the early December 2020 (Fig. 3a) and in the January 2021 (Fig. 3b). We can say that during a month and the half of the monitoring, the temperature of the detected anomaly (Fig. 3a, shaded in red) dropped to zero (Fig. 3a, white-red color). This means that the thawed soils almost froze during this period of the winter. This is provided by the norms for building on the principle of preserving permafrost. Obviously, the analysis of the current temperature field allows one to detect the zones with anomalous temperatures, which highly likely means the weakening of the bearing capacity of the soil. This information can prevent possible accidents in time by a proper plan of actions.

In addition, to control the temperature of the permafrost at the base of the foundation, the dense enough grid of in-borehole thermal sensors and a measurement period (every 3 hours) will allow one to promptly respond to water lines breakdowns (pipe breaks). Note that these will be detected by an unexpected temperature jump in data of near-surface (at the zero depth) sensors.

The further temperature monitoring under the buildings in the city of Salekhard will provide data that will be used to the numerical modelling of the non-stationary thermal field and to calculate the bearing capacity of the foundations of the monitored buildings for the forthcoming years. The numerical calculations will be carried out using the program developed by specialists of the N.N. Krasovskii Institute of Mathematics and Mechanics, Ural Branch of RAS together with the Arctic Research Center of the Yamal-Nenets autonomous district. In this paper, the algorithm of the program and the first calculations using the real data are presented.

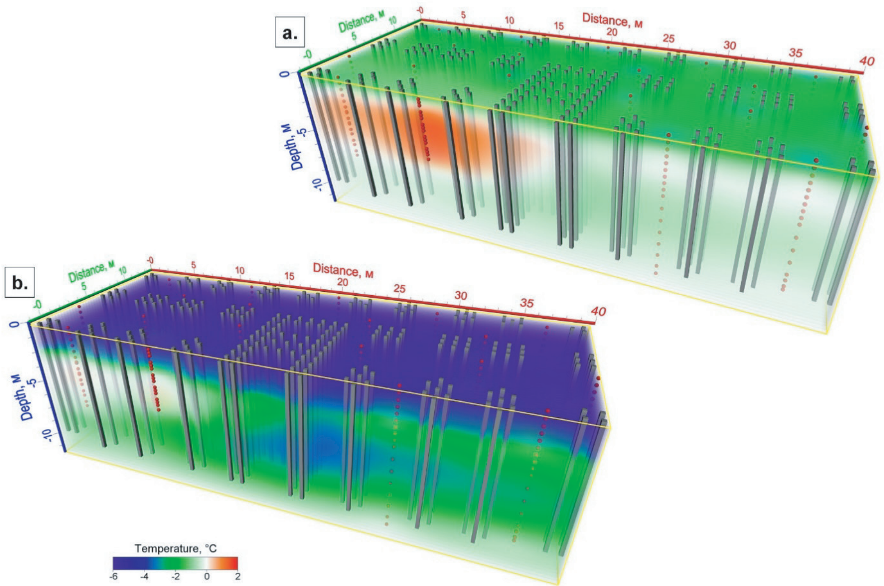

Fig. 3. Scheme of the pile base (grey piles) and the location of thermistors (red spheres) and 3D interpolation of weekly average temperature of soils that measured at the base of the foundation of the Residential building I: (a) – 30.11.2020–06.12.2020; (b) – 11.01.2021–17.01.2021

DISCUSSION

It is easy to imagine that if not to make a minimal effort for the geotechnical monitoring of the soils of buildings foundation in the future, the young cities located in the permafrost zones will inevitably repeat the history of older ones. Investigation of the rate of permafrost degradation in the natural and anthropogenic conditions will improve the construction norms and regulations. The infrastructure and residential buildings should be built already taking into account the predictions of the future permafrost changes obtained using real thermometry data.

In the last decade, the development of the Arctic regions by oil and gas companies has given the instrumental, scientific, methodological, and technological impetus to the system of geotechnical monitoring. This system has recently outlined, the needs and abilities are determined. It is necessary to have the real-time monitoring system as an enough dense grid of the in-borehole thermal sensors, which have to be examined and justified by specialists of the geocryology. Such systems are already developing, but mainly for the oil and gas infrastructure (Arhgeo.com 2020; Permafrost-engineering.com 2021; Pugach V.N. et al. 2019). The idea of automated monitoring in the urban environment has been conceiving for more than three years by the Arctic Research Center of the Yamal-Nenets Autonomous District together with colleagues of the Moscow State University (Gromadsky et al. 2019; Shein et al. 2020) and is currently being tested in Salekhard.

A combination of temperature monitoring in the pile foundation area of the residential buildings together with mathematical modeling methods that use data from the grid of the in-borehole thermal sensors is a promising direction. It will cumulate the advantages of these approaches. The thorough monitoring will allow one to quickly respond to technogenic and natural factors affecting on the bearing capacity of the soil, but, in addition, the computer modelling will allow one to make prognosis of the observed tendencies. Moreover, in contrast to the three-dimensional interpolation of the average soil temperature, reconstructed from the data of thermometric boreholes, the zones of influence of SCDs are clearly visible in the temperature fields obtained by the numerical simulation (Fig. 4). The mathematical modeling in the evaluation of the thermometry data will allow one both to test hypotheses about the detected anomalies and to predict the long-term impact of climatic and anthropogenic factors.

The models developed earlier for the processes of thawing of permafrost (Filimonov et al. 2013; Vaganova N.A. et al. 2017, 2019) are easily transferred to the modeling of processes in pile foundations. To complete the model for simulating thermal fields in the ground with a pile base, it is necessary to take into account the position of the piles, dimensions, as well as the SCDs and possible sources of heat in the ground that may be detected by thermistors.

Mathematical modeling is a convenient forecasting tool that makes it possible to assess not only the current temperature regime of the foundation, but also to test hypotheses of the causes of possible deviations in planned regimes, as well as to highlight trends of different scenarios. The main areas of application of modeling in the monitoring system may be considered as follows:

• creation of a foundation model for the buildings pointing out the essential parameters;
• assignment or correction of the parameters necessary for calculations in conditions of incomplete data and possible assumptions;
• comparison of the calculated data with the monitoring data;
• updating the model in real time, for example, when weather conditions change;
• formulation of criteria for evaluating various modeled states of the system;
• ability to respond to observed deviations in real time.

A preliminary numerical simulation of the Residential building I is carried out for December and January in 2020–2021 season of the monitoring. A geometric model of the building is suggested, the data of thermometric boreholes (Fig. 3a) are taken as the initial data.

The following parameters typical for the sandy soils like in the base are used in the calculations: the thermal conductivity of frozen/thawed soil is 1.89/1.74 W/(m K), the volumetric heat capacity of frozen/thawed soil is 2.17/2.42 10^3 kJ/(m^3 K), the phase transition heat is 6.699 10^4 kJ/(m^3 K), phase transition temperature is -0.1°C.

The preliminary modeling is carried out for December (average air temperature is -15.3°C) and January (average air temperature is -21.2°C). The data were obtained from

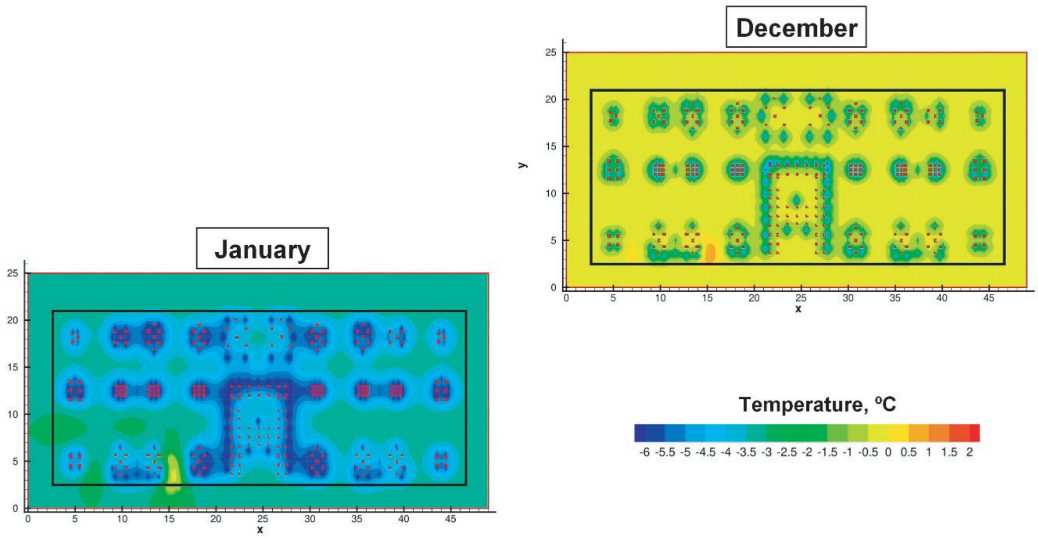

Fig. 4. The computed temperature at the deep of 2.3 m under the Residential building I in December and January

four air temperature thermistors installed in different parts of the ventilated basement at a height of 1-1.5 m. The ventilated basement area is shaded, so the solar radiation can be neglected. The square concrete piles at the base have dimensions of 0.3m×0.3m×10m, with the thermal conductivity is 1.74 W/(m K), the volumetric heat capacity is 2.42 10^3 kJ/(m^3 K). SCDs are the metal tubes with the diameter of 0.02 m and the depth of 10 m and are considered as the internal sources of cold, and the temperature on which depends on the difference of air temperatures on the surface and the soil temperature (Vaganova N.A. et al. 2019). In Fig. 4, the temperature at the deep of 2.3 m is shown in (x,y) plane for December and January. The SCDs work and the resulting freezing is stronger in January. The warmer area in the soil (detected in the previous stage, Fig. 3) became cooler and freezes due to the SCDs influence. This is observed by the following monitoring of the ground. In the future development, the authors plan to analyze the calculated temperature fields and compare it with the temperatures recorded by the thermistors. The model should be verified with using of the data of one-year period at least.

A complex approach to the geotechnical monitoring of the buildings and structures located in the permafrost areas will allow one to link the data obtained with the mathematical modeling of the thermal processes and to reach the accurate (as far as numerical calculations will allow) assessment of the bearing capacity of the foundation. But «this system itself will be effective if it will be based both on the results of the engineering surveys and project design, and on the information about the conditions for their implementation (construction). That is, on the balanced system: survey – project design – construction (building) – operation (monitoring)» (Rivkin 2020).

The projects of creation of the monitoring systems in the permafrost zones are necessary to be supported by all stakeholders, executive and legislative authorities, construction organizations, management companies, etc. At the same time, it is necessary to develop appropriate laws and legal norms. The complex geotechnical monitoring systems are directly related to sustainable development of Northern cities and apply to the modern technical and the informational technologies.

CONCLUSIONS

The thermal monitoring in the boreholes T1–T4 started from summer of 2018 and allows one to say that the ground in the base of the Residential building I is stable. We have to note that the temperature increased by 2.5°C in the borehole T1 at the depth of 12–14 m. It points out the detrimental effects (permafrost thawing) and detects the heat transfers in this zone. The scope of the detected thawing and the source of heat (presumably groundwater) are advisable to be investigated with using the geophysical methods, for example, the electrotomography.

The reconstruction of the full-scale thermal fields by the monitoring data will allow one to detect the zones of possible weakening of the bearing capacity of the soils or thawing zones. This information sharing can prevent in time possible accidents by a proper plan of actions.

The enough dense grid of the in-borehole thermal sensors will allow one to promptly respond to utility breakdowns (pipe breaks), which will be detected by an unexpected temperature jump in the data of the near-surface (at the zero depth) sensors. The full-scale reconstruction of temperature in the ground with using the numerical simulation of the inserted devices will clarify the temperature in the soil in the zones out of reach of the thermistors, in particular, on the pile surfaces. In contrast to the thermal monitoring, the data of the computer simulations can predict the development of various temperature processes depending on the changes in the climatic parameters. Moreover, including technogenic heat sources into the model may be detected with delay or too lately to prevent destructive processes. But accumulation and analysis of the data of the long-time observation can make contribution to the refinement and adjustment of the model and computer simulation program in order to obtain more thorough results.

REFERENCES

Aalto J., Karjalainen O., Hjort J. and Luoto M. (2018). Statistical forecasting of current and future circum – Arctic ground temperatures and active layer thickness. Geophysical Research Letters, 45(10), 4889-4898, DOI: 10.1029/2018GL078007.

Anisimov Oleg A. and Nelson Frederick E. (1996). Permafrost distribution in the Northern Hemisphere under scenarios of climatic change. Global and Planetary Change, 14(1–2), 59-72, DOI: 10.1016/0921-8181(96)00002-1.

Arhgeo.com (2021). Automated system for collecting and transmitting geotechnical monitoring data [online] Available at: http://arhgeo.com/home/geo/data/ [Accessed 15 Feb. 2021 in Russian].

BBC News. Russian Arctic oil spill pollutes big lake near Norilsk (2020). [online] Available at: https://www.bbc.com/russian/features-52926977 [Accessed 15 Feb. 2021].

BBC News. Norway landslide: Buildings swept away in Alta disaster (2020). [online] Available at: https://www.bbc.com/news/av/world-europe-52920766 [Accessed 15 Feb. 2021].

Brown J., Ferrians Jr, O.J., Heginbottom J.A. and Melnikov E.S. (1997). Circum-Arctic map of permafrost and ground-ice conditions. Reston, VA: US Geological Survey, 45.

Brown J., Ferrians, Heginbottom J.A. and Melnikov E. (2002). Circum-Arctic Map of Permafrost and Ground-Ice Conditions, Version 2. [online]. Boulder, Colorado USA. NSIDC: National Snow and Ice Data Center, DOI: 10.7265/skbg-kf16. [Accessed 15 Feb. 2021].

Filimonov M. and Vaganova N. (2017). Permafrost thawing from different technical systems in Arctic regions. IOP Conf. Series: Earth and Environmental Science, 72, 012006, DOI: 10.1088/1755-1315/72/1/012006.

Filimonov M. and Vaganova N. (2013). Simulation of thermal stabilization of soil around various technical systems operating in permafrost. Applied Mathematical Sciences, 7(141-144), 7151-7160, DOI: 10.12988/ams.2013.311669.

Grebenets V., Streletskiy D. and Shiklomanov N. (2012). Geotechnical safety issues in the cities of Polar Regions. Geography, Environment, Sustainability, 5(3), 104-119, DOI: 10.15356/2071-9388_03v05_2012_08.

Gromadsky A.N, Arefiev S.V., Volkov N.G., Kamnev Y.K. and Sinitsky A.I. (2019). Remote temperature regime monitoring of permafrost soils under the buildings in Salekhard. Scientific Bulletin of the Yamal-Nenets Autonomous District, 104(3), 17-21, DOI: 10.26110/ARCTIC.2019.104.3.003. (in Russian with English summary).

Hjort J., Karjalainen O., Aalto J., Westermann S., Romanovsky V.E., Nelson F.E., Bernd Etzelmüller and Luoto M. (2018). Degrading permafrost puts Arctic infrastructure at risk by mid-century. Nature communications, 9(1), 1-9, DOI: 10.1038/s41467-018-07557-4.

Kiselyov F. and Sergeyev F. (2020). Prediction of construction bases frozen soil temperature development under intense heating. Journal of Physics: Conference Series, 1425, 012208, DOI: 10.1088/1742-6596/1425/1/012208.

KrioLab. Equipment for geotechnical monitoring [online] Available at: https://kriolab.ru/ [Accessed 30 June 2021 in Russian].

Kuzin I.L. (1963). Geomorphological levels of the north of Western Siberia. Geology and oil-and-gas potential of the north of Western Siberia, Proceedings of VNIGRI, 225, 330-339.

McClymont A.F., Hayashi M., Bentley L.R. and Christensen B.S. (2013). Geophysical imaging and thermal modeling of subsurface morphology and thaw evolution of discontinuous permafrost. Journal of Geophysical Research: Earth Surface, 118(3), 1826-1837, DOI: 10.1002/jgrf.20114.

Msu-geophysics. Geotechnical monitoring. [online] Available at: http://www.msu-geophysics.ru/uslugi/geotexnicheskij-monitoring [Accessed 30 June 2021 in Russian].

Nelson F.E., Anisimov O.A. and Shiklomanov N.I. (2001). Subsidence risk from thawing permafrost. Nature, 410, 889-890, DOI:10.1038/35073746.

Nelson F.E., Anisimov O.A. and Shiklomanov N.I. (2002). Climate Change and Hazard Zonation in the Circum-Arctic Permafrost Regions. Natural Hazards, 26, 203-225, DOI: 10.1023/A:1015612918401.

Olenchenko V.V., Kartoziya A.A., Tsibizov L.V., Osipova P.S. and Esin E.I. (2019). Geoelectrical characteristics of Samoylov Island coastline (Lena River delta). Russian Journal of geophysical technologies, (4), 39-49, DOI: 10.18303/2619–1563–2018–4–5.

Pugach V.N. and Boiychov S.V. (2019). Experience in the application and development of systems for monitoring the temperature of permafrost soils production of JSC research-and-industrial enterprise «Etalon». Materials of the III International Scientific and Practical Conference. Architectural, construction and road transport complexes: problems, prospects, innovations, 262-268. (in Russian with English summary).

Resolution of the State Construction Committee of the Russian Federation of 27.09.2003 N 170 «On approval of the Rules and norms of technical operation of housing» [online] Available at: http://www.consultant.ru/document/cons_doc_LAW_44772/ [Accessed 15 Feb. 2021 in Russian].

Rivkin F.M. (2020) Changes in geocryological conditions in the foundations of buildings and structures in the Arctic and Subarctic. Bulletin of Engineering Surveys, 45(6), 18-22 (in Russian).

Romanovsky V.E. and Osterkamp T.E. (2001) Permafrost: Changes and impacts / In R. Paepe & V. Melnikov (eds), Permafrost Response on Economic Development, Environmental Security and Natural Resources, Dordrecht, Netherlands: Kluwer Academic Publishers, 297-315.

RUSGEOTECH. Realization of solutions in the field of geotechnical monitoring. [online] Available at: https://www.rgtekh.ru/ [Accessed 30 June 2021 in Russian].

Permafrost-engineering.com (2021). Services in geotechnics on permafrost LLC PermafrostEngineering [online] Available at: http://permafrost-engineering.com/ [Accessed 15 Feb. 2021 in Russian].

Shein A.N. and Kamnev Y.K. (2020). Review of Scientific Publications and Industrial Works Devoted to the Study of Permafrost Formations in Natural and Anthropogenic Conditions. Scientific Bulletin of the Yamal-Nenets Autonomous District, 108(3), 42-50, DOI: 10.26110/ARCTIC.2020.108.3.007 (in Russian with English summary).

SP 25.13330.2012 (2012). Construction Regulations. Soil bases and foundations on permafrost soil . Updated version SNiP 2.02.04–88 Construction Norms and Regulations for Foundations on Permafrost. Ministry of Regional Development of the Russian Federation. Moscow, Russia. (in Russian).

Streletskiy D.A., Shiklomanov N.I. and Grebenets, V.I. (2012). Changes of foundation bearing capacity due to climate warming in Northwest Siberia. Earth Cryosphere, 16(1), 22-32. (in Russian with English summary).

Streletskiy D.A., Suter L.J., Shiklomanov N.I., Porfiriev B.N. and Eliseev D.O. (2019). Assessment of climate change impacts on buildings, structures and infrastructure in the Russian regions on permafrost. Environmental Research Letters, 14(2), 025003, DOI: 10.1088/1748-9326/aaf5e6.

Suter L., Streletskiy D. and Shiklomanov N. (2019). Assessment of the cost of climate change impacts on critical infrastructure in the circumpolar Arctic. Polar Geography, 42(4), 267-286, DOI: 10.1080/1088937X.2019.1686082.

System of automated geocryological monitoring (2021). [online] Available at: https://monitoring.arctic.yanao.ru/ [Accessed 15 Feb. 2021 in Russian].

The Siberian Times. Two-storey residential building breaks apart in Yakutsk, Russia's permafrost capital (2020). [online] Available at: https://siberiantimes.com/other/others/news/two-storey-residential-building-breaks-apart-in-yakutsk-russias-permafrost-capital/ [Accessed 15 Feb. 2021].

Vaganova N.A. and Filimonov M.Yu (2019). Simulation of Cooling Devices and Effect for Thermal Stabilization of Soil in a Cryolithozone with Anthropogenic Impact. Lecture Notes in Computer Science, 11386, 580-587, DOI:10.1007/978-3-030-11539-5_68.

Vaganova N. and Filimonov M. (2017). Simulation of freezing and thawing of soil in Arctic regions. IOP Conf. Ser.: Earth Environ, 72, 012006, DOI:10.1088/1755-1315/72/1/012005.

Yeltsov I.N., Olenchenko V.V. and Faguet A.N. (2017). Electrotomography in the Russian Arctic based on field studies and three-dimensional numerical modeling. Business magazine Neftegaz. RU, (2), 54-64 (in Russian).

You Y., Yu Q., Pan X., Wang X. and Guo L. (2013). Application of electrical resistivity tomography in investigating depth of permafrost base and permafrost structure in Tibetan Plateau. Cold Regions Science and Technology, 87, 19-26, DOI:10.1016/j.coldregions.2012.11.004.

Zhang T., Barry R.G., Knowles K., Heginbottom J.A. and Brown J. (1999). Statistics and characteristics of permafrost and ground-ice distribution in the Northern Hemisphere. Polar Geography, 23(2), 132-154, DOI:10.1080/10889379909377670.

Zhang Y., Chen W. and Cihlar J. (2003). A process-based model for quantifying the impact of climate change on permafrost thermal regimes. J. Geophys. Res., 108(D22), 4695, DOI: 10.1029/2002JD003354.

RESEARCH PAPER

THE VALUE OF BUILDINGS AND STRUCTURES FOR PERMAFROST DAMAGE PREDICTION: THE CASE OF EASTERN RUSSIAN ARCTIC

Svetlana V. Badina[1,2*], Alexey A. Pankratov[3]
[1]Lomonosov Moscow State University, Faculty of Geography, GSP-1, Leninskie Gory, 1, 119991, Moscow, Russia
[2]Plekhanov Russian University of Economics, Stremyanny lane, 36, 117997, Moscow, Russia
[3]Lomonosov Moscow State University, Faculty of Economics, Leninskiye Gory, 1, 46 bld, 119991, Moscow, Russia
***Corresponding author:** bad412@yandex.ru

Received: May 21th, 2021 / Accepted: November 9th, 2021 / Published: December 31st, 2021
https://doi.org/10.24057/2071-9388-2021-058

ABSTRACT. The relevance of the study lay in the need to obtain reliable information on the possible economic consequences of changing geocryological conditions in the Russian Arctic, to find methods for preventing (reducing) potential damage, increasing the safety of the population and economy in the areas of the highest geocryological risks, and ensuring balanced socio-economic development in the Russian Arctic permafrost zone for the long term. The study aimed to assess the cost of fixed assets, including their most vulnerable part – buildings and structures (case study: municipalities of the Russian Arctic Asian sector). Economic sectoral structure was evaluated in accordance with the Russian Standard Industrial Classification of Economic Activities using primary statistical data – closed data from companies accounting reports. The work used statistical, cartographic, and visual-graphic methods, as well as methods for analyzing spatial information and microeconomic data. According to calculations, the Russian Arctic Asian sector concentrates the fixed assets of commercial companies with a total value of about 14.8 trillion rubles, including buildings and structures worth 10.7 trillion rubles. The obtained calculated data can be used in modeling the directions of state policy in the field of climate change adaptation and territory protection from natural hazards.

KEYWORDS: Active Layer Thickness (ALT), permafrost, thaw subsidence, CALM (Circumpolar Active Layer Monitoring) program, Russia, Taymyr Peninsula

CITATION: Svetlana V. Badina, Alexey A. Pankratov (2021). The Value Of Buildings And Structures For Permafrost Damage Prediction: The Case Of Eastern Russian Arctic. Geography, Environment, Sustainability, Vol.14, No 4, p. 83-92
https://doi.org/10.24057/2071-9388-2021-058

ACKNOWLEDGEMENTS: The reported study was funded by the Russian Science Foundation (RSF project No 21-77-00047, https://rscf.ru/project/21-77-00047/).

Conflict of interests: The authors reported no potential conflict of interest.

INTRODUCTION

According to modern studies, the expected global climate changes will be most intensely manifested exactly in the circumpolar latitudes (Anisimov et al. 2016; The second assessment…, 2014; Arctic…, 2017; Volodin et al. 2017), i.e. primarily in the territories belonging to the Arctic zone of the Russian Federation (AZRF), most of which is located in the permafrost zone. The predicted climate warming may bring both positive economic effects (first of all, a decrease in costs of construction, passengers and cargo transportation, geological exploration and geological production, an increase in the navigation period duration in the Arctic seas basins, a reduction in energy consumption for life support in the Arctic regions, etc.), and negative economic effects, associated primarily with a damage increase from the natural hazards activation (Kislov et al. 2011; Porfiriev et al. 2017, Orttung et al. 2021). According to some forecasts (Porfiriev et al. 2017), the cumulative effect of the positive consequences of climate change for the AZRF and the country economy as a whole until 2030 will be characterized by a noticeable excess of costs over benefits.

In this case, permafrost degradation, where more than two-thirds of the total Russian Arctic urban population lives (and 100% of the population in the Russian Arctic Asian sector), seems to be a key problem associated with colossal direct and indirect damage. In the Arctic the temperature of upper permafrost horizons rises much faster than the air temperature (Streletsky et al. 2012), and over the past 30 years it has increased by about 0.5-2.0°C in general in the Russia permafrost zone (Romanovsky et al. 1997; Romanovsky et al. 2010). At the same time, the warming trend continues (Kukkoneni et al. 2020; Vasiliev et al. 2020a; Vasiliev et al. 2020b). According to various estimates as a warming result by the end of the XXI century, thawing may occur from 30% to 85% of the upper permafrost horizons (Scholes et al. 2018). Exceeding the values of the soil temperatures optimal range laid down in the design of buildings and structures with pile type of foundations leads to their deformation and destruction (Grebenets et al. 2012). A one-time and massive decommissioning of a significant share of residential buildings, buildings and structures of the economy, regional and local road infrastructure elements will inevitably lead to a rapid deterioration of the socio-economic situation in the Arctic regions, impose disproportionately high loads on grassroots budgets, since the fixed assets restoration is a long and capital-intensive process, (Badina 2020). The significance of the permafrost degradation problem, need to renew its monitoring system is highlighted in such key modern strategic planning documents as the «Strategy for the AZRF development and national security until 2035» and the «Strategy for the spatial development of the Russian Federation until 2025», as well as in the «National action plan for the first stage of adaptation to climate change for the period up to 2022».

However, the formation of timely adaptation strategies to changing geocryological conditions and preventive measures require a scientifically grounded understanding of intraregional differences in the vulnerability level of the Arctic territories, potential damage amount, and geocryological risk integral level. The permafrost degradation consequences forecasting is a pioneering area of scientific researches, since for the first time in world history, society may face such catastrophic socio-economic damage within the permafrost zone. Thus, the need for reliable and scientifically based forecasts is an important challenge for modern science. Economic studies of engineering and geocryological risk in the context of climate change are currently at the initial stage, both in conceptual and methodological aspects. There are serious methodological difficulties associated primarily with a high degree of uncertainty (an extremely wide range of values for forecast scenarios of climatic and geocryological changes), difficulties in comparing natural and socio-economic parameters in order to predict damage both in space (natural boundaries with synthetic administrative-territorial division boundaries) and in time (economic processes, and, accordingly, forecasts, in general, are shorter than climatic and geocryological ones), but the most important limitation is the imperfection of Russian statistics necessary to probable damage assessment. Exactly the statistical limitations predetermined the fact that in all previous researches, the assessment of fixed assets value (its elements) was given very approximately, using many assumptions (Table 1).

Table 1. Analysis of key researches in the field of material damage assessing from permafrost degradation

Damage indicators	Key weaknesses of economic assessments	Key strengths of economic assessments	Amount of damage
Hjort et al. 2018. The study area is the permafrost zone of the Northern Hemisphere in «unprecedented high (~ 1 km) spatial resolution»			
Infrastructure (buildings and structures): residential (settlements and buildings), transport (roads, railways and airports), industrial facilities (pipelines and industrial areas)	The authors show the share of infrastructure (in %) that will be affected by permafrost thawing (its cost estimates are not given). There is a very significant range of probable damage, for example, from 24 to 70% for pipelines. Polygonal objects were converted to point objects in order to estimate their number in hazardous areas, which is a very significant simplification	Geospatial data analysis. Reliance on satellite images, clear geo-referencing of economic objects to specific permafrost degradation areas	33% of the total number of consider infrastructure objects (without a cost estimate)
Suter et al, 2019. Study area – permafrost regions of Russia			
Objects of linear (roads and pipelines) and point (housing, airports and ports) infrastructure	Buildings and structures for the main economy sectors (industry, services, etc.) are not taken into account. The regional level does not allow recognizing intraregional differences in terms of infrastructure maintaining costs, while they are quite significant. The current (at the study time) cost of infrastructure is considered, however the change for the forecast period is not estimated (for the second half of the XXI century, taking into account the new infrastructure projects implementation)	The average annual costs of infrastructure maintaining during its operational period and direct damage are shown in relation to the GRP of the corresponding regions, which makes it possible to assess the scale of the expected consequences	The cost of Arctic infrastructure maintaining in case of permafrost degradation will increase by 27.5% (in Russia) and will be $ 6.63 billion by 2050–2059. The cost of influenced infrastructure will be $ 40339.14 million (32% of the total Russian infrastructure in the permafrost zone)
Streletskiy et al, 2019. Study area – regions (for some indicators – municipalities) of the Russian permafrost zone			
Residential buildings, non-residential commercial and social facilities, linear infrastructure, heavy machinery and industrial equipment, vehicles and intangible assets	The calculation is based on the assumption that the spatial structure of fixed assets in the region corresponds to the spatial structure of the population (proportional dependence). But this dependence is far from always linear, especially for the Arctic, where industry plays a key role in the economy, the subsectors of which differ greatly in terms of labor intensity and fixed assets intensity	Integrative spatial analysis made it possible to best compare socio-economic and environmental (climate, permafrost) data	The total population of the Russia permafrost zone is 5.4 million people; the cost of fixed assets is $1.29 trillion. The cost of structures in the permafrost degradation zone is $ 39.3 billion, the cost of infrastructure – is $ 209.2 billion, and the cost of residential real estate – is $ 52.6 billion. The total cost of infrastructure maintenance costs associated with permafrost changes will rise to $ 105.07 billion by the middle of the 21st century

Melnikov et al. 2021. Study area – municipalities of AZRF			
Buildings and structures by economy sectors; housing stock	Re-estimates of damage parameters for municipalities are based on many assumptions. Authors examples of obtained results verification show in a number of cases a discrepancy with the actual data	The damage assessment method was developed for the municipal level with a high degree of information detailing; intraregional differences in the expected damage amount are well sown. The authors used a most comprehensive set of parameters characterizing damages (however, railways and roads were not considered separately)	5.7 – 7.7 trillion rubles (in 2020 prices)

Source: compiled by the authors

Scientists (Streletsky et al. 2019) were among the first who proposed an approach to assessing the value of fixed assets in the municipalities of the Russian permafrost zone. However, their estimates are based on very bold assumptions, which does not allow their conclusions to be considered correct. For example, in order to move from the regional to the municipal level, they guessed that the spatial structure of fixed assets in the region was proportional to the spatial structure of the population (simple proportional dependence): «it was assumed that the spatial pattern of the fixed assets within a given region corresponds to that of population: higher and denser population indicates higher fixed assets». Earlier, in 2015, researchers (Baburin and Badina 2015) proposed an identical solution for fixed assets value calculating for municipalities: «The value of regional fixed assets should be distributed in proportion to the size of the population (rural, urban or total, depending on the economic activity type) or in proportion to the value of the product produced for the relevant type of economic activity. The latter option is more rational, since the relationship between fixed assets and the population is not always linear, especially in the Arctic and the Far East, where it is impossible to ignore the specific features of industries with different fixed-asset needs. Indeed, a distinctive feature of Russian Arctic regions is pronounced industrial specialization. Industry represents an average of 52% of the gross regional product (GRP) of Arctic regions, compared to an average of 33% for all Russian regions. This is reflected in the structure of fixed assets. Industrial assets also represent 44% of the total value of fixed assets in the Arctic regions, exceeding the average of 31% for all Russian regions (Badina 2021). As a result, it would be better to use correlation dependence of fixed asset value and the value of production in the relevant type of economic activity (but not population size).

Therefore, a common problem for all of the above works is the limited primary statistical information characterizing fixed assets value, which predetermines the need to develop various kinds of re-estimates for more detailed large-scale calculations or to present the results in a very generalized and approximate form at the regional level. In this regard, the expected damage amount varies quite strongly among themselves, even in the works of one researchers group, depending on the selected assessment methods of fixed assets value. Unlike damages to housing stock and infrastructure, damages to the commercial companies fixed assets are practically not paid attention to in modern scientific research. Although exactly they form regional economy, GRP, population employment and local and regional budgets revenues, in other words, with this type of fixed assets associated the greatest share of not only direct (Melnikov et al. 2021), but also indirect damages to regional and local economies. It is important to note that indirect damage from buildings and structures deformation and destruction in the Arctic can negatively affect the economies of other regions, since some of the enterprises directly operating in the AZRF are legally registered in other regions, often far beyond the permafrost zone.

Researches in modern Russian and foreign science devoted to the issue of fixed assets value assessing can be divided into several key directions (Table 2).

Table 2. Analysis of key researches in the field of fixed assets value assessing

Russian researches	Foreign researches
Methodological approaches to assessing the fixed assets value of individual enterprises	
(Didkovsky 1997): approaches to assessing the replacement value of fixed assets; (Gribovsky 1998): accounting for depreciation models in case of assessing the fixed assets market value of enterprises; (Shichkov 2003): assessment of the intrinsic value of the company's fixed assets; (Petruk 2016): approaches to assessing the fixed assets value of an enterprise; (Zhurkina et al. 2018): improving of methods for company's fixed assets analyzing	(Fernandes 2007): methods for assessing the value of a company's fixed assets
Assessment of the fixed assets value of large territorial units: countries and regions	
(Ableeva 2011): comparative assessment of fixed assets of the Bashkortostan Republic; (Adamadziev et al. 2011): statistical relationships between economic parameters and fixed assets values in Russian regions	(Gourfinkel 2007): regional study on the management, control and accounting of fixed assets: Latin America and the Caribbean
Assessment of the fixed assets value in the context of industries and economic activity types	

(Khanin 2010): assessment of the fixed assets replacement value of the Russian industry; (Fomin et al. 2012): assessment of the fixed assets value of railway transport in Russia	(Daniels 1933): assessment of industrial fixed assets
Alternative approaches to assessing the fixed assets value	
(Sapritsky et al. 1996): computer methods for assessing the fixed assets value; (Eidelman et al. 2010): approaches to replacement value assessing in the framework of fixed assets revaluation	(Carpenter et al. 2005): fixed asset accounting software evaluation: a structured methodology for the mid-market firm

Source: compiled by the authors

At the same time, the development of methodological approaches, as well as a direct assessment of the fixed assets value of economic sectors, and even more so the value of buildings and structures, on municipal level in case of the Russian Arctic, have not yet been undertaken due to the limited and imperfect statistical data, the need for significant temporary and labor costs for this task implementation. Another problem is the discrepancy between the data of regional statistics and the obtained calculated data on municipal level.

In this research, key attention is paid to the study of the real territorial organization of companies fixed assets in the case of the Russian Arctic Asian sector. Thus, for the first time in the Russian and world (in relation to the Russian territory) practice of permafrost thawing damage forecasting, the cost of fixed assets (in particular, buildings and structures) was estimated at the microeconomic level – in the context of enterprises, that is, the most detailed and reliable statistical observation level. The basis is the data of the companies financial statements provided by the info-analytical system «SPARK-Interfax»[1].

Thus, based on the obtained data analysis, it becomes possible for the first time to make the most realistic forecast of probable damage from the permafrost degradation, provided they are compared with the geocryological changes forecasts. In the context of the fixed assets vulnerability of companies, it is important to note one significant aspect. Many directly operating in the AZRF enterprises are registered on the territory of other regions. There are prerequisites for a change in this situation with the introduction of a preferential regime in the Russian Arctic[2], however, preferences are designed primarily for the creation of new companies not related to the minerals extraction, therefore, cardinal changes, most likely, will not happen soon (Kuznetsova et al. 2021; Pilyasov 2020).

The discrepancy between the registration of legal entities and the real localization of production determines the key problem for the Russian Arctic, when companies, in case of completion of their activities in the Arctic territories, or in case of emergencies, including due to climate change, «leave» the region, not wanting to eliminate the negative consequences of their activities. This problem was raised at the highest level by the Russian President V. Putin in the course of his message to the Federal Assembly in April 2021: «Our approaches to environmental protection are absolutely principle and cannot be revised ... I ask you to speed up the law adoption, which will establish the financial responsibility of the enterprises owners for the elimination of accumulated damage, for the reclamation of industrial sites ... if you got it at the expense of nature – clean up after yourself»[3]. At the same time, this issue is seen more deeply by the authors, as businesses need to eliminate not only the consequences of their activities, but also prevent and eliminate the consequences of likely climate change that could lead to environmental and man-made disasters, such as diesel leaks in Norilsk on May 29, 2020.

Accordingly, part of the regional and local taxes goes outside the AZRF, thereby, on the one hand, the potential of the Arctic regions' resistance to permafrost degradation decreases. On the other hand, the damage caused to the fixed assets of commercial companies localized in the Russian Arctic will cause indirect damage from permafrost thawing in regions located often far beyond the permafrost zone, which will undoubtedly entail negative multiplier effects spreading throughout the country. In the context of such negative scenario, the possibility of implementing the state course for the priority Arctic socio-economic development as a special geostrategic territory (Pankratov et al. 2020, 2021), investment activity stimulating and population consolidating (Badina et al. 2020) is excluded.

MATERIALS AND METHODS

The methodological approach adopted in this study is based on the «risk» concept, which is a function of the natural hazard likelihood (in this case, an engineering-geocryological hazard) and the value of potential consequences for the population and the economy (damage value) (Akimov et al. 2013; Korolev et al. 2007; Myagkov et al. 2004; Osipov et al. 2017; Porfiriev 2011). Thus, it is planned to estimate the total value of buildings and structures of commercial companies on permafrost in the AZRF Asian sector: Yamalo-Nenets Autonomous Okrug, Chukotka Autonomous Okrug, arctic municipalities of Krasnoyarsk krai and Sakha Republic (Yakutia), taking into account the specifics of the engineering-geocryological hazard. In this study, primary attention is paid to the Asian sector of the Russian Arctic, because exactly there the most catastrophic changes in engineering-geocryological conditions are expected (Anisimov et al. 2015; SWIPA 2017).

To assess the market value of fixed assets, including buildings and structures for the AZRF Asian sector municipalities, the authors have created a technique based on statistical and cartographic methods, visual-graphic methods, as well as methods for spatial information and microeconomic data analysis. The informational basis of the study is data on the Russian companies of the «SPARK-Interfax» system, collected from all enterprises operating in the studied territory. In addition, in some cases, in order to exclude emissions, annual reports of companies (mostly large companies) were used. In the framework of the analysis, a database was formed. This database contains information on the fixed assets market value, the company's belonging to the corresponding economic activity type (according to Russian Standard Industrial Classification of

[1]SPARK-Interfax – a system for professional analysis of markets and companies. http://www.spark-interfax.ru/Front/Index.aspx (accessed May 1, 2021)

[2]Federal Law of July 13, 2020 N 193-FZ "On state support of entrepreneurial activity in the Arctic zone of the Russian Federation". http://www.consultant.ru/document/cons_doc_LAW_357078/ (accessed May 1, 2021)

[3]Message from the President of Russia to the Federal Assembly, April 21, 2021, http://www.kremlin.ru/events/president/transcripts/messages/65418, (accessed July 18, 2021)

Economic Activities-2), addresses of operating and legal registration, the tax revenues volume, revenue volume and other significant technical-economic indicators. In total, about 13.5 thousand commercial companies were analyzed.

The calculation of the economy fixed assets value for the AZRF Asian sector municipalities was carried out for all companies, regardless of its legal registration place. At the same time, in the manual setting mode, the data on the biggest Russian interregional companies were adjusted in terms of the fixed assets accounting directly in the AZRF in order to increase the reliability, quality and representativeness of statistical information (using data from annual reports or information from the official websites of the relevant companies). In order to additional verification, the obtained data were compared with the available Rosstat data on the fixed assets value and the tax revenues volume in the case of the regions or the largest cities. The calculation of the commercial organizations buildings and structures values was carried out based on its average share values[1] in the total fixed assets values (by multiplying the total fixed assets values by the calculated decreasing coefficients for corresponding economic activity type (Table 3). These coefficients were developed and tested in previous studies of the authors (Badina 2021).

Thus, within the framework of this study, for the first time in Russian scientific and managerial practice, the buildings and structures value of companies as the most vulnerable to permafrost degradation part of the economy fixed assets was calculated.

As an alternative method for measuring the value of fixed assets on municipal level, it is possible to use the data on property tax of organizations. The Federal Taxation Service of the Russian Federation provides this data in the public domain. It should be noted that this approach has been repeatedly used by Russian researchers in the framework of the implementation of tasks in terms of assessing the gross municipal product in the Russian Federation (Zemlyansky et al. 2021; Dmitriev et al. 2020).

In particular, taking into account the fact that the tax rates on the property of organizations are established by the laws of the Russian regions and cannot exceed 2.2%[2], as well as on the basis of available open data on tax reporting, it seems possible to estimate the total value of the taxable base, which theoretically will correspond to the fixed assets value. At the same time, without making these calculations, it is also possible to directly use the available data on the residual value of real estate recognized as an object of taxation.

Table 3. Average contribution of the buildings and structures costs to the total fixed assets value by the economy sectors, %, 2019 (case study – commercial organizations)

Economic sector	Average contribution, %
Average	62.53
Agriculture, forestry, hunting, fishing and fish farming	44.16
Mining industry	74.43
Manufacturing industries	41.24
Electricity, gas and steam supply; air conditioning	57.16
Water supply; sewerage, organization of waste collection and disposal, pollution elimination	83.13
Building	33.40
Wholesale and retail trade; repair of motor vehicles and motorcycles	80.40
Transportation and logistics	67.07
Hotels and catering	74.93
Information and communication	25.65
Finance and insurance	28.94
Real estate transactions	85.19
Professional, scientific and technical activities	63.19
Administrative activities and related additional services	31.05
Public administration and military security; social security	32.76
Education	54.94
Health and social services	53.50
Culture, sports, leisure and entertainment	71.38
Other types of services	50.42

Source: calculated by the authors based on Rosstat data (https://fedstat.ru/indicator/58656, (accessed July 18, 2021))

[1]meaning the average for the Russian economy

[2]Article 380 "Tax rate" of the Tax Code of the Russian Federation, URL: https://base.garant.ru/10900200/ece92382efb38f5899252c9982390b2d/ (accessed October 18, 2021)

At the same time, these method contains a number of limitations, which ultimately largely distort the real picture in terms of assessing the fixed assets value, and, thus, cannot be considered as a representative approach in the framework of the proposed study.

Firstly, in relation to real estate objects, the taxable base is determined as their cadastral value, which, as a rule, is several times less than their market value. Thus, the measurement of the fixed assets value by the revaluation method based on data on property tax of organizations is several times lower than the real fixed assets market value. Secondly, it is inappropriate to make quantitative estimates by the method of correlation of cadastral and market values for different regions and municipalities, without taking into account the existing interregional differences in approaches to assessing the cadastral value of buildings and structures. These differences may be even more significant for the territories of the AZRF.

Thirdly, it is important to take into account that cadastral values are calculated once every several years. In addition, this important limitation determines the presence of significant discrepancies between the cadastral values of fixed assets of different organizations in the context of the possibility of linking them to the current price level.

Nevertheless, within the framework of these study, in order to determine interregional differences between the fixed assets market value, calculated using closed data from the accounting reports of companies (SPARK-Interfax) and their cadastral value in accordance with the data of the Federal Tax Service of the Russian Federation, it is advisable to supplement the calculated data with data on the residual value of real estate recognized as an object of taxation in the studied municipalities of the AZRF Asian Sector.

RESULTS AND DISCUSSION

According to Rosstat, the total fixed assets carrying value of the Russian Federation in 2019 amounted to 349.7 trillion rubles (at full accounting value for a full range of organizations); the studied Arctic regions (Yamalo-Nenets Autonomous Okrug, Krasnoyarsk krai, Sakha Republic (Yakutia), Chukotka Autonomous Okrug) – 22.6 trillion rubles, or 6.5% of the total fixed assets value in Russia. Fixed assets value of AZRF Asian sector municipalities, according to the SPARK-Interfax database, amounted to 14.8 trillion rubles, or 65.7% of the total fixed assets value of considered Arctic regions. It is important to note that the obtained results will make it possible to clarify the results of the fixed assets assessment proposed by the previous authors' works (for example, Baburin et al. 2020; Badina, 2020; Melnikov et al. 2021) by further detailed analysis of each municipality (Table 4):

Based on the calculations results, it can be argued that the territorial organization of fixed assets in study municipalities varies significantly. Therefore, the territory of the AZRF Asian sector can be divided into two parts according to the accumulated social-economic potential volume:

- Western sector: municipalities of Yamalo-Nenets Autonomous Okrug and Krasnoyarsk krai, for the overwhelming majority of which the accumulated fixed assets volume exceeds 100 billion rubles;
- Eastern sector: municipalities of Sakha Republic (Yakutia) and Chukotka Autonomous Okrug, for which the accumulated fixed assets volume is less than 100 billion rubles.

The largest fixed assets volume is concentrated in Novy Urengoy – 3 890 billion rubles, Salekhard – 2 998 billion rubles, Yamal district – 2 899 billion rubles, Purovsky district – 1,201 billion rubles, Noyabrsk – 954 billion rubles, Shuryshkarsky district – 438 billion rubles, Taimyr Dolgan-Nenets district – 359 billion rubles, Turukhansky district – 339 billion rubles, Nadym – 310 billion rubles, Gubkinsky – 267 billion rubles, Tazovsky district – 229 billion rubles and Norilsk – 186 billion rubles (Fig. 1).

Taking into account the average coefficients that characterized the share of buildings and structures in fixed assets value by economy sectors, the value of buildings and structures in AZRF Asian sector municipalities was estimated. According to these calculations, the total value of buildings and structures is 10.7 trillion rubles (72% of the total fixed assets value in 2019). In addition, based on the open data of tax reporting of the Russian Federal Tax Service (FTS) (information about the property tax of organizations), the cadastral values of buildings and structures of the studied municipalities in 2019 were calculated. (Table 5):

The highest value of buildings and structures, both in absolute and relative terms, is typical for the municipalities of the Yamalo-Nenets Autonomous Okrug and Krasnoyarsk krai. More than 75% of buildings and structures in the fixed assets are on the territory of Shuryshkarsky, Tazovsky, Priuralsky districts, Nadym. The high value of buildings and structures in Yamalo-Nenets AO is a consequence of its highest territorial development, the highest population density relative to the rest of the studied regions, the most developed urban network, as well as the increased importance of housing and communal services and the presence of a highly developed oil and gas production complex. The Arctic territories of the Krasnoyarsk krai have a high accumulated industrial potential related, first of all, to the fixed assets of «Norilsk Nickel».

The smallest buildings and structures share corresponds to the Iultinsky and Providensky districts of the Chukotka Autonomous Okrug (less than 55%), as well as the Arctic

Table 4. The cost of fixed assets in the regions and municipalities of the AZRF Asian sector in 2019, billion rubles

Region	Regions of the AZRF Asian sector (Rosstat)	Municipalities of the AZRF Asian sector (SPARK-Interfax)	Municipalities of the AZRF Asian sector (according to previously approved author's methods)
Yamalo-Nenets Autonomous Okrug	13 937	13 515	13 937
Krasnoyarsk krai	4 856	884	2 070
Sakha Republic (Yakutia)	3 589	221	151
Chukotka Autonomous Okrug	212	216	212
Sum	22 594	14 836	16 370

Source: calculated by the authors based on Rosstat and «SPARK-Interfax» data

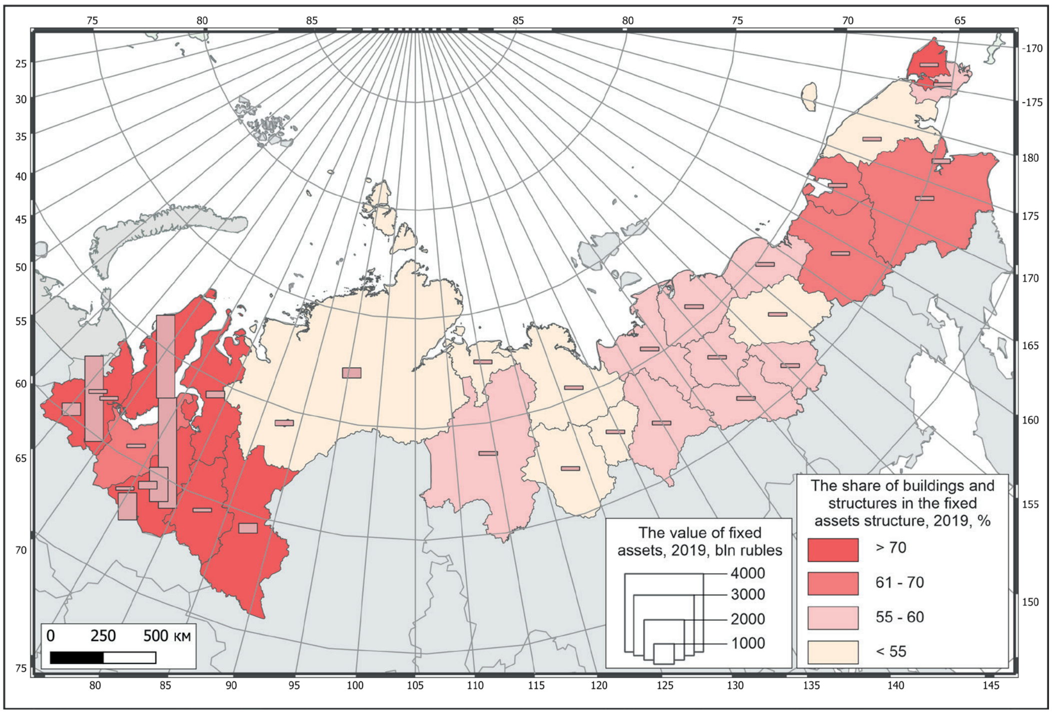

Fig. 1. Fixed assets value in municipalities of the AZRF Asian sector, 2019

Table 5. The value of buildings and structures in municipalities of the AZRF Asian sector, 2019

Region	Value of buildings and structures, billion rubles, 2019		The difference between the market and cadastral values, times	Share of the total fixed assets value (according to calculated data),%
	FTS data (cadastral value)	Calculated data (market value)		
Yamalo-Nenets AO	5 185	9 955	1,9	74
Krasnoyarsk krai	370	517	1,4	58
Sakha Republic (Yakutia)	65	122	1,9	55
Chukotka AO	55	139	2,5	64
Sum	5 675	10 733	1,9	72

Source: calculated by the authors based on «SPARK-Interfax» and Russian Federal Tax Service data

municipalities of the Sakha Republic (Yakutia), which are characterized by low territorial development, insignificant socio-economic potential.

The data of the Russian Federal Tax Service on the cadastral value of buildings and structures in considered municipalities, presented in Table 5, as a whole, make it possible to verify the calculated market fixed assets value. A number of Russian studies provide analytical and empirical average ratios of cadastral and market values for real estate objects. In particular, a number of Russian researchers indicate that in most cases the cadastral value is one third or even half less than the market value (Kotlyarov et al. 2012; Myasnikov et al. 2019; Berdnikova 2019). This pattern is generally reproduced within the specified range with the ratio of the cadastral and market values in studied municipalities of the AZRF Asian sector.

On average, for Arctic territories, the market value of buildings and structures exceeds their cadastral value by 1.9 times (by 47%), while the smallest difference is typical for the Arctic districts of the Krasnoyarsk krai – 1.4 times (by 28%), the largest – for the Chukotka Autonomous Okrug – 2.5 times (60%). These interregional differences may indicate, on the one hand, the existing differences in assessing the cadastral value in different regions of Russia and for different types of economic activities, on the other hand, about the limitations of the SPARK-Interfax database – lack of statistical data on a number of companies. Taking into account these circumstances, it can be assumed that the real market value of buildings and structures in Asian Arctic municipalities is slightly higher than the calculated values.

CONCLUSIONS

An analysis of the fixed assets (including buildings and structures) territorial organization in the AZRF Asian sector municipalities shows a significant heterogeneity of the study area in terms of their density distribution. It determines the need to develop a differentiated approach to the state system modeling aimed at natural risks preventing, in particular, those associated with engineering-geocryological conditions changes. Based on this, it is advisable to plan the financial support of this system, taking into account the real fixed assets carrying value concentrated in areas of maximum permafrost throwing danger, as well as the regional and local budgets financial capabilities.

The largest probable damage, as well as the financial burden associated with adaptation measures implementation, will be in the regions and municipalities that concentrate the largest fixed assets volume, ceteris paribus. In total, according to our estimates, fixed assets of commercial companies with a total value of about 14.8 trillion rubles (including buildings and structures – 10.7 trillion rubles) are concentrated in the AZRF Asian sector permafrost zone.

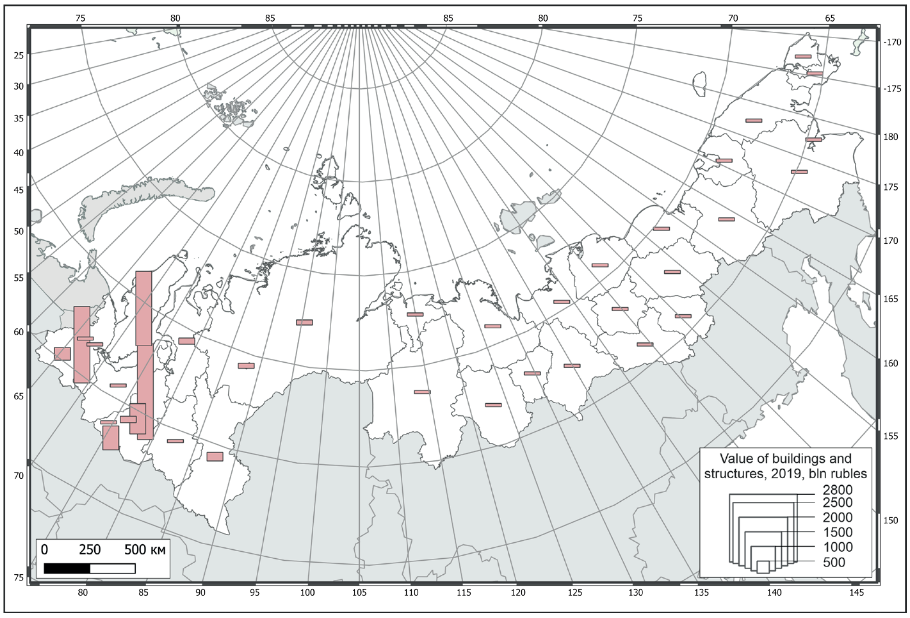

Fig. 2. The value of buildings and structures in the municipalities of the AZRF Asian sector, 2019

This research is pioneering; therefore, the results presented in the article are only the first necessary generalization, taking into account promising clarifying and improvements in methods. First, at the next iteration, it is planned to create a GIS, where specific enterprises with already known fixed assets (buildings and structures) values will be georeferenced to specific permafrost degradation areas in order to damage prediction. It requires scientific cooperation and work with specialized cryolithologists.

This study results can be used in developing and correcting strategic planning documents (both sectoral and territorial planning), adaptation programs at various territorial levels, including the subsequent stages of the National Action Plan for Adaptation to Climate Changes developing. Based on the obtained results, the development and early application of measures set aimed at geocryological risk level reduction can be carried out.

REFERENCES

Ableeva A.M. (2010). Assessment of the dynamics of the cost of fixed assets of agriculture in the Republic of Bashkortostan, Economic aspects of anti-crisis development of modern society. Materials of the II International Scientific and Practical Conference, 6-8. (in Russian).

Adamadziev K.R., Adamadzieva A.K. (2011). Assessment of the dependence of GRP on investment, the number of people employed in the economy and the cost of fixed assets using panel data models (on the example of Russian regions), International Journal of Applied and Basic Research, 9, 68-70. (in Russian).

Akimov V.A., Voronov S.P., Radaev N.N. (2013). Risk concepts and risk analysis concepts, Civil protection strategy: problems and researches, 3, 2(5), 562-567 (in Russian).

Anisimov O.A., Streletsky D.A. (2015). Geocryological risks during the thawing of permafrost soils. Arctic XXI century, Natural sciences, 2(3), 60-74 (in Russian).

Anisimov O.A., Kokorev V.A. (2016). Climate in the Arctic zone of Russia: analysis of modern changes and model projections for the XXI century, Vestnik Moskovskogo Universiteta, Seriya 5: Geografiya, 1, 61-69 (in Russian).

Baburin V.L., Badina S.V. (2015). Evaluation of the social-economic potential of natural hazard- subjected territories, Vestnik Moskovskogo universiteta, Seriya 5: Geografiya, 5, 9-16. (In Russian).

Baburin V.L., Badina S.V. (2020). Forecasting of damages from natural hazards for the «Northern Caucasus Resorts» tourist cluster, Sustainable Development of Mountain Territories, 12(3), 349-356. (In Russian).

Badina S.V. (2020). Prediction of socioeconomic risks in the cryolithic zone of the Russian Arctic in the context of upcoming climate changes, Studies on Russian Economic Development, 31, 4, 396-403.

Badina S.V. (2021). Estimation of the value of buildings and structures in the context of permafrost degradation: The case of the Russian Arctic, Polar Science, DOI: 10.1016/j.polar.2021.100730.

Badina S.V., Pankratov A.A., Yankov K.V. (2020). Transport accessibility problems of the isolated settlements in Russian European Arctic zone, InterCarto. InterGIS. GI support of sustainable development of territories: Proceedings of the International conference. Moscow: Moscow University Press, 26(1), 305-317 (in Russian).

Berdnikova V.N. (2019). The relationship between cadastral and market value, Bulletin of the Chelyabinsk State University, 9(431), Economic sciences, Issue 66, 210–216. (in Russian).

Carpenter C.G. (2005). Fixed Asset Accounting Software Evaluation: A Structured Methodology For The Mid-Market Firm, The Review of Business Information Systems s – Spring 2005, 9(2), 55-68.

Daniels M.B. (1993). The Valuation of Fixed Assets. The Accounting Review (Published By: American Accounting Association), 8(4), 302-316.

Didkovsky V.M., Tabakova S.A. (1997). Methodological approaches to assessing the replacement cost of fixed assets, Evaluation issues, 1(5-10). (in Russian).

Dmitriev M.E., Chistyakov P.A., Romashina A.A. (2020). Approbation of the methodology for estimating municipal gross value added, Studies on Russian Economic Development, 31 (1), 36-43.

Eidelman G.I., Barashev A.F., Lylova T.Yu., Medvedev Yu.A. Determination of the full replacement cost in the appraisal and revaluation of fixed assets. Deposited manuscript,185-B2010 05.04.2010. (in Russian).

Fernandes P. (2007). Company valuation methods. The most common errors in valuations. IESE Business School – University of Navarra. January 2002. SSRN Electronic Journal.

Fomin D.A., Khanin G.I. (2012). An alternative assessment of the cost of fixed assets and the financial position of the railway transport in Russia, Forecasting problems, 3(132), 55-70. (in Russian).

Gourfinkel D. (2007). Regional Study on the Management, Control, and Recording of Fixed Assets: Latin America and the Caribbean. World Bank, Washington, DC.

Grebenets V.I., Streletsky D.A., Shiklomanov N.I. (2012). Changes in the bearing capacity of frozen soils due to climate warming in the north of Western Siberia, Cryosphere of the Earth, 16(1), 22-32 (in Russian).

Gribovsky S.V. (1998). The concept of accounting for depreciation models of fixed assets of enterprises when assessing their market value, Evaluation issues, No. 3, 2–12. (in Russian).

Melnikov V.P., Osipov V.I., Brushkov A.V. et al. (2021). Assessment of damage to residential and industrial buildings and structures during temperature changes and permafrost thawing in the Arctic zone of the Russian Federation by the middle of the XXI century, Geoecology, 1, 14-31 (in Russian).

Khanin G.I., Kopylova N.V. (2011). Alternative assessment of the replacement cost of fixed assets of Russian industry in 2005–2008, ECO, 1(439), 83-98. (in Russian).

Kislov A.V., Grebenets V.I., Evstigneev V.M. et al. (2011). Consequences of possible climate warming in the XXI century in the north of Eurasia, Vestnik Moskovskogo Universiteta, Seriya 5: Geografiya, 3, 3-8. (in Russian).

Korolev V.Yu., Bening V.E., Shorgin S.Ya. (2007). Mathematical foundations of risk theory. Moscow: FIZMATLIT (in Russian).

Kotlyarov M.A., Tatarkin D.A., Animitsa P.E. (2012). The relationship between the market and cadastral value of real estate for tax purposes, Economy. Taxes. Right, 6, 25-30. (in Russian).

Kukkoneni I., Suhonen E., Ezhova E. et al. (2020). Observations and modelling of ground temperature evolution in the discontinuous permafrost zone in Nadym, north-west Siberia, Permafrost and Periglacial Processes, 31(2), 264-280.

Kuznetsova O.V., Badina S.V., Mikhailov A.A., Bobrovsky R.O. (2021). Development trends and modernization of the industry in Russian regions, Moscow: Research Association of the Plekhanov Russian University of Economics, 2. (in Russian).

Myagkov S.M., Shnyparkov A.L. (2004). Risk concept. Section of the monograph «Natural hazards of Russia. «Nature, Society and Environment». Moscow: Publishing house «Gorodets», 4, 265-274 (in Russian).

Myasnikov V.F., Pokhorukova E.I. (2019). Cadastral and market value of residential real estate: what is the difference? Regulation of land and property relations in Russia: legal and geospatial support, real estate appraisal, ecology, technological solutions, 1, 208-211. (in Russian).

Osipov V.I., Larionov V.I., Burova V.N. et al. (2017). Methodology of natural risk assessment in Russia, Natural Hazards, 88(S1), 17-41.

Orttung R.W., Anisimov O., Badina S. et al. (2021). Measuring the sustainability of Russia's arctic cities, Ambio, 50(11), 2090-2103.

Pankratov A.A., Musaev R.A., Badina S.V. (2020). Innovation clusters in the Arctic zone of Russian Federation, IOP Conference Series: Materials Science and Engineering, 941, 012023-012024.

Pankratov A.A., Kuvshinova E.A., Galstyan L.S. (2021). Quantitative Assessment of the Socioeconomic Potential of Advanced Development Territories of Regions of the Far Eastern Federal District, Studies on Russian Economic Development, 32(4), 407-414.

Petruk Yu.S. (2016). Essence, classification and assessment of the cost of fixed assets of the enterprise, Science in modern society: patterns and development trends. Collection of articles of the international scientific and practical conference: in 2 parts, 84–87. (in Russian).

Pilyasov A.N. (2020). Arctic entrepreneurship development factors. GEOGRAPHY, ENVIRONMENT, SUSTAINABILITY, 13(1), 46-56.

Porfiryev B.N. (2011). Nature and economics: risks of interaction. (Ecological and economic essays). Edited by Academician V.V. Ivanter. Moscow: Ankil (in Russian).

Porfirev B.N., Voronina S.A., Semikashev V.V. et al. (2017). Consequences of climate change for economic growth and development of individual sectors of the Russian Arctic economy, Arctic: ecology and economics, 4(28), 4-17. (in Russian).

Scholes R., Montanarella L., Brainich A. et al. (2018). IPBES (2018): Summary for policymakers of the thematic assessment report on land degradation and restoration of the Intergovernmental Science-Policy Platform on Biodiversity and Ecosystem Services. Bonn, Germany (in Russian).

The second assessment report of Roshydromet on climate changes and their consequences on the territory of the Russian Federation. General summary. (2014). Moscow: FGBU «Research Center «Planeta» (in Russian).

Romanovsky V.E., Osterkamp T.E. (1997). Thawing of the active layer on the coastal plain of the Alaskan Arctic, Permafrost and Periglacial Processes, 8, 1-22.

Romanovsky V.E., Smith S.L., Christiansen H.H. (2010). Permafrost thermal state in the Polar Northern Hemisphere during the International Polar Year 2007–2009: a Synthesis, Permafrost and Periglacial Processes, 21, 106-116.

Sapritsky E.B., Rudnev Yu.A., Dubinsky A.R., Khalatov S.A. (1996). Computer systems for assessing the value of fixed assets, Evaluation issues, 4, 57-62. (in Russian).

Shichkov A.N. (2003). Assessment of the intrinsic value of fixed assets of the enterprise. Ministry of Education of the Russian Federation, Vologda State Technical University. Vologda. (in Russian).

Streletsky D.A., Shiklomanov N.I., Grebenets V.I. (2012). Changes in the bearing capacity of frozen soils in connection with climate warming in the north of Western Siberia, Cryosphere of the Earth, XVI(1), 22-32.

Streletskiy D.A., Suter L., Shiklomanov N.I. et al. (2019). Assessment of climate change impacts on buildings, structures and infrastructure in the Russian regions on permafrost, Environmental Research Letters, 14(2), 025003.

Suter L., Shiklomanov N., Streletskiy D. (2019). Assessment of the cost of climate change impacts on critical infrastructure in the circumpolar Arctic, Polar Geography, 42, 267-286.

SWIPA (2017). Snow, Water, Ice and Permafrost in the Arctic. Arctic Monitoring and Assessment Programme (AMAP). Oslo, Norway.

Vasiliev A.A., Drozdov D.S., Gravis A.G. et al. (2020a). Permafrost degradation in the western Russian arctic, Environmental Research Letters, 15, 045001.

Vasiliev A.A., Gravis A.G., Gubarkov A.A. et al. (2020b). Permafrost degradation: results of long-term geocryological monitoring in the western sector of the Russian arctic, Cryosphere of the Earth, 24(2), 15-30 (in Russian).

Volodin E.M., Mortikov E.V., Kostrykin S.V. et al. (2017). Simulation of the present-day climate with the climate model INMCM5, Climate Dynamics, 49, 11-12, 3715-3734.

Hjort J., Karjalainen O., Aalto J. et al. (2018). Degrading permafrost puts Arctic infrastructure at risk by midcentury, Nature communications, 9(1), 5147.

Zemlyanskiy D.Y., Kalinovskiy L.V., Makhrova A.G. et al. (2021). Integrated socioeconomic development index for Russian cities, Regional Research of Russia, 11(1), 29-39.

RESEARCH PAPER

RADON HAZARD IN PERMAFROST CONDITIONS: CURRENT STATE OF RESEARCH

Andrey V. Puchkov[1*], Evgeny Yu. Yakovlev[1], Nicholas Hasson[2], Guilherme A. N. Sobrinho[3], Yuliana V. Tsykareva[4], Alexey S. Tyshov[1], Pavel I. Lapikov[1], Ekaterina V. Ushakova[5]
[1]N. Laverov Federal Centre for Integrated Arctic Research of the Ural Branch of Russian Academy of Sciences, 109 Severnoj Dviny Emb., Arkhangelsk, 163000, Russia.
[2]Water and Environmental Research Center, University of Alaska Fairbanks, 1731 South Chandalar Drive, Fairbanks, AK 99775, USA.
[3]Institute of Radiation Protection and Dosimetry, Av. Salvador Allende s/n – Barra da Tijuca, Rio de Janeiro, Brasil, CEP – 22783-127
[4]Northern (Arctic) Federal University named after M.V. Lomonosov, 17 Severnaya Dvina Emb., Arkhangelsk, 163002, Russia.
[5]Yuri Gagarin State Technical University of Saratov, 77 Politechnicheskaya street, Saratov, 410054, Russia.
***Corresponding author:** andrey.puchkov@fciarctic.ru
Received: March 31th, 2021 / Accepted: November 9th, 2021 / Published: December 31st, 2021
https://doi.org/10.24057/2071-9388-2021-037

ABSTRACT. In this paper, we review both practical and theoretical assessments for evaluating radon geohazards from permafrost landforms in northern environments (>60º N). Here, we show that polar amplification (i.e. climate change) leads to the development of thawing permafrost, ground subsidence, and thawed conduits (i.e. Taliks), which allow radon migration from the subsurface to near surface environment. Based on these survey results, we conjecture that abruptly thawing permafrost soils will allow radon migration to the near surface, and likely impacting human settlements located here. We analyze potential geohazards associated with elevated ground concentrations of natural radionuclides. From these results, we apply the main existing legislation governing the control of radon parameters in the design, construction and use of buildings, as well as existing technologies for assessing the radon hazard. We found that at present, these laws do not consider our findings, namely, that increasing supply of radon to the surface during thawing of permafrost will enhance radon exposure, thereby, changing prior assumptions from which the initial legislation was determined. Hence, the legislation will likely need to respond and reconsider risk assessments of public health in relation to radon exposure. We discuss the prospects for developing radon geohazard monitoring, methodical approaches, and share recommendations based on the current state of research in permafrost effected environments.

KEYWORDS: Radon hazard, radiation safety, permafrost, Arctic, climate warming, radon-hazardous territory, natural radioactivity, uranium ore, legislation, measurement method

CITATION: Andrey V. Puchkov, Evgeny Yu. Yakovlev, Nicholas Hasson, Guilherme A. N. Sobrinho, Yuliana V. Tsykareva, Alexey S. Tyshov, Pavel I. Lapikov, Ekaterina V. Ushakova (2021). Radon Hazard In Permafrost Conditions: Current State Of Research. Geography, Environment, Sustainability, Vol.14, No 4, p. 93-104 https://doi.org/10.24057/2071-9388-2021-037

ACKNOWLEDGMENTS: The work was supported by the Russian Science Foundation grant No. 20-77-10057 «Diagnostics of permafrost degradation based on isotope tracers (234U/238U, δ18O+δ2H, 292 δ13C+14C) and by Russian Foundation for Basic Research grant No. 20-35-70060 «Investigations of the conditions for increased radon emanation in the sedimentary cover of areas of kimberlite magmatism (on example the Arkhangelsk diamondiferous province)».

Conflict of interests: The authors reported no potential conflict of interest.

INTRODUCTION

At present, the problem of rapid warming in northern latitudes (>60º N) is quite acute, particularly for landscape changes, vegetation productivity, and ground subsidence or thawing of permafrost soils. Such changes lead to consequences for the population, infrastructure and the ecosystem as a whole (Zolkos et al. 2021). At the same time, the fact remains undeniable that climate warming trends over the past hundreds of years will continue in the future in accordance with the 5th Assessment Report of the Intergovernmental Panel on Climate Change (IPCC, 2014).

Recently, the most important indicator of global climate change was the phenomenon of permafrost degradation, which in turn causes the release of various substances into the atmosphere, for example, stored organic carbon. (Obu et al. 2019; Biscaborn et al. 2019). Permafrost is a key element of the cryosphere (Obu et al. 2019), occupying a significant part of the land and sea of the northern hemisphere (Brown et al. 1997; Rachold et al. 2007), and 17% of the Earth's land surface (Biscaborn et al. 2019). Recent studies indicate that the permafrost boundary is gradually shifting from south to north, and its depth is progressively increasing (Zhang et al. 2021). The indicators of such a phenomenon as the degradation of permafrost are craters in Yamal (Buldovicz et al. 2018), man-made incidents (Norilsk) (Koptev, 2020), and changes in landform (Ji et al. 2019; Doloisio et al. 2020). Every year, new scientific studies enhance the concern of permafrost degradation across northern latitudes (Liu et al. 2021; Vaisanen et al. 2020; Heslop et al. 2019). One promising area of development is the assessment of radiation safety in conditions of thawing of soils, bedding of rocks with an increased content of radium-226, and subsequent release of radioactive radon gas to the near surface, but remains poorly understood (Glover 2006; Glover 2007).

The aim of this scientific work is to show the relevance and importance of a comprehensive study of the effect of thawing of permafrost on the radiation safety of the territory from the point of view of the radon hazard, as well as the need to take this predictor into account in the normative assessment of the potential radon hazard parameter. We find the lack of scientific literature in this area indicates a knowledge gap, if we are to safeguard public health in response to polar amplification, and its consequences, as mentioned. We discuss here the field studies of two parameters: the concentration of radon and pathway mechanisms involving permafrost thaw.

Our study examines four areas of inquiry (1-4):

(1) we show how radon is distributed in the conditions of the spread of permafrost soils, as well as their degradation due to progressive climate change.

(2) we identify territories where complex factors are widespread, for example, the presence of soils and rocks with an increased content of radium-226, as well as the population factor of the territory living on these permafrost landforms; the latter factor plays an important role, because if the major hypothesis of increased radon production developing from conditions of permafrost degradation is confirmed, this will ultimately lead to the re-evaluating methods for monitoring the potential radon effects on the public health of populated areas living near such geohazards.

(3) we apply the current legislation regarding the environmental radiation safety or standards in response to natural sources of ionizing radiation, in order to understand the need for further clarification and adjustment of the norms for the control of the potential radon hazard.

(4) Finally, it is important to study the recent developments, methods, and technologies for assessing the potential radon hazards, which are currently available; the parameters or predictors we must consider for effective public safety measures and the remaining hidden variables, which are poorly understood in this context.

PERMAFROST AS A BARRIER TO RADIOACTIVE RADON GAS

Radon is a member of the radioactive chain of uranium-238 and is continuously formed in all natural environments during the radioactive decay of its parent isotope, radium-226, which has a half-life of about 1600 years (Sabbarese et al. 2021; Giustini et al. 2019; Miklyaev et al. 2010; Baskaran et al. 2016; Daraktchieva et al. 2021). Due to its physical and chemical properties, as well as being an inert gas with a relatively long half-life (3.82 days), it is an optimal indicator for studying many processes occurring in the environment (Loisy et al. 2012, Kuo et al. 2014, Baskaran et al. 2016, Selvam et al. 2021), including in geological research, for example, for predicting seismic phenomena and other geodynamic processes (Sahoo et al. 2020; Kawabata et al. 2020). Free radon exhibits the ability to easily migrate in the geological environment in the gas phase or dissolved in pore waters. This is especially true when the geological system is open or has conduits, for example, pores, cracks, and faults (e.g. Taliks) (Miklyaev et al. 2010; Moreno et al. 2018; Tsapalov et al. 2016; Yang et al. 2018). The process of release of radon-222 from solids to the surface (into the external space or into the open pore space) is called radon emanation, the quantitative characteristics of which are the intensity of emanation, emanation ability and the coefficient of emanation (Miklyaev et al. 2010; Nuccetelli et al. 2020; Domingos et al. 2018; Pinto et al. 2020).

The behavior of free radon can depend on a high degree of influencing factors, starting with climatic parameters (temperature, humidity, pressure) and physical parameters of the geological environment (for example, gas permeability of rocks, soils, porosity, density), as well as mineralogical composition and complex geochemical processes and relationships, on which the existence of both the parent radionuclide radium-226 and its daughter radionuclide, radon-222, depends (IAEA 2013; Krupp et al. 2017). Some authors (Banerjee et al. 2011; Pereira et al. 2017; Li et al. 2018; Coletti et al. 2020) indicate the importance of considering the parameters of porosity and density of the rock, which in turn depend on the temperature processes occurring after magmatic crystallization. Radon formed in a solid can enter the surrounding space both due to radioactive recoil and due to diffusion (Titaeva, 2000). In the case of radioactive recoil, the radon atoms formed during the radioactive decay of radium-226 acquire a certain recoil energy, which they subsequently lose while transporting. Part of the atoms remaining in the solid phase that make up bound radon. But the recoil energy of about 86 keV is quite enough for some of the atoms to be released outside the solid, forming free radon (IAEA 2013; Thu et al. 2020).

Considering the above, there are three scenarios for the behavior of the radon atom after its formation as a result of the decay of the radium-226 atom. In the first case, the radon-222 atom remains in the solid phase. In the second case, the recoil energy is enough to overcome the boundaries of one grain of solid matter, to pass through the pore space, but to be included in the composition of another grain of solid matter. In the third case, the radon atom remains in the pore space and enters the environment, which in turn constitutes the process of radon emanation (Hassan et al. 2009; Eakin et al. 2016; Thu et al. 2020).

In order to understand the behavior of radon, scientists have developed and supplemented the previously existing models of radon transport in solid media. There are three groups of radon transport models: (1) diffusion (Telford et al. 1983; Pavlov et al. 1996; Minkin et al. 2002, 2003; Klimshin et al. 2010; Livshits et al. 2017); (2) convective (Rogers et al. 1991; Arvela et al. 1995) and diffusion-convective; and (3) diffusion-advective (Al-Ahmady et al. 1994). However, the latest results of mathematical calculations obtained from convective and diffusion-convective models have shown poor correlation with experimental data, since the calculated versions of the models are usually very simplified, and most of them require very specific input parameters, which in some cases unrealistic for determining in-situ (Bakaeva et al. 2016). The group (1-2) of diffusion models showed cogent results in convergence with experimental data, and at the moment the diffusion mechanism is considered to be the main one for the radon transfer process (Minkin et al. 2008, Livshchits et al. 2017).

In the context of permafrost thawing and the dependence of radon flux on seasonal variations, the prior work of thermo diffusion model (Minkin et al. 2003) seems to be of interest here, where radon transfer in the absence of a pressure difference occurs at a temperature gradient and therefore, during the mass transfer equation, where the radon flux includes two components:

(1) thermal diffusion radon flux and (2) flux concentration diffusion. Later, this theory was refined by the authors themselves, based on the already known temperature fluctuations in soils (Minkin et al. 2016; Shapovalov et al. 2016). Livshchits et al. 2017 also calculate radon transport using a diffusion model, but considers thermal diffusion in the form of an «equivalent» diffusion coefficient.

In fractured and fractured-porous geological areas, fracture geometry plays an important role in the study of radon flux. For such environments, among others, discrete fracture network (DFN) models have been created, which is generally considered one of the most effective methods for predicting the flow of fluids such as groundwater, carbon-dioxide, oil and natural gas (Blonsky et al. 2017). In the case of fractured porous media, a tetrahedral mesh is used for their geometric description. Tetrahedrons describe a porous matrix, while tetrahedron faces describe cracks. In the case of purely fractured media, the fractures are described by a two-dimensional triangular mesh matched at the intersection lines of the fractures. In this case, the gas flow is described as the sum of diffusion and advective flows. However, such a description of media does not consider the anisotropy, which is quite costly in terms of the required computational resources needed for modeling. In recent work (Feng et al. 2020), the author proposed to use fractals to describe the geometry of coupled fractures in the DFN model, which makes it possible to take into account the fractured anisotropy and optimizes the numerical calculation algorithm by presenting equations for the fracture network in matrix form.

Moving from the physical processes of radon transfer to the issue of the effect of permafrost on radon, it should be noted that as early as 1990, work was carried out to assess the distribution of permafrost based on the results of measuring the radon concentration as a tracer (Sellmann et al. 1990). Results showed that the radon concentration correlates well with frozen areas under conditions of permafrost cover. Low values of radon concentration were found where the permafrost thickness is high. And high values of radon concentration were found where there is a weak level of permafrost (or there is no permafrost at all). The authors concluded that permafrost has a significant impact on the dynamics of radon distribution. At the same time, it was not concluded that an increase in the amount of radon occurs at a higher level of thawing of frozen soils due to the release of radium-226 and radon from ice crystals. That is, the permafrost layer, on the one hand, retains radioactive substances, and on the other hand, it is an excellent barrier for mobile forms of radionuclides.

The need to consider permafrost factors when assessing the distribution of radon was first indicated by prior work (Evangelista et al. 2002) and conducted studies of the radon exhalation rate on King George Island and the Antarctic Peninsula. They assumed that surface ice and permafrost largely screen the radon flux to the Earth's surface.

Some theoretical studies in the field of assessing radon distribution under permafrost thawing conditions were started in 2006–2008 (Glover 2006; Glover 2007). The authors developed models showing the fact of an increase in the supply of radon to the surface, including buildings, in the process of permafrost degradation. They showed that with an average world content of radium-226 in soil with concentration of 40 Becquerels per kilogram ($Bq \cdot kg^{-1}$), a permafrost layer of 13 m can lead to a decrease in the radon concentarion in a building to 5-10 Becquerels per cubic metre ($Bq \cdot m^{-3}$) (model of an unventilated room). However, as a result of melting permafrost, the level of radon concentration can increase up to 100 times (1000-1500 $Bq \cdot m^{-3}$). According to the model constructed by the authors, this level can persist for several years and then gradually decrease. The authors believe this fact is extremely relevant considering the control level of 100-300 $Bq \cdot m^{-3}$ (for different countries), as well as considering the extremely negative effect of radon on the incidence of cancer.

It is noted that the values of the radon contration were obtained under the condition of the radium-226 content in the soil at a level of 40 $Bq \cdot kg^{-1}$. In the world as a whole, there are many territories having increased content of radium-226 in soils, rocks, but particularly interesting in the presence of permafrost up to 1500 m in layer thickness, and where human settlements and/or infrastructure exist. Some Russian scientists (Klimshin et al. 2010) have made conclusions about the significant effect of the level of seasonal soil freezing (up to 1 m) in winter on radon emanation to the earth's surface. Based on these results, appropriate guidelines were developed with criteria for assessing the potential radon hazard, considering the level of soil freezing. Recently, it was found by (Chuvilin et al. 2018) by experimental methods, soil freezing significantly affects gas permeability, depending on the initial value of moisture content. The authors investigated sand types and sandy-clay mixture mediums. For most sand samples with an initial moisture content of about 10%, permeability in thawed and frozen states differed within 1.5-4 times, whereas samples represented by silty sand, gas permeability in thawed and frozen states differed by more than 10 times.

As part of a series of international expeditions TROICA (Transcontinental Observations into the Chemistry of the Atmosphere), passing along the Trans-Siberian Railway from 1999 to 2007, an analysis of spatial and temporal variations in the concentration of radon-222 in the surface layer of the atmosphere over the continental part of Russia was carried out. Scientists (Berezina et al. 2009; Berezina 2014) noted a significant increase in the surface concentration of radioactive gas (approximately 3 times) with an increase in the depth of seasonal soil thawing from summer 1999 to autumn 2005 in the permafrost zone in the Eastern Siberia region Russia due to the intensive migration of radon-222, accumulated in frozen soils, into the near-surface layer of the soil and its subsequent exhalation into the atmosphere. All the above facts about climate warming, melting of permafrost and its barrier function for the entry of gases to the surface, an increase in the radon concentration during thawing of frozen soils, were based on a few studies, as well as the fact that radon has an extremely negative effect on human health from the point of view of oncology. This indicates the relevance and need for fundamental research in potentially hazardous areas and from the point of view of radiation safety or public health assessment but remains poorly understood. In such case of confirmation, a significant increase in the flow of radon to the earth's surface during thawing of frozen soils, it will then be necessary to recognize that permafrost is one of the predictors (indicators) that characterizes the territory in terms of potential radon hazard. Under such context and conclusions, this warrants further development of the regulatory legal framework in terms of radiation safety and radiation control when planning the construction of residential and industrial buildings, as well as their operation, and the methodology for assessing the potential radon hazard of the Arctic territories. It then become necessary to consider certain geological parameters of the spread of permafrost (power, rate of degradation, etc.), which we will now consider.

DYNAMIC GEOHAZARDS: PARAMETERS OF RADON IN PERMAFROST LANDFORMS

In order to understand the need and relevance of research on the subject of radon hazard of territories in the conditions of thawing permafrost, it is necessary to identify the territories in which the increased content of radioactive elements and the spread of permafrost are most pronounced, as well as characterized by the presence of settlements.

Figure 1 shows the distribution of permafrost over the earth's surface, which covers ~24% of the Northern Hemisphere surface area. The territories covered by permafrost are represented by such countries/areas as the United States (Alaska), Canada, Scandinavia (e.g. Sweden) and Russia. Permafrost covers to a lessor area Mongolia, Greenland (Denmark), and Alpine regions.

Due to the fact that radon is a decay product in the uranium-238 chain (Baskaran et al. 2016), we will focus on uranium-containing ore fields to identify promising territories. From this point of view, two countries remain interesting for study: Russia and Canada.

On the territory of Russia, within the permafrost distribution, the following uranium-bearing ore fields can be distinguished: Polar-Ural field; Taimyr field; Chukchi field; Anabar field; Sayano-Yenisei field; North Baikal field; Vitimskoye deposit; East Transbaikal field; Streltsovskoe deposit; Elkon field; East Aldan field. Figure 3 shows a diagram of the location of the main

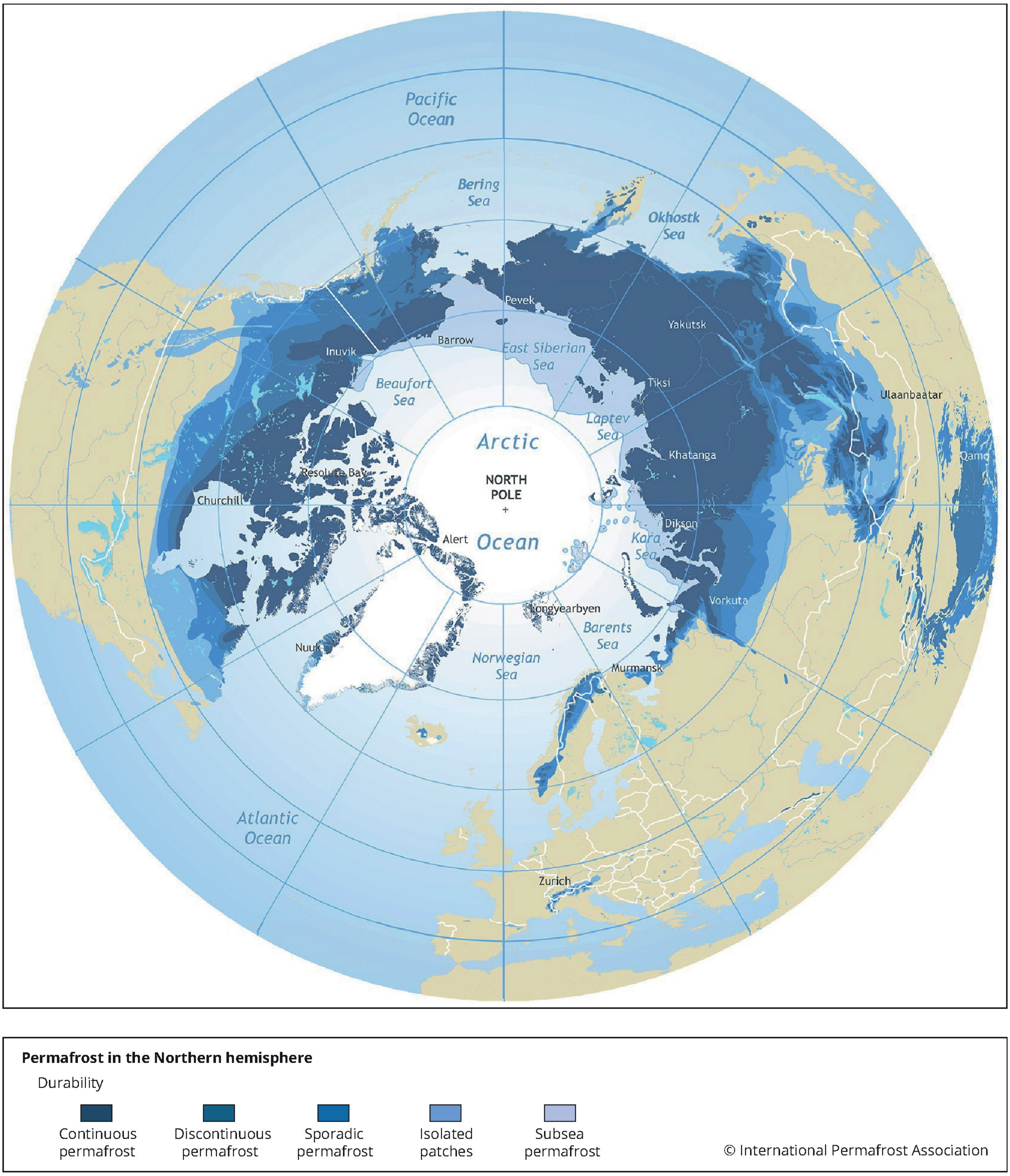

Fig. 1. Distribution of permafrost on the earth's surface in the Northern Hemisphere (based on materials from https://www.eea.europa.eu. Copyright holder: European Environment Agency (EEA))

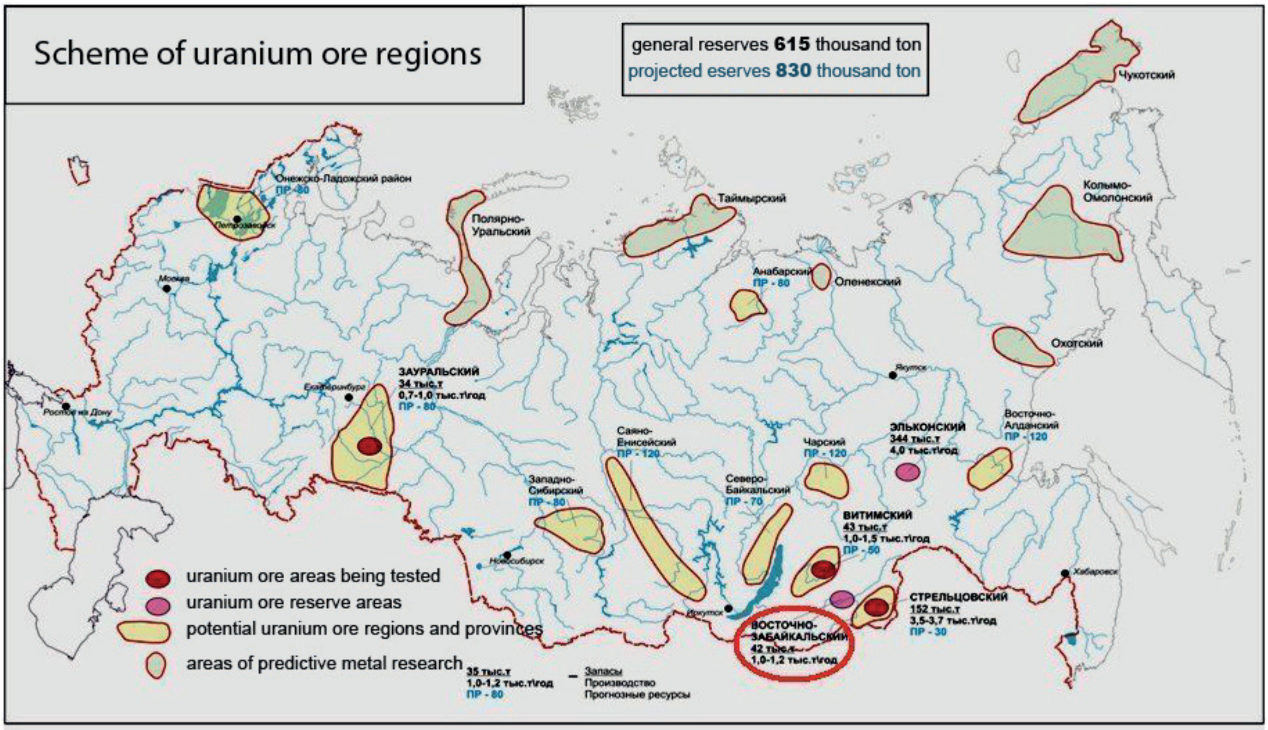

Fig. 2. The diagram of the location of the main uranium-containing regions of Russia (based on materials from https://promtu.ru/dobyicha-resursov/dobyicha-urana-v-rossii-i-mire)

uranium-containing regions of Russia (https://promtu.ru/dobyicha-resursov/dobyicha-urana-v-rossii-i-mire).

Ores vary in uranium content in the territory. Moreover, the distribution of uranium in the ore is described not by the normal (Gaussian) rule, but as logarithmic one, i.e. very rich ores are possible, but they are extremely rare. Uranium does not occur naturally as a native element. This is due to the fact that uranium can be in several stages of oxidation, it occurs in a very diverse geological setting (Nizinski et al. 2020).

From the ore fields presented above, two of the most interesting regions were identified, which are located on the territory of permafrost, near settlements and within the seismically active zone: the Polar-Ural field and the Republic of Buryatia, which includes the Severo-Baikalskoe field, Vitimskoe deposit, Streltsovskoe deposit and the Khiagda ore field. The Polar-Ural field is located within the Russian Arctic. These facts are confirmed by the information presented in Figures 3, 4. Buryatia especially stands out given the presence of permafrost, a seismically active zone and an increased dose of radon exposure.

From a historical perspective on the area, it should be noted that in 1960, large scale geological surveys were conducted within the Polar Urals, discovering the Kharbeysky molybdenite deposit and Novo-Kharbeysky uranium ore occurrence. These discoveries served as one of the initial beginnings of prospecting work in the northern Urals or

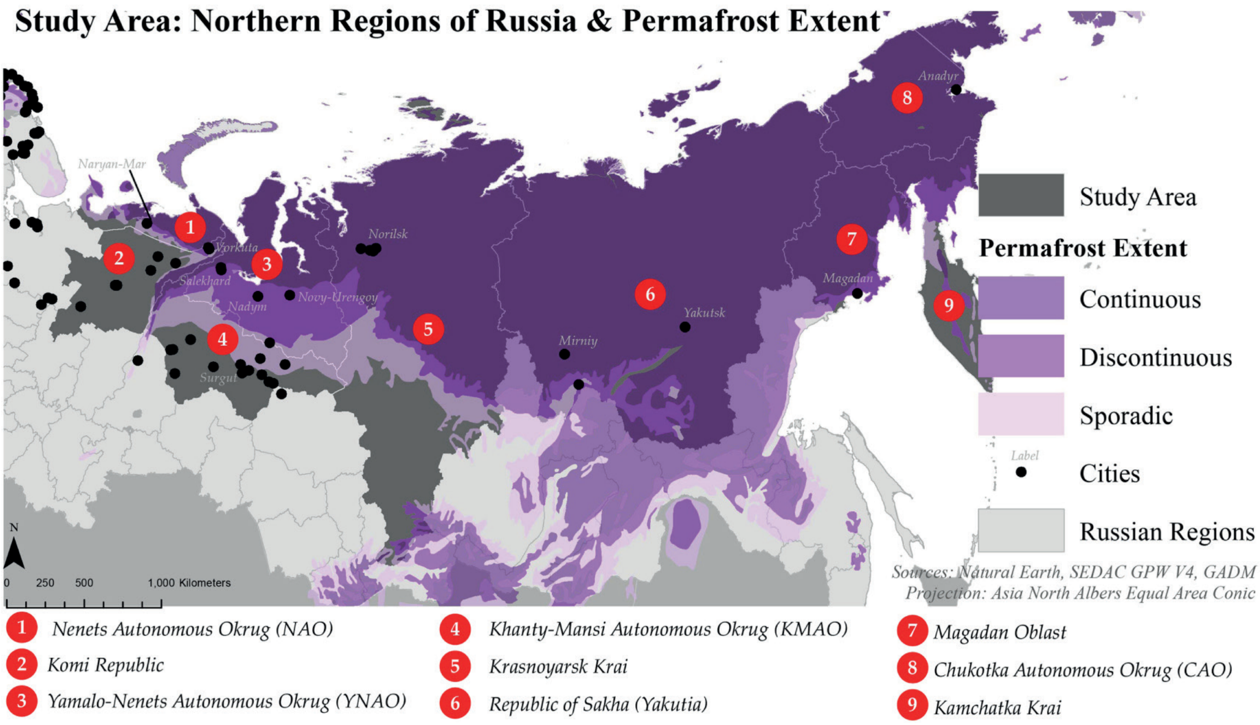

Fig. 3. Permafrost distribution and administrative division of Russia. The boundaries of nine administrative regions considered in this study are shown in gray. Location of major cities is shown with black circles (Streletskiy et al. 2019)

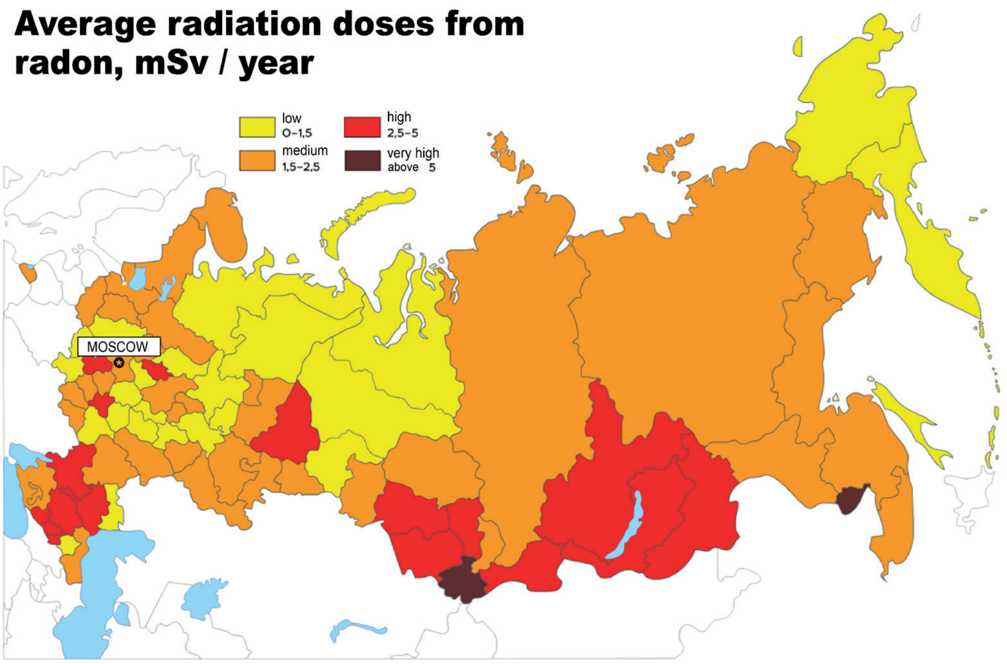

Fig. 4. Average radiation doses from radon in Russia (based on materials from https://eksorb.com/radon)

polar and sub-polar division. Here, between 1961 and 1965, Uranium-bearing ores were discovered (Verkhovtsev 2000).

A more detailed study in this area, discovered clastic diorites on the surface with the dose rate of gamma radiation reaching 612 $\mu R \cdot h^{-1}$. The radioactivity was sourced in shallow deposition of a radioactive minerals from the near surface. Later, geophysicists during search routes on the southern slope of the mountain discovered a bedrock outcrop of dark gray chloritized rocks with resinous mineralization 0.7 m thick, having a gamma dose rate of over 7500 $\mu R \cdot h^{-1}$ (Dushin et al. 1997).

As for the Republic of Buryatia, the unique position of the territory in the Trans-Baikal radio-geochemical province of the Sayano-Baikal folded seismically active region with a significant number of natural radioactive objects (deposits, ore occurrences and radioactive anomalies) and associated high levels of radiation background in terms of the exposure dose rate of gamma radiation and radon allow us to objectively classify the territory of the Republic of Buryatia as a province of radiation distress, high radon risk with very high radon concentrations in the geological environment (rocks, faults, water and soil) and in residential buildings. It is necessary to conduct extensive radon metric studies in the geological environment, as well as studies of the air environment within the permafrost in order to identify risk groups of the population in accordance with dose loads due to radon (Astakhov et al. 2015), as well as to form predictive estimates for the development of radioecological situation in the region.

Canada is a good example of an area outside of Russia characterized by both permafrost and rock outcrops with increased levels of naturally occurring radionuclides. Canada is a vast country with most of the population living on a small portion of the land. But despite this, control over the radon hazard is carried out throughout the country as a whole (Chen

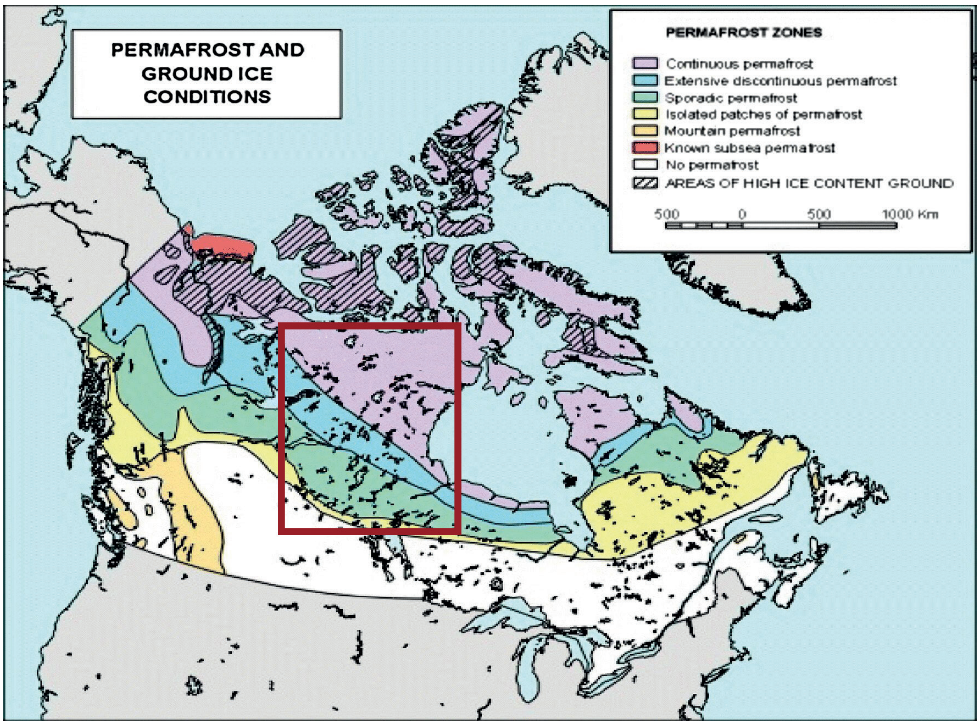

Fig. 5. Uranium-bearing ore field in Canada – northern part of Saskatchewan (based on materials from http://gsc.nrcan.gc.ca)

2009). One province are especially interesting in terms of potential radon hazard – the northern part of Saskatchewan shown in Fig. 5. This province is covered (from north to south) with continuous to discontinuous permafrost and also characterized by seismic hazard zones (Leonard et al. 2010; Chi et al. 2018).

The uranium ore deposits in this area are located on the Canadian Shield (Chi et al. 2018). They are associated with Precambrian quartz conglomerates containing brannerite, uraninite, and uranium-rich monzonite, with veins containing uranium tar, and pegmatite facies of syenite and granite with uraninite and uranotorite (Chi et al. 2018). The main deposits of uranium are known in the Elliot Lake (Blind River) area (Clulow et al. 1998). Deposits of the second type, initially mined for radium, are known in the structural provinces of Ber (the eastern coast of Lake Bolshoye Medvezhye and southeast of it) and Churchill (the northern coast of Lake Athabasca and areas southeast of Lake Slavolnichye) (Bridge et al. 2009); the main deposits are in the regions of Port Radium (Great Bear Lake) and Uranium City (Lake Athabasca) (http://nuclearsafety.gc.ca/).

The above facts indicate the presence of large territories in the world (mainly Russia, Canada and, probably, the United States (Alaska)) on which a combination of three factors is revealed: permafrost, uranium-containing ores, and human settlement or temporary residence of people in such territories. This conclusion indicates the need for research in the field of radon distribution in certain areas as mentioned. At the moment, we are working on a program for conducting scientific research in the territories of Russia (the Republic of Buryatia, the Nenets Autonomous Okrug) and the USA (Interior Alaska), landforms of which covered by permafrost.

LEGISLATIVE REGULATION AND ASSESSMENT POTENTIAL RADON HAZARD

Much attention is directed to the problem of radon hazard in aforementioned ecosystems. In 2009, UNSCEAR, based on a detailed scientific assessment of epidemiological data, made a statement at the UN General Assembly that there is direct evidence to support a detectable risk of lung cancer for the population from radon in dwellings. The statement concluding that there is no effective lower threshold of radon concentration, below which radon exposure poses no danger. Strong scientific evidence demonstrates that radon-induced lung cancer is a significant public health risk, with children at greater risk than adults (as is often the case with exposure to toxic substances/radiation) (Radon indoor air, Canada 2014). The presence of a carcinogenic effect was noted, particularly when such exposure to radon levels of concentration for dwellings exceeding 50–100 Bq·m^{-3}. Most radon-induced lung cancers are due to low to moderate levels of radon concentration rather than high levels, because fewer people are generally exposed to high radon concentrations. Therefore, continuous low doses pose the major risk (UNSCEAR 2019).

Back in 2009, the World Health Organization published the book «WHO handbook on indoor radon: A public health perspective», where recommendations established a number of rules to reduce the level of radon hazard in rooms, for example, setting a control level for the the radon concentration in buildings of no more than 100 Bq·m^{-3}; the introduction of preventive measures to reduce the level of radon in the design and construction of buildings and structures; the improvement of technologies for monitoring the level of radon both in the territories and in buildings were recommended (World Health Organization, 2009).

The European directive (Council Directive 2013) establishes basic safety standards to protect various categories of the population and personnel from the dangers associated with human exposure to ionizing radiation. In this document, including the main categories of the population and personnel, reference levels of the the radon concentration is again established at 100 Bq·m^{-3}. If it is impossible to reach this level and in excess of 300 Bq·m^{-3}, it is necessary to take measures for radon protection of the population and personnel. This document is distinguished by the involvement of a wide range of categories of the population and personnel in the process of standardizing the characteristics of ionizing radiation: children, students, pregnant women, adults, workers, etc.

Longstanding recognition of radon as a public health concern has been established internationally. For example, in Canada, this has led to the establishment of guideline norms for indoor air concentrations of radon, recommending no greater level of 200 Bq·m^{-3}, established by Health Canada. This is 4-fold lower than a previous guideline reference level of 800 Bq·m^{-3}, but still higher than the guidelines set by the World Health Organization (100 Bq·m^{-3}) and in the United States (4 pCi·L^{-1}, equivalent to about 148 Bq·m^{-3}) (Radon indoor air, Canada 2014). Health Canada's surveys of indoor radon levels in federally owned or operated buildings and of private homes across Canada indicate certain geographic areas in Canada of particular concern (parts of Manitoba, New Brunswick, Saskatchewan, and the Yukon), but also that high radon levels may be present anywhere and therefore that all buildings should be tested (Radon indoor air, Canada 2014).

ICRP publication 103 considers radon exposure in the context of the existing exposure situation. The introduction of a new concept of radiation protection in situations of existing exposure served as the basis for a modern strategy for the implementation of national programs to protect the population from radon. The current vision for solving the radon problem is to consider two related problems. The first is aimed at reducing the number of people exposed to unacceptably high individual risks associated with radon, the second is aimed at reducing the average value of individual radon risk for the entire population of the country. The systematic solution of both problems, calculated for the long-term perspective of its implementation, will allow to achieve the ultimate goal – to reduce he morbidity and mortality of the population from radon-induced lung cancers (ICRP 2007).

New recommendations from WHO, ICRP and IAEA have initiated the development of new or revision of existing radon programs in many countries. For the member states of the European Union, their development is mandatory in accordance with the approved (Council Directive 2013). According to (Marennyy et el. 2019), in world practice, the understanding that the national radon program should be carried out in the format of multi-level cooperation between organizations responsible for radiation protection and public health policy, public and private enterprises specializing in radiation measurements and engineering and construction activities by scientific organizations interested in informal and non-governmental organizations, emerging information policies in this area.

The experience of implementing a strategy for solving the radon problem, aimed at reducing individual risks from radon in existing buildings, has shown that the main difficulties in all countries are the extremely low awareness of the population about radon and its effects on the human body, as well as the lack of experience in the application of radon protection measures.

The requirements of Russian legislation are aimed at limiting the impact of ionizing radiation on humans from all types of radiation. Such requirements are reflected in the basic federal laws (Russian Federal Law N 3-FZ, 1996, Russian Federal Law N 384-FZ, 2009), as well as in the basic sanitary rules for ensuring radiation safety (NRB-99/2009, OSPORB-99/2010). In accordance with the requirements of the (NRB-99/2009), the reduction of exposure of the population is achieved by establishing a system of restrictions on exposure of the population from individual natural sources of radiation. At higher values of the radon concentration, protective measures should be taken to reduce the intake of radon into the air of buildings and improve ventilation of buildings (NRB-99/2009, OSPORB-99/2010). If it is impossible to reduce the values of one or both indicators to the standard level without violating the integrity of the building, the issue of relocation of residents and re-profiling of the building or part of the premises or the demolition of the building is considered.

To check the compliance of residential and public buildings with legal requirements at all stages of construction, reconstruction, overhaul and operation of residential and public buildings, radiation monitoring is carried out. In cases of detection of an excess of the standard values, an analysis of the reasons associated with this should be carried out and the necessary protective measures should be taken to reduce the dose rate of gamma radiation and / or the content of radon in the indoor air.

Assessment of the radiation situation at the site is part of the program of engineering and environmental surveys during construction work on the construction of residential and non-residential buildings, industrial development, linear and square structures, as well as during construction work on the dismantling of previously erected facilities.

The engineering and environmental surveys include a whole list of the main types of work, including the study and assessment of the radiation situation (SP 47.13330.2016).

In accordance with (SP 47.13330.2016), radiation and environmental studies should include an assessment of the gamma background on the construction site, determination of the radiation characteristics of water supply sources, an assessment of the radon hazard of the area. At the same time, the radon hazard of the territory is determined by the density of the radon flux from the soil surface and the radon content in the air of constructed buildings and structures. The assessment of the potential radon hazard of the territory is carried out according to a complex of geological and geophysical characteristics. Geological features include: the presence of certain petrographic types of rocks, faults, seismic activity of the territory, the presence of radon in groundwater and the outcrops of radon sources to the surface. Geophysical features include: high concentration of radium in the rocks composing the geological section; levels of radon concentration in soil air, equivalent equilibrium the radon concentration in buildings and structures operated in the study area and in the adjacent area. Therefore, at the pre-design stages, a preliminary assessment of the potential radon hazard of the territory should be carried out, and at the design stage, the radon hazard of the area is clarified and the class of the required anti-radon protection of buildings is determined.

For the implementation of engineering and environmental surveys for construction and sanitary supervision, unified approaches to the procedure for monitoring the potential radon hazard of land plots and assessing the results of monitoring were developed (MU 2.6.1.038-2015). This document covers a significant list of geological and geophysical features that allow to reliably determine the potential radon hazard of a territory. It should be noted that, in accordance with this document, an assessment of the potential radon hazard is not carried out (not required) in areas located in the permafrost zone during construction without thawing of the base soils. However, in the calculations of the radon exhalation rate based on the results of field measurements, a soil freezing factor was introduced with a value of up to 1.7 when freezing more than 1 m, which indicates a significant screening of radon entry to the surface by frozen soils. Moreover, the guidelines indirectly take into account the sign of permafrost when assessing the radon hazard of a territory. This fact is indicated by the calculation of the radon exhalation rate based on the results of standard measurements of the characteristics of soil samples and the comparison of the calculation results with the permissible levels of the radon exhalation rate given in (NRB-99/2009, OSPORB-99/2010). But it does not take into account that the process of degradation of permafrost can lead to an increase in radon flux to the surface, which in turn can transfer the investigated area into the category of «abnormally radon hazardous area».

Thus, we wanted to show that a lot of attention is paid to the radon hazard problem in the world both at the level of research and at the level of legislative regulation. The main conclusion of the numerous documents is the fact that today scientists have studied radon production in populated areas thoroughly. However, they ignore individual territorial predictors such as permafrost. This stems from the fact that permafrost has only been extensively studied recently and does not immediately come into consideration.

EXISTING METHODS AND TECHNOLOGIES FOR ASSESSING THE POTENTIAL RADON HAZARD AND THEIR MODERNIZATION

Until now, a unified approach to the methodology for assessing the radon hazard of sites planned for development has not been developed (Ryzhakova et al. 2018), including due to a large number of factors affecting the formation of the radon field of the territory. We conducted a patent search for existing technologies and methods for assessing the radon hazard. In this section, we will describe some of these methods, which most fully take into account various indicators when assessing the potential for radon hazard.

European scientists are faced with a number of difficulties when using individual physical quantities as criteria for the radon hazard, on the basis of which the radon potential or radon index is calculated (Ryzhakova et al. 2018; Ciotoli 2017). For example, in the Czech Republic and Germany, a complex of two parameters is widely used – the gas permeability of the soil and the radon concentration in the subsoil air, with further calculation of the quantitative indicator – the radon potential (Neznal 2004). This method for assessing the radon hazard is based on measuring the radon concentration at a depth of 0.8 m after a short air sampling using a special rod with a syringe. In parallel with the radon concentration at the same depth, the gas permeability parameter is determined using the Radon-Jok installation. Further, using the classification table, the category of the radon index is determined – low, medium or high level of radon hazard.

A known method for assessing the radon hazard of building sites (Kropat et al. 2016) is a complicated process that includes several steps such as:

(1) Measuring the dose of gamma radiation at a height of 1 m from the earth's surface;

(2) Measuring the gas permeability of soils at depths from 0.8 m to 1 m using a device Radon-Jok;

(3) Studying the geological structure of the overburden based on regional databases to: a) identify geologically homogeneous units; b) determine the density of fault lines.

(4) Processing by means of logistic regression data on: a) types of geologically homogeneous units; (b) doses of gamma radiation; (c) gas permeability of soils and density of fault lines.

Russian scientists (Ryzhakova et al. 2018) have recently developed and patented a method for assessing the risk of radon, which entails choosing control points at the bottom of the foundation of a building under construction at the bottom of the excavation located at a distance of 10 m from each other. At the control points, the top layer with a thickness of 3 cm to 5 cm is removed, and the surface is carefully leveled out. A storage chamber with carbon adsorbers is installed at each point to accumulate radon for 1 hour, and the radon exhalation rate is determined by the beta radiation of short-lived daughter products of radon decay 214Pb and 214Bi. If the average value of the radon exhalation rate exceeds 80 $mBq \cdot m^{-2} \cdot s^{-1}$, then the territory is considered radon-hazardous, and if it is less than 80 $mBq \cdot m^{-2} \cdot s^{-1}$, then the territory is radon-safe.

The most detailed and comprehensive method for assessing the radon hazard of a territory is the radon exhalation rate method described in detail in (MR 2.6.1.038-2015 «Assessment of the potential radon danger of land plots for construction of residential, public and industrial buildings»). These guidelines cover a significant list of geological and geophysical signs (predictors) that allow to reliably determine the potential radon hazard of a territory. Among other things, the document contains recommendations for taking into account the level of soil freezing, which is significant in the context of the influence of the northern climate and the geographical location of the northern countries. It should be noted that in other countries except Russia, when assessing the potential radon hazard of a territory, this factor is not taken into account.

All of the above methods and technologies take into account a variety of factors and predictors of potential radon hazard, but the phenomenon of permafrost remains ignored. Only one document (MR 2.6.1.038-2015) takes into account the factor of seasonal soil freezing. But in our opinion, this factor has one negative feature. After the completion of the construction of the building, the factor of soil freezing will be absent due to the warming effect of the foundation. On the other hand, permafrost will remain. And despite the technologies that allow not to disturb this geological environment, climate warming will lead to thawing of permafrost and an increase in the flow of radon to the earth's surface.

In view of the above, we believe that the existing methods and technologies should be supplemented with an assessment of the level of permafrost degradation if an assessment of the potential radon hazard is carried out in such territories. To do this, we can choose ways to assess the permafrost level: electrical prospecting, the method of contactless measurement of the electric field, electromagnetic sounding, ground penetrating radar, seismic exploration, microgravimetry. Recently, the method of low-frequency electromagnetic mapping (VLF-method) seems to be of interest (Wright 1988, Oskooi and Pedersen 2006, Sundararajan et al 2007, Ramesh et al. 2007), which began to develop in Alaska from the 1970s (McNeill 1973; Hoekstra 1978). This method is also interesting for the detection of uranium ores, respectively, rocks with an increased content of natural radionuclides. In this case, the complex of methods of emanation survey, low-frequency magnetometry and, as an auxiliary, drilling and determination of the radiation and physical characteristics of the rock and soil core looks interesting. Such a set of methods will allow the most complete assessment of the potential radon hazard, taking into account all possible predictors.

CONCLUSIONS

The issue of assessing the radon hazard at the current moment in the whole world is quite deeply worked out. Organizations conducting radiation-ecological surveys have at their disposal modern instrumental and methodological complexes that take into account a significant number of factors affecting the behavior of radon in conditions of various soils.

But despite this, over time, events arise that lead to the need to adjust already created methods or develop new ones. One of such events was global warming and the associated phenomenon of melting permafrost. This process began to lead to the release of a significant amount of various kinds of substances (organic matter, methane, carbon dioxide), including radioactive ones. One of these radioactive substances was radon gas, which is still in the crystal lattice of ice, permafrost.

Perhaps in the absence of elevated radium-226 content in the soil, thawing of permafrost will not lead to a significant increase in the radon content in the near-surface soil layers, and, accordingly, in buildings. But in those territories where there are outcrops of rocks enriched in natural radionuclides, this predictor can play a significant role.

We assume that the greatest release of radon will be observed during thawing of icy dispersed sediments. The rocks with which uranium deposits are associated in most cases contain significantly less ice and their thawing is not accompanied by significant structural changes. Thus, during their thawing, the additional release of radon will be less significant. But if the rocks are covered with a layer of frozen soil, then it will be a barrier for radon. And when such a layer thaws, we will be able to observe an increased concentration of radon on the earth's surface.

The few facts and theoretical studies presented in this work on the effect of the thawing of permafrost on an increase in radon flux to the earth's surface show the relevance and need for full-fledged fundamental research work aimed at confirming the proposed theory. In addition, the fact of the increased interest of countries in the Arctic territory, its progressive development and settlement adds relevance to the conduct of such studies.

In case of a successful result of such work, it will be extremely necessary to revise the existing methods and methods for assessing the radon hazard of the Arctic territories, as well as those territories that are in the permafrost zone. Additionally, it will be extremely necessary to take into account the predictor presented in this work when correcting existing laws. Such changes in the legislation will lead to the prevention of a possible situation in the future associated with increased exposure of the population of the Arctic countries due to the natural radioactive background.

REFERENCES

Adopted I.P.C.C. (2014). Climate Change 2014 Synthesis Report. IPCC: Geneva, Szwitzerland.

Al-Ahmady K.K., & Hintenlang D.E. (1994). Assessment of temperature-driven pressure differences with regard to radon entry and indoor radon concentration. AARST. Atlantic City: The American Association of Radon Scientists and Technologists.

Arvela H. (1995). Seasonal variation in radon concentration of 3000 dwellings with model comparisons. Radiation Protection Dosimetry, 59(1), 33-42, DOI: 10.1093/oxfordjournals.rpd.a082634.

Astakhov N.E., Bartanova S.V., Tubanov C.A. (2015). Radon anomalies of some break zones in buryatia as the factor of radiation risk. Bulletin of the Samara Scientific Center of the Russian Academy of Sciences, 17, 5-1 (in Russian with English summary).

Bakaeva N., Kalaydo A. (2016). About the radon transport mechanisms into the buildings. Construction and reconstruction, (5), 51-59, (in Russian with English summary).

Banerjee K.S., Basu A., Guin R., & Sengupta D. (2011). Radon (222Rn) level variations on a regional scale from the Singhbhum Shear Zone, India: A comparative evaluation between influence of basement U-activity and porosity. Radiation Physics and Chemistry, 80(5), 614-619, DOI: 10.1016/j.radphyschem.2010.12.015.

Baskaran M. (2016). Radon: A tracer for geological, geophysical and geochemical studies (Vol. 367). Basel: Springer, DOI: 10.1007/978-3-319-21329-3.

Berezina E.V., & Elansky N.F. (2009). 222 Rn concentrations in the atmospheric surface layer over continental Russia from observations in TROICA experiments. Izvestiya, Atmospheric and Oceanic Physics, 45(6), 757-769 (in Russian with English summary), DOI: 10.1134/S0001433809060097.

Berezina E.V., Elansky N.F., Moiseenko K.B., Safronov A.N., Skorokhod A.I., Lavrova O.V., ... & Shumsky R.A. (2014). Estimation of biogenic CH_4 and CO_2 emissions and dry deposition of O_3 using 222 Rn measurements in TROICA expeditions. Izvestiya, Atmospheric and Oceanic Physics, 50(6), 583-594 (in Russian with English summary), DOI: 10.1134/S000143381406005X.

Biskaborn B.K., Smith S.L., Noetzli J., Matthes H., Vieira G., Streletskiy D. A., ... & Lantui H. (2019). Permafrost is warming at a global scale. Nature communications, 10(1), 1-11, DOI: 10.1038/s41467-018-08240-4.

Blonsky A.V., Mitrushkin D.A., & Savenkov E.B. (2017). Simulation of flows in a discrete crack system: computational algorithms. Preprints of the Institute of applied mathematics. M. V. Keldysh RAS, (0), 66-30, (in Russian with English summary), DOI: 10.20948/prepr-2017-66.

Bridge N.J., Banerjee N.R., Finnigan C.S., Carpenter R., & Ward J. (2009, December). The Lac Cinquante Uranium Deposit, Nunavut, Canada. In AGU Fall Meeting Abstracts, 2009, V33D-2065.

Brown J., Ferrians Jr.O.J., Heginbottom J.A., & Melnikov E.S. (1997). Circum-Arctic map of permafrost and ground-ice conditions, Reston, VA: US Geological Survey, 45, DOI: 10.3133/CP45.

Buldovicz S.N., Khilimonyuk V.Z., Bychkov A.Y., Ospennikov E.N., Vorobyev S.A., Gunar A.Y., ... & Amanzhurov R.M. (2018). Cryovolcanism on the earth: Origin of a spectacular crater in the Yamal Peninsula (Russia). Scientific reports, 8(1), 1-6.

Chen J. (2009). A preliminary design of a radon potential map for Canada: a multi-tier approach. Environmental Earth Sciences, 59(4), 775-782, DOI: 10.1007/s12665-009-0073-x.

Chi G., Haid T., Quirt D., Fayek M., Blamey N., & Chu H. (2017). Petrography, fluid inclusion analysis, and geochronology of the End uranium deposit, Kiggavik, Nunavut, Canada. Mineralium Deposita, 52(2), 211-232, DOI: 10.1007/s00126-016-0657-9.

Chuvilin E.M., Grebenkin S.I., & Zhmaev M.V. (2018). Influence of hydrate and ice formation on the gas permeability of sandy rocks. Vesti gas science, 3(35), (in Russian with English summary).

Ciotoli G., Voltaggio M., Tuccimei P., Soligo M., Pasculli A., Beaubien S.E., & Bigi S. (2017). Geographically weighted regression and geostatistical techniques to construct the geogenic radon potential map of the Lazio region: A methodological proposal for the European Atlas of Natural Radiation. Journal of environmental radioactivity, 166, 355-375, 10.1016/j.jenvrad.2016.05.010.

Clulow F.V., Davé N.K., Lim T.P., & Avadhanula R. (1998). Radionuclides (lead-210, polonium-210, thorium-230, and-232) and thorium and uranium in water, sediments, and fish from lakes near the city of Elliot Lake, Ontario, Canada. Environmental Pollution, 99(2), 199-213., DOI: 10.1016/S0269-7491(97)00187-5.

Coletti C., Brattich E., Cinelli G., Cultrone G., Maritan L., Mazzoli C., ... & Sassi R. (2020). Radionuclide concentration and radon exhalation in new mix design of bricks produced reusing NORM by-products: The influence of mineralogy and texture. Construction and Building Materials, 260, 119820, DOI: 10.1016/j.conbuildmat.2020.119820.

Council Directive 2013/59/Euratom (05.12.2013)

Daraktchieva Z., Wasikiewicz J.M., Howarth C.B., & Miller C.A. (2021). Study of baseline radon levels in the context of a shale gas development. Science of The Total Environment, 753, 141952, DOI: 10.1016/j.scitotenv.2020.141952.

Doloisio N., & Vanderlinden J.P. (2020). The perception of permafrost thaw in the Sakha Republic (Russia): Narratives, culture and risk in the face of climate change. Polar Science, 26, 100589, DOI: 10.1016/j.polar.2020.100589.

Domingos F., & Pereira A. (2018). Implications of alteration processes on radon emanation, radon production rate and W-Sn exploration in the Panasqueira ore district. Science of The Total Environment, 622, 825-840, DOI: 10.1016/j.scitotenv.2017.12.028.

Dushin V.A., Kuznetsov V.I., & Grigoriev V.V. (1997). Assessment of the prospects and conditions for the localization of new and unconventional types of mineral raw materials in the north of the Urals. In Polar Ural-new mineral resource base of Russia (proceedings of the 1st Polar-Ural scientific and practical conference). Tyumen-Salekhard, 26. (in Russian).

Eakin M., Brownlee S.J., Baskaran M., & Barbero L. (2016). Mechanisms of radon loss from zircon: microstructural controls on emanation and diffusion. Geochimica et Cosmochimica Acta, 184, 212-226, DOI: 10.1016/j.gca.2016.04.024.

Eksorb.com (2016). NPP «EXORB» LLC. [online] Available at: https://eksorb.com/radon/ [Accessed 20 Mar. 2021].

Evangelista H., & Pereira E. B. (2002). Radon flux at king George island, Antarctic peninsula. Journal of environmental radioactivity, 61(3), 283-304, DOI: 10.1016/S0265-931X(01)00137-0.

Federal Law as of 09.01.1996 No. 3-FZ «About Radiation Safety of the Public», Russia.

Federal Law as of 30.12.2009 No. 384-FZ «Technical Regulations for Safety of Buildings and Structures», Russia.

Feng S., Wang H., Cui Y., Ye Y., Liu Y., Li X., ... & Yang R. (2020). Fractal discrete fracture network model for the analysis of radon migration in fractured media. Computers and Geotechnics, 128, 103810, DOI: 10.1016/j.compgeo.2020.103810.

Giustini F., Ciotoli G., Rinaldini A., Ruggiero L., & Voltaggio M. (2019). Mapping the geogenic radon potential and radon risk by using Empirical Bayesian Kriging regression: A case study from a volcanic area of central Italy. Science of the Total Environment, 661, 449-464, DOI: 10.1016/j.scitotenv.2019.01.146.

Glover P.W.J. (2006). Increased domestic radon exposure caused by permafrost thawing due to global climate change, EGU General Assembly, Vienna, Austria, 2-7 April. EGU06-A-01439.

Glover P.W., & Blouin M. (2007). Modelling increased soil radon emanation caused by instantaneous and gradual permafrost thawing due to global climate warming.

Hassan N.M., Hosoda M., Ishikawa T., Sorimachi A., Sahoo S.K., Tokonami S., & Fukushi M. (2009). Radon migration process and its influence factors; review. Japanese Journal of Health Physics, 44(2), 218-231, DOI: 10.5453/jhps.44.218.

Heslop J.K., Winkel M., Walter Anthony K.M., Spencer R.G.M., Podgorski D.C., Zito P., ... & Liebner S. (2019). Increasing organic carbon biolability with depth in yedoma permafrost: ramifications for future climate change. Journal of Geophysical Research: Biogeosciences, 124(7), 2021-2038, DOI: 10.1029/2018JG004712.

Hoekstra P. (1978). Electromagnetic methods for mapping shallow permafrost. Geophysics, 43(4), 681-874, DOI: 10.1190/1.1440853.

IAEA (2013). Measurement and Calculation of Radon Releases from NORM Residues. Technical Reports Series, 474. IAEA, Austria.

Ji M., Kong W., Liang C., Zhou T., Jia H., & Dong X. (2020). Permafrost thawing exhibits a greater influence on bacterial richness and community structure than permafrost age in Arctic permafrost soils. The Cryosphere, 14(11), 3907-3916, DOI: 10.5194/tc-14-3907-2020.

Kawabata K., Sato T., Takahashi H. A., Tsunomori F., Hosono T., Takahashi M., & Kitamura Y. (2020). Changes in groundwater radon concentrations caused by the 2016 Kumamoto earthquake. Journal of Hydrology, 584, 124712, DOI: 10.1016/j.jhydrol.2020.124712.

Klimshin A.V., Kozlova I.A., Rybakov E.N., Lukovskoy M.Yu. (2010). Effect of freezing the surface layer of soil on the radon transport. Vestnik Kamchatskoy regional'noy assotsiatsii «Uchebno-nauchnyy tsentr». Seriya: Nauki o Zemle, 16(2), 146-151 (in Russian with English summary).

Koptev D.P. (2020). Norilsk spill: lessons and consequences. Drilling and Oil, (7-8), 3-9. (in Russian with English summary).

Kropat G., Bochud F., Murith C., Palacios M., & Baechler S. (2017). Modeling of geogenic radon in Switzerland based on ordered logistic regression. Journal of environmental radioactivity, 166, 376-381, DOI: 10.1016/j.jenvrad.2016.06.007.

Krupp K., Baskaran M., & Brownlee S.J. (2017). Radon emanation coefficients of several minerals: How they vary with physical and mineralogical properties. American Mineralogist: Journal of Earth and Planetary Materials, 102(7), 1375-1383, DOI: 10.2138/am-2017-6017.

Kuo T., & Tsunomori F. (2014). Estimation of fracture porosity using radon as a tracer. Journal of Petroleum Science and Engineering, 122, 700-704, DOI: 10.1016/j.petrol.2014.09.012.

Leonard L.J., Mazzotti S., Cassidy J.C., Rogers G., & Halchuk S. (2010). Seismic hazard in western canada from global positioning system strain rate data. Proceedings of the 9th U.S. National and 10th Canadian Conference on Earthquake Engineering Compte Rendu de la 9ième Conférence Nationale Américaine et 10ième Conférence Canadienne de Génie Parasismique July 25-29, 753, 1-10.

Li Y., Tan W., Tan K., Liu Z., Fang Q., Lv J., ... & Guo Y. (2018). The effect of laterite density on radon diffusion behavior. Applied Radiation and Isotopes, 132, 164-169, DOI: 10.1016/j.apradiso.2017.12.001.

Liu L., Zhao D., Wei J., Zhuang Q., Gao X., Zhu Y., ... & Zheng D. (2021). Permafrost sensitivity to global warming of 1.5° C and 2° C in the Northern Hemisphere. Environmental Research Letters, 16(3), 034038, DOI: 10.1088/1748-9326/abd6a8.

Livshits M., Gulabyants L. (2017). The mathematical solution of the boundary problem of radon transfer in the system «soil – atmosphere – building». Fundamental, exploratory and applied research of the russian academy of natural sciences on scientific support for the development of architecture, urban planning and the construction industry of the russian federation in 2016, 218-226. (in Russian with English summary).

Loisy C., & Cerepi A. (2012). Radon-222 as a tracer of water–air dynamics in the unsaturated zone of a geological carbonate formation: Example of an underground quarry (Oligocene Aquitain limestone, France). Chemical Geology, 296, 39-49, DOI: 10.1016/j.chemgeo.2011.12.010.

Marenniy A.M., & Kiselev S.M. (2019). National radon programs: implementation experience and challenges for the future. Radiation Hygiene , 12 (2 (sv)), 97-108, DOI: 10.21514/1998-426X-2019-12-2s-97-108. (in Russian with English summary)

McNeill D., Hoekstra P. (1973). In-situ measurements on the conductivity and surface impedance os sea ice at VLF. Radio Science, 8(1), 23-30, DOI: 10.1029/RS008i001p00023.

Miklyaev P.S., Petrova T.B. (2010). The study of radon emanation in clay. Geoecology. Engineering geology, hydrogeology, geocryology, (1), 13-22, (in Russian).

Minkin L. (2002). Is diffusion, thermodiffusion, or advection a primary mechanism of indoor radon entry? Radiation protection dosimetry, 102(2), 153-161, DOI: 10.1093/oxfordjournals.rpd.a006084.

Minkin L. (2003). Thermal diffusion of radon in porous media. Radiation protection dosimetry, 106(3), 267-272, DOI: 10.1093/oxfordjournals.rpd.a006360.

Minkin L., & Shapovalov A.S. (2008). Indoor radon entry: 30 years later.

Minkin L., & Shapovalov A.S. (2016). Thermo-diffusional radon waves in soils. Science of the Total Environment, 565, 1-7, DOI: 10.1016/j.scitotenv.2016.04.131.

Moreno V., Bach J., Zarroca M., Font L., Roqué C., & Linares R. (2018). Characterization of radon levels in soil and groundwater in the North Maladeta Fault area (Central Pyrenees) and their effects on indoor radon concentration in a thermal spa. Journal of environmental radioactivity, 189, 1-13, DOI: 10.1016/j.jenvrad.2018.03.001.

MU 2.6.1.038-2015 Assessment of the potential radon danger of land plots for construction of residential, public and industrial buildings.

Neznal M., Neznal M., Matolin M., Barnet I., & Miksova J. (2004). The new method for assessing the radon risk of building sites, Prague: Czech Geological Survey, 48.

Nizinski C.A., Hanson A.B., Fullmer B.C., Mecham N.J., Tasdizen T., & McDonald IV L.W. (2020). Effects of process history on the surface morphology of uranium ore concentrates extracted from ore. Minerals Engineering, 156, 106457.

NRB-99/2009, Radiation Safety Standarts, Sanitary rules and regulations, Russia.

Nuccetelli C., Leonardi F., & Trevisi R. (2020). Building material radon emanation and exhalation rate: Need of a shared measurement protocol from the european database analysis. Journal of Environmental Radioactivity, 225, 106438, DOI: 10.1016/j.jenvrad.2020.106438.

Nuclearsafety.gc.ca, (2019). Canadian Nuclear Safety Commission. [online] Available at: http://nuclearsafety.gc.ca/eng/waste/uranium-mines-and-millswaste/index.cfm/ [Accessed 21 Mar. 2021].

Obu J., Westermann S., Bartsch A., Berdnikov N., Christiansen H. H., Dashtseren A., ... & Zou D. (2019). Northern Hemisphere permafrost map based on TTOP modelling for 2000–2016 at 1 km2 scale. Earth-Science Reviews, 193, 299-316, DOI: 10.1016/j.earscirev.2019.04.023.

Oskooi B., & Pedersen L.B. (2006). Resolution of airborne VLF data. Journal of applied geophysics, 58(2), 158-175, DOI: 10.1016/j.jappgeo.2005.06.002.

OSPORB 99/2010 Basic sanitary rules for ensuring radiation safety, Russia.

Pavlov I.V. (1996). Mathematical model of the process of radon exhalation from the earth's surface and criteria for assessing the potential radon hazard of a built-up area. HENRI, 97, 15-26.

Pereira A.J.S.C., Godinho M.M., & Neves L.J.P.F. (2010). On the influence of faulting on small-scale soil-gas radon variability: a case study in the Iberian Uranium Province. Journal of environmental radioactivity, 101(10), 875-882, DOI: 10.1016/j.jenvrad.2010.05.014.

Pinto P.V., Kumara K.S., & Karunakara N. (2020). Mass exhalation rates, emanation coefficients and enrichment pattern of radon, thoron in various grain size fractions of monazite rich beach placers. Radiation Measurements, 130, 106220, DOI: 10.1016/j.radmeas.2019.106220.

PromTu.ru (2018). Industrial goods and services in Russia. [online] Available at: https://promtu.ru/dobyicha-resursov/dobyicha-urana-v-rossii-i-mire/ [Accessed 21 Mar. 2021].

Protection R. (2007). ICRP publication 103. Ann ICRP, 37(2.4), 2.

Rachold V., Bolshiyanov D.Y., Grigoriev M.N., Hubberten H.W., Junker R., Kunitsky V.V., ... & Schneider W. (2007). Nearshore Arctic subsea permafrost in transition. Eos, Transactions American Geophysical Union, 88(13), 149-150, DOI: 10.1029/2007EO130001.

Radon in Indoor Air: A Review of Policy and Law in Canada. Canadian Environmental Law Association, 2014.

Ramesh Babu, V., Ram, S., & Sundararajan, N. (2007). Modeling and inversion of magnetic and VLF-EM data with an application to basement fractures: A case study from Raigarh, India. Geophysics, 72(5), B133-B140, DOI: 10.1190/1.2759921.

Rogers, V. C., & Nielson, K. K. (1991). Multiphase radon generation and transport in porous materials. Health Physics, 60(6), 807-815, DOI: 10.1097/00004032-199106000-00006.

Ryzhakova N.K., Stavitskaya K.O., & Udalov A.A. (2018). Issues in assessment of potential radon hazard at building sites.Radiatsionnaya Gygiena= Radiation Hygiene, 11(2), 37-44, DOI: 10.21514/1998-426X-2018-11-2-37-44 (in Russian with English summary).

Ryzhakova, N. K., & Shilova, K. O. (2018). Method for assessing the radon hazard of building sites.

Sabbarese C., Ambrosino F., D'Onofrio A., Pugliese M., La Verde G., D'Avino V., & Roca V. (2021). The first radon potential map of the Campania region (southern Italy). Applied Geochemistry, 104890, DOI: 10.1016/j.apgeochem.2021.104890.

Sahoo S.K., Katlamudi M., Barman C., & Lakshmi G.U. (2020). Identification of earthquake precursors in soil radon-222 data of Kutch, Gujarat, India using empirical mode decomposition based Hilbert Huang Transform. Journal of Environmental Radioactivity, 222, 106353, DOI: 10.1016/j.jenvrad.2020.106353.

Sellmann P.V., & Delaney A.J. (1990). Radon measurements as indicators of permafrost distribution. Cold regions science and technology, 18(3), 331-336, DOI: 10.1016/0165-232X(90)90029-V.

Selvam S., Muthukumar P., Sajeev S., Venkatramanan S., Chung S. Y., Brindha K., ... & Murugan R. (2021). Quantification of submarine groundwater discharge (SGD) using radon, radium tracers and nutrient inputs in Punnakayal, south coast of India. Geoscience Frontiers, 12(1), 29-38, DOI: 10.1016/j.gsf.2020.06.012.

SP 11-102-97 Engineering and environmental surveys for construction.

SP 47.13330.2016 Engineering surveys for construction.

Streletskiy D.A., Suter L.J., Shiklomanov N.I., Porfiriev B.N., & Eliseev D.O. (2019). Assessment of climate change impacts on buildings, structures and infrastructure in the Russian regions on permafrost. Environmental Research Letters, 14(2), 025003.

Sundararajan N., Nandakumar G., Chary M.N., Ramam K., & Srinivas, Y. (2007). VES and VLF—an application to groundwater exploration, Khammam, India. The Leading Edge, 26(6), 708-716, DOI: 10.1190/1.2748489.

Sundararajan, N., Ramesh Babu, V., Shiva Prasad, N., & Srinivas, Y. (2006). VLFPROS-: A Matlab code for processing of VLF-EM data. Computers & Geosciences, 32(10), 1806-1813.

Telford W.M. (1983). Radon mapping in the search for uranium. In Developments in Geophysical Exploration Methods—4, Springer, Dordrecht, 155-194

Thu H.N.P., & Van Thang N. (2020). The effects of some soil characteristics on radon emanation and diffusion. Journal of environmental radioactivity, 216, 106189, DOI: 10.1016/j.jenvrad.2020.106189.

Titaeva N.A. (2000). Nuclear Geochemistry, 336. (in Russian).

Tsapalov A., Kovler K., & Miklyaev P. (2016). Open charcoal chamber method for mass measurements of radon exhalation rate from soil surface. Journal of environmental radioactivity, 160, 28-35, DOI: 10.1016/j.jenvrad.2016.04.016.

UNSCEAR, 2019. Sources, effects and risks of ionizing radiation. United Nations, NewYork: Report.

Väisänen M., Krab E.J., Monteux S., Teuber L.M., Gavazov K., Weedon J.T., ... & Dorrepaal E. (2020). Meshes in mesocosms control solute and biota exchange in soils: A step towards disentangling (a) biotic impacts on the fate of thawing permafrost. Applied Soil Ecology, 151, 103537, DOI: 10.1016/j.apsoil.2020.103537.

Verkhovtsev V.A. & Dushin, V.A. (2000). On the prospects for the discovery of complex uranium deposits «Type of unconformity» in the north of the Urals. Bulletin of the Ural State Mining University, (10). (in Russian).

World Health Organization. (2009). WHO handbook on indoor radon: a public health perspective. World Health Organization.

Wright J.L. (1988) VLF Interpretation Manual. EDA Instruments (now Scintrex. Ltd.), Concord, Ont.

Yang Y., Li Y., Guan Z., Chen Z., Zhang L., Lv C. J., & Sun F. (2018). Correlations between the radon concentrations in soil gas and the activity of the Anninghe and the Zemuhe faults in Sichuan, southwestern of China. Applied Geochemistry, 89, 23-33 DOI: 10.1016/j.apgeochem.2017.11.006.

Zavyalov A.D., Peretokin S.A., Danilova T.I., Medvedeva N.S., & Akatova K.N. (2019). General Seismic Zoning: From maps GSZ-97 to GSZ-2016 and new-generation maps in the parameters of physical characteristics. Seismic Instruments, 55(4), 445-463, DOI: 10.3103/S0747923919040121.

Zhang Z.Q., Wu Q.B., Hou M.T., Tai B.W., & An Y. K. (2021). Permafrost change in Northeast China in the 1950s–2010s. Advances in Climate Change Research, DOI: 10.1016/j.accre.2021.01.006.

Zolkos S., Fiske G., Windholz T., Duran G., Yang Z., Olenchenko V., ... & Natali S. M. (2021). Detecting and Mapping Gas Emission Craters on the Yamal and Gydan Peninsulas, Western Siberia. Geosciences, 11(1), 21, DOI: 10.3390/geosciences11010021.

EDITORIAL PAPER

INTRODUCTION TO GEOGRAPHY OF COVID-19 PANDEMIC: ENVIRONMENTAL ISSUES, PUBLIC HEALTH AND SOCIO-ECONOMIC CONSEQUENCES

Alexander Baklanov[1,5,6*], Natalia E. Chubarova[2], Vladimir A. Kolosov[3], Svetlana M. Malkhazova[2], Boris N. Porfiriev[4]

[1]Science and Innovation Department, World Meteorological Organization (WMO), Geneva, Switzerland
[2]Faculty of Geography, Lomonosov Moscow State University, Leninskie Gory 1, Moscow, 119991, Russia
[3]Institute of Geography, Russian Academy of Sciences, Staromonetnyi per., 29, 119017 Moscow, Russia
[4]Institute of Economic Forecasting of the Russian Academy of Sciences, Moscow, Russia
[5]Niels Bohr Institute, University of Copenhagen, Copenhagen, Denmark
[6]Institute of Atmospheric Physics of the Russian Academy of Sciences, Moscow, Russia
***Corresponding author:** abaklanov@wmo.int

Received: November 3rd, 2021 / Accepted: November 9th, 2021 / Published: December 31st, 2021
https://doi.org/10.24057/2071-9388-2021-044

ABSTRACT. The COVID-19 pandemic has severely affected all countries and the global scientific agenda, particularly that of health, economy, environment, geography and geosciences in general. This Special Issue is also a contribution to the global efforts of the scientific community in the analysis of the geography of the COVID-19 pandemic with public health, economic and environmental consequences. Two blocks of papers are considered: (1) the socio-spatial, statistical and geographical analysis of COVID-19 distributions; and (2) the impacts of the pandemic lockdown on the environment, air pollution, and the quality of water.

KEYWORDS: COVID-19 pandemic, lockdown, environment, air pollution, quality of water, geographical analysis of COVID-19 distribution

CITATION: Alexander Baklanov, Natalia E. Chubarova, Vladimir A. Kolosov, Svetlana M. Malkhazova, Boris N. Porfiriev (2021). Introduction To Geography Of Covid-19 Pandemic: Environmental Issues, Public Health And Socio-Economic Consequences. Geography, Environment, Sustainability, Vol.14, No 4, p. 105-108 https://doi.org/10.24057/2071-9388-2021-044

Conflict of interests: The authors reported no potential conflict of interest.

INTRODUCTION

The COVID-19 pandemic has greatly affected all countries and the global scientific agenda, particularly that of health, economy, environment, geography and geosciences in general. The pandemic has highlighted the importance of international solidarity and unity in the face of the worst global health and economic crisis in contemporary lifetime. Thousands of papers have been published during the last year in different journals around the world analyzing different aspects of current experience and possible further scenarios.

However, the virus is still with us, with more potent variants. It remains the most immediate challenge for geosciences and health, including its impacts on geoscience development and the achievement of the United Nations Sustainable Development Goals.

Long-term visions based on transdisciplinary scientific advances are therefore essential. As a consequence, the global research community calls for contributions based on data-driven and theory-based approaches to health in the context of global change (Schertzer et al. 2020). This includes: (i) main lessons from lockdowns, (ii) how to get the best scientific results during the corona pandemic? (iii) how to manage field works, geographical monitoring and planetary missions? (iv) qualitative improvements in epidemic modelling, with nonlinear, stochastic, and complex system science approaches; (v) eventual interactions between environmental, weather, climate factors and epidemic/health problems; (vi) new surveillance capabilities (including contact tracing), data access, assimilation and multidimensional analysis techniques; (vii) a fundamental revision of our urban systems, their greening and their need for mobility; (viii) a special focus on urban biodiversity, especially to better managing virus vectors; (ix) national and urban resilience must include the resilience to epidemics, and therefore requires revisions of urban governance.

A number of recently published global review papers analyzed experience of different countries in solving the above-mentioned issues.

International symposia and programmes, in particular the World Meteorological Organization, elucidated what is known, understood, and can be reliably predicted about environmental variables' influence on the trajectory of the COVID-19 epidemic, from global, hemispheric, regional and local perspectives. Outcomes of this work (WMO 2021) include a synthesis of the information presented and recommendations for further research at local to global scales. This report presents a summary of key findings to date, as informed by peer reviewed literature. It is motivated both by the global relevance of the subject and by the staggering number of papers and pre-prints currently available, which emphasizes the need for careful review and communication of the state of the science. Main findings include to date: (i) Epidemiological studies of COVID-19 have offered mixed results regarding the meteorological sensitivity of the disease; (ii) COVID-19 transmission dynamics appear to have been controlled primarily by government interventions rather than meteorological factors; (iii) Respiratory viral infections frequently exhibit some form of seasonality, however the underlying mechanisms that drive seasonality of respiratory viral infections are not yet well understood; (iv) Laboratory studies have yielded some evidence that the virus survives longer under cold, dry, and low ultraviolet radiation conditions; (v) There is evidence that chronic and short-term exposure to air pollution exacerbates symptoms and increases mortality rates for some respiratory diseases. Another global study (Sokhi et al. 2021) provides a comprehensive observational analysis, focuses on changes in air quality in and around cities across the globe for main air pollutants during different phases of the lockdown, with the following conclusions: (i) NO2 - major reductions in emissions (traffic) will be effective but need to be equivalent to full lockdown; (ii) PM – Measures similar to pandemic lockdown will not be effective for decreasing PM2.5 and PM10 to meet WHO guidelines (WHO 2021). Complexities from precursor emissions, chemistry and meteorology; (iii) O3 – reductions in precursor emissions, chemistry, meteorology and urban background are important; (iv) Updated WHO Air Quality Guidelines pose additional challenges – even during full lockdown there will be guideline exceedances globally; (v) International policies need to be more ambitious (e.g. Convention of Long-range Transboundary Air Pollution and the Gothenburg Protocol) (precursor emissions for PM and O_3); (vi) Complexities from regionally dependent meteorological and episodic emissions from natural or anthropogenic sources (e.g., dust and biomass burning events) can add further complexity; (vii) Potential for co-benefits - reducing the impact of short-lived climate pollutants and GHGs, e.g. cleaner energy transition, low or zero emission traffic, and other control measures targeted at source.

Forster et al (2020) and Jones et al. (2021) analyzed the climate response to emissions reductions due to COVID-19 for current and future global climate scenarios and concluded that (i) Air pollutants interact with climate and have resulted in both warming and cooling over the historical period; (ii) Emission reductions lead to benefits for air quality and health but with differing impacts on climate; (iii) Emission reductions during COVID-19 restrictions impacted air quality but with a small to negligible effect on climate; (iv) Ultimately it is important to consider both climate and air quality policies together to maximize any potential co-benefits in any future measures.

This special issue «Geography of the COVID-19 pandemic: public health, economic and environmental consequences» of the «Geography, Environment, Sustainability» journal is also a contribution to these global efforts to analyze the geography of the COVID-19 pandemic with public health, economic and environmental consequences.

Two main blocks of the papers within the issue can be distinguished: (1) Socio-spatial, statistical and geographical analysis of COVID-19 distributions; and (2) Impacts of the pandemic lockdown on the environment, air pollution, and the quality of water.

SOCIO-SPATIAL AND GEOGRAPHICAL ANALYSIS OF COVID-19

The problems concerning socio-spatial and geographical analysis of COVID-19 are discussed in the papers (Kolosov et al. 2021; Kieu et al. 2021; Rahardjo et al. 2021; Sahu and Mishra 2021; Vu et al. 2021; Talib 2021; Wetchayont and Waiyasusri 2021).

Kolosov et al. (2021, this issue) reviewed the main areas and methods of human-geographical studies. The authors distinguished between three areas in this field: studies of the spatial spread of infection on the different stages of the pandemic; analysis of its demographic, (geo) political and economic implications, and attempts to forecast the impact of social and technological changes accelerated by the pandemic on territorial structures.

Kieu et al. (2021, this issue) reviewed over hundred scientific papers on applications of GIS and Remote Sensing methods in studies of the COVID-19 pandemic distribution, including spatio-temporal changes, WebGIS-based mapping, the correlation between the COVID-19 and natural, socio-economic factors, and the environmental impacts. They provided recommendations on how to apply new techniques to better understand and manage the evolution of the COVID-19 pandemic and effectively assess its impacts.

Rahardjo et al. (2021, this issue) assessed the contribution of crowdsourcing data from social media in understanding locations and geographical distribution patterns of COVID-19 in Indonesia. The accuracy of the resulted data and visualization maps in this study was assessed by comparing the results with the official data from the Ministry of Health of Indonesia. Although the accuracy of crowdsourcing data remains a challenge, the authors argued that crowdsourcing platforms can be a potential data source for an early assessment of the disease spread especially for countries lacking possibilities to build a systematic data structure to monitor the disease spread.

In the paper (Sahu and Mishra 2021, this issue) the Vulnerability Index (VI) distribution over the 28 states and 8 Union Territories of India is discussed. The VI aims at identifying the sources and forms of vulnerability of population due to COVID-19. The results of the assessment support that the factors involved in the three-section exposure, sensitivity, and adaptive capacity had a significant impact on the vulnerability of the population. This study identified that people in Puducherry, Delhi, Goa, Tripura, and Andhra Pradesh are more vulnerable and need more attention from the government and policymakers. The adaptive capacity pattern shows that small states with relatively better medical infrastructure and COVID-19 specific health care facilities can effectively erode the vulnerability. It is expected that the proposed method will have good practical applications.

The analysis of the spatial clustering of the COVID-19 pandemic using spatial auto-correlation analysis is shown in (Vu et al. 2021, this issue) for conditions of the Fourth COVID-19 Wave in Vietnam. The spatial clustering including spatial clusters (high-high and low-low), spatial outliers (low-high and high-low), and hotspots of the COVID-19 pandemic were explored using the local Moran's I and Getis-Ord's statistics in two phases of the fourth COVID-19 wave. Significant low-high spatial outliers and hotspots of COVID-19 were first detected in the north-eastern region in the first phase, whereas, high-high clusters and low-high outliers and hotspots were then detected in the southern region of Vietnam. The present findings confirm the effectiveness of spatial autocorrelation in the fight against the COVID-19 pandemic, especially in the study of spatial clustering of COVID-19.

The results presented in (Talib 2021, this issue) also concern the application of geospatial analysis of the data in South-Eastern Asia. The author provides an accurate estimation of the cluster tracking system of the

COVID-19 by using geospatial technology in Malaysia. This study is important for raising public awareness of the virus, especially among Malaysian citizens making them more concerned, obeying all the Standard Operating Procedure provided by the government to prevent the spread of COVID-19.

The geospatial analysis has also been applied in **(Wetchayont and Waiyasusri, 2021, this issue)** for the detection and monitoring of the spreading stage during Third Wave of the COVID-19 Pandemic in Thailand. The authors showed that Bangkok, the capital of Thailand, was a significant hotspot for incidence rates, whereas other cities across the region have been less affected. Bivariate Moran's I showed a low relationship between COVID-19 incidences and the number of adults, whereas a strong positive relationship was found between COVID-19 incidences and population density. Daily changes in global Moran's I successfully indicated the Early and Spreading stages during the third wave of the COVID-19 pandemic. These findings could be used to create monitoring tools and aid in policy prevention planning.

IMPACTS OF THE PANDEMIC LOCKDOWN ON THE ENVIRONMENT, AIR POLLUTION, AND THE QUALITY OF WATER

The impacts of the pandemic lockdown on the environment, air pollution, and water quality are considered in **(Chubarova et al. 2021; Sari et al. 2021; Islam et al. 2021; Arakelov et al. 2021)**. The analysis of changes in concentration of different atmospheric gas and aerosol species during the COVID-19 lockdown has been made using ground-based and satellite measurements for different geographical regions: Iran **(Sari et al. 2021)**, India **(Islam et al. 2021)** and Moscow megacity in Russia **(Chubarova et al. 2021)**.

In **(Chubarova et al. 2021, this issue)** the dynamics of the atmospheric pollutants and meteorological conditions has been analyzed during the lockdown due to the COVID-19 pandemic in spring-summer of 2020 in Moscow, Russia, according to the ground-based measurements. The decrease in traffic emissions during the lockdown played an important role in the decrease (up to 70%) and much smoother daily cycles of many gaseous species and aerosol PM10 concentrations. On contrary, there was an increase in surface ozone concentration (up to 18%). The additional comparisons of situations with similar synoptic conditions of northern advection, prevailing during the lockdown period, with additional removing the cases affected by fire smoke advection, have revealed similar tendencies, but with the substantial decrease in absolute concentrations, except ozone. The authors obtained a statistically significant negative correlation between the Yandex self-isolation indices (SII), which can be used as an inverse proxy of traffic intensity, and daily concentrations of all pollutants, except surface ozone, using Pearson partial correlation analysis with fixed temperature factor. In situations with SII>2.5 more favorable conditions for surface ozone generation were observed due to smaller NOx and the higher O_3/NO_x ratios at the same ratio of VOC/NOx. The ozone increase during lockdown may also happen, since in conditions with the prevailing northern air advection the growth of ozone could be observed due to the downward flux of the ozone-rich air from the higher layers of the atmosphere.

In **(Sari et al., 2021, this issue)** the columnar content of main polluted trace gases NO_2, CO and SO_2 was analyzed over Iran and its several districts with high population. The study was based on the retrievals from the TROPO spheric Monitoring Instrument (TROPOMI) on board ESA Sentinel -5P mission as a part of Copernicus program. The concentrations of the polluted gases observed during the lockdown period were compared with those for the period before and after the COVID-19 lockdown. The authors showed that the content of these gases significantly decreased, especially over the urban areas with high population activity such as Tehran and some other large industrial cities (about 80% for SO_2, up to 50% for NO_2 and CO). Some effects of the decrease in the content of the pollutants were also observed after lockdown period compared with pre-lockdown conditions.

Sentinel-5P TROPOMI data were also used in the analysis of the columnar content of nitrogen dioxide due to the lockdown during the COVID-19 pandemic in India **(Islam et al. 2021, this issue)**. The spatio-temporal characteristics of the tropospheric column NO_2 concentration during 45 days of the lockdown were compared with the same days of 2019. Results showed that the mean NO_2 concentration reduced from 0.00406 mol/m^2 before the lockdown (2019-03-25 to 2019-05-10) to 0.0036 mol/m^2 during the lockdown period (2020-03-25 to 2020-05-10). The maximum decline of NO_2 concentration was observed in large cities like Gautam Buddha Nagar (- 40.5%) and Delhi (- 37.5%). Positive standard residuals in the results of the applied Ordinary Least Squares (OLS) method indicate that the concentration of NO_2 has reduced more than expected in the OLS model. The large value of z-score (24.11) from spatial autocorrelation showed that residuals are highly clustered and there is less than a 1% likelihood that this clustered pattern could be a result of a random chance.

The effects of lockdown due to COVID-19 on the quality of water were studied in **Arakelov et al. 2021**, this issue). In this paper the results of the hydrochemical analysis of the Kuban's Black Sea Waters were considered in the conditions of the 2020 quarantine. They concluded that its most visible impact was a disproportionate decrease of the recreational pressure which reduced the concentration of the main pollutants. The authors revealed a proportional relationship between biochemical oxygen demand and the concentration of mobile forms of ammonium nitrogen. Interestingly, though the petroleum refineries in the city of Tuapse did not stop during the quarantine period, the concentration of petroleum derivates dropped sharply.

CONCLUSION

The COVID-19 pandemic is the most immediate challenge for geosciences and health, including its impacts on geoscience development and the achievement of the United Nations Sustainable Development Goals. The papers in this special issue of Geography, Environment, Sustainability would be helpful for understanding the problems in economical, socio-spatial and geographical analysis of COVID-19 pandemic and its consequences, as well as in its impact on the environment, air pollution, and the quality of water.

REFERENCES

Arakelov M. S. , Lipilin D. A., Dolgova-Shkhalakhova A. V. (2021). Influence of Quarantine Measures Against COVID-19 on the State of Black Sea Coastal Waters. Geography, Environment, Sustainability, 4(14), 199-204, DOI: 10.24057/2071-9388-2021-089.

Chubarova N. Ye., Androsova E. Ye., Lezina E. A. (2021). The Dynamics of the Atmospheric Pollutants during the Covid-19 Pandemic 2020 and their Relationship with Meteorological Conditions in Moscow. Geography, Environment, Sustainability, 4(14), 168-182, DOI: 10.24057/2071-9388-2021-012.

Forster P.M., Forster H.I., Evans M.J. et al. (2020). Current and future global climate impacts resulting from COVID-19. Nat. Clim. Chang, 10, 913-919, DOI: 10.1038/s41558-020-0883-0.

Jones C.D., Hickman J.E., Rumbold S.T., Walton J., Lamboll R.D., Skeie R.B., et al. (2021). The climate response to emissions reductions due to COVID-19: Initial results from CovidMIP. Geophysical Research Letters, 48, e2020GL091883, DOI: 10.1029/2020GL091883.

Kolosov V.A., Tikunov V.S., Eremchenko E.N. (2021). Areas of Socio-Geographical Study of the COVID-19 Pandemic in Russia and the World. Geography, Environment, Sustainability, 4(14), 109-116, DOI: 10.24057/2071-9388-2021-091.

Rahardjo Noorhadi, Djarot Heru Santosa, Hero Marhaento (2021). Crowdsourcing Data to Visualize Potential Hotspots for Covid-19 Active Cases in Indonesia. Geography, Environment, Sustainability, 4(14), 125-130, DOI: 10.24057/2071-9388-2021-011.

Sahu Netrananda, Martand Mani Mishra (2021). Assessing the Vulnerability Index of COVID-19 Pandemic in India. Geography, Environment, Sustainability, 4(14), 131-139, DOI: 10.24057/2071-9388-2021-059.

Sari Nurwita Mustika, Muhammad Nur Sidiq Kuncoro (2021). Monitoring of CO, NO_2 and SO_2 Levels During the COVID-19 Pandemic in Iran Using Remote Sensing Imagery. Geography, Environment, Sustainability, 4(14), 183-191, DOI: 10.24057/2071-9388-2020-74.

Schertzer D. et al. (2020). Great e-Debate «Epidemics, Urban Systems and Geosciences». «EGU2020: Sharing Geoscience Online». European Geosciences Union (EGU) session ITS2.10 / NP3.3: «Urban Geoscience Complexity: Transdisciplinarity for the Urban Transition».

Sokhi R.S., V Singh X Querol, Finardi S., Créso Targino A., de Fatima Andrade M., Pavlovic R., Garland R.M., Massagué J., Kong S., Baklanov A., Ren L., Tarasova O., Carmichael G., Peuch V-H., et al., (2021). A global observational analysis to understand changes in air quality during exceptionally low anthropogenic emission conditions, Environment International, 157, 106818, DOI: 10.1016/j.envint.2021.106818.

Talib Noorfatekah, Nur Nabila Mohd Fuad, Nurhafiza Md Saad, Nurul Ain Mohd Zaki, Nurhanisah Hashim (2021). Towards a Strategic Approach of COVID-19 Cluster Web Mapping in Malaysia. Geography, Environment, Sustainability, 4(14), 148-154, DOI: 10.24057/2071-9388-2021-088.

Vu Danh-tuyen, Tien-thanh Nguyen, Anh-huy Hoang (2021). Spatial Clustering Analysis of the COVID-19 Pandemic: A Case Study of the Fourth Wave in Vietnam. Geography, Environment, Sustainability, 4(14), 140-147, DOI: 10.24057/2071-9388-2021-086.

Wetchayont Parichat, Katawut Waiyasusri (2021). Detection and Monitoring of the Spreading Stage during Third Wave of the COVID-19 Pandemic in Thailand Using Moran's I Approach. Geography, Environment, Sustainability, 4(14), 155-167, DOI: 10.24057/2071-9388-2021-090.

WHO (2021). WHO global air quality guidelines. Particulate matter (PM2.5 and PM10), ozone, nitrogen dioxide, sulfur dioxide and carbon monoxide. Geneva: World Health Organization; Licence: CC BY-NC-SA 3.0 IGO.

WMO (2021). First Report of the WMO COVID-19 Task Team: Review on Meteorological and Air Quality Factors Affecting the COVID-19 Pandemic (WMO-No. 1262). Part I: First COVID-19 report, Part II: Executive Summary (multilingual). World Meteorological Organization, https://library.wmo.int/index.php?lvl=notice_display&id=21857#.YZF8GGDMI2w

REVIEW PAPER

AREAS OF SOCIO-GEOGRAPHICAL STUDY OF THE COVID-19 PANDEMIC IN RUSSIA AND THE WORLD

Vladimir A. Kolosov[1*], Vladimir S. Tikunov[2], Evgeny N. Eremchenko[2]

[1]Insitute of Geography of Russian Academy of Sciences, Staromonentny per., 29. Moscow 119017, Russia

[2]Faculty of Geography, Moscow State University, Leninskie Gory 1, Moscow 119899, Russia

***Corresponding author:** kolosov@igras.ru

Received: August 1th, 2021 / Accepted: November 9th, 2021 / Published: December 31st, 2021

https://doi.org/10.24057/2071-9388-2021-091

ABSTRACT. The natural and socio-economic characteristics of the territory play a decisive role in the spread of the pandemic of COVID-19. It provoked a restructuring process in practically all fields of the social life. Its main areas were laid before the pandemic, but the changes were sharply accelerated by the pandemic. In analyzing a number of Russian and foreign publications, the authors discuss the main areas and methods of human-geographical study of the development and consequences of the pandemic. The constantly growing flow of publications in this field can be divided into three major parts: studies of the spatial spread of infection on the different stages; analysis of demographic, (geo) political and economic implications of the pandemic, and attempts to forecast the impact of social and technological changes accelerated by it on territorial structures. The authors note in particular that the geopolitical picture of the world with the division of countries into developed and developing, rich and poor, authoritarian and democratic, Eastern and Western, became much less clear. The most obvious geopolitical consequence of the pandemic is the further fragmentation of the political and socio-economic space. Not only state, but often also administrative boundaries have turned into almost insurmountable barriers for people and trade. The COVID crisis has opened new opportunities for a reasonable combination of the concentration of social life in the «archipelago» of large cities and the development of other territories.

KEYWORDS: Pandemic, COVID-19, social-territorial implications, geographical analysis

CITATION: Vladimir A. Kolosov, Vladimir S. Tikunov, Evgeny N. Eremchenko (2021). Areas Of Socio-Geographical Study Of The Covid-19 Pandemic In Russia And The World. Geography, Environment, Sustainability, Vol.14, No 4, p. 109-116
https://doi.org/10.24057/2071-9388-2021-091

ACKNOWLEDGMENT: The article was prepared with partial support of the State Assignment IGRAS (0148-2019-0008, AAA-A-A19-119022190170-1).

Conflict of interests: The authors reported no potential conflict of interest.

INTRODUCTION

The COVID-19 pandemic has caused a deep crisis in the relationship between nature and society, and many, if not all, social systems are undergoing a restructuring process. Its main areas were laid before the pandemic, but the course of this process was sharply accelerated by the spread of infection and its consequences. The impetus for the restructuring of the international geopolitical order and world economic shifts, intensified by the pandemic, was given by the loss of the collective West of centuries-old domination and a radical change in the balance of power in the world.

The natural and socio-economic characteristics of the territory play a decisive role in the spread of the pandemic. These include the diffusion of morbidity in accordance with the hierarchy of settlements and their involvement in international and national interactions, and the staging of epidemic processes. Their analysis and zoning of the territory are necessary for the correct maneuvering of resources in the fight against a pandemic and the adaptation of the health care system to epidemic risks, considering the regional specifics. The need for an early economic recovery after the crisis provoked by the fight against infection requires considering the unique geographical and cultural diversity of the territory when developing forecasts for the development of the situation in different regions and justifying political decisions.

The objective of this paper is to review the main areas of the human-geographical study of the coronavirus infection. The authors realize that the flow of publications on the pandemic is constantly increasing and by no means pretend to comprehensiveness of their brief outlook. This flow can be divided into three major parts: studies of the spatial spread of infection on the different stages; analysis of demographic, (geo) political and economic implications of the pandemic, and attempts to forecast the impact of social and technological changes accelerated by it on territorial structures. The structure of the paper is based on this division.

The spread of coronavirus infection

The development of the pandemic in space and time attracted the attention of scholars already in the first weeks of the pandemic. The authors studying and mapping this process use such indicators as the number of registered cases of infection per 100 thousand inhabitants, mortality from coronavirus, the number of tests carried out, the severity of restrictive measures and the scale of protests against them (Kalabikhina and Panin 2020; Analytical commentary 2021).

These studies can be conditionally divided into «global», the authors of which consider the spread of the virus at the country level, and «national», based on state regional statistics. The main questions posed in both groups of publications are similar and are aimed at identifying the influence of different factors on the course of the pandemic: 1) territorial mobility of citizens (cross-border or internal), depending, in turn, on their income and social composition; 2) the density of social contacts, and, consequently, the level of urbanization and the nature of settlement; 3) the age structure of the population and the level of health care, in general, determined by the size of the economy and GDP per capita.

The pandemic is spreading across the countries of the world extremely unevenly. Polish geographers J. Banski, M. Mazur and W. Kaminska, studying daily information on the number of new cases of infection by countries at the first stage of the pandemic (until April 5 2020) with the use of statistical models, concluded that at first the pandemic affected almost exclusively the «rich»countries whose residents often travel abroad. At the beginning of the pandemic, the healthier «old» members of the EU suffered much more from its consequences than the «new» and even more so the United States, which holds the sad primacy in the number of cases and deaths (Kam Wing Chan et al. 2020; Zyryanov, Balaban and Zyryanov 2020; Society and pandemic… 2020; Panin, Rylsky, Tikunov 2021).In the same countries, the largest number of deaths from COVID was recorded. No significant correlation was found between population density and the frequency of infections at that stage, but its dependence on the level of urbanization was traced. There is also no relationship between morbidity and mortality with age structure and level of health care. The distribution of 24 economically most important countries in the world, each of which produced more than 1% of global GDP for at least one year from 1980 to 2019, in terms of mortality of infected people per 1 million population, did not depend on the Global Health Security Index for 2019 (Chetverikov 2020). But at an early stage the grouping of countries showed the importance of lifestyle and culture. For instance, it was noted that the relative «atomization» of Japanese society, the rituals of greetings and law-abidingness adopted in it, slowed down the course of the pandemic in comparison with other countries, especially the Mediterranean ones – Spain, Italy (Banski, Mazur and Kaminska 2021).

At the national level in Poland, the first wave of the pandemic (March – late September 2020, that is, at an early stage, before the much wider spread of infection in autumn and winter) affected only a limited number of powiats (counties), reflecting the effectiveness of the government's measures to limit social contacts. The point, however, is not only the timeliness of these measures, but also the relative social homogeneity of Polish society compared to Italy or the UK, with their large migrant communities, less inclined to comply with restrictions. The most affected powiats were distributed at this stage across the territory in a mosaic manner – as well as at the global level, regardless of the population density (Krzysztofik, Kantor-Pietraga and Spórna 2020; Więckowski 2020).

Modeling the spread of morbidity and staging of epidemic processes showed again the importance of the classical model of diffusion of innovations. In Russia, the infection initially spread to Moscow, other large metropolitan areas, coastal and border cities with a high intensity of internal and external migration. The further course of the pandemic depended on the hierarchy of settlements and their involvement in international and national interactions, the number and composition of the most vulnerable social groups, and territorial mobility of the population. In turn, it is determined by the level of income and the geographical location of cities and other settlements, transport accessibility, the prevailing pattern of migrations, cultural features, and the capital of the population's health. The set and role of factors changed over time (Zemtsov, Baburin 2020).Tourist regions and centers in Europe and other regions of the world were among the first to be attacked by the coronavirus (Zyryanov, Balaban and Zyryanov 2020).

Studies of the spread of phenomena across the territory, which, as a rule, are multifaceted and difficult to formalize, are associated with a number of reasons that affect the direction and speed of the process. Considering a large number of factors significantly complicates its imitation. Sometimes secondary, subordinate causes obscure the picture. In this regard, it is very tempting to simulate a multiparametric process using the minimum number of the most accessible indicators.

Among the class of deterministic models, the bulk of works is devoted to the application of the so-called «gravitational» models or their modifications. In this case, the model was based on Stewart's formula for the interaction of settlements, created by analogy with Newton's model of gravity. Therefore, the results obtained are considered as indicative, and the model itself as the first approximation to the mathematical description of the process. As an example, the development of an epidemic between British cities with a population of more than 100 thousand was modeled (Tikunov 1997).

The most often simulated are the flows of the population or its individual categories, freight flows, the volume of telephone conversations between points, etc. A whole class of processes of the spread of phenomena over the territory has similar aspects. For example, it is logical to assume that the flow of vacationers rushing to the Black Sea coast or buyers to retail outlets, as well as the flow of nonresident applicants to universities, will be associated with the population of settlements from which migration occurs and the distance from centers of attraction.

For most types of migrations, these are the two most common factors affecting the volume of migration flows. But it is possible also name a number of specific factors, for example, for the latter case it will be the connection between the profile of the university and the predominant type of occupation of the population, the prestige of this profile at the university, the nature of information about it, the number of students, etc. However, these are less accessible and significant factors. Therefore, as a concrete example, the problem was chosen to simulate some «abstract» epidemic over the territory, which characterizes the process in its most general form (Tikunov 1981a). In this example, there were no typical sources of laughter, which, according to some scholars, cause discrepancies between facts and Stewart's formula. This is the absence of strong flows of a non-local nature and the non-use of data on small settlements.

When justifying the possibilities of using the model, it is assumed that the development of the epidemic is directly proportional to the number of contacts between people, and therefore is determined by the migrations between settlements. As it was noted, for most types of migrations, the number of populations in different settlements and the distance between them are the most common factors of migration. But a number of other specific factors can also be named, for example, distortions in the nature of the spread of epidemics caused by preventive vaccinations, quarantine measures, etc. It is also possible to experiment with modeling «waves» of population, the development of epidemics (Rushton, Mautner 1955) and using the logistic models (Koltsova, Kurkina and Vasetsky 2020), etc.

Among the stochastic models of the spatial development of phenomena, the Monte Carlo method is particularly important. It has a well-developed computational algorithm and provides good results. Apparently, all this led to the widespread use of this method for solving various problems of the spatial development of phenomena. In geographic research, models based on Markov chains and the game theory are also widely used for predicting the spatial distribution of phenomena was interesting (Tikunov 1997).

Socio-territorial consequences of the pandemic

Demographic implications. The most serious consequences of the pandemic are the loss of human lives. Comparing mortality from coronavirus in different countries and even regions of the same country is not easy due to the use of different statistical methods and completeness of reporting. The simplest, although not entirely accurate, method is to estimate the so-called excessive mortality, that is, the excess of its level during a pandemic over «normal» – for the previous year or another period. It is impossible to explain all excessive mortality only by losses from the pandemic, since it was influenced by the isolation regime, the reduction in planned care due to the mobilization of health care system to treat primarily patients with COVID, and a decrease in income. In most countries of the world, the pandemic did not start at the beginning of the year, but in February or March, which affects the baseline. Nevertheless, this method shows a fairly reliable overall picture.

According to a study by Israeli demographers (Karlinsky and Kobak 2021)[1], the highest excessive mortality per 100 thousand inhabitants compared to the average for 2015-2019 was registered in 2020 in Peru (290), Bolivia (260), Bulgaria (250), Ecuador (230), Lithuania (230) and Mexico (210). At the same time, in Western European countries where the morbidity was assessed by world media as critical (Italy, Spain, UK), this figure was significantly lower (respectively, 110, 170 and 120). For comparison, in Russia for 11 months (January-November) it was 180. Since mortality from coronavirus infection is especially high in older age cohorts, the difference in mortality adjusted for the «young» age structure of the population, between Western European and Latin American countries is even more significant.

The comparability of the official data on the number of deaths from coronavirus infection with the actual picture was questionable due to differences in the methodology and completeness of registration. In most countries excessive mortality exceeds the official data by 3 times and more. However, in Uzbekistan, the difference was 30 times, Belarus – 15, Egypt -13, Kazakhstan -12, Russia – 6.7. In France and Belgium and some other countries, the reported deaths number from COVID is higher than the excessive mortality, as they included cases in which the suspected infection was not confirmed. There are the countries in which, despite the pandemic, mortality in absolute terms even decreased, which is associated with an effective lockdown (Karlinsky and Kobak 2021).

According to official statistics, the demographic losses of China from the pandemic were much lower as compared with and the United States. It is explained by the rapid and total isolation of the initial focus of infection in Wuhan and the effectiveness of similar measures in other cities, high availability of protective equipment, but especially by strict discipline, and mutual understanding between the authorities and the population (Ryazantsev and Ange 2020).

Demographic losses from COVID varied greatly between regions of individual countries, depending on the level of urbanization, the structure of settlement, the sectoral composition of the economy, age, ethnic structure, level of education and population mobility, cultural characteristics, and other factors. In Russia, the highest excessive mortality in 2020 was observed not in the capitals, but in the North Caucasian republics – in Chechnya (44.5% more than in 2019), Dagestan (34.0%) and Ingushetia (29.1%). Compliance with traditions did not allow the inhabitants of these republics to stay in self-isolation; social contacts remained close (weddings, funerals, holidays and anniversaries). Apparently, information is affected by both the rate of spread of infection in isolated mountain settlements and the reliability of reporting on the number of deaths from COVID. Excessive mortality is naturally higher in the Western Siberian autonomous districts – Yamalo-Nenets (28.8%) and Khanty-Mansi (26.5%), as well as Tatarstan (27.1%). In isolated settlements located in oil and gas fields, the infection spread especially rapidly. Moscow is only the 9th in the ranking of regions in terms of excessive mortality (23.3%), and St. Petersburg shares the 12-14th places with Mordovia and Chuvashia (22.9%). They are followed by Moscow region (22.5%) (Coronavirus in Russia 2021; Firsov 2021).

Socio-economic implications. The importance of state and administrative borders and informal boundaries is also determined by social polarization, sharply intensified by the pandemic. Closed state and administrative borders have rigidly divided «rich» and «poor» territories, successful and unsuccessful in the fight against the pandemic. According to the UN, in 2020, an additional 131 million people lived below the poverty threshold. Among them, the most vulnerable social groups, including women, constitute a significant proportion, since many of them are employed in the tertiary sector most affected by the crisis. Accordingly, the crisis has especially affected those employed in small and medium-sized enterprises, small entrepreneurs and the self-employed. In Russia, in late March-early June 15 million people suspended work, of which 680 thousand lost their jobs. Registered unemployment rose rapidly. In April 2020, it was 0.7 million people, and in June it was already 3.0 million (Society and the Pandemic: 105).

Before the start of the mass production of vaccines, isolation was the only way to fight the pandemic, but in the countries of Tropical Africa and large parts of Asia and Latin America, only the upper strata of society have the physical ability to isolate (Lieven 2020). The inhabitants of the multimillion-dollar slums in the cities of these regions of the world provide ideal environments for the explosive spread of infection. At the same time, vaccination campaigns are hampered by the high cost of vaccines and the lack of logistics conditions.

Not only in these, but also in much more developed regions the economic impossibility of isolating affects socio-territorial polarization during a pandemic. Border closures have increased the economic differentiation of

[1]The compatibility of these data is limited by the difference in information by countries: some of them provided for the whole year, the others – for 11 months (January – November) and even 10 months (January – October).

states, provinces and municipalities and, indirectly, racial and ethnic discrimination. In Russia, as evidenced by a study carried out by R. Dokhov and M. Topnikov (2020) and based on monitoring population mobility and data on average wages in the poorest rural and small-town areas and in some of areas in the south of Siberia and in the republics of the North Caucasus, citizens have no savings even for minimal downtime in the event of a lockdown. In such areas and on ordinary holidays, mobility falls 2-3 times less than in the rich.

The pandemic has led to a global economic crisis and a sharp drop in GDP in most countries. In 2020, the global economy contracted by 4.3% – more than two and a half times more than during the 2009 global financial crisis. At the same time, in developed countries, which tried to prevent an overload of the health care system and the lives of their citizens through tough lockdowns, the new crisis was deeper: in the first year of the pandemic, their economies shrank by 5.6%. However, these countries have more resources to provide economic assistance to their citizens and businesses, so their expected recovery rates are higher. In total, according to UN experts, $ 12.7 trillion was spent on emergency measures in the world in 2020. Funding government programs to stimulate the economy forced governments to take the largest borrowing in the entire post-war period, increasing public debt by 15%, which will have a negative impact on future prospects (Post-Pandemic… 2021).

The service industries, such as retail, tourism, and the entertainment industry, have been particularly hard hit, and their activities are only possible with guaranteed security. Accordingly, unlike previous crises, the consequences of which were felt more strongly in industrial centers of a certain specialization, the pandemic affected primarily the tourist countries and regions, capital centers and other large cities with a predominance of the tertiary sector in the gross urban product and employment, including retail trade, catering, culture and sports, passenger transport.

The most powerful blow of the pandemic fell on tourism and transport, primarily aviation. The global turnover of the tourism industry, according to the OECD, fell by about 80% in 2020, or more than $ 1 trillion. More than 10 million people lost their jobs. The pandemics affected in March – May 2020 98% of air routes. About 70% of the world aviation fleet (16 thousand aircrafts) was stopped. During the first quarantine in France (April 2020) the traffic at Paris-Orly airport fell from the usual 600 takeoffs and landings per day to 20 associated with the return of French citizens, and passenger traffic fell from 90 thousand to 1,000 (Więckowski 2021). Airlines suffered from big losses: they were forced to pay for aircraft parking and periodic maintenance. Thus, the daily passenger turnover of the Lufthansa group fell from 350 thousand people to 3 thousand. Despite unprecedented government subsidies, airlines were forced to cut staff, including the most valuable personnel – pilots (Dagaeva 2020). According to forecasts, global aviation transport will recover no earlier than 2023.

Other modes of transport also experienced great difficulties. In maritime transport, container freight has risen sharply, ship delays and disruptions to the schedule of shipping lines have become more frequent. The reason was the shortage of containers in Asia due to the asymmetry of foreign trade flows: the high loading of transportation capacities in China and the lack of a sufficient amount of cargo in North America and Europe. Because of this, a crisis arose in the market of fresh vegetables and fruits in the Russian Far East. In the confined spaces of ships, especially cruise ships, the infection spread especially quickly (there were at least 25 of them in late March 2020). Seaports have refused to accept such floating foci of the coronavirus (Mallapaty 2020).

It is obvious that the economic recovery after the coronavirus crisis will be rather slow. This process will be uneven, selective, both in the sectoral and territorial context, and will obviously not lead to the reproduction of the picture that existed before 2020.

Geopolitical implications. The pandemic has led to the largest geopolitical upheavals that will have long-term consequences. Firstly, the state has regained and strengthened its role as the main actor in world politics. Thus, the concept of the weakening of the state as a result of globalization and the strengthening of such powerful actors as transnational corporations or cross-border non-governmental organizations and social movements was at least partially refuted. The American geographer John Agnew urged not to be limited to the study of spatial political systems only within the boundaries of the state. The expression «territorial trap» has become widespread in political geography (Agnew 1994, 2015). Indeed, large transnational corporations surpass in financial power and influence on world processes almost most of the individual states. However, just practically only the states had to really fight the spread of infection, took on the heavy burden of social protection of the most vulnerable groups and subsidies to the economy affected by lockdowns.

Secondly, many experts started talking about de-globalization. At the same time, a discourse arose about the disintegration of the liberal economic order associated with the deregulation of various spheres of activity, the free movement of people, goods and capital, the further strengthening of transnational companies, many of which are superior in power even to relatively large states, and the expansion of integration processes. The struggle for the repatriation of foreign investments and industries flared up with renewed vigor.

Indeed, even before the pandemic, researchers noted attempts by leading states to isolate themselves from the negative and unforeseen consequences of globalization, including by erecting thousand-kilometer physical barriers along the borders and severe restrictions on international migration, strengthening protectionism, establishing new customs barriers and quotas. Gross violations of WTO principles, sanctions and counter-sanctions, restrictions on investments in certain industries, and other manifestations of «economic patriotism» have become more frequent. The ongoing changes were also reflected in the fragmentation of the global political space – the reverse side of integration processes: many regions of the world have become the arena of religious fundamentalism, separatist, nationalist movements, and cultural isolationism. New territories appeared on the political map that were not controlled by legitimate governments.

International organizations at various levels were unable to take urgent action. The activities of international organizations did not match the urgent need to coordinate the efforts, their global reach and solidarity – to help countries and regions in the most difficult situation. The pandemic clearly highlighted the return in international relations of Realpolitik – sharp competition, not mitigated by supranational political and legal institutions, national egoism, domination of the strongest, imposing their interests on weaker partners, increasingly using «soft power». International humanitarian aid in the form of services of qualified specialists, supplies of vaccines, equipment, medicines has become a new powerful source of geopolitical influence, including China and

Russia. Leadership in vaccine development and the lead in vaccination has become a reason for national pride and a demonstration of advantages over political opponents.

For example, the aid of China to Serbia has considerable improved its image in this country, although Russia has also helped Belgrade in the most difficult moments. At the same time, the authority of the United States, where the health care system did not cope with the challenge on the early stage of the pandemic, has been noticeably damaged (Šantić and Antić 2020). The usual geopolitical picture of the world with the division of countries into developed and developing, rich and poor, authoritarian and democratic, eastern and western, has been greatly shaken.

Thirdly, the actualization of Realpolitik and the aggravation of the competitive struggle between states caused an intensification of the confrontation between Russia and China, on the one hand, and the collective West, on the other, revived comparisons of the effectiveness of authoritarian and democratic political regimes. Authoritarian states have often resisted the pandemic better than democracies, and relatively poor states have fought better than richer ones. Democracies with post-industrial economies and market-oriented health systems have found themselves in short supply of beds, ventilators, protective suits, and even masks. At the same time, in authoritarian countries with a disciplined and obedient population – primarily in China – it was possible to take quick and effective measures to contain the infection. However, it is impossible to draw a final conclusion about the advantages of democratic or authoritarian regimes in the fight against the pandemic, since it turned out that territorially differentiated cultural factors, such as lifestyle, forms of leisure, culture of everyday life and governance, trust in government institutions, are of great importance. For example, in Switzerland, the epidemic map reveals a completely different course of the pandemic in the German, French and Italian cantons, though all of them make part of the same country that has self-isolated along its external borders (Baunov 2020).

The unprecedented quarantine measures that many countries were forced to introduce, including those related to the use of artificial intelligence and other modern methods of controlling the behavior and movement of people, have caused widespread fears that states will use these methods to spy on citizens, which will strengthen authoritarian tendencies in political life, as happened in the Xinjiang Uygur Autonomous Region of China. The Italian philosopher Giorgio Agamben, the author of the concept of «biopolitics», wrote that since the enemy (virus) is inside us, the fight against him inevitably stimulates the growth of authoritarian tendencies in political life. The adoption of tough measures without the formal declaration of the state of emergency, requiring the approval of the parliament, was a sign of this tendency. Characteristically, residents of democratic and authoritarian states were equally ready to accept the restriction of personal freedoms in the sake of security (Filippov 2020; Lieven 2020).

Fourth, the pandemic has caused internal political turmoil in many countries and regions, and has changed the nature of relations between central governments and regional authorities, center and periphery. Regardless of the nature of the regime, in some cases the pandemic has led to an increase in the popularity of political leaders, in others, on the contrary, it has brought down their ratings. The uneven course of the pandemic caused the need to consider its regional and local characteristics and decentralize political decisions, and therefore increased the importance of regional and local authorities, which could mix the spread of the infection, relying on the help of volunteers and NGOs. Decentralization of solutions to combat the pandemic provided flexibility in responding to a rapidly changing epidemic situation, made it possible not to automatically impose restrictions where they were not urgently needed, and to reduce their economic consequences. However, acute conflict situations arose when regional and local authorities did not agree with the central government, for example, in France and Spain.

The most obvious geopolitical consequence of the pandemic is the further fragmentation of the political and socio-economic space. Not only state, but also internal administrative boundaries became its instrument. Some of them have turned into almost insurmountable barriers for people and trade. Limiting territorial mobility of the population at all levels is seen as the main way to reduce the spread of infection and reduce the burden on the healthcare system. Paradoxically, it turned out that on the twenty-fifth anniversary of the Schengen agreement, almost all movement within its area was prohibited. The trend towards erecting barriers to the movement of individuals, which had emerged a few years earlier to limit migration flows that had swept the EU countries, reached its climax (Filippov 2020; Wassenberg 2020). The closure of the borders took place in an atmosphere of extreme alarm and haste, asynchronously and asymmetrically, and it was not agreed even between the EU countries. As a result, it happened that the border between neighboring countries was closed to the citizens of one country and remained open to the other. As the incidence of the disease declined in the EU countries, so-called bubbles formed – the territories of several countries with a more favorable epidemic situation, which opened the borders between themselves – for example, the borders of Finland were open to citizens of Norway, the three Baltic states, as well as Denmark and Iceland. The closures have affected the mobility and daily interests of more than 90% of the world's population. The return of millions of labor migrants who have lost their jobs and tourists to the countries of their permanent residence has become a big problem. Millions of trapped migrants have become one of the most vulnerable groups during the pandemic. The outbreak of the pandemic found more than 600 thousand EU citizens abroad, including 200 thousand in Germany and 160 thousand in France (Więckowski 2020). After the termination of regular flights, many countries, including Russia, have organized special flights to take their citizens home.

Attempts to contain the pandemic by establishing and closing borders increased the negative image of neighbors, spawned a search for «scapegoats» guilty of the hypothetical creation of the COVID-19 virus (repeated statements by President Trump about China) or the spread of infection («irresponsible» neighbors who did not accept timely measures) (Mionel, Neguţ and Mionel 2020). As a result, the pandemic contributed to the geopolitical fragmentation of the world, its further division into «us» and «Others». This tendency was clearly manifested in the unrecognized (partially recognized) states in the post-Soviet space – Abkhazia, DPR and LPR, Nagorno-Karabakh, Transnistria and South Ossetia. Their leadership has never closed the borders with the patron states (Russia and Armenia) on its own initiative and, on the contrary, used the pretext of the pandemic to block the borders with the parent states (Georgia, Azerbaijan, Ukraine) for a long time, which caused strong discontent among certain groups of population (Kolosov and Zotova 2021).

At the domestic level, in many countries «red», «orange», «yellow», «green» areas with different levels of morbidity and the degree of border barrier have appeared. Many cities and entire regions were almost completely isolated from the outside world.

The emergence of many, if not almost all of them, is far from accidental. Their analysis gives a new understanding of the division of space and its possible fragmentation. Traffic controls and barriers suddenly reappeared where checkpoints had long been boarded up. Invisible borders between the regions with different levels of morbidity divided the territories with different levels of urbanization, age structure and income and, accordingly, population mobility, and finally, different cultural characteristics and lifestyle. These boundaries do not necessarily coincide with the administrative ones, but often reveal various kinds of historical boundaries (relict or phantom). An example of such boundaries at the interstate level was the dividing line Western and Central Europe (former socialist countries). In more developed Western countries, the number of infected per 100,000 inhabitants and mortality were higher. It was explained by the universal vaccination against tuberculosis during socialism, which affects immunity, the mechanism of which has not yet been clarified, and the peculiarities of the socialist health care system. Former socialist counties still have a higher number of hospital beds per 1,000 inhabitants and the custom of hospitalizing patients for reasons that in other countries are considered insufficient. The UK, Spain and Italy lag significantly behind the countries of Central Europe in the relative number of beds, which greatly affected the most acute stages of the pandemic.

Structural changes in society and a new configuration of space

The economic crisis caused by the pandemic is not just another recession. It sharply intensified the previously observed profound structural shifts in the economy, in the labor market, in the social field and in many other spheres of life. The results of the first year of the pandemic have revealed the evolution of the territorial structures and changes in the functions of various elements of social and economic space.

First of all, the crisis contributed to a sharp acceleration of digitalization, the expansion of the use of artificial intelligence and the automation of many work processes, which leads to a reduction in jobs, not only in production, but also in offices, the transfer of employees to a distant mode of work and partial employment. Traditional retail is being replaced by electronic and all kinds of delivery services, which has significantly transformed consumer behavior. Apparently, the period of rapid construction of shopping malls on the periphery of large cities is coming to an end. The use of unmanned aerial vehicles in the delivery of goods opens up new markets and, along with distant work, the prospects for the revival of the most advantageously located and attractive settlements in depopulated areas.

The freeing up of labor as a result of the cumulative impact of falling production and structural transformation creates significant stagnant unemployment. According to experts from the Danish Saxo Bank, it will induce many developed countries to establish an unconditional basic income, which will affect the quality of life, change people's attitudes towards work and life strategies, reduce mobility (Khvostik 2020).

The decline of some industries in a pandemic was accompanied by a boom or restructuring of others. The demand for the products of the medical and pharmaceutical industries and health services has grown even more. A huge new industry has emerged – «corona-business» of tens, if not hundreds of billions of dollars – for example, tracking the immune status of citizens. Further widespread is distant learning, which can revolutionize the field of education: students get the opportunity to follow courses from different universities and in different disciplines, which creates opportunities for a more even distribution of leading universities. The book market has revived in a number of countries, including Russia.

According to TsIAN agency in Russia, the potential demand (number of site visits and search queries) for suburban housing was 28% higher in the first quarter of 2021 compared to the first quarter of 2020 for land plots and by 27% for houses or summer cottages. At the same time, within a radius of 50 km from the Moscow Ring Road, there were a quarter fewer individual housing construction sites on sale than last year, and the average cost increased by 3%. The number of summer cottages and cottages for sale with an area of less than 200 sq.m. decreased by a third – from 6 thousand in 2020 to 3.95 thousand in 2021, and the average price increased by 10%. During the pandemic the demand for building materials increased sharply, which, in turn, is largely due to a significant increase in demand for suburban real estate around large cities(Sobol 2021). City dwellers re-evaluate the role of second homes as shelters and investment targets. As A.G. Makhrova and T.G. Nefedova (2021) point out, «dachas» (country homes) around Moscow and St. Petersburg have long been gradually turned into permanent dwellings where there is the necessary social and transport infrastructure, while maintaining housing in the city. The pandemic has also reinforced the pulsating seasonal migration of residents of large centers to small towns.

Changes in the tourism industry are characteristic. According to the media platform HotelTechReport, the coronavirus will accelerate the previously outlined digital transformation in the hospitality industry by 10-15 years (Shabalina, Tikunova 2016). These include the transition to «online tourism», that is, the rejection of group package tours and independent travel planning using Internet services, which will integrate not only the booking of tickets for transport and accommodation, but also the purchase of tickets to museums, car rental, food delivery, etc. It is estimated that the global online tourism market will grow from $ 570 billion in 2017 to $ 1,135 billion in 2023. In accordance with the individualization of demand, the diversification of destinations and types of tourism, and the growing demand for «urban» domestic tourism are observed, while the duration and distance of trips are decreasing.

No less impressive structural changes are taking place in the world's air transport. During the pandemic, the hubs suffered serious losses – the largest transit airports, which became especially dangerous due to the large congestion of passengers. Experts believe that many of them will not revive, as demand has shifted to point-to-point flights, which are more comfortable and reliable, although often more expensive. This has already caused a change in the aviation industry: the use of aircrafts of large capacity for transportation between hubs is diminishing. The Airbus company announced the termination of the production of its flagship A-380 aircraft in the near future (Aksenov 2020; Dagaeva 2020).

The crisis caused by the pandemic calls into question the current paradigm of finding ways to reduce costs in production and the social sphere, mainly due to the consolidation and deep specialization of enterprises and facilities, which dooms small cities and entire regions to depopulation and decline. Large cities have long become a source of not only innovation, but also social destabilization – environmental pollution, crime, unrest, new infections, the vulnerability of the entire society in case of unforeseen events. The crisis has shown the importance of a reasonable combination of the concentration of social life in the «archipelago» of large cities and the simultaneous development of other territories by expanding the availability of medical care, various services, creating cultural and leisure centers, and preserving small schools.

The closure of borders has reduced the length of production chains and often forced the search for suppliers of goods and services within the state territory. Thus, it turned out that agriculture in the Russian Far East is quite capable of doing without seasonal Chinese workers (Zuenko 2020).

However, in our opinion, it is too early to draw a final conclusion about the beginning of the de-globalization of the world economy. The pandemic has accelerated the development of technologies that enhance the interdependence and interconnectedness of the modern world. Satellite data exchange is revolutionizing international electronic banking and the access of billions of people to the digital economy.

CONCLUSION

Already in the first weeks after the outbreak of the COVID-19 pandemic, a rapidly growing flow of human-geographical publications about its progress and consequences appeared as part of interdisciplinary research of this unprecedented natural and social phenomenon. Attempts to model and predict the spatial spread of the infection, proceeding in accordance mainly with social laws occupies an important place in this flow. Such attempts are based so far mainly on the application of already known statistical methods and their modifications, but the pandemic has become a stimulus for the development of new approaches. It became obvious that its consequences are extremely deep and long-term and sharply accelerated the trends of changes in all fields of social life emerged in recent years. They will lead to the transformation of its entire territorial organization of society – settlement and migration, the structure and location of economic activity, especially transport. They will transform political systems and the network of political and administrative borders. The pandemic is not over, and its consequences are far from clear. They will undoubtedly be the subject of a powerful flow of further research.

ACKNOWLEDGEMENTS

The parts on consequences of the pandemic and structural changes in society was prepared thanks to the support of the State Assignment IGRAS (0148-2019-0008, AAAA-A19-119022190170-1).

The part about cartographic oriented systems was prepared thanks to the support on the State Assignment theme "Studying the dynamics of socio-natural systems using geoinformation mapping and digital technologies" (No. 121051100163-3).

The part on new configuration of space was prepared thanks to the grant of RSF "Development of the concept, technologies and services of a new generation atlas information system for monitoring the characteristics of the ecological state of the regions and cities of Europe and Russia" (No. 20-47-01001).

REFERENCES

Agnew J. (1994). The Territorial Trap: The Geographical Assumptions of International Relations Theory. Review of International Political Economy, 1(1), 53-80.

Agnew J. (2015). Revisiting the Territorial Trap. Nordia Geographical Publications, 44(4), 43-48.

Aksenov P. (2020). Hubs are a thing of the past. How the pandemic will change the world's aviation [online]. Available at: htpps://www.bbc.com/Russian/features-54715695 [Accessed on 30 July 2021].

Analytical commentary [Foundation «Petersburg's Policy]. [online]. Available at:https://fpp.spb.ru/fpp-rating-2021-02 [Accessed on 30 July 2021].

Banski J., Mazur M. and Kaminska W. (2021). Socioeconomic Conditioning of the Development of the COVID-19 Pandemic and Its Global Spatial Differentiation. Int. J. Environ. Res. Public Health, 18(4802).

Baunov A. (2020). Revision of borders. What will international relations be like after the pandemic? [online]. Available at: https://carnegie.ru/commentary/81714. [Accessed on 30 July 2021].

Coronavirus in Russia: death rate in 2020 increased by almost 18% (2021). [online] Available at: https://www.bbc.com/russian/news-55984574 [Accessed on 30 July 2021].

Dagaeva A. (2020). How the pandemic will change aviation in Russia and the world. [online]. Available at: https://carnegie.ru/commentary/81585 [Accessed on 30 July 2021].

Dokhov R., Topnikov M. (2020). Self-isolation for the rich: who could afford to quarantine [online]. Available at: https://www.forbes.ru/obshchestvo/400409-samoizolyaciya-dlya-bogatyh-kto-smog-pozvolit-sebe-uyti-na-karantin. [Accessed on 30 July 2021].

Filippov A. (2020). Normality and abnormality of the emergency. Russia in global affairs. [online]. Available at: https://globalaffairs.ru/articles/normalnost-chrezvychajnogo [Accessed on 30 July 2021].

Firsov A. (2021). Chechnya, Dagestan and Ingushetia lead in excess mortality. The media outlook on the COVID-19 epidemic did not coincide with reality [online]. Available at:https://www.vedomosti.ru/opinion/articles/2021/03/15/861389-chechnya-dagestan?utm_campaign=newspaper_15_3_2021&utm_medium=email&utm_source=vedomosti [Accessed on 30 July 2021].

Ilnitskiy A. (2020). Civilization of space [online]. Available at : https://www.pnp.ru/politics/civilizaciya-prostranstva.html [Accessed on 30 July 2021].

Karlinsky A. and Kobak D. (2021). The World Mortality Dataset: Tracking excess mortality across countries during the COVID-19 pandemic [online], DOI: 10.1101/2021.01.27.21250604 [Accessed on 30 July 2021].

Kolosov V. and Zotova M. (2021). «De-Facto Borders» as a Mirror of Sovereignty. The Case of the Post-Soviet Non-Recognized States, Historical Social Research.

Khvostik E. (2020). Vaccination against COVID-19 will destroy corporations, and large cities will be empty [online]. https://www.kommersant.ru/doc/4604064 [Accessed on 30 July 2021].

Kalabikhinal. Ye., Panin A.N. (2020). Spatial choreography of the coronavirus. Population and Economics, 4(2), 123-152.

Kam Wing Chan, Gentile M., Kinossian N., Oakes T. and Young C. (2020). «More-than-viral» Eurasian geographies of the covid-19 pandemic: interconnections, inequalities, and geopolitics, Eurasian Geography and Economics, 61(4-5), 343-361.

Koltsova E.M., Kurkina E.S., Vasetsky A.M. (2020). Mathematical modeling of the spread of the COVID-19 coronavirus epidemic in a number of European, Asian countries, Israel and Russia. Problems of Economics and Legal Practice, 2, 154-165.

Krzysztofik R., Kantor-Pietraga I. and Spórna T. (2020). Spatial and functional dimensions of the COVID-19 epidemic in Poland, Eurasian Geography and Economics, 61(4-5), 573-586.

Lieven A. (2020). Coronavirus as a mirror: what we see. Russia in global affairs [online]. Available at: https://globalaffairs.ru/articles/korona-zerkalo-obshhestva [Accessed on 30 July 2021].

Makhrova A.G., Nefedova T.G. Can the COVID-19 pandemic stimulate sub- and de-urbanization in Russia? Vestnik Mosk. Universiteta, ser. 5, Geografia. 2021.

Mallapaty S. (2020). What the cruise-ship outbreaks reveal about COVID-19. Nature, 580(7801), 18.

Mionel V., Neguț S. and Mionel O. (2020). Pandemopolitics. How a public health problem become a geopolitical and geoeconomic issue, Eurasian Geography and Economics, 61(4-5), 389-403.

Society and pandemic. Experience and lessons of the fight against COVID-19 in Russia. Moscow: 2020, 744. [in Russian].

Panin A.N., Rylsky I.A., Tikunov V.S. (2021). Spatial patterns of the spread of the COVID-19 pandemic in Russia and the world: spatial and cartographic analysis, Vestnik Moskovskogo Universiteta, Series 5, Geography, 1, 62-77.

Post-Pandemic World Economy: UN Calls for Global Consolidation (2021). [online]. Available at: https://news.un.org/ru/story/2021/01/1395082 [Accessed on 30 July 2021].

Ryazantsev S.V., Anghe (2020). COVID-19 epidemic in China: socio-demographic aspects, Scientific Review, Series 1, Economics and Law, 3, 156-165.

Rushton S., Mautner A.J. (1955). The deterministic model of a simplt epidemic for more than one community. Biometrika, 42, 126-132.

Šantić D. and Antić M. (2020). Serbia in the time of COVID-19: between «corona diplomacy», tough measures and migration management, Eurasian Geography and Economics, 61 (4-5), 546-558.

Shabalina N.V., Tikunova I.N. Modern processes and phenomena in the international tourist market. In: Kolosov V.A. and Sluka N.A., eds. Geography of the World Economy: Traditions, Modernity, Prospects. Moscow-Smolensk: Oikumena, 2016, 230-246 [in Russian].

Sobol M. (2021). Extend the dacha amnesty: Rosreestr intends to simplify the registration of land rights [online]. Available at: https://www.gazeta.ru/business/2021/04/05/13548146.shtml [Accessed on 30 July 2021].

Tikunov V.S. (1981). Imitation of spatial development of phenomena on the example of the gravitational model of the spread of epidemics and their mapping. Geodesy, cartography and aerial photography. Issue 33. Lvov, Vishcha shkola, 104-110. [in Russian].

Tikunov V.S. (1997). Modelling in cartography. Moscow University Publ. House, 405.

Wassenberg B. (2020). The Schengen Crisis and the End of the Myth of «Europe Without Borders», Borders in Globalization Review, 1(2), 30-39.

Więckowski M. (2020). Can a pandemic stop or slow the Anthropocene? Geographia Polonica, 93(4), 473-492.

Zyryanov A.I., Balaban M.O., Zyryanov G.A. (2020). Geography of coronavirus and issues of tourism, Geography and Tourism, 2, 5-17.

Zuenko I. (2020). Without Chinese. How the pandemic is changing agriculture in the Far East [online]. Available at: https://carnegie.ru/commentary/83423[Accessed on 30 July 2021].

REVIEW PAPER

GIS AND REMOTE SENSING: A REVIEW OF APPLICATIONS TO THE STUDY OF THE COVID-19 PANDEMIC

Quoc-lap Kieu[1], Tien-thanh Nguyen[2*], Anh-huy Hoang[3]
[1]Faculty of Natural Resources and Environment, Thainguyen University of Sciences, Tan Thinh Ward, Thainguyen, 250000, Vietnam
[2]Faculty of Surveying, Mapping and Geographic Information, Hanoi University of Natural Resources and Environment, No. 41A, Phu Dien Road, North-Tu Liem District, Hanoi,100000, Vietnam
[3]Faculty of Environment, Hanoi University of Natural Resources and Environment, No. 41A, Phu Dien Road, North-Tu Liem District, Hanoi, 100000, Vietnam
*Corresponding author: tdgis_ntthanh@163.com; ntthanh@hunre.edu.vn
Received: May 16th, 2021 / Accepted: November 9th, 2021 / Published: December 31st, 2021
https://doi.org/10.24057/2071-9388-2021-054

ABSTRACT. The spread of the 2019 novel coronavirus disease (COVID-19) has engulfed the world with a rapid, unexpected, and far-reaching global crisis. In the study of COVID-19, Geographic Information Systems (GIS) and Remote Sensing (RS) have played an important role in many aspects, especially in the fight against COVID-19. This review summarises 102 scientific papers on applications of GIS and RS on studies of the COVID-19 pandemic. In this study, two themes of GIS and RS-related applications are grouped into the six categories of studies of the COVID-19 including spatio-temporal changes, WebGIS-based mapping, the correlation between the COVID-19 and natural, socio-economic factors, and the environmental impacts. The findings of this study provide insight into how to apply new techniques (GIS and RS) to better understand, better manage the evolution of the COVID-19 pandemic and effectively assess its impacts.

KEYWORDS: GIS; remote sensing; applications; COVID-19; viral infection; impacts; environment

CITATION: Quoc-lap Kieu, Tien-thanh Nguyen, Anh-huy Hoang (2021). Gis And Remote Sensing: A Review Of Applications To The Study Of The Covid-19 Pandemic. Geography, Environment, Sustainability, Vol.14, No 4, p. 117-124
https://doi.org/10.24057/2071-9388-2021-054

ACKNOWLEDGEMENTS: We wish to thank the editors and anonymous reviewers for their valuable and constructive comments and suggestions on this paper that have helped us to greatly improve the quality of the paper.

Conflict of interests: The authors reported no potential conflict of interest.

INTRODUCTION

The COVID-19 pandemic has been a global health concern due to the rapid spread of the disease (WHO 2020) since a deadly new coronavirus strain, the SARS-CoV-2 virus was initially discovered in Wuhan city, PR China. The COVID-19 pandemic has been described as a social, human, and economic crisis (United Nations 2020). Globally, as of October 22, 2021, there were more than 242.3 million confirmed cases of the COVID-19, including more than 4.9 million deaths reported to WHO (WHO 2021). Geography is considered a key part of fighting the COVID-19 Coronavirus outbreak (Shepherd 2020). Later, Rose-Redwood et al. (2020) highlight that the COVID-19 pandemic is thoroughly spatial in nature. It is, therefore, the assessment of the scale of the COVID-19 pandemic from a geographical perspective that can offer a better understanding of the spatial distribution, better manage the COVID-19 infection, and effectively study its impacts.
A Geographic Information System (GIS) is an essential tool to examine the spatial distribution of spatial objects. Many COVID-19-related data such as the locations of (visited) COVID-19 cases can be considered a type of spatial object which has a spatial dimension and can be mapped by a GIS. When assessing potential geographical accessibility for health utilization studies, Graves (2012) showed the importance of GIS in analyzing epidemiological data, revealing trends and interrelationships that would be difficult to discover in tabular format and the visualization of problems in relation to existing health and social services and the natural environment and so more effectively target resources. Later, the use of GIS in geospatial health has been also firmly established as a useful tool for collating, exploring, visualizing, and analyzing health data in a graphic manner (Cicalò and Valentino 2019). Along with GIS, remote sensing allows acquiring information about the Earth's surface without actually being in contact with it. The applications of remote sensing data to studies of human health, especially in infectious disease research have been reviewed by Viana et al. (2017). It is, therefore, GIS and remote sensing data are fundamental to keep infectious diseases and their geographical distribution under control (Cicalò and Valentino 2019). In this study, to understand the spatial patterns, effects, and consequences of COVID-19 in the context of geography, this study aims to review the applications of GIS and remote sensing in the study of the COVID-19 pandemic. In this study, we first review the applications of GIS to detect the spatio-temporal changes, Web-GIS-based mapping of the COVID-19, and the identification of the correlation between the

COVID-19 and natural, social-economical variables. It will then go on to discuss the applications of remote sensing techniques on the environmental impacts of the COVID. The environmental impacts of the COVID-9 will mainly focus on studies of its impacts on water and air quality.

APPLICATIONS OF GIS IN THE STUDY OF THE COVID-19 PANDEMIC

Spatio-temporal changes

GIS can help to study the COVID-19 epidemic spread at the country or state scale (Kodge 2021; Saeed et al. 2021), at the regional scale (Amdaoud et al. 2021; Onafeso et al. 2021), and at the global scale (Bisanzio et al. 2020; Gelfand et al. 2021; Meng 2021). When the SARS-CoV-2 virus was initially discovered at the end of 2019 in Wuhan city, Hubei province, central China, and quickly spread throughout China, application studies of GIS on the fight of the COVID-19 pandemic in China have been conducted by many authors. One of the most cited studies was carried out by Guan et al. (2020). With the help of GIS, Guan et al. (2020) extracted data regarding 1099 patients with laboratory-confirmed Covid-19 from 552 hospitals in 30 provinces, autonomous regions, and municipalities in mainland China through January 29, 2020. Later, by analyzing the spatial distribution of COVID-19 cases in the early stages of the epidemic and determining their correlation with the population migration from Wuhan city and Hubei province using ArcGIS software and the Bayesian space-time model, Chen et al. (2020) concluded that the population that emigrated from Wuhan was the main infection source in other cities and provinces. This is of great importance for strictly implementing isolation or social distancing rules and early warning and prevention of future outbreaks. After COVID-19 rapidly spread across China and the rest of the world, many studies make use of GIS to detect the spatio-temporal changes in many countries, especially in the worst-affected countries such as the USA (Feng et al. 2020; Rui et al. 2021; Wang et al. 2021), Italy (Giuliani et al. 2020; Gross et al. 2020; He et al. 2020), England (Elson et al. 2021; Sartorius et al. 2021), South Korea (He et al. 2020; Kim and Castro 2020; Lee et al. 2020), Iran (He et al. 2020), Brazil (Castro et al. 2021), Russia (Kuznetsov et al. 2020a) and most recently in India (Bag et al. 2020; Bhunia et al. 2021).

When characterizing the dynamics and quantifying the trends of the COVID-19 epidemic in the United States using spatial and space-time scan statistics and the Joinpoint analysis, Wang et al. (2021) indicate that higher risks of clustering and incidence of COVID-19 were consistently observed in metropolitan versus rural counties, counties closest to core airports, the most populous counties, and counties with the highest proportion of racial/ethnic minorities. Feng et al. (2020) revealed that GIS can help to effectively characterize spatio-temporal transmission of COVID-19 and its mitigation strategies. Most recently, when analyzing the spread of COVID-19 in the USA, Rui et al. (2021) found that the spatio-temporal multivariate time-series model is especially suitable for envisioning the virus transmission tendency across a geographic area over time. Using an endemic-epidemic multivariate time-series mixed-effects generalized linear model for areal disease counts, Giuliani et al. (2020) successfully modeled and predicted the spatio-temporal spread of COVID-19 in Italy. In the early stages of the COVID-19 pandemic between January and June 2020 in England, using spatial and spatio-temporal kernel estimates developed by Davies and Lawson (2019), Elson et al. (2021) discovered the spatio-temporal distribution of COVID-19 infection. In Brazil, Castro et al. (2021) successfully used daily data on reported cases and deaths to understand, measure, and compare the spatio-temporal pattern of the spread across municipalities. In South Korea, to understand the COVID-19 clustering across districts in South Korea and how the spatial pattern of COVID-19 changes, Kim and Castro (2020) successfully applied the global Moran's I statistic and the retrospective space-time scan statistic to analyze spatio-temporal clusters of COVID-19. Most recently, when identifying spatial patterns of COVID-19 disease clustering in India using another global spatial autocorrelation statistic, the Getis-Ord G^*_i statistic, Bhunia et al. (2021) discovered that this statistic can help public health professionals to effectively identify risk areas for disease and take decisions in real-time to control this viral disease.

WebGIS-based mapping

When considering the usage of Web-based (or Web-GIS-based) mapping during the COVID-19 pandemic, Mooney and Juhász (2020) concluded that Web-GIS maps have been widely used for delivering public information on this fast-moving, epidemiologically complex, and geographically unbounded process. Similar to those reported by Mooney and Juhász (2020), Franch-Pardo et al. (2020) also showed the importance of WebGIS-based mapping in the dissemination and provision of (official) information on COVID-19, especially for the spatial representation of the pandemic and its evolution. When conducting a study on geographical tracking and mapping of coronavirus disease COVID-19/SARS-CoV-2 epidemic and associated events around the world, Boulos and Geraghty (2020) successfully employed different types of WebGIS-based mapping such as practical online/mobile GIS and mapping dashboards for tracking the 2019/2020 coronavirus epidemic. According to Franch-Pardo et al. (2020), the most international information compiled, the most widely referenced viewer, and the first to go online out is an interactive WebGIS-based dashboard to track COVID-19 in real-time developed by John Hopkins University (see Dong et al. (2020) for more detail). At the same time, Cicalò and Valentino (2019) successfully used the web-based for the study of epidemics and design of the web maps on COVID-19. Since then, more WebGIS-based applications for mapping COVID-9 have been created for each country such as Russia (Kuznetsov et al. 2020a; Momynaliev et al. 2021), the USA (Cicalò and Valentino 2019; Gao et al. 2020), China (Xu et al. 2020), UK (Mooney and Juhász 2020), Israel (Rossman et al. 2020) and Italy (Mooney and Juhász 2020).

Typically, to obtain a real-time nationwide view of symptoms across the entire population in Israel, an online questionnaire was employed in a study by Rossman et al. (2020) to identify geographic clusters in which the virus is spreading. This study is potential for the detection of COVID-19 outbreaks. And recently, to help increase risk awareness of the public, support data-driven public health and governmental decision-making, and help enhance community responses to the COVID-19 pandemic, Gao et al. (2020) successfully used daily updated human mobility statistical patterns derived from large-scale anonymized and aggregated smartphone location big data at the county-level in the United States to provide timely quantitative information on how people in different counties and states reacted to the social distancing guidelines.

In Russia, a number of authors have successfully applied WebGIS to mapping the COVID-19 epidemic.

Kuznetsov et al. (2020b) focused on the investigation and design of the methodology and software prototype for GIS-based support of medical administration and planning on a city scale when accounting and controlling infectious diseases. Later, with the aim of evaluating the usefulness of Internet queries related to the smell to assess the effectiveness of anti-epidemic measures of preventing the spread of COVID-19 in some regions of Russia, Momynaliev et al. (2021) concluded that the rise in the sudden interest in smell among Internet users can be seen as a valuable minimally invasive indicator of the spread of the coronavirus in the population, as well as to assess the effectiveness of anti-epidemic measures against COVID-19. WebGIS for mapping the COVID-19 pandemic has been also proved effective by other scholars (Bachilo et al. 2020; Nekliudov et al. 2020).

Identification of correlations between COVID-19 and natural, socio-economic factors

To analyze the correlation between confirmed cases of COVID-19 and several geographic, meteorological, and socio-economic variables at the province level in Spain, Oto-Peralías (2020) points out that the arrival of the summer heat may play in limiting the spread of the virus. From a different angle, using GIS-based approaches such as spatial lag and spatial error models to investigate spatial dependence and multiscale geographically weighted regression models to locally examine spatial non-stationarity, Mollalo et al. (2020) point out the effects of significant explanatory variables (income inequality, median household income, the proportion of black females, and the proportion of nurse practitioners) on a relatively high spatial variability of COVID-19 incidence rates in the continental United States. Also in the United States, when investigating the correlation between the geographic spread of COVID-19 and the structure of social networks as measured by Facebook, Kuchler et al. (2020) concluded that a social connectivity index can help epidemiologists predict the spread of communicable diseases.

In the first COVID-19 wave, Russia has the third-highest number of confirmed cases after the United States and Brazil (Pramanik et al. 2020). Many contributions to apply GIS in the fight against the second COVID-19 wave have been made by scholars in Russia. Typically, using the Random Forest algorithm, Pramanik et al. (2020) successfully investigated the relationship between climatic factors (air temperature, relative humidity, wind speed, sunshine, diurnal temperature change, and temperature seasonality) and the rise of COVID-19 intensity. Later, when investigating the meteorological controls on the spread of SARS-CoV-2 in Russia using correlation analysis and factor analysis, Shankar et al. (2021) indicated that the increase of temperature increases the spreading and the decreased humidity with increase death rates. Spatial dynamics and diffusion factors across Russian regions were analyzed in a study by Zemtsov and Baburin (2020). In that study, Zemtsov and Baburin (2020) have revealed that the SARS-CoV-2 has spread faster in regions where the population has a higher susceptibility to diseases.

When India experienced the third wave of COVID-19, much effort has been put into the identification of correlations between COVID-19 and natural, socio-economic factors. Using GIS-based proximity analysis and census data of Jaipur city and socio-economic parameters (population, population density, percentage of main workers, and percentages of literates), Kanga et al. (2021) researched the risk of COVID-19 infection utilizing integrated hazard and vulnerability components associated with this pandemic for effective risk mitigation. Also in India, using a GIS-based geostatistical approach, risk analysis of COVID-19 infections in Kolkata Metropolitan city was carried out by Nath et al. (2021). With the help of GIS-based approaches in combination with related socio-economic variables, extensive studies on the risk assessment to COVID-19 infection have been conducted in many badly-affected countries by COVID-19 such as the United States (Ali et al. 2021b; DuClos et al. 2021), Italy (Tiboni et al. 2020), England (Sartorius et al. 2021), Brazil (Gomes et al. 2020; Martines et al. 2021), Peru (Badillo-Rivera et al. 2020), India (Kanga et al. 2021; Nath et al. 2021) and Bangladesh (Masrur et al. 2020; Rahman et al. 2021a).

APPLICATIONS OF REMOTE SENSING IN THE STUDY OF THE COVID-19 PANDEMIC

Studies of impacts on water quality

When the SARS-CoV-2 virus was initially identified in December 2019 in Wuhan city, China, and quickly spread throughout China Sivakumar (2021) point out that the spread of COVID-19 will increase the water demand and worsen the water quality, leading to additional challenges in water. It is, therefore, the impacts of the COVID-19 pandemic on water quality employing remote sensing techniques have been studied by many authors in China. One of the first studies on the impacts of the COVID-19 on water quality in China was carried out by Avtar et al. (2020) to quantitatively estimate the chlorophyll-a (Chl-a) concentrations in different lake bodies of Wuhan, China. In that study, Avtar et al. (2020) concluded that there was an elevated concentration of Chl-a during the COVID-19 lockdown. Also in Wuhan city, Sun et al. (2021) employed multi-sensor satellite images (Landsat-8/OLI, Sentinel-2/MSI, and HY-1C/CZI) to estimate the turbidity of lakes. It was found that the mean turbidity showed a 24.9% decline from 33.4 NTU to 25.1 NTU after the lockdown in Wuhan, which dropped 16.0% compared to that in the previous year (Sun et al. 2021). Later, when investigating the lockdown effects of the COVID-19 on total suspended solids (TSS) concentrations in the Lower Min River (China) during COVID-19 using different multi-temporal optical remotely sensed images acquired from November 2019 to April 2020 such as Landsat-5 Thematic Mapper (TM), Landsat-8 Operational Land Imager (OLI), and China's GaoFen-1 (GF-1) Wide Field of View (WFV) images, Xu et al. (2021) indicated that the lockdown measures have resulted in a 48% fall in TSS concentrations in February 2020. Xu et al. (2021) also concluded that industrial production, social and economic activities, and river shipping appear to be the main factors contributing to the river's TSS decline in the lockdown period. These findings were consistent with those reported in a most recent study of Liu et al. (2022) that COVID-19 lockdown improved river water quality in China.

After the SARS-CoV-2 virus quickly spread across the globe, this problem has received much attention from several authors in the worst-affected countries such as India, Spain, and Italy. To understand the effects of COVID-19 lockdown, Wagh et al. (2021) assessed the indicative lake water quality for the Lake Hussain Sagar (India) using Landsat-8 sensor Operational Land Imager (OLI). This study results have shown that there were a reduction in Chlorophyll-a (Chl-a) and Colored Dissolved Organic Matter (CDOM) concentrations and a significant reduction in lake water pollution (Wagh et al. 2021). From the above discussion, it can be concluded that there has been an improvement in the water quality during the COVID-19 lockdown. These findings were consistent with those reported by many studies (Arif et al. 2020; Najah et al. 2021; Yunus et al. 2020). In this study, Adwibowo (2020) investigated the effects of social distancing on water quality in the Jakarta coast based on remote sensing data captured by Copernicus Sentinel-3B Ocean and Land Color Instrument in January and February of 2020, Adwibowo (2020) figured out that there were reductions of levels and areas of chlorophyll-a in the coast as a function of social distancing and activity restrictions. Weeks later, with the help of Sentinel-2A images and the ArcGIS software, Parra Boronat (2020) conducted a study on the effects of before (since February 3rd, 2020) and during (until June 22nd, 2020) the quarantine caused by COVID-19 on the Alboran Sea (Spain). The study results of Parra Boronat (2020) indicated that seawater quality has been improved after the quarantine caused by COVID-19. Later, to study the impacts of the 2020 COVID-19 lockdown and the 2019 extreme flood in the Venice lagoon (northeast Italy), Niroumand-Jadidi et al. (2020) employed Planet Scope imagery to retrieve water quality. The results of Niroumand-Jadidi et al. (2020) have shown that a remarkable reduction of the turbidity during the lockdown, due to the COVID-19 pandemic and capture the high values of total suspended matter (TSM) during the flood condition. Using Sentinel-2A, -2B, and optical satellite data, Tripathi et al. (2020) showed that the Ganga River's water quality has been improved during COVID-19 lockdowns in India (24th March to 18th May 2020) while comparing with the normal days.

Studies of impacts on air quality

In the early stages of the COVID-19 pandemic initially discovered in Wuhan city, PR China, nitrogen dioxide (NO_2) concentrations estimated from remotely sensed images had been proved to fall by as much as 30% across China and by as much as 50% across areas of central Europe (NASA 2020). Later, one of the first studies on the impacts of the COVID pandemic on air quality was carried out by Talukdar et al. (2020). When modeling the global air quality conditions in the perspective of COVID-19 stimulated lockdown periods using MERRA-2and AIRS data, Talukdar et al. (2020) concluded that amid lockdown aerosol optical depth (AOD), sulfur dioxide (SO_2), ozone, carbon monoxide (CO), particulate matter ($PM_{2.5}$), and black carbon (BC) concentration level have been significantly reduced in fully lockdown countries. Later, studies on specific countries and regions through remotely sensed images were gradually reported. One of the Google Scholar rankings of most highly cited studies on spatio-temporal patterns of COVID-19 impact on human activities and environment in mainland China using nighttime light and air quality data was carried out by Liu et al. (2020). In that study, Liu et al. (2020) discovered a significant decreasing trend in the daily average Air Quality Index for mainland China from January to March 2020, with cleaner air in most provinces during February and March, compared to January 2020. With the help of satellite data, Zheng et al. (2020) estimated the decline and rebound in China's CO_2 emissions during the COVID-19 pandemic. Similar to those reported in a study by Zheng et al. (2020), Chen et al. (2021) also revealed the driving force of China's CO_2 emissions fell by more than 40% compared with the same period in 2019 when the city was closed from the end of January to the beginning of 2020.

Using the ground-based remote sensing techniques, Ionov et al. (2021) found that there was a decrease in CO_2 emission obtained during the COVID-19 lockdown period in 2020 and the same period of 2019 in the city of St. Petersburg, Russia. Singh et al. (2020) explored the dynamics of different air pollutants and qualitatively highlight potential links with COVID-19 pressures during different phases of the pandemic in Russia using Sentinel-5P based datasets. It was found that regional concentrations of NO_2 and O_3 increased significantly, in some cases by more than 50% during the "lockdown" in Russia. Employing OMI and AIRS data to estimate the extent of the reduction of major pollutants such as carbon monoxide, nitrogen dioxide, and sulfur dioxide in the south-east Asian regions from January to April 2020, Metya et al. (2020) discovered air quality improved in India and China during the COVID-19 outbreak in which NO_2 was reduced the most; CO to some extent and SO_2 experienced a nominal reduction. Similar to those reported by Metya et al. (2020), there were also a decrease in NO_2 in the Beijing-Tianjin-Hebei region and most of Northeast and Central China during COVID-19 (Nichol et al. 2020) and drastic reductions in NO_2 (up to -54.3%) in the urban area during partial lockdown (Nakada and Urban 2020). Using low spatial resolution images, Das et al. (2020) have shown that most of the countries, for example, Italy, Spain, Germany, the UK, the USA, Russia, India, Mexico, China, Australia, Brazil show a decreasing trend of NO_2 during COVID-19 lockdown in March 2020 when comparing with those obtained from the previous year. Most recently, when investigating the COVID-19 transmission change under different lockdown scenarios in Dhaka city, Bangladesh, study results of Rahman et al. (2021b) showed that overall, 26, 20.4, 17.5, 9.7, and 8.8% declined in $PM_{2.5}$, NO_2, SO_2, O_3, and CO concentrations, respectively, in Dhaka City during the partial and full lockdown compared to the period before the lockdown. Late work using different types of remotely sensed images also confirmed the air quality improvement during the COVID-19 lockdown, quarantine, and social distancing, with studies from badly affected countries such as England (Wyche et al. 2021), Italy (Filippini et al. 2020; Sannino et al. 2020), Brazil (Brito et al. 2020), and most recently India (Naqvi et al. 2021; Sathe et al. 2021).

Studies of other impacts on the environment

Apart from the main impacts on water and air quality as reviewed above, using remotely sensed images, many studies have been conducted on the other environmental impacts of the COVID-19 pandemic such as urban heat islands (Ali et al. 2021a; Alqasemi et al. 2021; Teufel et al. 2021) and ecology (Firozjaei et al. 2021). In the study of urban heat islands, when conducting a study on the remote sensing-based assessment of changes in urban heat island effect associated with the lockdown implementations to retard the spread of the COVID-19 virus in Pakistan, Ali et al. (2021a) had come to a conclusion that restrictions on transportation in the cities resulted in an evident drop in the surface urban heat island effect, particularly in megacities. This finding is consistent with those recently reported in studies of Alqasemi et al. (2021) using the Level 2 Sentinel 5P data in the United Arab Emirates and of Teufel et al. (2021) using MODIS images in Montreal (Canada). Most recently, in the study of ecological status, the impact of the COVID-19 lockdowns on urban surface ecological status in Milan and Wuhan cities was assessed in the research of Firozjaei et al. (2021). It was found that, due to the COVID-19 lockdowns, built-up, bare soil, and green spaces for Milan and Wuhan dramatically decreased (Firozjaei et al. 2021). To investigate the effect of lockdown during COVID-19 on land surface temperature using the TIRS sensor data acquired during the COVID-19 lockdown and post-lockdown in Dehradun city, India, Maithani et al. (2020) discovered that there was an increase in a number of hot spots accompanied by a decrease in thermal comfort level post-lockdown. In Russia, one of the most affected country by COVID-19, when studying the reduction of surface radiative forcing observed from remote sensing data during global COVID-19 lockdown in April 2020, Mazhar et al. (2021) revealed that aerosol optical depth and NO_2 shows a significant increase in some part of Russia. Also in Russia, when comparing environmental noise measurements in urban conditions before and during the COVID-19 period, Vasilyev (2021) indicated that transport noise level is reduced, but the industrial noise level is almost the same, especially in low-frequency range. These findings were also consistent with those reported in the worst-affected countries such as China (Fan et al. 2020; Filonchyk et al. 2020), the United States (Acharya et al. 2021; Wei et al. 2020), and European countries (Li et al. 2020).

CONCLUSIONS

This study is an addition to studies of the applications of GIS and remote sensing on the COVID-19 pandemic. Two themes of GIS and RS-related applications are grouped into six categories of the COVID-19-related studies including spatio-temporal changes, WebGIS-based mapping, the identification of the correlation between the COVID-19 pandemic and natural, socio-economical variables using GIS, and the use of remote sensing to assess the environmental impacts of the COVID-19. GIS methods play an important role in COVID-19 related-decision-making, more importantly, social mobilization and community responses. COVID-19 studies with remote sensing can be an effective tool in the assessment of the impacts of COVID-19. This study provides insight and a better understanding of the applications of GIS and RS on studies of the COVID-19 pandemic. It can be concluded from this review that both GIS and RS have played an important role in many aspects of COVID-19 studies, especially in the fight against COVID-19.

AUTHOR CONTRIBUTIONS

Quoc-lap Kieu conceived, designed, and prepared the research. Tien-thanh Nguyen carried out the formal analysis, wrote and edited the manuscript. Anh-huy Hoang supervised the research and provided conceptual advice. All authors discussed the results, implications and commented on the manuscript at all stages.

REFERENCES

Acharya P et al. (2021). Revisiting the levels of Aerosol Optical Depth in South-Southeast Asia, Europe and USA amid the COVID-19 pandemic using satellite observations Environmental research,193(110514).

Adwibowo A (2020). Does social distancing have an effect on water quality?: An evidence from Chlorophyll-a level in the water of populated Southeast Asian coasts.

Ali G, Abbas S, Qamer F.M, Wong M.S, Rasul G., Irteza S.M, Shahzad N. (2021a). Environmental impacts of shifts in energy, emissions, and urban heat island during the COVID-19 lockdown across Pakistan Journal of Cleaner Production, 291(125806).

Ali T., Mortula M., Sadiq R. (2021b). GIS-based vulnerability analysis of the United States to COVID-19 occurrence Journal of Risk Research, 1-16.

Alqasemi A.S., Hereher M.E., Kaplan G., Al-Quraishi A.M.F., Saibi H. (2021). Impact of COVID-19 lockdown upon the air quality and surface urban heat island intensity over the United Arab Emirates Science of The Total Environment, 767(144330).

Amdaoud M., Arcuri G., Levratto N. (2021). Are regions equal in adversity? A spatial analysis of spread and dynamics of COVID-19 in Europe The European Journal of Health Economics, 1-14.

Arif M., Kumar R., Parveen S., Verma N. (2020). Reduction in water pollution in Yamuna river due to lockdown under COVID-19 pandemic ChemRxiv Preprint.

Avtar R., Kumar P., Supe H., Jie D., Sahu N., Mishra B.K., Yunus A.P. (2020). Did the COVID-19 lockdown-induced hydrological residence time intensify the primary productivity in lakes? Observational results based on satellite remote sensing Water, 12(2573).

Bachilo E., Barylnik J., Shuldyakov A., Efremov A., Novikov D. (2020). Mental health of medical workers during the COVID-19 pandemic in Russia: Results of a cross-sectional study medRxiv.

Badillo-Rivera E., Fow-Esteves A., Alata-López F., Virú-Vásquez P., Medina-Acuña M. (2020). Environmental and social analysis as risk factors for the spread of the novel coronavirus (SARS-CoV-2). using remote sensing, GIS and analytical hierarchy process (AHP): Case of Peru medRxiv.

Bag R., Ghosh M., Biswas B., Chatterjee M. (2020). Understanding the spatio–temporal pattern of COVID–19 outbreak in India using GIS and India's response in managing the pandemic Regional Science Policy & Practice, 12, 1063-1103.

Bhunia G.S., Roy S, Shit PK (2021). Spatio-temporal analysis of COVID-19 in India–a geostatistical approach Spatial Information Research, 1-12.

Bisanzio D., Kraemer M.U., Bogoch II, Brewer T., Brownstein J.S., Reithinger R. (2020). Use of Twitter social media activity as a proxy for human mobility to predict the spatiotemporal spread of COVID-19 at global scale Geospatial health 15.

Boulos M.N.K., Geraghty E.M. (2020). Geographical tracking and mapping of coronavirus disease COVID-19/severe acute respiratory syndrome coronavirus 2 (SARS-CoV-2) epidemic and associated events around the world: how 21st century GIS technologies are supporting the global fight against outbreaks and epidemics. BioMed Central.

Brito P.L., Kuffer M., Koeva M., Pedrassoli J.C., Wang J., Costa F., Freitas A.Dd. (2020). The Spatial Dimension of COVID-19: The Potential of Earth Observation Data in Support of Slum Communities with Evidence from Brazil ISPRS International Journal of Geo-Information, 9(557).

Castro M.C. et al. (2021). Spatiotemporal pattern of COVID-19 spread in Brazil Science.

Chen J., Gao M., Huang S., Hou W. (2021). Application of remote sensing satellite data for carbon emissions reduction Journal of Chinese Economic and Business Studies, 1-9.

Chen Z-L et al. (2020). Distribution of the COVID-19 epidemic and correlation with population emigration from Wuhan, China Chinese medical journal.

Cicalò E., Valentino M. (2019). Mapping and visualisation on of health data. The contribution on of the graphic sciences to medical research from New York yellow fever to China Coronavirus Disegnarecon, 12:12-11-12.19.

Das R.D., Bandopadhyay S., Das M., Chowdhury M. (2020). Global Air Quality Change Detection During Covid-19 Pandemic Using Space-Borne Remote Sensing and Global Atmospheric Reanalysis. In: 2020 IEEE India Geoscience and Remote Sensing Symposium (InGARSS), IEEE, 158-161.

Davies T.M., Lawson A.B. (2019). An evaluation of likelihood-based bandwidth selectors for spatial and spatiotemporal kernel estimates Journal of Statistical Computation and Simulation, 89(1131-1152).

Dong E., Du H., Gardner L. (2020). An interactive web-based dashboard to track COVID-19 in real time The Lancet infectious diseases, 20(533-534).

DuClos C et al. (2021). Peer Reviewed: Mapping Chronic Disease Risk Factors With ArcGIS Online in Support of COVID-19 Response in Florida Preventing Chronic Disease 18.

Elson R., Davies T.M., Lake I.R., Vivancos R., Blomquist P.B., Charlett A., Dabrera G. (2021). The spatio-temporal distribution of COVID-19 infection in England between January and June 2020 Epidemiology & Infection 149.

Fan C., Li Y., Guang J., Li Z., Elnashar A., Allam M., de Leeuw G. (2020). The impact of the control measures during the COVID-19 outbreak on air pollution in China Remote Sensing, 12(1613).

Feng Z., Xiao C., Li P., You Z., Yin X., Zheng F. (2020). Comparison of spatio-temporal transmission characteristics of COVID-19 and its mitigation strategies in China and the US Journal of Geographical Sciences, 30(1963-1984).

Filippini T., Rothman K.J., Goffi A., Ferrari F., Maffeis G., Orsini N., Vinceti M. (2020). Satellite-detected tropospheric nitrogen dioxide and spread of SARS-CoV-2 infection in Northern Italy Science of The Total Environment, 739(140278).

Filonchyk M., Hurynovich V., Yan H., Gusev A., Shpilevskaya N. (2020). Impact assessment of COVID-19 on variations of SO2, NO2, CO and AOD over East China Aerosol and Air Quality Research, 20, 1530-1540.

Firozjaei M.K., Fathololomi S., Kiavarz M., Arsanjani J.J., Homaee M., Alavipanah S.K. (2021). Modeling the impact of the COVID-19 lockdowns on urban surface ecological status: A case study of Milan and Wuhan cities Journal of environmental management, 286(112236).

Franch-Pardo I., Napoletano B.M., Rosete-Verges F., Billa L. (2020). Spatial analysis and GIS in the study of COVID-19. A review Science of The Total Environment, 739 (140033).

Gao S., Rao J., Kang Y., Liang Y., Kruse J. (2020). Mapping county-level mobility pattern changes in the United States in response to COVID-19 SIGSpatial Special, 12, 16-26.

Gelfand M.J. et al. (2021). The relationship between cultural tightness–looseness and COVID-19 cases and deaths: a global analysis The Lancet Planetary Health, 5, e135-e144.

Giuliani D., Dickson M.M., Espa G., Santi F. (2020). Modelling and predicting the spatio-temporal spread of coronavirus disease 2019 (COVID-19) in Italy Available at SSRN 3559569.

Gomes D. et al. (2020). Risk clusters of COVID-19 transmission in northeastern Brazil: prospective space–time modelling Epidemiology & Infection 148.

Graves B.A. (2012). A model for assessment of potential geographical accessibility: a case for GIS Online Journal of Rural Nursing and Health Care, 9(6-55).

Gross B. et al. (2020). Spatio-temporal propagation of COVID-19 pandemics EPL (Europhysics Letters), 131, 8003.

Guan W-j et al. (2020). Clinical characteristics of coronavirus disease 2019 in China New England journal of medicine, 382, 1708-1720.

He J. et al. (2020). Comparative infection modeling and control of COVID-19 transmission patterns in China, South Korea, Italy and Iran Science of the Total Environment 747:141447.

Ionov D.V. et al. (2021). The CO 2 integral emission by the megacity of St. Petersburg as quantified from ground-based FTIR measurements combined with dispersion modelling Atmospheric Chemistry and Physics Discussions:1-29.

Kanga S., Meraj G., Farooq M., Nathawat M., Singh S.K. (2021). Analyzing the Risk to COVID–19 Infection using Remote Sensing and GIS Risk Analysis.

Kim S., Castro M.C. (2020). Spatiotemporal pattern of COVID-19 and government response in South Korea (as of May 31, 2020) International Journal of Infectious Diseases, 98, 328-333.

Kodge B. (2021). A review on current status of COVID19 cases in Maharashtra state of India using GIS: a case study Spatial Information Research, 29, 223-229.

Kuchler T., Russel D., Stroebel J. (2020). The geographic spread of COVID-19 correlates with the structure of social networks as measured by Facebook. National Bureau of Economic Research.

Kuznetsov I., Panidi E., Kolesnikov A., Kikin P., Korovka V., Galkin V. (2020a). Gis-based infectious disease data management on a city scale, case study of St. Petersburg, Russia The International Archives of Photogrammetry, Remote Sensing and Spatial Information Sciences, 43, 1463-1467.

Kuznetsov I., Panidi E., Korovka V., Galkin V., Voronov D. (2020b). Web-based representation and management of infectious disease data on a city scale, case study of St. Petersburg, Russia The International Archives of Photogrammetry, Remote Sensing and Spatial Information Sciences, 44, 87-91.

Lee W. et al. (2020). COVID-19 in South Korea: epidemiological and spatiotemporal patterns of the spread and the role of aggressive diagnostic tests in the early phase International journal of epidemiology, 49, 1106-1116.

Li W., Thomas R., El-Askary H., Piechota T., Struppa D., Ghaffar K.A.A. (2020). Investigating the significance of aerosols in determining the coronavirus fatality rate among three European Countries Earth Systems and Environment, 4, 513-522.

Liu D., Yang H., Thompson J.R., Li J., Loiselle S., Duan H. (2022). COVID-19 lockdown improved river water quality in China Science of The Total Environment, 802(149585).

Liu Q. et al. (2020). Spatiotemporal Patterns of COVID-19 Impact on Human Activities and Environment in China Using Nighttime Light and Air Quality Data arXiv preprint arXiv:200502808.

Maithani S., Nautiyal G., Sharma A. (2020). Investigating the effect of lockdown during COVID-19 on land surface temperature: study of Dehradun city, India Journal of the Indian Society of Remote Sensing, 48, 1297-1311.

Martines M.R., Ferreira R.V., Toppa R.H., Assunção L., Desjardins M.R., Delmelle E.M. (2021). Detecting space–time clusters of COVID-19 in Brazil: mortality, inequality, socioeconomic vulnerability, and the relative risk of the disease in Brazilian municipalities Journal of Geographical Systems, 23, 7-36.

Masrur A., Yu M., Luo W., Dewan A. (2020). Space-time patterns, change, and propagation of COVID-19 risk relative to the intervention scenarios in Bangladesh International journal of environmental research and public health, 17(5911).

Mazhar U., Jin S., Bilal M., Ali M.A., Khan R. (2021). Reduction of surface radiative forcing observed from remote sensing data during global COVID-19 lockdown Atmospheric Research, 105729.

Meng T. (2021). Clusters in the Spread of the COVID-19 Pandemic: Evidence From the G20 Countries Frontiers in Public Health, 8(948).

Metya A., Dagupta P., Halder S., Chakraborty S., Tiwari Y.K. (2020). COVID-19 lockdowns improve air quality in the South-East Asian regions, as seen by the remote sensing satellites Aerosol and Air Quality Research, 20, 1772-1782.

Mollalo A., Vahedi B., Rivera K.M. (2020). GIS-based spatial modeling of COVID-19 incidence rate in the continental United States Science of the total environment, 728(138884).

Momynaliev K., Khoroshun D., Akimkin V. (2021). Web-queries as an evaluation marker for epidemiological situation of SARS-COV-2 infection in Russia Antimicrobial Resistance and Infection Control.

Mooney P., Juhász L (2020). Mapping COVID-19: How web-based maps contribute to the infodemic Dialogues in Human Geography, 10,265-270.

Najah A. et al. (2021). Surface water quality status and prediction during movement control operation order under COVID-19 pandemic: Case studies in Malaysia International Journal of Environmental Science and Technology, 18, 1009-1018.

Nakada L.Y.K., Urban R.C. (2020). COVID-19 pandemic: Impacts on the air quality during the partial lockdown in São Paulo state, Brazil Science of the Total Environment, 730, 139087.

Naqvi H.R., Datta M., Mutreja G., Siddiqui M.A., Naqvi D.F., Naqvi A.R. (2021). Improved air quality and associated mortalities in India under COVID-19 lockdown Environmental Pollution, 268, 115691.

NASA (2020). NASA, ESA, JAXA Release Global View of COVID-19 Impacts. https://svs.gsfc.nasa.gov/13647. [Accessed May 8, 2021].

Nath B., Majumder S., Sen J., Rahman M.M. (2021). Risk Analysis of COVID–19 Infections in Kolkata Metropolitan City: A GIS–Based Study and Policy Implications GeoHealth, 5, e2020GH000368.

Nekliudov N.A. et al. (2020). Excessive media consumption about COVID-19 is associated with increased state anxiety: outcomes of a large online survey in Russia Journal of medical Internet research, 22, e20955.

Nichol J.E., Bilal M., Ali M., Qiu Z. (2020). Air pollution scenario over China during COVID-19 Remote Sensing, 12, 2100.

Niroumand-Jadidi M., Bovolo F., Bruzzone L., Gege P. (2020). Physics-based bathymetry and water quality retrieval using planetscope imagery: Impacts of 2020 Covid-19 lockdown and 2019 extreme flood in the Venice Lagoon Remote Sensing, 12, 2381.

Onafeso O.D. et al. (2021). Geographical trend analysis of COVID-19 pandemic onset in Africa Social Sciences & Humanities Open, 4, 100137.

Oto-Peralías D. (2020). Regional correlations of COVID-19 in Spain.

Parra Boronat M. (2020). Analysis of the evolution of sea water quality in the Spanish coast from satellite images before and during the quarantine caused by COVID-19.

Pramanik M., Udmale P., Bisht P., Chowdhury K., Szabo S., Pal I. (2020). Climatic factors influence the spread of COVID-19 in Russia International journal of environmental health research, 1-15.

Rahman M.H., Zafri N.M., Ashik F.R., Waliullah M., Khan A. (2021a). Identification of risk factors contributing to COVID-19 incidence rates in Bangladesh: A GIS-based spatial modeling approach Heliyon, 7, e06260.

Rahman M.S., Azad M.A.K., Hasanuzzaman M., Salam R., Islam A.R.M.T., Rahman M.M., Hoque M.M.M. (2021b). How air quality and COVID-19 transmission change under different lockdown scenarios? A case from Dhaka city, Bangladesh Science of The Total Environment, 762(143161).

Rose-Redwood R. et al. (2020). Geographies of the COVID-19 pandemic Dialogues in Human Geography, 10(97-106).

Rossman H. et al. (2020). A framework for identifying regional outbreak and spread of COVID-19 from one-minute population-wide surveys Nature Medicine, 26,634-638.

Rui R., Tian M., Tang M.-L., Ho GT-S., Wu C-H. (2021). Analysis of the spread of COVID-19 in the USA with a spatio-temporal multivariate time series model International Journal of Environmental Research and Public Health, 18(774).

Saeed U., Sherdil K., Ashraf U., Younas I., Butt H., Ahmad S. (2021). Identification of potential lockdown areas during COVID-19 transmission in Punjab, Pakistan Public health, 190, 42-51.

Sannino A., D'Emilio M., Castellano P., Amoruso S., Boselli A. (2020). Analysis of Air Quality during the COVID-19 Pandemic Lockdown in Naples (Italy) Aerosol and Air Quality Research, 20.

Sartorius B., Lawson A., Pullan R. (2021). Modelling and predicting the spatio-temporal spread of COVID-19, associated deaths and impact of key risk factors in England Scientific reports, 11, 1-11.

Sathe Y., Gupta P., Bawase M., Lamsal L., Patadia F., Thipse S. (2021). Surface and satellite observations of air pollution in India during COVID-19 lockdown: Implication to air quality Sustainable cities and society, 66(102688).

Shankar K., Gnanachandrasamy G., Mahalakshmi M., Devaraj N., Prasanna M., Chidambaram S., Thilagavathi R. (2021). Meteorological parameters and COVID-19 spread-Russia a case study. In: Environmental Resilience and Transformation in Times of COVID-19. Elsevier, 179-190.

Shepherd M. (2020). Why Geography is a key-part of fighting the COVID-19 Coronavirus outbreak Forbes.

Singh R.K. et al. (2020). Prediction of the COVID-19 pandemic for the top 15 affected countries: advanced autoregressive integrated moving average (ARIMA) model JMIR public health and surveillance, 6(e19115).

Sivakumar B. (2021). COVID-19 and water. Springer.

Sun X., Liu J., Wang J., Tian L., Zhou Q., Li J. (2021). Integrated monitoring of lakes' turbidity in Wuhan, China during the COVID-19 epidemic using multi-sensor satellite observations International Journal of Digital Earth, 14(443-463).

Talukdar S., Mahato S., Pal S., Debanshi S., Das P., Rahman A. (2020). Modelling the Global Air Quality Conditions in Perspective of COVID-19 Stimulated Lockdown Periods Using Remote Sensing Data.

Teufel B. et al. (2021). Impact of COVID-19-Related Traffic Slowdown on Urban Heat Characteristics Atmosphere, 12(243).

Tiboni M., Pezzagno M., Vetturi D., Alexander C., Botticini F. (2020). Data analysis and mapping for monitoring health risk. What has the spread of the Covid-19 pandemic in northern Italy taught us? TeMA-Journal of Land Use, Mobility and Environment, 343-360.

Tripathi G., Pandey A.C., Parida B.R. (2020). Spatio-Temporal Analysis of Turbidity in Ganga River in Patna, Bihar Using Sentinel-2 Satellite Data Linked with Covid-19 Pandemic. In: 2020 IEEE India Geoscience and Remote Sensing Symposium (InGARSS), IEEE, 29-32.

United Nations (2020). The Social Impact of COVID-19. https://www.un.org/development/desa/dspd/2020/04/social-impact-of-covid-19/. [Accessed May 2021].

Vasilyev A. (2021). EXPERIMENTAL RESEARCH OF ENVIRONMENTAL NOISE IN URBAN CONDITIONS BEFORE AND DURING COVID-19 PERIOD ON THE EXAMPLE OF SAMARA REGION OF RUSSIAN FEDERATION Journal Akustika, 39.

Viana J., Santos J.V., Neiva R.M., Souza J., Duarte L., Teodoro A.C., Freitas A. (2017). Remote sensing in human health: A 10-year bibliometric analysis Remote Sensing, 9(1225).

Wagh P., Sojan J.M., Babu S.J., Valsala R., Bhatia S., Srivastav R. (2021). Indicative Lake Water Quality Assessment Using Remote Sensing Images-Effect of COVID-19 Lockdown Water, 13(73).

Wang Y., Liu Y., Struthers J., Lian M. (2021). Spatiotemporal characteristics of the COVID-19 epidemic in the United States Clinical infectious diseases, 72, 643-651.

Wei Z., Kondragunta S., Yang K., Zhang H., McDonald B.C. (2020). Correlating Economic Activity Indicators and Tropospheric Column Nitrogen Dioxide during COVID-19 Pandemic in the United States. In: AGU Fall Meeting Abstracts, A005-0026.

WHO (2020). Report of the WHO-China Joint Mission on Coronavirus Disease 2019 (COVID-19). https://www.who.int/docs/default-source/coronaviruse/who-china-joint-mission-on-covid-19-final-report.pdf. [Accessed May 2020]

WHO (2021). WHO Coronavirus (COVID-19) Dashboard. https://covid19.who.int/. [Accessed October 2021].

Wyche K., Nichols M., Parfitt H., Beckett P., Gregg D., Smallbone K., Monks P. (2021). Changes in ambient air quality and atmospheric composition and reactivity in the South East of the UK as a result of the COVID-19 lockdown Science of the Total Environment, 755(142526).

Xu C., Zhang X., Wang Y. (2020). Mapping of health literacy and social panic via web search data during the COVID-19 public health emergency: infodemiological study Journal of Medical Internet Research, 22(e18831).

Xu H., Xu G., Wen X., Hu X., Wang Y. (2021). Lockdown effects on total suspended solids concentrations in the Lower Min River (China) during COVID-19 using time-series remote sensing images International Journal of Applied Earth Observation and Geoinformation, 98(102301).

Yunus A.P., Masago Y., Hijioka Y. (2020). COVID-19 and surface water quality: Improved lake water quality during the lockdown Science of the Total Environment, 731(139012).

Zemtsov S., Baburin V. (2020). COVID-19: Spatial dynamics and diffusion factors across Russian regions Regional Research of Russia, 10(273-290).

Zheng B. et al. (2020). Satellite-based estimates of decline and rebound in China's CO2 emissions during COVID-19 pandemic Science Advances 6:eabd4998.

RESEARCH PAPER

CROWDSOURCING DATA TO VISUALIZE POTENTIAL HOTSPOTS FOR COVID-19 ACTIVE CASES IN INDONESIA

Noorhadi Rahardjo[1*], Djarot Heru Santosa[2], Hero Marhaento[3]
[1]Faculty of Geography, Universitas Gadjah Mada, Yogyakarta 55281, Indonesia
[2]Faculty of Cultural Sciences, Universitas Gadjah Mada, Yogyakarta 55281, Indonesia
[3]Faculty of Forestry, Universitas Gadjah Mada, Yogyakarta 55281, Indonesia
*Corresponding author: noorhadi@ugm.ac.id
Received: February 1th, 2021 / Accepted: May 25th, 2021 / Published: July 1st, 2021
https://DOI-10.24057/2071-9388-2021-011

ABSTRACT. As the COVID-19 outbreak spread worldwide, multidisciplinary researches on COVID-19 are vastly developed, not merely focusing on the medical sciences like epidemiology and virology. One of the studies that have developed is to understand the spread of the disease. This study aims to assess the contribution of crowdsourcing-based data from social media in understanding locations and the distribution patterns of COVID-19 in Indonesia. In this study, Twitter was used as the main source to retrieve location-based active cases of COVID-19 in Indonesia. We used Netlytic (www.netlytic.org) and Phyton's script namely GetOldTweets3 to retrieve the relevant online content about COVID-19 cases including audiences' information such as username, time of publication, and locations from January 2020 to August 2020 when COVID-19 active cases significantly increased in Indonesia. Subsequently, the accuracy of resulted data and visualization maps was assessed by comparing the results with the official data from the Ministry of Health of Indonesia. The results show that the number of active cases and locations are only promising during the early period of the disease spread on March – April 2020, while in the subsequent periods from April to August 2020, the error was continuously exaggerated. Although the accuracy of crowdsourcing data remains a challenge, we argue that crowdsourcing platforms can be a potential data source for an early assessment of the disease spread especially for countries lacking the capital and technical knowledge to build a systematic data structure to monitor the disease spread.

KEYWORDS: covid-19, crowdsourcing data, map visualization, netlytic, phyton, Indonesia

CITATION: Noorhadi Rahardjo, Djarot Heru Santosa, Hero Marhaento (2021). Crowdsourcing Data To Visualize Potential Hotspots For Covid-19 Active Cases In Indonesia. Geography, Environment, Sustainability, Vol.14, No 4, p. 125-130
https://DOI-10.24057/2071-9388-2021-011

ACKNOWLEDGMENTS: The authors acknowledge the Institute for Research and Community Services (LPPM) Universitas Gadjah Mada, Indonesia for providing the research grant entitled «Pemanfaatan Hasil Penelitian Dan Penerapan Teknologi Tepat Guna». We greatly appreciate Abghy Aunurrahim and Damar for their help during conducting this research.

Conflict of interests: The authors reported no potential conflict of interest.

INTRODUCTION

A coronavirus disease-19 (COVID-19) caused by a novel coronavirus has been considered the most crucial global health calamity of the century. It was started appeared in China by the end of 2019, and the first reported death from COVID-19 also in China in January 2020 (WHO 2020). The first case outside of China was found in Thailand on 13 January 2020 (Hui 2020). Ever since, the COVID-19 has become a global concern because of its high transmission rate that is from person-to-person via airborne respiratory droplets, direct contact with body fluids or secretions, or through contaminated objects (Xu et al. 2020). As results, on March 11th 2020 the World Health Organization (WHO) declared the COVID-19 outbreak as a global pandemic since it has affected all aspects of human life and has challenged health care systems worldwide (Arora et al. 2020).

With all global attentions are currently on the COVID-19, governments and the scientific community including health professionals are challenged in response to this pandemic e.g., to develop vaccines as well as curative medicines (Iyer et al. 2020). Furthermore, multidisciplinary researches on COVID-19 are then vastly developed not only focusing on the medical sciences like epidemiology and virology but also to the social behaviour issues since COVID-19 has affected much more far-reaching rather than just medical issues, like affecting social and economic of nations (Zhang and Shaw 2020).

One of the particular studies that have been demanded in COVID-19 measures are to understanding the spread of disease (Ponjavic et al. 2020). By understanding the transmission speed which the disease has spread throughout the world and visualizing the data with a clear presentation of the geographical area and time interval, it may help to clarify the extent and impact of the pandemic (Franch-Pardo et al. 2020). However, to develop such a system that integrates data structure analysis and modelling to geocoding and mapping of active cases and visualizing infection spread over time may require a large investment for hardware and software as well as man-hours that is a challenge for low- and middle-income countries like Indonesia.

In order to tackle this limitation, crowdsourcing may offer huge potential to contribute to the modelling and visualizing the spread of coronavirus. Crowdsourcing basically is a process of outsourcing a business task or activity to a network of individuals (Paniagua & Korzynski 2017). Heipke (2010) defined crowdsourcing is an effort to recruit human workers to perform tasks that are inherently hard for computers to perform, for instances sentiment analysis of text, image or video classification or tagging, and matching data records that belong to the same entity. In the geospatial study, Heike (2010) described crowdsourcing is data acquisition by large and diverse groups of people, who in many cases are not trained surveyors and who do not have special computer knowledge, using web technology. During this COVID-19 pandemic, crowdsourcing and social media have played an unprecedented role which can help understand disease dynamics in space and time when testing is limited (Al-Omoush et al. 2020). This is because social media has been the preferred platforms to communicate, collaborate, and convey a sense of unity during the times of crisis e.g., during pandemic COVID-19 (Gui et al. 2017; Abdulhamid et al. 2020).

Social media platforms such as Facebook, Instagram, and Twitter have provided direct access to account users' preferences and attitudes, algorithms mediate, and facilitate content promotion (Kulshrestha et al. 2017). This has attracted the attention of researchers from various fields including cartography to analysing and synthesizing social media data. However, like no other platforms, Twitter provides a feature called «geo-location» that is open-access information regarding the user's location when uploading information. According to Twitter (developer.twitter.com), there are three metadata sources for geo-referencing tweets that can be used for map visualization: 1) tweet location: tweets that are geo-tagged with an exact location (i.e. a single landmark with longitude and latitude coordinates) or twitter place (i.e. an area with four pairs of longitude and latitude coordinates that define a bounding box), 2) mentioned location: parsing the Tweet message for geospatial location, and 3) profile location: parsing the account-level location for locations of interest. These facilities have helped to carry out a spatial analysis as well as map visualization.

This study aims to review the implementation of crowdsourcing-based data from social media in understanding locations and the distribution patterns of COVID-19 in Indonesia. In this study, we used Twitter as crowd-sourced data to retrieve location-based active cases of COVID-19 in Indonesia. According to the latest report of statistica.com, Twitter users in Indonesia reach 13.2 Million is the seventh-largest Twitter user in the world. From these users, approximately around 80% are active users producing 5 billion tweets a year. By these large number of Twitter users in Indonesia, our hypothesis is that crowdsourcing-based data from Twitter may provide an early assessment of the disease spread in Indonesia.

MATERIALS AND METHODS

Data source

In this study, tweets contain information related to COVID-19 active cases in Indonesia were used and analysed. We used Netlytic (www.netlytic.org) to retrieve the relevant online content about COVID-19 cases including audiences' information such as username, time of publication, and locations. Netlytic is a community-supported text and social networks analyser that can capture publicly available posts from social media sites, discover popular topics, find and explore emerging themes of discussions, analyse online communication networks using social network analysis, and map geo-coded social media data (www.netlytic.org). However, since the accessible data from netlytic.org is only limited to the maximum data acquisition up to the past 7 days, we used another method by using Phyton's script namely GetOldTweets3 and pandas packages to retrieve older tweet data. We determined the range time period from January 2020 to August 2020 when COVID-19 active cases significantly increased.

In order to find related information needed, we searched queries including several keywords (some words are in Bahasa Indonesia, the national language) such as: covid, corona, pasien covid, odp, pdp, otg, virus, virus covid, physical distancing, social distancing, positif corona, psbb, new normal, pandemi, karantina, quarantine, stay at home, bantuan covid, and vaksin covid which were all posted in Indonesia. It should be noted that all data collected were publicly available and obtained legally.

Data Analysis

All tweets retrieved by data-crawling using Netlytic and Phython script was then filtered according to the required criteria such as containing chosen keywords with information of active cases of COVID-19, geo-referenced tweets, and tweeted between January 2020 and August 2020. Subsequently, selected data is transformed into a shapefile format that can be visualized in Geographic Information System (GIS) environment. In this study, we used Quantum GIS (QGIS) to carry out map editing and map visualization of the geo-referenced tweets. QGIS is a cross-platform desktop (open source) software on geographic information systems (GIS) that has been widely used worldwide to analyse spatial data (Jaya & Fajar 2019; Ahmad & Kim 2020).

The resulted data and maps were then compared with the official data from the Ministry of Health of Indonesia in order to validate the results. We used a commonly used t-test to determine whether the results from crowdsourcing data are equal with the official data. The null hypothesis is that the two means are equal, and the alternative is that they are not. In addition, we also visually observed the resulted scatter-plot graph by comparing it relative with the x = y line as well as the resulted map visualizations.

RESULTS

Data and Map visualizations

By using Netlytic and Phyton, we were able to retrieve the suspected COVID-19 active cases within thirty-four provinces in Indonesia. However, both methods worked in different time periods, which Netlytic only covered in the period from July to August 2020, while Phyton was able to cover old tweet data from January 2020 to August 2020. In total, from the Netlytic in the period July – August 2020, we discovered 89 active cases in Indonesia spread over nine provinces (see Figure 1), where Jawa Barat (West Java) province has the largest cases with 35 active cases, followed by Jawa Tengah (Central Java) and Jawa Timur (East Java) provinces. However, it should be noted that these were based on tweeted spots which in each spot often contained more than one active cases.

Different from Netlytic, by using Phyton script to crawl the old tweets, we were able to retrieve monthly information from January 2020 to August 2020. The results show that the top six provinces having the most tweets contain information about the COVID-19 active cases were all on the Java Island. DKI Jakarta, Indonesia's capitol, has consistently been the

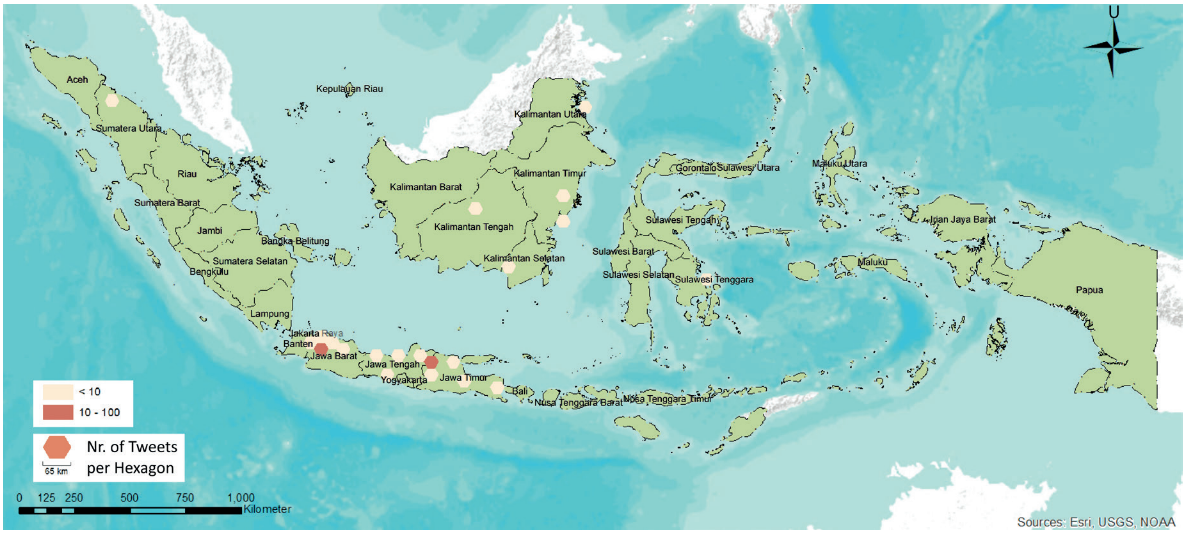

Fig. 1. Map visualization of the tweets contains information on COVID-19 active cases in Indonesia from July to August 2020 based on Netlytic

largest COVID-19 active cases in Indonesia which reach the peak reported cases on March 2020, and slowly decreased in the subsequent months. The following provinces having the largest informed COVID-19 active cases after DKI Jakarta from January 2020 to August 2020 were Banten, Jawa Barat, D.I. Yogyakarta, Jawa Timur, and Jawa Tengah (see Figure 2). Figure 3 shows the map visualization from the tweets contains information on COVID-19 active cases in Indonesia from January to August 2020 where most of the tweeted active cases were located in Java Island. Some provinces outside Java Island i.e. Sumatra Barat (West Sumatra), Papua, Kalimantan Timur (East Kalimantan), and Riau were also reported having quite high number of COVID-19 active cases but only by less than 200 tweets of cases.

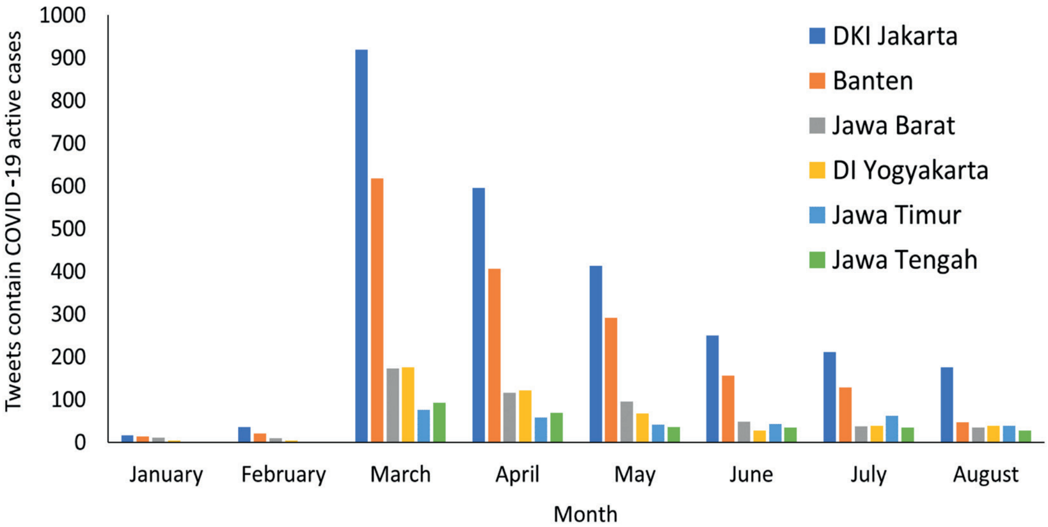

Fig. 2. Number of tweets contain information of COVID-19 active cases in the top six provinces in Indonesia

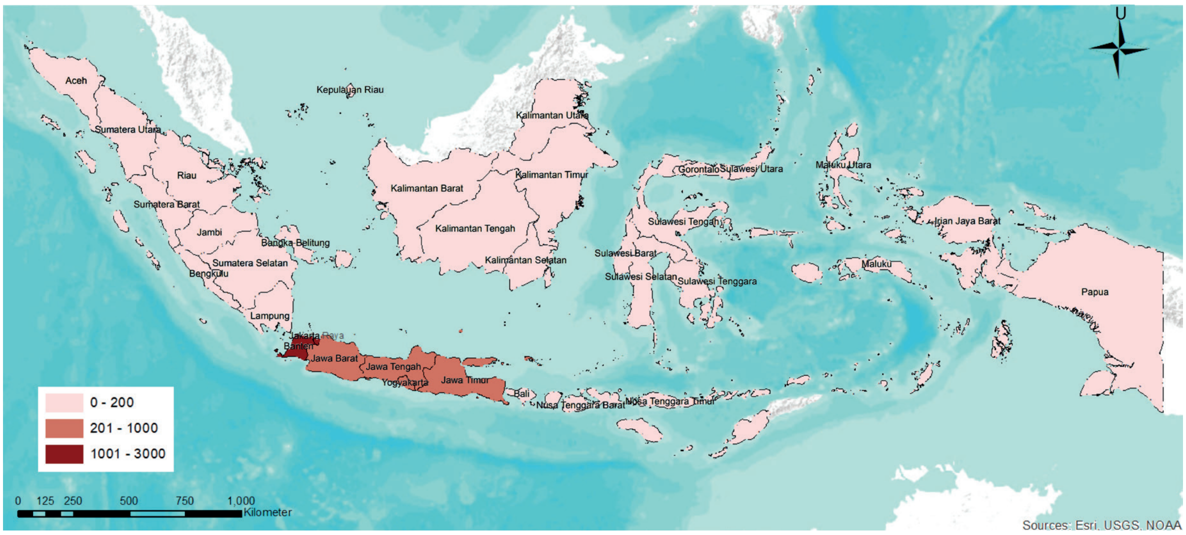

Fig. 3. Map visualization of the tweets contains information on COVID-19 active cases Indonesia from January to August 2020 based on data crawling using Phyton

Accuracy of results

We carried out the accuracy analysis by performing t-test statistic to the two sets data from crowdsource-based data (i.e. Twitter) and official data from the Ministry of Health of Indonesia. For this study, the comparisons were applied for three different periods: March – April, May – June, and July – August. The results show that in the period of March – April, the null hypothesis was accepted with the p-value was 0.736295, greater than 0.05, the applied statistic significant level. While for the subsequent period, May – June and July – August, the alternative hypothesis was accepted with the p-values for both periods were 0.004341 ($p < 0.01$) and 0.000982 ($p < 0.001$). These statistical test results show that the crowdsourcing data was relatively accurate to predict the COVID-19 active cases only for the period of March – April, while the accuracy was getting worst for the subsequent periods. By visual inspections of the scatter-plot graphs, it was observable that during the period March – April, the resulted scatter-plot was relatively closer to the x = y line (see Figure 4a). However, during the May – June period, the resulted scatter-plot was below the x = y line indicating an under-estimation from the crowdsourcing data compared to the official data (see Figure 4b). This bias due to under-estimation was exaggerated in the period of July – August (see Figure 4c).

Similar results were shown by comparing the visualization maps of COVID-19 active cases between the crowdsourcing-based data and the official data as seen in Figure 5. It was observable that in the period of March – April 2020, crowdsourcing data has comparable results with the official data, where the Java Island was the epicentre of the spread disease. However, in the subsequent periods, the crowdsourcing data were not able to match the official data due to under-estimation results. As seen in Figure 5c and 5d, while the results of crowdsourcing data visually pointed Java Island as the most findings COVID-19 active cases, the government data showed that the active cases of COVID-19 have been spread in all over Indonesia (i.e., 27 provinces out of 34 provinces) with a range of 101 – 10,000 cases/province. In the subsequent period, the differences become larger as seen in Figure 5e and 5f, which the crowdsourcing data only resulted in 7 provinces in Indonesia that have 101 – 10,000 cases/province. This is far below the government data which found 33 provinces out of 34 provinces have COVID-19 active cases more than 100 cases/province.

DISCUSSION

Research on social media and its unique communities have now been often studied (Marwick & Boyd 2011; Gaffney & Puschmann 2013). Carley et al. (2015) argue that following patterns on social media e.g. Twitter, Facebook, Instagram can help in making accurate predictions about future trends. Through social media, public involvement in the scientific processes is now openly available; not just in the data collection process, but also in the planning and data visualization (Lamoureux & Fast 2019). However, it should be noted that information spread through social media has been often inaccurate (Thomson et al. 2012), outdated, and contain irrelevant information (Acar & Muraki 2011). For this reason, it is necessary to explore to what extent the crowdsourcing data from social media can be used to provide reliable information.

In this research, we used Twitter as the main source of information to visualize potential hotspots for COVID-19 active cases in Indonesia. We found a promising result of crowdsourcing data visualisation only during the early period of COVID-19 transmission, when it was going viral on the social media of Twitter. In the subsequent periods, a

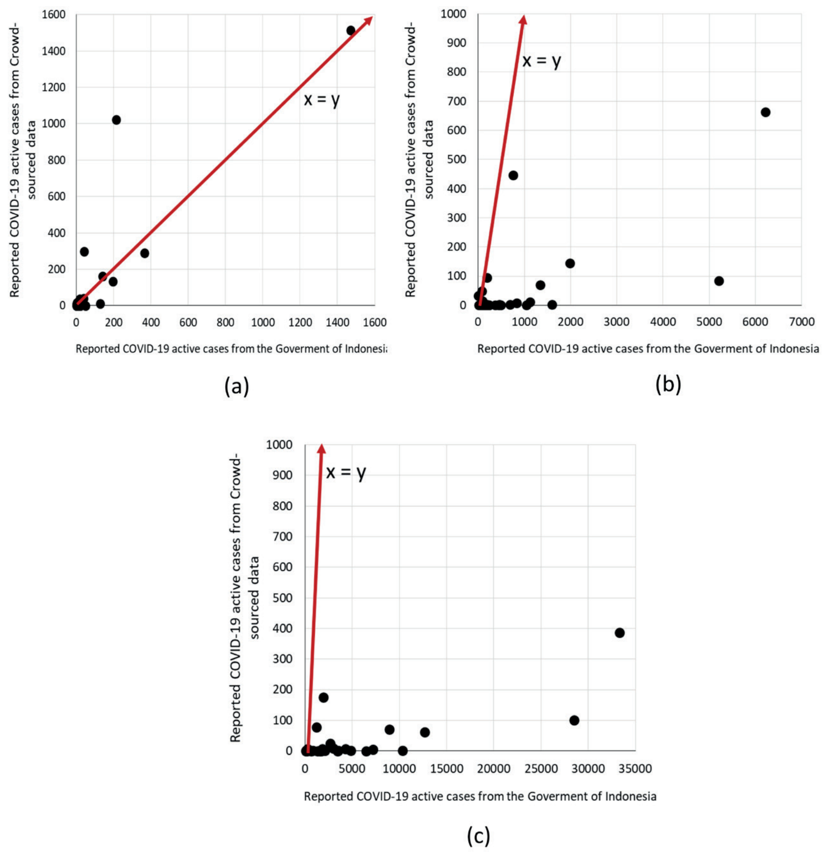

Fig. 4. Scatter-plot graphs between reported COVID-19 active cases from crowdsourcing data and government data relative to the x = y line for the period March – April 2020 (a), May – June 2020 (b), and July – August (c)

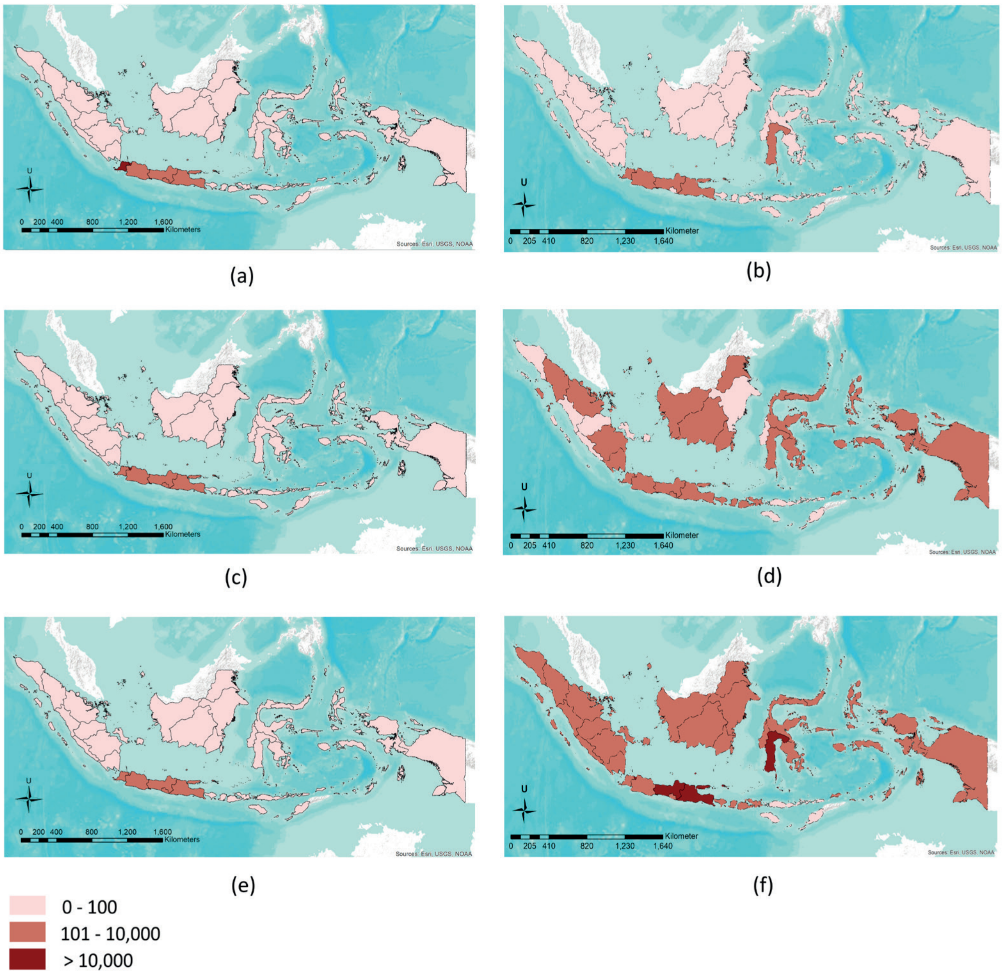

Fig. 5. Maps of COVID-19 active cases in Indonesia from March 2020 to April 2020 according to Crowdsourcing (a) and Government data (b), from May 2020 to June 2020 according to Crowdsourcing (c) and Government data (d), and from July 2020 to August 2020 according to Crowdsourcing (e) and Government data (f)

significant decrease in the accuracy was observable when it was compared to the government data. This phenomenon apparently can be explained by a social media behaviour which during a meaningful event like COVID-19 initial spread, social excitement has influenced social media user in content creation and sharing (Wakefield & Wakefield 2016). However, once the meaningful event was over, in this study the COVID-19 initial cases, the only social excitement was not sufficient to motivate content creation and sharing activities in social media resulting inaccuracies of crowdsourcing data.

Despite revealing the challenge on its accuracy, the crowdsourcing platform used and discussed in this research can be a potential source for those lacking the capital and technical knowledge to build a systematic data structure for data collection, management, and visualization platforms of the COVID-19 spread. Our findings are similar to the results of Larson (2018) and Chakraborty et al. (2020), among others that during the pandemic, crowdsourcing data can support monitoring of social distancing, contact tracing, as well as the disease spread. However, as found in our research that the accuracy of crowdsourcing data has remained questionable. This is similar to the finding of Moturu & Liu (2010) who argue that only a fair portion of social media information is useful and has proven to be a great source of knowledge, which most of the information shared should be taken carefully. One of the reasons is that much of the information shared through social media has been contributed by strangers with little or no apparent reputation to share information. For this reason, Chung et al. (2012) emphasized the importance of the source of information that transmits the news. Our results showed that crowdsourcing data make citizen science-based project more attractive and accessible to everyone. Indeed, the accuracy and information credibility remain the main issues of working with the crowdsourcing data requiring more study focusing on the information credibility and crowdsourcing data verifications.

CONCLUSIONS

In this study, we were able to visualize the distribution patterns of COVID-19 active cases in Indonesia by using crowdsourcing-based data from social media Twitter. However, based on the accuracy-test using independent t-test and visual inspection to the resulted scatter plots against the official data, it was found that the prediction is only promising during the early period of the disease spread on March – April, 2020, where most of people (i.e. netizen) tweeted about COVID-19 active cases. In the subsequent periods from April to August 2020, the prediction error was exaggerated from time to time. Although it has challenges on the data accuracy, we argue that crowdsourcing platform can be a potential data source for an early assessment of the disease spread especially for those (e.g. countries) lacking the capital and technical knowledge to build a systematic data structure.

REFERENCES

Abdulhamid N.G., Ayoung D.A., Kashefi A., & Sigweni B. (2020). A survey of social media use in emergency situations: A literature review. Information Development, DOI: 10.1177/0266666920913894.

Acar A., & Muraki Y. (2011). Twitter for crisis communication: lessons learned from Japan's tsunami disaster. International Journal of Web Based Communities, 7(3), 392-402.

Ahmad S., & Kim D.H. (2020). Quantum GIS based descriptive and predictive data analysis for effective planning of waste management. IEEE Access, 8, 46193-46205.

Al-Omoush K.S., Orero-Blat M., & Ribeiro-Soriano D. (2020). The role of sense of community in harnessing the wisdom of crowds and creating collaborative knowledge during the COVID-19 pandemic. Journal of Business Research.

Arora G., Kroumpouzos G., Kassir M., Jafferany M., Lotti T., Sadoughifar R., Sitkowska Z., Grabbe S. and Goldust M. (2020). Solidarity and transparency against the COVID–19 pandemic. Dermatologic Therapy.

Carley K.M., Malik M.M., Kowalchuck M., Pfeffer J., & Landwehr P. (2015). Twitter usage in Indonesia. Computational Analysis of Social and Organizational Systems (CASOS) Technical Report CMU-ISR-15-109. Available at SSRN 2720332.

Chakraborty K., Bhatia S., Bhattacharyya S., Platos J., Bag R., & Hassanien A.E. (2020). Sentiment Analysis of COVID-19 tweets by Deep Learning Classifiers—A study to show how popularity is affecting accuracy in social media. Applied Soft Computing, 97, 106754.

Chung C.J., Nam Y., & Stefanone M.A. (2012). Exploring online news credibility: The relative influence of traditional and technological factors. Journal of Computer–Mediated Communication, 17(2), 171-186.

Franch-Pardo I., Napoletano B.M., Rosete-Verges F., & Billa L. (2020). Spatial analysis and GIS in the study of COVID-19. A review. Science of The Total Environment, 140033.

Gaffney D., & Puschmann C. (2013). Data collection on Twitter. In K. Weller, A. Bruns, J. Burgess, M. Mahrt, & C. Puschmann (Eds.), Twitter and Society, New York: Peter Lang, 55-68.

Gui X., Kou Y., Pine K.H., & Chen Y. (2017, May). Managing uncertainty: using social media for risk assessment during a public health crisis. In Proceedings of the 2017 CHI Conference on Human Factors in Computing Systems, 4520-4533.

Heipke C. (2010). Crowdsourcing geospatial data. ISPRS Journal of Photogrammetry and Remote Sensing, 65(6), 550-557.

Hui D.S., Azhar E.I., Madani T.A., Ntoumi F., Kock R., Dar O., ... & Zumla A. (2020). The continuing 2019-nCoV epidemic threat of novel coronaviruses to global health—The latest 2019 novel coronavirus outbreak in Wuhan, China. International Journal of Infectious Diseases, 91, 264-266.

Iyer M., Jayaramayya K., Subramaniam M.D., Lee S.B., Dayem A.A., Cho S.G., & Vellingiri B. (2020). COVID-19: an update on diagnostic and therapeutic approaches. BMB reports, 53(4), 191.

Jaya M.T.S., & Fajar A.N. (2019). Analysis of The Implementation Quantum GIS: Comparative Effect and User Performance. J. Theor. Appl. Inf. Technol, 97, 2596-2605.

Kulshrestha J., Eslami M., Messias J., Zafar M.B., Ghosh S., Gummadi K.P., & Karahalios K. (2017, February). Quantifying search bias: Investigating sources of bias for political searches in social media. In Proceedings of the 2017 ACM Conference on Computer Supported Cooperative Work and Social Computing, 417-432.

Lamoureux Z. & Fast V. (2019). The tools of citizen science: An evaluation of map-based crowdsourcing platforms. Spatial Knowl. Inf. Canada, 7(4), 1.

Larson H.J. (2018). The biggest pandemic risk? Viral misinformation. Nature, 562(7726), 309-310.

Marwick A.E. & Boyd D. (2011). I tweet honestly, I tweet passionately: Twitter users, context collapse, and the imagined audience. New Media & Society, 13(1), 114-133, DOI: 10.1177/1461444810365313.

Moturu S.T., & Liu H. (2011). Quantifying the trustworthiness of social media content. Distributed and Parallel Databases, 29(3), 239-260.

Paniagua J. & Korzynski P. (2017). Social Media Crowdsourcing. E.G. Carayannis (ed.), Encyclopedia of Creativity, Invention, Innovation and Entrepreneurship. Springer Science+Business Media LLC, DOI: 10.1007/978-1-4614-6616-1_200009-1.

Ponjavic M., Karabegovic A., Ferhatbegovic E., Tahirovic E., Uzunovic S., Travar M., Pilav A., Mulić M., Karakaš S., Avdić N., Mulabdić Z., Pavić G., Bičo M., Vasilj I., Mamić D., Hukić, M. (2020). Spatio-temporal data visualization for monitoring of control measures in the prevention of the spread of COVID-19 in Bosnia and Herzegovina. Med Glas (Zenica), 17(2), 265-274.

Thomson R., Ito N., Suda H., Lin F., Liu Y., Hayasaka R., ... & Wang Z. (2012, April). Trusting Tweets: The fukushima disaster and information source credibility on Twitter. In 9th ISCRAM conference, 10.

Wakefield R., & Wakefield K. (2016). Social media network behavior: A study of user passion and affect. The Journal of Strategic Information Systems, 25(2), 140-156.

World Health Organization W. (2020). Coronavirus disease (COVID-19) pandemic. Retrieved August 12, 2020, from https://www.who.int/emergencies/diseases/novel-coronavirus-2019.

Xu C., Luo X., Yu C., & Cao S.J. (2020). The 2019-nCoV epidemic control strategies and future challenges of building healthy smart cities.

Zhang H., & Shaw R. (2020). Identifying research trends and gaps in the context of covid-19. International journal of environmental research and public health, 17(10), 3370.

RESEARCH PAPER

ASSESSING THE VULNERABILITY INDEX OF COVID-19 PANDEMIC IN INDIA

Netrananda Sahu[1*], Martand Mani Mishra[2]
[1]Assistant Professor, Department of Geography, Delhi School of Economics, University of Delhi, Delhi 110007, India
[2]Ph.D. Research Scholar, Senior Research Fellow, Department of Geography, Delhi School of Economics, University of Delhi, Delhi 110007, India
*Corresponding author: babunsahu@gmail.com
Received: May 21th, 2021 / Accepted: November 9th, 2021 / Published: December 31st, 2021
https://doi.org/10.24057/2071-9388-2021-059

ABSTRACT. The coronavirus (COVID-19) outbreak has created havoc all across the States and Union Territories (UTs) of India since its beginning on 30th January 2020. As of 1st January 2021, India has recorded 10,305,788 cases and 149,218 deaths from this deadly pandemic. It has been observed through the data; across states and UTs, the trend and pattern of this disease are not similar at all. There are many reasons for these dissimilarities which are categorized into indicators to assess the vulnerability in this study. We have examined vulnerabilities in 28 states and 8 UTs of India. Livelihood Vulnerability Index (LVI) has been applied with certain modifications to calculate the Vulnerability Index (VI). The figure resulting from the vulnerability assessment corresponds that the factors involved in the three-section exposure, sensitivity, and adaptive capacity had a significant impact on deciding the vulnerability of the population. The result identified the states and UTs which are more vulnerable and need more attention from the government and policymakers. The proposed method of study is unique in its sense as vulnerability index calculation is purely based on a secondary source of data and therefore has an expectation of a higher degree of practical application.

KEYWORDS: India, COVID-19, Exposure, Sensitivity, Adaptive Capacity, Population Density, Vulnerability Assessment

CITATION: Netrananda Sahu, Martand Mani Mishra (2021). Assessing The Vulnerability Index Of Covid-19 Pandemic In India. Geography, Environment, Sustainability, Vol.14, No 4, p. 131-139 https://doi.org/10.24057/2071-9388-2021-059

ACKNOWLEDGEMENTS: We are grateful to acknowledge the support provided by the Department of Geography, Delhi School of Economics, University of Delhi, Government of India, and www.indiastat.com

Conflict of interests: The authors reported no potential conflict of interest.

INTRODUCTION

Pathogens like viruses, bacteria, fungi, and parasites that are responsible for communicable diseases (CDS) have a long history of their inception (Freedman 1966). There has been reporting of different virus-related deadly CDS earlier like that of the Spanish Influenza, Human Immunodeficiency Virus (HIV), Ebola, and others that had affected several globally. Novel Coronavirus (SARS-CoV-2) is responsible for COVID-19, the infectious communicable disease that has been expanding across the length and breadth of the globe (Acharya and Porwal 2020; Avtar et al. 2020; Chaurasiya et al. 2020; Coronavirus Disease (COVID-19); Giovanetti et al. s2020; Lai et al. 2020; Phan et al. 2020; Tosepu et al. 2020). This rapidly spreading disease primarily travels from one infected person to the other through respiratory or saliva droplets via symptomatic, pre-symptomatic, and asymptomatic carriers (Jernigan 2020; Wiersinga et al. 2020). COVID-19 infected patients mostly experience mild to moderate respiratory illness with the serious illness being developed by those having severe underlying medical issues. The first case to be reported in the world was from the Wuhan city of China in early December 2019 (Martínez-Piédrola et al. 2021; Mazinani & Rude 2021). Since then, it has been incresing at an alarming rate with COVID-19 spreading its wings around over 86 million cases globally (Coronavirus Disease (COVID-19). The rate of its gradual expansion and accompanying consequences had resulted in the World Health Organization (WHO) declaring it as a global pandemic on 11th of March 2020. All the COVID-19 hit nations and most importantly nations with friable health infrastructure were affected accordingly (Coronavirus Disease (COVID-19); Lupia et al. 2020; Sohrabi et al. 2020).

Communicable diseases are a major public cause of concern in developing countries where available health infrastructure is not sufficient with the bulging population. These countries are more susceptible because of their high population densities, inadequate health care infrastructure, meager income, and poverty (Gupte and Mitlin 2020). India, a developing country with a population of over 1.3 billion and being home to the world's second-highest population, stands in a high-risk situation owing to its large number of reported cases of infection and death. As of September 2020, COVID-19 had spread its wings around over 32.7 million globally and over 5 million in India (Coronavirus Disease (COVID-19). The first COVID-19 case in India was reported from the state of Kerala on January 30, 2020, whose origin was Wuhan, China (Chaurasiya et al. 2020; Ogen 2020). COVID-19 has not only restricted itself to an increase in infection numbers and deaths but also has wider corresponding implications in terms of social consequences, economic repercussions, environmental changes as well political adverse (Shah and Farrow 2020).

In this article, we empirically try to show the inter-relation between COVID-19 and related vulnerabilities in the States and UTs of India. The article tries looking deeply and demarcating regions depending on the rate of exposure, sensitivity traits, and its nature to adapt. Thus, this piece of original research contributes in three ways firstly, by understanding the scenario of COVID-19 in the country and its corresponding health infrastructure, second looking at the health vulnerabilities of India, state-wise through a range of indicators thereby clearing the cloud on the country's probability to adapt to the pandemic situation and finally, developing the VI to decipher the zonation of health vulnerabilities for quick identification of problem-centric states and UTs for enacting guidelines accordingly.

MATERIAL AND METHODOLOGY

Study area

India, the study area comprises 28 states and 8 union territories located between latitudes 8°4′N and 37°6′N and longitudes 68°7′E and 97°25′E. Physiographically, India is divided into Plains, Himalayas, Plateaus, Coastal areas, Desert regions, and Islands. There is an extensive difference among the Indian states in terms of population density, age structure, social condition, and cultural diversity. The UTs of Jammu & Kashmir and Ladakh have been combined as one entity which is divided into two parts in the year 2019 (Fig. 1a). Previously these two UTs were considered as a single state and therefore some socio-economic data is not available separately for these. In this study, some UTs namely (1. Dadra and Nagar Haveli and Daman and Diu, 2. Lakshadweep) are not included due to the non-availability of COVID-19 of data.

Data collection

The basic idea of the study is to calculate the vulnerability index value for all the states and UTs based on multiple indicators that are divided into three broad categories of exposure, sensitivity, and adaptive capacity according to the IPCC concept (Hahn et al. 2009) Table 1. The dataset used in the study is obtained from secondary sources. The major sources include Central Government official publications, Census of India, (2011), and data available from the website (https://www.indiastat.com/) (Coronavirus Data India - COVID-19 Pandemic Data India with State Wise Growth Statistics Details Figures | Indiastat)

Vulnerability Analysis

Coronavirus vulnerability analysis has been done to calculate the state and UTs level vulnerability related to COVID-19 cases and deaths. Some modifications have been made in the Livelihood Vulnerability Index (LVI) method to adapt the methodology fit for our specific study. The

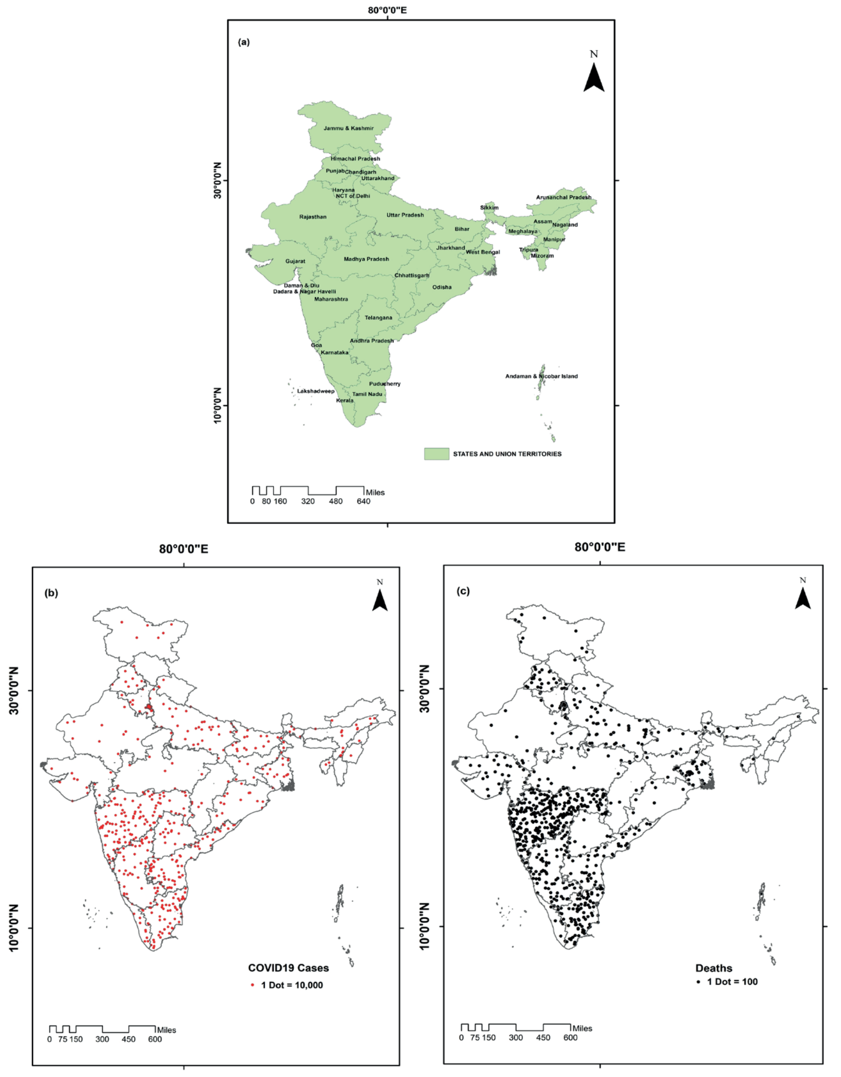

Fig. 1(a). Locational map showing Indian states and Union Territories (UTs). The name of each States and UTs are on the map is inside the administrative boundary (b) total number of COVID19 cases (c) total deaths in Indian states and UTs

stepwise calculation of the VI has been summarized below.

Steps to calculate the Vulnerability Index (VI)

Step 1: Indicators
Values for all the indicators are to be standardized for all the states.
Step 1
The steps can be broadly summarized as:

$$(Ix) = \frac{Ib - I(\min)}{I(\max) - I(\min)}$$

Where, **Ix** = Standardized value for the indicator
Ib= Value for the Indicator I for a particular state or UT, b.
I (min) = Minimum Value for the indicator across all the states and UTs
I (max) = Maximum Value for the indicator across all the states and UTs

Step 2: Profiles
Indicator index Values are combined to get the values for

$$(P) = \sum_{i=1}^{n} \frac{Indicator\ \ Index}{n} i$$

the profiles
Where, **n** – no. of indicators in the profile
Indicator Index i – Index of the i th indicator.

Step 3: Vulnerability Index: The three contributing factors are combined to calculate the VI
Vulnerability Index = (Exposure – Adaptive Capacity) x Sensitivity. The obtained data for the profile section and VI have been classify according to the natural breaks (Jenks) classification. The VI has been scaled from -1 (least vulnerable) to +1 (most vulnerable) and categorized value into four categories very low, medium, high, and very highly vulnerable blocks.

RESULT AND DISCUSSION

India has recorded the second-highest number of COVID-19 cases after the USA since the inception of the disease. Country continues to face a serious threat of outbreak not only due to its large population size, but other factors related to demographics, social negligence, and poor health infrastructure (Acharya and Porwal 2020). COVID-19 pandemic has become a serious challenge to the health and economic status of people. This disease has impacted the economy, social life, health, and other areas and added more vulnerability to human life (Fong et al. 2020). Many factors are responsible for its transmission at many levels of interaction (Deziel et al. 2020). In a recently published pioneer work, it has been observed that COVID-19 has not been evenly distributed on a geographical space due to factors related to uneven demographic distribution and differential available health care infrastructure(Amram et al. 2020). COVID-19 vulnerability index is an effective tool to demarcate the areas of high vulnerability by adding composite scores of factors associated with exposure, sensitivity, and adaptability (Mishra et al. 2020). In the present study, the indicators are based on several studies on disease vulnerability analysis (Bae et al. 2019; Acharya & Porwal 2020; Sarkar and Chauhan 2021; Mishra et al. 2021; Paul 2021).

We have calculated the percentage of COVID-19 cases and related deaths to the total population for each state and UTs separately to understand the level of exposure (Table 2). In the exposure section, the percentage of the population having COVID19 and related deaths both specify the level of exposure to the COVID19 pandemic. The death of people in a region moreover accentuates the insecurity of life. It exposes the populace and the region to much ardent needs of identifying the vulnerable and controlling the deteriorating covid situation. The striking variation could be noted among states and UTs through the calculation which in turn impacts the health of people. We have found huge variation among the states and UTs through the calculation which is certainly affecting the health of the people. The final composite score values of exposure show that Puducherry (0.97) has the highest component value, followed by Delhi (0.86), Goa (0.86), and Maharashtra (0.70). The high population density in these states has accentuated the infection rates causing a high number of cases and deaths (Fig. 2). The least exposure component scores are recorded in Mizoram (0.0), Meghalaya (0.01), and Himachal Pradesh (0.02). A sparse population and physical inaccessibility mainly due to hilly terrain are the major reasons for relatively lower exposure in terms of the number of cases and deaths per capita due to COVID-19 (Fig. 2). Bihar has a less composite score of exposure (0.02) due to fewer deaths and recorded cases attributed to under-reporting and poor diagnosis of cases in the state, otherwise composite score would have

Table 1. The broad categorization of Exposure, Sensitivity, and Adaptive Capacity and their related indicators to calculate Vulnerability Index

COMPONENT	PROFILE	INDICATORS
Exposure	COVID- 19	• % Cases of COVID-19 to the total population • % COVID-19 related deaths to the total population
Sensitivity	Vulnerable factors	• % (age group 0-6 Years) • % (age group above 60 Years) • Density of population
Adaptive Capacity	Healthcare Capacity	• % Total isolation beds (excluding intensive care unit (ICU) Beds) to the total population • % Isolation beds of confirmed cases to the total population • % Isolation beds for suspected cases to the total population • % Oxygen (O2) supported beds to the total population • % ventilators to the total population • % Total ICU beds to the total population

*Data on the indicators of exposure and adaptive capacity section have been compiled from https://www.indiastat.com/, and for the vulnerable population from https://www.indiastat.com/data/demographics/

Table 2. Represents the calculated value for COVID- 19 total confirmed cases and related deaths to the total population in Indian states and UTs

States/ UTs	% Cases of COVID-19 to the total population	% COVID-19 related deaths to the total population
Andaman and Nicobar Islands (UT)	0.92	0.013
Andhra Pradesh	1.11	0.010
Arunachal Pradesh	0.42	0.001
Assam	0.44	0.001
Bihar	0.15	0.001
Chandigarh (UT)	0.69	0.008
Chhattisgarh	0.23	0.002
Delhi (UT)	1.25	0.028
Goa	1.61	0.019
Gujarat	0.18	0.005
Haryana	0.35	0.004
Himachal Pradesh	0.13	0.001
Jammu and Kashmir	0.43	0.007
Jharkhand	0.18	0.002
Karnataka	0.72	0.012
Kerala	0.31	0.001
Madhya Pradesh	0.12	0.002
Maharashtra	0.90	0.026
Manipur	0.27	0.002
Meghalaya	0.12	0.001
Mizoram	0.13	0.000
Nagaland	0.25	0.001
Odisha	0.34	0.001
Puducherry (UT)	1.52	0.029
Punjab	0.27	0.008
Rajasthan	0.14	0.002
Sikkim	0.33	0.001
Tamil Nadu	0.68	0.011
Telangana	0.44	0.003
Tripura	0.50	0.005
Uttarakhand	0.29	0.004
Uttar Pradesh	0.15	0.002
West Bengal	0.22	0.004

been higher like other similar states of Andhra Pradesh (0.50), Karnataka (0.40) and Tamil Nadu (0.38), and Uttar Pradesh (0.12). A relatively lesser number of foreign travelers can also be attributed to fewer cases in Bihar and Madhya Pradesh (0.04). Interestingly, major developed states like Delhi (0.86), Maharashtra (0.70), Andhra Pradesh (0.50), Karnataka (0.40), and Tamil Nadu (0.38) have high composite scores of exposures in comparison to relatively poor states (Fig. 2). Through the map, it is easy to say that the Southern region of the country is highly exposed to this disease in terms of exposure and related deaths. There is need to adopt several strategies like

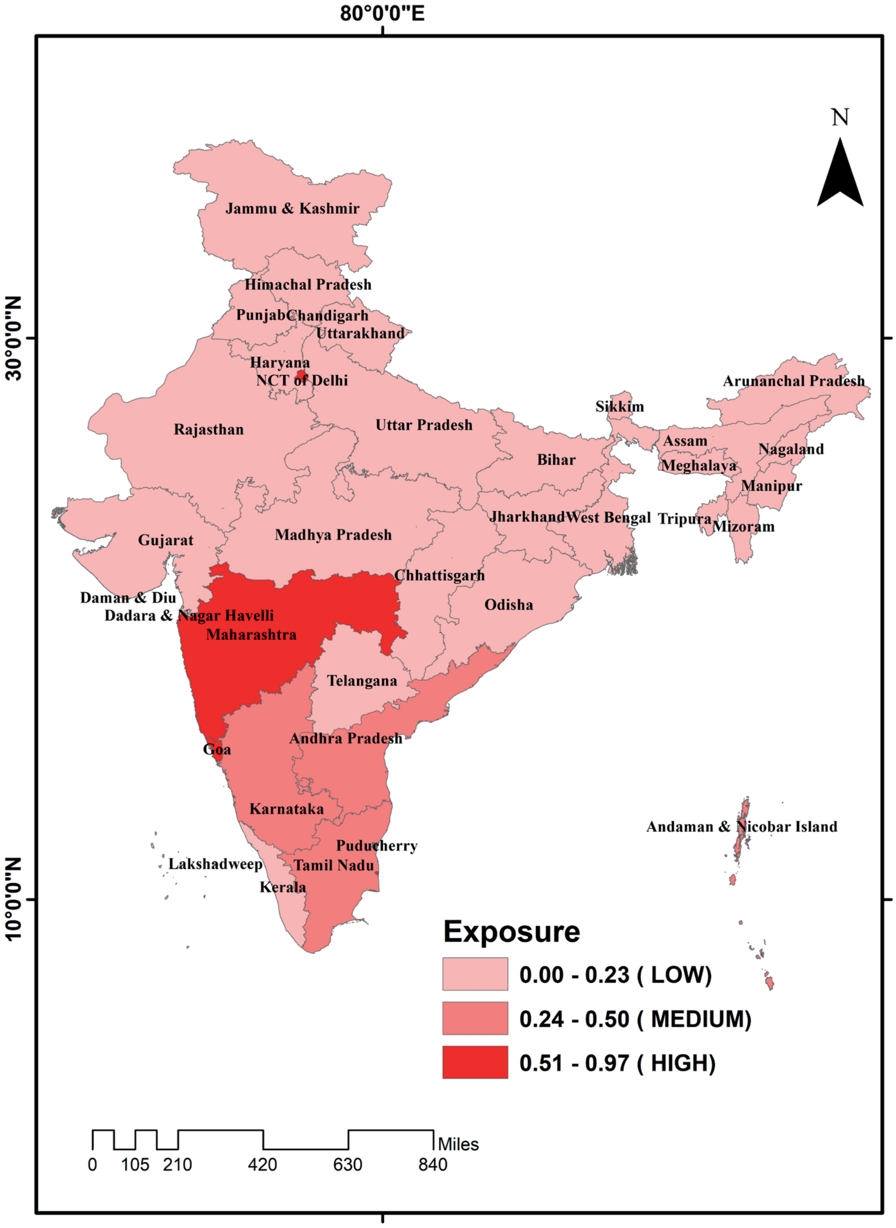

Fig. 2. Exposure value distribution in different States and UTs of India. Value ranges for the exposure are between (0-1)

social distancing, wearing masks, and hygienic practices to reduce exposure in the states and UTs. The availability of better healthcare infrastructure and high literacy rates in the southern states have contributed to high reporting of cases from these states.

The term sensitivity addresses the degree of the impact caused by the exposure factors. Sensitivity is a crucial factor in assessing the vulnerability of the population against the COVID-19 (Mishra et al. 2020). Higher density areas provide fertile ground for the virus to exacerbate its spread (Bhadra et al. 2020). As COVID-19 has its higher ramification on the aged population and spread rapidly in a densely populated region data have been taken for both as an indicator of sensitivity. In addition to this, data of the age group of population between (0-6) years is also included in this study. Both these groups of the population are the most vulnerable group (Acharya and Porwal 2020; Haleemunnissa et al. 2021). The aged population suffers from many comorbidities which makes them sensitive. In a developing country like India, the infant population is facing several challenges like hunger, malnutrition, and diseases. Because of these three major contributing factors, population (0-6) years has been taken as an indicator for our study. It has been observed in the final value for the sensitivity section that states and UTs with relatively high population density and a high share of vulnerable populations have higher scores (Fig. 3). According to health experts, population density plays an important role in the rapid spread of infectious diseases like COVID-19 (Benz et al. 2011; Bray et al. 2020; Coşkun et al. 2021; Zhang and Schwartz 2020). Delhi (0.50) has the highest composite sensitivity score mainly due to very high population density and a greater number of people age sixty and above. It is followed by Bihar (0.45) and Chandigarh (0.40), mainly attributed to high population density and a greater number of people in the age group 0-6 years (Fig. 3). Among the states and UTs, north Indian states have recorded the highest fertility rate. Highly vulnerable states like Bihar, Delhi, Chandigarh, Uttarakhand, Jharkhand, and Jammu & Kashmir fall in the northern region of the country. All the insular states with the least population densities have lesser composite scores e.g., Sikkim (0.11), Andaman and Nicobar (0.12), Arunachal Pradesh (0.20), Nagaland (0.20), Manipur (0.22), Tripura (0.24). As mentioned earlier these states are physically inaccessible and have a sparse population due to hilly terrain. It is, therefore, necessary to ensure better COVID-19 specific medical infrastructure in densely populated states with a high proportion of sensitive age groups. States with high population density

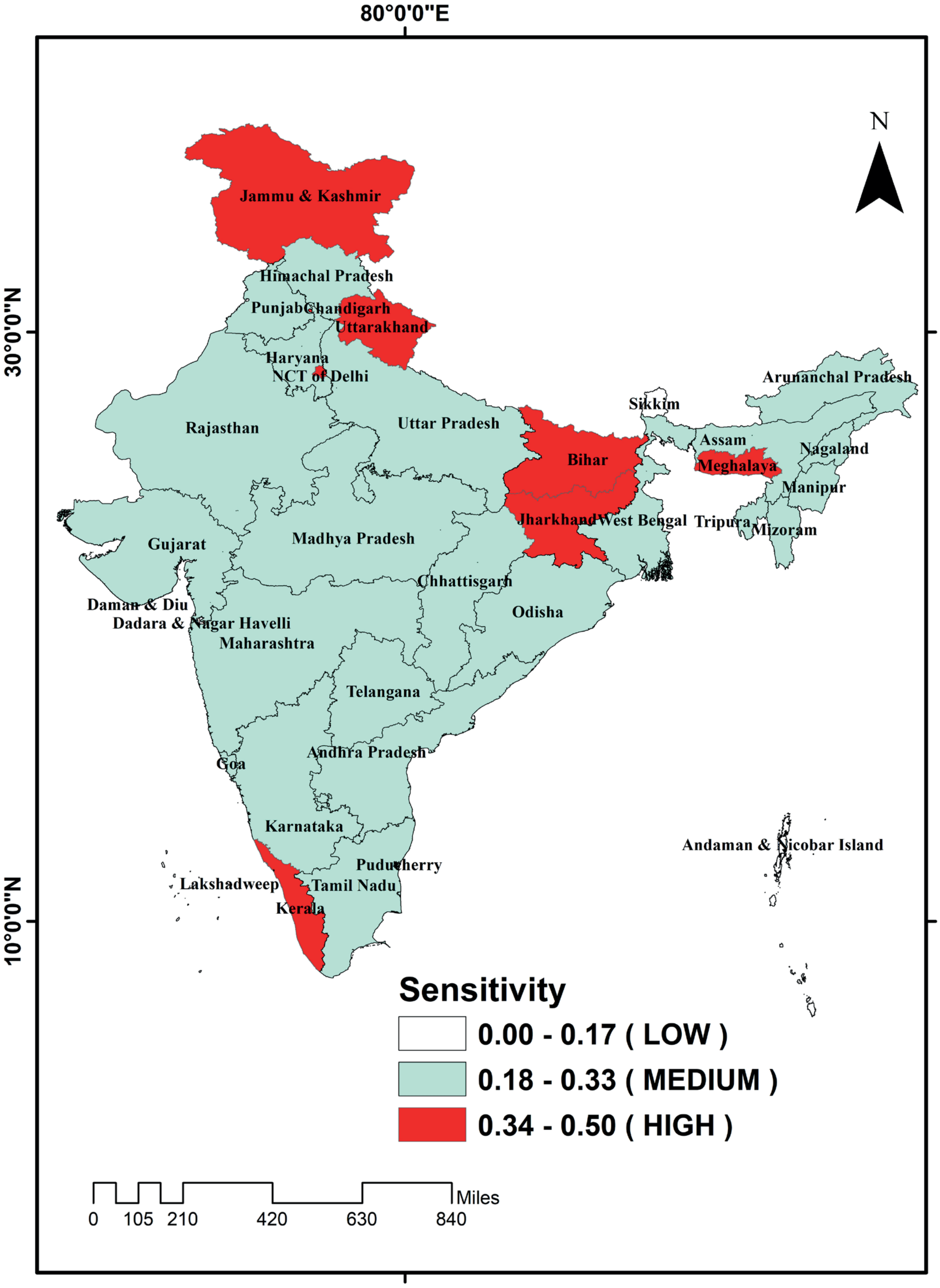

Fig. 3. The map is showing the final Sensitivity value distribution in different States and UTs of India. The final composite value ranges for the exposure is between (0-0.5)

should also make sure that the age-sensitive population with weak immune system should be the priority in dealing with COVID-19.

Adaptive capacity is the ability to effectively tackle the risks associated with COVID-19 exposure (Sarkar and Chouhan 2020). It includes the necessary medical infrastructures to deal with cases and related fatalities. This is particularly good in the states and union territories with relatively viable economic conditions and dynamic social structures with the smooth flow of information and medical practices. The adaptive capacity pattern shows that small states with relatively better medical infrastructure and COVID-19 specific health care facilities can effectively erode the vulnerability. The composite profile values for adaptive capacity underscore the overall status of medical infrastructure linked to COVID-19 control and treatment. Chandigarh (0.74) has the highest composite profile score particularly due to the very effective medical infrastructure preceding the actual COVID-19 outbreaks. This is followed by Maharashtra (0.71), Andaman and Nicobar (0.62), Tamil Nadu (0.59), Uttarakhand (0.57), and Delhi (0.56) (Fig. 4). The Maximum number of COVID-19 cases and related death is recorded in two major cities of the country, Delhi and Mumbai. New Delhi as the capital city of the country situated in Delhi and Mumbai as the economic capital of the country have well-developed and equipped medical facilities. The Government of India has provided full attention to these two cities which places them in a very high adaptive capacity zone. The least composite profile scores were recorded Bihar (0.02), Jharkhand (0.06), Nagaland (0.06), Tripura (0.06), and Himachal Pradesh (0.07) (Fig. 4). It has been observed that the states which are less populous and have viable socio-economic conditions have performed well on the selected indicators, unlike in the underdeveloped states (Fig. 4).

COVID-19 VI has been obtained using the formula (Exposure – Adaptive Capacity) x Sensitivity (Hahn

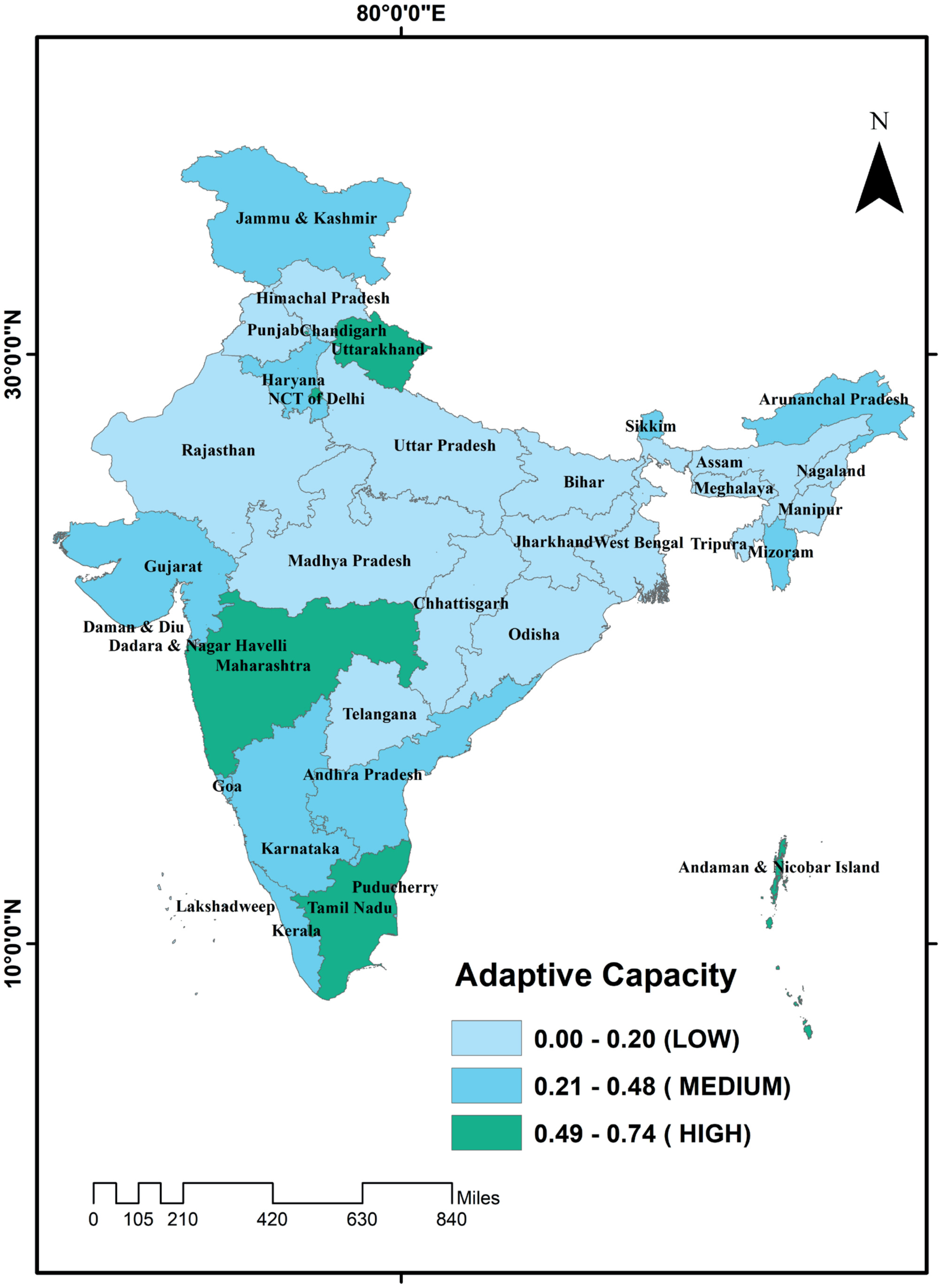

Fig. 4. The map is representing the composite value of Adaptive Capacity in different States and UTs of the country. The final composite value ranges for the adaptive capacity is between (0- 0.74)

et al. 2009). Adaptive capacity erodes the COVID-19 vulnerability whereas exposure and sensitivity accentuate the risks. The scores of the VI range as high as +0.25 to -0.15. The positive values indicate high vulnerability while the negative scores indicate lower vulnerability. The final VI values show that people in Puducherry, Delhi, Goa, Tripura, and Andhra Pradesh, among other states, are relatively more vulnerable to COVID-19 (Fig. 5), on account of high exposure and sensitivity. Though the states like Delhi (0.57), Goa (0.43) and, Puducherry (0.35) scores well on adaptive capacity parameters, the exposure and sensitivity offset the gains when final vulnerability scores are calculated (Fig. 5). People in the states of Uttarakhand, Chandigarh, Mizoram, Haryana, Kerala, and Tamil Nadu have lower vulnerability against COVID-19. Uttarakhand performs well on the adaptive capacity (0.57) parameter against its peers and has relatively less exposure (0.05) (Fig. 5). Chandigarh Performs well due to very good adaptive capacity (0.74) measures, effectively offsetting the high exposure and sensitivity. It is important to note that only relatively smaller states have either very high or very less vulnerability, unlike the big states which have either medium or high vulnerability scores.

CONCLUSION

VI helps understand the priority states, and there is a need for intervention in the high and right direction. Nowadays, globally it has been observed that COVID-19 has developed new strains that spread faster than the original. It can further be added that along with the responsibility of the Government and associated health and related authorities, equal conscious citizens of a nation can play their important role in combating Coronavirus by adopting preventive measures and following guidelines issued by authorities (Shah and Farrow 2020; Zu et al. 2020). Restoring the confidence of the general public in public health measures is crucial,

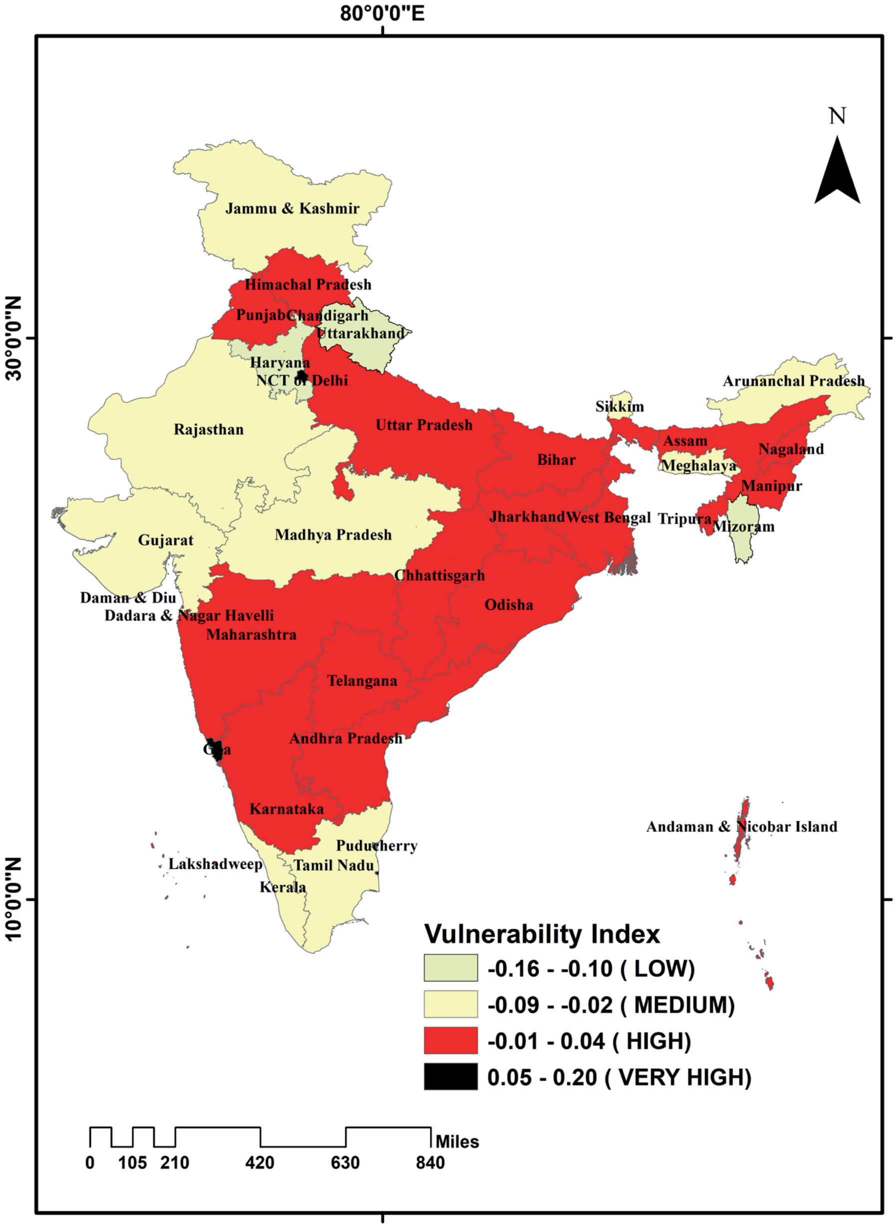

Fig. 5. The Choropleth map is showing the VI value distribution in different States and UTs of the country. The values of the final VI calculation lie between -1 to +1 and have been divided into four classes according to Jenks Natural Breaks classification. The States and UTs having high negative values are categorized as low vulnerable category whereas the States and UTs near positive values and above are categorized into three classes as a medium, high, and very high vulnerable zones

otherwise fear and apprehension might limit the local, national, regional, and international efforts and measures aimed at tackling the COVID-19 outbreak. This is only possible through the joint and coordinated efforts and cooperation between diverse stakeholders at local, national, and global levels (Shah and Farrow 2020). In this situation of wave kind movement of COVID-19 pandemic in the country, this study will be of significant importance for policymakers and will be very helpful to them in identifying the vulnerable states and UTs of the country.

REFERENCES

Acharya R., & Porwal A. (2020). A vulnerability index for the management of and response to the COVID-19 epidemic in India: an ecological study. The Lancet Global Health, 8(9), e1142–e1151, DOI: 10.1016/S2214-109X(20)30300-4.

Amram O., Amiri S. Lutz R.B., Rajan B., & Monsivais P. (2020). Development of a vulnerability index for diagnosis with the novel coronavirus, COVID-19, in Washington State, USA. Health and Place, 64, 102377, DOI: 10.1016/j.healthplace.2020.102377.

Avtar R., Kumar P., Supe H., Jie D., Sahu N., Mishra B. and Yunus A. (2020). Did the COVID-19 Lockdown-Induced Hydrological Residence Time Intensify the Primary Productivity in Lakes? Observational Results Based on Satellite Remote Sensing. Water, 12(9), 2573, DOI: 10.3390/w12092573.

Bae H.-J., Kang J.E., & Lim Y.-R. (2019). Assessing the health vulnerability caused by climate and air pollution in Korea using the fuzzy topsis. Sustainability, 11(10), 2894, DOI: 10.3390/su11102894.

Benz J.K., Espinosa O., Welsh V., and Fontes A. (2011). Awareness of racial and ethnic health disparities has improved only modestly over a decade. Health Affairs, 30(10), DOI: 10.1377/hlthaff.2010.0702.

Bhadra A., Mukherjee A., & Sarkar K. (2021). Impact of population density on Covid-19 infected and mortality rate in India. Model Earth

System Environ, 7, 623-629, DOI: 10.1007/s40808-020-00984-7.

Bray I., Gibson A., & White J. (2020). Coronavirus disease 2019 mortality: a multivariate ecological analysis in relation to ethnicity, population density, obesity, deprivation and pollution. Public Health, 185, 261-263, DOI: 10.1016/j.puhe.2020.06.056.

Chaurasiya P., Pandey P., Rajak U., Dhakar K., Verma M., & Verma T. (2020). Epidemic and Challenges of Coronavirus Disease-2019 (COVID-19): India Response. SSRN Electronic Journal, DOI: 10.2139/ssrn.3569665.

Coronavirus Data India - COVID-19 Pandemic Data India with State wise growth statistics details figures | Indiastat. Retrieved January 18, 2021, available at https://www.indiastat.com/health-data/16/diseases/77/coronavirus-covid-19/1314071/stats.aspx.

Coronavirus disease (COVID-19). Retrieved January 5, 2021, available at https://www.who.int/emergencies/diseases/novel-coronavirus-2019.

Coşkun H., Yıldırım N., and Gündüz S. (2021). The spread of COVID-19 virus through population density and wind in Turkey cities. Science of the Total Environment, 751, DOI: 10.1016/j.scitotenv.2020.141663

Deziel N.C., Allen J.G., Scheepers P.T.J., & Levy J.I. (2020). The COVID-19 pandemic: a moment for exposure science. Journal of Exposure Science and Environmental Epidemiology, 30(4), 591-593, DOI: 10.1038/s41370-020-0225-3.

Fong M.W., Gao H., Wong J.Y., Xiao J., Shiu E.Y.C., Ryu S., & Cowling B.J. (2020). Nonpharmaceutical measures for pandemic influenza in nonhealthcare settings-social distancing measures. In: Emerging Infectious Diseases , Vol. 26, Issue 5, 976–984. Centers for Disease Control and Prevention (CDC), DOI: 10.3201/eid2605.190995.

Freedman B. (1966). HISTORY AND GEOGRAPHY OF THE MOST IMPORTANT DISEASES. American Journal of Public Health and the Nations Health, 56(11), 1973. https://www.ncbi.nlm.nih.gov/pmc/articles/PMC1257350/

Giovanetti M., Benvenuto D., Angeletti S., & Ciccozzi M. (2020). The first two cases of 2019-nCoV in Italy: Where they come from? Journal of Medical Virology, 92(5), DOI: 10.1002/jmv.25699.

Gupte J., & Mitlin D. (2020). COVID-19: what is not being addressed. Environment and Urbanization, 095624782096396, DOI: 10.1177/0956247820963961.

Hahn M.B., Riederer A.M., & Foster S.O. (2009). The Livelihood Vulnerability Index: A pragmatic approach to assessing risks from climate variability and change-A case study in Mozambique, DOI: 10.1016/j.gloenvcha.2008.11.002.

Haleemunnissa S., Didel S., Swami M. K., Singh K., & Vyas V. (2021). Children and covid19: Understanding impact on the growth trajectory of an evolving generation. Children and Youth Services Review, 120, 105754, DOI: 10.1016/j.childyouth.2020.105754.

Jernigan D.B. (2020). Update: Public Health Response to the Coronavirus Disease 2019 Outbreak — United States, February 24, 2020. MMWR. Morbidity and Mortality Weekly Report, 69(8), 216-219, DOI: 10.15585/mmwr.mm6908e1.

Lai C.C., Shih T.P., Ko W.C., Tang H.J., & Hsueh P.R. (2020). Severe acute respiratory syndrome coronavirus 2 (SARS-CoV-2) and coronavirus disease-2019 (COVID-19): The epidemic and the challenges. In: International Journal of Antimicrobial Agents, 55(3). Elsevier B.V., DOI: 10.1016/j.ijantimicag.2020.105924.

Lupia T., Scabini S., Mornese Pinna S., Di Perri G., De Rosa F.G., & Corcione S. (2020). 2019 novel coronavirus (2019-nCoV) outbreak: A new challenge. Journal of Global Antimicrobial Resistance, 21, DOI: 10.1016/j.jgar.2020.02.021

Martínez-Piédrola M.M., Guadarrama-Ortega D., Pérez-Fernández E., Ortigosa-Barriola A., Parra-García S., Molinares-Juarrero B., & Díaz-Cuasante A.I. (2021). Strategy for planning and execution of a large-scale SARS-CoV-2 seroprevalence study on teaching hospital workers during a pandemic situation. Journal of Healthcare Quality Research, 36(1), 3-11, DOI: 10.1016/j.jhqr.2020.11.003.

Mazinani M., & Rude B.J. (2021). The novel zoonotic Coronavirus disease 2019 (COVID-19) pandemic: Health perspective on the outbreak. In: Journal of Healthcare Quality Research, 36(1), 47-51. Elsevier Espana S.L.U., DOI: 10.1016/j.jhqr.2020.09.004.

Mishra M.M., Sahu N., Pandey BW., Singh RB. (2021). Assessing Human Health Vulnerabilities in the Blocks of Kalahandi district of Odisha, India. Disaster Advances,14, 32-40.

Mishra S.V., Gayen A., & Haque S.M. (2020). COVID-19 and urban vulnerability in India. Habitat International, 103(August), 102230, DOI: 10.1016/j.habitatint.2020.102230.

Ogen Y. (2020). Assessing nitrogen dioxide (NO2) levels as a contributing factor to coronavirus (COVID-19) fatality. Science of the Total Environment, 726, 138605, DOI: 10.1016/j.scitotenv.2020.138605.

Paul S. (2021). Vulnerability and the resilience against covid-19 in India. Journal of the Asia Pacific Economy, 1-19, DOI: 10.1080/13547860.2021.1915545.

Phan L.T., Nguyen T. V., Luong Q.C., Nguyen T.V., Nguyen H.T., Le H.Q., Nguyen T.T., Cao T.M. & Pham Q.D. (2020). Importation and Human-to-Human Transmission of a Novel Coronavirus in Vietnam. New England Journal of Medicine, 382(9), DOI: 10.1056/nejmc2001272.

Sarkar A., & Chouhan P. (2020). COVID-19: District level vulnerability assessment in India. Clinical Epidemiology and Global Health, June, 0–1. DOI: 10.1016/j.cegh.2020.08.017

Shah S.G.S., & Farrow A. (2020). A commentary on "World Health Organization declares global emergency: A review of the 2019 novel Coronavirus (COVID-19)." In: International Journal of Surgery , Vol. 76, 128–129. Elsevier Ltd., DOI: 10.1016/j.ijsu.2020.03.001.

Sohrabi C., Alsafi Z., O'Neill N., Khan M., Kerwan A., Al-Jabir A., Iosifidis C., & Agha R. (2020). World Health Organization declares global emergency: A review of the 2019 novel coronavirus (COVID-19). In: International Journal of Surgery, 76, DOI: 10.1016/j.ijsu.2020.02.034.

Tosepu R., Gunawan J., Effendy D.S., Ahmad L.O.A.I., Lestari H., Bahar H., & Asfian P. (2020). Correlation between weather and Covid-19 pandemic in Jakarta, Indonesia. Science of the Total Environment, 725, 138436, DOI: 10.1016/j.scitotenv.2020.138436.

van den Broek-Altenburg E., Atherly A., Diehl S., Gleason K., Hart V., MacLean C., Barkhuff D., Levine M., & Carney J. (2020). Risk Factors for COVID-19: Community Exposure and Mask-Wearing. SSRN Electronic Journal, 05405, 1-19, DOI: 10.2139/ssrn.3676570.

Wiersinga W.J., Rhodes A., Cheng A.C., Peacock S.J., & Prescott H.C. (2020). Pathophysiology, Transmission, Diagnosis, and Treatment of Coronavirus Disease 2019 (COVID-19): A Review. In: JAMA - Journal of the American Medical Association, 324(8), 782-793, American Medical Association, DOI: 10.1001/jama.2020.12839.

Zhang C.H., and Schwartz G.G. (2020). Spatial Disparities in Coronavirus Incidence and Mortality in the United States: An Ecological Analysis as of May 2020. Journal of Rural Health, 36(3), DOI: 10.1111/jrh.12476.

Zu Z.Y., Di Jiang M., Xu P.P., Chen W., Ni Q.Q., Lu G.M., & Zhang L.J. (2020). Coronavirus Disease 2019 (COVID-19): A Perspective from China. In: Radiology , Vol. 296, Issue 2, E15–E25. Radiological Society of North America Inc., DOI: 10.1148/radiol.2020200490.

RESEARCH PAPER

SPATIAL CLUSTERING ANALYSIS OF THE COVID-19 PANDEMIC: A CASE STUDY OF THE FOURTH WAVE IN VIETNAM

Danh-tuyen Vu[1], Tien-thanh Nguyen[1*], Anh-huy Hoang[3]
[1]Faculty of Surveying, Mapping and Geographic Information, Hanoi University of Natural Resources and Environment, No. 41A, PhuDien Road, North-TuLiem District, Hanoi,100000, Vietnam
[2]Faculty of Environment, Hanoi University of Natural Resources and Environment, No. 41A, PhuDien Road, North-TuLiem District, Hanoi, 100000, Vietnam
*Corresponding author: tdgis_ntthanh@163.com; ntthanh@hunre.edu.vn
Received: July 31th, 2021 / Accepted: November 9th, 2021 / Published: December 31st, 2021
https://DOI-10.24057/2071-9388-2021-086

ABSTRACT. An outbreak of the 2019 Novel Coronavirus Disease (COVID-19) in China caused by the emergence of Severe Acute Respiratory Syndrome CoronaVirus 2 (SARSCoV2) spreads rapidly across the world and has negatively affected almost all countries including such the developing country as Vietnam. This study aimed to analyze the spatial clustering of the COVID-19 pandemic using spatial auto-correlation analysis. The spatial clustering including spatial clusters (high-high and low-low), spatial outliers (low-high and high-low), and hotspots of the COVID-19 pandemic were explored using the local Moran's I and *Getis-Ord's* G^*_i statistics. The local Moran's I and Moran scatterplot were first employed to identify spatial clusters and spatial outliers of COVID-19. The *Getis-Ord's* G^*_i statistic was then used to detect hotspots of COVID-19. The method has been illustrated using a dataset of 86,277 locally transmitted cases confirmed in two phases of the fourth COVID-19 wave in Vietnam. It was shown that significant low-high spatial outliers and hotspots of COVID-19 were first detected in the North-Eastern region in the first phase, whereas, high-high clusters and low-high outliers and hotspots were then detected in the Southern region of Vietnam. The present findings confirm the effectiveness of spatial auto-correlation in the fight against the COVID-19 pandemic, especially in the study of spatial clustering of COVID-19. The insights gained from this study may be of assistance to mitigate the health, economic, environmental, and social impacts of the COVID-19 pandemic.

KEYWORDS: Spatial clustering; Spatial auto-correlation; COVID-19 pandemic; Vietnam's fourth wave

CITATION: Danh-tuyen Vu, Tien-thanh Nguyen, Anh-huy Hoang (2021). Spatial Clustering Analysis of the COVID-19 Pandemic: A Case Study of the Fourth Wave in Vietnam. Geography, Environment, Sustainability, Vol.14, No 4, p. 140-147
https://DOI-10.24057/2071-9388-2021-086

ACKNOWLEDGEMENTS: We wish to thank the editors and three anonymous reviewers for their valuable and constructive comments and suggestions on this paper that have helped us to greatly improve the quality of the paper.

Conflict of interests: The authors reported no potential conflict of interest.

INTRODUCTION

The 2019 COVID-19 is a pandemic illness that was discovered in Wuhan of China at the end of 2019. The COVID-19 epidemic quickly spreads worldwide rapidly to emerge as a global public health concern (Das et al. 2021). Globally, as of 26 October 2021, a total of more than 243.6 million confirmed cases of the COVID-19 and more than 4.9 million deaths were reported (WHO 2021). The COVID-19 pandemic has been described as a social, human, and economic crisis (United Nations 2020). It is, therefore, the understanding of the spatial distribution of the COVID pandemic, in general, and of the spatial clustering, in particular, plays an important role in the fight of COVID-19.

In studies of the COVID-19 pandemic, Shepherd (2020) indicated that geography is considered a key part of fighting the COVID-19 coronavirus outbreak. Especially, after Rose-Redwood et al. (2020) discovered the COVID-19 pandemic is thoroughly spatial in nature, a lot of efforts have been made on the study of the COVID-19 pandemic from a geographical perspective to better understand the spatial distribution and better manage the COVID-19 infection. Using *Getis-Ord's* G^*_i statistic and geographically weighted principal component analysis, Das et al. (2021) successfully examined the impact of living environment deprivation on the COVID-19 hotspot in Kolkata megacity, India. The result study of Das et al. (2021) revealed that living environment deprivation was an important determinant of spatial clustering of COVID-19 hotspots in the Kolkata megacity. Xie et al. (2020) used the exploratory spatial data analysis and the geodetector method to analyze the spatial and temporal differentiation characteristics and the influencing factors of the COVID-19 epidemic spread in mainland China based on the cumulative confirmed cases, average temperature, and socio-economic data. The results of Xie et al. (2020) demonstrate two things. First, the population inflow from Wuhan and the strength of economic connection are the main factors affecting the epidemic's spread. Second, when the average temperature in winter is maintained at 11-16°C, the epidemic spread rate is higher. Later, with the aim to analyze the spatial distribution characteristics of the COVID-19 pandemic in Beijing and its relationship with the environmental factors, based on the incidences of new local COVID-19 cases in Beijing, Han et al. (2021) investigated the spatial clustering characteristics of the COVID-19 pandemic in Beijing using spatial autocorrelation analysis. In line with those obtained by Xie et al. (2020), Han et al. (2021) also indicated that population density and distance to the market are key factors of the pandemic. When a rapid increase in the number of COVID-19 cases was reported in Iran in 2020, Ramírez-Aldana et al. (2020) developed a spatial statistical approach to describe how COVID-19 cases are spatially distributed and to identify significant spatial clusters of cases and how socioeconomic and climatic features of Iranian provinces might predict the number of cases. In that study, Ramírez-Aldana et al. (2020) successfully applied global (Moran's I) and local indicators of spatial autocorrelation (LISA), both univariate and bivariate, to derive significant clustering of COVID-19 pandemic. In South Korea, to understand the COVID-19 clustering across districts in South Korea and how the spatial pattern of COVID-19 changes, Kim and Castro (2020) successfully applied the global Moran's I statistic and the retrospective space-time scan statistic to analyze spatio-temporal clusters of COVID-19. A similar conclusion was reached by Choi (2020), Kim and Castro (2020) also showed that the spatial pattern of clusters changed and the duration of clusters became shorter over time in this country. Most recently, when identifying spatial patterns of COVID-19 disease clustering in India using another global spatial autocorrelation statistic, the *Getis-Ord's* G^*_i statistic, Bhunia et al. (2021) discovered that this statistic can help public health professionals to effectively identify risk areas for disease and take decisions in real-time to control this viral disease. Similar to those obtained from these studies, a recent study by Robinson (2000) has also indicated that commonly used statistics such as global spatial statistics (Moran's I, *Getis-Ord's* G^*_i and Geary's C) and LISA have been successfully applied in epidemiological studies in general and in the study of COVID-19 pandemic in particular. Among these spatial statistics, local Moran's I and *Getis-Ord's* G^*_i statistics have been most widely used for the analysis of spatial auto-correlation (Zhang and Zhang 2007) because of their effectiveness in displaying the spatial distribution of infectious diseases (Tran et al. 2004; Wang et al. 2015), thus, these two statistics will be employed to analyze the spatial clustering of the COVID-19 pandemic in this study.

A Delta-driven fourth wave of COVID-19 has profoundly affected the world including such countries in Southeast Asia as Vietnam. Although, a lot of efforts have been put into the study of the COVID-19 pandemic in Vietnam (Duy et al. 2021; Hoang et al. 2020; Huang et al. 2020; La et al. 2020; Le and Tran 2021; Nguyen and Vu 2020), so far, very little attention has been paid to the role of geographical methods. Most recently, Hoang et al. (2020) described the pattern of the COVID-19 epidemic in Vietnam, however, no spatial autocorrelation also has been taken into account. Particularly, to date, no previous study has investigated the spatial clustering of the COVID-19 pandemic in Vietnam. Accordingly, this study aims to analyze spatial clustering of the COVID-19 pandemic using spatial auto-correlation analysis. It is believed that this is the first study on the identification of spatial clustering of COVID-19 pandemic in Vietnam that accounts for spatial auto-correlation among locally transmitted cases COVID-19 cases.

STUDY AREA AND DATA USED

According to the Ministry of Health of Vietnam (MHV), as of 24 June 2021, the COVID-19 pandemic in Vietnam can be divided into four COVID-19 waves and resulted in a total of 89,992 confirmed cases (87,847 locally transmitted cases and 2,145 internationally imported cases) and 63 deaths (MHV 2021). The first wave started from 23 January to 24 July 2020 causing 415 confirmed cases (106 locally transmitted cases and 309 internationally imported cases). Vietnam was ranked 94th on the list of 206 countries and territories affected by COVID-19 (Ha et al. 2020). The second wave ranged from 25 July 2020 to 27 January 2021 with 1,136 confirmed cases (554 locally transmitted cases and 582 internationally imported cases) (Ha et al. 2020) and 35 deaths as of February 2021 (Phuong et al. 2021). The third wave was from 28 January 2021 to 26 April 2021 with 1,301 cases (910 locally transmitted cases and 391 internationally imported cases) (MHV 2021). A total of 25 COVID-19 clusters related to the outbreaks had been identified mainly in Van Don international airport (VnExpress 2021a) and Dong Trieu town in Quang Ninh province (VnExpress 2021b), and POYUN company and Haiduong city in Hai Duong province (HanoiTimes 2021). The latest data show that, as of 24 June 2021, the on-going fourth wave has resulted in 87,140 (86,277 locally transmitted cases and 863 internationally imported cases) since a series of COVID-19 confirmed cases occurred due to viral virus strain from the UK and India was declared on 27 April 2021 in industrial zones in Bac Giang and Bac Ninh provinces, North-East of Vietnam (VietNamNews 2021a; VnExpress 2021c) and the presence of the Delta variant (VietNamNews 2021b). In this study, the focus will be made on the fourth wave of COVID-19 in all 63 provinces and cities in Vietnam. Consequently, a total of 86,277 locally transmitted cases confirmed in the fourth wave of COVID-19 was used to identify the spatial clustering of the COVID-19 pandemic. Data from Figure 1 demonstrates the daily number of new locally transmitted cases were reported in Vietnam by MHV (2021) since the ongoing fourth wave of COVID-19 infections started on 27 April 2021. The spatial distribution of these locally transmitted cases in the first, second phase of the fourth COVID-19 wave and the whole fourth wave was shown in Figures 2-a, b, and c, respectively.

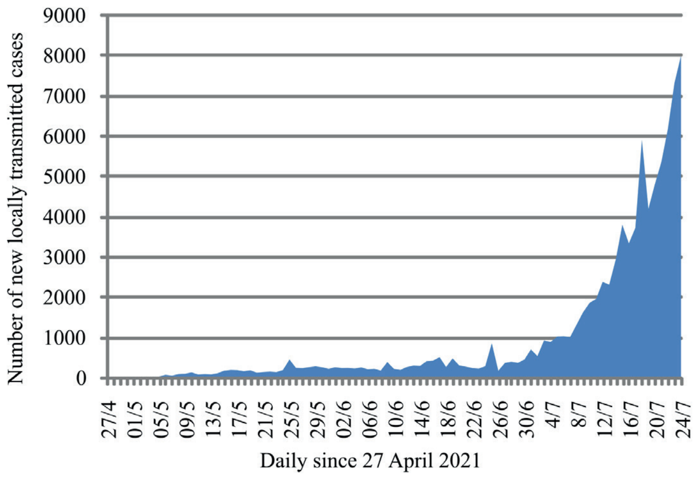

Fig. 1. Daily new confirmed cases in the fourth wave of COVID-19 in Vietnam

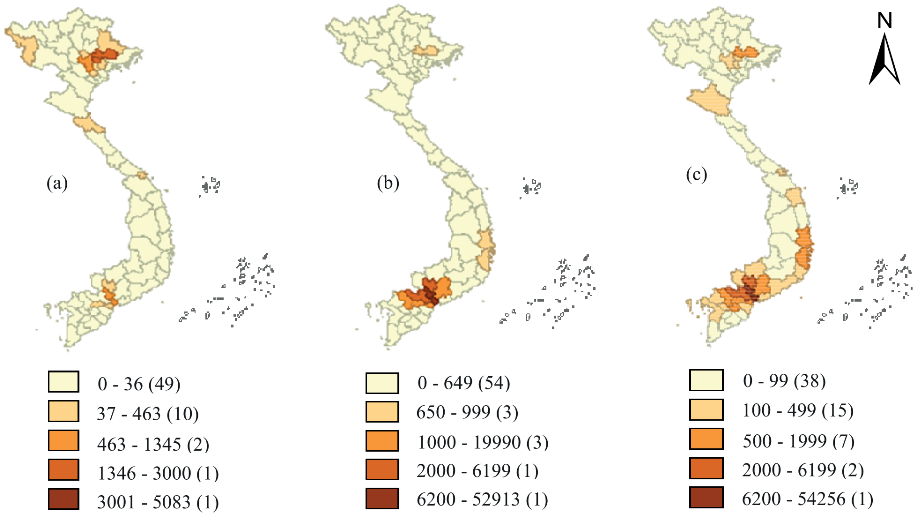

Fig. 2. Spatial distribution of confirmed cases in the fourth wave of COVID-19 in Vietnam

METHODOLOGY

The workflow for spatial clustering analysis of the COVID-19 pandemic is shown in Figure 3. The number of locally transmitted COVID-19 cases was firstly collected from a database provided by the official websites of the Ministry of Health of Vietnam (MHV 2021). After the spatial weight matrix was constructed, with the help of GeoDA software developed by Anselin et al. (2016), Moran's I and *Getis-Ord's* G^*_i statistics were then computed to create LISA and hotspot maps. These maps were finally used for the evaluation of the spatial clustering of the COVID-19 pandemic.

Identifying spatial clustering of the COVID-19 pandemic using *Moran's I* statistic

In this study, the degree of spatial clustering of the COVID-19 pandemic as a whole is measured using global *Moran's I* statistic (Cliff and Ord 1981; Getis and Ord 1996). The global Moran's I statistic is defined as follow:

$$I = \frac{n}{S_0}\frac{\sum_{i=1}^{n}\sum_{j=1}^{n} W_{ij}\left(x_i - \bar{x}\right)\left(x_j - \bar{x}\right)}{\sum_{i=1}^{n}\sum_{j=1}^{n} W_{ij}\sum_{i=1}^{n}\left(x_i - \bar{x}\right)^2} \quad (1)$$

where x_i and x_j are the cumulative numbers of confirmed cases for province/city *i* and province/city *j* in the fourth wave of COVID-19; $\bar{x}$ is the mean of COVID-19 cases and be given $x = \sum_{i=1}^{n}\frac{x_i}{n}$; n is the total number of provinces/cities (all 63 provinces and cities in Vietnam) in the whole study area; and W_{ij} is a (n x n) spatial queen contiguity weight matrix.

The global *Moran's I* coefficient takes values in the interval [-1, +1]. Positive spatial autocorrelation in the data translates into positive values of *Moran's I*, whereas negative spatial autocorrelation produces negative values of *Moran's I* (Nguyen and Vu 2019a). The values of global *Moran's I* coefficients are close to zero indicating no spatial clustering or random distribution of COVID-19 pandemic.

The global *Moran's I* reflects the presence or lack of spatial clustering as a whole (Nguyen et al. 2016; Nguyen and Vu 2019a). Therefore, the spatial clustering of low and high COVID-19 pandemic at each province/city was then measured utilizing the local *Moran's I* statistic. The local *Moran's I* statistic (I_i) for COVID-19 pandemic at province/city i is given by the following equation (Anselin 1995):

$$I_i = \frac{\left(x_i - x\right)}{\sigma^2}\sum_{j\#i, j\in J_i}^{N} W_{ij}\left(x_j - \bar{x}\right) \quad (2)$$

where x_i, x_j, $\bar{x}$, and W_{ij} are defined in equation (1); *N* is the total number of neighborhood provinces/cities; J_i denotes the neighborhood set of COVID-19 confirmed cases at province/city *i*; j#i implies that the sum of all (x_j-$\bar{x}$) of nearby neighbourhood provinces/cities of province/city *i* but not including x_i; and σ^2 is the variance of *x*, given in equation (3).

$$\sigma^2 = \frac{1}{N}\sum_{j=1}^{N}\left(x_i - \bar{x}\right) \quad (3)$$

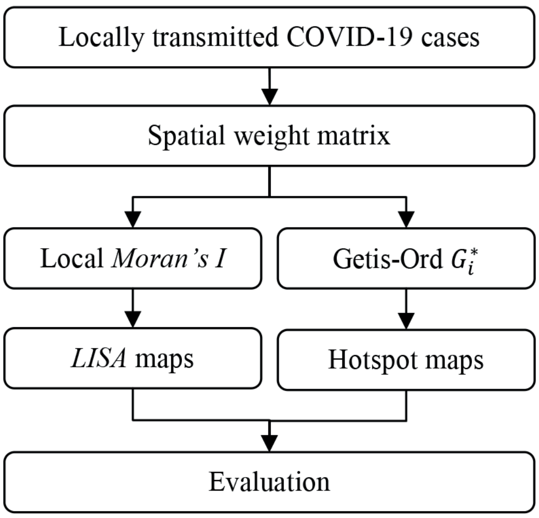

Fig. 3. The workflow for spatial clustering analysis of the COVID-19 pandemic

Local *Moran's I* reflects the degree of spatial clustering of the COVID-19 pandemic at each province/city. Similar to the global *Moran's I* statistic, the local *Moran's I* value at province/city i (I_i) also ranges between -1 and +1. If the local *Moran's I* coefficient at province/city i equals zero (I_i= 0) then there is no spatial clustering of COVID-19 cases. If I_i> 0 then there will be a positive spatial clustering of COVID-19 cases. If I_i< 0 then there will be a negative spatial clustering of COVID-19 cases. A high positive I_i shows the province/city i has a similarly high or low number of COVID-19 cases as its neighbors and is called the «spatial cluster» by Nguyen and Vu (2019a). In this case, when there exists a positive local spatial autocorrelation, the local *Moran's I* statistic identifies two types of spatial clusters for COVID-19 cases: high-high clusters and low-low clusters. Based on the findings in previous studies (Nguyen et al. 2016; Nguyen and Vu 2019a), if the p-value of local Moran's I at location *i*, $p(I_i)$, is less than a predetermined level (α), $p(I_i)<\alpha$, $I_i>0$ and $x_i-\bar{x}>0$, then x_i and $x_{j\in Ji}$ belong to a spatial cluster between high numbers of COVID-19 cases. This means a high number of COVID-19 at province/city *i* are clustered with high numbers of COVID-19 at neighborhood provinces/cities. If $p(I_i)<\alpha$, $I_i>0$, and $x_i-\bar{x}<0$, then x_i and $x_{j\in Ji}$ belong to a spatial cluster between the low number of COVID-19 cases. This means a low number of COVID-19 cases at province/city *i* is clustered with low numbers of COVID-19 at neighborhood provinces/cities. Meanwhile, Lalor and Zhang (2001) defined spatial outliers as those values that are significantly different from the values of their surrounding locations. In this case, similar to those reported in Nguyen et al. (2016) when there exists a negative local spatial autocorrelation, local *Moran's I* identifies two types of spatial outliers: low-high and high-low clusters. If $p(I_i)<\alpha$, $I_i<0$, and $x_i-\bar{x}>0$ then a province/city with a high number of COVID-19, x_i, is surrounded by provinces/cities with low numbers of COVID-19, $x_{j\in Ji}$, (high-low outliers). If $p(I_i)<\alpha$, $I_i<0$, and $x_i-\bar{x}>0$ then a province/city with a low number of COVID-19, x_i, is surrounded by provinces/cities with high numbers of COVID-19, $x_{j\in Ji}$, (low-high outliers).

Anselin (1995) indicates that testing for the significance of spatial autocorrelation statistics such as the global and local Moran's I, and *Getis-Ord's* G^*_i can be carried out based on an assumption of a normal distribution. However, these statistics are very sensitive to a strongly skewed distribution (Hoang et al. 2017; Nguyen et al. 2014; Nguyen 2018; Nguyen et al. 2016; Nguyen and Vu 2019a; Nguyen and Vu 2019b) due to the existence of a high and very high number of COVID-19 cases in some provinces or cities. Wherefore, in this study, testing for the significance of these spatial autocorrelation statistics was carried out by a randomization test which recalculates the statistic many times to generate a reference distribution (Anselin 2005). The data values are reassigned among the N fixed locations in the randomization test, providing a randomization distribution against which we can judge our observed value (Nguyen 2018). With the help of the spatial statistics software, GeoDA 095i, developed by Anselin et al. (2016), all spatial autocorrelation coefficients including the *Getis-Ord's* G^*_i statistic (see below for more details) were calculated and tested at the significance of 0.05 using 999 permutations.

Identifying hotspots of the COVID-19 pandemic using Getis-Ord's G^*_i statistic

The *Getis-Ord's* G^*_i statistic can be employed to measure the degree of spatial clustering of COVID-19 incidence in a study location (Liu et al. 2021). *Getis-Ord's* G^*_i statistic-based hotspot analysis characterizes the presence of hotspots (high clustered values) and coldspots (low clustered values) over an entire area by looking at each feature within the context of its neighboring features (Mitchel 2005; Nguyen and Vu 2019b). Accordingly, in this study, *Getis-Ord's* G^*_i statistic was applied to measure the degree of hotspot of COVID-19. Ord and Getis (1995) defined the form of *Getis-Ord's* G^*_i statistic as follows:

$$G_i^* = \frac{\sum_{j=1}^{N} W_{ij}x_j - \bar{x}\sum_{j=1}^{N} W_{ij}}{S\sqrt{\frac{N\sum_{j=1}^{N}\left[W_{ij}^2 - \left(W_{ij}\right)^2\right]}{N-1}}} \quad (4)$$

$$\text{with } \bar{x} = \frac{1}{N}\sum_{j=1}^{N} x_j \text{ and } S = \sqrt{\frac{\sum_{j=1}^{N} x_j^2}{N} - \left(\bar{x}\right)^2}$$

where G^*_i is computed for the number of COVID-19 cases at province/city *i*; x_i, x_j, $\bar{x}$, and W_{ij} are defined in equation (1); and N is the total number of neighborhood provinces/cities as defined in equation (2).

Similar to those obtained from global and local *Moran's I* statistics, the *Getis-Ord's* G^*_i coefficient at province/city *i* (G^*_i) also ranges from -1 to +1. If $G^*_i>0$ and $p(G^*_i)<\alpha$ then there exists a spatial clustering of the high number of COVID-19 cases. In this case, these high-high values, so-called a hotspot, reflects the presence of high numbers of COVID-19 cases among province/city i and its neighborhood provinces/cities ($j\in J_i$). On the contrary, if $G^*_i<0$ and $p(G^*_i)<\alpha$ then there exists a spatial clustering of low-low values. These low-low values are called a coldspot indicating low numbers of COVID-19 cases among provinces/cities i and its neighborhood provinces/cities ($j\in J_i$). Similar to those in the definition of local Moran's I statistic, if the value of G^*_i close zero and $p(G^*_i)<\alpha$ then there will be no spatial clustering (neither hotspots nor coldspots) or random distribution of COVID-19 cases.

Several studies (Alves et al. 2021; Liu et al. 2021; Nguyen and Vu 2019b) have computed the *Getis-Ord's* G^*_i statistic with the help of ArcGIS software using *Getis z-scores* defined in a study by Mitchel (2005). If provinces/cities with 1.65<*Getis z-scores*<1.96, 1.96<*Getis z-scores*<2.58, and *Getis z-scores*>2.58 were considered to be significant at the 90% confidence level (p < 0.1), 95% confidence level (p < 0.05), and 99% confidence level (p < 0.01), respectively. However, as discussed in the previous section on *Moran's I* statistic, the presence of a strongly skewed distribution in the dataset fails the test. Therefore, testing for the significance of the *Getis-Ord's* G^*_i statistic in this study was also carried out by a randomization test using 999 permutations.

RESULTS AND DISCUSSIONS

Spatial clustering of the COVID-19 pandemic

Global Moran's I coefficients (p<0.001) were 0.1 for the first phase, 0.06 for the second phase, 0.05 for the whole of the ongoing fourth COVID-19 wave, respectively (Figure 4). The global *Moran's I* value of 0.1 indicates the strongest spatial association for the first phrase. Whereas, global *Moran's I* values reduce to 0.06 and 0.05 indicating weaker spatial associations for the second phase and the whole of the fourth COVID-19 wave, respectively. However, these global *Moran's I* coefficients were close to zero indicating, as a whole, there were no spatial auto-correlation or random distribution of the COVID-19 pandemic in this fourth wave. In addition, global *Moran's I* ignore the presence of spatial auto-correlation of COVID-19 confirmed cases at local or provincial scales. To overcome this limitation, local

Moran's I-based LISA was employed to measure the degree of spatial clustering at local scales (province/city level).

A total of 9,192 locally transmitted cases were reported in the first phase of the fourth wave of the COVID-19 pandemic in Vietnam. The spatial distribution of the COVID-19 clustering area was illustrated by LISA maps in Figure 5. Data from Figure 5-a demonstrates that, in the first phase of the ongoing COVID-19 wave, the local *Moran's I* statistic identified a total of three high-high clusters in Bac Giang (5,083 cases), Bac Ninh (1,407 cases), and Hanoi (464 cases); and nine low-low clusters including Ninh Thuan (12 cases), Binh Thuan (11 cases), Dak Lak (6 cases) in South-central region and very low number of COVID-19 cases in Southern provinces of Vietnam such as Lam Dong, An Giang, Kien Giang, Can Tho, Hau Giang, and Bac Lieu. Spatial clustering of COVID-19 pandemic including high-high clusters and low-high outliers was mainly identified in the North-Eastern provinces of Vietnam. These spatial clusters and outliers were mainly caused by more than 6,500 infected workers in industrial parks in Bac Giang and Bac Ninh provinces (VietNamNews 2021a; VnExpress 2021c) after a series of COVID-19 confirmed cases declared on 27 April 2021 due to the rapid spread of the viral virus strain from the UK and India (VietNamNews 2021a; VnExpress 2021c).

Data from Figures 5-b and 5-c illustrates that comparing with those obtained in the first phase, the locations of spatial clustering of COVID-19 pandemic have been quickly changed from the North-Eastern region in the first phase to the Southern region of Vietnam in the second phase of the fourth COVID-19 wave (Figure 5-b). The local *Moran's I* statistic successfully identified five high-high, eleven low-low clusters, and two low-high outliers. Five high-high clusters included Ho Chi Minh city (52,913 cases), the epicenter of the ongoing fourth wave, followed by the Southern provinces of Binh Duong (6,146 cases), Long An (2,178 cases) and Dong Nai (1,778 cases), and Tieng Giang (1,245 cases). Two low-high outliers were detected in the provinces of Ba Ria – Vung Tau (471 cases) and Tay Ninh (204 cases). Whereas, eleven low-low clusters were identified in North-Western provinces of Vietnam with a low number of COVID-19 cases. Policy solutions for COVID-19 response used by local authorities in these provinces have shown effectiveness in stopping the community transmission in these areas. Since the presence of the Delta variant was detected in the second phase of the fourth wave (VietNamNews 2021b), Vietnam recorded 77,085 locally transmitted cases mainly detected in Southern provinces. Similar to those obtained in the second phase, spatial clustering of the COVID-19 pandemic in the whole of the fourth COVID-19 wave was mainly detected in cities/provinces in the Southern region of Vietnam. This is due to the number of locally transmitted cases in this phase accounts for 97% of the total number confirmed in the fourth wave of COVID-19. To effectively fight the COVID-19 in the ongoing fourth wave, social distancing rules under the Government's Directive No. 16 are being imposed in these Southern localities of COVID-19 hotspots (VGP 2021). The rapid spread of infections has prompted strict movement restrictions in around one-third of the country, with both Hanoi and Ho Chi Minh City under lockdown (Reuters 2021).

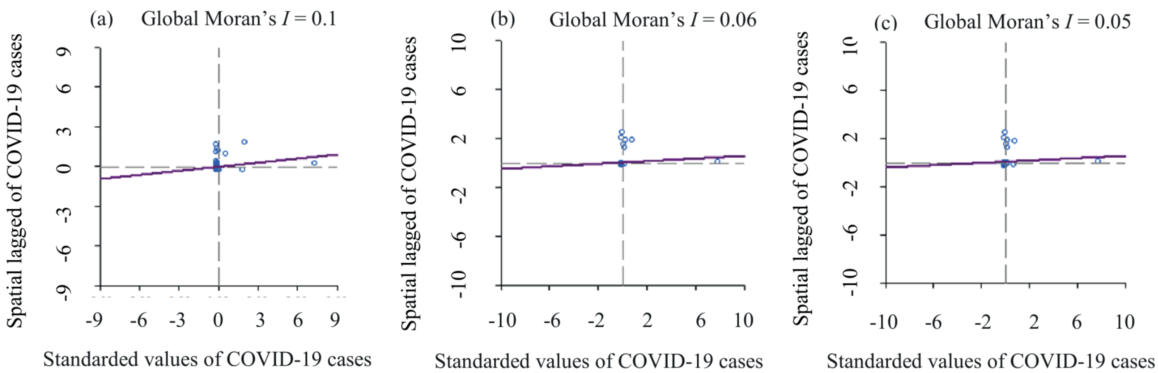

Fig. 4. Moran scatterplot of confirmed cases in the fourth wave of COVID-19 in Vietnam

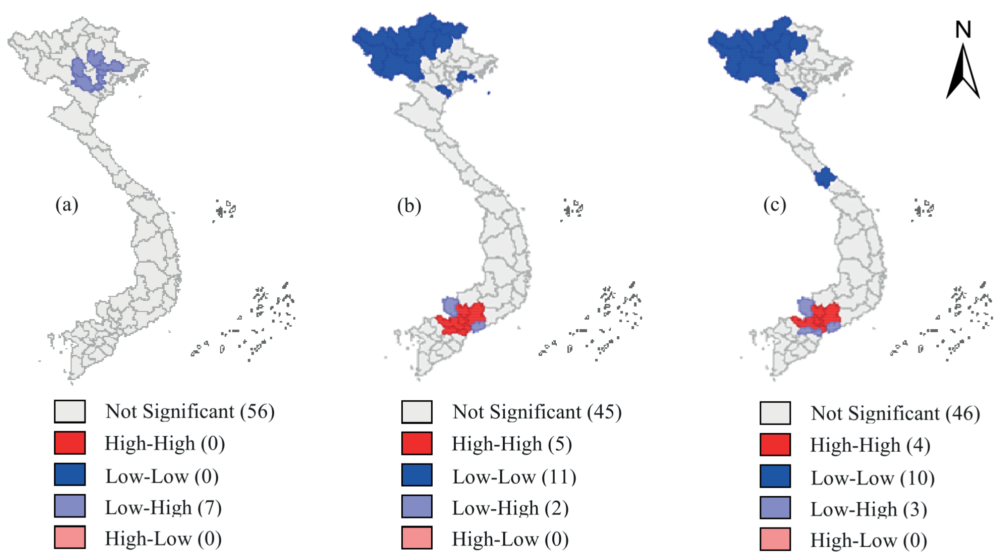

Fig. 5. Spatial clustering of the COVID-19 pandemic in the fourth wave in Vietnam

Hotspots of the COVID-19 pandemic

Maps from Figure 6 illustrate the spatial distribution of hotspots and coldspots of the COVID-19 pandemic in the fourth wave in Vietnam. In the first phase of the fourth COVID-19 wave (Figure 6-a), the local *Getis-Ord's* G^*_i statistic successfully identified a total of six COVID-19 hotspots in the North-Eastern region of Vietnam, including Bac Giang (5,083 cases), Bac Ninh (1,470 cases), Hanoi (464 cases), Hai Duong (51 cases), Thai Nguyen (7 cases), and Quang Ninh (1 case). Especially, two provinces have reported the highest number of new cases including Bac Giang (5,083 cases) and Bac Ninh (1,407 cases). In addition, 11 coldspots with a very low number of COVID-19 cases in provinces and cities of the central and Southern region were successfully detected. A recent study by Nguyen et al. (2021) has shown that effective policy solutions for COVID-19 response of the Vietnamese government such as swift governmental action, strict border control measures, effective communication of health promotion measures, widespread community engagement, expanded testing capacity and effective social measures can be account for the presence of these coldspots in this phrase. But in late April 2021, the highly transmissible Delta variant began to take hold in the Southern region of Vietnam, especially in Ho Chi Minh city – the country's economic engine (Tough 2021) and has caused the second phrase of COVID-19 in Vietnam.

Similar to those obtained using the local Moran's I (see Figure 5-b), the locations of hotspots of the COVID-19 pandemic quickly changed from the North-Eastern region in the first phase to the Southern region of Vietnam in the second phase of the fourth COVID-19 wave (Figure 6-b). In this second phase, the local *Getis-Ord's* G^*_i statistic successfully identified seven COVID-19 hotspots in the southern region of Vietnam and 11 coldspots in the North-Western cities/provinces in Vietnam. Similar to those obtained in the second phase by the local *Moran's I*, seven hotspots of COVID-19 included Ho Chi Minh city (52,913 cases), Binh Duong (6,146 cases), Long An (2,178 cases), and Dong Nai (1,778 cases), Tien Giang (1,245 cases), Ba Ria – Vung Tau (471 cases) and Tay Ninh (204 cases). Similar to those obtained in the second phase, hotspots of the COVID-19 pandemic in the whole of the fourth COVID-19 wave were also mainly detected in cities/provinces in the southern region of Vietnam (Figure 6-c). Among these hotspots of the COVID-19 pandemic, an unknown source of a COVID-19 cluster from a Christian congregation based in Go Vap district caused Ho Chi Minh city the most-affected local with 52,913 confirmed cases and 356 deaths (VnExpress 2021). A most recent study by Tough (2021) has also indicated that social distancing measures used to control previous variants have proven ineffective against the virulent Delta strain in these COVID-19 hotspot areas in Vietnam, and this prompted the Vietnamese authorities to impose increasingly strict lockdowns in these hotspot areas. Another important reason might be the very low testing capacities. In addition, a total of 10 coldspots caused by a very low number of COVID-19 cases was identified in the North-Western provinces. Travel restrictions and the effectiveness of local policies for COVID-19 response play an important role in the effective prevention and control of COVID-19 in these coldspot areas.

CONCLUSIONS

In this study, the spatial clustering of the COVID-19 pandemic was analyzed using spatial auto-correlation analysis. The spatial clustering including spatial clusters (high-high and low-low), spatial outliers (low-high and high-low), and hotspots of the COVID-19 pandemic were explored using the local *Moran's I* and *Getis-Ord's* G^*_i statistics. Results from a case study on 86,277 locally transmitted cases confirmed in two phases of the fourth COVID-19 wave in Vietnam showed that significant low-high spatial outliers and hotspots of COVID-19 were first detected in the North-Eastern region in the first phase. Significant high-high clusters and low-high outliers and hotspots were then identified in the Southern region of Vietnam in the second phase. It can be concluded that spatial statistics (Moran's I and *Getis-Ord's* G^*_i statistics) are of great help in understanding the spatial clustering of the COVID-19 pandemic. The study is limited by the lack of the relative values of the total COVID-19 confirmed cases and deaths to the total population of a municipality in the data used. It is, therefore, further studies regarding the role of the relative values would be worthwhile. Notwithstanding these limitations, the present findings confirm the effectiveness of spatial statistics, particularly spatial clustering analysis, in the fight against the COVID-19 pandemic. These empirical findings not only provide a new understanding of how the COVID-19 pandemic is spatially clustered, but also may be help mitigate the effects of the COVID-19 clustering area and making appropriate decisions related to the health, economic, and social system.

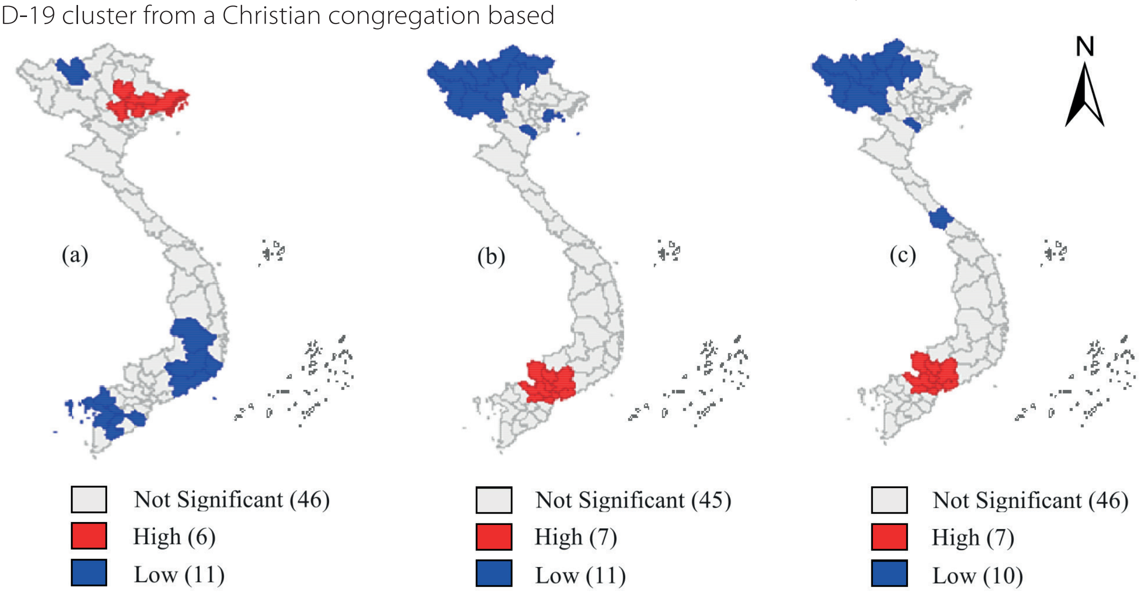

Fig. 6. Hot spots of the COVID-19 pandemic in the fourth wave in Vietnam

AUTHOR CONTRIBUTIONS

Tien-thanh Nguyen conceived and designed the study. Danh-tuyen Vu and Anh-huy Hoang collected the data. Tien-thanh Nguyen and Anh-huy Hoang performed the statistical analysis. Tien-thanh Nguyen and Danh-tuyen Vu prepared the manuscript. All authors discussed the results, implications and commented on the manuscript at all stages.

REFERENCES

Alves J. D., Abade A.S., Peres W.P., Borges J.E., Santos S.M., Scholze A.R. (2021). Impact of COVID-19 on the indigenous population of Brazil: A geo-epidemiological study. MedRxiv, DOI: 10.1101/2021.01.12.21249703.

Anselin L. (1995). Local indicators of spatial association—LISA. Geographical analysis, 27, 93-115, DOI: 10.1111/j.1538-4632.1995.tb00338.x.

Anselin L. (2005). Exploring spatial data with GeoDaTM: a workbook. Center for spatially integrated social science.

Anselin L., Syabri I., Kho Y. (2016). GeoDa: An introduction to spatial data analysis. 2005 Reference Source, DOI: 10.1007/978-3-642-03647-7_5.

Bhunia G.S., Roy S., Shit P.K. (2021). Spatio-temporal analysis of COVID-19 in India–a geostatistical approach. Spatial Information Research, 29, 661-672, DOI: 10.1007/s41324-020-00376-0.

Choi J.Y. (2020). COVID-19 in South Korea. Postgraduate medical journal, 96, 399-402, DOI: 10.1136/postgradmedj-2020-137738.

Cliff A.D., Ord J.K. (1981). Spatial processes: models & applications. Taylor & Francis.

Das A., Ghosh S., Das K., Basu T., Dutta I., Das M. (2021). Living environment matters: Unravelling the spatial clustering of COVID-19 hotspots in Kolkata megacity, India. Sustainable Cities and Society 65, 102577, DOI: 10.1016/j.scs.2020.102577.

Duy C., Nong V.M., Van Ngo A., Doan T.T., Nguyen T.Q., Truong P.T. (2021). Nosocomial coronavirus disease outbreak containment, Hanoi, Vietnam, March–April 2020. Emerging infectious diseases, 27(1), 10-17, DOI: 10.3201/eid2701.202656.

Getis A., Ord J. K. (1996). Local spatial statistics: an overview. Spatial analysis: modelling in a GIS environment, 374, 261-277.

Ha B.T.T., La Quang N., Mirzoev T., Tai N.T., Thai P.Q., Dinh P.C. (2020). Combating the COVID-19 epidemic: experiences from Vietnam. International journal of environmental research and public health, 17, 3125, DOI: 10.3390/ijerph17093125.

Han Y., Yang L., Jia K., Li J., Feng S., Chen W. (2021). Spatial distribution characteristics of the COVID-19 pandemic in Beijing and its relationship with environmental factors, Science of The Total Environment 761:144257, DOI: 10.1016/j.scitotenv.2020.144257.

HanoiTimes. (2021). Why does Hai Duong become a hotspot of Covid-19? http://hanoitimes.vn/why-does-hai-duong-become-a-hotspot-of-covid-19-316326.html. [Accessed 01 Nov. 2021].

Hoang H.A., Vu T.D., Nguyen T.T. (2017). Spatial Variability Analysis of Cu Content: A Case Study in Jiurui Copper Mining Area. International Journal of Applied Geospatial Research (IJAGR), 8,81-93, DOI: 10.4018/IJAGR.2017010105.

Hoang V.M., Hoang H.H., Khuong Q.L., La N.Q., Tran T.T.H. (2020). Describing the pattern of the COVID-19 epidemic in Vietnam. Global health action, 13, 1776526, DOI: 10.1080/16549716.2020.1776526.

Huang R., Xia J., Chen Y., Shan C., Wu C. (2020). Outbreak investigation for COVID-19 in northern Vietnam. The Lancet Infectious Diseases, 20(5), 535-536, DOI: 10.1016/S1473-3099(20)30159-6.

Kim S., Castro M.C. (2020). Spatiotemporal pattern of COVID-19 and government response in South Korea (as of May 31, 2020). International Journal of Infectious Diseases 98, 328-333, DOI: 10.1016/j.ijid.2020.07.004.

La V.P., Pham T.H., Ho M.T., Nguyen M.H., Nguyen K.L., Vuong T.T., Vuong Q.H. (2020). Policy response, social media and science journalism for the sustainability of the public health system amid the COVID-19 outbreak: the Vietnam lessons. Sustainability, 12(7), 2931, DOI: 10.3390/su12072931.

Lalor G.C., Zhang C. (2001). Multivariate outlier detection and remediation in geochemical databases Science of the total environment 281(1-3), 99-109, DOI: 10.1016/S0048-9697(01)00839-7.

Le T.H., Tran T.P.T. (2021). Alert for COVID-19 second wave: A lesson from Vietnam. Journal of global health, 11: 03012, DOI: 10.7189/jogh.11.03012.

Liu M. et al. (2021). The spatial clustering analysis of COVID-19 and its associated factors in mainland China at the prefecture level, Science of The Total Environment, 777, 145992, DOI: 10.1016/j.scitotenv.2021.145992.

MHV (2021). COVD-19 Information Website of Ministry of Health, Vietnam. Ministry of Health of Vietnam. https://ncov.moh.gov.vn/. [Accessed 01 Nov. 2021]

Mitchel A. (2005). The ESRI Guide to GIS analysis, Volume 2: Spartial measurements and statistics ESRI Guide to GIS analysis. ESRI press.

Nguyen T., Liu X., Ren Z. (2014). A Study Of Geochemical Exploration Spatial Cluster Identificaton Based On Local Spatial Autocorrelation. Geophysical and Geochemical Exploration. 38, 370-376 (In Chinese with English summary).

Nguyen T.H., Vu D.C. (2020). Summary of the COVID-19 outbreak in Vietnam–Lessons and suggestions. Travel medicine and infectious disease, 37, 101651, DOI: 10.1016/j.tmaid.2020.101651.

Nguyen T.T. (2018). Use of Moran's I and robust statistics to separate geochemical anomalies in Jiurui area (Southeast China). Bulletin Of The Mineral Research and Exploration, 156(156), 179-192, DOI: 10.19111/bmre.01695.

Nguyen T.T., Vu D.T., Trinh L.H., Nguyen T.L.H. (2016). Spatial Cluster and Outlier Identification of Geochemical Association of Elements: A Case Study in Juirui Copper Mining Area. Bulletin Of The Mineral Research and Exploration, 153(153), 159-167, DOI: 10.19111/bulletinofmre.351376.

Nguyen T.T., Vu T.D. (2019a). Identification of multivariate geochemical anomalies using spatial autocorrelation analysis and robust statistics. Ore Geology Reviews, 111:102985, DOI: 10.1016/j.oregeorev.2019.102985.

Nguyen T.T., Vu T.D. (2019b). Use of Hot Spot Analysis to Detect Underground Coal Fires from Landsat-8 TIRS Data: A Case Study in the Khanh Hoa Coal Field, North-East of Vietnam. Environment and Natural Resources Journal, 17(3), 1-10, DOI: 10.32526/ennrj. 32517.32523.32019.32517.

Nguyen T.V., Dai Tran Q., Phan L.T., Vu L.N., Truong D.T.T., Truong H.C., Pham Q.D. (2021). In the interest of public safety: rapid response to the COVID-19 epidemic in Vietnam. BMJ global health, 6(1), e004100, DOI: 10.1136/bmjgh-2020-004100.

Ord J.K., Getis A. (1995). Local spatial autocorrelation statistics: distributional issues and an application. Geographical analysis, 27, 286-306, DOI: 10.1111/j.1538-4632.1995.tb00912.x.

Phuong H.V.M., Dai Tran Q., Phan L.T., Vu L.N., Truong D.T.T., Truong H.C., Pham Q.D. (2021). Novel Mutation of SARS-CoV-2, Vietnam, July 2020. Emerging Infectious Diseases, 27(1519), DOI: 10.1136/bmjgh-2020-004100.

Ramírez-Aldana R., Gomez-Verjan J. C., Bello-Chavolla O. Y. (2020). Spatial analysis of COVID-19 spread in Iran: Insights into geographical and structural transmission determinants at a province level. PLoS neglected tropical diseases, 14:e0008875, DOI: 10.1371/journal.pntd.0008875.

Reuters (2021). Vietnam taps private hospitals as Delta-driven COVID-19 infections rise. Reuters. https://www.reuters.com/world/asia-pacific/vietnam-taps-private-hospitals-delta-driven-covid-19-infections-rise-2021-07-30/. [Accessed 01 Nov. 2021].

Robinson T.P. (2000). Spatial statistics and geographical information systems in epidemiology and public health. Advances in Parasitology, 47, 81-128, DOI: 10.1016/S0065-308X(00)47007-7

Rose-Redwood R. et al. (2020). Geographies of the COVID-19 pandemic Dialogues in Human. Geography, 10(2), 97-106.

Shepherd M. (2020). Why Geography is a key-part of fighting the COVID-19 Coronavirus outbreak. Forbes.

Tough R. (2021). Ho Chi Minh City during the fourth wave of COVID-19 in Vietnam. City & Society 33(3), 1-13. Available at: https://ueaeprints.uea.ac.uk/id/eprint/81878/1/Accepted_Manuscript.pdf [Accessed 01 Nov. 2021]

Tran A., Deparis X., Dussart P., Morvan J., Rabarison P., Remy F., Gardon J. (2004). Dengue spatial and temporal patterns, French Guiana, 2001. Emerging infectious diseases, 10(615), DOI: 10.3201/eid1004.030186.

United Nations (2020). The Social Impact of COVID-19. https://www.un.org/development/desa/dspd/2020/04/social-impact-of-covid-19/. [Accessed 01 Nov. 2021].

VGP (2021). Gov't may impose stricter social distancing in COVID-19 hotspots. http://news.chinhphu.vn/Home/Govt-may-impose-stricter-social-distancing-in-COVID19-hotspots/20217/44715.vgp. [Accessed 01 Nov. 2021].

VietNamNews (2021a). Bắc Giang sees highest daily cases amid COVID-19 fourth wave. https://vietnamnews.vn/society/956680/bac-giang-sees-highest-daily-cases-amid-covid-19-fourth-wave.html. [Accessed 01 Nov. 2021].

VietNamNews (2021b). Fourth wave of COVID-19 in Việt Nam longer and much more serious than previous ones: Health Minister. VietNamNews. https://vietnamnews.vn/society/994206/fourth-wave-of-covid-19-in-viet-nam-longer-and-much-more-serious-than-previous-ones-health-minister.html. [Accessed 01 Nov. 2021].

VnExpress (2021). HCMC detects four new Covid clusters with unidentified transmission sources. https://e.vnexpress.net/news/news/hcmc-detects-four-new-covid-clusters-with-unidentified-transmission-sources-4292516.html. [Accessed 01 Nov. 2021].

VnExpress (2021a). Van Don airport in Covid-19 cluster reopens after more than a month. https://e.vnexpress.net/news/news/van-don-airport-in-covid-19-cluster-reopens-after-more-than-a-month-4242771.html. [Accessed 01 Nov. 2021].

VnExpress (2021b). Vietnam records nine more Covid-19 community transmissions. https://e.vnexpress.net/news/news/vietnam-records-nine-more-covid-19-community-transmissions-4231748.html. [Accessed 01 Nov. 2021].

VnExpress. (2021c). Covid-19 hotspot Bac Ninh permits reopening of Canon factory. https://e.vnexpress.net/news/business/companies/covid-19-hotspot-bac-ninh-permits-reopening-of-canon-factory-4281449.html. [Accessed 01 Nov. 2021].

Wang H., Du Z., Wang X., Liu Y., Yuan Z., Liu Y., Xue F. (2015). Detecting the association between meteorological factors and hand, foot, and mouth disease using spatial panel data models. International Journal of Infectious Diseases 34:66-70, DOI: 10.1016/j.ijid.2015.03.007.

WHO (2021). WHO Coronavirus (COVID-19) Dashboard. https://covid19.who.int/. [Accessed May 2021].

Xie Z., Qin Y., Li Y., Shen W., Zheng Z., Liu S. (2020). Spatial and temporal differentiation of COVID-19 epidemic spread in mainland China and its influencing factors. Science of The Total Environment 744:140929. DOI: 10.1016/j.scitotenv.2020.140929.

Zhang S.L., Zhang K. (2007). Comparison between general Moran's Index and Getis-Ord general G of spatial autocorrelation. Acta Scientiarum Naturalium Universitatis Sunyatseni, 4(022).

RESEARCH PAPER

TOWARDS A STRATEGIC APPROACH OF COVID-19 CLUSTER WEB MAPPING IN MALAYSIA

Noorfatekah Talib[1*], Nur Nabila Mohd Fuad[1], Nurhafiza Md Saad[1], Nurul Ain Mohd Zaki[1], Nurhanisah Hashim[2], Mohd Amsyar Abdullah[3]
[1]Centre of Studies for Surveying Science and Geomatics, Faculty of Architecture, Planning and Surveying, Universiti Teknologi MARA, Cawangan Perlis, Kampus Arau, 02600, Arau, Perlis, Malaysia
[2]Centre of Studies for Surveying Science and Geomatics, Faculty of Architecture, Planning and Surveying, Universiti Teknologi MARA, Shah Alam, Selangor, Malaysia
[3]Affinivo Consultant Plt, 43300 Seri Kembangan, Selangor, Malaysia
*Corresponding author: noorf492@uitm.edu.my
Received: July 31th, 2021 / Accepted: November 9th, 2021 / Published: December 31st, 2021
https://doi.org/10.24057/2071-9388-2021-088

ABSTRACT. The world was shocked by an unprecedented outbreak caused by coronavirus disease 2019 (COVID-19). In Malaysia, it started with the largest number of COVID-19 cases with the first wave of infection on 25 January 2020. The objectives of this paper are to obtain the perspective of the respondents about the need for web-mapping in the form of mapping the geospatial data in Malaysia and to visualize the current online datasets of COVID-19 disease case clusters. The study area would cover the entire Malaysia since a rapidly increasing number of citizens were affected by this virus. To be specific, this study focused on the active clusters of COVID-19 in Malaysia. The data were freely shared in real-time by referring to the Ministry of Health (MOH) channel. The hotspots map were explored using the Map Editor by Cloud GIS. The approach has been illustrated using a dataset of whole Malaysia which are locally transmitted confirmed cases in four phases of COVID-19 wave in Malaysia. This study is significant to raise public awareness of the virus, especially among Malaysian citizens. It can provide an accurate estimation of the cluster tracking of the COVID-19 system by using geospatial technology. Therefore, people are more concerned and followed all the Standard Operating Procedure (SOP) provided by the government to prevent the spread of COVID-19.

KEYWORDS: COVID-19; cluster cases; geospatial data; GIS

CITATION: Noorfatekah Talib, Nur Nabila Mohd Fuad, Nurhafiza Md Saad, Nurul Ain Mohd Zaki, Nurhanisah Hashim (2021). Towards A Strategic Approach Of Covid-19 Cluster Web Mapping In Malaysia. Geography, Environment, Sustainability, Vol.14, No 4, p. 148-154 https://doi.org/10.24057/2071-9388-2021-088

ACKNOWLEDGEMENTS: The authors would like to express their gratitude to the Ministry of Higher Health (MOH), Malaysia for data sharing, Universiti Teknologi MARA, Arau Campus, Malaysia, for the administrative support and Mr. Mohd Amsyar who offered invaluable guidance in this research. The authors also thank the editors and the anonymous reviewers for their valuable comments that significantly improved the manuscript.

Conflict of interests: The authors reported no potential conflict of interest.

INTRODUCTION

SARS-CoV-2 is the virus that causes COVID-19. This contagion is a new coronavirus recently announced by the World Health Organization (WHO), and it can cause severe pneumonia and acute respiratory distress syndrome (ARDS) (Li et al. 2020). According to WHO (2020), since the COVID-19 pandemic, more than 332,930 people from 147 countries and regions have been reported to be sick. As of 23rd March 2020, 14,510 people have died from the rapidly spreading virus, including Malaysia. The case in Malaysia began on the 25th January 2020. The Health Minister in Malaysia, Datuk Seri Dr Dzulkefly Ahmad confirmed that the first case of COVID-19, involving three Chinese citizens who entered from Singapore via Johor on 23rd January 2020. The Ministry of Health of Malaysia advised the people not to travel to China without a concrete reason Bernama (2020). As a result of the virus infection, there were various COVID-19 clusters in Malaysia, with the biggest clusters being the tabligh assembly cluster at Sri Petaling Mosque. The biggest challenge in the battle against the spreading epidemic is identifying ways to change the conventional technological approaches and to increase the pace and precision of social management delivery (Zhou et al. 2020). As the COVID-19 virus is still active and data collection is continuing worldwide, most countries are actively gathering data through various methods for the future. Therefore, this study used ArcGIS Online and GIS Cloud platform to convey information about the COVID-19 virus according to clusters in Malaysia in the form of mapping, and to display the data attributes obtained from MOH.

In Malaysia, many clusters exist because COVID-19 disease is highly transmissible even by touch. The collection of disease clusters was created to facilitate the MOH to detect potentially infected individuals and prevent it from spreading widely. In addition, there are about five largest clusters of COVID-19 infection in Malaysia which are Perhimpunan di Seri Petaling, Persidangan Keagamaan di Kuching, Majlis Perkahwinan di Bandar Baru Bangi, individu sejarah perjalan ke Itali, and Sub-cluster Seri Petaling di Daerah Rembau (Amirudin Shari, 2020 and Michael, 2020). According to Ruzki and Karim (2020), the MOH was still investigating the cause of the infection that led to the emergence of new clusters in the capital's construction sector. To help counter the COVID-19 pandemics, the government of Malaysia initiated the Movement Control Order (MCO), effective on 18 March 2020, in order to increase social distancing and slow down the transmission rate of the virus. The MCO order was extended multiple times and has, at times, switched to either the Conditional Movement Control Order (CMCO), the Recovery Movement Control Order (RMCO), or the Enhanced Movement Control Order (EMCO). Following the MCO stages, the National Recovery Plan (NRP) was put in place starting June 1, 2021. NRP consists of a four – phase recovery plan that is developed to steer Malaysia out of the pandemic. The three key conditions to be met to move to a next phase are related to daily COVID – 19 cases, the rate of bed use in ICUs, and the percentage of the population fully vaccinated.

At the latest news, MOH has identified a new COVID-19 cluster of six cases at the Depot Tahanan Imigresen Sepang (DTI), Selangor, the third cluster involving DTI as stated by Bernama (2020). Husain and Adnan (2020) stated that the number of DTI Bukit Jalil cluster cases jumped to 608. New cases recorded in this cluster involved illegal immigrants detained at the centre. All cases detected involved foreigners. Apart from that, referring to Iwan Shu-Aswad Shuaib (2020), most of the cases that increased in September were from the Fortress Cluster in Sabah.

Meanwhile, some clusters have been declared to come to an end, meaning that no new cases are recorded in the cluster based on the specified time. The key criterion for terminating clusters is that there are no new cases after two incubation cycles (14 days or one incubation) using the symptom date of the last case or no symptoms 28 days after the date of the previous COVID-19 positive case Ministry of Health Malaysia (2020). Particularly, there is no previous study that has investigated cluster cases in Malaysia. It is believed that this study can be visualized as real time data using web mapping to locate the transmitted cluster COVID-19 cases.

STUDY AREA AND DATA USED

The study area as shown in Figure 1 focused on Malaysia as a whole. Malaysia is located north of the Equator, consisting of two unconnected areas, namely Peninsular Malaysia or known as West Malaysia, and East Malaysia, located in the Borneo island. The country consists of 14 states including federal states with a total area of 329 847 km^2 . This area was chosen because, until 25th October 2020 (Ministry of Health 2020), Malaysia was the fifth country in the list of Asian countries with an increasing number of cases day by day.

Data collected through individuals infected with the COVID-19 virus were obtained from the MOH via websites Ministry of Health (2020) and social media, such as Facebook and Telegram to achieve the first objective. Data collection focused on the cluster data. All data collected was entered manually into the Mobile Data Collection (MDC) platform and continued to be updated daily. Based on Table 1, the

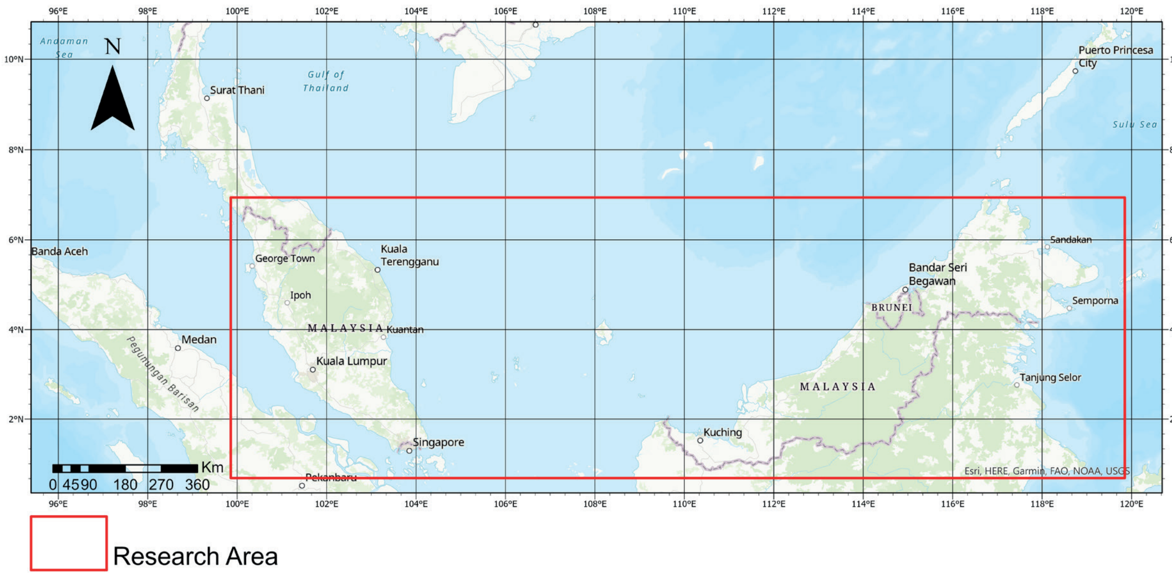

Fig. 1. The location of the research area, Malaysia

Table 1. Sample of Cluster Data From 18th March 2020 until 14th April 2020 during Movement Control Order (Source: https://t.me/cprckkm)

Cluster	State	New Cases	Total Cases	Total Active Cases	Total ICU Cases	Total Cured Cases	Total Cases Died
Majlis Perkahwinan Bandar Baru Bangi	Putrajaya, Kedah, Perak, Selangor, Negeri Sembilan, Johor, Melaka, Kelantan & Terengganu	0	96	72	1	24	0
PUI Itali	Sarawak	0	50	34	1	11	5
PUI Bali	Pahang & Kelantan	0	20	16	3	3	1
Rembau	Negeri Sembilan	0	53	9	0	44	0
Persidangan Gereja	Sarawak	0	50	34	1	11	5

clusters existed from 18th March 2020 until 14th April 2020. That was an example of data taken daily using the MDC platform. However, the complete number of infections, and data on clusters were updated through the same platform.

METHODOLOGY

The questionnaire was created to determine the need for web mapping among the public, and the analysis was done using Statistical Package for Social Sciences (SPSS) software to analyze the findings from the respondents through questionnaires provided. Then, all the data processing is continued using MDC throughout the Map Editor mode Attributes which have been added to in Map Editor is basically the number of COVID-19 cluster cases collected from a database provided by the official website of the Ministry of Health of Malaysia (MOH 2020). The data is collected during Movement Contro Order (MCO) from 18th Mac 2020 until 9th November 2020.

In addition, the daily data appears with a great base map, and from that, the data can be downloaded to import to ArcGIS Online. A form is created (Figure 2) using MDC Mobile App to facilitate the information filling process. The beauty is, the form can be customized based on the user's requirement. Therefore, the data can be inserted easily as it is in real time data. After that, the data is saved automatically in the cloud through Map Editor as shown in Figure 3(a). Once a user clicks on an existing point that has been created, it will display all the cluster's attribute data. Users also can view the images as shown in Figure 3(b) after clicking the image icon in the attribute data.

Lastly, ArcGIS Online is used to facilitate sharing with the public to view the map and provide views through the web-mapping questionnaires. After the processing is done, it started with mapping the data collection and shared the link of online mapping with the public to know their perspective. After the spatial attributes were constructed in the software, the hotspot maps can be automatically applied. The map shows the distribution of cluster cases of COVID-19 in Malaysia from MCO 1 until RMCO finally used for the evaluation of the spatial clustering of the COVID-19 pandemic. The public could see the map and turn on or off the layer according to MCO's phase. Therefore, the public could learn about the existence of COVID-19 clusters by district more carefully.

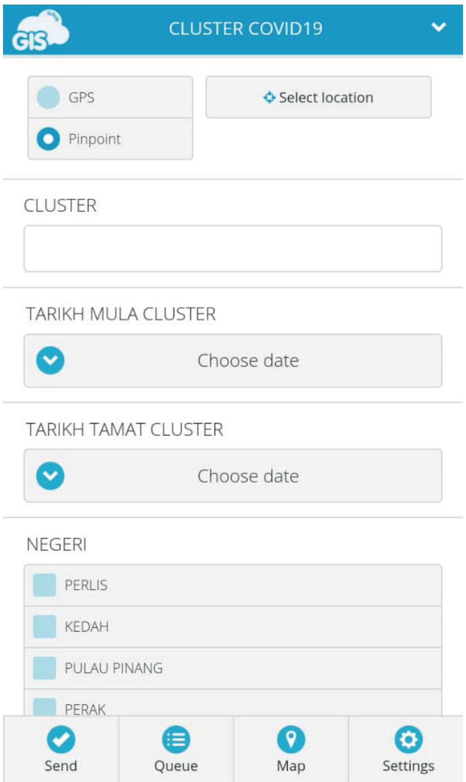

Fig. 2. Customize Form in MDC Application

RESULTS

Data Analysis

From the questionnaire 75 percent of the respondents preferred information of COVID-19 cases to be presented using interactive maps. Next, about 17.11 percent chose the graph method as an alternative to information delivery. The rest, about 9.89 percent, chose the table as a method of information delivery. For a better understanding, Table 2 shows the frequency and percentage of respondents on their preference for information presentation. The frequency of respondents choosing the

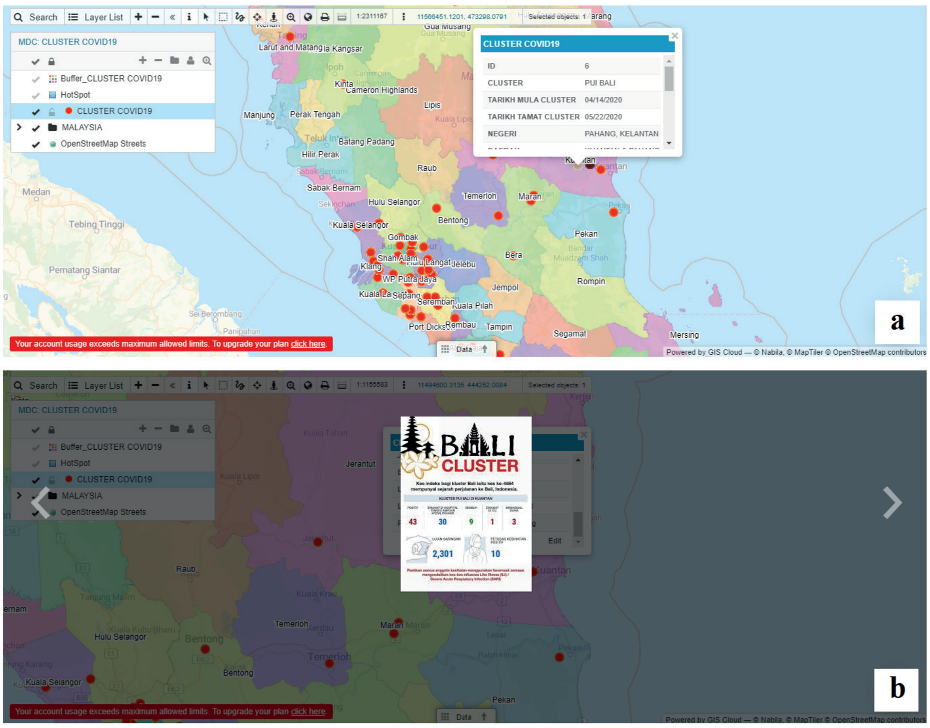

Fig. 3. Map View with the attribute data of cluster cases (a) and the image window of the attribute data (b)

Table 2. The Frequency and Percentage of The Preference for Information Presentatio

Preference for Information Presentation	Frequency	Percentage
Graph	13	17.1
Interactive Map	57	75.0
Table	6	7.9

interactive map as an information delivery platform was 57 respondents; 13 respondents chose the graph, and six respondents chose the table as the method of information delivery. Thus, most respondents chose the interactive map as the platform to deliver the information about the COVID-19 clusters.

In addition to that, according to the bar graph in Figure 4(a), 92.11 percent of respondents agreed that this application was informative, and only 7.895 percent thought that it may be useful. Table 3 shows the frequency and percentage of the opinion on the content. Seventy respondents considered it informative compared to the other six respondents. Thus, the content provided was informative to the public. Table 3 shows the frequency and percentage of rating on online mapping, showing that 51.3 and 40.8 percent rated the online mapping as «Very Good» and «Good». The remaining 7.9 percent only rated «Neutral». The histogram in Figure 4(b) shows an ascending chart with 39 respondents as the highest respondents. The lowest was six respondents while the mean respondents were 4.43, and the standard deviation was 0.639. Therefore, the rating of this application was good.

Data and Map Visualizations

Figure 5 below shows the Interactive Map-COVID-19 Cluster in Malaysia. It showed from the MCO 1 until RMCO, where all the data is collected from 18th March 2020 until 9th November 2020. Besides, the public user can view the map through ArcGIS Online. On the website view, users could view the detailed data about each cluster available in Malaysia. From the content, users can turn on or off the button layers which are referring to the designated MCO phases. In addition, at each layer, as shown in (a), the users are able to click the attribute data on the map. Following,

Table 3. The Frequency and Percentage of The Preference for Information Presentation

Rating on Online Mapping	Frequency	Percentage
Neutral	6	7.9
Good	31	40.8
Very Good	39	51.3

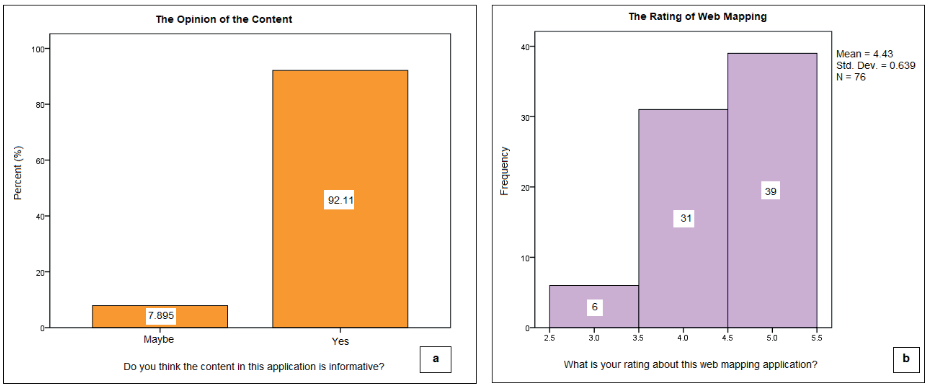

Fig. 4. Bar graph of the opinion on the content (a) and Histogram of the rating on online mapping (b)

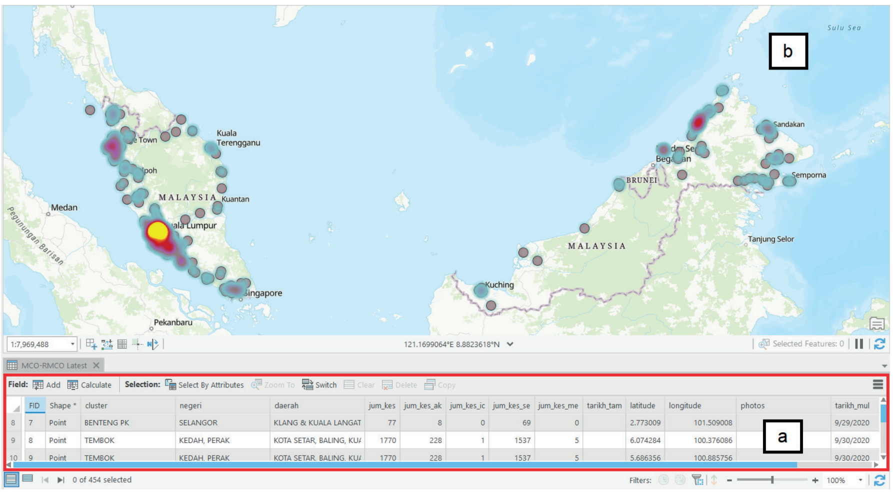

Fig. 5. An Interactive Map of Cluster COVID-19 Cases in Malaysia using ArcGISPro

the table is shown at the bottom of the interface in the interactive map (b). All the details of the spatial data are save in the attribute field. To be specific, if users clicked on the point area, it would pop out the attribute table. Hence, this map is user friendly for everyone. According to the previous study by Howell et al. (2019), for practitioners interested in researching the scope of the existing aspen sciences, they created a user-friendly, map-based online tool.

DISCUSSION

Figure 6 shows the map distribution of COVID-19 cluster during MCO 1 until MCO 4. The data in MCO 1 were taken from 18th March 2020 to 31st March 2020. About eight districts have been involved in the same cluster case, namely the Majlis Perkahwinan Bandar Baru Bangi Cluster. The districts affected were Kota Setar, Kinta, Melaka Tengah, Klang, Sepang, Seremban, Kota Baharu, and Johor Bharu. The total number of cases in this cluster was 96 cases. However, this cluster did not spread to Sarawak and Sabah. Only states in the peninsular were involved.

Next, the result shows the map distribution of cluster COVID-19 along with MCO 2. This phase starts on 1st April 2020, until 14th April 2020. In this phase, there are five clusters, and seven districts are involved. During MCO 3, the data were taken from 15th April 2020 to 28th April 2020. During this phase, about 20 districts were recorded as clustered. Subsequently, during MCO 4, this phase starts on 29th April 2020 until 12th May 2020. During this phase, the cases have started to decrease, and only six clusters are recorded.

Besides, Figure 7 shows the map distribution of COVID-19 cluster during the Recovery Movement Control Order (RMCO). This phase took place from 10th June 2020 to 31st March 2021, and the data were taken until 9th November 2020. Referring to the figure, the green dot indicates that the recorded cluster case has expired while the red dot indicates that the cluster case is still ongoing at that time. For the clusters that have expired, the most scattered cluster was the Tawar cluster. This cluster involved seven districts, specifically Baling, Kuala Muda, Kulim, Sik, Barat Daya, Timur Laut and Seberang Prai Utara. The PUI Sivagangga cluster spread to five districts: Kangar, Kubang

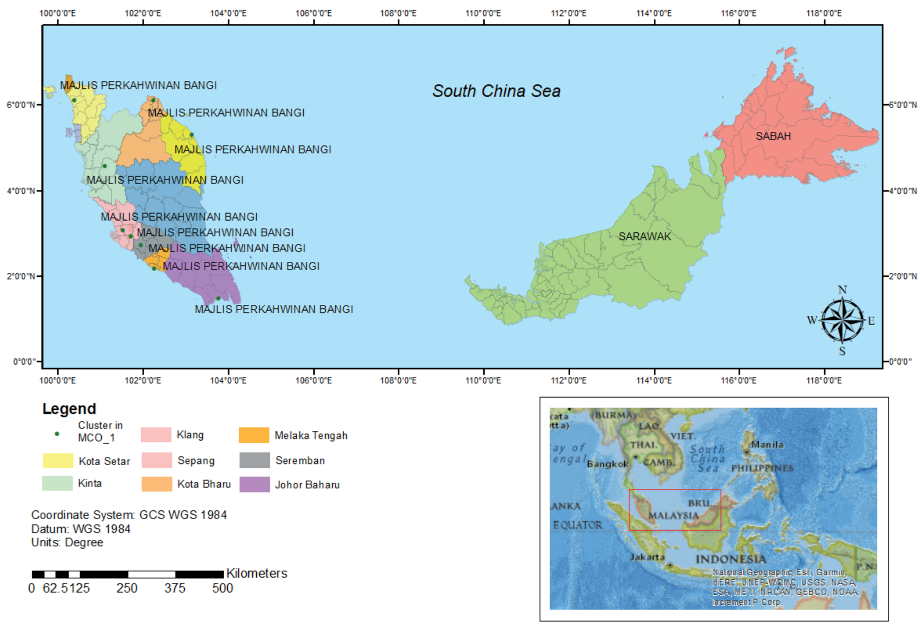

Fig. 6a. Map Distribution of Cluster COVID-19 along movement control order (MCO 1) in Malaysia

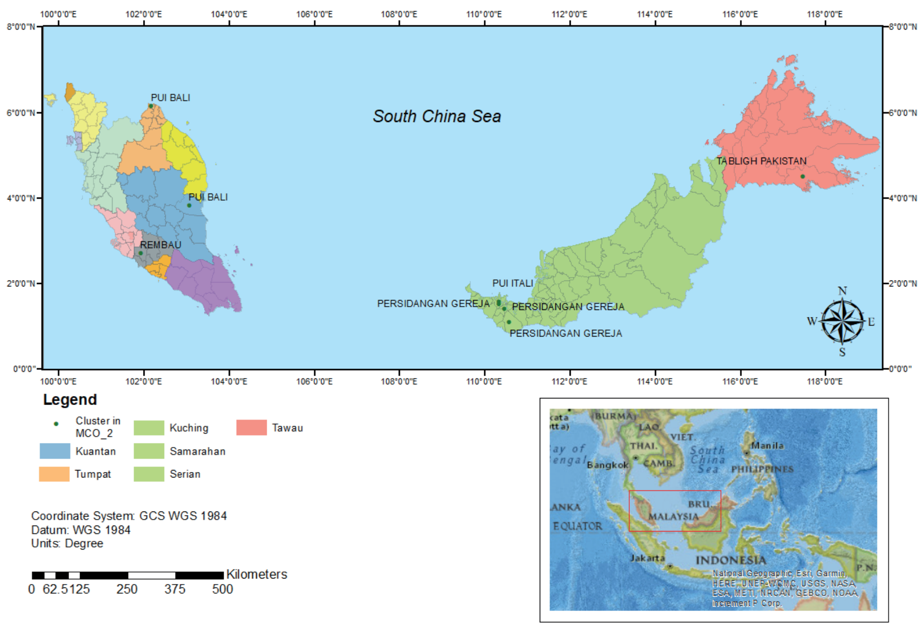

Fig. 6b. The Map Distribution of Cluster COVID-19 along movement control order (MCO 2) in Malaysia

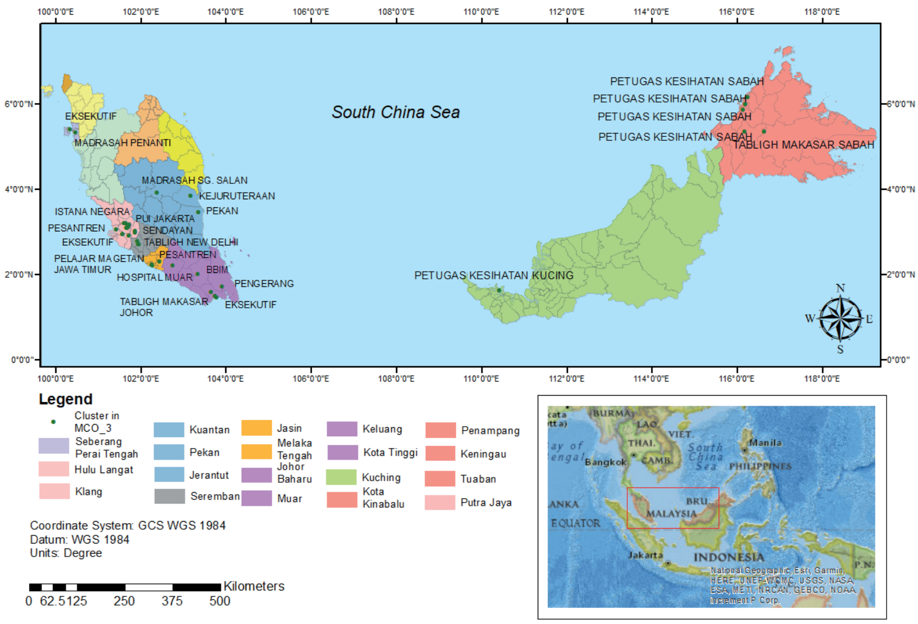

Fig. 6c. The Map Distribution of Cluster COVID-19 along movement control order (MCO 3) in Malaysia

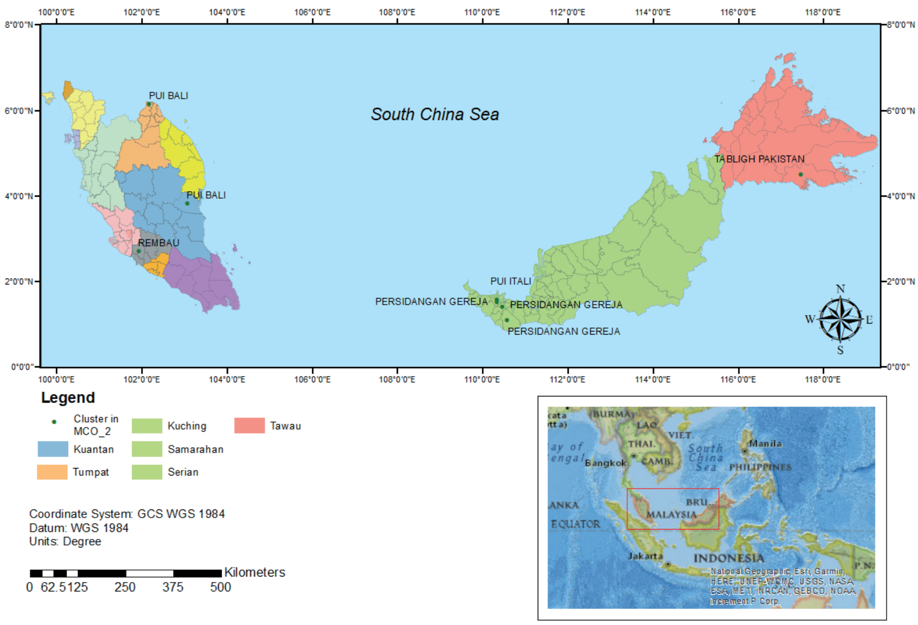

Fig. 6d. Map Distribution of Cluster COVID-19 along movement control order (MCO 4) in Malaysia

Pasu, Padang Terap, Kulim, and Seberang Prai Tengah. The Selasih Cluster spread to four districts: Putrajaya, Sepang, Johor Bharu, and Seremban. The Bah Puchong cluster also spread to four districts: Klang, Kinta, Larut Matang and Selama, and Titiwangsa.

However, the cluster categories from 10th June 2020 until 9th November 2020 were represented by a red dot. The Jalan Meru cluster was a cluster spread to 15 districts starting from 1st October 2020. The districts involved were Hulu Langat, Klang, Gombak, Petaling, Hulu Selangor, Kuala Selangor, Johor Bharu, Batu Pahat, Kota Baharu, Titiwangsa, Lembah Pantai, Kepong, Cheras, Temerloh, and Muallim. Although the number of cases was not high, its spread to the districts was the highest. Next, the Kaya Cluster also spread to 15 districts. The districts involved were Seremban, Port Dickson, Kuala Pilah, Lembah Pantai, Cheras, Kepong, Putrajaya, Melaka Tengah, Sepang, Klang, Kuala Langat, Kuala Selangor, Petaling, Hulu Langat, and Kluang. The Simera cluster, on the other hand, involved 14 districts, namely Besut, Kuantan, Petaling, Klang, Hulu Langat, Gombak, Port Dickson, Manjung, Hilir Perak, Johor Bharu, Muar, Lembah Pantai, Putrajaya and Tanah Merah.

Over the map below, the district in Sabah recorded 14 districts affected by COVID-19 infection. However, it might increase rapidly because the state had 26 districts; hence, the cluster cases could spread to several districts. Referring to other states, almost all districts in some states had clusters of cases.

In addition, a survey about recommendations also has been collected. Overall, positive feedback from the respondent said that all the information given is easy to understand by the public, not just for geospatial or geomatic users. Subsequently, some of the respondents suggested in adding some facts about how COVID-19 can spread or awareness about themselves from the virus. Another recommendation is to add some statistical graphics and area status according to the allowed movement control. The next suggestion is to update the new distribution cluster of their location.

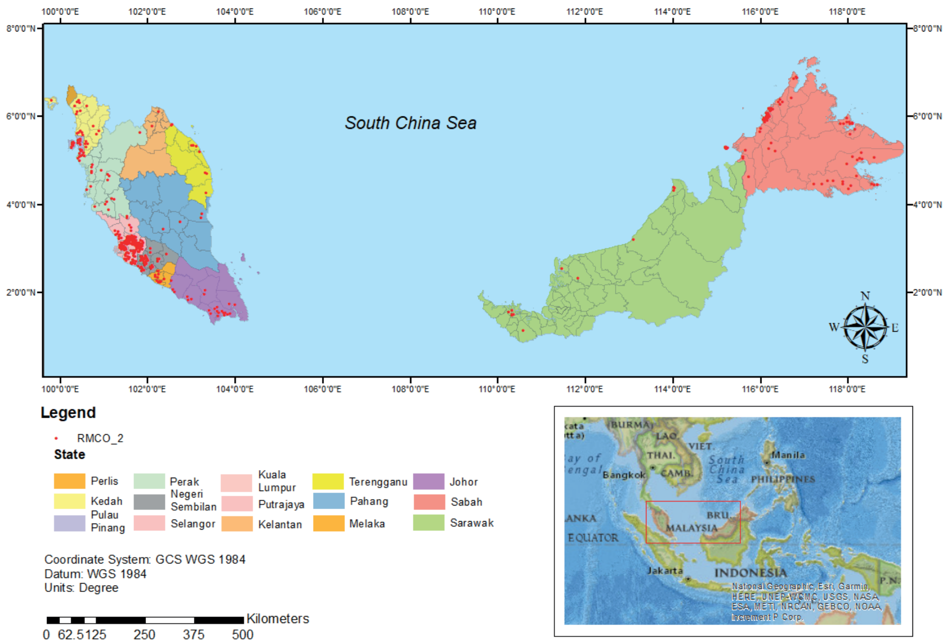

Fig. 7. Map distribution of COVID-19 cluster during the Recovery Movement Control Order (RMCO)

CONCLUSIONS

From this study, the society preferred interactive maps rather than graphics and tables. This has been proven in the first objective: to obtain the respondents' perspective on the need for web mapping. The questionnaires helped address the next goal. Overall, all the feedback from the respondents is in good vibes and constructive. The second objective was achieved by visualizing an online dataset of COVID-19 clusters. The clusters' daily data were collected and visualized through web mapping. This process was carried out using the Cloud GIS approaches. Next, from the generated map, the spatial analysis is automatically defined to find out the number of clusters scattered and the hotspot area. Furthermore, the map also recorded the highest number of cases according to the specified period or cluster. COVID-19 is the latest pandemic that involves the entire world, and it is very dangerous to human health. Hopefully, by generating this map, it can help our nation to create awareness in fighting the COVID-19.

REFERENCES

Amirudin Shari (2020). 5 Kluster Jangkitan Covid-19 Terbesar di Malaysia. Available at: https://www.amirudinshari.com/posts/5-kluster-jangkitan-covid-19-terbesar-di-malaysia.

Bernama (2020a). KKM sahkan kluster baharu DTI di Sepang. MalayMail. Available at: https://www.projekmm.com/news/berita/2020/05/24/kkm-sahkan-kluster-baharu-dti-di-sepang/1869169.

Bernama. (2020b). Kronologi Covid-19 di Malaysia sehingga 16 Mac 2020. Harian Metro. Available at: https://www.hmetro.com.my/mutakhir/2020/03/555424/kronologi-covid-19-di-malaysia-sehingga-16-mac-2020.

Forouzan B.A. (2007). Cryptography & network security. McGraw-Hill, Inc.

Howell R.G., Petersen S.L., Balzotti C.S., Rogers P.C., Jackson M.W., & Hedrich A.E. (2019). Using WebGIS to Develop a Spatial Bibliography for Organising, Mapping, and Disseminating Research Information: A Case Study of Quaking Aspen. Rangelands, 41(6), 244-247, DOI: 10.1016/j.rala.2019.10.001.

Husain N.H., & Adnan T.B.T.M. (2020). Kluster DTI Bukit Jalil melonjak, 270 kes baru. Sinar Harian. Available at: https://www.sinarharian.com.my/article/86293/KHAS/Covid-19/Kluster-DTI-Bukit-Jalil melonjak-270-kes-baharu.

Iwan Shu-Aswad Shuaib (2020). Malaysia Catat 45 Kes Baharu Covid-19, 40 libatkan Kluster Benteng di Sabah. MStar. Available at: https://www.mstar.com.my/lokal/semasa/2020/09/10/malaysia-catat-45-kes-baharu-covid-19-40-libatkan-kluster-benteng-di-sabah.

Kamel Boulos M.N., Geraghty E.M. (2020). Geographical tracking and mapping of coronavirus disease COVID-19/severe acute respiratory syndrome coronavirus 2 (SARS-CoV-2) epidemic and associated events around the world: how 21st century GIS technologies are supporting the global fight against outbreaks and epidemics. Int J Health Geogr 19(8), DOI: 10.1186/s12942-020-00202-8.

Li L., Huang T., Zheng W., Liang Y., Huang T., Zhang H., Sun W., & Wang Y. (2020). COVID-19 Patients ' Clinical Characteristics, Discharge Rate, And Fatality Rate of Meta – Analysis. Medical Virology, March, 577-583, DOI: 10.1002/jmv.25757.

Michael J.T. (2020). Sebanyak 5 Kluster Covid-19 Dikenal Pasti Di Malaysia. Borneo Today. Available at: https://www.borneotoday.net/sebanyak-5-kluster-covid-19-dikenal-pasti-di-malaysia/

Ministry of Health Malaysia. (2020). Ministry of Health Malaysia website. Available at: https://covid-19.moh.gov.my/

Ministry of Health Malaysia (2015). Ministry of Health Malaysia. Health Facts 2015. Available at: https://doi.org/MOH/S/RAN/31.12(TR).

Ruzki R.M., & Karim L.A.A. (2020). COVID-19: Kluster pembinaan dikaitkan dengan 3 kluster. Berita Harian. Available at: https://www.bharian.com.my/berita/nasional/2020/05/684765/covid-19-kluster-pembinaan-dikaitkan-dengan-3-kluster.

WHO. (2020). Coronavirus disease (COVID-19) Pandemic. Available at: https://www.who.int/emergencies/diseases/novelcoronavirus2019?gclid=CjwKCAjwte71BRBCEiwAU_V9h520leJVCv7n3fl9TFuSZpd43kHSCw617BqiukllhME0uTBjVMoxoCJ78QAvD_BwE.

Zhou C., Su F., Pei T., Zhang A., Du Y., & Luo B. (2020). COVID-19 : Challenges to GIS with Big Data. Geograpgy and Sustainability, 1(1), 77-87, DOI: 10.1016/j.geosus.2020.03.005.

RESEARCH PAPER

USING MORAN'S I FOR DETECTION AND MONITORING OF THE COVID-19 SPREADING STAGE IN THAILAND DURING THE THIRD WAVE OF THE PANDEMIC

Parichat Wetchayont[1*], Katawut Waiyasusri[2]
[1]Department of Geography, Faculty of Social Sciences, Srinakharinwirot University, 114 Sukhumvit 23, Khlong Toei Nuea, Wattana District, Bangkok 10110 Thailand
[2]Geography and Geo-Informatics Program, Faculty of Humanities and Social Sciences, Suan Sunandha Rajabhat University, 1 U-Thong Nok Road, Dusit, Bangkok 10300 Thailand
***Corresponding author:** parichatw@g.swu.ac.th
Received: August 31th, 2021 / Accepted: November 9th, 2021 / Published: December 31st, 2021
https://doi.org/10.24057/2071-9388-2021-090

ABSTRACT. Spatial distribution and spreading patterns of COVID-19 in Thailand were investigated in this study for the 1 April – 23 July 2021 period by analyzing COVID-19 incidence's spatial autocorrelation and clustering patterns in connection to population density, adult population, mean income, hospital beds, doctors and nurses. Clustering analysis indicated that Bangkok is a significant hotspot for incidence rates, whereas other cities across the region have been less affected. Bivariate Moran's I showed a low relationship between COVID-19 incidences and the number of adults (Moran's I = 0.1023-0.1985), whereas a strong positive relationship was found between COVID-19 incidences and population density (Moran's I = 0.2776-0.6022). Moreover, the difference Moran's I value in each parameter demonstrated the transmission level of infectious COVID-19, particularly in the Early (first phase) and Spreading stages (second and third phases). Spatial association in the early stage of the COVID-19 outbreak in Thailand was measured in this study, which is described as a spatio-temporal pattern. The results showed that all of the models indicate a significant positive spatial association of COVID-19 infections from around 10 April 2021. To avoid an exponential spread over Thailand, it was important to detect the spatial spread in the early stages. Finally, these findings could be used to create monitoring tools and policy prevention planning in future.

KEYWORDS: COVID-19, Spatio-temporal, Detection, Moran's I, Socioeconomic, Health care

CITATION: Parichat Wetchayont, Katawut Waiyasusri (2021). Using Moran's I For Detection And Monitoring Of The Covid-19 Spreading Stage In Thailand During The Third Wave Of The Pandemic. Geography, Environment, Sustainability, Vol.14, No 4, p. 155-167 https://doi.org/10.24057/2071-9388-2021-090

ACKNOWLEDGEMENTS: We appreciate everyone who worked hard in the healthcare system to combat the COVID-19 epidemic. The authors are sincerely grateful for supporting from the Faculty of Social Sciences, Srinakharinwirot University and the Digital Government Development Agency (DDC) of Thailand for providing daily COVID-19 confirmed case data which was used in the study. We gratefully acknowledge the National Statistical Office of Thailand for providing the demographic data. This study was performed under the Earth and Atmospheric Research Laboratory (EAR).

Conflict of interests: The authors reported no potential conflict of interest.

INTRODUCTION

On 13 January 2020, the Thailand government reported they had first detected a tested positive of coronavirus disease (COVID-19) from a Wuhan resident who had travelled to Bangkok. A COVID-19 outbreak then rapidly spread from Bangkok into all provinces of Thailand. To prevent the coronavirus from spreading, Thailand's government announced a nationwide lockdown and curfew from March 26 to May 31, 2020. These actions immediately changed the daily life activities of Thai people, had impacts on the environment, pollution, the economy, jobs and other things, and has since been the subject of various debates (Wetchayont 2021, Wetchayont et al. 2021). Figure 1 illustrates a time series plot of daily confirmed new cases (DDC 2021). Considering that COVID-19 was spreading like an ocean wave, the first wave of COVID-19 in Thailand, which began in March 2020 and extended across 68 provinces, had initially started at boxing events and nightclubs in Bangkok. By May 25 2020, the number of total confirmed cases had reached 3,042 cases with 57 deaths (Rajatanavin et al. 2021). The second wave was spurred by some Thai workers who entered Thailand illegally from Myanmar and were not apprehended by state quarantine. They transported the infection and disseminated it across Thailand's Northern provinces. In addition, a huge number of infected migrant laborers traveled directly and illegally from Myanmar to work in industries and seafood markets in Bangkok's neighboring province of Samut Sakhon. Between December 18, 2020 and February 27, 2021, new cases rise from 3,042 cases in the first wave to 21,584 cases in the second wave. However, daily incidences had reduced to less than 100 by the last week of February 2021, indicating that the problem was progressively being brought under control (Rajatanavin et al. 2021). The most recent wave of the coronavirus outbreak in Thailand is now number three. As of 23 July 2021, 467,707 cases of COVID-19 were officially confirmed in Thailand, including 3,811 deaths, with a record high of 14,575 new COVID-19 cases and 114 fatalities over one 24 hour period. For every day since 10 April 2021, the total number of COVID-19 cases in Thailand increased rapidly due to the Songkran holiday because of a new variant virus. The Songkran holiday, which runs from April 10 to 15, saw a large number of workers return to their hometowns from Bangkok and other big cities where infection rates were high, causing COVID-19 to spread nationwide. Over 2020 Thailand had a commendably low number of cases and successfully slowed the rate of infections by using strict measures. Nevertheless, on this current wave, the infection rate is rising exponentially and has not stopped up till now. This has caused a hospital bed shortage and left medical officials exploring home isolation for asymptomatic cases. Regular hospitals have been advised to treat only those patients with moderate symptoms or severe conditions. Early in the first wave of this COVID-19 pandemic, sex differences in the incidence of the disease were observed. The incidence rate in males was about 15% higher than in females in younger age groups, as shown in Figure 2. The same results were also found in the European region. A study by Green et al. (2021) provided evidence of sex and age differences in the case-fatality rates (CFR) of infection from COVID-19 in seven countries throughout Europe. They found that higher CFRs in males within younger age groups could be related to hormonal factors. Meanwhile, in the second wave, females tended to have higher incidence rates by about 30%, but then the incidence rates came down to become equal. There could be several factors responsible for the increased number of cases in the third wave. One of the reasons is that the mutant virus is more effective at transmitting and has a shorter incubation period (Li et al. 2021).

Previous studies have evaluated the geographical heterogeneity of chronic respiratory diseases (CRDs) in Thailand by using spatial statistics and found that high cluster areas of CRDs associate with population and industrial booms which generally contribute to epidemics (Laohasiriwong et al. 2018). Other studies have looked at the spatial spread of severe acute respiratory syndrome (SARS) in Beijing and mainland China (Meng et al. 2005; Fang et al. 2009). The findings show that there were different spatial connections between provinces in terms of possible pathways for the spread. Recently, there have been some studies that explored spatiotemporal clustering patterns of COVID-19 outbreaks at the provincial level by using global and local Moran's I indices in mainland China, which were also attributed to changes in social and demographic factors (Wang et al. 2021; Kang et al. 2020; Li et al. 2020; Zhang et al. 2020). COVID-19 incidence rates showed spatial connections between the district level and socioeconomic determinants, according to studies conducted in Brazil and Iran, which employed the global Moran's index and the Local Index of Spatial Association (LISA) as tools (Raymundo et al. 2021; Ramírez-Aldana et al. 2020). Moreover, a study among European nations, discovering a substantial positive association between income/population and COVID-19 cases/deaths, implied that these two variables could be important control variables for assessing COVID-19-related human casualties (Sannigrahi et al. 2020).

There was an assessed effort over temporal and spatiotemporal reproduction numbers to track transmission of COVID-19 dynamics in Thailand during the first wave (Rotejanaprasert et al. 2020). Results showed that the outbreak could contain reproduction numbers when it was under the control of strict measures. However, the real situation was difficult to determine in the early transmission stage due to limited incidence numbers. Additionally, Triukose et al. (2021) reported on the causes and lessons learned from the first wave of COVID-19 spread in Thailand. Their study used effective reproduction numbers to characterize the spread of COVID-19 across the country in five stages. Their results revealed that COVID-19 was mostly limited to Bangkok in the Early stage, but then started to cross over Bangkok's borders during the Spreading stage. After that, it spread nationwide, primarily due to a massive movement to people's hometowns after the Bangkok lockdown on 26 March 2020 in the Intervention I stage. In the Intervention II stage, the infectious rate downturned and became stable. Finally, the average of daily confirmed cases declined to zero and held the country in the Easing stage.

So far, the number of studies on spatial association of COVID-19's spread in Thailand are limited. Understanding the early stages of the COVID-19 outbreak's spatial spread is critical, as it may aid in the prediction of local epidemics and the development of public health policies based mainly on outbreak data (Kang et al. 2020). Even if those studies show how well temporal and spatial reproduction numbers track the transmission of COVID-19 dynamics in Thailand, in order to utilize these tools for tracking a spreading wave, or for preventive and crisis management policy planning, it requires extensive study to assess the effect of other variables on the spread of COVID-19. Thus, the goal of this study is to detect early transmission by using spatial distribution of COVID-19 incidence in Thailand's provinces and its relationship with sociodemographic factors. The expected results of this study could gain better understanding of the social environment and the epidemic's spread for utilizing tools needed to inform disease control activities in the future.

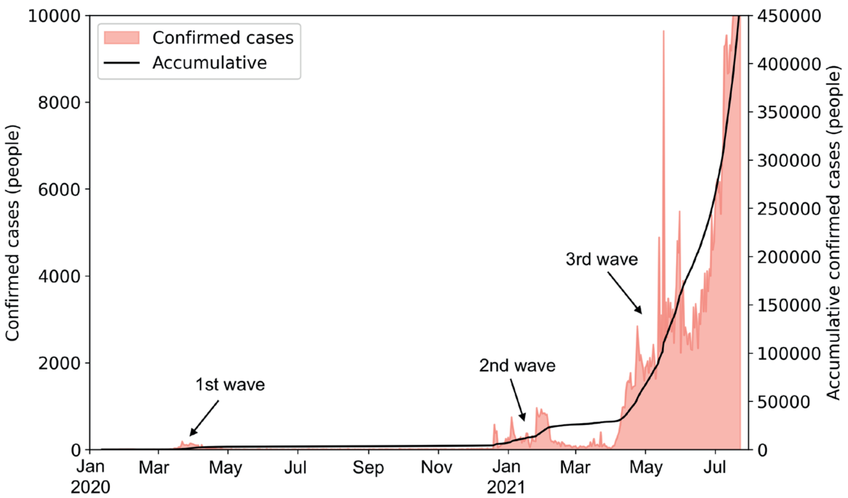

Fig. 1. Trend chart of new confirmed cases in Thailand during the period of January 1, 2020 to July 23, 2021. The first (March-May 2020), second (January-February 2021) and third waves (April-July 2021) are indicated by the daily new number of confirmed cases

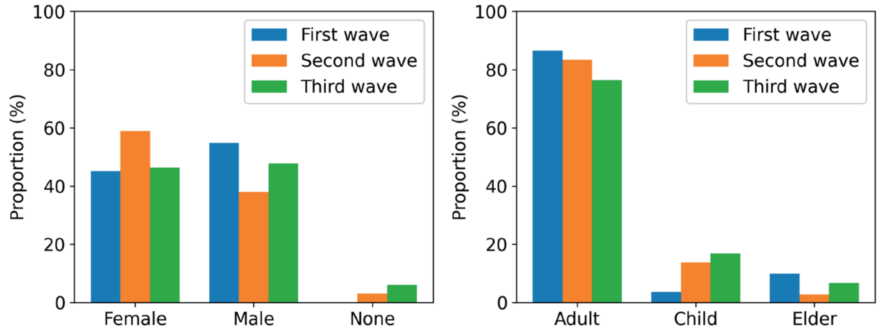

Fig. 2. Distribution by gender and age groups of patients admitted for COVID-19 during the first (March-May 2020), second (January-February 2021) and third waves (April-July 2021)

MATERIALS AND METHODS

Data collections

The number of confirmed COVID-19 cases, as registered by the Department of Disease Control of Thailand and updated daily, were obtained from their Thai website at the Digital Government Development Agency (https://data.go.th/dataset/covid-19-daily). There are 76 provinces and one special administrative area (Bangkok) in Thailand. This study used 4 months' data from 1 April to 19 July 2021, which was during the early stages of the third wave of COVID-19 in Thailand. Other datasets were obtained from the National Statistical Office of Thailand (NSO) website, including population, population density, number of doctors, and hospital beds by province (NSO 2021). All population-related and medical resource datasets were collected in 2020, making this the most up-to-date demographic information available (Table 1).

Figure 3 depicts a province-by-province map of monthly cumulative cases. The total number of instances is the sum of newly confirmed cases from 1 April–23 July 2021. The largest number of cases was in Bangkok, which is the capital city. Figure 4(a) presents the total population and population density (population/km^2) for each province in 2020. Metropolitan Bangkok had the highest population density, number of adult people and mean household income. As shown in Figure 4(d) – (f), Bangkok also has the highest number of hospital beds, doctors and nurses, whereas Chiang Mai and Nakhon Ratchasima Provinces ranks third and fifth for the number of hospital beds and doctors, respectively.

Data analysis

The number of COVID-19 cases as confirmed from the laboratory in the 76 provinces and one special administrative area (Bangkok) in Thailand, including the total population in each province, were used to compute the incidence rates in this section. The cumulative number of all reported cases between 1 January and 23 July 2021, as announced by the Department of Disease Control (DDC) of Thailand on July 23, 2021 (DDC 2021), were calculated to get the incidence of COVID-19 in each province according to the following formula:

$$COVID-19\ incidence = confirmed\ case\,/\,total\ population \quad (1)$$

The most commonly used measure of global spatial autocorrelation is Moran's I, which represents the overall distribution of deviations from randomness (Tu and Xia 2008). To provide information on spatial clusters and outliers, as well as forms of spatial correlation, we presented both global and local Moran's I. By using global Moran's Index (global Moran's I) based on Queen's contiguity spatial-lag of order 1: immediate neighbors (Moran 1950), the COVID-19 incidence rates in Thailand for each month from April to July 2021 were used as a variable. Global Moran's I is a spatial autocorrelation test that determines whether or not the spatial patterns of COVID-19 incidence are clustered by considering that space and location presents an influence on a single variable. Global Moran's I and P test values were used to determine the number of incidence rates with different types of neighbors using the spatial weight matrix, based on geographical adjacency at a 5% level of significance. Spatial autocorrelation was measured using the global Moran's I statistic, which was derived as follows:

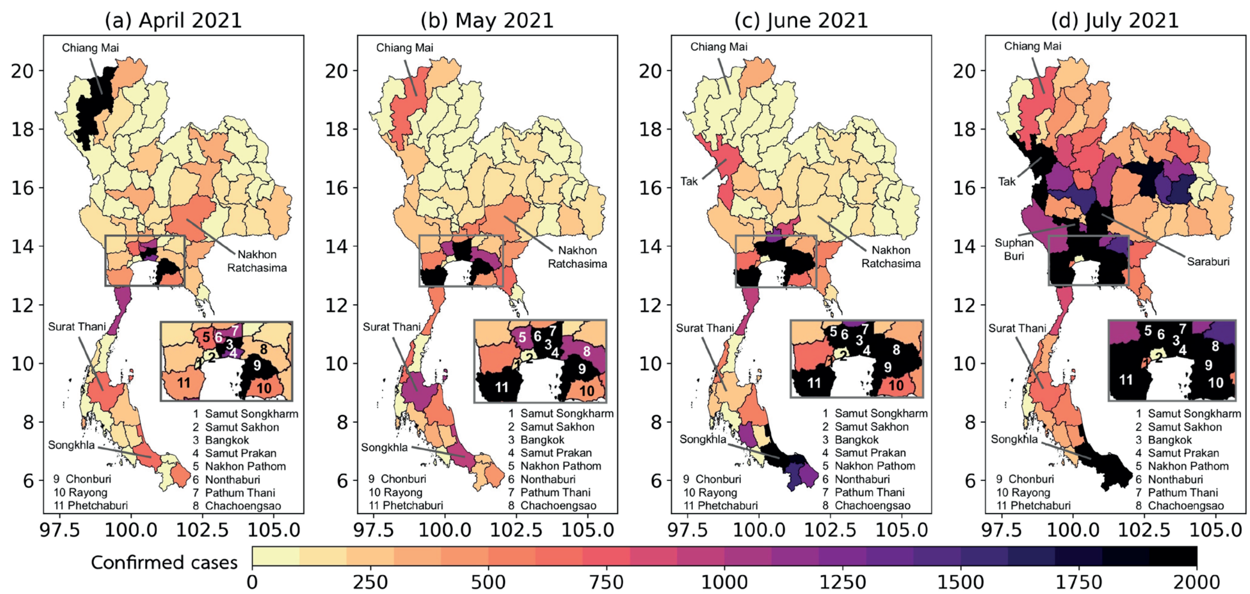

Fig. 3. Spatial distribution of monthly accumulative COVID-19 confirmed cases in Thailand by province during the period of April 1, 2021 to July 23, 2021

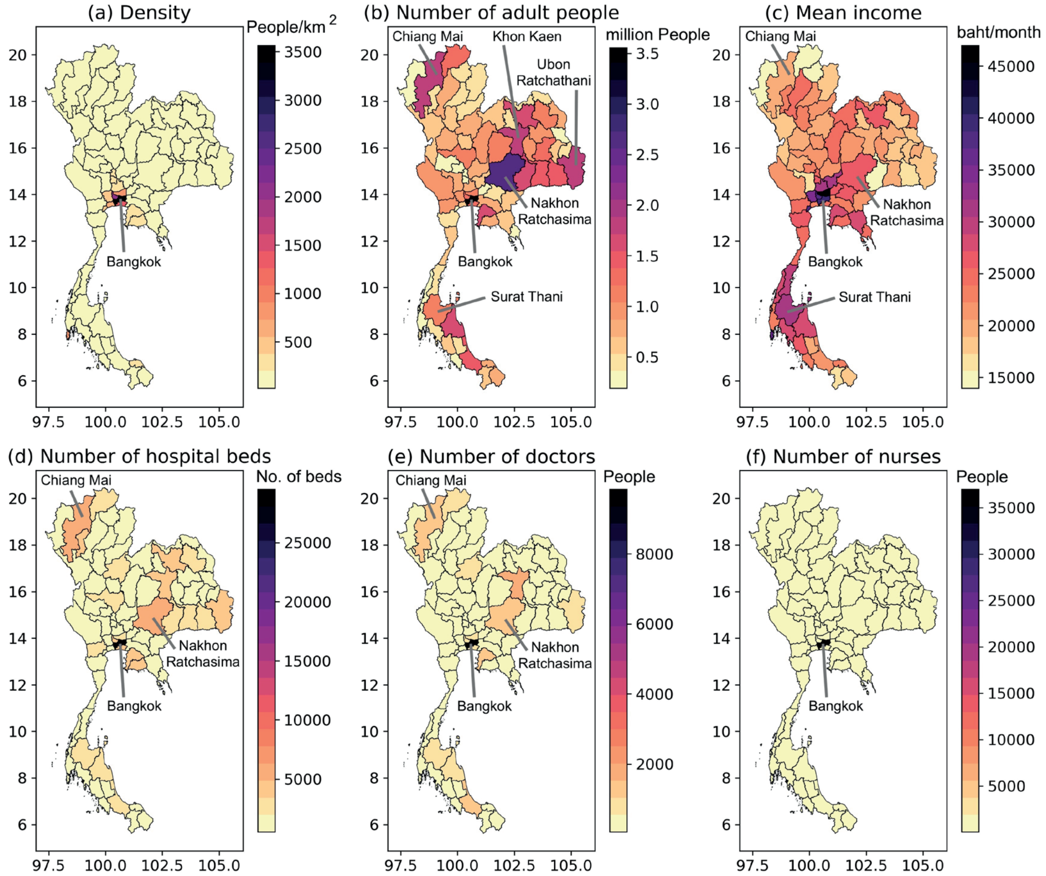

Fig. 4. Spatial distribution of (a) population density (people/km2), (b) number of adult people (million), (c) mean household income (baht/month), (d) number of hospital beds, (e) doctors (people) and (f) nurses (people) in 2020

Table 1. Description of parameters, data sources, and periods used in this study

Type	Description of variable	Data source	Period
Pandemic	COVID-19 confirmed cases	https://data.go.th/dataset/covid-19-daily	January-July 2021
Demographic	Total population of province	http://statbbi.nso.go.th/staticreport/page/sector/th/index.aspx	2020
	Population density		
	Number of adults in province		
Healthcare	Number of Hospital beds in province	http://statbbi.nso.go.th/staticreport/page/sector/th/index.aspx	2020
	Number of Doctors in province		
	Number of Nurses in province		
Socioeconomic	Mean monthly household income in province	http://statbbi.nso.go.th/staticreport/page/sector/th/index.aspx	2020

$$I = \frac{N}{\sum_{i=1}^{N}\sum_{j=1}^{N} w_{ij}} \times \frac{\sum_{i=1}^{N}\sum_{j=1}^{N} z_i w_{ij} z_j}{\sum_{i=1}^{N} z_i^2} \tag{2}$$

where N is the total number of analysis locations, zi is the variable value for each location i, and wij is the spatial weight (or connectivity) for location i and j. Notice that locational information for this formula is found in the weights. For non-neighboring tracts, the weight is zero, so these add nothing to the correlation. Global Moran's I ranges from -1 to +1, where +1 indicates strong positive spatial autocorrelation (clustered pattern), 0 indicates no spatial autocorrelation (random pattern), and -1 indicates strong negative spatial autocorrelation (checkered pattern).

The local Moran's I, or local indicators of spatial association (LISA), (Anselin 1995) was used to identify the location of local clusters for each individual location in the region as either a hot or cold spot, which is the likelihood of a unit's attribute value being associated with values in neighboring regions. The LISA spreading maps (LISA map) and LISA significance maps were then created with the following equation:

$$I_i = z_i \sum_j w_{ij} z_j \tag{3}$$

where zi and zj are the deviation of the variable with respect to the mean values for location i and j, and j is a location in the neighboring region of location i.

The LISA significance map and cluster map are used to visualize clusters of COVID-19 incidence more thoroughly. The maps highlight significant provinces with the LISA statistics using four alternative methods of clustering. Each one is based on a province's local spatial relationship with its neighbors (Anselin and Bao 1997; Anselin 2019): High-High (indicates a province with a high value surrounded by provinces of high values), Low-High (a province with a low value surrounded by provinces of high values), Low-Low (a province with a low value surrounded by provinces of low values), and High-Low (a province with a high value surrounded by provinces of low values). The spatial dependence of the provinces are represented on a map and color-coded based on the type of interaction. Positive local spatial correlations are detected as spatial clusters: High-High and Low-Low areas (red and light green color, respectively), whereas negative local spatial correlations are defined as spatial outliers in the High-Low and Low-High sectors (orange and dark green color, respectively).

Moreover, bivariate Moran's I statistic is a spatial version of the correlation coefficient. It captures the changing relationship between two variables at multiple locations and embeds this information in a geographical context (Lee 2001). We also calculated the bivariate spatial autocorrelation between province-level demographics, healthcare, socioeconomic parameters and COVID-19 incidence rates. The spatial correlations of COVID-19 incidence based on the two variables are as follows (Anselin 2019):

$$I_{x,y} = \frac{N}{\sum_{i=1}^{N}\sum_{j=1}^{N} w_{ij}} \times \frac{\sum_{i=1}^{N}\sum_{j=1}^{N} w_{ij}\left(x_i - \bar{x}\right)\left(y_j - \bar{y}\right)}{\sqrt{\sum_{i}^{N}\left(x_i - \bar{x}\right)^2 \sum_{j}^{N}\left(y_j - \bar{y}\right)^2}} \quad (4)$$

Six distinct types of neighborhood were selected, as in a prior study (Kang et al. 2020; Meng et al. 2005). Three groups of parameters (Table 1) that may describe the spatial relationship with incidence rates of the COVID-19 pandemic were examined using bivariate Moran's I statistic: demographic (population density and age), socioeconomic (mean income) and healthcare (hospital beds, number of doctors and nurses). To employ the bivariate Moran's I method, the incidence rates were analyzed within those parameters, providing six models in this stage. Because COVID-19 travels from person to person, the coronavirus spreads from places with the largest to the smallest population size (Kang et al. 2020; Meng et al. 2005). Model 1 took into account population density. As seen in Fig.2, the key inflection age group is adults, thus, numbers of adult people were important factors to consider for Model 2. In Model 3, we considered the mean household income in each province by assuming that COVID-19 spread refers to socioeconomic factors, from the largest to the smallest provinces (Mollalo et al. 2020). In terms of healthcare resources, Models 4, 5 and 6 took into account the number of hospital beds, as well as doctors and nurses, respectively. Its assumes that the spread of COVID-19 goes from where the largest to the smallest healthcare resources exist (Kang et al. 2020; Mollalo et al. 2020; Meng et al. 2005). Spatial autocorrelation analyses in this study were implemented using a PySAL package, Version 1.14.0 (Rey and Anselin 2007), based on a Python Version 3.8 package.

RESULTS

Spatial Distribution of monthly COVID-19 incidence

Monthly COVID-19 incidence rates in the third wave are shown in Figure 5(a-d) for April, May, June and July, respectively. The incidence rates in Thailand clearly increased from month to month. The infection rate first increased in Bangkok, Chonburi and Prachuap Khiri Khan Provinces, then came first-order neighboring provinces like Nonthaburi, Pathum Thani, Samutprakarn, and Phetchaburi (Figure 5b), and eventually second-order neighboring provinces such as Nakhon Pathom, Chachoengsao and Samut Songkhram (Figure 5c). Finally, the epidemic spread to neighboring regions in the third-order, including Nakhon Nayok, Saraburi, Ayutthaya, Suphan Buri, Ang Thong, Sing Buri, Lopburi, Tak, Ratchaburi, Ranong, Songkhla, Pattani, Yala and Narathiwat (Figure 5d). This confirms that COVID-19 is regionally dispersed and that investigating spatial dependency is necessary.

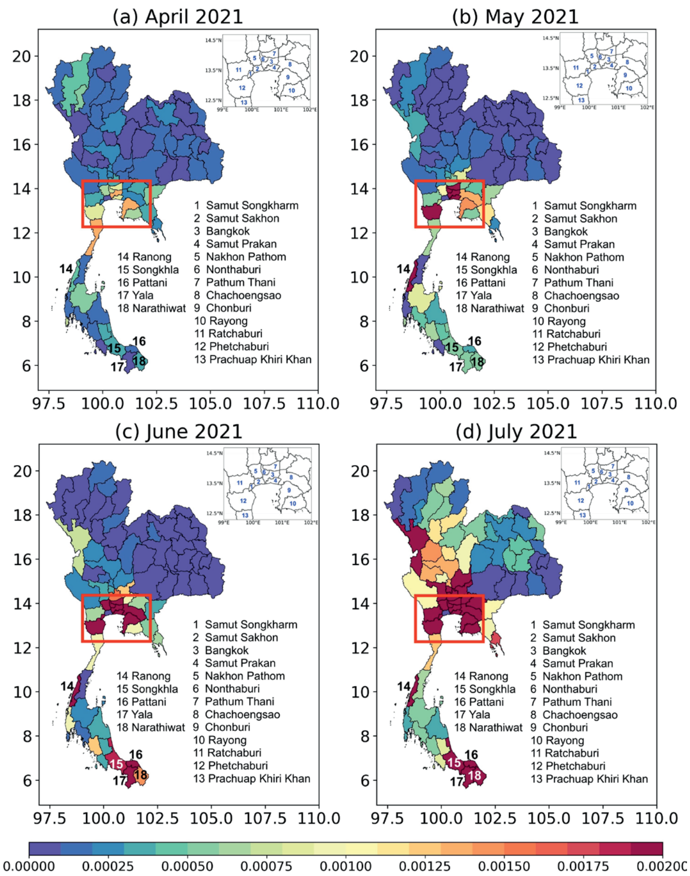

Fig. 5. Spatial distribution map of Thai COVID-19 incidence rates at the provincial level during the period of (a) April 2021, (b) May 2021, June 2021 and July 2021

Univariate spatial correlation

The goal of this research was to examine if COVID-19 incidences in Thailand had a spatial correlation. To measure spatial dependency, Moran's I statistic was utilized to determine COVID-19 incidence in various types of neighborhoods. The global Moran's I value for COVID-19 incidence was 0.3290, 0.3739, 0.5789 and 0.7605 for April, May, June and July, respectively ($P < 0.05$), which indicates that COVID-19 incidence at the province-level showed a very significant spatial dependence. Additionally, Figure 6 presents the LISA map (upper panel) and its p-value (lower panel) for each month during the third wave of the pandemic at Thailand's province level. The LISA map highlights the main clusters of COVID-19 incidence, where the High-High clustering zones (red) indicate regions with high numbers of incidence relative to the average, surrounded by regions that also present high numbers. The Low-Low clustering zones (light green) denote spatial association groups with low numbers of incidence (below the average) surrounded by low-valued regions. In April, most provinces in Central Thailand (including Bangkok) and surrounding provinces belonged to a High-High clustering zone. In contrast, Samut Sakorn and Samut Songkarm Provinces were close to these High-High clustering zones but contained significant Low-Low clustering zones. Since those provinces were the main COVID-19 clusters in the second wave, most of its citizens received a COVID-19 vaccine afterward. Therefore, these regions have had low incidence rates in the third wave. In May, the High-High clustering zone from East of Bangkok decreased, and a Low-Low clustering zone appeared in North and Northeast Thailand, indicating that COVID-19 had spread across the country (Fig.9a). It became apparent during May to July (Fig 9b-d) that a Low-Low clustering zone is continuously increasing its distribution in the North and Northeast regions, and a High-High clustering zone has also expanded.

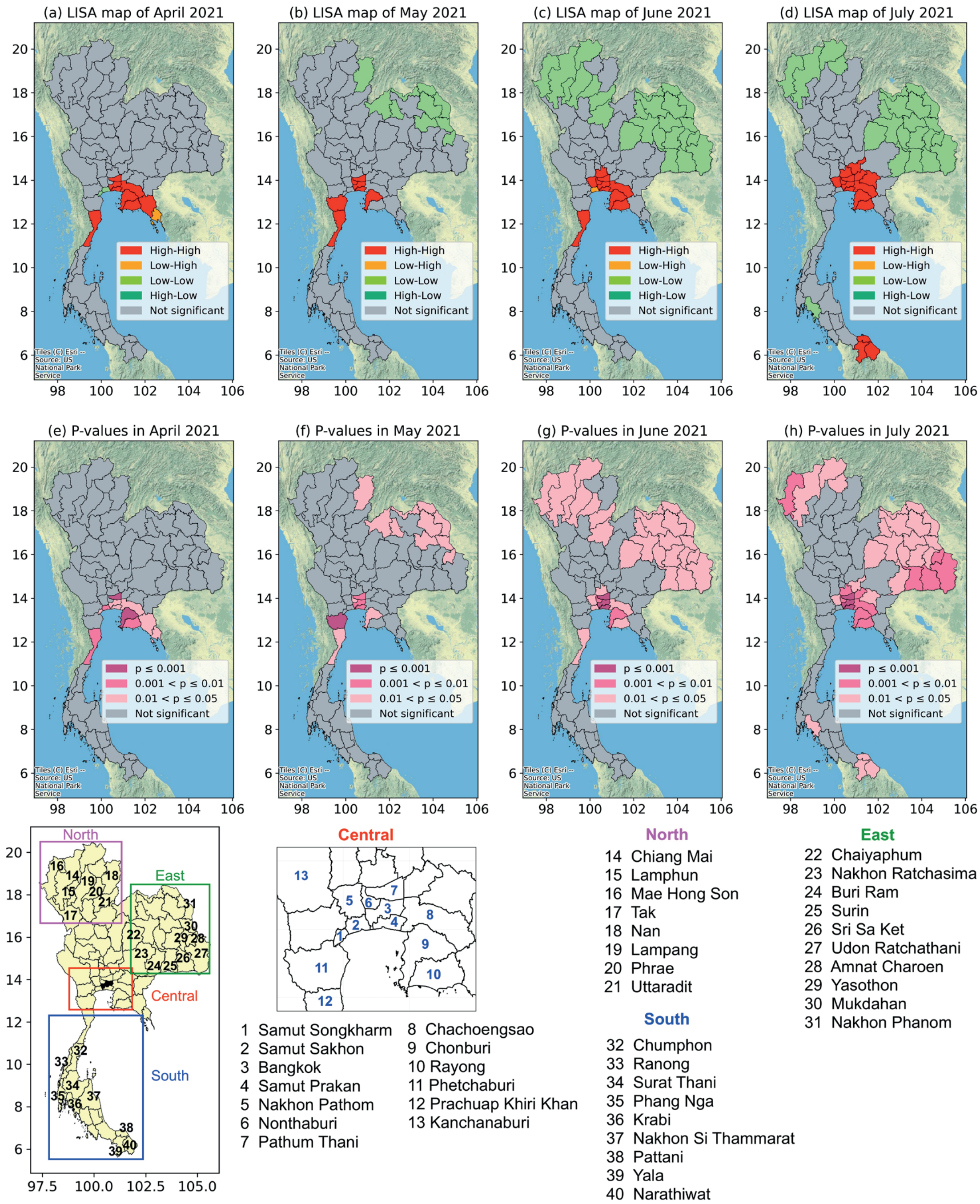

Fig. 6. Global Moran's I and univariate LISA cluster map of monthly COVID-19 incidence in provinces of Thailand, (a) April 2021, (b) May 2021, (c) June 2021, and (d) July 2021. Significance of the LISA map for monthly COVID-19 incidence in (e) April 2021, (f) May 2021, (g) June 2021, and (h) July 2021

Bivariate spatial correlation

Figure 7 shows the summary of results obtained from Pearson correlation analysis. Factors of population density and mean income showed the highest significant positive correlation (0.55) with COVID-19 incidence rates, followed by healthcare resources, which also represented a significant positive correlation (0.33). Meanwhile, the adult age group showed a weak positive (0.2) association with COVID-19 incidence rates. Additionally, population density showed a strong significant positive correlation (0.8) with the number of hospital beds, as well as doctor and nurse numbers. Accordingly, the distribution of medical resources in Thailand leans towards regions with greater population size and economic development.

Bivariate Moran's I analysis of demographics, health care and socioeconomics with COVID-19 incidence revealed a positive spatial autocorrelation, with Moran's I values shown in Table 2. With a significance threshold of 0.05, these values were statistically significant, except for Model 2: number of adult people in April and May. Based on these results, all the Models exhibit strong spatial association for COVID-19 incidence, and Moran's I value increases as the number of COVID-19 incidences increase. Figure 8 shows changes in the global Moran's I and P-values over time. The incidence rates of confirmed COVID-19 cases in all models showed significant global spatial correlation (Moran's $I > 0.0$, $p < 0.05$), except for the first few days in April 2021 and in early May 2021 of Model 2 (Figure 8b). Features of Moran's I index trend changes are evident in three stages: they first increase in a low slope from April to May 2021; then, an increasing slope appears from May to June; after that, the trend becomes steadier in July (Fig. 8). These results are inconsistent with a change in the incidence trend that rapidly increased from May to July. This indicates that, even though the incidence rates were increasing, the number of clusters did not change or were slightly less than previously (Fig. 5 and 6). Cluster features still influence global spatial correlation, however, reflecting that COVID-19 incidence tends to develop into a spread. Global bivariate Moran's I revealed that Model 1 had the highest spatial dependence between COVID-19 cases and population density in July 2021 (Moran's I = 0.6022, p = 0.001), as shown in Table 2 and Fig. 8a. The primary High-High clustering zones were located in big cities of Thailand such as Bangkok, Rayong, Samut Prakan, Patumthani and Nonthaburi (Fig. 9a-d). The Low-Low clustering zones were mainly located in Northern Thailand. This implies that high COVID-19 incidence rates occurred in regions with high population density such as big cities, then distributed to rural areas with low population density. Because COVID-19 spreads primarily from people to people by touching, breathing and talking, high population density should be considered to have a high possibility of infection. Model 2 indicates that the number of adult people determines the highest proportion among COVID-19 infections in people. Global bivariate Moran's I dramatically increased each month with weak positive spatial autocorrelation (Moran's I = 0.1023-0.1985), as shown in Table 2 and Fig. 8b. The LISA map for April and June presented three groups of clustering zones: High-High, Low-Low and Low-High. A High-High clustering zone was located in Bangkok, Samut Prakan and Chonburi, similar to Model 1, indicating a high incidence rate with high numbers of adult people in the surrounding area. A Low-Low clustering zone was found in Suphanburi, Nakhonsawan and Chiang Mai, and a Low-High clustering zone appeared in Samut Sakorn, Chaiyaphoom and Buriram, which indicates low incidence rates with a low and high number of adult people in the surrounding area, respectively. Then in July, the Low-Low clustering zone in Chiang Mai disappeared, while the Low-Low clustering zone in Suphanburi became a High-Low clustering zone. These results suggest that Chiang Mai successfully reduced the incidence rate, whereas Suphanburi increased its incidence rate in other age groups. For the mean household income variable, Model 3 had strong positive spatial autocorrelation (Moran's I = 0.2980-0.3523), as shown in Table 2 and Fig. 8c. Most of the LISA map reveals two primary clustering zones - one High-High and one Low-Low (Fig. 9 i-l). It can be observed how dynamically changes between the High-High and Low-High clustering zones occurred, depending on how the incidence rates changed. The results indicate that a region with high income tends to have a high possibility of infection due to being densely populated. Model 4 (hospital beds), Model 5 (doctor numbers) and Model 6 (nurse numbers) indicated moderate positive spatial autocorrelation (Moran's I = 0.1986-0.4853), as shown in Table 2 and Fig. 8d-f, with a uniform pattern of High-High and Low-Low clustering zones (Fig.10). The results show that hospital beds were not more essential than doctors or nurses in COVID-19's third wave, and they were significant throughout the whole period.

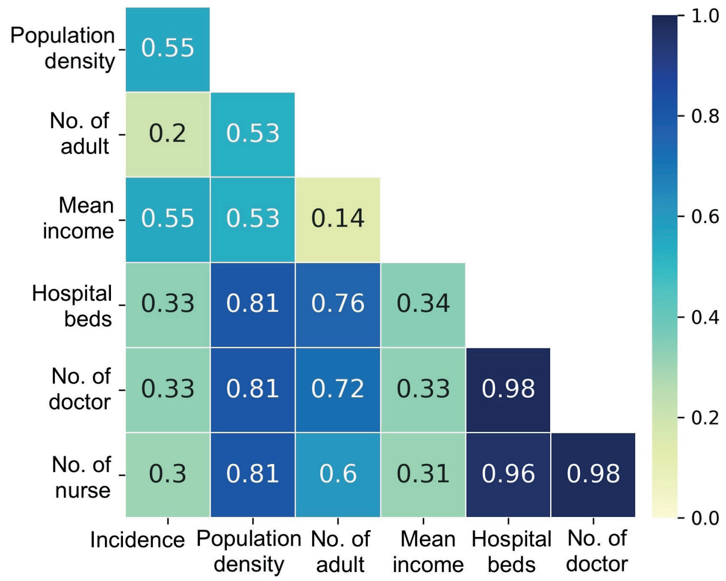

Fig. 7. Summary of Pearson correlation analysis between COVID-19 incidence rates and factors related to demographic, socio-economic, and healthcare resources.

Table 2. Moran's I statistical and P-values for Models 1 to 6

	April		May		June		July	
	Moran's I	P-value	Moran's I	P-value	Moran's I	P-value	Moran's I	P-value
Model 1	0.2776	0.0020	0.3788	0.0010	0.5765	0.0010	0.6022	0.0010
Model 2	0.1023	0.0570	0.1081	0.0840	0.1985	0.0340	0.1885	0.0400
Model 3	0.2980	0.0010	0.3908	0.0010	0.4663	0.0010	0.4853	0.0010
Model 4	0.1986	0.0210	0.2237	0.0080	0.3424	0.0020	0.3457	0.0040
Model 5	0.1881	0.0140	0.2223	0.0030	0.3440	0.0010	0.3523	0.0050
Model 6	0.1718	0.0210	0.2144	0.0050	0.3295	0.0020	0.3340	0.0070

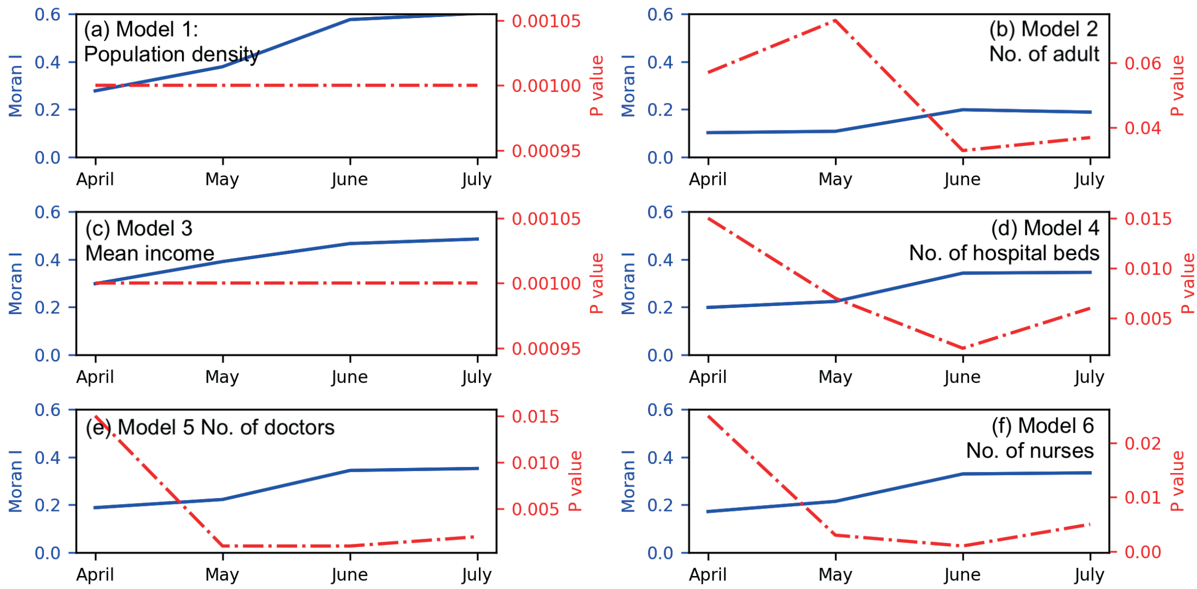

Fig. 8. Monthly changes in local Moran's I statistics and p-values from April 1, 2021 to July 23, 2021 in Thailand for six models: (a) Model 1: population density, (b) Model 2: number of adults, (c) Model 3: mean income, (d) Model 4: number of hospital beds, (e) Model 5: number of doctors, and (f) Model 6: number of nurses

For each day, Moran's I statistics and associated p-values are shown in Figure 10. Except for the first few days and Model 2, the p-values in Figure 11 are all very close to zero. All the models show systematically spatial clustering correlation with the COVID-19 incidence rates since 10 April, being especially strongest in Model 1 (Fig.10a). In Figure 11, the features of Moran's I index trend changes are seen in three phases: they first increase and then fall from April 10; after that, they increase again and then fall from May 20; after that, they increase again from June 7. Interestingly, after they went down, they then increased with higher Moran's I values, indicating that the COVID-19 spread was continuously increasing. Moreover, the different Moran's I value in each stage demonstrated the transmission level of infectious COVID-19, particularly in the Early (first phase) and Spreading stages (second and third phases).

In addition, daily changes in the bivariate global Moran's I value expressed the key factors affecting the spread of the COVID-19 epidemic. The results reveal that COVID-19 incidence has a significant spatial dependence on all six variables, indicating that effecting factors on the outbreak and transmission of an epidemic occur primarily through the source of infection, the channel of transmission, and the receptive population. As seen in Model 1, the results point to the fact that COVID-19 expanded significantly, from crowded areas to adjacent areas. During the periods with no significant spatial dependence in Model 2, we demonstrated that COVID-19 was spreading to other age groups. The third wave of the COVID-19 pandemic in Thailand started with a spike in daily confirmed cases on 10 April associated with the Songkran holiday. Workers went back to their hometowns and spread COVID-19 to their family members, resulting in a wider spread and transmitting it to other age groups. It has been demonstrated that the factors that affect the outbreak and transmission of an epidemic occur mainly through influences on the sources of infection, the routes of transmission, and the susceptible population. COVID-19's spread may be linked to ecological, social, and economic factors, as well as preventative measures and controlling activities such as limiting the infection sources and shutting off transmission routes.

DISCUSSION

This study provides information on the spatial and temporal patterns of the third wave of the COVID-19 pandemic in Thailand. In the early stage of the COVID-19 outbreak, new cases occurred intensively in Bangkok and Rayong, Chonburi and Prachuap Khiri Khan Provinces. The pandemic extended to bordering provinces over time, with the first-order, second-order and third-order neighboring provinces showing a notably high number of confirmed cases after May 2021. Results on the spatial distribution patterns of COVID-19 incidence rates in Thailand show a

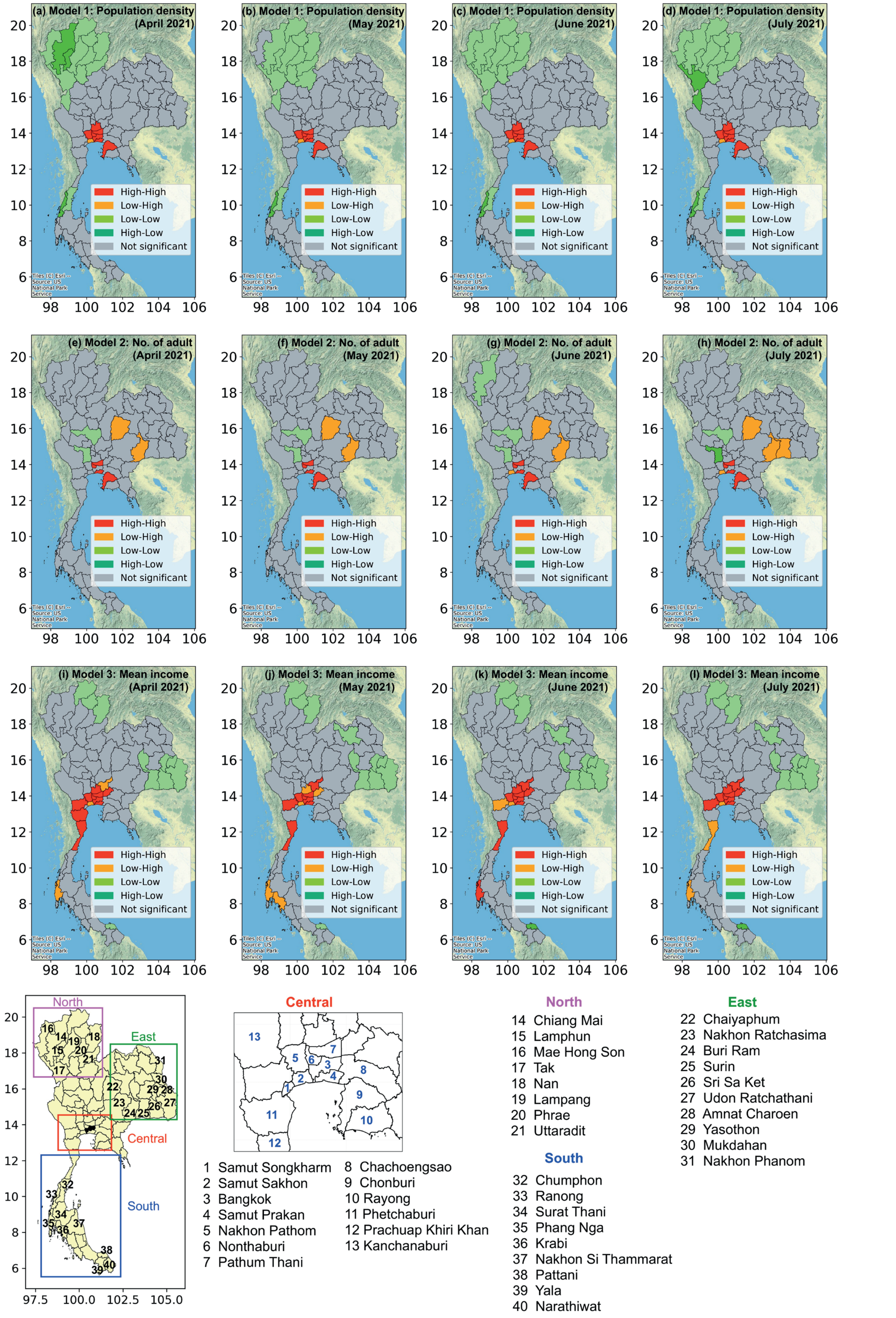

Fig. 9. Spatial distribution of LISA cluster maps between COVID-19 incidence and related parameters: Model 1: population density (a-d), Model 2: number of adults (e-h), and Model 3: mean household income (i-l) from April to July 2021

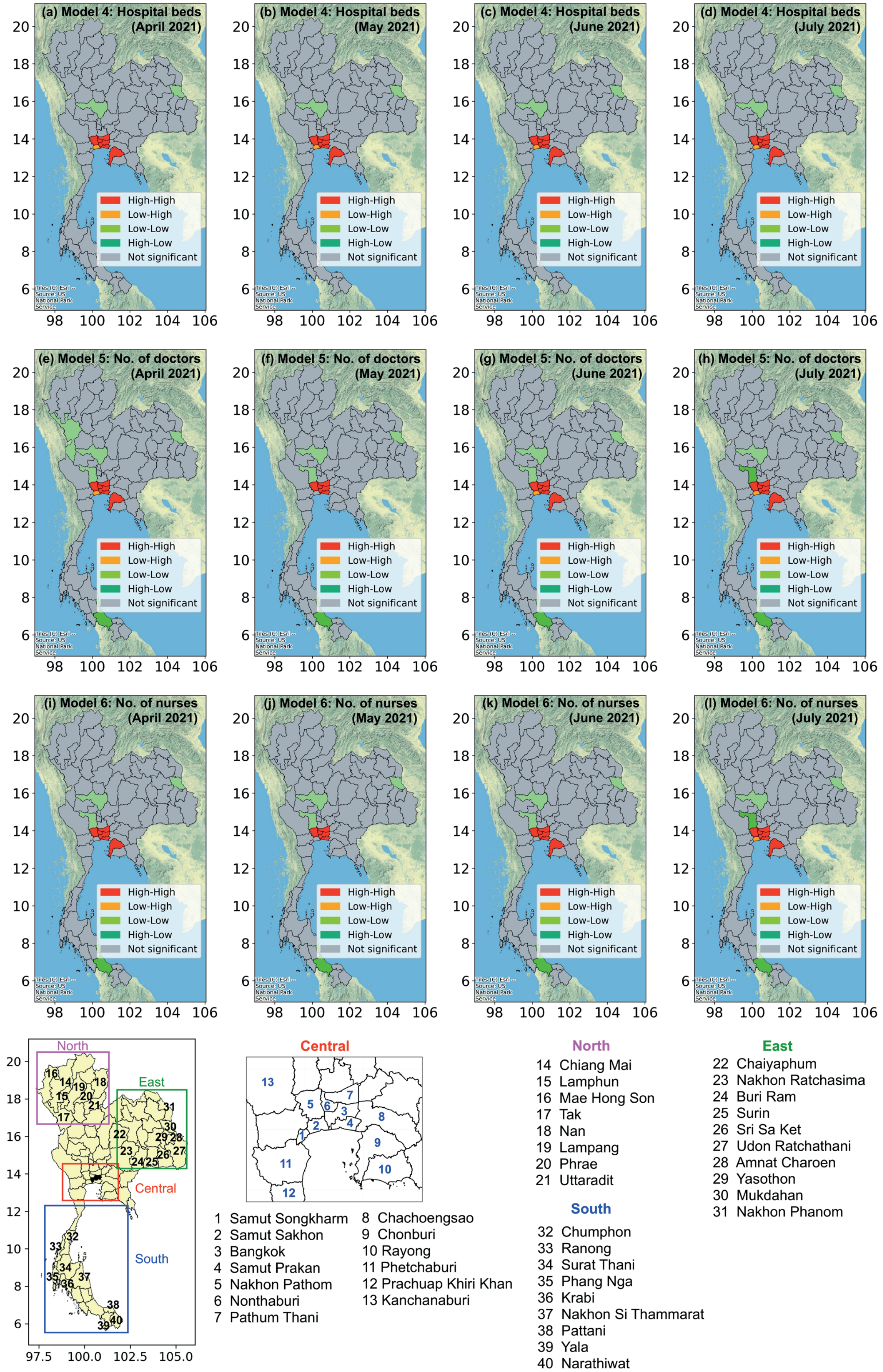

Fig. 10. Spatial distribution of LISA cluster maps between COVID-19 incidence and related parameters: Model 4: hospital beds (a-d), Model 5: number of doctors (e-h), and Model 6: number of nurses (i-l) from April to July 2021

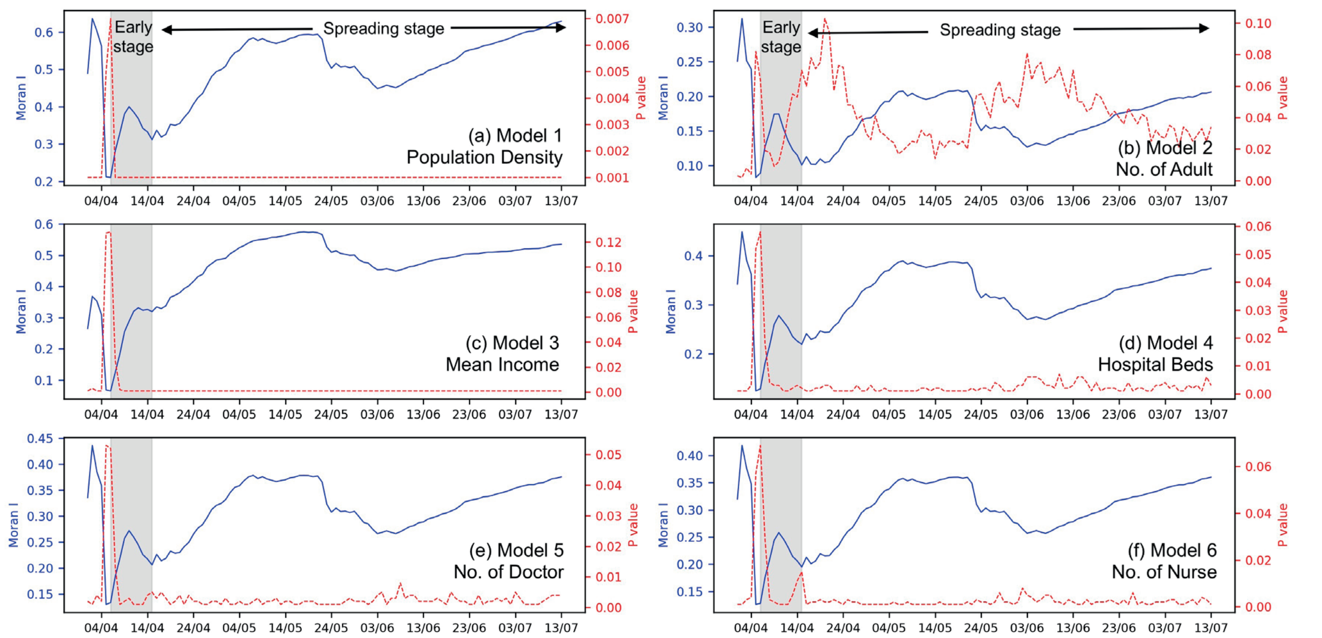

Fig. 11. Daily changes in the global Moran's I statistic and p-values from April 1, 2021 to July 23, 2021 in Thailand for six models: (a) Model 1: population density, (b) Model 2: number of adults, (c) Model 3: mean income, (d) Model 4: number of hospital beds, (e) Model 5: number of doctors, and (f) Model: 6 number of nurses

clear systematic pattern among provinces: high incidence rates surrounded by provinces with similar levels of incidence, and provinces with low incidence surrounded by provinces with low values. The highest infected clusters have occurred in Bangkok and its neighboring provinces, while lower infection rates have been in the countryside. The same pattern was observed for the relationship between incidence rates and population density, adult numbers, mean household income, hospital beds, and doctor and nurse numbers.

Meng et al. (2005) modeled the influence of demographic, socioeconomic and healthcare resources on the (SARS) respiratory syndrome in Beijing and found that population density and medical care resources did influence the spatial spread of SARS in Beijing. However, the major variables that caused the epidemic to spread were different at different times. Kang et al. (2020) provides information on the spatial and temporal patterns of the COVID-19 pandemic in mainland China. They show that, in the early phases of the COVID-19 pandemic, the disease distributed rapidly from region to region in mainland China. Moreover, they also evaluated the influence of demographic, socioeconomic and healthcare resource factors on COVID-19 cases. The results presented significant spatial autocorrelation between COVID-19 cases and population density and the number of doctors, but no significant spatial autocorrelation existed with hospital beds. Population size is a key factor in COVID-19 spread.

Their findings are in line with our results, except that we found a significant spatial autocorrelation between COVID-19 incidence and hospital beds, as it showed strong correlation between population density and healthcare resources. Having a large number of beds, doctors and nurses in a location means that the area can handle a large number of critically ill patients, this could lead to the infection spreading. Moreover, the daily change in global Moran's I values in this study could indicate the Early and Spreading stages during the COVID-19 pandemic's third wave. Similarly, Triukose et al. (2021) used effective reproduction numbers to identify the COVID-19 transmission level in Bangkok. On the other hand, the LISA statistic showed the dynamics of cluster distribution to be consistent with the Spreading stages, which were found by the daily change in global Moran's I values. Therefore, global and local Moran's I can be used as a monitoring and policy-decision-making tool to inform disease control activities in the future. (Laohasiriwong et al. 2018; Triukose et al. 2021). There are several limitations to this paper. The factors that influence the epidemic's propagation are numerous. This paper developed an indicator system based on the available data that influences the epidemic's multiple factors (Meng et al. 2005; Kang et al. 2020). Other non-quantitative factors may have been overlooked, adding to the inadequacy of the study's evaluation. Without access to precise information on those diagnosed with COVID-19, such as medical history, weight, smoking status, and so on, the study's findings may have been weakened. Nevertheless, attempts to investigate probable external environmental impacts are critical for protecting healthcare workers and containing the COVID-19 outbreak (Wang et al. 2021). Future research may be useful in delving deeper into the epidemiological factors and social environment of COVID-19.

CONCLUSIONS

A new geographic database for studying the COVID-19 epidemic was created based on the COVID-19 outbreak in 76 provinces and one special administrative region (Bangkok) in Thailand. A PySAL package based on python language was used to detect early transmission by using the spatial distribution of COVID-19 incidence in Thailand's provinces and its relationship with sociodemographic factors in order to better understand the outbreak and transmission of the disease in Thailand from April to July 2021. Thus, the following conclusions were found. Global spatial autocorrelation was employed to confirm that COVID-19 incidence in Thailand has a spatial association, and the correlation characteristics increased at a slow rate in April, and then rapidly increased in June and July 2021. However, considering local spatial autocorrelation, the correlation characteristics tended to remain steady over time and mostly consisted of High/Low aggregation zones. In the provinces surrounding Bangkok, hotspots have stabilized over time (Nonthaburi, Pathum Thani, Samutprakarn Chonburi, and Prachuap Khiri Khan Provinces). Among social factors, population density exhibited the highest positive correlation with incidence. Our results revealed that the diverse spatiotemporal clustering patterns we discovered may represent variances in social and demographic characteristics, public health emergency readiness and response capacities, as well as differences in transmission patterns and mechanisms of these coronaviruses. Finally, daily changes in global Moran's I successfully indicated the Early and Spreading stages during the third wave of the COVID-19 pandemic. These findings could be used to create monitoring tools and aid in policy prevention planning. Future researches may be useful in delving deeper into the epidemiological factors and social environment of the COVID-19.

REFERENCES

Anselin L. (1995). Local Indicators of Spatial Association LISA, Geographical Analysis, 27, DOI: 10.1111/j.1538-4632.1995.tb00338.x.

Anselin L. (2004). GeoDa 0.95i Release Notes. Urbana-Champaign, IL: Spatial Analysis Laboratory (SAL), Department of Agricultural and Consumer Economics, University of Illinois.

Anselin L. (2019). A local indicator of multivariate spatial association: extending Geary's C. Geogr Anal, 51, 133-50, DOI: 10.1111/gean.12164.

Anselin L., and Bao S. (1997). Exploratory Spatial Data Analysis Linking Space Stat and ArcView, Chapter 3 in Recent Developments in Spatial Analysis, Spatial Statistics, Behavioral Modeling and Computational Intelligence, M.M. Fischer and A. Getis (Eds.). Berlin: Springer-Verlag, 35-59.

DDC (2021). The Digital Government Development Agency, https://data.go.th/dataset/covid-19-daily, (Accessed 23 July 2021).

Fang L.Q., Vlas S.J., Feng D., Liang S., Xu Y.F., and Zhou J.P. (2009). Geographical spread of SARS in mainland China, Trop Med Int Health, 14, DOI: 10.1111/j.1365-3156.2008.02189.x.

Green M.S., Nitzan D., Schwartz N., Niv Y., Peer V. (2021). Sex differences in the case-fatality rates for COVID-19 — A comparison of the age-related differences and consistency over seven countries, PLoS ONE, 16, 4, DOI: 10.1371/journal.pone.0250523.

Kang D., Choi H., Kim J.H., and Choi J. (2020). Spatial epidemic dynamics of the COVID-19 outbreak in China, Int J Infect Dis, 94, DOI: 10.1016/j.ijid.2020.03.076.

Laohasiriwong W., Puttanapong N., and Luenam A. (2018). A comparison of spatial heterogeneity with local cluster detection methods for chronic respiratory diseases in Thailand, F1000Research, 6,1819, DOI: 10.12688/f1000research.12128.2.

Lee S.I. (2001). Developing a bivariate spatial association measure: An integration of Pearson's r and Moran's I, J. Geograph Syst, 3, DOI: 10.1007/s101090100064.

Li B., Deng A., Li K., Hu Y., Li Z., Xiong Q., Liu ,Z., Guo Q., Zou L., Zhang H., Zhang M., Ouyang F., Su J., Su W., Xu J., Lin H., Sun J., Peng J., Jiang H., Zhou H., Zhen H., Xiao J., Liu T., Che R., Zeng H., Zheng Z., Huang Y., Yu J., Yi L., Wu J., Chen J., Zhong H., Deng X., Kang M., Pybus O., Hall M., Lythgoe K., Li Y., Yuan J., He J., and Lu J. (2021). Viral infection and transmission in a large well-traced outbreak caused by the Delta SARS-CoV-2 variant, medRxiv, Published online: July 12, 2021:2021.07.07.21260122, DOI:10.1101/2021.07.07.21260122.

Li H., Calder C.A., and Cressie N. (2007). Beyond Moran's I: testing for spatial dependence based on the spatial autoregressive model, Geogr Anal, 39, 4, DOI: 10.1111/j.1538-4632.2007.00708.x.

Li H., Li H., Ding Z., Hu Z., Chen F., Wang K., Peng Z., and Shen H. (2020). Spatial statistical analysis of Coronavirus Disease 2019 (Covid-19) in China, Geospatial Health, 15, 1, DOI: 10.4081/gh.2020.867.

Meng B., Wang J., Liu J., Wu J., Zhong E. (2005). Understanding the spatial diffusion process of severe acute respiratory syndrome in Beijing. Public Health, 119, 12, DOI: 10.1016/j.puhe.2005.02.003.

Mollalo A., Vahedi B., and Rivera K.M. (2020). GIS-based spatial modeling of COVID-19 incidence rate in the continental United States, Science of the Total Environment, 728, DOI: 10.1016/j.scitotenv.2020.138884.

Moran P.A. (1950). A test for the serial independence of residuals. Biometrika, 37, DOI: 10.1093/biomet/37.1-2.178.

NSO (2021). The National Statistical Office of Thailand, http://statbbi.nso.go.th/staticreport-/page/sector/th/index.aspx, (Accessed 23 July 2021).

Pei Z., Han G., Ma X., Su H., and Gong W. (2020). Response of major air pollutants to COVID-19 lockdowns in China, Sci Total Environ, 743, DOI: 10.1016/j.scitotenv.2020.140879.

Rajatanavin N., Tuangratananon T., Suphanchaimat R., and Tangcharoensathien V. (2021). Responding to the COVID-19 second wave in Thailand by diversifying and adapting lessons from the first wave BMJ Global Health, 6, 7, DOI: 10.1136/bmjgh-2021-006178.

Ramírez-Aldana R., Gomez-Verjan J.C., and Bello-Chavolla O.Y., (2020). Spatial analysis of COVID-19 spread in Iran: Insights into geographical and structural transmission determinants at a province level, PLoS Negl Trop Dis, 18, 14(11), DOI: 10.1371/journal.pntd.0008875. PMID: 33206644; PMCID: PMC7710062.

Raymundo C.E., Oliveira M.C., Eleuterio T. A., André S. R., da Silva M. G., Queiroz ERDS, and Medronho R.A. (2021). Spatial analysis of COVID-19 incidence and the sociodemographic context in Brazil, PLoS One, 6, 3, DOI: 10.1371/journal.pone.0247794.

Rey S.J., and Anselin L. (2010). PySAL: A Python Library of Spatial Analytical Methods. In: Fischer M., Getis A. (eds) Handbook of Applied Spatial Analysis. Springer, Berlin, Heidelberg, DOI: 10.1007/978-3-642-03647-7_11.

Rotejanaprasert C., Lawpoolsri S., Panngum W., and Maude R.J. (2020). Preliminary estimation of temporal and spatiotemporal dynamic measures of COVID-19 transmission in Thailand, PLoS ONE, 15, 9, DOI: 10.1371/journal. pone.0239645.

Sannigrahi S., Pilla F., Basu B., Basu A.S., and Molter A. (2020). Examining the association between socio-demographic composition and COVID-19 fatalities in the European region using spatial regression approach, Sustain Cities Soc, 62, DOI: 10.1016/j.scs.2020.102418.

Triukose S., Nitinawarat S., Satian P., Somboonsavatdee A., Chotikarn P., Thammasanya T., Wanlapakorn N., Sudhinaraset N., Boonyamalik P., Kakhong B., and Poovorawan Y. (2021). Effects of public health interventions on the epidemiological spread during the first wave of the COVID-19 outbreak in Thailand, PLoS ONE, 16, 2, DOI: 10.1371/journal. pone.0246274.

Tu J., and Xia Z.G. (2008). Examining spatially varying relationships between land use and water quality using geographically weighted regression I: Model design and evaluation, Sci Total Environ., 407, 358-378, DOI: 10.1016/j.scitotenv.2008.09.031.

Tu, J. and Xia Z.G., (2008). Examining spatially varying relationships between land use and water quality using geographically weighted regression I: Model design and evaluation, Sci Total Environ., 407, 358-378, DOI: 10.1016/j.scitotenv.2008.09.031.

Wang Q., Dong W., Yang K., Ren Z., Huang D., Zhang P., and Wang J. (2021). Temporal and spatial analysis of COVID-19 transmission in China and its influencing factors, Int J Infect Dis., 105, DOI: 10.1016/j.ijid.2021.03.014.

Wetchayont P. (2021). Investigation on the Impacts of COVID-19 Lockdown and Influencing Factors on Air Quality in Greater Bangkok, Thailand, Advances in Meteorology, 2021, 6697707, DOI: 10.1155/2021/6697707.

Wetchayont P., Hayasaka T., and Khatri P. (2021). Air Quality Improvement during COVID-19 Lockdown in Bangkok Metropolitan, Thailand: Effect of the Long-range Transport of Air Pollutants, Aerosol Air Qual. Res., 21, 200662, DOI: 10.4209/aaqr.200662.

Zhang X., Rao H., and Wu Y. (2020). Comparison of spatiotemporal characteristics of the COVID-19 and SARS outbreaks in mainland China, BMC Infect Dis, 20, 805, DOI: 10.1186/s12879-020-05537-y.

RESEARCH PAPER

THE DYNAMICS OF THE ATMOSPHERIC POLLUTANTS DURING THE COVID-19 PANDEMIC 2020 AND THEIR RELATIONSHIP WITH METEOROLOGICAL CONDITIONS IN MOSCOW

N. Ye. Chubarova[1*], Ye. Ye. Androsova[1], Ye. A. Lezina[2]
[1]Faculty of Geography of Lomonosov Moscow State University, Moscow, Russia
[2]GPU «Mosecomonitoring « Environmental Protection State Agency, Moscow, Russia
***Corresponding author:** chubarova@geogr.msu.ru
Received: February 9th, 2021 / Accepted: May 25th, 2021 / Published: July 1st, 2021
https://doi.org/10.24057/2071-9388-2021-012

ABSTRACT. The relationship between the dynamics of the atmospheric pollutants and meteorological conditions has been analyzed during the COVID-19 pandemic in Moscow in spring, 2020. The decrease in traffic emissions during the lockdown periods from March 30th until June 8th played an important role in the decrease (up to 70%) of many gaseous species and aerosol PM_{10} concentrations and in the increase of surface ozone (up to 18%). The analysis of the pollutant concentrations during the lockdown showed much smoother diurnal cycle for most of the species due to the reduced intensity of traffic, especially during rush hours, compared with that before and after the lockdown. The specific meteorological conditions with low temperatures during the lockdown periods as well as the observed smoke air advection have made a considerable contribution to the air quality. After removing the cases with smoke air advection the decrease in concentration of many pollutants was observed, especially in NO_x and PM_{10}. The analysis of Pearson partial correlation coefficients with fixed temperature factor has revealed a statistically significant negative correlation between the Yandex self-isolation indices (*SII*), which can be used as a proxy of traffic intensity, and daily concentrations of all pollutants, except surface ozone, which has a statistically significant positive correlation with *SII* caused by specific photochemical reactions. In situations with *SII>2.5* more favorable conditions for surface ozone generation were observed due to smaller NOx and the higher O_3/NOx ratios at the same ratio of VOC/NOx. In addition, this may also happen, since during the Arctic air advection, which was often observed during the lockdown period, the growth of ozone could be observed due to the downward flux of the ozone-rich air from the higher layers of the atmosphere.

KEYWORDS: COVID-19 pandemic, urban pollution, aerosol, gas, lockdown, traffic emission, PM_{10}, ozone, nitrogen oxides, CO, SO_2, long-term measurements, Yandex self-isolation indices, meteorological factors

CITATION: N. Ye. Chubarova, Ye. Ye. Androsova, Ye. A. Lezina (2021). The Dynamics Of The Atmospheric Pollutants During The Covid-19 Pandemic 2020 And Their Relationship With Meteorological Conditions In Moscow. Geography, Environment, Sustainability, Vol.14, No 4, p. 168-182 https://doi.org/10.24057/2071-9388-2021-012

ACKNOWLEDGMENTS: The analysis of meteorological conditions, the development of the datasets, and the analysis of several gas species concentrations have been carried out with the partial support of the RGO grant (agreement 08/07-2020-Mo). The analysis of the gas-aerosol regime in 2020 was partially supported by the Ministry of Education and Science of the Russian Federation (grant number 075-15-2021-574). This research was performed according to the Development program of the Interdisciplinary Scientific and Educational School of M.V.Lomonosov Moscow State University «Future Planet and Global Environmental Change».

Conflict of interests: The authors reported no potential conflict of interest.

INTRODUCTION

The COVID-19 pandemic has affected the air quality, especially in large urban areas (Li et al. 2020; Mahato et al. 2020; Krecl et al. 2020; Sharma et al. 2020). The adoption of strict quarantine measures and the almost complete lockdown have been reflected in the reduction of anthropogenic emissions, including greenhouse gases emissions (https://www.icos-cp.eu/event/933), and resulted in the decrease of the content of harmful substances in the atmospheric air over several geographical regions (Zambrano-Monserrate et al. 2020; Mahato et al. 2020). As a result of the reduction in transport traffic and economic activities, an improvement in air quality was observed in a number of cities. It has been expressed in a statistically significant decrease in the concentration of major air pollutants (Jain et al. 2020; Li et al. 2020) such as nitrogen oxides, carbon dioxide, mass concentration of particulate matter (PM) with a diameter smaller than 10 and 2.5 micrometer (PM10 and PM2.5, respectively). At the same time, the specific features of meteorological conditions could also affect the variability of the concentration of pollutants (Şahin et al. 2020; Briz-Redón et al. 2020).

The objective of this study was to analyze the dynamics of atmospheric air quality in the Moscow metropolitan area during the COVID pandemic in spring-summer 2020 taking into account the changing meteorological conditions. It should be noted that in Moscow, the isolation measures were introduced gradually. Firstly, on March 30, 2020 a self–isolation regime was adopted. Secondly, on April 13, 2020 more strict measures were accepted. The quarantine ended on June 9, 2020. Since the variability of the concentration of small gaseous and aerosol species also depends on meteorological conditions, a detailed study of the dynamics of the main meteorological parameters during the pandemic was carried out for the evaluation of their role in air quality changes.

For the analysis we used the meteorological observations and the measurements of the gas-aerosol composition of the atmosphere, which were carried out at the territory of the Meteorological Observatory of the Moscow State University (MO MSU). The MO MSU is considered as a background urban station (Chubarova et al., 2014) due to its location in the green area of the MSU Botanical Garden at a distance of about 350-400 m from the nearest highway.

The data and method description

The analysis of meteorological conditions and the dynamics of atmospheric pollution during the COVID-19 pandemic in Moscow was made for the 01.01.2020–30.06.2020 period. We compared the conditions before the lockdown, during the two lockdown periods and after them. To characterize the meteorological regime during this natural experiment we used the 1-minute resolution data on air temperature, atmospheric pressure, relative humidity, partial pressure of water vapor from the Vaisala MAWS-301 automatic weather station and the standard meteorological measurements from the MO MSU dataset. The measurement errors for the air temperature and relative humidity from the Vaisala station in comparison with standard measurements are 0.2°C and 2%, respectively (Environmental and climatic characteristics… 2013). In addition, we used sun/sky photometer measurements from the AERONET (Aerosol Robotic Network) program at the MO MSU (Chubarova et al. 2011) for the evaluation of the absorption Angstrom exponent (*AAE*) over the 440-870 nm spectral range for attributing the smoke air advection.

Since the gas-aerosol composition of the atmosphere depends not only on the emissions of pollutants, but also on the direction of air advection and synoptic situation, we also analyzed the periods with quasi-homogeneous meteorological conditions (QHMC). These situations were determined taking into account for the direction of air advection, circulation mode and the absence of significant changes in meteorological parameters. In addition, we consider the meteorological indicator of the intensity of pollution dispersion (IPD) (Kuznetsova et al. 2014), which characterizes the mixing conditions in the boundary layer of the atmosphere. Its value varies from 1 to 3 and is based on a complex of meteorological parameters such as the type of atmospheric circulation, the type of stratification in the boundary layer, wind speed, and precipitation. A value of 1 corresponds to the meteorological conditions favorable to the accumulation of pollution in the atmosphere, and 3 – to the conditions of its active dispersion. The IPD was calculated using the 24-hour forecast of the COSMO[1]-Ru operational model with 1-hour resolution.

In order to more accurately identify the dynamics of the urban effect on air pollution, an additional analysis of the possible advection of the smoke air from the biomass burning areas in the process of agricultural activity was also carried out, since the properties of the smoke air differ significantly from those of typical Moscow air. The following scheme of the analysis has been applied: for separating air masses influenced by the smoke air advection we used the data service for fire monitoring (https://earthdata.nasa.gov/earth-observation-data/near-real-time/firms) based on MODIS/Terra[2] measurements. In addition, using the HYSPLIT[3] model we calculated the backward trajectories at an altitude of 500 m with a time step of 24-hour. The data at 500 m usually reflect air transport at higher altitudes up to 2-3 km, which is the typical upper aerosol height in the troposphere. The location of the fire spots is considered to be important within about 50 km distance from the trajectory line. This distance is similar to the Moscow area size and can be used as a first proxy for removing the fire advection cases. If the number of fires is small and/or the spots are located within a border of a 50-km area, in addition, the data on the AERONET absorption Angstrom exponent (*AAE*) are used. A value of *AAE*=1 was applied as the threshold for the low-temperature combustion processes of smoke aerosol (Kirchstetter et al. 2004; Sun et al. 2017). If the *AAE* values are smaller than 1, then this indicates that there is no absorption by organic carbon, which efficiently absorbs in the UV and blue spectral range. Hence, these conditions corresponds to a typical Moscow air. A detailed scheme for detecting cases of smoke aerosol is described in (Chubarova et al. 2020). Fig. 1 shows the examples of the assimilation of data on fire spots and backward trajectories for Moscow conditions. Note, that on April 4, 2020, a small number of fires were observed (Fig. 1b) along the trajectory line. However, according to the AERONET data during this day, the *AAE*=1.06, which is higher than the threshold, and therefore, this day was excluded from the sample. As a result, we identified 8 periods (March 17-18, March 25-29, April 4, April 7, April 9, April 13, April 23, and June 18), when the effects of smoke on the composition of atmospheric air were observed in the Moscow metropolitan area.

The 20-minute resolution data on mass concentrations of aerosol PM10 and various trace gases (NO, NO_2, SO_2, CO, O_3, volatile organic compounds VOCs or CHx) at the MO MSU site were provided by the «Mosecomonitoring « Environmental Protection State Agency of Russia. The site is equipped by the TEOM 1400a for PM10 measurements, by the internationally certified Russian instruments from the OPTEC company (www.optec.ru) including ME 9841 for NOx, ME 9810B for O_3, ME 9850B for SO_2, K-100 for CO. The detailed description of the instrumentation and the quality assurance procedure can be found at http://mosecom.mos.ru. In order to estimate the typical mass concentrations over these months we also analyzed the data for the previous five- year period (2015–2019). The choice of this period for the comparison is due to the fact that the air quality in Moscow has significantly improved during recent years (https://mosecom.mos.ru/wp-content/uploads/2020/07/report2019.pdf), and the comparisons of the air pollution during the lockdown period in 2020 with the earlier measurements could lead to a systematic bias. In case of CHx, a 3-year period (2017–2019) was used due to the absence of measurements in the earlier years. The analysis of the data revealed the necessity of the additional correction of data. So, we removed small negative values, the cases with more than 50% difference from the

[1] COSMO is the acronym of Consortium of Small scale Modelling
[2] MODIS/TERRA is a Moderate Resolution Imaging Spectroradiometer on board of Terra satellite
[3] HYSPLIT- is the acronym of the Hybrid Single-Particle Lagrangian Integrated Trajectory model

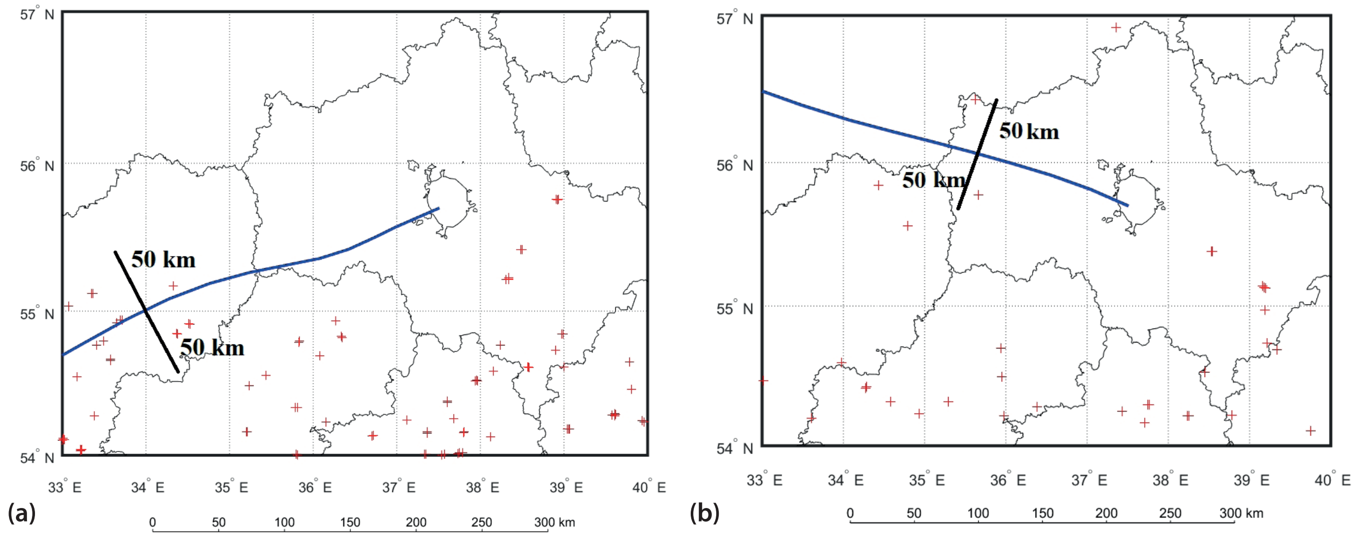

Fig. 1. The examples of data assimilation of fire locations and the direction of air particle transport for the detection of smoke advection in the Moscow region. (a) – 17/03/2020, (b) – 04/04/2020. The red marker indicates the fire centers based on satellite data from the FIRMS/MODIS dataset, the blue line – the particle 24-hour backward trajectory using the HYSPLIT model

neighboring values, zero values immediately before or after data omissions, zero values repeated two and more times in the absence of measurements simultaneously for several other parameters. In most cases, in 2020 the additional number of excluded values is small – i.e. less than 0.2% – with the exception of CO (3.1%). However, for the analyzed 5-year period, these quality criteria were not met for 17% of NO, 4% of SO_2, and 3% of CO measurements. Table 1 summarizes the total statistics on the available and removed cases. It should be mentioned that the total number of such cases, which includes the quality control tests provided at the Mosecomonitoring State Agency, are higher: from 2.9 to 22.5% depending on species for the 2015–2019 period, and from 1 to 11.9% – for 2020.

In order to characterize the main features before, within and after lockdown periods the following dates were chosen: the first lockdown period began from March, 30th – the date of the start of self-isolation regime; the second lockdown period lasted from April 13th up to June, 9th -the date of removing the self-isolation regime. These dates were determined in accordance with the Decrees of the Head of the Moscow city administration from March 29, 2020 (No. 34-UM), and the Supplement to the Decree from April 11, 2020 (No. 43-UM), and the Decree from 08.06.2020 (No. 68-UM).

In addition, the analysis of the dynamics of pollutants was carried out together with the daily values of the self-isolation index (*SII*), which was developed by the Yandex company (https://yandex.ru/company/researches/2020/podomam). The calculation of the self-isolation indices was carried out using the data from the Yandex «Transport» and «Yandex.Maps» platforms. These provide the most accurate picture of the dynamics of the transport situation in the city. Since this index is generated using the information on transport activity, it is natural to assume that it is related to the dynamics of pollutant emissions. The value has several thresholds, indicating the number of people on the street during the day. The *SII* zero corresponds to the conditions of the rush hour of a normal weekday. The *SII* from 0 to 3 qualifies the situation, when no strict lockdown conditions are observed. The *SII* from 3 to 4 qualifies the conditions, when people are rare on the streets. The *SII* in the range from 4 to 5 characterizes the conditions, when there is almost no people on the streets.

Table 1. The ratio (in %) of the additionally removed cases (N) relative to the measured case number for different pollutants. The measured case number and the number of the removed values ($C / C_{removed}$) are given in the parentheses. N_{all} – the percent of the total removed case numbers against the number of all 20-min intervals for the January-June period

Parameter	2015–2019 N% (C / Cr_{emoved}) $N_{all\%}$ (total case number =65232)	2020 N% ($C / C_{removed}$) $N_{all\%}$ (total case number =13104)
PM_{10}	0.07% (60 824 / 45) 6.8%	0.17% (12 953 / 22) 1.3%
NO	17.1% (60 927 / 10 391) 22.5%	0.01% (12 976 / 1) 1.0%
NO_2	0.07% (60 927 / 43) 6.7%	0.01% (12 972 / 1) 1.0%
SO_2	4.2% (58 322 / 2444) 14.3%	0.03% (12 955 / 4) 1.2%
CO	3.3% (62 280 / 2042) 7.7%	3.1% (11 911 / 371) 11.9%
CH_x^*	0% (37 975 / 0) 2.9%	0% (12 381 / 0) 5.5%
O_3	0.07% (55 213 / 37) 15.4%	0% (12 376 / 0) 5.6%

* for CHx the total case number is 39096 due to the shorter period of observation (2017–2019)

RESULTS

Meteorological conditions during the COVID-19 pandemic

For the Moscow region, the year 2020 was characterized by a uniquely warm winter. Table 2 shows the monthly mean meteorological characteristics for the January-June period in comparison with the long-term observations at the MO MSU from 1954 to 2013 (Chubarova et al. 2014). In winter, a stable snow cover has not been formed, since the air temperature in January and February was near zero, which was 7-8°C higher than the climatic value. In March, the average monthly air temperature also significantly exceeded the climatic value by more than 6°C. The increased air temperature affected the increase in the partial pressure of water vapor during January-March period. In April and May, on the contrary, the air temperature was slightly lower than the climatic values: by 1.4°C and 1.7°C, respectively. It happened due to the predominance of air advection from the northern regions. Low temperatures were accompanied by frequently observed low atmospheric pressure. The partial pressure of water vapor and the relative humidity were also low. In April, small amount of precipitation was recorded (22.9 mm), both relative to the climatic value, and relative to other months of 2020. In May and June, the amount of precipitation significantly, almost 3 times, exceeded the climatic value. June 2020 was characterized by warmer weather compared to the typical conditions. In general, during this month, the air temperature, and the partial pressure of water vapor were higher (by 1.5°C and 2.5 hPa, respectively) than the climatic values. The atmospheric pressure was also higher, indicating the predominance of the anticyclonic type of weather. A large amount of precipitation was associated with the active frontal systems at the beginning and at the end of June.

For a detailed analysis of weather conditions over March-June, 2020, we considered 21 periods, which were characterized by quasi-homogeneous meteorological conditions. Fig. 2 presents the variations of the meteorological parameters for these QHMC periods. During the periods of March 4-10, May 4-7, and June 4-9, there was an advection of warm and humid air masses from the southern directions. The average temperatures were about 5.8, 15.0 and 18.8°C, respectively, which is significantly higher than those in adjacent periods. The average relative humidity values were about 83, 79 and 74%. In some of these periods, the average indices of intensity of particle dispersion were significantly less than 3, reaching 2.4 during the period of May 23-28, and 2.2 – during the period of June 16-19.

During the periods of March 15-20, March 21-27, April 5-7, and May 8-22, the advection of cold and dry Arctic air masses was observed, providing a significant decrease in temperature and relative humidity in Moscow. For these periods, the average temperatures were about 3, 3, 2.2, 10.2°C, and the relative humidity comprised 56, 38, 46 and 61%, which were lower than those values in the adjacent periods. Similar conditions with the predominance of the cold air advection from the north-west direction were observed from April 12 to 29. In the periods of March 21-27, April 5-7, and May 23-28, the highest values of atmospheric pressure (i.e. >1000 hPa) were observed with the deviation from the monthly mean value by more than 15 hPa. The cyclonic circulation was the most pronounced during the period of March 11-14, when the average atmospheric pressure decreased to 975 hPa, and the deviation from the monthly mean value was -18 hPa. In the periods of May 4-7 and June 4-19, higher temperatures were observed compared with the climatic values. During the period of June, 16-19, the deviation typical conditionswas more than 5°C. The largest amount of precipitation (132.5 mm) was recorded during the period from May 29 until June 3, which comprised 37% of their total for May and June. This led to a significant excess of monthly values, especially in May, when the absolute maximum of monthly precipitation was recorded.

Figure 3 shows the average air temperature with confidence intervals at a significance level of 0.05 for the various lockdown stages during March-June 2020 compared to the 2015–2019 period. It is clearly seen, that the temperature in March (before the first stage of the lockdown) was even higher than that during the first lockdown period from March 30 until April 12, 2020. The temperature for the second lockdown period (from April 13 until June 9, 2020) was also significantly lower than the mean temperature for the 2015–2019 period. The low spring air temperature values were observed due to the prolonged influence of the cold Arctic air advection.

Table 2. Monthly mean values of meteorological parameters in January-June 2020 and their climatic characteristics for the period of 1954–2013 (adapted from Chubarova et al. 2014). For the data obtained according to long-term measurements, the values of the standard error are given in parentheses at a significance level of 0.05

	January 2020 / 1954–2013	February 2020 / 1954–2013	March 2020 / 1954–2013	April 2020 / 1954–2013	May 2020 / 1954–2013	June 2020 / 1954–2013
Air temperature (°C)	-0.2 / -8.0 (±0.96)	-0.3 / -7.5 (±0.95)	4.2 / -2.0 (±0.68)	4.8 / 6.2 (±0.57)	11.6 / 13.3 (±0.59)	18.7 / 17.2 (±0.55)
Atmospheric pressure (hPa)	988.6 / 992.4 (±1.65)	982.4 / 993.6 (±1.77)	991.8 / 993.1 (±1.46)	986.1 / 992.2 (±0.80)	988.6 / 992.4 (±0.67)	992.6 / 989.9 (±0.70)
Relative humidity (%)	85 / 83 (±0.84)	79 / 79 (±0.99)	64 / 72 (±1.23)	57 / 64 (±1.56)	66 / 61 (±1.37)	71 / 65 (±1.40)
Partial pressure of water vapor (hPa)	5.2 / 3.2 (±0.22)	4.9 / 3.1 (±0.23)	5.3 / 4.0 (±0.20)	4.9 / 6.1 (±0.25)	9.1 / 9.2 (±0.31)	15.0 / 12.5 (±0.35)
Precipitation (mm)	56 / 47 (±5.2)	35 / 40 (±5.0)	49 / 37 (±4.6)	17 / 41 (±5.1)	168 / 55 (±7.5)	193 / 76 (±8.7)

Features of atmospheric air pollution during the COVID-19 pandemic and its relationship with natural and anthropogenic factors

The main characteristics of the mass concentration of pollutants for the January-June period in 2020 and over the 2015–2019 period are summarized in Table A (in the Annex) and Fig. 4.

Before the lockdown in winter months and March, there were changes in concentrations in the range of 10-15%, with an exception of NOx and SO_2. For these species the concentrations were significantly lower (by 40-60%), and more likely due to the lower consumption of fuel for heating during the abnormally warm winter and in March. A more complex pattern was identified for ozone in January, when a significant increase (by 46%) in its concentration was observed. This could occur due to the specific features of chemical reactions at low NOx level.

In April, when quarantine measures have been already imposed and emissions significantly reduced there was a noticeable decrease up to 70%, in the concentration of almost all pollutants, except O_3, which, on the contrary, increased by 18%. The increase in O_3 during the COVID-19 lockdown periods was also reported for other geographic regions (Lee et al. 2020). In May, the picture became more complex. For some substances (NO_2, CO, SO_2, CHx, and PM10) the lower values continued to be observed, while the concentration of NO and O_3 values approached to the typical ones (to the 5-year averages). In June the concentrations of most pollutants deviated from the 5-year average in the range of 10-20%. The lowest concentrations were observed for NO_2 and SO_2 (-30 and -63%, respectively), although their concentration increased relative to the previous periods. The reason of the low values for these two species in June could be the reduction of number of cars and, possibly, an incomplete

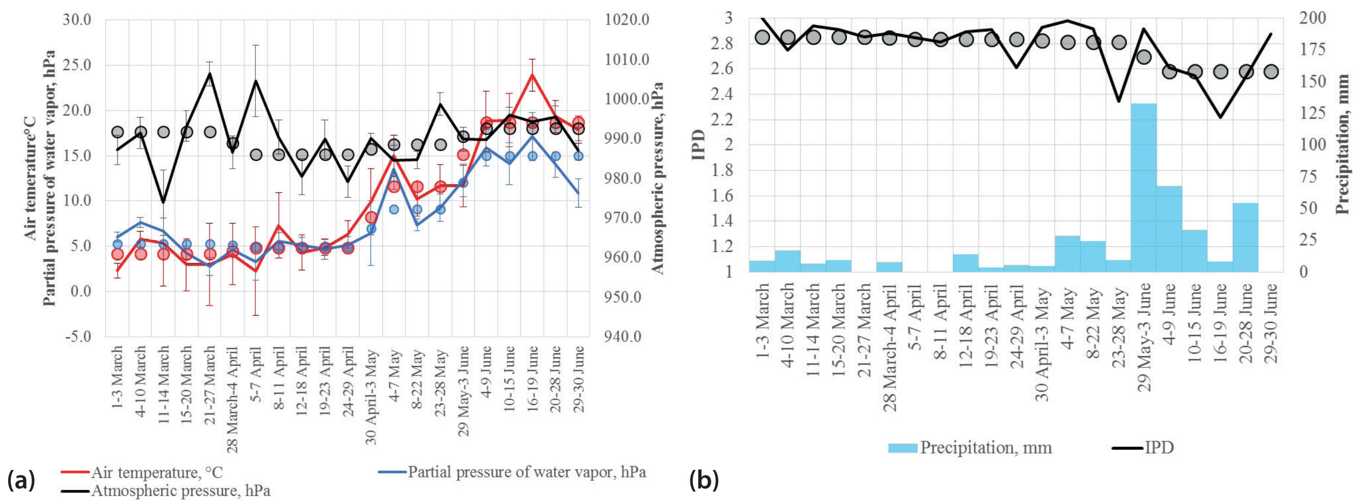

Fig. 2. Meteorological parameters (a – atmospheric pressure, air temperature, and partial pressure of water vapor; b – amount of atmospheric precipitation, and intensity of particle dispersion, (IPD) for the selected periods with quasi-homogeneous meteorological conditions, QHMC. The markers indicate the monthly mean values of the corresponding parameters

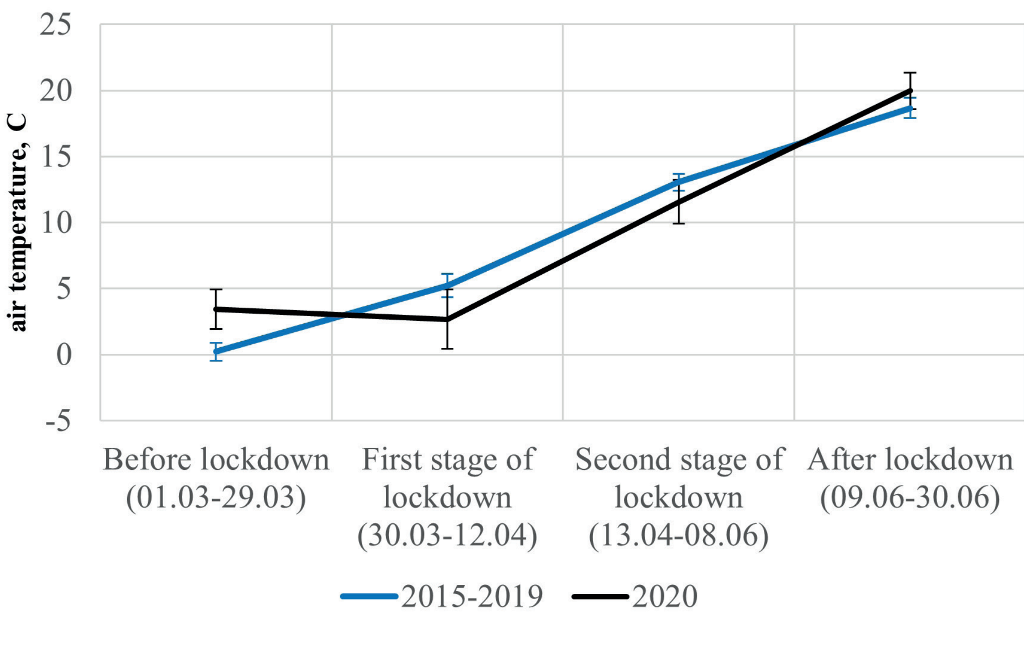

Fig. 3. The changes in the air temperature averaged over the different stages of the quarantine regime (lockdowns) in 2020 and during the 2015–2019 period in Moscow according to the measurements at the MO MSU. Confidence intervals are shown at 0.05 significance level

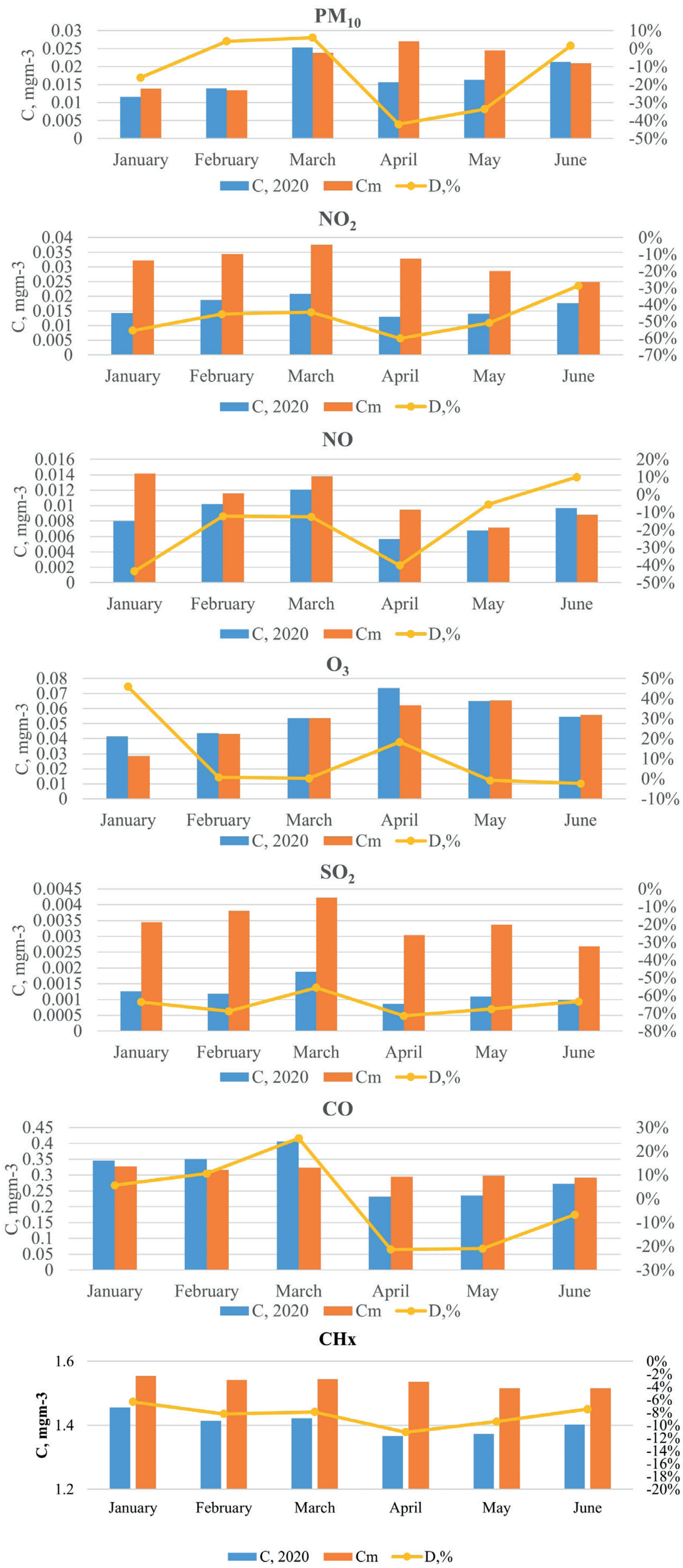

Fig. 4. Monthly mean values of the mass concentration (C, mgm^{-3}) of different pollutants – PM_{10}, NO_2, NO, O_3, SO_2, CO, CHx – observed in 2020, and in the 2015–2019 period (Cm, mgm^{-3}) and their relative differences D (in %). D=100%*(C-Cm)/Cm). Moscow

restoration of the transport activities of trucks (leading to lower emissions). Note, that the concentrations of SO_2 are extremely low in Moscow, and they are near the limit level of their detection (see Table A). The change between the relative differences of the normalized concentration between April and March (ΔD,%=D(April),%-D(March),%) was also negative for all substances, except ozone. This indicates a significant clearance of the urban atmosphere. However, the values of ΔD varied greatly: about -50% for CO and PM_{10}, about 20-30% for NOx and SO_2, and about -4% for CHx. For O_3, on the contrary, during March-April, the value of ΔD was +18%. In June a recovery in concentrations for some substances was observed. A noticeable, more than 10% increase in the normalized concentrations, compared with the May values, was observed for PM_{10} (ΔD=35%), NO (ΔD=16%) NO_2 (ΔD=22%), and CO (ΔD=14%). These changes in concentrations could be caused not only by the dynamics of anthropogenic emissions with a minimum in April-May, but also due to specific meteorological conditions during the period and the additional influence of the events with smoke advection.

For better evaluating the effects of meteorological factors we analyzed the situations for the QHMC periods. Figure 5 shows the dynamics of the average mass concentrations of pollutants and the IPD indices during these periods for all cases and for the cases without smoke advection in March-June 2020. Removing the days with smoke advection leads to a significant decrease in the concentrations of gaseous species (especially, NOx) and PM_{10}. For example, the extremely high concentrations of pollutants during the period of March 21-27 were observed due to a significant influence of smoke air advection. The effects of additional pollutants accumulation due to the stable atmospheric conditions (low IPD indices) can be only seen during the periods of May, 23-28 and June, 16-19. During these periods the average IPD values were below 2.5 and the increased concentrations of pollutants were recorded (see Figure 5b). On the whole, during the March-June period relatively high IPD indices were observed, indicating that there were no long-term conditions favorable for the accumulation of pollutants.

The lowest values of PM_{10}, SO_2, and CO were observed during the April 12-18, April 19-23 and May 8-22 periods, when there was an advection of the air from the north and north-western directions with high values of IPD.

In order to better understand the relationship between different pollutants and IPD indices we evaluated the correlation matrix between them using the QHMC bins for all cases and for cases without smoke advection. A good agreement is seen between the PM_{10} and NOx mass concentrations for both samples (Table 3). The high consistency of the surface concentrations of PM_{10} and NOx was also confirmed by the results of observations described in (Chubarova et al. 2019; Chubarova et al. 2020). There are statistically significant Pearson correlation coefficients between the IPD indices, PM_{10} and NOx. However, removing the cases with smoke advection provided a better agreement between them. In addition, in conditions without smoke advection one can see much more pronounced negative correlation between the O3 and NOx concentrations due to photochemical reactions in the same regime with typical organic and NOx emissions.

Fig. 6 shows the daily cycle of the pollutant concentrations evaluated for the studied periods: before lockdown, during the first and the second stages of lockdown and after lockdown. The cases with smoke advection were excluded from the analysis. In addition, the conditions with the advection of the cleanest Arctic air with potentially low values of the pollutants were considered separately in Fig. 6b. Note, that 42-45% of the days with the Arctic advection were observed during the analyzed periods, except for the first lockdown period, when 82% of days with such conditions were recorded.

In general, one can see much smoother diurnal cycle for most of the species due to the reduced intensity of traffic, especially during rush hours, smaller concentrations for all species, except O_3, during the lockdown periods, and some effects of seasonal changes.

The diurnal variability of PM_{10} is significantly lower in the lockdown periods, both when analyzing all cases and the cases, which are associated with the Arctic

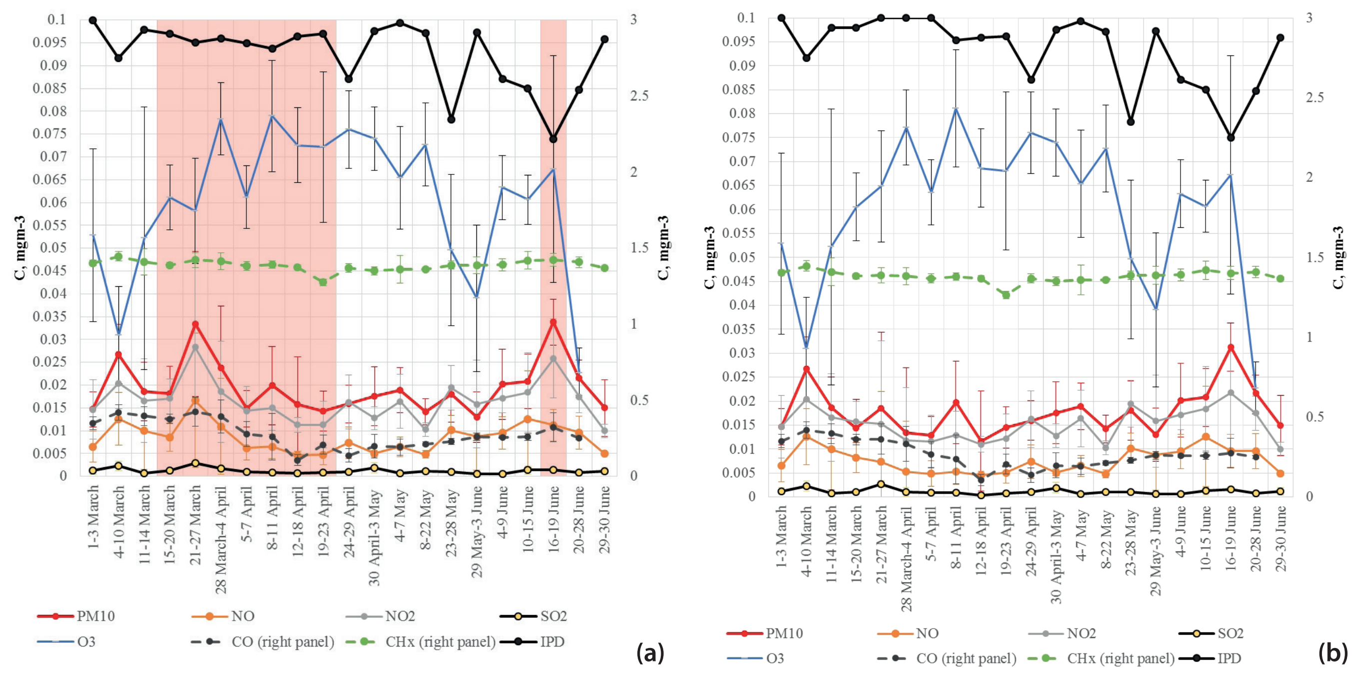

Fig. 5. Mean mass concentrations (mgm^{-3}) of pollutants – PM_{10}, NO, NO_2, SO_2, O_3, CO, CHx – and the average indices of intensity of pollution dispersion (IPD) for quasi-homogeneous meteorological periods in March-June 2020. a – all cases, b – only the cases without smoke advection. The periods, when smoke advection was observed, are marked in pink

Table 3. Correlation matrix for pollutants (PM_{10}, NO, NO_2, SO_2, CO, CHx, O_3) and the intensity of pollution dispersion (IPD) for the periods with quasi-homogeneous meteorological conditions during March-June 2020. a – all cases, b – excluding cases with smoke advection.

(a)

All cases	PM_{10}	NO	NO_2	SO_2	CO	CH_x	O_3	IPD
PM_{10}	1	**0.79**	**0.89**	**0.66**	0.56	0.62	-0.12	-0.47
NO		1	**0.91**	0.60	**0.68**	**0.74**	-0.41	-0.42
NO_2			1	0.58	0.60	**0.67**	-0.28	-0.52
SO_2				1	0.57	0.41	-0.05	-0.02
CO					1	0.64	-0.35	0.08
CHx						1	-0.46	-0.34
O_3							1	0.18
IPD								1
n	21							
p	0.95	**0.999**						

(b)

No fires	PM_{10}	NO	NO_2	SO_2	CO	CH_x	O_3	IPD
PM_{10}	1	**0.65**	**0.79**	0.46	0.29	0.50	-0.27	**-0.66**
NO		1	**0.89**	0.24	0.46	**0.70**	**-0.64**	-0.60
NO_2			1	0.27	0.34	0.59	-0.53	**-0.71**
SO_2				1	0.46	0.32	-0.06	-0.05
CO					1	0.55	-0.41	0.19
CHx						1	-0.52	-0.30
O_3							1	0.23
IPD								1
n	21							
p	0.95	**0.999**						

advection. The increased aerosol concentration outside the lockdown periods during such advection may be associated with more active urban aerosol generation due to increased anthropogenic emissions and some effects of seasonal changes, which provides higher PM generation in warm conditions after lockdown. For NOx and CHx, which concentrations are directly related to motor transport emissions, the smoothed morning and evening peaks are associated with the decreased traffic density in the lockdown period. This tendency is most pronounced in case of the Arctic advection. Note, that during the lockdown periods in the latter conditions, the concentrations of these chemical species outside of rush hours are close to those observed in typical situations. The diurnal changes in O_3 are determined by photochemical and dynamical processes and have some seasonal features. During the lockdown period, elevated O_3 values are observed throughout the day. It is due to the specific chemical reactions in the absence of large emissions of NOx. In the diurnal cycle, the maximum is observed during the daytime at any conditions. Note, that before the lockdown the smaller diurnal O_3 maximum is associated with a lower rate of photochemical reactions at low levels of UV radiation during the cold period, which is typical for the Moscow metropolitan area conditions (Elansky et al. 2018).

The opposite dependence with higher O_3 concentrations was observed during the lockdown periods partly due to lower NOx emissions, which also provided much more smoothed diurnal O_3 cycle. For cases with the Arctic advection, the O_3 concentrations are close to those observed before the lockdown. This is probably due to the influence of a downward flux of the ozone-rich air from the upper atmosphere during the Arctic advection. Hence, the natural factors play here an important role.

The CO concentrations were lower than before and after the lockdown. However, during the first period of the lockdown they were higher than those during the second stage. This may be explained by more active chemical loss of CO due to hydroxyl, which concentration was higher in May-June at increased levels of solar radiation.

In the diurnal cycle CO and CHx had much more smoother character during the lockdown periods without peaks during rush hours, and their concentrations were lower. The concentrations of CHx during the first and second stages of the lockdown were slightly reduced (by

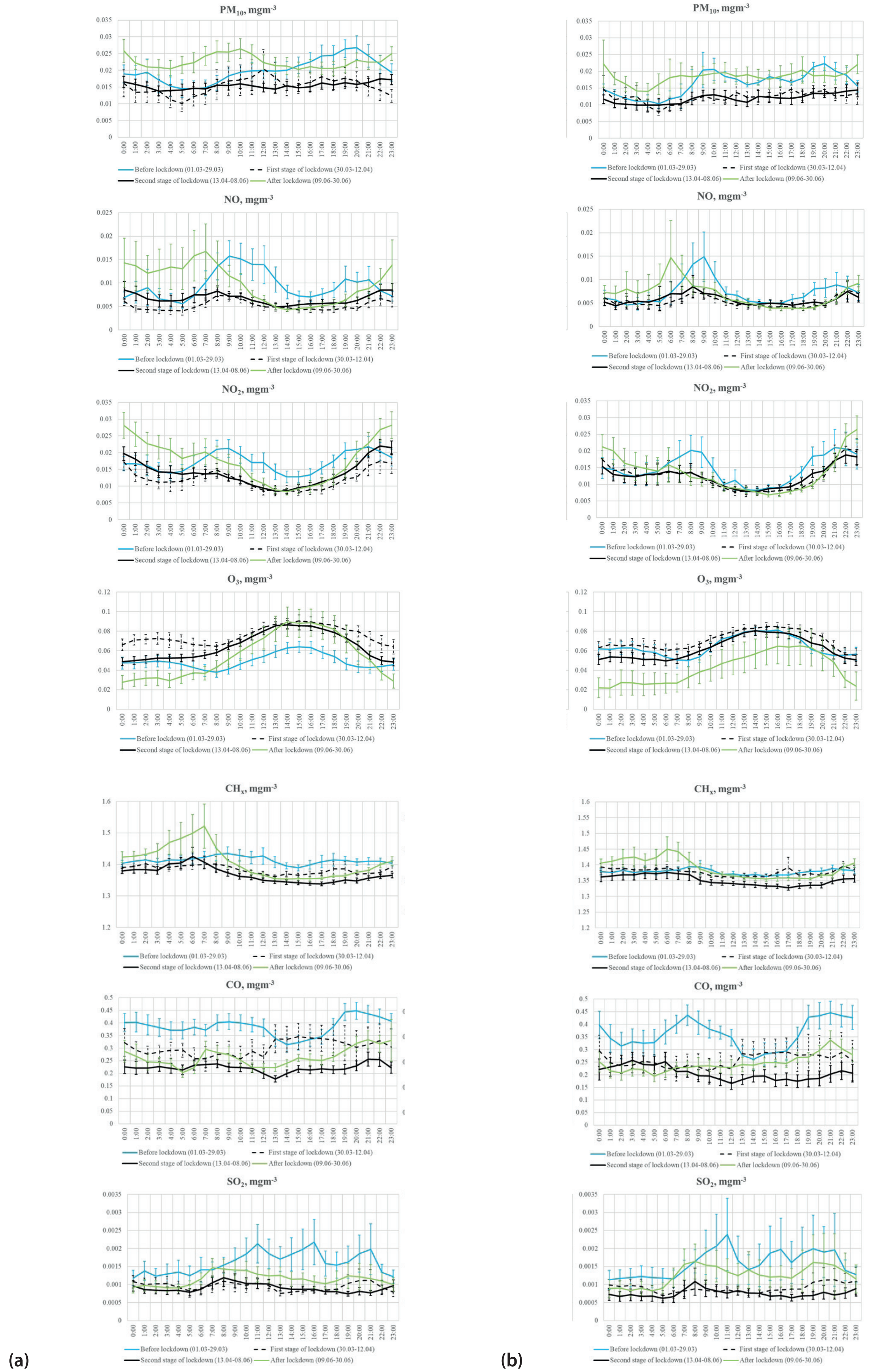

Fig. 6. Diurnal cycle of pollutants (PM_{10}, NO, NO_2, SO_2, CO, CHx, O_3) before lockdown (01.03-29.03), during the first stage of lockdown (30.03-12.04), the second stage (13.04-08.06), and after lockdown (09-30.06). a – all cases, b – only the cases with Arctic advection. The days with smoke situations were removed from the dataset

10%) to some extent due to the colder weather during these periods (see Fig. 3) and reflected smaller emission of organic matter due to lower vegetation activity.

In order to reveal the effects of emissions from traffic on the pollutants' concentrations we analyzed their relationship with the self-isolation index (*SII*) obtained from the Yandex. Figure 7 shows the *SII* dynamic during the March-June 2020 period. One can see that the *SII* values were above 2.5 during the first and partly the second lockdown periods from March 29 until May 11, 2020. At the same time, the increase in the *SII* on weekends and holidays before and after the lockdown can be sometimes as high as during the lockdown period.

The *SII* data reflect the dynamics of pollutants' emissions mainly from traffic, and, hence, the variations in concentrations of pollutants. Figure 8 shows the dependences of the daily mean concentration of various pollutants on *SII* over the March-June, approximated by a linear regression. For all species, statistically significant correlations were obtained at α=0.05, demonstrating that with the *SII* increase, the concentrations of all substances decreased. Exception is for O_3, which has a positive correlation. This result is in agreement with the analysis given above.

However, when considering the dependence only on, *SII* the changes in weather conditions were not taken into account. As shown above, during the lockdown in Moscow,

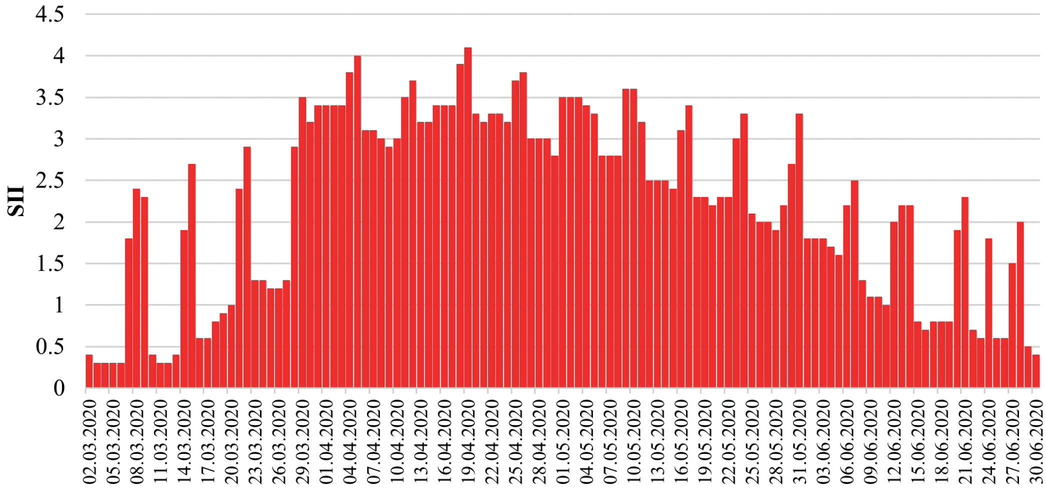

Fig. 7. The dynamics of self-isolation index (*SII*) in Moscow during March-June 2020 according to the Yandex dataset (https://yandex.ru/company/researches/2020/podomam)

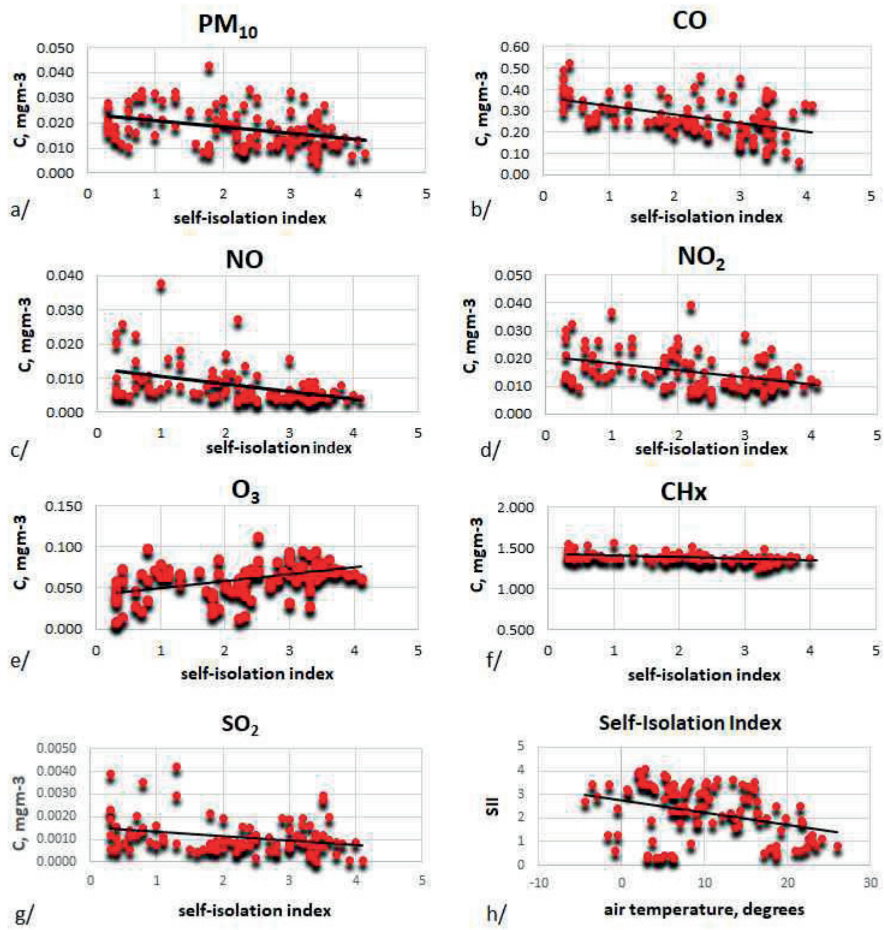

Fig. 8. The correlation between daily mean mass concentration (C, mgm^{-3}) of pollutants (PM_{10}, NO, NO_2, SO_2, CO, CHx, O_3) with self-isolation index, *SII* (a-g), and the correlation of *SII* with air temperature (h). No cases with smoke advection. March-June, 2020. Moscow

weather was characterized by cold Arctic air advection. This had an additional effect on air clearance and provided virtual *SII* dependence on the air temperature (see Fig. 8h). In order to remove the influence of the temperature changes (taken as a first proxy of different air mass advection) in variations of the pollutants' concentrations, the partial correlation coefficients were estimated. This allowed to identify the relationship between the two values at a fixed value of the third parameter (i.e. the air temperature). A comparison of the Pearson correlation coefficients between *SII* and the concentrations of pollutants with their partial correlation coefficients, when taking into account for temperature factor, is shown in Figure 9. One can see that all partial correlation coefficients remained statistically significant at α=0.05 for all species. However, in some cases, the partial correlation for coefficients were getting slightly smaller (for example, PM_{10} and NO_2) after accounting the air temperature changes.

This means that at higher temperatures, the concentrations of these pollutants are getting higher. And in some cases, on the contrary, the partial correlation coefficients increased (for example, for SO_2, CO). For SO_2, we may explain this due to large emissions of SO_2 during the heating season at relatively low temperatures. For CO, these effects were observed due to more active chemical loss in photochemical reactions during the warm period with higher temperatures at high levels of the solar radiation. As for CHx and O_3, there were no any significant changes in the sign and level of correlation coefficients. For O_3 this means that the most important factor in its dynamic is the photochemistry, and not the downward O_3 flux, which can be important only in specific conditions of the Arctic advection. Thus, we confirmed the presence of statistically significant relationships between the emissions of pollutants due to traffic, the indicator of which was the value, and the concentrations of the pollutants in the atmosphere.

A special attention was paid to the changes in concentration of surface O_3, since this is the gas of the first class of danger. Therefore, we analyzed its generation for different periods before, during, and after lockdown, as well as its changes due to *SII* variation. Fig. 10 shows the dependence of the O_3 mass concentration on NOx for different lockdown periods and *SII* ranges. In general, for all conditions we obtained non-linear relationship between O3 and NOx similar to that obtained by Zillman (1999) and Berezina et al. (2020).

The *SII* ranges qualified well the NOx limits during lockdown periods. The highest daily mean O_3 values were observed (see Fig. 10) at relatively high *SII* (>2.5), associated with a decrease in emissions of NOx. However, the O_3 generation also depends on the ratio of NOx and CHx. Figure 11 shows the ratio of O_3 concentrations to NOx as a function of ratio of CHx to NOx, which demonstrates the efficiency of O_3 formation per unit concentration of NOx at different ratios of CHx to NOx. These ratios are also given for different ranges of the *SII* values.

One can see that for all *SII* ranges, O_3 increased more efficiently with an increase in the proportion of organic compounds at the same content of NOx, which is consistent with data analysis shown by Berezina et al. (2020). At the same time, in conditions with relatively high *SII* (i.e. >2.5) the most effective O_3 generation is observed at the same CHx/NOx ratios (see Fig. 11). This may happen, since *SII*

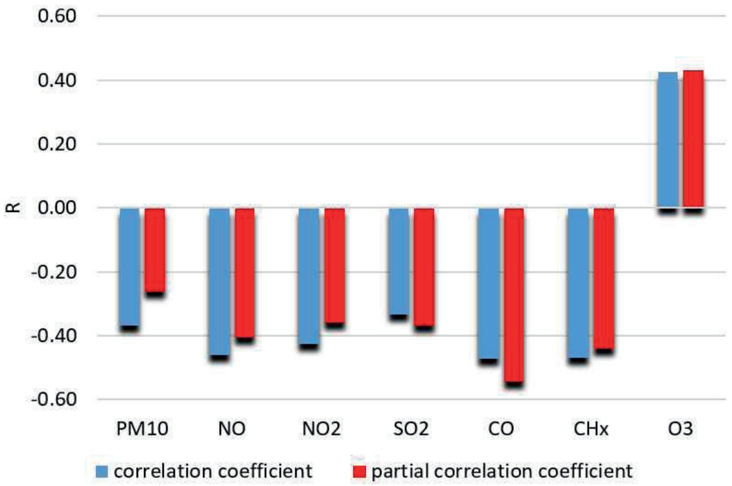

Fig. 9. The Pearson correlation coefficients between the daily mean concentration of pollutants and self-isolation index, *SII* and the partial Pearson correlation coefficients with accounting for the air temperature changes. No cases with smoke advection. All coefficients are statistically significant at α= 0.05

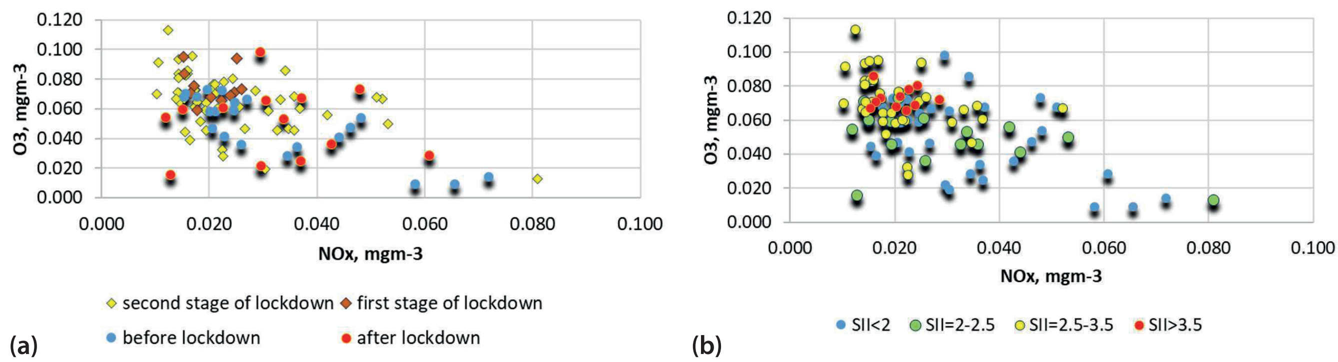

Fig. 10. The O_3 dependence on NOx concentration for different lockdown periods (a) and for different ranges of self-isolation index, *SII* (b) for the Moscow metropolitan area. Cases with smoke advection are not included

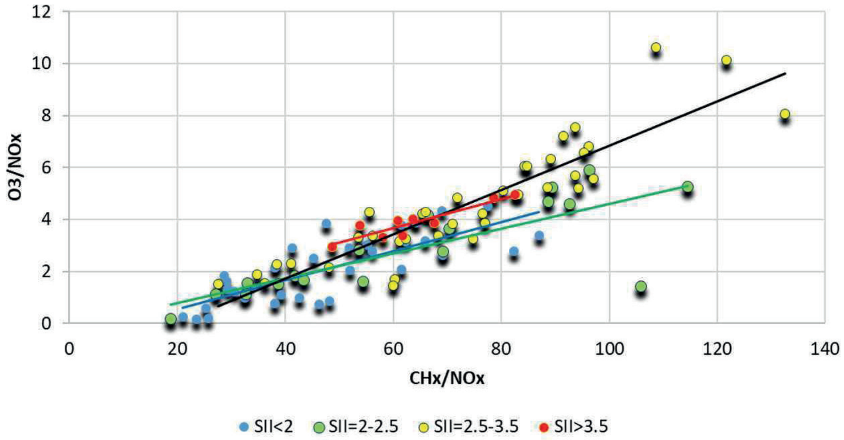

Fig. 11. The surface O_3 production per 1 mgm^{-3} of NOx at different CHx/NOx ratios for various *SII* ranges. No cases with fire advection. Moscow

values were usually higher 2.5 in April-May, 2020, when the Arctic air advection was often observed. This provided additional increase in ozone, associated with the advection of ozone-rich air from higher layers of the atmosphere.

DISCUSSION

Meteorological conditions during the analyzed period were characterized by exceptionally high monthly mean air temperatures in cold months (i.e. 6-8^{0}C above the climatic values in January-March, 2020) and the lower temperatures observed in April-May (by 1.5-2^{0}C), which affected the dynamics of the pollutants during the spring lockdown of 2020. Before the first stage of the lockdown the air temperature over the period from March, 1st until March, 30, 2020 was even higher than that during the first lockdown period (from March 30 until April 12, 2020). The temperature for the second lockdown period (from April 13 until June 9, 2020) was also significantly lower than the average temperature for the 2015–2019 period. These specific low spring air temperature conditions were observed due to the prolonged influence of the cold Arctic air advection.

In April, 2020 the average monthly mean concentrations of NO_2, NO, PM_{10}, SO_2 were 40-70% lower than those observed during the 2015–2019 period, while CO and CHx concentrations were only 10-20% lower. On the contrary, there was an increase in the concentration of surface O_3 by 18%.

The additional filters on smoke air advection resulted in removing the cases with high concentrations of pollutants (mainly, $PM1_0$ and NOx), especially at the end of March, 2020. These cases provided extremely high noise to the signal from urban pollution. The analysis without cases with smoke air advection has revealed much more pronounced relationship between O_3 and NOx, as well as between the IPD indices and concentrations of some pollutants.

The analysis of the pollutants' concentrations evaluated for considered periods before the lockdown, during the first and the second stages of the lockdown and after the lockdown provided much smoother diurnal cycle for most of the chemical species due to the reduced intensity of traffic, especially during rush hours. We also revealed the lower concentrations for all species, except O_3, during the lockdown periods, and some effects of seasonal changes in their variability. During the lockdown period, the elevated O_3 values were observed, which is due to the specific chemical reactions in the absence of large emissions of NOx. However, for the cases with the Arctic air advection, the elevated O_3 concentrations were closer to those observed before the lockdown periods due to the influence of the downward flux of ozone-rich air from the upper atmosphere in these situations.

The statistically significant negative correlation was identified between the self-isolation indices, and the daily mean concentrations of all pollutants, except surface O_3, when the positive correlation was observed. A comparison of the Pearson correlation coefficients between *SII* and the concentrations of pollutants with their partial correlation coefficients, when taking into account for the air temperature factor, revealed that the partial correlation coefficients remained statistically significant at α=0.05 for all the pollutants. However, in some cases, the partial correlation coefficients were getting slightly smaller (for PM_{10} and NOx) after accounting for the air temperature changes. This means that at higher temperatures, for example, the concentrations of these species are getting higher. In some cases, on the contrary, correlation coefficients increased (for SO_2 and CO). For SO_2, it can be explained due to larger emissions of SO_2 during the heating season at relatively low air temperatures. For CO, these effects were observed due to more active chemical loss in photochemical reactions at higher levels of the solar radiation during the warm period with the higher temperatures. For O_3, no significant changes in the sign and level of correlation coefficients were detected. This means that the process of O_3 photochemistry played more important role, than the effects of the downward O_3 flux, which can be important only in specific conditions of the Arctic air advection.

Results also showed that there is a pronounced negative nonlinear dependence of O_3 on NOx concentrations for different lockdown periods and *SII* ranges. The most active formation of O_3 was observed at the highest *SII* indices. These are associated with a decrease in emissions of NOx into the atmosphere and, accordingly, resulted in reduction of their concentration. It was also shown that for all *SII* ranges with the increase in the CHx/NOx ratio, the ozone increased more efficiently at the same content of NOx. It is consistent with results shown by Berezina et al. (2020). At the same time, the most favorable conditions for O_3 generation existed in conditions with *SII* >2.5 at the same CHx/NOx ratios. Since *SII*>2.5 were observed in April and May, we explained this feature by the additional influence of the Arctic advection during this period, which created favorable conditions for downward ozone-rich air flux from the higher layers of the atmosphere.

CONCLUSIONS

The results of our study showed that the specific meteorological conditions with extremely high air temperatures in cold months and low temperatures during the lockdown periods as well as the situation with smoke air advection have made a considerable contribution to the air quality during the COVID-19 pandemic. Nevertheless, the decrease in traffic emissions during the lockdown periods played important role for the decrease in concentration of many pollutants and the increase in O_3 concentration. However, the growth of O_3, especially during the Arctic air advection, was observed due to natural processes of the downward flux of the ozone-rich air from higher layers of the atmosphere. The analysis of the pollutant concentrations also revealed that the lockdown periods were characterized by much smoother diurnal cycles for most of the chemical species considered due to the reduced intensity of traffic, and especially during rush hours.

A statistically significant negative relationship was obtained between the self-isolation indices, *SII* and the average daily concentrations of all pollutants, except surface O_3, which was characterized by positive correlation with . The accounting for the air temperature effects using the analysis of the partial correlation coefficients confirmed the statistically significant (at α=0.05) dependences between and the concentrations of all pollutants. It was shown that for O_3 the process of photochemistry plays more important role than the effects of the downward O_3 flux, which can be important only in specific conditions of the Arctic air advection. These relationships between the pollutant concentration and *SII* can be used in future for assessing the dynamics of urban pollution in different traffic conditions.

It was found that for all ranges with the growth of the CHx/NOx ratio, the O_3 concentration increased more efficiently at the same content of NOx. The most favorable conditions for O_3 generation were created at the same CHx/NOx ratio in conditions with *SII*>2.5. Since *SII*>2.5 were usually observed in April and May, this feature can be explained by the additional influence of the Arctic air advection during this period, which created favorable conditions for the downward ozone-rich air flux from the higher layers of the atmosphere.

REFERENCES

Berezina E., Moiseenko, K., Skorokhod A., Pankratova N.V., Belikov I., Belousov V. and Elansky N.F. (2020). Impact of VOCs and NOx on Ozone Formation in Moscow. Atmosphere, 11(11), 1262, DOI: 10.3390/atmos11111262.

Briz-Redón Á. and Serrano-Aroca Á. (2020). A spatio-temporal analysis for exploring the effect of temperature on COVID-19 early evolution in Spain. Science of The Total Environment, 728, 138811, DOI: 10.1016/j.scitotenv.2020.138811.

Chubarova N.E. Nezval' E.I., Belikov I.B. et al. (2014). Climatic and environmental characteristics of Moscow megalopolis according to the data of the Moscow State University Meteorological Observatory over 60 years. Russian Meteorology and Hydrology, 39(9), 602-613, DOI: 10.3103/S1068373914090052.

Chubarova N.E., Androsova E.E., Kirsanov A.A., Vogel B., Vogel H., Popovicheva O.B. and Rivin G.S. (2019). Aerosol and Its Radiative Effects during the AeroRadcity 2018 Moscow Experiment. Geography, Environment, Sustainability, 12(4), 114-131, DOI: 10.24057/2071-9388-2019-72.

Chubarova N., Smirnov A., Holben B. (2011). Aerosol Properties in Moscow According to 10 Years of AERONET Measurements at The Meteorological Observatory of Moscow State University. Geography, Environment, Sustainability. 4(1), 19-32, DOI: 10.24057/2071-9388-2011-4-1-19-32.

Chubarova N.E., Zhdanova E.Yu., Androsova E.E. et al. (2020). Aerosol pollution of cities and its effects on weather forecast, regional climate and geochemical processes. Moscow: MAX Press (in Russian), DOI: 10.29003/m1475.978-5-317-06464-8.

Environmental and climate characteristics of the atmosphere in 2013 according to the measurements of the Meteorological Observatory of Moscow State University. (2014). Ed. by N.Ye. Chubarova, Moscow, MAKS Press (In Russian).

Elansky N. F., N. A. Ponomarev and Ya. M. Verevkin. (2018). «Air quality and pollutant emissions in the Moscow megacity in 2005–2014», Atmos. Environ. 175, 54–64 DOI: 10.1016/j.atmosenv.2017.11.057.

Jain S. and Sharma T. (2020). Social and Travel Lockdown Impact Considering Coronavirus Disease (COVID-19) on Air Quality in Megacities of India: Present Benefits, Future Challenges and Way Forward. Aerosol and Air Quality Research, 20(6), 1222-1236, DOI: 10.4209/aaqr.2020.04.0171.

Kirchstetter T.W., Novakov T. and Hobbs P.V. (2004). Evidence that the spectral dependence of light absorption by aerosols is affected by organic carbon. Journal of Geophysical Research, 109, D21208, DOI: 10.1029/2004JD004999.

Krecl P., Targino A.C., Oukawa G.Y. and Cassino Junior R.R. (2020). Drop in urban air pollution from COVID-19 pandemic: Policy implications for the megacity of São Paulo. Environmental Pollution, 265, part B, 114883, DOI: 0.1016/j.envpol.2020.114883.

Kuznetsova I.N., Shalygina I.Yu. et al. (2014). Unfavorable for air quality meteorological factors. Proceedings of Hydrometcentre of Russia, 351, 154-172. (in Russian).

Lee J.D., Drysdale W.S., Finch D.P., Wilde S.E. and Palmer P.I. (2020). UK surface NO2 levels dropped by 42 % during the COVID-19 lockdown: impact on surface O3. Atmos. Chem. Phys., 20, 15743-15759, DOI: 10.5194/acp-20-15743-2020.

Li L., Li Q., Huang L., Wang Q. et al. (2020). Air quality changes during the COVID-19 lockdown over the Yangtze River Delta Region: An insight into the impact of human activity pattern changes on air pollution variation. Science of The Total Environment, 732, 139282, DOI: 10.1016/j.scitotenv.2020.139282.

Mahato S., Pal S. and Ghosh K.G. (2020). Effect of lockdown amid COVID-19 pandemic on air quality of the megacity Delhi, India. Science of the Total Environment, 730, 139086, DOI: 10.1016/j.scitotenv.2020.139086.

Şahin M. (2020). Impact of weather on COVID-19 pandemic in Turkey. Science of The Total Environment, 728, 138810, DOI: 10.1016/j.scitotenv.2020.138810.

Sharma S., Zhang M., Gao A.J., Zhang H. and Kota S.H. (2020). Effect of restricted emissions during COVID-19 on air quality in India. Science of The Total Environment, 728, 138878, DOI: 10.1016/j.scitotenv.2020.138878.

Sillman S. (1999). The relation between ozone, NOx and hydrocarbons in urban and polluted rural environments. Atmospheric Environment, 33(12), 1821-1845.

Sun J., Guorui Z., Hitzenberger R. et al. (2017). Emission factors and light absorption properties of brown carbon from household coal combustion in China. Atmos. Chem. Phys., 17(7), 4769-4780, DOI: 10.5194/acp-17-4769-2017.

Quinio V. and Enenkel K. (2020). How have the Covid pandemic and lockdown affected air quality in cities? [online] Centre of Cities briefing, 10th December 2020. Available at: https://www.centreforcities.org/publication/covid-pandemic-lockdown-air-quality-cities/ [Accessed 22 Jan. 2021].

Zambrano-Monserrate M.A., Ruano M.A. and Sanchez-Alcalde L. (2020). Indirect effects of COVID-19 on the environment. Science of The Total Environment, 728, 138813, DOI: 10.1016/j.scitotenv.2020.138813.

Appendix

Table A. Main statistical characteristics of the mass concentration of pollutants (in mgm-3) in 2020 and for the period of 2015–2019 according to the measurements at the MO MSU. All cases, including smoke situations.

Month	Mean 2020/ 2015–2019	Minimum 2020/ 2015–2019	Maximum 2020/ 2015–2019	50th percentile 2020/ 2015–2019	Number of cases 2020/ 2015–2019
PM_{10}					
January	0.012 / 0.014	0.001 / 0.001	0.091 / 0.094	0.009 / 0.012	2232 / 8907
February	0.014 / 0.013	0.001 / 0.001	0.133 / 0.058	0.013 / 0.012	1969 / 8568
March	0.025 / 0.024	0.001 / 0.001	0.143 / 0.464	0.020 / 0.016	2219 / 10882
April	0.016 / 0.027	0.001 / 0.001	0.083 / 0.260	0.013 / 0.021	2157 / 10665
May	0.016 / 0.025	0.001 / 0.001	0.077 / 0.185	0.014 / 0.021	2220 / 11009
June	0.021 / 0.021	0.002 / 0.001	0.109 / 0.161	0.020 / 0.007	2134 / 10748
NO					
January	0.008 / 0.014	0.001 / 0.001	0.075 / 0.329	0.006 / 0.006	2232 / 9569
February	0.010 / 0.012	0.001 / 0.001	0.057 / 0.331	0.007 / 0.006	1997 / 7702
March	0.012 / 0.014	0.001 / 0.001	0.259 / 0.353	0.007 / 0.006	2207 / 8769
April	0.006 / 0.010	0.001 / 0	0.066 / 0.275	0.004 / 0.005	2149 / 8703
May	0.007 / 0.007	0.001 / 0	0.074 / 0.199	0.005 / 0.004	2230 / 7321
June	0.010 / 0.009	0.001 / 0.001	0.128 / 0.294	0.006 / 0.006	2160 / 8472
NO_2					
January	0.014 / 0.032	0.001 / 0.001	0.052 / 0.137	0.013 / 0.030	2232 / 11156
February	0.019 / 0.034	0.003 / 0.001	0.058 / 0.125	0.016 / 0.030	1997 / 9692
March	0.021 / 0.038	0.003 / 0.002	0.164 / 0.156	0.015 / 0.032	2207 / 10941
April	0.013 / 0.033	0.002 / 0.001	0.071 / 0.155	0.011 / 0.026	2148 / 10273
May	0.014 / 0.029	0.002 / 0.001	0.064 / 0.133	0.010 / 0.022	2231 / 8927
June	0.018 / 0.025	0.002 / 0.001	0.087 / 0.144	0.013 / 0.019	2156 / 9895
SO_2					
January	0.0013 / 0.0035	0.0003 / 0.0001	0.0127 / 0.0360	0.0012 / 0.0027	2228 / 8668
February	0.0012 / 0.0038	0.0001 / 0.0001	0.0038 / 0.0790	0.0011 / 0.0030	1988 / 8702
March	0.0019 / 0.0042	0 / 0.0001	0.0161 / 0.0731	0.0013 / 0.0028	2217 / 9326
April	0.0009 / 0.0030	0 / 0	0.0084 / 0.0566	0.0007 / 0.0025	2152 / 9110
May	0.0011 / 0.0034	0 / 0	0.0089 / 0.0480	0.0009 / 0.0028	2224 / 9916
June	0.0010 / 0.0027	0 / 0.0001	0.0092 / 0.0391	0.0008 / 0.0023	2142 / 10156
CO					
January	0.35 / 0.33	0.01 / 0.10	1.73 / 2.72	0.35 / 0.30	2231 / 8930
February	0.35 / 0.32	0.02 / 0.02	0.84 / 1.92	0.34 / 0.30	1996 / 8706
March	0.41 / 0.32	0.01 / 0.01	2.41 / 2.60	0.38 / 0.30	2222 / 10442
April	0.23 / 0.29	0.01 / 0.01	0.92 / 2.50	0.21 / 0.27	1899 / 10543
May	0.24 / 0.30	0.01 / 0.01	0.91 / 2.90	0.23 / 0.25	1612 / 10951
June	0.27 / 0.29	0.02 / 0.06	1.37 / 3.37	0.25 / 0.26	1580 / 10666

CH_x					
January	1.46 / 1.55	1.28 / 1.37	1.78 / 2.81	1.45 / 1.52	2228 / 6613
February	1.41 / 1.54	1.34 / 1.36	1.91 / 2.46	1.40 / 1.52	1997 / 5732
March	1.42 / 1.54	1.32 / 1.37	2.16 / 3.22	1.40 / 1.50	2148 / 6424
April	1.37 / 1.54	1.23 / 1.21	1.67 / 2.98	1.36 / 1.52	1924 / 6383
May	1.37 / 1.52	1.22 / 1.15	2.36 / 3.21	1.35 / 1.48	1951 / 6356
June	1.40 / 1.52	1.31 / 1.08	2.75 / 3.20	1.37 / 1.49	2133 / 6465
O_3					
January	0.042 / 0.029	0.002 / 0.001	0.094 / 0.084	0.043 / 0.026	2231 / 9830
February	0.044 / 0.043	0.002 / 0.001	0.089 / 0.100	0.046 / 0.045	1979 / 7677
March	0.054 / 0.054	0.002 / 0.001	0.146 / 0.126	0.057 / 0.057	2230 / 8738
April	0.074 / 0.062	0.004 / 0.001	0.140 / 0.283	0.074 / 0.062	2158 / 10106
May	0.065 / 0.065	0.002 / 0.001	0.149 / 0.169	0.066 / 0.065	2231 / 8926
June	0.055 / 0.56	0.001 / 0.001	0.193 / 0.272	0.047 / 0.052	1547 / 9899

RESEARCH PAPER

MONITORING OF CO, NO_2 AND SO_2 LEVELS DURING THE COVID-19 PANDEMIC IN IRAN USING REMOTE SENSING IMAGERY

Nurwita Mustika Sari[1,2]*, Muhammad Nur Sidiq Kuncoro[3]
[1]Department of Geography, Faculty of Mathematics and Natural Science, Universitas Indonesia
[2]Remote Sensing Application Center, LAPAN, Indonesia
[3]Department of Management, Faculty of Economics and Business, Universitas Indonesia
*Corresponding author: nurwita_sutaat@yahoo.com; nurwita.mustika@lapan.go.id
Received: April 16th, 2020 / Accepted: August 2nd, 2021 / Published: October 1st, 2021
https://doi.org/10.24057/2071-9388-2020-74

ABSTRACT. The COVID-19 pandemic has had a major impact on various sectors. Iran is one of the countries most affected by this pandemic. After considering the huge impact, the government imposed strict rules prohibiting social gatherings and restricting travel for the entire population following the large number of victims in the country. These restrictions lead to changes in the environment, especially air quality. The purpose of this study was to find out how the COVID-19 pandemic affected air quality in Iran following the activity restrictions in the region. The method used in this research was based on the use of multitemporal Sentinel-5P data processing with scripts available on the Google Earth Engine applied on the images, acquired in the period before and after the COVID-19 pandemic. The data used included the image collection of Sentinel-5P NRTI CO: Near Real-Time Carbon Monoxide, Sentinel-5P NRTI NO_2: Near Real-Time Nitrogen Dioxide and Sentinel-5P NRTI SO_2: Near Real-Time Sulphur Dioxide. The results showed, that for Iran in general, changes in the concentration of CO are clearly visible in urban areas with high population activity such as Tehran, where there was a decrease from 0.05 to 0.0286 mol/m^2, while for other areas it is also influenced by the varying climate conditions, which affect the level of pollution. For the NO_2 pollutant, there was a significant decrease in pollution levels in big cities such as Tehran, Qom, Isfahan and Mashhad from 0.0002 to 0.000114 mol/m^2. For the SO_2 pollutant, there was a decrease in pollution levels in Iran's big cities from 0.0005 to 0.0000714 mol/m^2. For Tehran province, which is the most populous and busiest province in Iran, it can be observed that there was also a decrease in the concentration of pollutants after the lockdown compared to the pre-lockdown period. The CO concentration decreased from 0.043 to 0.036 mol/m^2, while for the NO_2 pollutant there was a decrease from 0.0002 to 0.000142 mol/m^2 and for the SO_2 pollutant, there was a decrease from 0.0005 to 0.000143 mol/m^2.

KEYWORDS: COVID-19, global pandemic, Iran, air pollution, Sentinel-5P imagery

CITATION: Nurwita Mustika Sari and Muhammad Nur Sidiq Kuncoro (2021). Monitoring Of Co, No_2 And So_2 Levels During The Covid-19 Pandemic In Iran Using Remote Sensing Imagery . Geography, Environment, Sustainability, Vol.14, No 4, p. ??=??
https://doi.org/10.24057/2071-9388-2020-74

ACKNOWLEDGEMENTS: The author would like to express our gratitude to the Indonesia Endowment Fund for Education (LPDP Kementerian Keuangan Republik Indonesia) for supporting this research fund and Dr. Eng. Masita Dwi Mandini Manessa for the guidance.

Conflict of interests: The authors reported no potential conflict of interest.

INTRODUCTION

The COVID-19 outbreak was caused by the SARS-CoV-2 novel coronavirus which appeared around the end of 2019 in the Wuhan area, Hubei Province, China. Since the emergence of this disease, various sectors were shocked many times not only medically but also economically around the world due to the ease of its transmission between humans and the resulting impact of late handling. COVID-19 has been declared a global pandemic by WHO circa March 2020, following its spread throughout the world regardless of climate, the race of population and even the development stage of the country.

Considering the situation in Iran, in late October 2020, Iran reported a death due to COVID-19 every four minutes (Reuters 2020). Not only citizens were infected, several country officials such as the leader of parliament and dozens of parliament members have tested positive for COVID-19. Following the large number of positive COVID-19 cases which is getting worse and the increasing number of victims, the Iranian government began to enact regulations related to mitigation of the COVID-19 outbreak, as has been done in many affected countries. These rules include the prohibition of social gatherings and frequent travel within the territory of the country.

Research related to COVID-19 was still limited but increasing very rapidly in various aspects because of the consequences caused by this global pandemic. The existing research was related to the characteristics, mode of transmission and origin of this COVID-19 infection (Adnan et al. 2020); the correlation between weather variables and the pandemic in Jakarta (Tosepu et al. 2020); epidemiology and pathogenesis which also studies the transmission and phylogenetics of coronaviruses (Rothan & Byrareddy 2020); and the comparison of COVID-19 with the predecessors, SARS and MERS, which were also caused by the coronavirus (Petrosillo et al. 2020).

The pollution of air by various types of contaminants is mainly associated with motor vehicle emissions and smoke from industrial chimneys. The impact caused by air pollution includes the spread of heart diseases, which suggests a close relationship between exposure to air pollution and diseases of the cardiovascular system (Andersson et al. 2020); (Miller 2020). Its other impacts are related to mental health as it causes depressive symptoms (Altuğ et al. 2020) and the influence on the health of children due to their imperfect breathing system and immunity (Kurata et al. 2020). Another thing that also turns out to be related to air pollution is frequent traffic accidents (Wan et al. 2020).

In terms of economy and finance, air pollution can even affect the disposition of financial transactions and influence the transition from direct shopping in stores to online shopping (J. (Jie) Li et al. 2019). Research related to the effect of COVID-19 on air pollution in China has been carried out by looking at the implications of lockdown in North China (Wang et al. 2020). On the other hand, it has also been studied how the COVID-19 pandemic affects NO^2 and $PM_{2.5}$ concentrations in the US through federal air monitoring network data (Berman & Ebisu 2020). Based on this study, the COVID-19 pandemic had a major impact on behavior change, causing a reduction in NO_2 concentration by 25.5% with an absolute decrease of 4.8 ppb compared to previous years. In addition, the pandemic caused a decrease in $PM_{2.5}$ due to the closure of business activities.

Various remote sensing data have been extensively used for observing air pollution. Remote sensing was used for air pollution monitoring through the IASI (Infrared Atmospheric Sounding Interferometer) feature of the Metop series satellites, which allows to observe ammonia, sulphur dioxide (SO_2) and Ozone (O_3) pollutants (Clerbaux et al. 2017). In addition, air pollution sources were detected from MODIS remote sensing data to view aerosols in 1 km resolution using Glowworm Swarm Optimization (GSO) (Chen et al. 2017). Other studies on monitoring air pollution with remote sensing data are related to determining industrial pollution emissions from VIIRS Nightfire data (Sun et al. 2020), measuring aerosols in the metropolitan area (Vratolis et al. 2020), measuring $PM_{2.5}$ concentration with MODIS data and machine learning (X. Li & Zhang 2019), measuring air pollution from motor vehicles on urban roads (Smit et al. 2019), and detection of aerosols using MODIS data (Filonchyk et al. 2017). In another study, research of methane variability in Pakistan, Afghanistan and surrounding areas was carried out using Sciamachy/Envisat data (ul-Haq et al. 2015)

Other studies related to the use of remote sensing data for air pollution analysis are studies that look at air pollution inputs to a specific desert area, the Mojave Desert, using the airborne, in-situ and remote sensing satellite data as desert ecosystems are particularly vulnerable to pollution from urban activities. Measurement data in this study were obtained from the mobile air quality laboratory, AMOG (AutoMObile trace Gas), with additional GHG and O_3 data from AJAX – Alpha Jet Atmospheric eXperiment. Further, the aerosol modeling was carried out using LiDAR (Leifer et al. 2019). To detect vehicle emissions on roads, an on-road remote sensing system with infrared (IR) and ultraviolet (UV) bands was used, which also has a speed detector and a camera to capture the image of vehicle plates (Huang et al. 2018). Another study has predicted the concentrations of $PM_{2.5}$ using MODIS Terra and Aqua remote sensing data and dynamic spatial panel model (Fu et al. 2020). A study comparing the use of direct on-site measurements and remote sensing data for monitoring air pollution and health aspects in Canada has shown that they give similar results and are associated with each other (Prud et al. 2013).

Sentinel-5P data, which is still relatively new in monitoring air quality, was used to investigate NO_2 pollution in France (Omrani et al. 2020). In another study, Sentinel-5P was used for monitoring sulphur dioxide and nitrogen dioxide in the South African region as a result of coal-fired power plants (Shikwambana et al. 2020). TROPOMI on Sentinel-5P was used to analyse the level of NO_2 concentration in Ecuador after the COVID-19 lockdown, which emphasizes the importance of air quality for human health. From this research, a reduction of NO_2 concentrations (-13%) was observed in Ecuador (Pacheco et al. 2020).

Sentinel-5P was launched in October 2017 with a specific mission of monitoring air pollution, which is the focus of this study. This satellite is dedicated to monitoring the atmosphere with an instrument called the TROPOspheric Monitoring Instrument (TROPOMI). Its aim is to reduce gaps in the availability of global atmospheric data such as SCIAMACHY/Envisat (which ended in April 2012), the OMI/AURA mission and the future Copernicus Sentinel-4 and Sentinel-5 missions. TROPOMI combines the power of SCIAMACHY data, OMI, and state-of-the-art technology to provide observations with performance that other instruments currently cannot meet. Its advantages include higher sensitivity as well as spectral, spatial and temporal resolution (ESA 2021). That is why the use of Sentinel-5P data has a very high potential for observing air pollution conditions in a wide area and over a long period. Iran as one of the countries that have been heavily affected by the pandemic had to implement a strict lockdown to control the spread of the virus. This study aims to analyse the effect of social activity and travel restrictions due to the COVID-19 global pandemic on air pollution in Iran.

MATERIALS AND METHODS

Materials

This research focuses on the Tehran province of Iran where the capital city is located. The data used in this study includes the Sentinel-5P NRTI CO: Near Real-Time CO, Sentinel-5P NRTI NO_2: Near Real-Time NO_2 and Sentinel-5P NRTI SO_2: Near Real-Time SO_2. The dataset version used in this research is Near Real-Time, or NRTI, which covers a smaller area than the offline version but appears more quickly after acquisition. These datasets were provided by European Space Agency (ESA) and are available on Earth Engine Data Catalog developed by Google (Google 2020).

As explained by ESA, the CO pollutant dataset used is global CO data in the clear-sky and cloudy-sky conditions in the 2.3 m spectral range of the shortwave infrared (SWIR) part of the solar spectrum. Noise in the data causes negative values to appear. Negative vertical column values are often observed especially over clean regions or very low SO_2 emissions. It is stated that is recommended not to filter these negative values except for outliers, i.e., vertical columns lower than -0.001 mol/m^2. In the NO_2 data collection used, the dataset represents the collective nitrogen oxide concentration that occurs as a result of the photochemical cycle during the day involving ozone and sunlight.

The TROPOMI NO_2 processing system is based on the algorithm developments for the DOMINO-2 product and the EU QA4ECV NO_2 dataset reprocessed for OMI, which has been adapted for TROPOMI. This uptake assimilation modeling system uses a 3-dimensional global TM5-MP chemical transport model at 1x1 degree resolution as an essential element. As for CO data, negative vertical column values are often observed because of noise, particularly over clean regions with low NO_2 emissions. It is also recommended not to filter these values except for outliers, i.e., vertical columns lower than -0.001 mol/m^2.

For the SO_2 data collection, S5P/TROPOMI performs a one-day return visit of the Earth's surface at an unprecedented 3.5 x 7 km spatial resolution, which allows to investigate fine details and detect much smaller SO_2 areas. Same as for CO and NO_2 data, due to noise, negative vertical column values are often observed especially in clean areas with low SO_2 emissions. It is recommended not to filter these negative values except for outliers, i.e., vertical columns lower than -0.001 mol/m^2.

For the period before the lockdown, the period right before the outbreak occurred, namely 2 months at the end of 2019, was selected. For the period after the lockdown, the closest period when the impact of the pandemic was starting to get heavy and restrictions began was chosen. The period was chosen right after the Nowruz, Persian New Year in Iran because at that time there was a lot of activity and it was feared that it would not be representative. The data period ranged from 1 October 2019 to 1 December 2019 represented a period before the outbreak and from 25 March to 31 May 2020 represented a period during the COVID-19 lockdown as the local activity restrictions started around that period. Other data used included open-source administrative boundary data of Iran and Tehran Province.

Methods

The air pollution distribution pattern analysed in the study were measured using Sentinel-5P data in the period as previously described. Carbon Monoxide (CO), Nitrogen Dioxide (NO_2) and Sulphur Dioxide (SO_2) are the main pollutants in the air and have a significant impact on human physical and environmental conditions if present in large quantities. That is why these pollutants were chosen to study the effect of social restrictions in Iran on the level of pollutants in the research area.

The distribution of pollutants is obtained by extracting the data using scripts that are available in the Google Earth Engine. In this research, the first band used is CO_column_number_density which describes vertically integrated CO column density. The second band used is NO2_column_number_density which describes vertically integrated NO_2 column density. The third band is SO2_column_number_density which describes vertically integrated SO_2 column density. The measurement units are mol/m2. The datasets used represent the periods before and after the COVID-19 outbreak. Furthermore, the analysis of pollutants was also conducted for the Iranian capital, Tehran, to see more clearly the effect of social restrictions in the country's capital, which is the center of government and citizen activity. After the results were obtained, an analysis was carried out to identify the differences in the distribution of pollutants before and after the outbreak in accordance with the limitation of social activities. The research flowchart is shown in Fig. 1.

RESULTS AND DISCUSSION

Iran

The distribution of Carbon Monoxide (CO) levels in Iran before lockdown is shown for the period from 1 October 2019 to 1 December 2019 and during intensive lockdown from 25 March 2020 to 31 May 2020 (Fig. 2). The period before lockdown represents the time before the COVID-19 outbreak emerged in Iran. CO can originate from incomplete combustion processes, like the ones that occur in vehicle engines, including cars and motorcycles, various other types of engines, trains or industries (Somvanshi et al. 2019).

From Figure 2 it can be seen that in Iran in general there is no significant difference in the CO exposure before

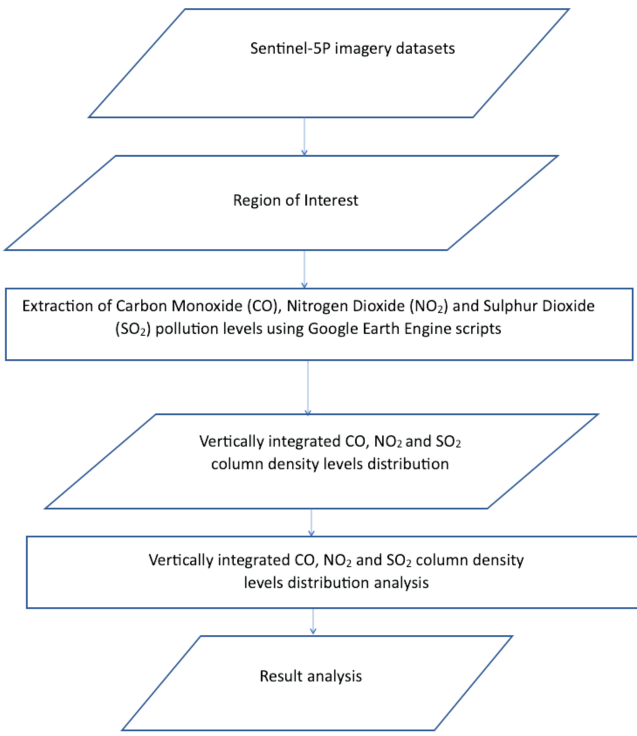

Fig. 1. Flowchart of the CO, NO_2 and SO_2 pollution levels distribution analysis

and after the lockdown that occurred in this region as an effort to control the spread of the virus. Overall, there was a slight increase in CO exposure from 0.0214 mol/m2 to 0.0286 mol/m^2. In some areas, the pollution level slightly increased from 0.0286 to 0.0357 mol/m^2, while in the others, the concentration of CO before and after the lockdown stayed the same, namely 0.0286 mol/m^2.

During the intensive lockdown period, the government began to impose restrictions on social activities such as limitations on travelling between regions and gatherings. The result shows that during the lockdown period from the end of March to the end of July 2020, there was no significant decrease in CO pollution in the Iran region which, in addition to natural levels in the atmosphere, is generally caused by motor vehicles or industrial fumes (TROPOMI 2020). Carbon monoxide and oxygen can be quickly converted to CO_2 in the air. As one of the greenhouse gases associated with global warming, this pollutant is closely related to the temperature: the higher the temperature, the higher the concentration level of CO_2 (NASA 2011).

The climate in Iran varies significantly, the northern part of the country has a cold climate and the western part is mountainous. Both these areas are characterized by low temperatures. This also results in the low CO concentration in these regions before and after the lockdown period compared to the eastern region. The eastern region is a dry desert valley with high temperatures (Wikipedia 2021) and it is marked by higher CO levels before and after the lockdown period. The contrasting climate differences in Iran also affects the differences in greenhouse gas levels over the entire observation period. On the other hand, in a densely populated province such as Tehran where the capital is located, there was a significant decrease in CO concentration during the intensive lockdown period from 0.05 mol/m^2 to 0.0286 mol/m^2. This decrease indicates that the lockdown in that area has been effective in reducing the CO exposure due to the limitation of the population activity which resulted in the reduction of anthropogenic emissions in urban areas.

The effect of the intensive lockdown on pollutant concentrations can be seen more clearly for Nitrogen Dioxide (NO_2) levels, which were obtained for Iran from 1 October 2019 to 1 December 2019 and during intensive lockdown from 25 March 2020 to 31 May 2020 (Fig. 3). NO_2 exists in the atmosphere as a result of anthropogenic activities like burning fossil fuels and biomass as well as natural processes like forest fires and microbiological processes on the ground (TROPOMI 2021).

From the map of NO_2 distribution in Iran, it can be seen that most of the area has NO_2 exposure of 0.0000857 mol/m^2. From the figure, it can be seen how the level of NO_2 in Iran's big cities decreased during the intensive lockdown period. In the area of Tehran, the capital of Iran, as well as the cities of Qom, Isfahan and Mashhad, it can be seen that the concentration of NO_2 in the city center reaches 0.0002 mol/m^2. Further away from the city center the concentration of NO_2 decreases successively to 0.000171 and 0.000142 mol/m^2.

It can also be observed that during the lockdown period there was a decrease in the area that had a high concentration of NO_2. In the main cities of Tehran, Qom, Isfahan and Mashhad, the concentration decreased from 0.0002 to 0.000114 – 0.000171 mol/m^2. Meanwhile, in other cities such as Ahvaz and Yazd, the value of NO_2 decreased from 0.000142 to 0.000114 mol/m_2. From spatial observation and analysis of the pollutant concentrations, it can be seen that in Iran's big cities there was a decrease in NO_2 pollution during the intensive lockdown period. This was triggered by a reduction in anthropogenic activities in that period such as the burning of fossil fuels which is one of the sources of NO_2.

The next result shows the distribution of Sulphur Dioxide (SO_2) levels in Iran from 1 October 2019 to 1 December 2019 as the period before lockdown and 25 March 2020 to 31 May 2020 as the period during intensive COVID-19 lockdown (Fig. 4). The majority of SO_2 pollutant comes from anthropogenic origin namely from the burning of petroleum and coal, while only a small amount of SO_2 comes from natural sources (TROPOMI 2020).

In the distribution map of SO_2 pollution levels, it can be seen that in the period before the lockdown, high SO_2 concentrations of 0.0005 mol/m^2 were found in big cities such as Tehran, Isfahan, Qom, Mashhad, Ahvaz and Kerman. Apart from burning fuel, oil and coal, SO_2 exposure also usually occurs in coal-fired power plants such as in South Africa (Shikwambana et al. 2020). The presence of a number of power plants in the region can increase SO_2 exposure.

Furthermore, the map of SO_2 distribution during the intensive lockdown period shows a significant decrease in SO_2 exposure in Iran. It can be observed that the exposure

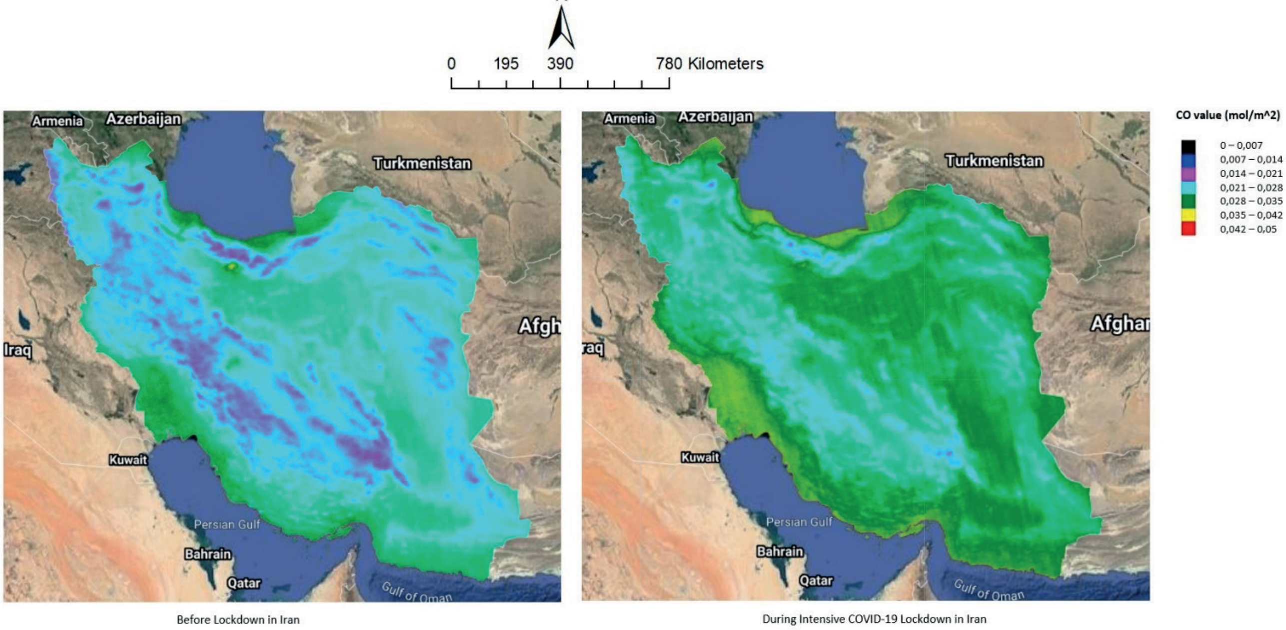

Fig. 2. Distribution of CO levels before and during the COVID-19 lockdown in Iran

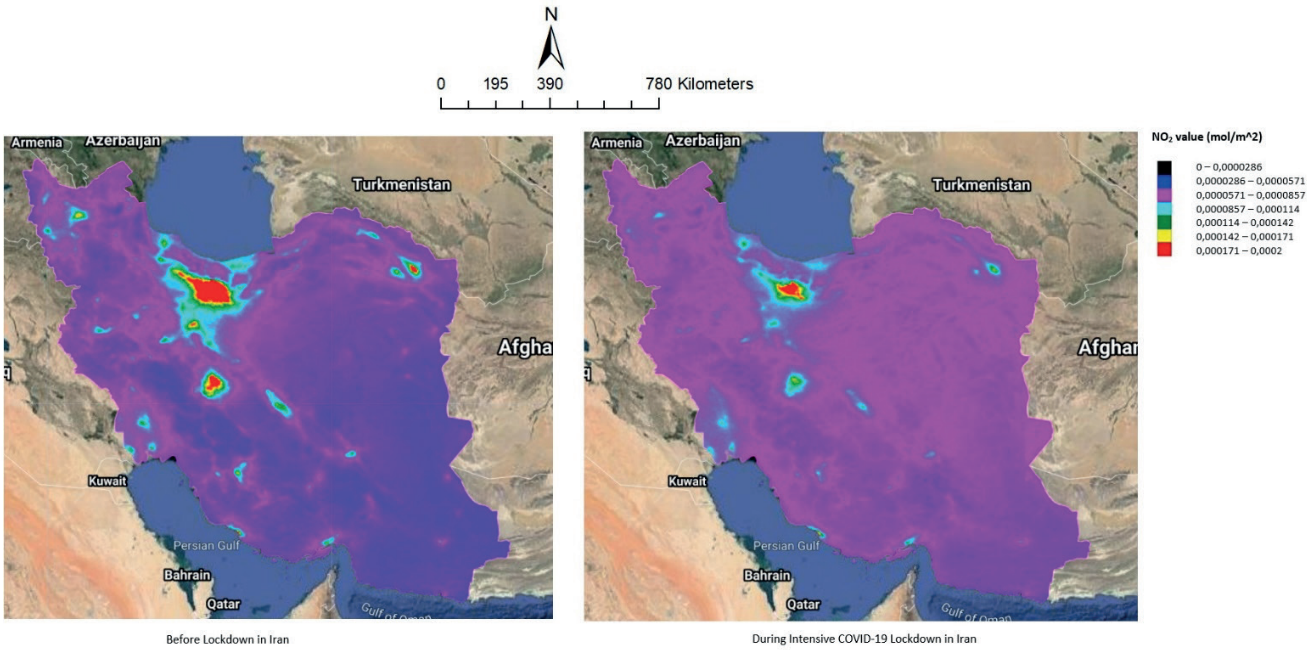

Fig. 3. Distribution of CO levels before and during the COVID-19 lockdown in Iran

level in the areas of Tehran, Qom, Isfahan, which before the lockdown reached up to 0.0005 mol/m^2, decreased after the intensive lockdown to 0.0000714 – 0.000143 mol/m^2. Meanwhile, SO_2 concentration in the central and eastern regions of Iran, which originally stood at 0.000143 mol/m^2 for most of the area, decreased to 0 – 0.0000714 mol/m^2. These findings suggest that the period of intensive lockdown along with restrictions on anthropogenic activities in the form of burning oil and coal as one of the sources of this pollutant contributed to a decrease in SO_2 pollution in Iran.

Tehran Province

The province of Tehran is the place where the capital city of Iran is located and the richest province in the country. It has more than 12 million inhabitants, making it the most populous region in Iran, about 18% of the country's population resides in the province of Tehran. As the province where the capital is located, Tehran is the commercial center of Iran. Tehran province has over 17.000 industrial units employing approximately 390.000 people, which is 26% of all units in Iran. The province contains more or less 30% of Iran's economy and comprises 40% of Iran's consumer market (Wikipedia 2021). As a center of economic and business activity, it is very interesting to examine the impact of the lockdown due to the COVID-19 pandemic on the air quality of this busiest province in Iran.

Subsequent results show the level of pollution by CO, NO_2 and SO_2 in Tehran province before and after the intensive lockdown (Fig. 5, Fig. 6 and Fig. 7). The period for the condition before the outbreak is from 1 October to 1 December 2019 and for the condition after the lockdown is from 25 March to 31 May 2020. As the heart of commercial, business and citizen activities, it can be seen how the level of all types of air pollution in this region is increasing closer to the capital city, Tehran, which is the most populous city in Iran and Western Asia.

As mentioned before, the period chosen for the intensive lockdown starts after 20 March 2020 because on 20 March 2020, there is a celebration of Nowruz or the Persian New Year and pollution related to the effects of this celebration can result in an anomaly in the data. That is

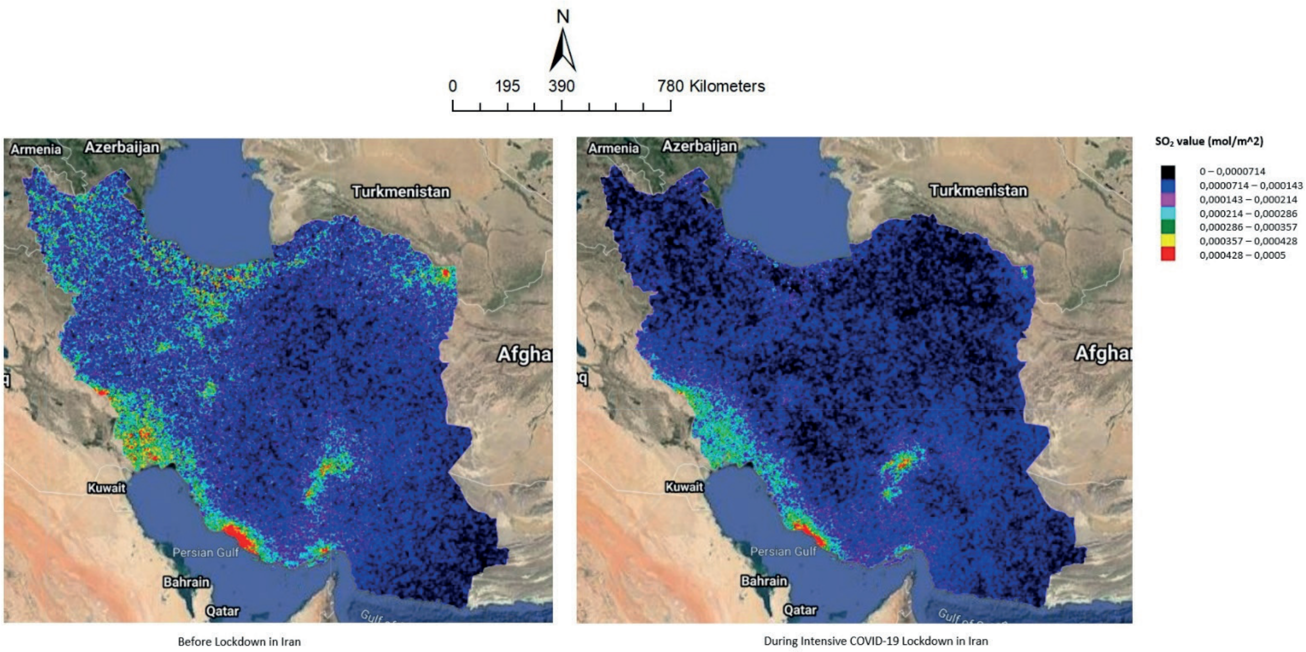

Fig. 4. Distribution of SO_2 levels before and during the COVID-19 lockdown in Iran

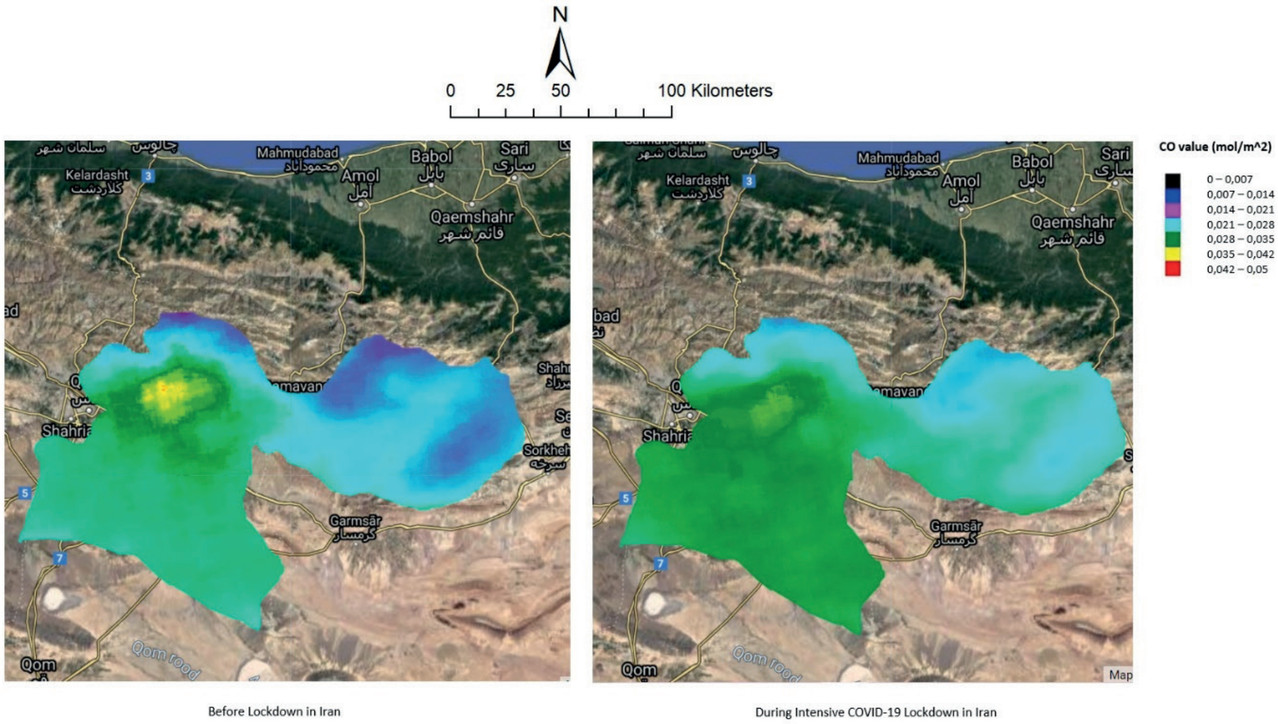

Fig. 5. Distribution of CO levels before and during the COVID-19 lockdown in Tehran Province

why the period chosen for the intensive lockdown is from 25 March to 31 May 2020. Besides restrictions on human activities that have an impact on the emissions from gasoline-powered vehicles, a decrease in CO levels in the air is also related to a decrease in other types of activities such as the metal and building materials industry as well as reduced input from housing sources (Zheng et al., 2018). In another case, the reduction in CO levels can also be due to reduced biomass combustion, biogenic emission and photochemical production (I et al. 2020).

Fig. 5 shows that according to the distribution of air pollution, there was a change in the pattern of CO as it concentrated in the center of Tehran before the outbreak and spread to the surrounding area after the outbreak. Based on CO levels, there was a decrease in pollution in the region. Before the outbreak occurred, CO pollution levels ranged from 0.014 – 0.0428 mol/m^2, while after the lockdown was enforced, it reduced to 0.014 – 0.036 mol/m^2, which means that there was a decrease in CO levels in Tehran province. In downtown Tehran, it is clearly visible that before the lockdown there was a high CO concentration of 0.043 mol/m^2 which then dropped to 0.036 mol/m^2 after entering the lockdown period.

From Fig. 6, it can be seen how the level of the NO_2 pollutant in this region is increasing closer to the Tehran city center. As with the CO pollutant, the highest concentration of NO_2 is observed closest to downtown Tehran where it reaches 0.0002 mol/m^2. In the period before the lockdown, the region with high NO_2 level covered a wide area in downtown Tehran, occupying up to half of Tehran Province. However, after the lockdown, the area with a NO_2 level of

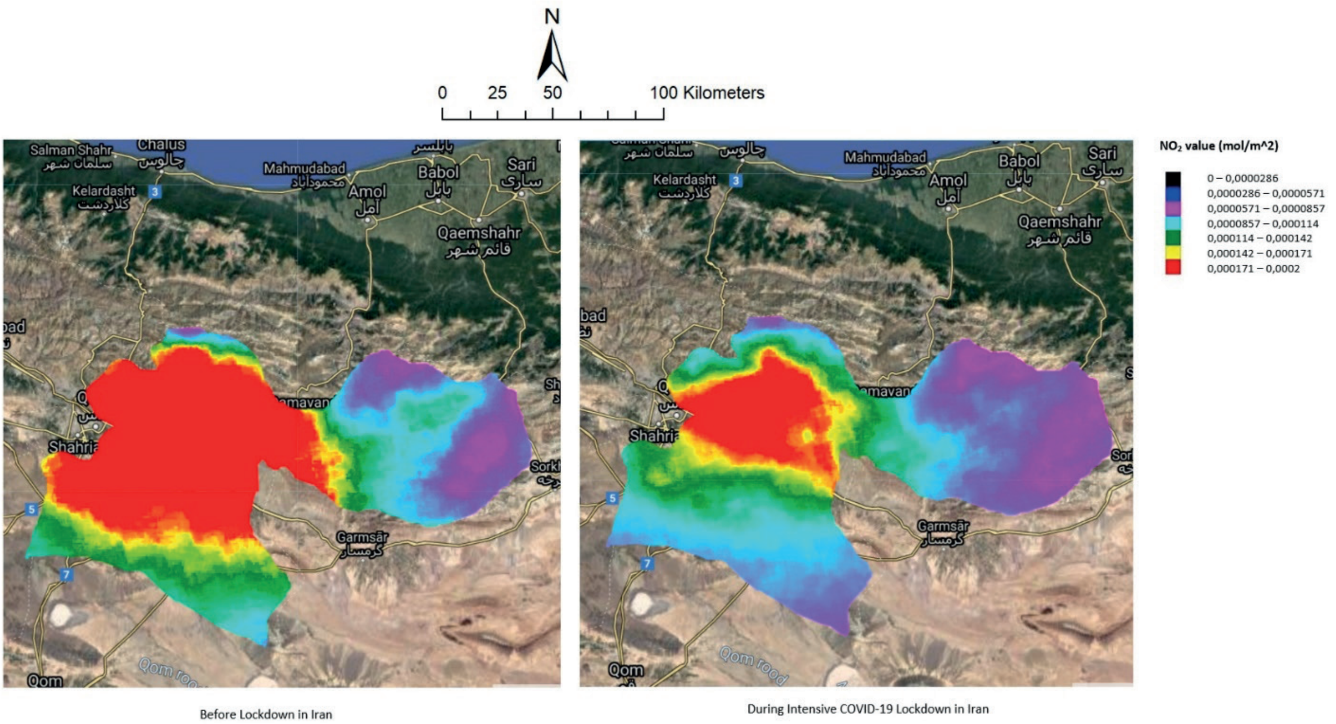

Fig. 6. Distribution of NO_2 levels before and during the COVID-19 lockdown in Tehran Province

0.0002 mol/m^2 decreased and covered only the city center and a few areas around it.

The counties (shahrestan) around Tehran that have high levels of NO_2 reaching 0.0002 mol/m^2 include Ray, Eslamshahr, Baharestan, Shahriar, Qarchak, Pakdasht, Pardis, Shemiranat, Qods and Robat Karim. Meanwhile, after the lockdown, these districts experienced a decrease in their NO_2 levels from 0.0002 to 0.000142 mol/m^2, except for Tehran, Qods, Eslamshahr and Shahriar which still had high NO_2 levels. The decreasing value means that there was a reduction of NO_2 levels in the Tehran province due to the limitation of anthropogenic activity that produces this pollutant during the lockdown. In several studies, it was revealed that NOx emissions are mostly associated with activities such as coal combustion at coal-fired power plants, air traffic, road traffic, biomass burning and the N microbial cycle (Adams et al. 2020; Dahlmann et al. 2011; Zong et al. 2018).

From the results that show the level of SO_2 pollutant in Tehran province (Fig. 7), it can be seen that its distribution pattern differs from CO and NO_2 as it tends to be irregular and evenly distributed in this province. Fig. 7 also shows that the level of SO_2 pollution in this province which originally stood at a high value of 0.0005 mol/m^2 decreased to 0.000143 mol/m2. This indicates a decrease in the amount of SO_2 after the implementation of a strict lockdown in Tehran province. In some areas of Tehran Province, where originally an SO_2 value of 0.000357 mol/m^2 was observed, it decreased to 0 – 0.0000714 mol/m^2 in the period after the lockdown. This change means that there was a significant decrease in SO_2 levels in the province of Tehran due to the reduction of anthropogenic activities that produce SO_2. Sources of SO_2 include burning coal at coal-fired power plants and motor vehicle fumes (Adams et al. 2020; Azimi et al. 2018). Negative values in the obtained pollutant concentrations can arise when the sky conditions are very clear or the pollutant level is very low. This can indeed happen because the lowest range of the minimum SO_2 vertical column density in the band used in Sentinel-5P data is a negative value, which indicates a very low or zero density of pollutant molecules (Google Earth Engine 2021).

From the overall results obtained in this study, it can be seen that the Sentinel-5P data is able to present both spatial and temporal distribution of pollutants as well as their concentration in Iran and Tehran Province. From the results, it can be concluded that after the lockdown there was a decrease in the concentration of pollutants in the Iran region compared to the period before the COVID-19 pandemic. Changes in the CO pollutant values are clearly visible in urban areas with high population activity such as Tehran, where CO concentration decreased from 0.05 to 0.0286 mol/m^2, while in other areas it is also influenced by the varying climate in Iran. Meanwhile, for the NO_2 pollutant, there was a significant decrease in pollution levels in big cities such as Tehran, Qom, Isfahan and Mashhad, where it reduced from 0.0002 to 0.000114 mol/m^2. Furthermore, for the SO_2 pollutant, the pollution levels in Iran's big cities decreased from 0.0005 to 0.0000714 mol/m^2.

Meanwhile for Tehran province, which is the most populous and busiest province in Iran, it can be observed that there was also a decrease in the concentration of pollutants after the lockdown compared to the pre-lockdown period. The CO concentration decreased from 0.043 to 0.036 mol/m^2, while for the NO_2 pollutant there was a decrease from 0.0002 to 0.000142 mol/m^2 and for the SO_2 pollutant, there was a decrease from 0.0005 to 0.000143 mol/m^2.

CONCLUSION

Based on the results of processing the Sentinel-5P imagery data for Iran and Tehran province, an analysis was done to monitor both spatial and temporal distribution of air pollution, particularly CO, NO_2 and SO_2 pollutants.

For Iran in general, changes in the concentration of CO are clearly visible in urban areas with high population activity such as Tehran, where there was a decrease from 0.05 to 0.0286 mol/m^2, while for other areas it is also influenced by the varying climate conditions, which affect the level of pollution. For the NO_2 pollutant, there was a significant decrease in pollution levels in big cities such as Tehran, Qom, Isfahan and Mashhad from 0.0002 to 0.000114 mol/m^2. For the SO_2 pollutant, there was a decrease in pollution levels in

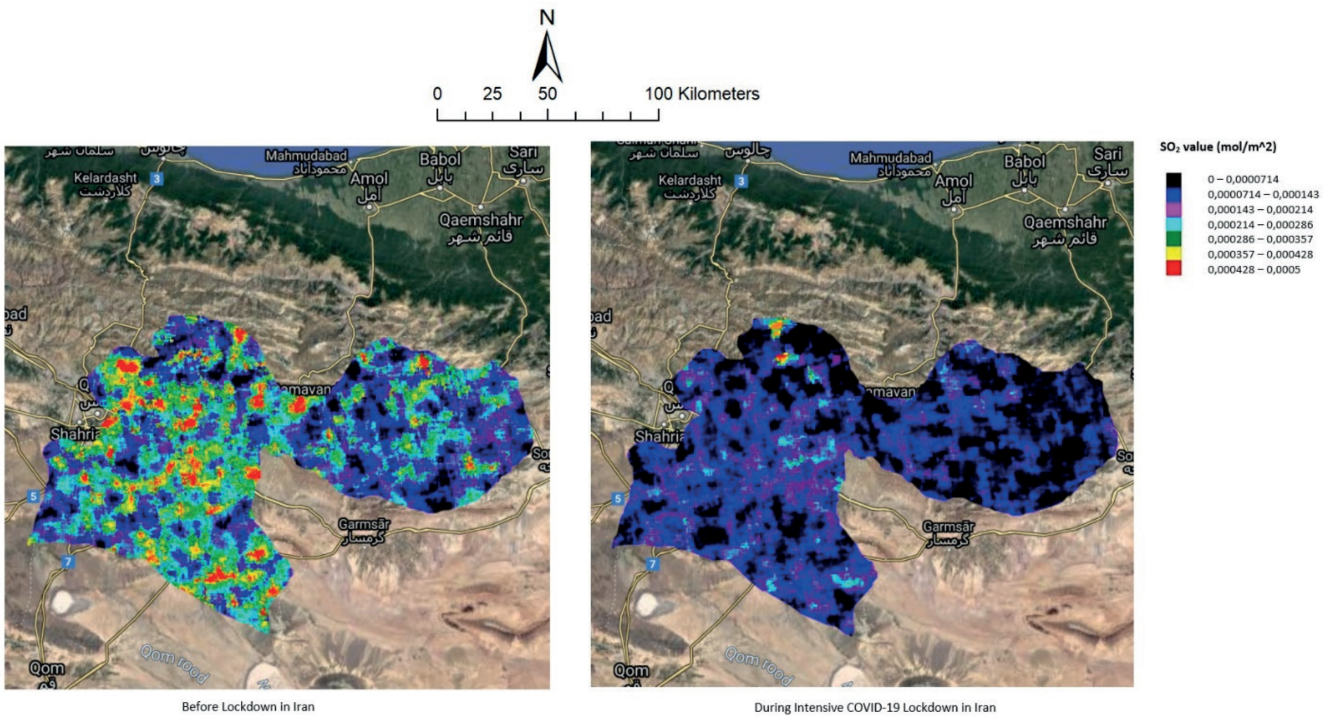

Fig. 7. Distribution of SO_2 levels before and during the COVID-19 lockdown in Tehran Province

Iran's big cities from 0.0005 to 0.0000714 mol/m^2. For Tehran province, which is the most populous and busiest province in Iran, it can be observed that there was also a decrease in the concentration of pollutants after the lockdown compared to the pre-lockdown period. The CO concentration decreased from 0.043 to 0.036 mol/m^2, while for the NO_2 pollutant there was a decrease from 0.0002 to 0.000142 mol/m^2 and for the SO_2 pollutant, there was a decrease from 0.0005 to 0.000143 mol/m^2.

These findings suggest that the period of intensive COVID-19 lockdown contributed to the reduction of CO, NO_2 and SO_2 pollution in Iran, along with the restriction of anthropogenic activities which are the sources of these pollutants.

REFERENCES

Adams D., Oh D.H., Kim D.W., Lee C.H. & Oh M. (2020). Prediction of SOx–NOx emission from a coal-fired CFB power plant with machine learning: Plant data learned by deep neural network and least square support vector machine. Journal of Cleaner Production, 270, 122310, DOI: 10.1016/j.jclepro.2020.122310.

Adnan M., Khan S., Kazmi A., Bashir N., & Siddique R. (2020). COVID-19 infection : Origin , transmission , and characteristics of human coronaviruses. Journal of Advanced Research, 24, 91-98, DOI: 10.1016/j.jare.2020.03.005.

Altuğ H., Fuks K.B., Hüls A., Mayer A.K., Tham R., Krutmann J. & Schikowski T. (2020). Air pollution is associated with depressive symptoms in elderly women with cognitive impairment. Environment International, 136(January), DOI: 10.1016/j.envint.2019.105448.

Andersson E.M., Ögren M., Molnár P., Segersson D., & Stockfelt L. (2020). Road traffic noise, air pollution and cardiovascular events in a Swedish cohort. Environmental Research, 109446, DOI: 10.1016/j.envres.2020.109446.

Azimi M., Feng F., & Yang Y. (2018). Air pollution inequality and its sources in SO2 and NOX emissions among Chinese Provinces from 2006 to 2015. Sustainability (Switzerland), 10(2), DOI: 10.3390/su10020367.

Berman J.D., & Ebisu K. (2020). Science of the Total Environment Changes in U . S . air pollution during the COVID-19 pandemic. Science of the Total Environment, 739, 139864, DOI: 10.1016/j.scitotenv.2020.139864.

Chen Y., Wang S., Han W., Xiong Y., Wang W., & Tong L. (2017). A New Air Pollution Source Identification Method Based on Remotely Sensed Aerosol and Improved Glowworm Swarm Optimization. 3454 IEEE JOURNAL OF SELECTED TOPICS IN APPLIED EARTH OBSERVATIONS AND REMOTE SENSING, 10(8), 3454-3464.

Clerbaux C., Bauduin S., Boynard A., Clarisse L., Coheur P., George M., Hadji-lazaro J., Hurtmans D., Safieddine S., Damme M. Van, & Whitburn S. (2017). Observation of Air Pollution over China Using the IASI Thermal Infrared Space Sensor. In Air Pollution in Eastern Asia: An Integrated Perspective, 309-322, DOI: 10.1007/978-3-319-59489-7.

Dahlmann K., Grewe V., Ponater M., & Matthes S. (2011). Quantifying the contributions of individual NOx sources to the trend in ozone radiative forcing. Atmospheric Environment, 45(17), 2860-2868, DOI: 10.1016/j.atmosenv.2011.02.071.

European Space Agency. (2021). Sentinel. https://sentinel.esa.int/web/sentinel/missions/sentinel-5p accessed on June 12th, 2021.

Filonchyk M., Yan H., Yang S., & Lu X. (2017). Detection of aerosol pollution sources during sandstorms in Northwestern China using remote sensed and model simulated data. Advances in Space Research, DOI: 10.1016/j.asr.2017.11.037.

Fu M., Kelly J.A., & Clinch J.P. (2020). Prediction of PM2.5 daily concentrations for grid points throughout a vast area using remote sensing data and an improved dynamic spatial panel model. Atmospheric Environment, 117667, DOI: 10.1016/j.atmosenv.2020.117667.

Google Earth Engine (2020). Sentinel-5P NRTI CO Near Real-Time Carbon Monoxide. Earth Engine Data Catalog.

Huang Y., Organ B., Zhou J.L., Surawski N.C., Hong G., Chan F.C., & Yam Y.S. (2018). Remote sensing of on-road vehicle emissions: mechanism, applications and a case study from Hong Kong. Atmospheric Environment, DOI: 10.1016/j.atmosenv.2018.03.035.

Srivastava I.N., Yarragunta S., Kumar Y., & Mitra D. (2020). Distribution of surface carbon monoxide over the Indian subcontinent: Investigation of source contributions using WRF-Chem. Atmospheric Environment, 243, DOI: 10.1016/j.atmosenv.2020.117838.

Kurata M., Takahashi K., & Hibiki A. (2020). Gender differences in associations of household and ambient air pollution with child health: Evidence from household and satellite-based data in Bangladesh. World Development, 128, 104779, DOI: 10.1016/j.worlddev.2019.104779.

Leifer I., Melton C., Chatfield R., Cui X., Fischer M.L., Fladeland M., Gore W., Hlavka D.L., Iraci L., Marrero J., Ryoo M., Tanaka T., Yates E., & Yorks J. (2019). Air pollution inputs to the Mojave Desert by fusing surface mobile and airborne in situ and airborne and satellite remote sensing: A case study of interbasin transport with numerical model validation. Atmospheric Environment, 117184, DOI: 10.1016/j.atmosenv.2019.117184.

Li J. (Jie), Massa M., Zhang H., & Zhang J. (2019). Air pollution, behavioral bias, and the disposition effect in China. Journal of Financial Economics, xxxx, DOI: 10.1016/j.jfineco.2019.09.003.

Li X., & Zhang X. (2019). Predicting ground-level PM 2 . 5 concentrations in the Beijing-Tianjin- Hebei region : A hybrid remote sensing and machine learning. Environmental Pollution, 249, 735-749, DOI: 10.1016/j.envpol.2019.03.068.

Miller M.R. (2020). Oxidative stress and the cardiovascular effects of air pollution. Free Radical Biology and Medicine, January, DOI: 10.1016/j.freeradbiomed.2020.01.004.

NASA (2011). Effects of Changing the Carbon Cycle. In Earth Observatory

Omrani H., Omrani B., Parmentier B., & Helbich M. (2020). Spatio-temporal data on the air pollutant nitrogen dioxide derived from Sentinel satellite for France. Data in Brief, 28, 105089, DOI: 10.1016/j.dib.2019.105089.

Pacheco H., Díaz-López S., Jarre E., Pacheco H., Méndez W., Zamora-Ledezma E. (2020). NO2 levels after the COVID-19 lockdown in Ecuador: A trade-off between environment and human health. Urban Climate, 34(December), 100674, DOI: 10.1016/j.uclim.2020.100674.

Petrosillo N., Viceconte G., Ergonul O., Ippolito G., & Petersen E. (2020). COVID-19, SARS and MERS: are they closely related? Clinical Microbiology and Infection, DOI: 10.1016/j.cmi.2020.03.026.

Prud G., Dobbin N.A., Sun L., Burnett R.T., Martin R.V, Davidson A., Cakmak S., Villeneuve P.J., Lamsal L.N., Donkelaar A.Van, Peters P.A., & Johnson M. (2013). Comparison of remote sensing and fixed-site monitoring approaches for examining air pollution and health in a national study population. Atmospheric Environment, 80, 161-171, DOI: 10.1016/j.atmosenv.2013.07.020.

Reuters (2020). Iran reports COVID-19 death every four minutes, extends curbs. In Health News.

Rothan H.A., & Byrareddy S.N. (2020). The epidemiology and pathogenesis of coronavirus disease (COVID-19) outbreak. Journal of Autoimmunity, February, 102433, DOI: 10.1016/j.jaut.2020.102433.

Shikwambana L., Mhangara P., Mbatha N. (2020). Trend analysis and first time observations of sulphur dioxide and nitrogen dioxide in South Africa using TROPOMI/Sentinel-5 P data. International Journal of Applied Earth Observation and Geoinformation, 91(September), 102130, DOI: 10.1016/j.jag.2020.102130.

Smit R., Kingston P., Neale D.W., Brown M.K., Verran B. & Nolan T. (2019). Monitoring on-road air quality and measuring vehicle emissions with remote sensing in an urban area. Atmospheric Environment, 218(September), 116978, DOI: 10.1016/j.atmosenv.2019.116978.

Somvanshi S.S., Vashisht A., Chandra U., & Kaushik G. (2019). Delhi Air Pollution Modeling Using Remote Sensing Technique. In Handbook of Environmental Materials Management, 1-27, DOI: 10.1007/978-3-319-58538-3_174-1.

Sun S., Li L., Wu Z., Gautam A., Li J., & Zhao W. (2020). Variation of industrial air pollution emissions based on VIIRS thermal anomaly data. Atmospheric Research, 244(May), 105021, DOI: 10.1016/j.atmosres.2020.105021

Tosepu R., Gunawan J., Effendy D.S., Ahmad L.O.A.I., Lestari H., Bahar H., & Asfian P. (2020). Correlation between weather and Covid-19 pandemic in Jakarta, Indonesia. Science of the Total Environment, 138436, DOI: 10.1016/j.scitotenv.2020.138436.

TROPOMI (2020). Carbon Monoxide. In Data Products

TROPOMI (2020). Nitrogen Dioxide. In Data Products

TROPOMI (2020). Sulphur Dioxide. In Data Products

ul-Haq Z., Tariq S., Ali M. (2015). Atmospheric variability of methane over Pakistan, Afghanistan and adjoining areas using retrievals from SCIAMACHY/ENVISAT. Journal of Atmospheric and Solar-Terrestrial Physics, 135(December), 161-173, DOI: 10.1016/j.jastp.2015.11.002.

Vratolis S., Fetfatzis P., Argyrouli A., Soupiona O., Mylonaki M., & Maroufidis J. (2020). Comparison and complementary use of in situ and remote sensing aerosol measurements in the Athens Metropolitan Area. Atmospheric Environment, 228(March), 117439, DOI: 10.1016/j.atmosenv.2020.117439.

Wan Y., Li Y., Liu C., & Li Z. (2020). Is traffic accident related to air pollution? A case report from an island of Taihu Lake, China. Atmospheric Pollution Research, September 2019, 0-1, DOI: 10.1016/j.apr.2020.02.018

Wang P., Chen K., Zhu S., Wang P., & Zhang H. (2020). Severe air pollution events not avoided by reduced anthropogenic activities during COVID-19 outbreak. Resources, Conservation and Recycling, 158(March), 104814, DOI: 10.1016/j.resconrec.2020.104814.

Wikipedia (2021). Geography of Iran. https://en.wikipedia.org/wiki/Geography_of_Iran accessed on June 14th, 2021.

Wikipedia (2021). Tehran Province. https://en.wikipedia.org/wiki/Tehran_Province accessed on June 15th, 2021.

Zheng B., Chevallier F., Ciais P., Yin Y., Deeter M.N., Worden H.M., Wang Y., Zhang Q., & He K. (2018). Rapid decline in carbon monoxide emissions and export from East Asia between years 2005 and 2016. Environmental Research Letters, 13(044007) , DOI: 10.1088/1748-9326/aab2b3.

Zong Z., Tan Y., Wang X., Tian C., Fang Y., Chen Y., Fang Y., Han G., Li J., & Zhang G. (2018). Assessment and quantification of NOx sources at a regional background site in North China: Comparative results from a Bayesian isotopic mixing model and a positive matrix factorization model. Environmental Pollution, 242, 1379-1386, DOI: 10.1016/j.envpol.2018.08.026.

RESEARCH PAPER

CHANGE IN NITROGEN DIOXIDE (NO_2) CONCENTRATION DUE TO THE LOCKDOWN AMID THE COVID-19 PANDEMIC IN INDIA

Zubairul Islam[1*], Sudhir Kumar Singh[2], Saroj Ahirwar[3]
[1]Department of Geography and Environmental Studies, Adigrat University. Ethiopia. Email: zubairul@gmail.com, ORCID: 0000-0002-6591-2241
[2]K. Banerjee Centre of Atmospheric & Ocean Studies, IIDS, Nehru Science Centre, University of Allahabad, Prayagraj, Uttar Pradesh, India Email: sudhirinjnu@gmail.com
[3]Department of Industrial Microbiology, Jacob Institute of Biotechnology and Bioengineering (JIBB) Sam Higginbottom Institute of Agriculture, Technology and Sciences (SHUATS), Prayagraj, Uttar Pradesh, India
Email: sarojahirwar86@gmail.com
*Corresponding author: zubairul@gmail.com
Received: June 2th, 2021 / Accepted: November 9th, 2021 / Published: December 31st, 2021
https://doi.org/10.24057/2071-9388-2021-065

ABSTRACT. The study aimed to examine the change in the concentration of nitrogen dioxide due to the lockdown amid the COVID-19 pandemic in India at the district level using Sentinel-5P TROPOMI. The spatio-temporal characteristics of the tropospheric column NO_2 concentration during 45 days of the lockdown were compared with the same days of 2019. Further, to model spatially varying relationships of NO_2 during the lockdown period, it was given as a dependent variable whereas NO_2 during the pre-lockdown period was considered as an independent variable. Results show that the mean NO_2 concentration was reduced from 0.00406 mol/m^2 before the lockdown (2019-03-25 to 2019-05-10) to 0.0036 mol/m^2 during the lockdown period (2020-03-25 to 2020-05-10). The maximum decline of NO_2 concentration was observed in Gautam Buddha Nagar and Delhi. This indicates the high level of atmospheric pollution due to the excess use of fuel in human activities. The results of the Ordinary Least Squares (OLS) method show a strong positive relationship between both variables. Positive standard residuals indicate that the concentration of NO_2 has reduced more than expected as per the OLS model. The z-score (24.11) was obtained from spatial autocorrelation. It indicates that residuals are highly clustered and there is less than a 1% likelihood that this clustered pattern could be a result of a random chance. The highest decrease was observed in districts/urban agglomerations of Gautam Buddha Nagar (-40%), Delhi (-37%), Greater Bombay (-31%), Hyderabad (-29%), Faridabad (-29%), Bangalore Urban (-28%), Gandhinagar (-27%), Chennai (-27%) and Gurgaon (-26%) respectively.

KEYWORDS: COVID-19, Coronavirus, Nitrogen dioxide (NO_2), Sentinel-5P

CITATION: Zubairul Islam, Sudhir Kumar Singh, Saroj Ahirwar (2021). Change In Nitrogen Dioxide (No_2) Concentration Due To The Lockdown Amid The Covid-19 Pandemic In India. Geography, Environment, Sustainability, Vol.14, No 4, p. 192-198
https://doi.org/10.24057/2071-9388-2021-065

ACKNOWLEDGEMENTS: We wish to thank Royal Netherlands Meteorological Institute (KNMI) for providing useful information about the products used in this work.

Conflict of interests: The authors reported no potential conflict of interest.

INTRODUCTION

Nitrogen dioxide (NO_2) is an ambient trace gas which originates from both natural and anthropogenic processes. Long-term exposure to NO_2 may cause a wide spectrum of severe health problems such as hypertension, diabetes, heart and cardiovascular diseases and even death (Ogen 2020). Breathing air with a high concentration of NO_2 can damage human respiratory system. Such exposure over short periods can aggravate respiratory diseases, particularly asthma, leading to respiratory symptoms such as coughing, wheezing or difficult breathing. Longer exposure to an elevated concentration of NO_2 may contribute to the development of asthma and potentially increase susceptibility to respiratory infections. People with asthma, children and the elderly are generally at greater risk to the elevated NO_2 concentration (US EPA OAR 2016). COVID-19 originated from Wuhan city of Hubei Province in China in December 2019. Since then, it has spread in more than 210 countries. It is a viral disease due to the Severe Acute Respiratory Syndrome Coronavirus 2 (SARS-CoV-2). The patients show flu-like symptoms with a dry cough, sore throat, high fever, and breathing problems (Ali & Alharbi 2020). WHO continues to provide updated information (World Health Organization: WHO 2020). More than 4.3 million cases of Covid-19 have been recorded worldwide, including at least 297,000 deaths as of 7th April 2020., According to the tally of deaths by Johns Hopkins University at least 300,074 people have died from COVID-19 across the world (Renton 2020).

The first confirmed case in India was reported on January 30 2020. A university student studying in Wuhan, China, had travelled back home to Kerala, a state on India's southern tip, during vacation. Over the next four days, two more people in Kerala tested positive for the disease (Ward 2020). The latest figures from the Health Ministry of India showed that the total number of coronavirus cases in India jumped by 3,722 over the past 24 hours, increasing the total number of confirmed COVID-19 cases as of 13th May 2020 to 78,003. The Health Ministry says that 70% of deaths occur due to co-morbidities.

A three-week lockdown in India started from 24th March 2020, which was an important initiative to control the spread of the coronavirus (Gettleman and Schultz 2020). India, which has the 2nd highest population, where the healthcare system is underdeveloped and the major portion of the population follow an unhygienic lifestyle, was able to restrict the rate of both infection and death of its citizens from COVID-19 (Paital et al. 2020).

According to a December 2019 report by the Global Alliance of Health and Pollution, India accounts for the highest number of pollution-related deaths in the world with more than 2 million people every year (Guardian 2019). Data from the Central Pollution Control Board (CPCB) showed, that the water quality of rivers in India has improved considerably during the lockdown, especially in industrial towns through which they pass. CPCB has three real-time monitoring stations in Kanpur, India. One is located upstream of the Ganga Barrage, the second is downstream of the barrage, and the third is at Shuklagunj. The monitoring station located upstream reported that the level of dissolved oxygen on March 28 was 8 mg/litre, BOD was 2.1 mg/litre, pH was 7.90 and ammonia was 0.49 mg/litre (Naqvi and Kumar 2020). Ray et al. (2021) studied carbon emissions of selected 184 countries and found that it is reduced by 438 Mt in 2020 than in 2019.

Venter et al. (2020) tested the hypothesis that lockdown has reduced tropospheric and ground-level air pollutant concentrations using satellite data and a network of >10,000 air quality stations. After accounting for the effects of meteorological variability, they found a decline in the population-weighted concentration of ground-level nitrogen dioxide. Research based on satellite data across India has shown a 15% reduction in NO_2 concentration level around the time of the shutdown (March 15 to April 30) compared to the same period in 2019. This was largely due to a temporary halt of vehicular traffic, which is one of the main sources of NO_2 emissions, due to the lockdown (World Bank 2020).

The main objective of this work was to measure the effect of lockdown amid the COVID-19 pandemic on the concentration of NO_2 in India. To meet the general objective, three specific objectives were set as (i) to study the tropospheric concentration of NO_2 during the pre-lockdown period from 2019-03-25 to 2019-05-10, (ii) to study the tropospheric concentration of NO_2 during the post-lockdown period from 2020-03-25 to 2020-05-10, and (iii) to study the change in the tropospheric concentration of NO_2 from pre-lockdown period (2019) to post-lockdown period (2020).

MATERIALS AND METHODS

DISTRICTS DATABASE

For districts vector data the Global Administrative Unit Layers (GAUL) were used. This data is prepared and provided by the Food and Agriculture Organization of the United Nations. It compiles and disseminates the best available information on administrative units for all the countries in the world, contributing to the standardization of the spatial dataset representing administrative units (FAO 2015).

NO_2 DATA

For the NO_2 concentration in the troposphere (from the surface up to ~10 km), the Sentinel-5 Precursor space-borne satellite (spatial resolution of 5.5 km), which is operated and managed by the European Commission under the «Copernicus» program, was used (Ogen 2020). Sentinel-5 Precursor is a satellite launched on 13 October 2017 by the European Space Agency to monitor air pollution. The onboard sensor is frequently referred to as Tropomi (Tropospheric Monitoring Instrument). The TROPOMI NO_2 processing system is based on the algorithm developments for the DOMINO-2 product (TROPOMI 2021) and the EU QA4ECV NO_2 reprocessed dataset for OMI, and has been adapted for TROPOMI. This retrieval-assimilation-modelling system uses the 3-dimensional global TM5-MP chemistry transport model at a resolution of 1x1 degree as an essential element (Sentinel-5P NRTI NO_2: Near Real-Time Nitrogen Dioxide 2018).

STATISTICAL ANALYSIS

The Ordinary Least Squares (OLS) method was applied to model the tropospheric concentration of NO_2 during the 2020 lockdown period (dependent variable) in terms of its relationship to tropospheric concentration of NO_2 during the 2019 pre-lockdown period (independent variable). The mean tropospheric concentration of NO_2 from 25th March to 25th April 2020 was given as a dependent variable and the mean tropospheric concentration of NO_2 from 25th March to 25th April 2019 was given as an independent variable.

$$y = \beta + \beta x + \varepsilon \quad (1)$$

Where y is the dependent variable, x is the independent/explanatory variable, β is the Regression coefficient (β) & ε is the Residual/random error.

Spatial Autocorrelation (Moran's I) Tool was used to identify the spatial pattern of the residuals (Islam et al. 2021).

The Moran's I statistic for spatial autocorrelation is given by Eq.2:

$$I = \frac{n}{S_0} \frac{\sum_{i=1}^{n} \sum_{j=1}^{n} w_{i,j} z_i z_j}{\sum_{i=1}^{n} z_i^2} \quad (2)$$

Where z_i is the deviation of an attribute for feature from its mean (x_i-$\bar{X}$), $w_{i,j}$ is the spatial weight between feature i and j, n is the total number of features, and S_0 is the aggregate of all spatial weights:

$$S_0 = \sum_{i=1}^{n} \sum_{j=1}^{n} w_{i,j} \quad (3)$$

The z_i-score for the statistic is computed as:

$$Z_I = \frac{I - E[I]}{\sqrt{V[I]}} \quad (4)$$

Where:

$$E[I] = -1/(n-1) \quad (5)$$

$$V[I] = E[I^2] - E[I]^2 \quad (6)$$

For conceptualization of spatial relationships among features, the inverse distance was used so that nearby neighbouring features have a larger influence on the computations for a target feature than features that are far away.

Euclidean distance method was used to calculate the distance from each feature to its neighbouring features. The distance threshold was set as 535109 m to cut off distance for the inverse distance options. Features outside the specified cutoff for a target feature were ignored in analyses for that feature.

For the Global Moran's I statistic, the null hypothesis (H0) stated that the residuals being analysed are randomly distributed among the features in the study area.

RESULTS

TROPOSPHERIC NO_2 CONCENTRATION

The mean tropospheric concentration of NO_2 was 0.00406 mol/m^2 during the pre-lockdown period in India. The major hot spots were observed in the National Capital Region (NCR), parts of certain states such as Chhattisgarh, Orissa, West Bengal, and metropolitan cities namely Ahmadabad, Greater Mumbai and Bangalore (Figure 1). The mean tropospheric concentration of NO_2 during the lockdown period were reduced to 0.0036 mol/m^2. Major changes were observed in urban agglomerations of Ahmadabad, Greater Mumbai and Bangalore (Figure 1). Table 1 shows the number of districts with different mean NO_2 concentration (mol/m^2) during the pre-lockdown and lockdown period.

CHANGE IN THE TROPOSPHERIC NO_2 CONCENTRATION

Figure 2 shows the change in tropospheric concentration of NO_2 in India during the lockdown period in 2020 compared to the same period of 2019. Tropospheric concentrations of NO_2 during the lockdown period was decreased in 540 districts (Table 2). The highest decrease was observed in districts namely Gautam Buddha Nagar (-40.47%), Delhi (-37.54%), Greater Bombay (-31.47%), Hyderabad (-29.53%), Faridabad (-28.60%), Bangalore Urban (-27.97%), Gandhinagar (-27.09%), Chennai (-26.52%) and Gurgaon (-26.39%) (Figure 2). The results were validated by the nitrogen dioxide concentration over India studied by the European Space Agency, which reported the new satellite maps, produced using data from the Copernicus Sentinel-5P satellite and showing average nitrogen dioxide concentrations over India from 1 January to 24 March 2020 and 25 March (the first day of the lockdown) to 20 April 2020 compared to the same period of the previous year. A significant reduction in the concentrations of NO_2 was

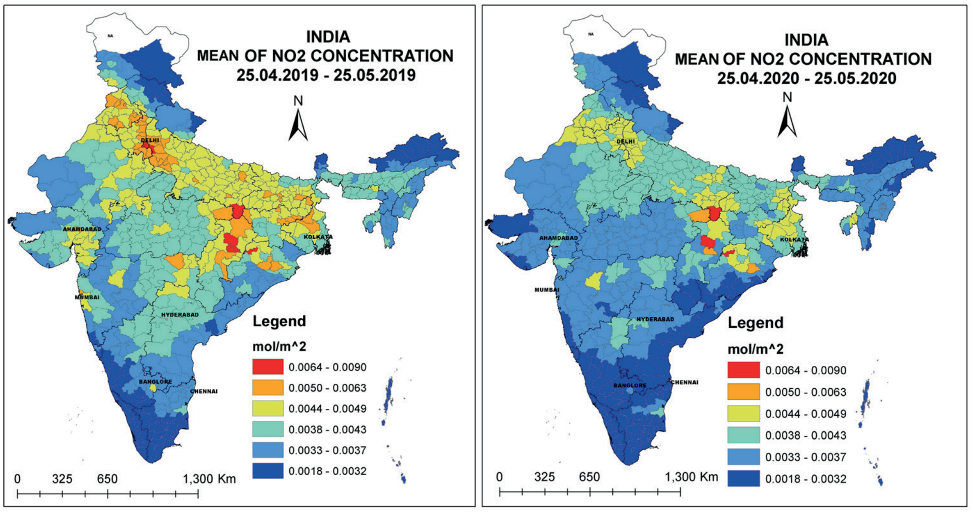

Fig. 1. Concentration of NO_2 during the pre- and post-lockdown period, large cities are shown in the map

Table 1. Number of districts with different mean NO_2 concentrations (mol/m^2)

Bin	Pre-lockdown period	Lockdown period
0.003161	71	129
0.003747	125	204
0.004256	170	171
0.00494	164	78
0.006278	51	3
0.008994	6	3
More	1	0

Data source: COPERNICUS_S5P_NRTI_L3_NO2

Table 2. Number of districts with different changes in tropospheric concentrations of NO_2 during the 2020 lockdown period compared to 2019

Change (%)	-26.4	-18.4	-14.8	-12.2	-9.8	-7.5	-4.8	1.9	0	12.3
Districts	9	35	76	80	93	101	90	56	14	34

Data source: COPERNICUS_S5P_NRTI_L3_NO2

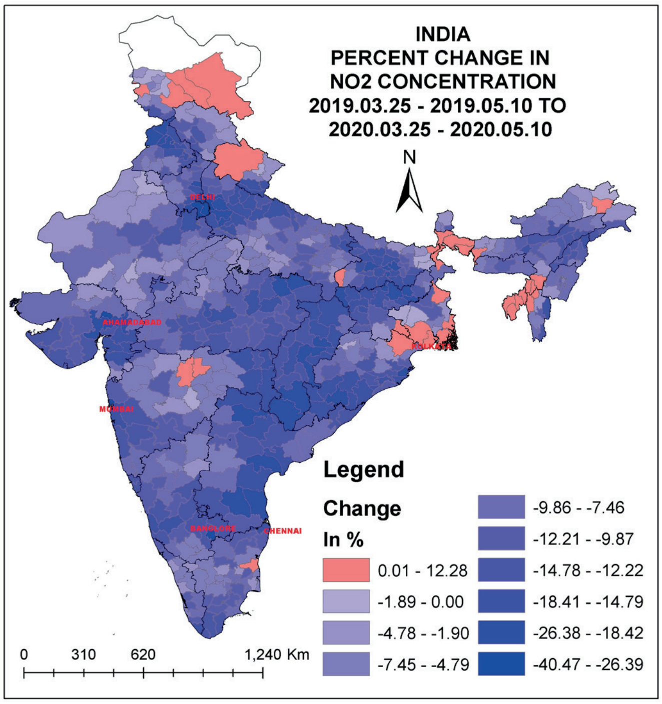

Fig. 2. Change in the concentrations of NO_2 during the pre- and post-lockdown period

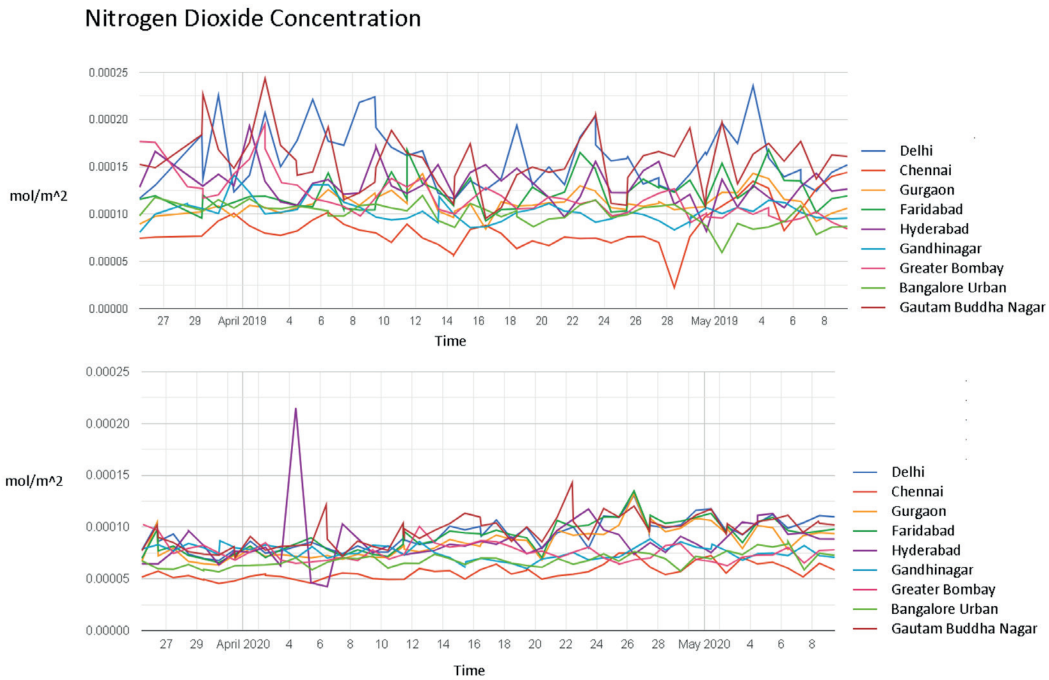

Fig. 3. Change in the mean nitrogen dioxide concentration in Indian mega cities

seen over major cities across India. Mumbai and Delhi saw drops of around 40-50% compared to last year (ESA 2020).

Table 2. Number of districts with different changes in tropospheric concentration of NO_2 during the 2020 lockdown period compared to 2019

NO_2 CONCENTRATION DURING PRE-LOCKDOWN AND LOCKDOWN PERIOD

The results of the Ordinary Least Squares (OLS) linear regression show a positive and strong relationship between both variables. The coefficient of the dependent (intercept) variable of -0.000094 and the coefficient of the independent variable of 1.142266 represent a positive and strong relationship between the explanatory and dependent variables. The results of probability ($p< 0.0000$) and Robust Probability ($p< 0.000000$) analysis indicate that these coefficients are statistically significant. The Koenker (BP) statistic test is not statistically significant ($p = 24.68$), which means that the modelled relationship is consistent. Jarque-Bera statistic test is also not statistically significant ($p=3280.74$) meaning that the model predictions are not biased (the residuals are close to the normal distribution) (Figure 4). Table 3 shows the number of districts belonging to different standard residual classes. Figure 5 helps to understand the spatial variation in the NO_2 concentration change during the lockdown (2020-03-25 to 2020-05-10) in relation to the pre-lockdown period (2019-03-25 to 2019-05-10).

SPATIAL PATTERN OF THE RESIDUALS

The computed z-score of 24.1 indicates that there is less than a 1% likelihood that this clustered pattern could be a result of a random chance (Table 4). Figure 6 shows the pattern of the NO_2 change in India at the district level.

Table 3. Number of districts belonging to different standard residual classes

Standard residual class	Districts
< -2.5 Std. Dev.	03
-2.5 - -1.5 Std. Dev.	21
-1.5 - -0.5 Std. Dev.	135
-0.5 - 0.5 Std. Dev.	291
0.5 - 1.5 Std. Dev.	114
1.5 - 2.5 Std. Dev.	13
> 2.5 Std. Dev.	12

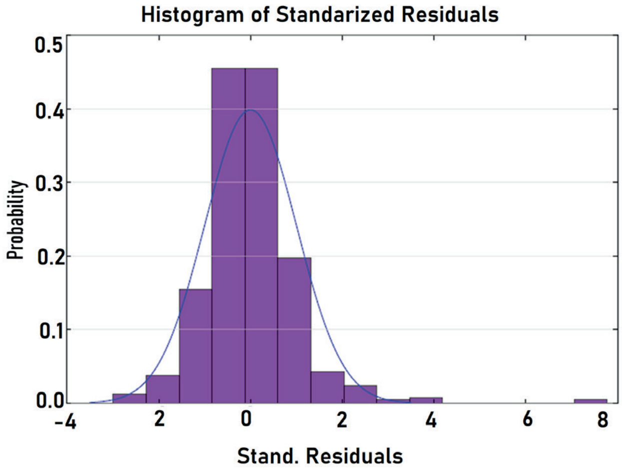

Fig. 4. Histogram of residuals

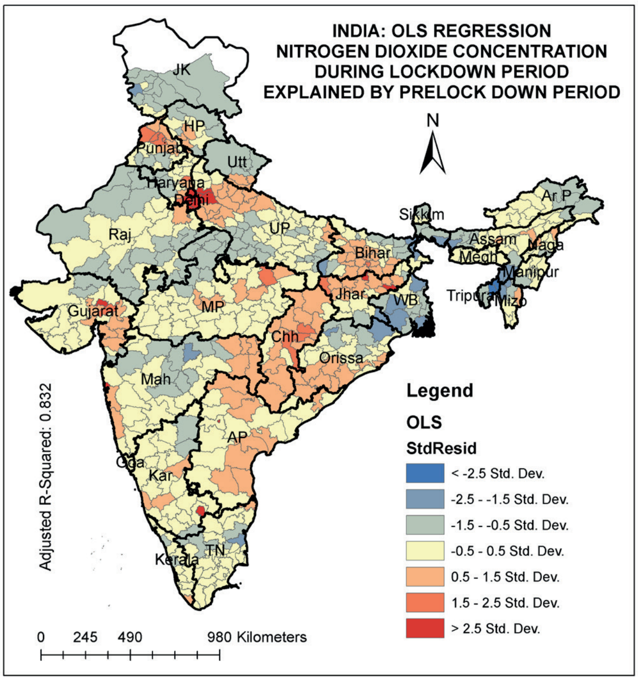

Fig. 5. NO_2 concentration during the lockdown in relation the pre-lockdown period

Table 4. Global Moran's I statistics

Moran's Index	0.158480
Expected Index	-0.001704
Variance	0.000044
z-score	24.115897
p-value	0.000000

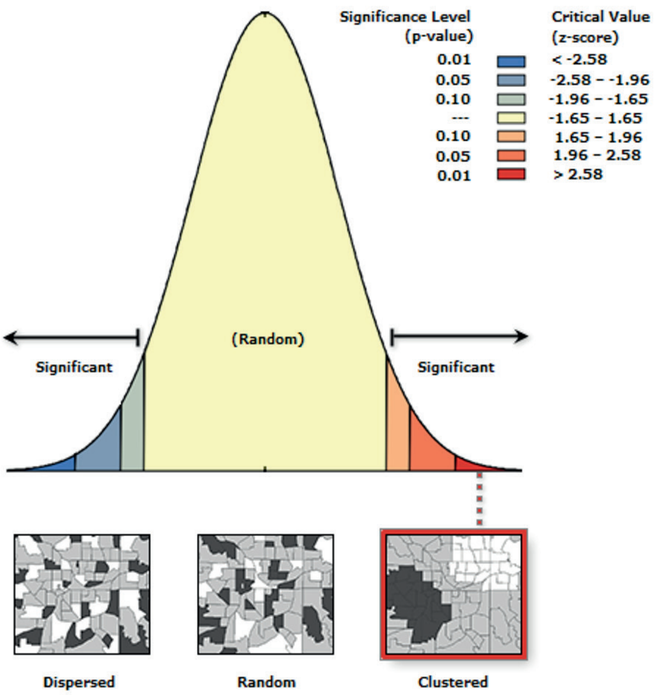

Fig. 6. Pattern of the NO_2 change in India at the district level

DISCUSSION

Describing air pollution due to COVID-19 has perhaps offered up hope of a practical way to reduce the effects of the virus, even if the change in outcomes is highly uncertain (Lewis 2020). The indirect impact of the virus on the environment has been little analysed. The first studies estimated a positive indirect impact on the environment (Zambrano-Monserrate et al. 2020). Satellite images have already revealed a dramatic reduction in concentrations of pollutant nitrogen dioxide in China and northern Italy, which coincided with lockdowns imposed to tackle the coronavirus pandemic (Gatenby 2020).

In highly populated areas the change in NO_2 was higher than predicted while in some areas this change was lower than predicted. Underpredicted areas, such as West Bengal, Northern Orissa, Maharashtra and Tamil Nadu, India, are known for the presence of heavy industries and thermal power stations. Heavy industries and thermal power stations were functioning during the lockdown period so the change there was lower than predicted. Misra et al. (2021) also presented similar results. They found a sharp decline in NO_2 in urban areas at Phase 1 and a slow recovery in subsequent phases. During Phase 1 of the lockdown, overall densities decreased substantially with a large negative mean anomaly (– 33.7% ± 12.1%), going as low as – 76.8% over central urban Delhi. Apart from urban areas, negative anomalies were also found above power plants and industries suggesting reduced emissions compared to 2019, which, however, were not as high as in densely populated areas (Misra et al. 2021).

CONCLUSION

Nitrogen oxides (NO_2 and NO) are important trace gases in the Earth's atmosphere, present in both the troposphere and the stratosphere. They enter the atmosphere as a result of anthropogenic activities (notably fossil fuel combustion and biomass burning) and natural processes (wildfires, lightning, and microbiological processes in soils). In this paper GIS and remote sensing techniques were used to find the change in the concentration of NO_2 during the pre-lockdown and lockdown period in India at the district level. To estimate the spatial variation in the NO_2 decline during the lockdown (2020), the same period was used from the previous year (2019). It was found that NO_2 concentration has decreased significantly due to the lockdown amid the COVID-19 pandemic in India. There is a spatial variation in this change; NO_2 concentration has decreased more (around 30 to 40%) in larger urban agglomerations. The results indicate that NO_2 concentration in highly populated areas was reduced more than in mineral-based industrial regions, as well as in remote, forested, mountainous and plateau regions of India. This change may be temporary but governments must plan to sustain this lower level of NO_2 concentration. The initiatives and planning to restart human activities in the post-lockdown period especially in megacities may be a benefit for public health and environmental sustainability.

REFERENCES

Ali I. and Alharbi OML. (2020). COVID-19: Disease, management, treatment, and social impact. Science of the Total Environment, [online], 728, 138861. Avilable at: https://pubmed.ncbi.nlm.nih.gov/32344226/ [Acessed 14 May, 2020], DOI: 1016/j.scitotenv.2020.138861

ESA. (2020). Air pollution drops in India following lockdown. Website. [online] available at: https://www.esa.int/Applications/Observing_the_Earth/Copernicus/Sentinel-5P/Air_pollution_drops_in_India_following_lockdown [Accessed 22 Aug, 2021].

FAO GAUL: Global Administrative Unit Layers 2015, First-Level Administrative Units. (2015). Website: [online]. Available at: https://developers.google.com/earth-engine/datasets/catalog/FAO_GAUL_SIMPLIFIED_500m_2015_level1#description [Accessed 14 May, 2020].

Ogen Y. (2020). Assessing nitrogen dioxide (NO2) levels as a contributing factor to coronavirus (COVID-19) fatality. Science of The Total Environment, [online], 726, 138605. Avilable at: https://www.ncbi.nlm.nih.gov/pmc/articles/PMC7151460/pdf/main.pdf [Accessed 14, May 2021], DOI: 10.1016/j.scitotenv.2020.138605.

Paital B. Das K. and Parida S.K. (2020). Inter nation social lockdown versus medical care against COVID-19, a mild environmental insight with special reference to India. Science of the Total Environment, [online], 728. 138914. Avilable at: https://www.sciencedirect.com/science/article/abs/pii/S0048969720324311 [Acessed 14 May, 2020], DOI: 10.1016/j.scitotenv.2020.138914.

Renton A. (2020). Coronavirus live news and updates from around the world-CNN. Website. [online]. Available at: https://edition.cnn.com/world/live-news/coronavirus-pandemic-05-14-20-intl/index.html [Accessed 14 May, 2020].

Gatenby J. (2020). Pollution levels in UK cities drop as coronavirus impacts on daily life, new data reveals. Website. [online]. Available at: https://phys.org/news/2020-03-pollution-uk-cities-coronavirus-impacts.html [Accessed 14 May, 2020].

Guardian. (2019). India suffers most pollution-linked deaths in world, study finds. Website. [online]. Available at: https://www.theguardian.com/world/2019/dec/19/india-suffers-most-pollution-linked-deaths-in-world-study-finds [Accessed 18 Aug, 2021].

Gerretsen I. (2020). How air pollution exacerbates Covid-19. Website. [online]. Available at: https://www.bbc.com/future/article/20200427-how-air-pollution-exacerbates-covid-19 [Accessed 14 May, 2020].

Gettleman J. and Schultz K. (2020). Modi Orders 3-Week Total Lockdown for All 1.3 Billion Indians. Website. [online]. Available at: https://www.nytimes.com/2020/03/24/world/asia/india-coronavirus-lockdown.html [Accessed 22 Aug, 2021].

Gohd C. (2020). Air pollution levels will bounce back as COVID-19 restrictions loosen, scientists say. Website. [online]. Available at: https://www.space.com/air-pollution-increase-covid-19-coronavirus.html [Accessed 14 May Aug, 2020].

Islam Z., Ranganathan M., Bagyaraj M., Singh S.K., and Gautam S.K., (2021). Multi-decadal groundwater variability analysis using geostatistical method for groundwater sustainability. Environment, Development and Sustainability, 1-19, DOI: 10.1007/s10668-021-01563-1.

Naqvi H. and Kumar S. (2020). Lockdown does what decades of schemes couldn't: Clean Ganga. Website. [online] available at: https://www.hindustantimes.com/india-news/anxiety-more-time-to-study-for-40k-students-stranded-in-kota/story-LgCluBkrFEITG9qyX16IEI.html [Accessed 14 May, 2021].

Lewis A. (2020). What we do and don't know about the links between air pollution and coronavirus. Website. [online]. Available at: https://theconversation.com/what-we-do-and-dont-know-about-the-links-between-air-pollution-and-coronavirus-137746 [Accessed 14 May, 2021].

Majumdar R. (2020). The silver lining: air pollution dips amid the lockdown. Website. [online] available at: https://www.indiatoday.in/india-today-insight/story/the-silver-lining-air-pollution-dips-amid-the-lockdown-1671422-2020-04-26 [Accessed 14 May, 2020].

Misra P. Takigawa M. Khatri P. et al. (2021). Nitrogen oxides concentration and emission change detection during COVID-19 restrictions in North India. Scientific Report 11, 9800, DOI: 10.1038/s41598-021-87673-2.

Ray, R. L., Singh, V., Singh, S. K., Acharya, B. S., & He, Y. (2021). What is the impact of COVID-19 pandemic on global carbon emissions?. Science of The Total Environment, 151503. https://doi.org/10.1016/j.scitotenv.2021.151503

Sentinel-5P NRTI NO2: Near Real-Time Nitrogen Dioxide. (2018). Website. [online]. Available at: https://developers.google.com/earth-engine/datasets/catalog/COPERNICUS_S5P_NRTI_L3_NO2 [Accessed 14 May, 2020].

Staff S. X. (2020). Coronavirus and air pollution: Does nitrogen dioxide impact fatalities? Retrieved Website. [online]. Available at: https://phys.org/news/2020-04-coronavirus-air-pollution-nitrogen-dioxide.html [Accessed 14 May, 2020].

Dasgupta S. (2020). Coronavirus update: Covid cases jump above 78,000 in India. State-wise status. Website. [online]. Available at: https://www.livemint.com/news/india/coronavirus-update-covid-cases-jump-above-78-000-in-india-state-wise-status-11589424303373.html [Accessed 14 May, 2020].

US EPA, OAR. (2016). Basic Information about NO2 | US EPA. Website. [online] available at: https://www.epa.gov/no2-pollution/basic-information-about-no2#What%20is%20NO2 [Accessed 15 May, 2020].

Venter Z.S. Aunan K., Chowdhury S. and Lelieveld J. (2020). COVID-19 lockdowns cause global air pollution declines. Proceedings of the National Academy of Sciences, 117(32), 18984-18990, DOI: 10.1073/pnas.2006853117.

Ward A. (2020). India's coronavirus lockdown and looming crisis, explained. Website. [online]. Available at: https://www.vox.com/2020/3/24/21190868/coronavirus-india-modi-lockdown-kashmir [Accessed 14 May, 2020].

World Health Organization: WHO. (2020). Coronavirus. Website. [online] available at: https://www.who.int/health-topics/coronavirus#tab=tab_1 [Accessed 14 May, 2020].

World Bank. (2020). COVID-19 lockdown. World Bank Blogs. https://blogs.worldbank.org/endpovertyinsouthasia/india-air-quality-has-been-improving-despite-covid-19-lockdown [Accessed 22 Aug, 2021].

Zambrano-Monserrate M.A., Ruano M.A. and Sanchez-Alcalde L. (2020). Indirect effects of COVID-19 on the environment. Science of the Total Environment, 728, 138813. Avilable at [Acessed 14 May, 2020], DOI: 10.1016/j.scitotenv.2020.138813.

RESEARCH PAPER

INFLUENCE OF QUARANTINE MEASURES AGAINST THE NEW CORONAVIRUS INFECTION COVID-19 ON THE STATE OF BLACK SEA COASTAL WATERS

Mikael S. Arakelov[1*], Dmitry A. Lipilin[2, 3], Alina V. Dolgova-Shkhalakhova[1]
[1]Tuapse Branch of Russian State Hydrometeorological University, 4 Morskaya St., Tuapse, 352800, Russia
[2]Kuban State Agrarian University named after I.T. Trubilin, 13 Kalinina St., Krasnodar, 350044, Russia
[3]Kuban State University, 149 Stavropolskaya St., Krasnodar, 350040, Russia
***Corresponding author:** m.arakelov@rshu.ru
Received: July 31th, 2021 / Accepted: November 9th, 2021 / Published: December 31st, 2021
https://doi.org/10.24057/2071-9388-2021-089

ABSTRACT. The Black Sea is one of the main recreational facilities in Russia subject to a high annual anthropogenic stress. Anthropogenic activity led to high coastal sea waters pollution, eutrophy, and endangered the sea's self-purification capabilities. The total quarantine introduced on the Black Sea coast of the Krasnodar territory associated with the new coronavirus infection COVID-19 pandemic led to a decrease in anthropogenic pressure on coastal ecosystems and provided a unique opportunity to trace the dynamics of the most important hydrochemical indicators of coastal waters in the Tuapse district. The study aimed to characterize the impact of quarantine measures against the coronavirus on the state of coastal waters in the eastern part of the Russian Black Sea. For this, we identified and characterized the hydrochemical indicators and determined the effect of quarantine measures on their dynamics. The study used the standardized methods. The results obtained showed that a decrease in the recreational stress led to a proportional decrease in the pollutants supply to coastal sea waters; with the recreational stress resumption the concentrations of mobile pollutants tended to increase; a proportional relationship was established between biochemical oxygen demand (BOD_5) and the ammonium nitrogen (NH_{4+}) concentration; the nitrates' (NO_{3-}) concentration, in the seawater did not depend on the recreational stress degree. In particular, a proportional increase in NH_{4+} concentration and BOD_5 in seawater was detected: in the third quarter of 2019 the concentration of NH_{4+} and BOD_5 amounted to 3.0 mg/dm^3 and 8.5 mg/dm^3, and 3.8 mg/dm^3 and 7.5 mg/dm^3 in the fourth quarter, respectively; in the 2020 samples, a decrease in the NH_{4+} concentration to 0.8 mg/dm^3 in the third and to 1.2 mg/dm^3 in the fourth quarter led to a proportional decrease in BOD_5 4.5 mg/dm^3 and 3.9 mg/dm^3, respectively. Thus, it was shown that the quarantine measures were shown to have a positive effect on the processes of self-purification of coastal sea waters in recreational zones.

KEYWORDS: COVID-19, quarantine restrictions, sea waters' hydrochemical indicators, pollutants concentration, recreational areas, recreational stress, seawater's self-purification capabilities

CITATION: Mikael S. Arakelov, Dmitry A. Lipilin, Alina V. Dolgova-Shkhalakhova (2021). Influence Of Quarantine Measures Against The New Coronavirus Infection Covid-19 On The State Of Black Sea Coastal Waters. Geography, Environment, Sustainability, Vol.14, No 4, p. 199-204 https://doi.org/10.24057/2071-9388-2021-089

ACKNOWLEDGEMENTS: The authors are grateful to Yulia A. Titova, leading researcher in microbiological control laboratory at All-Russian Research Institute of Plant Protection (FSBSE VIZR), PhD in biology, for her invaluable editory assistance in research styling.

Conflict of interests: The authors reported no potential conflict of interest.

INTRODUCTION

Currently, entering biological and chemical polluting components, including their derivatives, into the general circulation of substances threatens the self-purification capabilities of many water areas. This is due to an increase in the technogenic and anthropogenic recreational stress on the coast, which significantly outstrips the rate of biodestructors increase and distribution (Volkova et al. 2016; Gura et al. 2020). The greatest damage to the Black Sea is caused by pollution of rivers flowing into it. These rivers contain sewage and rainwater, petroleum products, cement dust, and chemicals' residues used in construction (Gogoberidze 2010; Matishov et al. 2015; Aleynikova et al. 2019). Nitrogen and phosphorus compounds enter the river runoff from household and industrial sources with fertilizers and detergents (Kosyan and Krylenko 2014, 2019). The coastal recreational area is polluted by accidental petroleum products spills occurring in the open part of the water area (Temirov et al. 2019; Antipceva et al. 2019).

Constant monitoring of the Black Sea water area state in the coastal zone conducted at the stations of the Federal Service for Hydrometeorology and Monitoring of the Environment State (Rosgidromet) (Chasovnikov et al. 2019) makes it possible to reveal some hydrochemical markers' indicating the role of the state of seawater and its self-purification capabilities in starting these processes and their dynamics. The stations are located in coastal areas with a maximum anthropogenic stress. They collect and analyze operational information on the pollution sources in the sea area and river mouths and assess the dynamics of hydrochemical and other parameters both throughout the year and over a long period. The Rosgidromet stations monitor the entire Russian Federation Black Sea coastal area and the largest estuaries on the coast, where industrial and domestic wastewater flows and from where it spreads (Krylenko et al. 2010; Zavyalov et al. 2014; Kostyleva 2015). The main quality indicators of the Black Sea coastal waters include the content of phosphates, nitrates, silicon and iron compounds, ammonium nitrogen, dissolved mercury, petroleum products, and synthetic surfactants (Korshenko 2016; Sergin et al. 2018). Exceeding the maximum concentration limit (MCL) for the above products (established in accordance with the standards of the Interstate Council for Standardization, Metrology, and Certification (ISC) and International Standardization Organization(ISO)), along with changing oxygen concentration in the surface water, cause fluctuations in number of dissective organisms and their activity, intensity of the organic substances formation and decomposition processes and, as a consequence, a decrease in the seawater's self-purification capabilities (Mironov et al. 1975; Korshenko 2020).

A decrease in the technogenic and anthropogenic recreational stress should maintain the main MCL indicators for the Black Sea coastal part within acceptable limits and contribute to restoration and acceleration of the seawater's self-purification capabilities (Arakelov et al. 2019). The pandemic of the new coronavirus infection COVID-19, which began at the end of 2019, has become one of the most important factors on a planetary scale, which had an inhibitory effect on the numerous sectors of global economy. The infection forced the people in the whole world to change their way of life. Many countries closed their borders and enterprises, transport traffic dropped sharply, people were called on self-isolation in their homes. Such a change in people's way of life and entire states influenced all life spheres on our planet, changed the environment. Russia was no exception, including the Krasnodar territory, which closed its borders and recreational areas on the coast of the Black Sea on March 31, 2020. Since the Black Sea is one of the main recreational facilities in Russia, the pandemic and the associated restrictive measures had a particularly strong negative impact on the resort and recreational industry state in the region. But in natural and ecological terms, this decreased anthropogenic pressure on coastal ecosystems, in particular, on the Black Sea coastal water area (RuNews24.ru). The introduced total quarantine on the Black Sea coast of the Krasnodar territory lasting from April to July 15, 2020 provided a unique opportunity to trace the hydrochemical indicators dynamics of coastal waters in the Tuapse district.

The research aim was to characterize the impact of quarantine measures against the coronavirus infection on the state dynamics of coastal waters in the Russian Black Sea eastern part within the Krasnodar territory's coast (the case of coastal waters in the Tuapse district). For this, we determined the concentrations of the most important hydrochemical indicators and assessed the impact of quarantine measures on their dynamics.

MATERIALS AND METHODS

The work was performed in the analytical chemical laboratory for environmental monitoring at the Affiliated Branch of the Russian State Hydrometeorological University (RSHU). Analysis of seawater samples and hydrochemical surveys were conducted on a quarterly basis according to the Standards of the Interstate Council for Standardization, Metrology, and Certification (ISC) and International Organization for Standardization (ISO); state standards of the Russian Federation; Management Directives (MD) and Federal Environmental Regulations (FER) of the Russian Federation Ministry for Environment Protection and Natural Resources, Russian Federation State Committee for Environment Protection (Arakelov et al. 2018). Water samples were taken directly in the recreational coastal areas confined to river mouths in the study areas. Hydrochemical indicators did not exceed the maximum concentration limit (MCL) (Korshenko 2020). In 2020, the hydrochemical indicators analysis could be conducted in the Tuapse region only due to the quarantine restrictions – the other Black Sea coastal waters monitoring points did not function.

The indicators were analyzed according to ISO 31861–2012: Water. General requirements for sampling and included biological oxygen demand (BOD_5); contents of ammonium nitrogen (NH_{4+}), total iron (Fe_{3+}), suspended substances, nitrates (NO_{3-}), petroleum hydrocarbons, and synthetic surfactants (Akhsalba and Marandidi 2021).

In the work, we used the following methods: gravimetric method for determining suspended substances and total content impurities in water and gravimetric method for measuring their mass concentration (MD 52.24.468-2005), jar method for estimating biochemical oxygen demand (BOD_5) in waters (MD 52.24.420-2006) (Tserenova and Muzalevsky 2015), photometric method for measuring mass concentration of ammonium nitrogen (NH_{4+}) in sea waters (MD 52.10.772-2013) (Akhsalba and Ekba 2017), photometric method for measuring indophenol blue NO_{3-}, quantitative chemical analysis of waters (ER F 14.1:2.4-95), photometric method for measuring mass concentration of nitrate ions in natural and waste water with salicylic acid and mass concentration of total iron (Fe_{3+}) and 1.10-phenanthroline in waters (MD 52.24.358-2006), extraction-photometric method for measuring mass concentration of synthetic surfactants and anion synthetic surfactants in water (MD 52.24.368-2006), and method for detecting them (LEKI SS2107 spectrophotometer, Republic of Korea), quantitative chemical analysis of waters and fluorometric method for measuring mass concentration of petroleumproducts in natural, drinking, and waste waters (ER F 14.1:2:4.128-98), and fluorophotometric method for estimating petroleum hydrocarbons content (FLUORAT 02, LUMEX, Russia) (Akhsalba 2018).

RESULTS

Fig. 1–4 show the assessment of the correspondence of the hydrochemical indicators of the seawater quality to their MCL.

A decrease in the recreational press in the research period of 2020 led to a reduction in the intake of pollutants into coastal sea waters – for all the estimated indicators, the concentrations approached the MCL values. The content of the petroleum derivates, nitrates (NO_{3-}), and suspended solids indicated a decrease in concentrations to a level below the MCL (Fig. 1–4).

Quarantine restrictions imposed on July 15, 2020 and the recreational stress resumption on the coast increased the concentrations of the most mobile pollutants in seawater: petroleum derivates and ammonium nitrogen (NH_{4+}) (Fig. 1a, 2a).

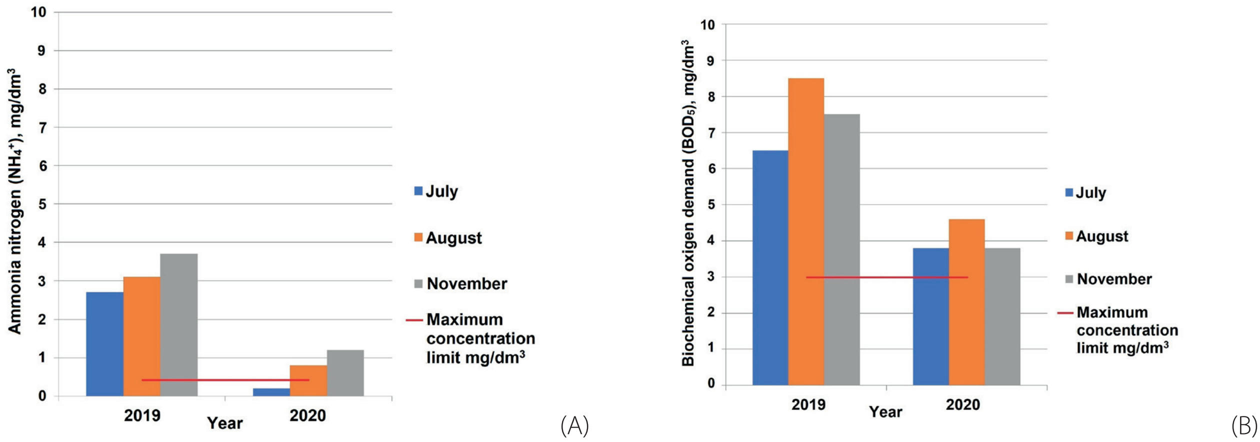

Fig. 1. Concentration dynamics of ammonium nitrogen (NH_{4+}) (a) and biochemical oxygen demand (BOD_5) (b) in seawater during periods of medium, minimum, and renewed recreational stress on the Black Sea coastal waters in the Tuapse district of the Krasnodar territory

We revealed a proportional increase in NH_{4+} concentration and BOD_5 in seawater: in the third quarter of 2019 the concentration of ammonia nitrogen and BOD_5 amounted to 3.0 mg/dm³ and 8.5 mg/dm³, and 3.8 mg/dm³ and 7.5 mg/dm3 in the fourth quarter, respectively; in the 2020 samples, a decrease in the NH_{4+} concentration to 0.8 mg/dm³ in the third and to 1.2 mg/dm³ in the fourth quarter led to a proportional decrease in BOD5 up to 4.5 mg/dm³ and 3.9 mg/dm³, respectively (Fig. 1).

The amount of petroleum derivates and suspended substances entering the seawater depended on the recreational stress onto the coast – imposition of quarantine measures coincided with a sharp decrease in the concentrations of the both indicators below the MCL: to 0.03 mg/dm³ in July 2020 for petroleum derivates and 4 mg/dm³ in August 2020 for suspended substances (Fig. 2).

A similar trend was noted in the total iron (Fe_{3+}) and synthetic surfactants concentrations' dynamics: with a decrease in the recreational stress on the coast due to imposing quarantine measures, the above substances concentrations decreased by 2–5 and 2–9 times, respectively (Fig. 3).

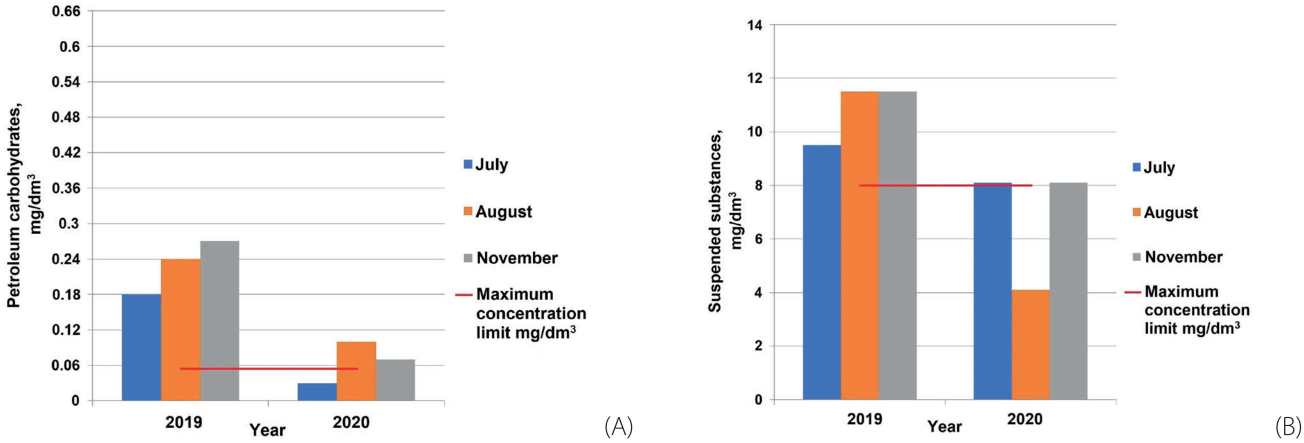

Fig. 2. Concentrations dynamics of petroleum products (a) and suspended solids (b) in seawater during periods of medium, minimum, and renewed recreational stress on the Black Sea coastal waters in the Tuapse district of the Krasnodar territory

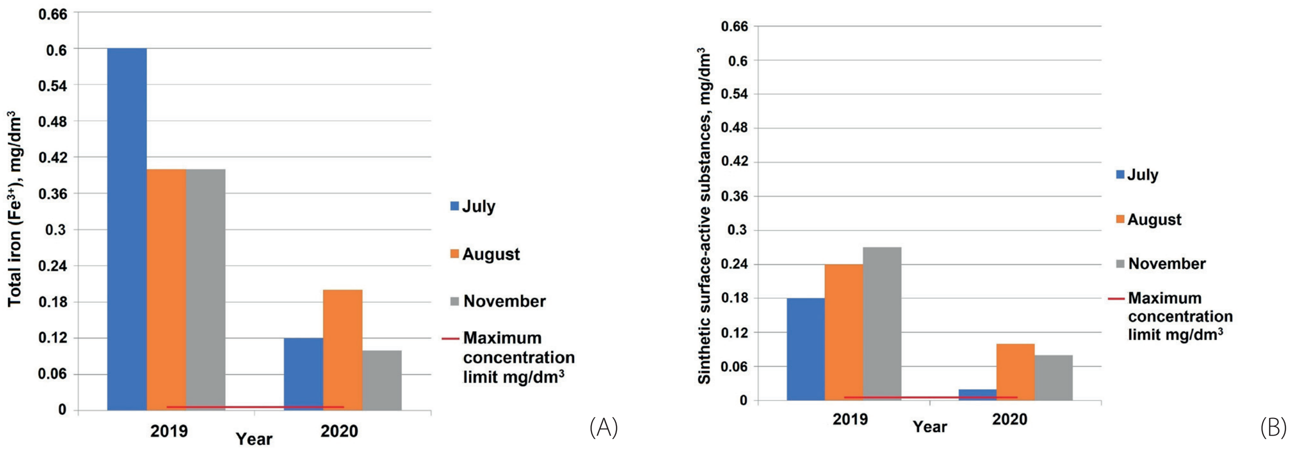

Fig. 3. Concentrations dynamics of total iron (Fe_{3+}) (a) and synthetic surfactants (b) in seawater during periods of medium, minimum, and renewed recreational stress on the Black Sea coastal waters in the Tuapse district of the Krasnodar territory

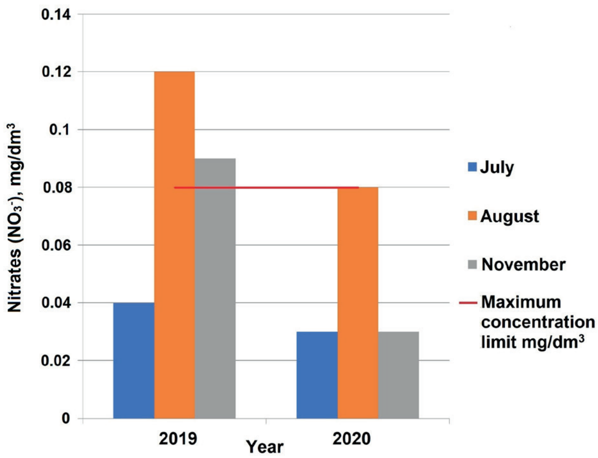

Fig. 4. Concentrations dynamics of nitrates (NO_{3-}) in seawater during periods of medium, minimum, and renewed recreational stress on the Black Sea coastal waters in the Tuapse district of the Krasnodar territory

In contrast to the abovementioned hydrochemical indicators, the quarantine measures did not have such a significant impact to the nitrates (NO_{3-}), although there is a tendency to decrease it (Fig. 4).

DISCUSSION

The seawater's self-purification capabilities is an important indicator of its state sustainability. Identifying the factors that determine such a state and its dynamics makes it possible to assess the Black Sea coastal water area self-purification capabilities (Ostroumova 2008; Baskakova et al. 2012). The hydrochemical indicators investigated during the periods of maximum, minimum, and renewed recreational stress of the Black Sea coastal waters in the Tuapse district of the Krasnodar territory revealed tendencies in the biodegradants development from eutrophy (BOD_5 = 3 MCL) to restoring seawater's self-purification capabilities (BOD_5 = MCL). Establishing a proportional relationship between biochemical oxygen demand (BOD_5) and the ammonium nitrogen (NH_{4+}) mobile forms concentration revealed the indicator function of these jointly considered parameters in assessing the possibilities of seawater's self-purification capabilities and the risks of developing its eutrophy (Dolgova-Shkhalakhova et al. 2020). We established a positive effect of quarantine measures on the sea coast state, since compared to the hydrochemical indicators of the most unfavourable 2019 year, the ecological state of the Black Sea coastal waters in the Tuapse region has improved (Gitsba and Ekba 2019; Dolgova-Shkhalakhova et al. 2020;). We established that the coastal recreational stress contributes to the seawater pollution with petroleum products. Despite the fact that the petroleum refineries in the Tuapse city worked at full capacity during periods of medium, maximum, minimum, and renewed recreational stress, imposition of the quarantine measures coincided with a sharp drop in the petroleum derivates concentration in the test samples. When the quarantine measures were cancelled, the petroleum derivates began to increase (Temirov et al. 2019; Arakelov et al. 2020).

CONCLUSIONS

Based on the results of the hydrochemical analysis conducted in 2020 and their comparison with the results of 2019, it was established that:

1. a decrease in the recreational stress led to a proportional decrease in the pollutants supply to coastal sea waters, which concentration reached the MCL level and below;
2. with the recreational stress resumption on the coast, the concentrations of the most mobile polluting components in seawater (petroleum derivates and ammonium nitrogen) tended to increase;
3. a proportional relationship has been established between biochemical oxygen demand (BOD_5) and the ammonium nitrogen (NH_{4+}) mobile forms concentration;
4. the amount of petroleum derivates and suspended solids entering the seawater is proportional to the recreational stress on the coast;
5. the nitrates' (NO_{3-}) concentration in seawater does not depend on the recreational stress on the coast.

REFERENCES

Akhsalba A.K. (2018). Chemical composition of atmospheric precipitation in Sukhum, Republic of Abkhazia, Bulletin of the Luhansk National University named after Vladimir Dal, 5 (11), 175-179 (in Russian with English summary).

Akhsalba A.K., Ekba Ya.A. (2017). Statistical analysis of the chemical composition of atmospheric precipitation in Sukhum, Republic of Abkhazia. Bulletin of the Krasnodar regional branch of the Russian Geographical Society, Krasnodar regional branch of the All-Russian public organization «Russian Geographical Society». Krasnodar: Platonov Igor, 54-59 (in Russian).

Akhsalba A.K., Marandidi S.I. (2021). Dynamics of carbon dioxide and oxygen content in the coastal waters of the Black Sea. Fundamental and applied aspects of geology, geophysics, and geoecology using modern information technologies, Proceedings of the VI International Scientific and Practical Conference, 31-38 (in Russian).

Aleynikova A.M., Lipka O.N., Krylenko M.V. (2019). Landscape structure of coastal cliffs of the Black Sea coast of the Caucasus, Bulletin of the Peoples' Friendship University of Russia. Series: Ecology and life safety, 27, 4, 298–306 (in Russian), DOI: 10.22363/2313-2310-2019-27-4-298-306.

Antipceva J., Volkova T., Lipilin D., Yarotskaya E. (2019). Tourist potential of specially protected areas of the Black Sea coast. 14th MEDCOAST Congress on Coastal and Marine Sciences, Engineering, Management, and Conservation, MEDCOAST 2019, 1, 233-240.

Arakelov M.S., Akhsalba A.K., Dolgova-Shkhalakhova A.V., Lipilin D.A., Yayli E.A. (2020). Hydrochemical indicators of waters in recreational zones of the Black Sea coast of Krasnodar territory and the Republic of Abkhazia, Advances in current natural sciences, 3, 50–56 (in Russian with English summary), DOI: 10.17513/use.37345.

Arakelov M.S., Akhsalba A.K., Gogoberidze G.G., Dolgova-Shkhalakhova A.V., Giba R.Yu., Yaili E.A. (2018). Analysis of geomorphological and geo-ecological condition and natural and anthropogenic risks reducing the resilience of coastal systems in the Eastern part of the Black Sea, Advances in current natural sciences, 12-2, 333-338 (in Russian with English summary).

Arakelov M.S., Dolgova-Shkhalakhova A.V., Merzakanov S.A., Akhsalba A.K. (2019). Assessing natural and anthropogenic risks of reducing the stability of coastal systems in the eastern part of the Black Sea in the context of recreational coastal management, Resorts. Service. Tourism, 1(42), 88-94 (in Russian with English summary).

Baskakova T.E., Aleksandrova Z.V., Belousova E.F., Dmitrienko V.M., Shevtsova E.A. (2012). Interannual and seasonal variability of hydrochemical indicators of the water in the north-eastern part of the Black Sea, The main problems of fisheries and the protection of fisheries reservoirs of the Azov-Black Sea basin. Collection of scientific papers (2010–2011), Rostov-on-Don: Azov Scientific Research Institute of Fisheries, 41-53 (in Russian with English summary).

Chasovnikov V.K., Zhu V.P., Chasovnikova L.A. (2019). Coastal-marine studies of the hydrochemical structure of waters in the monitoring section in the north-eastern part of the Black Sea, Modern problems of hydrometeorology and sustainable development of the Russian Federation, Collection of abstracts of the All-Russian scientific and practical conference, Saint Petersburg: RSHU, 428-429 (in Russian).

Dolgova-Shkhalakhova A.V., Arakelov M.S., Akhsalba A.K., Marandidi S.I. (2020). Hydrochemical indicators of the Black Sea waters in the Tuapse district from July to November 2020, Proc. of II Russian-Abkhaz Int. Res Pract. Seminar «the Black Sea coast: ecological guidelines in the present environmental trends – sustainable development in the future», Tuapse, 43-45 (in Russian).

Gitsba Ya.V., Ekba Ya.A. (2019). Hydrophysical processes in the Abkhaz Black Sea, Reports of Russian scientific and technical society of radio engineering, electronics, and communication named after A. S. Popov, Proceedings of the International Symposium. Ser. «Scientific International symposia. Engineering ecology», Moscow, 237-242 (in Russian with English summary).

Gogoberidze G.G. (2010). Methodology and methods for assessing the marine potential of coastal territories. Doctoral thesis in Economics. Moscow, 553 (in Russian).

Gura D.A., Gura A.Y., Volkova T.A., Lipilin DA (2020). Recreational space as a factor of sustainable development of coastal geosystems of the Krasnodar region. IOP Conference Series: Earth and Environmental Science, 579(1), 012007, DOI: 10.1088/1755-1315/579/1/012007.

Korshenko A.N. (2016). Quality of sea waters according to hydrochemical indicators. Annual 2015, Moscow: Nauka (in Russian).

Korshenko A.N. (2020). Quality of sea waters according to hydrochemical indicators. Annual 2019, Moscow: Nauka (in Russian).

Kostyleva A.V. (2015). Distribution of dissolved organic carbon in river mouth areas of the Greater Sochi region (north-eastern part of the Black Sea), Oceanology, 55, 2, 200-206 (in Russian), DOI: 10.7868/S0030157415020082.

Kosyan R.D., Krylenko M.V. (2019). Modern state and dynamics of the Sea of Azov coasts. Estuarine, Coastal and Shelf Science, 224, 314-323. DOI: 10.1016/j.ecss.2019.05.008.

Kosyan R.D., Krylenko V.V. (2014). Modern state of the marine accumulative coasts of the Krasnodar territory and the use of them. Moscow: Scientific world, 256 (in Russian).

Krylenko M.V., Isupova M.V., Dzaganiya E.V. (2010). Modern morpholithodynamics of estuarine seaside of the river Mzymta (Black Sea coast of Russia), Proceedings of the XXIII international coastal conference «the Doctrine of the development of sea shores: age-old traditions and ideas of modernity». Saint-Petersburg: RSHU, 222-224 (in Russian).

Matishov G.G., Stepanyan O.V., Grigorenko K.S., Kharkiv V.M., Povazhny V.V., Soyfer V.G. (2015). Features of the hydro-hydrochemical regime of the Azov and Black seas in 2013, Bulletin of the Southern Scientific Center of the Russian Academy of Sciences, 11, 2, 36-44 (in Russian with English summary).

Mironov O.G., Kiryukhina L.N., Kucherenko M.I., Tarkhova E.P. (1975). Self-cleaning in the coastal waters of the Black Sea, Kiev, 143 (in Russian).

Ostroumov S.A. (2008). Hydrobionts in the self-purification of waters and biogenic migration of elements. Moscow: MAKS Press, 197 (in Russian).

RuNews24.ru, (2020). Environmental impact of the COVID-19 pandemic, [online] The official site of the information agency «RuNews24.ru». Available at: https://runews24.ru/society/08/04/2020/71eb28sb6ad15457bfb5840e2779036a [Accessed July 25, 2021].

Sergin S.Ya., Tsai S.N., Magulyan A.O., Zemtsov R.V. (2018). Moderate and subtropical climate types of the Azov-black sea basin, Scientific notes of the Russian state Hydrometeorological University, 51, 58-62 (in Russian with English summary).

Temirov D.S., Ibragimov K.Kh., Konstantinidi Kh.A. (2019). Tourist and recreational sphere potential in the context of new goals of the state policy for the region socio-economic development. Krasnodar: Publishing House – South (in Russian).

Tserenova M.P., Muzalevsky A.A. (2015). Complex geo-ecological assessment of urbanized territory in the coastal zone. Ecological and economic aspects, Scientific notes of the Russian state Hydrometeorological University, 38, 189-200 (in Russian with English summary).

Volkova T.A., Filobok A.A., Belikov M.Yu., Pinchuk D.S., Kalustova I.S. (2016). Sustainable development and vulnerability of coastal geosystems of the Azov-Black Sea coast of the Krasnodar territory, Proc. of the VI Int. Res. and Pract. Conf. «Ecology and nature management: applied aspects», Ufa, 82-89 (in Russian with English summary).

Zavyalov P.O., Makkaveev P.N., Konovalov B.V., Osadchiev A.A., Khlebopashev P.V., Pelevin V.V., Grabovsky A.B., Izhitsky A.S., Goncharenko I.V., Soloviev D. M., Polukhin A. A. (2014). Hydrophysical and hydrochemical characteristics of marine waters near the mouths of small rivers of the Russian Black Sea coast, Oceanology, 54(3), 293 (in Russian), DOI: 10.1134/S0001437014030151.

ges.rgo.ru/jour/

ISSN 2542-1565 (Online)